Springer Proceedings in Physics 193

Ivan A. Parinov
Shun-Hsyung Chang
Muaffaq A. Jani *Editors*

Advanced Materials

Techniques, Physics, Mechanics and Applications

Springer

Springer Proceedings in Physics

Volume 193

The series Springer Proceedings in Physics, founded in 1984, is devoted to timely reports of state-of-the-art developments in physics and related sciences. Typically based on material presented at conferences, workshops and similar scientific meetings, volumes published in this series will constitute a comprehensive up-to-date source of reference on a field or subfield of relevance in contemporary physics. Proposals must include the following:

- name, place and date of the scientific meeting.
- a link to the committees (local organization, international advisors etc.)
- scientific description of the meeting
- list of invited/plenary speakers
- an estimate of the planned proceedings book parameters (number of pages/ articles, requested number of bulk copies, submission deadline).

More information about this series at http://www.springer.com/series/361

Ivan A. Parinov · Shun-Hsyung Chang
Muaffaq A. Jani
Editors

Advanced Materials

Techniques, Physics, Mechanics and Applications

Springer

Editors
Ivan A. Parinov
Institute of Mathematics, Mechanics
and Computer Sciences
Southern Federal University
Rostov-on-Don
Russia

Muaffaq A. Jani
Fakultas Teknik
University of 17 Agustus 1945 Surabaya
Surabaya
Indonesia

Shun-Hsyung Chang
Department of Microelectronics Engineering
National Kaohsiung Marine University
Kaohsiung
Taiwan

ISSN 0930-8989 ISSN 1867-4941 (electronic)
Springer Proceedings in Physics
ISBN 978-3-319-56061-8 ISBN 978-3-319-56062-5 (eBook)
DOI 10.1007/978-3-319-56062-5

Library of Congress Control Number: 2017936339

Printed on acid-free paper

This Springer imprint is published by Springer Nature
The registered company is Springer International Publishing AG
The registered company address is: Gewerbestrasse 11, 6330 Cham, Switzerland

Preface

Quickly developing theoretical, experimental and computational methods, directed to study and creation of numerous processing techniques, searching optimal compositions to process promising materials and composites are in the centre of modern Material Sciences and related areas of science and technology. Specific applications of materials and devices, manufactured on their base required quietly definite physical-mechanical and other structure-sensitive properties. Modern studies in this direction are found by very complex and fine fabrication techniques and constant searching of novel material compositions. A great attention is devoted to ecologically friendly material (for example, without lead ceramics). Industrial needs require devices and goods demonstrating very high accuracy, reliability, longevity and extended possibilities to operate under temperatures and pressures, changing into wide ranges. Characteristics of prepared devices are directly defined by the properties of materials and composites. Any movement in creation of optimal samples of materials and devices opens new possibilities in study of various physical processes and technologies.

This collection of 50 papers presents selected reports of the 2016 International Conference on "Physics, Mechanics of New Materials and Their Applications" (PHENMA-2016), which has taken place in Surabaya, Indonesia, during 19–22 July 2016 (http://phenma2016.math.sfedu.ru) The conference was sponsored the Ministry of Education and Science of the Russian Federation, South Scientific Center of the Russian Academy of Science, Russian Foundation for Basic Research, Ministry of Science and Technology of Taiwan, International Association of Certified Practicing Engineers (Indonesia), Ikatan Nasional Konsultan Indonesia, East Java Region (Indonesia), New Century Education Foundation (Taiwan), Ocean & Underwater Technology Association (Taiwan), Unity Opto Technology Co. (Taiwan), Fair Well Fishery Co. (Taiwan), Woen Jinn Harbor Engineering Co. (Taiwan), Lorom Group (Taiwan), Longwell Co. (Taiwan), Institute Technology of Bandung (Indonesia), Institute Technology of Sepuluh Nopember (Indonesia), University of 45, Surabaya (Indonesia), University of Islam Kadiri (Indonesia), Khon Kaen University (Thailand), Don State Technical University (Russia), South Russian Regional Centre for Preparation and Implementation of International Projects, Ltd.

The thematic of the PHENMA-2016 continued ideas of previous international symposia and conferences: PMNM-2012 (http://pmnm.math.rsu.ru), PHENMA-2013 (http://phenma.math.sfedu.ru), PHENMA-2014 (http://phenma2014.math.sfedu.ru), and PHENMA-2015 (http://phenma2015.math.sfedu.ru), whose results have been published in the following edited books "Physics and Mechanics of New Materials and Their Applications", Ivan A. Parinov, Shun Hsyung-Chang (Eds.), Nova Science Publishers, New York, 2013, 444, p. ISBN: 978-1-62618-535-7, "Advanced Materials – Physics, Mechanics and Applications", Springer Proceedings in Physics. Vol. 152. Shun-Hsyung Chang, Ivan A. Parinov, Vitaly Yu. Topolov (Eds.), Springer, Heidelberg, New York, Dordrecht, London, 2014, 380 p. ISBN: 978-3319037486, "Advanced Materials – Studies and Applications", Ivan A. Parinov, Shun-Hsyung Chang, Somnuk Theerakulpisut (Eds.), Nova Science Publishers, New York, 2015, 527 p. ISBN: 978-1-63463-749-7, and "Advanced Materials – Manufacturing, Physics, Mechanics and Applications", Springer Proceedings in Physics, Vol. 175, Ivan A. Parinov, Shun-Hsyung Chang, Vitaly Yu. Topolov (Eds.). Heidelberg, New York, Dordrecht, London: Springer Cham. 2016, 707 p. ISBN: 978-3319263229, respectively.

The presented papers are divided into four scientific directions: (i) processing techniques of advanced materials, (ii) physics of advanced materials, (iii) mechanics of advanced materials, and (iv) applications of advanced materials.

Into framework of the first theme are considered, in particular, the structural modification of sulfide minerals irradiated by high-power nanosecond pulses; the magnetic nanoparticles and heterogeneous persulfate oxidation of the nanoparticles and organic compounds. Then there are present the microstructure optimization of Pt/C catalysts for PEMFC; the synthesis of titanium dioxide, polyacrylonitrile-based materials, and also features of phase formation in bismuth ferrite. Moreover, this section contains investigations of growth of the strongly doped $LiNbO_3$: Zn single crystals and features of crystallization of sapphire melt. The first section is finished by considering the lignin degradation and production of slow release fertilizer from waste materials.

The second direction is opened by the numerical study of dielectric resonant gratings; the method of equilibrium density matrix in theory of superconductivity; new investigations of 1–3-type composites based on relaxor-ferroelectrics single crystals and ZTS-19/clay composite. Novel results are present at the modeling and characterization of advanced functional materials. In this section, in particular are studied diffusion of ferroelectric phase transition and glass-dipole state in the PZT-based solid solutions; the electromagnetic microwave radiation absorption by ferroelectric complex niobium oxides; the structural ordering in ceramic ferroelectromagnets. Special attention is devoted to physical properties of the graphene materials; morphology, atomic and electronic structure of metal oxide (CuO_x, SnO_x) nanocomposites and thin films; dispersion characteristics of zinc oxide nanorods organized in two-dimensional uniform arrays. Finally, new technical and technological solutions for measurement of displacements of the control object surfaces by laser interferometer and contactless method of temperature measurements are presented.

From viewpoint of mechanics, the models for nanosized magnetoelectric bodies with surface effects and general theory of polarization of the ferroelectric materials are presented. Moreover, there are studied the surface SH-waves in the weakly inhomogeneous pre-stressed piezoelectric structures; elastic waves in layered phononic crystals with strip-like cracks; ultrasonic guided waves in laminate fiber-reinforced composite plates; low-frequency elastic waves penetrating the triple periodic array of cracks and ultrasonic torsional guided waves in pipes with defects. Then why and how residual stress affects metal fatigue is discussed and also the mathematical modeling dynamics of prismatic body of two- and three-component materials and numerical study of three-dimensional anisotropic viscoelastic solids are presented. The third section is finished by investigations of the thermo-physical processes in boundary layers of metal-polymeric systems; the antifriction fillers influencing the characteristics of the metal polymer tribosystems and carbon brake discs with frictionally induced thermoelastic instability.

On the whole, the presented applications are devoted to lot of modern devices based on novel approaches. In particular, the developments of new metamaterials for advanced element base of micro- and nanoelectronics; the radiation detector with sensitive elements on the base of array of multi-walled carbon nanotubes and the magnetic field sensor with nanosized elements are discussed. Then the transducer designs for ultrasonic diagnostics and therapy, and also the electric power harvesting system based on the piezoelectric stack transducer and non-uniform polarization of multi-layered piezoelectric transducer are considered. Moreover, the multifrequency sonar equipment based on the self-action nonlinear effect is regarded. Finally, the singular nullor and mirror elements for circuit design; the usage of Markov chain model for wireless local area networks, and also the time-frequency features in the Berardius Baird whistles are discussed.

The book is addressed to students, postgraduate students, scientists and engineers, taking part in investigation of ferro-piezoelectrics, nano-structures and other advanced materials and composites. The book also covers many theoretical and experimental problems, connected with R&D of modern devices based on novel materials, which demonstrate wide applications in various scientific, technological and technical areas. The book includes new studies and results in the fields of Materials Science, Condensed Matter Physics, Physical and Mechanical Theory and Experiment, Processing Techniques and Engineering of Advanced Materials and Composites, Numerical Methods and numerous applications.

Rostov-on-Don, Russia — Ivan A. Parinov
Kaohsiung, Taiwan — Shun-Hsyung Chang
Surabaya, Indonesia — Muaffaq A. Jani

Contents

Contributors

Muslimin Abdulrahim Industrial Engineering Department, University of 17 Agustus 1945 Surabaya, Surabaya, Indonesia

A.G. Abubakarov Research Institute of Physics, Southern Federal University, Rostov-on-Don, Russia

Sergey M. Aizikovich Research and Educational Center "Materials", Don State Technical University, Rostov-on-Don, Russia; I.I. Vorovich Institute of Mathematics, Mechanics and Computer Science, Southern Federal University, Rostov-on-Don, Russia

Anastasia A. Alekseenko Southern Federal University, Rostov-on-Don, Russia

V.A. Aleshin Research Institute of Physics, Southern Federal University, Rostov-on-Don, Russia

Andrey A. Alexandrov Institute for Mathematics, Mechanics and Informatics, Kuban State University, Krasnodar, Russia

Abdulkarim A. Amirov Amirhanov Institute of Physics, Dagestan Scientific Center of the Russian Academy of Science, Makhachkala, Russia

E. Ananyeva Department of Physics, Southern Federal University, Rostov-on-Don, Russia

Nataliya E. Anashkina Institute of Comprehensive Exploitation of Mineral Resources of the Russian Academy of Science (IPKON RAS), Moscow, Russia

I.N. Andryushina Research Institute of Physics, Southern Federal University, Rostov-on-Don, Russia

A.G. Bakmaev Daghestan Scientific Center, H.I. Amirkhanov Institute of Physics, Russian Academy of Sciences, Makhachkala, Russia

Ekaterina M. Bayan Southern Federal University, Rostov-on-Don, Russia

Sergey V. Belenov Southern Federal University, Rostov-on-Don, Russia

Aleksandr A. Belov Research Institute for Mechanics, National Reasearch Lobachevsky State University of Nizhni Novgorod, Nizhny Novgorod, Russia

A.A. Bokov 4D LABS, Department of Chemistry, Simon Fraser University, Burnaby, BC, Canada

Nikita A. Boldyrev Research Institute of Physics, Southern Federal University, Rostov-on-Don, Russia

Igor Zh. Bunin Institute of Comprehensive Exploitation of Mineral Resources of the Russian Academy of Science (IPKON RAS), Moscow, Russia

A.A. Bush Moscow State Technical University of Radio Engineering, Electronics and Automation, Moscow, Russia

S. Chagovets Department of Physics, Southern Federal University, Rostov-on-Don, Russia

Chung-Chen Chang Department of Electrical Engineering, National Taiwan Ocean University, Keelung, Taiwan

Shun-Hsyung Chang Department of Microeletronic Engineering, National Kaohsiung Marine University, Kaohsiung, Taiwan

Valentine A. Chanturiya Institute of Comprehensive Exploitation of Mineral Resources of the Russian Academy of Science (IPKON RAS), Moscow, Russia

V.A. Chebanenko South Scientific Center of RAS, Rostov-on-Don, Russia; Vorovich Mathematics, Mechanics and Computer Science Institute, Southern Federal University, Rostov-on-Don, Russia

M.I. Chebakov Vorovich Institute of Mathematics, Mechanics and Computer Science, Southern Federal University, Rostov-on-Don, Russia

E. Chebanova Don State Technical University, Rostov-on-Don, Russia

A.I. Chechevatov Faculty of Physics, Southern Federal University, Rostov-on-Don, Russia

A-Li Chen Institute of Engineering Mechanics, Beijing Jiaotong University, Beijing, PR China

H. Chen University of Macau, Macau, China

T. Yu. Chernikova Department of Physics, Southern Federal University, Rostov-on-Don, Russia

A.V. Cherpakov Southern Federal University, Don State Technical University, Rostov-on-Don, Russia

Ksenia A. Chichay Laboratory of Novel Magnetic Materials, Immanuel Kant Baltic Federal University, Kaliningrad, Russia

C.-C. Chou National Taiwan University of Science and Technology, Taipei, Taiwan, China

Agus Darwanto Department of Informatics Engineering, Faculty of Engineering, University of 17 Agustus 1945 Semolowaru, Surabaya, Indonesia

Alexander V. Derkun I.I. Vorovich Institute of Mathematics, Mechanics and Computer Science, Southern Federal University, Rostov-on-Don, Russia

A. Dumitrescu Petroleum-Gas University of Ploiesti, Ploiesti, Romania

Le V. Duong Department of Mechanical Engineering, Le Quy Don Technical University, Hanoi, Vietnam

A.J. Emaimo Department of Physics, Southern Federal University, Rostov-on-Don, Russia

Artem Eremin Institute for Mathematics, Mechanics and Informatics, Kuban State University, Krasnodar, Russia

Evonda Department of Informatics Engineering, University 17 Agustus 1945 Surabaya, Surabaya, Indonesia

Aleksey G. Fedorenko Southern Scientific Center of Russian Academy of Sciences, Rostov-on-don, Russia

Sergey I. Fomenko Institute for Mathematics, Mechanics and Informatics, Kuban State University, Krasnodar, Russia

G.G. Gadjiev Daghestan Scientific Center, H.I. Amirkhanov Institute of Physics, Russian Academy of Sciences, Makhachkala, Russia

A.N. Gerasimenko Don State Technical University, Rostov-on-Don, Russia

E. Yu Gerasimenko Don State Technical University, Rostov-on-Don, Russia

R. Yu Gerasimenko Don State Technical University, Rostov-on-Don, Russia

Yu Ya Gerasimenko Don State Technical University, Rostov-on-Don, Russia

E.V. Glazunova Research Institute of Physics, Southern Federal University, Rostov-on-Don, Russia

Evgeny Glushkov Institute for Mathematics, Mechanics and Informatics, Kuban State University, Krasnodar, Russia

Natalia Glushkova Institute for Mathematics, Mechanics and Informatics, Kuban State University, Krasnodar, Russia

Mikhail V. Golub Institute for Mathematics, Mechanics and Informatics, Kuban State University, Krasnodar, Russia

Leonid V. Grigoryev ITMO University, Sant-Petersburg, Russia

Vladimir A. Gritskikh Lugansk Taras Shevchenko University, Lugansk, Ukraine

Roman U. Gruzdev I.I. Vorovich Institute of Mathematics, Mechanics and Computer Science, Southern Federal University, Rostov-on-Don, Russia

Vijay Kumar Gupta Design and Manufacturing, PDPM Indian Institute of Information Technology, Jabalpur, India

A.A. Gusev Institute of Solid State Chemistry and Mechanochemistry SB RAS, Novosibirsk, Russia

Vladimir E. Guterman Southern Federal University, Rostov-on-Don, Russia

Ahmad Habib Department of Informatics Engineering, Faculty of Engineering, University of 17 Agustus 1945 Semolowaru, Surabaya, Indonesia

Fajar Astuti Hermawati Department of Informatics Engineering, University 17 Agustus 1945 Surabaya, Surabaya, Indonesia

W.-L. Hong National Kaohsiung Marine University, Kaohsiung, Taiwan

Levan P. Ichkitidze National Research University "MIET", Zelenograd, Moscow, Russia

Leonid A. Igumnov Research Institute for Mechanics, National Reasearch Lobachevsky State University of Nizhni Novgorod, Nizhny Novgorod, Russia

Aleksandr A. Ipatov Research Institute for Mechanics, National Reasearch Lobachevsky State University of Nizhni Novgorod, Nizhny Novgorod, Russia

V.P. Isupov Institute of Solid State Chemistry and Mechanochemistry SB RAS, Novosibirsk, Russia

Y. Kabirov Department of Physics, Southern Federal University, Rostov-on-Don, Russia

E.M. Kaidashev Laboratory of Nanomaterials, Southern Federal University, Rostov-on-Don, Russia

Svetlana V. Kara-Murza Lugansk Taras Shevchenko University, Lugansk, Ukraine

Gevork Ya Karapetyan I.I. Vorovich Institute of Mathematics, Mechanics and Computer Science, Southern Federal University, Rostov-on-Don, Russia

I. Made Kastiawan Mechanical Engineering Department, University of 17 Agustus 1945 Surabaya, Kota Surabaya, Indonesia

S.V. Khasbulatov Research Institute of Physics, Southern Federal University, Rostov-on-Don, Russia

Evgenia V. Kirillova RheinMain University of Applied Sciences, Wiesbaden, Germany

A.B. Kleshenkov Faculty of Physics, Southern Federal University, Rostov-on-Don, Russia

A.G. Kochur Rostov State Transport University, Rostov-on-Don, Russia

N. Kofanova Department of Physics, Southern Federal University, Rostov-on-Don, Russia

Vladimir I. Kolesnikov Rostov State Transport University, Rostov-on-Don, Russia

Ekaterina V. Kolupaeva Southern Federal University, Rostov-on-Don, Russia

Georgy M. Konstantinov Research Institute of Physics, Southern Federal University, Rostov-on-Don, Russia

Elizaveta V. Koporulina Institute of Comprehensive Exploitation of Mineral Resources of the Russian Academy of Science (IPKON RAS), Moscow, Russia

Nataliya V. Korchikova Lugansk Taras Shevchenko University, Lugansk, Ukraine

Alexey T. Kozakov Scientific Research Institute of Physics, Southern Federal University, Rostov-on-Don, Russia

Tatyana V. Krasnyakova Lugansk Taras Shevchenko University, Lugansk, Ukraine; Institute of Physical Organic and Coal Chemistry, Donetsk, Ukraine

Leonid I. Krenev Research and Educational Center "Materials", Don State Technical University, Rostov-on-Don, Russia; I.I. Vorovich Institute of Mathematics, Mechanics and Computer Science, Southern Federal University, Rostov-on-Don, Russia

S.P. Kubrin Faculty of Physics, Research Institute of Physics, Southern Federal University, Rostov-on-Don, Russia

O.V. Kudryakov Don State Technical University, Rostov-on-Don, Russia

Yu. Kuprina Department of Physics, Southern Federal University, Rostov-on-Don, Russia

M.F. Kupriyanov Department of Physics, Southern Federal University, Rostov-on-Don, Russia

Erkki Lahderanta Lappeenranta University of Technology, Lappeenranta, Finland

Rolf Lammering Institute of Mechanics, Helmut-Schmidt-University/University of the Federal Armed Forces, Hamburg, Germany

Shi-Chun Lee Department of Electrical Engineering, National Taiwan Ocean University, Keelung, Taiwan

A.M. Lerer Faculty of Physics, Southern Federal University, Rostov-on-Don, Russia

Chin-Feng Lin Department of Electrical Engineering, National Taiwan Ocean University, Keelung, Taiwan

Timofey G. Lupeiko Southern Federal University, Rostov-on-Don, Russia

Aleksandr K. Lyubimov Research Institute for Mechanics, National Research Lobachevsky State University of Nizhni Novgorod, Nizhny Novgorod, Russia

Asfiah Mahdiani Department of Informatics, University of 17 Agustus 1945 Surabaya, Surabaya, Indonesia

M.A. Malitskaya Research Institute of Physics and Physics Department, Southern Federal University, Rostov-on-Don, Russia

M.B. Manuilov Faculty of Physics, Southern Federal University, Rostov-on-Don, Russia

Ivan P. Markov Research Institute for Mechanics, National Research Lobachevsky State University of Nizhni Novgorod, Nizhny Novgorod, Russia

Mark A. Mazurov ITMO University, Sant-Petersburg, Russia

Olga Miakisheva Institute for Mathematics, Mechanics and Informatics, Kuban State University, Krasnodar, Russia

Yuri F. Migal Rostov State Transport University, Rostov-on-Don, Russia

T.A. Minasyan Research Institute of Physics and Physics Department, Southern Federal University, Rostov-on-Don, Russia

I.P. Miroshnichenko Don State Technical University, Rostov-on-Don, Russia

Y.S. Miroshnichenko Institute of Nanotechnologies, Electronics and Equipment Engineering, Southern Federal University, Taganrog, Russia

I.S. Morozkin Rostov State Transport University, Rostov-on-Don, Russia

Muhyin Department of Mechanical Engineering, University of 17 Agustus 1945 Surabaya, Surabaya, Indonesia

T.N. Myasoyedova Institute of Nanotechnologies, Electronics and Equipment Engineering, Southern Federal University, Taganrog, Russia

A.V. Nagaenko Scientific Design and Technology Bureau “Piezopribor”, Southern Federal University, Rostov-on-Don, Russia

Andrey V. Nasedkin I.I. Vorovich Institute of Mathematics, Mechanics and Computer Science, Southern Federal University, Rostov-on-Don, Russia

Anna A. Nasedkina I.I. Vorovich Institute of Mathematics, Mechanics and Computer Science, Southern Federal University, Rostov-on-Don, Russia

R.D. Nedin Vorovich Institute of Mathematics, Mechanics and Computer Science, Southern Federal University, Rostov-on-Don, Russia

Vechaslav G. Nefedov Sant-Petersburg State University of Aerospase Instrumentation, Sant-Peterburg, Russia

Yuri M. Nikolaenko Donetsk Institute for Physics and Engineering Named After A.A. Galkin, Donetsk, Ukraine

A.V. Nikolskii Scientific Research Institute of Physics, Southern Federal University, Rostov-on-Don, Russia

Ivan N. Novomlinskiy Southern Federal University, Rostov-on-Don, Russia

Pavel A. Oganesyan Vorovich Institute of Mathematics, Mechanics and Computer Science, Southern Federal University, Rostov-on-Don, Russia

Z.M. Omarov Daghestan Scientific Center, H.I. Amirkhanov Institute of Physics, Russian Academy of Sciences, Makhachkala, Russia

Mikhail N. Palatnikov Kola Science Center, I.V. Tananaev Institute of Chemistry and Technology of Rare Elements and Mineral Raw Materials, Russian Academy of Sciences, Apatity, Murmansk Region, Russia

D. Pandey School of Materials Science & Technology, Institute of Technology, Banaras Hindu University, Varanasi, India

Ivan A. Panfilov Don State Technicla University, Rostov-on-Don, Russia

Guido Parchi Prometeon srl, Bologna, Italy

Ivan A. Parinov Vorovich Mathematics, Mechanics and Computer Sciences Institute, Southern Federal University, Rostov-on-Don, Russia

Lyubov I. Parinova Don State Technical University, Rostov-on-Don, Russia

A.A. Pavelko Research Institute of Physics, Southern Federal University, Rostov-on-Don, Russia

Anatoly V. Pavlenko Southern Scientific Center of the Russian Academy of Science, Rostov-on-Don, Russia

A.N. Pavlov Rostov State Technical University, Rostov-on-Don, Russia

Yu. V. Popov Institute of Earth Sciences, Southern Federal University, Rostov-on-Don, Russia

Vitaly V. Popuzin I.I. Vorovich Institute of Mathematics, Mechanics and Computer Science, Southern Federal University, Rostov-on-Don, Russia

Budi Prastio Mechanical Engineering Department, University of 17 Agustus 1945 Surabaya, Surabaya, Indonesia

Larisa E. Pustovaya Don State Technical University, Rostov-on-Don, Russia

S.I. Raevskaya Faculty of Physics, Research Institute of Physics, Southern Federal University, Rostov-on-Don, Russia

I.P. Raevski Faculty of Physics, Research Institute of Physics, Southern Federal University, Rostov-on-Don, Russia

Amirtham Rajagopal Indian Institute of Technology Hyderabad, Hyderabad, Telangana, India

J.A. Reyzenkind Research Institute of Physics, Southern Federal University, Rostov-on-Don, Russia

Larisa A. Reznichenko Research Institute of Physics, Southern Federal University, Rostov-on-Don, Russia

A.N. Reznitchenko Institute of Physics, Southern Federal University, Rostov-on-Don, Russia

Ahmad Ridho'i Department of Electrical Engineering, Universitas 17 Agustus 1945 of Surabaya, Surabaya, Indonesia

Valeria V. Rodionova Laboratory of Novel Magnetic Materials, Immanuel Kant Baltic Federal University, Kaliningrad, Russia

Elsen Ronando Department of Informatics Engineering, Faculty of Engineering, University of 17 Agustus 1945 Semolowaru, Surabaya, Indonesia

E.V. Rozhkov Vorovich Mathematics, Mechanics and Computer Science Institute, Southern Federal University, Rostov-on-Don, Russia

A.G. Rudskaya Department of Physics, Southern Federal University, Rostov-on-Don, Russia

Nikolay S. Runkevich I.I. Vorovich Institute of Mathematics, Mechanics and Computer Science, Southern Federal University, Rostov-on-Don, Russia

Maria V. Ryazantseva Institute of Comprehensive Exploitation of Mineral Resources of the Russian Academy of Science (IPKON RAS), Moscow, Russia

A.N. Rybyanets Institute of Physics, Southern Federal University, Rostov-on-Don, Russia

Evgeniy V. Sadyrin Research and Educational Center "Materials", Don State Technical University, Rostov-on-Don, Russia

D.A. Sarychev Faculty of Physics, Research Institute of Physics, Southern Federal University, Rostov-on-Don, Russia

Wolfgang Seemann Karlsruhe Institute of Technology, Karlsruhe, Germany

Sergei V. Selishchev National Research University "MIET", Zelenograd, Moscow, Russia

Harjo Seputro Mechanical Engineering Department, University of 17 Agustus 1945 Surabaya, Kota Surabaya, Indonesia

Vladimir P. Sergienko V.A. Biely Metal-Polymer Research Institute, National Academy of Sciences of Belarus, Gomel, Belarus

Oleg V. Shakin Sant-Petersburg State University of Aerospase Instrumentation, Sant-Peterburg, Russia

A. Shevchuk Department of Physics, Southern Federal University, Rostov-on-Don, Russia

Sergey N. Shevtsov South Scientific Center of Russian Academy of Sciences, Rostov-on-Don, Russia

Maria S. Shevtsova RheinMain University of Applied Sciences, Wiesbaden, Germany

Nikolai Yu Shichkin National Research University "MIET", Zelenograd, Moscow, Russia

Lidia A. Shilkina Research Institute of Physics, Southern Federal University, Rostov-on-Don, Russia

Evgenia I. Shprayzer Department of Theoretical and Applied Mechanics, Don State Technical University, Rostov-on-Don, Russia

I.A. Shvetsov Institute of Physics, Southern Federal University, Rostov-on-Don, Russia

N.A. Shvetsova Institute of Physics, Southern Federal University, Rostov-on-Don, Russia

Andrey V. Sidashov Rostov State Transport University, Rostov-on-Don, Russia

Nikolay V. Sidorov Kola Science Center, I.V. Tananaev Institute of Chemistry and Technology of Rare Elements and Mineral Raw Materials, Russian Academy of Sciences, Apatity, Murmansk Region, Russia

Evgeniy I. Sitalo Research Institute of Physics, Southern Federal University, Rostov-on-Don, Russia

A.S. Skaliukh Vorovich Institute of Mathematics, Mechanics and Computer Science, Southern Federal University, Rostov-on-Don, Russia

Slamet Department of Informatics Engineering, Faculty of Engineering, University of 17 Agustus 1945 Semolowaru, Surabaya, Indonesia

Boris V. Sobol Department of Information Technologies, Don State Technical University, Rostov-on-Don, Russia

Arkadiy N. Soloviev Department of Theoretical and Applied Mechanics, Don State Technical University, Rostov-on-Don, Russia; I.I. Vorovich Institute of Mathematics, Mechanics and Computer Science, Southern Federal University, Rostov-on-Don, Russia

V.V. Stashenko Faculty of Physics, Research Institute of Physics, Southern Federal University, Rostov-on-Don, Russia

Aman Subakti Department of Civil Engineering, Institut Teknologi Sepuluh Nopember, Surabaya, Indonesia

Sugiono Department of Informatics Engineering, University 17 Agustus 1945 Surabaya, Surabaya, Indonesia

Mezhlum A. Sumbatyan I.I. Vorovich Institute of Mathematics, Mechanics and Computer Science, Southern Federal University, Rostov-on-Don, Russia

A. Surahman Department of Physics, Southern Federal University, Rostov-on-Don, Russia; University of Lampung, Bandar-Lampung, Indonesia

Dmitri V. Telyshev National Research University "MIET", Zelenograd, Moscow, Russia

Natalya A. Teplyakova Kola Science Center, I.V. Tananaev Institute of Chemistry and Technology of Rare Elements and Mineral Raw Materials, Russian Academy of Sciences, Apatity, Murmansk Region, Russia

P. Teslenko Department of Physics, Southern Federal University, Rostov-on-Don, Russia

Alexandr A. Tikhii Lugansk Taras Shevchenko University, Lugansk, Ukraine; Donetsk Institute for Physics and Engineering Named After A.A. Galkin, Donetsk, Ukraine

P.E. Timoshenko Department of Physics, Southern Federal University, Rostov-on-Don, Russia; Laboratory of Nanomaterials, Southern Federal University, Rostov-on-Don, Russia

Roman A. Titov Kola Science Center, I.V. Tananaev Institute of Chemistry and Technology of Rare Elements and Mineral Raw Materials, Russian Academy of Sciences, Apatity, Murmansk Region, Russia

V.V. Titov Faculty of Physics, Research Institute of Physics, Southern Federal University, Rostov-on-Don, Russia

V.I. Torgashev Faculty of Physics, Southern Federal University, Rostov-on-Don, Russia

Retno Trimurtiningrum Department of Civil Engineering, Universitas 17 Agustus 1945, Surabaya, Indonesia

V.G. Trotsenko Faculty of Physics, Southern Federal University, Rostov-on-Don, Russia; Laboratory of Condensed Matter Physics, University of Picardy, Amiens, France

Anatoly V. Turik Research Institute of Physics, Southern Federal University, Rostov-on-Don, Russia

Gatut Priyo Utomo Mechanical Engineering Department, University of 17 Agustus 1945 Surabaya, Kota Surabaya, Indonesia

V.N. Varavka Don State Technical University, Rostov-on-Don, Russia

Pavel V. Vasiliev Department of Information Technologies, Don State Technical University, Rostov-on-Don, Russia

Aleksandr O. Vatulyan I.I. Vorovich Institute of Mathematics, Mechanics and Computer Science, Southern Federal University, Rostov-on-Don, Russia

Vadim A. Volochaev Southern Federal University, Rostov-on-Don, Russia

Yue-Sheng Wang Institute of Engineering Mechanics, Beijing Jiaotong University, Beijing, PR China

J.-K. Wu Department of Marine Engineering, National Kaohsiung Marine University, Kaohsiung, Taiwan

G.E. Yalovega Faculty of Physics, Southern Federal University, Rostov-on-Don, Russia

Alexander A. Yanichev Kola Science Center, I.V. Tananaev Institute of Chemistry and Technology of Rare Elements and Mineral Raw Materials, Russian Academy of Sciences, Apatity, Murmansk Region, Russia

M.-Y. Yeh Department of Microelectronics Engineering, National Kaohsiung Marine University, Kaohsiung, Taiwan

Yuriy I. Yurasov Research Institute of Physics, Southern Federal University, Rostov-on-Don, Russia; South Scientific Centre RAS, Rostov-on-Don, Russia

I. Yu. Zabiyaka Don State Technical University, Rostov-on-Don, Russia

Yu N. Zakharov Physics Research Institute, Southern Federal University, Rostov-on-Don, Russia

G. Zecheru Petroleum-Gas University of Ploieşti, Ploieşti, Romania

Chuanzeng Zhang Chair of Structural Mechanics, Department of Civil Engineering, University of Siegen, Siegen, Germany

Igor V. Zhikharev Donetsk Institute for Physics and Engineering Named After A. A. Galkin, Donetsk, Ukraine

Vladimir M. Zotov I.I. Vorovich Institute of Mathematics, Mechanics and Computer Science, Southern Federal University, Rostov-on-Don, Russia

Tatiana I. Zubar A.V. Luikov Heat and Mass Transfer Institute, National Academy of Sciences of Belarus, Minsk, Belarus

Part I
Processing Techniques of Advanced Materials

Chapter 1
Cu@Pt/C Catalysts: Synthesis, Structure, Activity in Oxygen Reduction Reaction

Anastasia A. Alekseenko, Sergey V. Belenov, Vadim A. Volochaev, Ivan N. Novomlinskiy and Vladimir E. Guterman

Abstract Nanostructured Cu@Pt_x/C catalysts with low platinum content (x = 0.8), comprising nanoparticles of core-shell architecture, were obtained by method of synthesis, which combines galvanic substitution of Cu at Pt and chemical reduction of Pt(IV). The obtained catalysts show high values of the electrochemically active surface area of platinum 80–100 m^2/g (Pt) and higher both activity in the oxygen electroreduction reaction (ORR) and stability compared with commercial Pt/C catalyst HiSPEC 3000 (Johnson Matthey).

1.1 Introduction

An actual problem of modern electrochemical power engineering is a preparation of electrocatalysts for low temperature fuel cells, which have desired characteristics for modern technologies [1, 2]. Looking for the ways to optimize of well-known synthesis methods is one of the most promising directions in the field of preparation and study of these materials [2, 3]. It is important reduce a cost of platinum catalysts, for example, by optimizing their composition, by enhancement of activity and stability, and by reducing the total cost of production.

The composition, size, shape and fine structure (architecture) of Pt and Pt-alloys nanoparticles (NPs) are the most important parameters, which affect the basic characteristics of catalysts [4–7]. Preparation of Pt-based electrocatalysts, containing bimetallic NPs with core-shell structure is primarily seen as a good possibility to reduce the loading of expensive platinum in the final material [3, 6]. At the same time, there is a positive influence (promoting effects) of metal core on the catalytic activity of platinum shell in some reactions [3, 6, 8]. As a rule, this effect is often observed in the case of a small thickness of the platinum shell [6, 8].

A.A. Alekseenko (✉) · S.V. Belenov · V.A. Volochaev · I.N. Novomlinskiy · V.E. Guterman
Southern Federal University, Zorge St. 7, 344090 Rostov-on-Don, Russia
e-mail: an-an-alekseenko@yandex.ru

I.A. Parinov et al. (eds.), *Advanced Materials*, Springer Proceedings in Physics 193, DOI 10.1007/978-3-319-56062-5_1

There are various ways of obtaining the electrocatalysts based on core-shell nanoparticles architecture by chemical reduction of precursors. In [6, 9, 10], the authors used a consistent chemical reduction of Pt(IV) on the pre-formed nuclei of *d*-metal (Cu, Ni, Ag, Pd, Co). By using these methods, bimetallic nanoparticles with thick (multilayer) Pt-shell are usually formed [6, 9]. In these NPs would be difficult to expect the promoting effect of the core on the catalytic activity of Pt-shell, and the mass fraction of precious metal in the catalyst is sufficiently high. In addition, the implementation of chemical reduction has difficulties to control the nanoparticles growth process and as usual rather thick Pt-shell is formed [6, 9, 10].

In order to produce NPs with core-shell structure the authors suggest the galvanic replacement method, it has been mentioned in a number of publications [11–17]. When non-noble metal nanoparticles M_1 (M_1 = Cu, Ag, Au, Pd, Ni, Co) are contacting with noble metal ions (M_2^{z+}), the reaction occurs [11–13, 16–18]:

$$M_1 + (n/z)M_2^{z+} \rightarrow M_1^{n+} + (n/z)M_2^0. \tag{1.1}$$

The reaction takes place for the following condition: E_p (M_2^{z+}/M_2) $\gg$ E_p (M_1^{n+}/M_1), where E_p is the equilibrium potential of the corresponding metal ion [11, 18]. During the electrochemical replacement process, Pt-atoms partially replace atoms M_1. By this mechanism 2D [12, 13, 17–19], and 3D-structure [5, 14, 17, 18] may be formed, in time it leads to the formation of a thin Pt-shell (up to a monolayer) on the surface of the *d*-metals. Core-shell nanoparticles with thin Pt layer, are obtained via this method, are often characterized by high activity [5, 13, 17], but the possibility of their long-term functioning as electrocatalyst is questionable due to the low Pt-layer thickness and consequently a low protecting ability of the shell to the metal core. In the most known studies, whose authors describe galvanic replacement method, the replacement of core atoms on platinum atoms is carried out in the sub-micron layers of *d*-metals, the size of these particles is large [11, 15–19]. In addition, a large number of studies [14, 16, 18, 19] describe the synthesis is carried out in an organic medium with stabilizers and without carbon support. Therefore, it is not quite clear what sorts of characteristics will show materials with nanoparticles deposited on the surface of the carbon support.

It should be noted that one of the possible method of improving the characteristics of M@Pt/C catalysts could be a thermo-treatment [20–23]. Evidently, the selected temperature conditions play an important role during this post-treatment [21–23].

In general, the questions about how to obtain the Pt-M nanoparticles with non-uniform distribution of components, suitable for the creation of high-level and relatively stable electrocatalysts, the optimal thickness of the Pt-shell and its control methods of thickness are still relevant.

In the present study, we investigated the possibility of using the combined method of synthesis: the combination of galvanic replacement (GR) of copper on platinum and chemical reduction Pt(IV) to Pt(0) in order to obtain bimetallic NPs with the structure including Cu-core and Pt-shell. In the development of synthesis methods, we proceeded from the assumption that at the first stage (GR) on surface of copper nuclei is formed thin (possibly defective) platinum shell. Pre-deposition

of calculated amount of platinum on the second stage—chemical reduction (ChR) should result in healing of the defects and the formation of a dense shell. Moreover, as noted in the literature review, conducting thermal post-treatment for the synthesized material could lead to higher crystallinity, reduced defectiveness, and consequently enhance the protective ability of Pt-shell relative to the core nanoparticle.

1.2 Experimental Part

Initially nanostructured Cu/C material, identified as A_1, was obtained by $CuSO_4$ reduction in carbon suspension (Vulcan XC72) by freshly prepared $NaBH_4$ solution. Mass loading of copper (12.5%) in the sample was determined by thermogravimetry. Formed copper nanoparticles were used as cores in further synthesis. The results of powder X-ray diffraction study show the presence of copper phase in combination with small amounts of copper (I) oxide (Fig. 1.1). The calculations according to Scherrer's equation confirmed the presence of the particles (crystallites) of copper with the average size of 10–11 nm.

At the next step, included the galvanic replacement, part of copper was replacing by platinum by adding a portion of $H_2PtCl_6 \cdot 6H_2O$ to Cu/C suspension in ethylene glycol solution:

$$2Cu^0 + [PtCl_6]^{2-} = Pt + 2Cu^{2+} + 6Cl^-. \quad (1.2)$$

Then a second portion of $H_2PtCl_6 \cdot 6H_2O$ and the excess $NaBH_4$ solution (freshly prepared) were added to reduce Pt(IV) and Cu^{2+} ions, passed into the solution at the previous stage of the synthesis by the reaction (1.2). It is known that

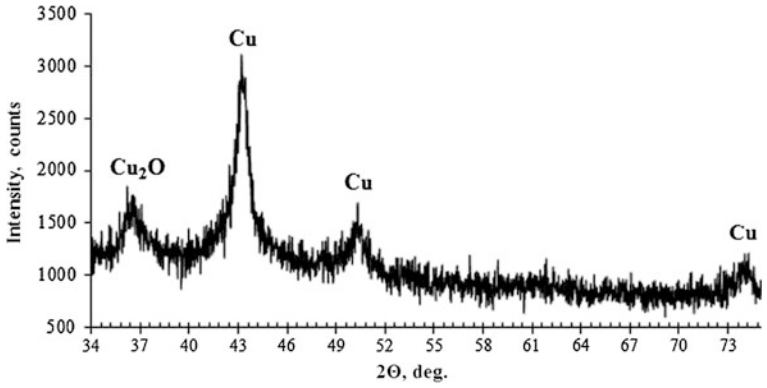

Fig. 1.1 The XRD-diffractogram of the synthesized Cu/C material (A_1)

during the reduction of Pt(IV) and Cu^{2+} by sodium borohydride can proceed the reactions (1.3)–(1.5) [24–26]. Side reaction in the decomposition of sodium borohydride is accompanied by evolution of hydrogen (see, reactions (1.6), (1.7)) can take place simultaneously [25].

$$8[PtCl_6]^{2-} + 5BH_4^- + 15H_2O = 8Pt^0 + 5H_3BO_3 + 35H^+ + 48Cl^- \quad (1.3)$$

$$[PtCl_6]^{2-} + BH_4^- + 2H_2O = Pt^0 + BO_{2^-} + 4H^+ + 6Cl^- + 2H_2 \quad (1.4)$$

$$Cu^{2+} + 2BH_4^- = Cu^0 + B_2H_6 + H_2 \quad (1.5)$$

$$BH_4^- + 2H_2O = BO_{2^-} + 4H_2 \quad (1.6)$$

$$BH_4^- + H_2O = B + OH^- + 2.5H_2 \quad (1.7)$$

The prepared powders of Cu@Pt/C electrocatalyst were separated by filtration of the suspension using a Buchner funnel, washed with acetone and water, and dried in a desiccator over P_2O_5 (sample A). Two portions of the resulting sample were chosen for the post-treatment procedure (one hour in an argon atmosphere) at the temperatures of 250 and 350 °C (samples are named as A_{250} and A_{350}). Additionally, Cu@Pt/C material was obtained by chemical reduction, as described in [9], and was used as a reference. In this case, the synthesis also was carried out using preformed copper nuclei (Cu/C). Solution of $NaBH_4$ was used as a reducing agent. The prepared Cu@Pt/C electrocatalyst powders were separated by filtration of the suspension using a Buchner funnel, washed with acetone and water, and dried in a desiccator over P_2O_5 (sample B).

Synthesis of the samples was repeated according to the described above methods at least three times, that allowed one to evaluate the reproducibility of characteristics for the obtained Cu@Pt/C materials.

The metal content was determined by TG method—the samples were calcined at 800 °C, the value of weight of the material after the calcination was used for calculations, taking in account the oxidation of metal copper to copper oxide (II). Electrochemical behavior of obtained catalysts was compared between the synthesized samples as well as the commercial electrocatalyst HiSPEC3000 (Johnson Matthey, 20% Pt), which was used for the comparison.

In order to determine the ratio of metals in the samples, X-ray fluorescence analysis was used on a Shimadzu EDX-800HS spectrometer at the following conditions: tube voltage—50 kV, current—15–25 mA, acquisition time—100 s. Processing of the X-ray fluorescence spectra was carried out using DXP-700E software (Version 1.00 Rel.017).

ARL X'TRA powder diffractometer with Bragg–Brentano geometry (θ-θ), CuKα—radiation ($\langle\lambda\rangle$ = 0.15418 nm) was used for powder X-ray data collection. Measurements were performed at room temperature. The samples were thoroughly mixed and placed into a cell on a depth of 1.5 mm or on a background-free substrate. Acquisition was carried out in a range of 15–55° with increments of 0.02°

and a rate from 4° to 0.5° per minute, depending on the task. The average size of crystallites was determined by Scherrer's equation for the most intensive peak (111) as described in [27]. Preliminary, the sizes of the crystallites, that are calculated via the FWHM of the (111) reflections for Cu@Pt/C materials are relative, because this peak may actually represent a superposition of the reflections of the two phases on the base of copper and platinum.

Transmission electron microscopy (TEM) analysis was performed using a JEM-2100 microscope operated at an accelerating voltage of 200 kV and resolution of 2 nm. Samples for TEM analysis were prepared by suspending the 0.5 mg catalyst powders in 1 ml of isopropanol. The suspension was ultrasonically dispersed, and one drop of the suspension was deposited onto a copper grid with carbon scattering.

Electrochemical measurements were performed at room temperature in a standard three-electrode cell. The electrolyte was 0.1 M $HClO_4$ solution saturated with Ar at atmospheric pressure. A saturated Ag/AgCl electrode was used as the reference electrode. All potentials cited here are referenced to the standard hydrogen electrode (SHE). The investigated catalyst was applied to the end of the rotating disk electrode in the catalyst's «ink» form, as described in [27].

One hundred cycles of potential sweep were initially recorded in the range from 0.03 to 1.2 V at a speed rate 200 mV/s. Then two CV cycles were registered in the same range of potentials, but upon a speed rate 20 mV/s. The electrochemically active surface area of Pt catalyst (ECSA) was determined by amount of electricity to be used for the electrochemical adsorption/desorption of atomic hydrogen during the registration of the second CV under 20 mV/s. The method of calculation is described in more detailed way in [29].

To evaluate the activity of catalysts in the oxygen reduction reaction (ORR), series of linear sweep voltammograms in a range from 0.020 to 1.2 V were measured (the scan rate 20 mV/s at speeds of disc electrode rotation 400, 900, 1600, 2500 rpm). To compare the activity of the tested catalysts, measured currents were normalized by the mass of platinum (A/g(Pt)).

To assess the stability of the electrocatalyst, a long-time (5000 cycles) voltammetric cycling method has been selected in the three-electrode cell with potential sweep in the range of 0.5–1.0 V with a scan rate of 100 mV/s. After every 500 cycles, two CVs were recorded to calculate ECSA (potential sweep rate of 20 mV/s, the potential range of 0.03–1.2). Stability was evaluated by the value of the degree of degradation (DD, %) by calculating $ECSA_{5000}/ECSA_0$ ratio.

1.3 Results and Discussion

The actual composition of obtained metal-carbon materials is close to the composition calculated by precursors loading: the mass fraction of metals—26–28% by weight, the content of Pt—15% by weight (Table 1.1). Thus, the composition of the metal component for each bimetallic material corresponds to the formula $Pt_{0.8}Cu$.

Table 1.1 Some characteristics of commercial catalyst HiSPEC 3000 and Cu@Pt/C materials prepared by the combined method (A, A250, A350) and chemical reduction (B)

Sample	Composition of metal component (XRF)	Metal loading (% wt)		Average size of crystallites, D (nm)	$ECSA_0$ (m^2/g (Pt))	Degree of degradation, DD (%)
		Estimated	Factual			
A	$Pt_{0.8}Cu$	28.2	28 ± 0.8	2.7 ± 0.2	100 ± 10	34
A_{250}				3.8 ± 0.3	89 ± 9	18
A_{350}				4.5 ± 0.4	80 ± 8	33
B	$Pt_{0.8}Cu$	30	26 ± 0.8	2.3 ± 0.2	55 ± 5	20
HiSPEC 3000	Pt	–	20	2.2 ± 0.2	81 ± 8	33

Powder X-ray diffractograms of the obtained materials have a typical for Pt/C and Pt-*M*/C catalysts shape [9, 12, 15]. Wide peaks on diffractograms of Cu@Pt/C samples confirm the presence of nano-sized ptatinum-contained particles (Fig. 1.2). Reducing the broadening of reflections for A_{250} and A_{350} samples (after the heat treatment) is due to the increase in the average crystallite size from 2.7 to 4.5 nm (Fig. 1.2, curves 2, 3; Table 1.1). The offset of platinum reflection (111) in the direction of larger values of 2Θ (the angle range 40–41°) is quite typical for the bimetallic catalysts, and it happens due to the influence of the alloying atoms (copper). Similar effects were observed in the case of formation of disordered solid solutions [12] and during the formation of NPs with Cu-core/Pt-shell architecture [9, 10]. Asymmetry of observed peaks in comparison with Pt/C reflections may be caused by inhomogeneity of phase's distribution (copper and platinum) in NPs. The appearance of small reflections in the area 2Θ nearly 36.2° for thermo-treated samples A_{250} and A_{350} (Fig. 1.2, curves 2 and 4) indicates the presence of copper (I) oxide phase. Apparently, a small amount of amorphous copper (I) oxide originally was contained in the sample A, and its heat treatment resulted to formation of crystal structure Cu_2O, visible for powder X-ray method. Even a little quantity of oxygen, contained in the pores of the carbon support, could oxidize the not protected by a continuous platinum shell copper, despite the fact that the heat treatment is conducted in an inert atmosphere.

Catalysts A and B were studied by transmission electron microscopy (TEM). It indicates the presence in their structure of NPs, which differ significantly in size and, possibly, in architecture. The initial copper cores in Cu/C material represent large NPs or their aggregates (Fig. 1.3a–c). So, it is not surprising that large NPs or aggregates of 10–12 nm size are presented in the TEM images of the sample A (Fig. 1.3d–f). We believe that such particles are formed, as a result, of platinum deposition during the synthesis on the surface of previously obtained copper particles. Calculation of interplanar distances, conducted by TEM results for the initial Cu/C material (Fig. 1.3b–c) indicated the presence of two phases—Cu and of Cu_2O. In this case, copper (I) oxide surrounds some copper NPs. It is not clear whether the formation of copper oxide (I) happens—directly during synthesis or later on: during filtering, washing, drying and storage of Cu/C samples. Apparently, during the

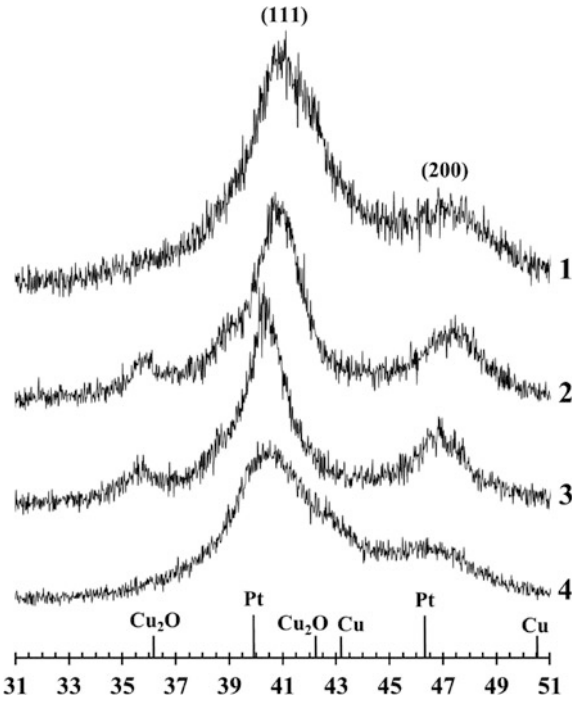

Fig. 1.2 XRD-diffractograms of *1*—A, *2*—A_{250}, *3*—A_{350}, *4*—B

subsequent formation of platinum shell, a significant portion of copper (I) oxide, previously dissolved in an acidic medium, was re-deposited as Cu^0 together with platinum. Platinum deposition process is accompanied by the destruction of large portion of copper nanoparticle aggregates. This conclusion can be made by comparing the particle size of Cu@Pt, formed during galvanic replacement, as previously observed in [11]. This fact may explain the smaller particle size after the formation of Pt-shell (Fig. 1.3d–f), compared with the size of initial copper nuclei (Fig. 1.3a–c). Significantly larger size of NPs in according with TEM results, compared with the size of the crystallites by XRD results (Table 1.1), could be caused by both a complex architecture of the NPs and by the presence of the amorphous transition layer on the interface boundary. In addition, individual bimetallic NPs can consist of a number of crystallites.

It is also possible to see large particles or nanoparticle's aggregates of 10–12 nm on TEM images for the sample B, which was prepared by chemical deposition of platinum on the Cu/C. Some NPs are in the size more than 10 nm and possess the expressed core-shell structure (Fig. 1.3g–i). Note that the presence of the contrast between the shell and core in the TEM images is not a precondition for confirmation of this architecture. Usually the contrast is characteristic of the large particles with thick shell [9, 15, 18]. A significant proportion of such Cu@Pt NPs is detected in the sample B. The TEM microphotographs of fragments of surface for

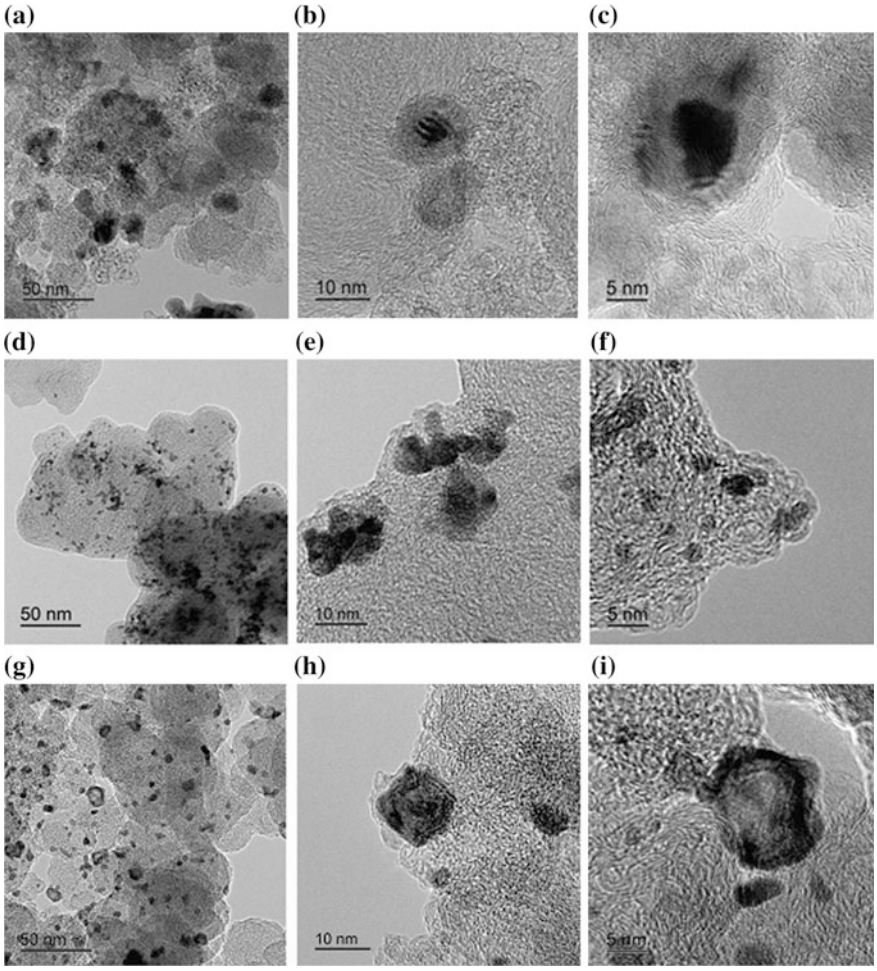

Fig. 1.3 Transmission electron microscopy photographs of the surface for Cu/C and Cu@Pt/C materials: **a–c** sample Cu/C—A_1 (core); **d–f** sample Cu@Pt/C—A (combined synthesis method); **g–i** sample Cu@Pt/C—B (chemical reduction method)

sample A (Fig. 1.3d–f) show NPs for which there is no contrast between the shell and the core. This does not exclude the possibility for them to have a relatively thin platinum shell [12].

In the microphotographs of A and B samples, 2–3 nm NPs can be seen (Fig. 1.3d–i). These NPs may represent a core-shell structure, or the one-phase particles. The latter could be formed by deposition of platinum (co-deposition of platinum and copper) on a carbon support during galvanic replacement step (by electrochemical mechanism, sample A), and at the stage of the chemical reduction (samples A and B). At the same time, it does not exclude the possibility of appearing small size NPs composed of a platinum or solid platinum-copper solution, in catalysts A and B.

A high copper content in the obtained samples A and B was confirmed by X-ray fluorescence analysis (Table 1.1). Moreover, during the pretreatment, Cu@Pt/C samples on the anodic branches CV copper dissolution peaks (Fig. 1.4a) were not recorded (Fig. 1.4b, c). This indicates the absence of direct contact of the electrolyte with copper NPs or copper cores, which poorly protected by the platinum shell.

Sample A demonstrates higher current values in the hydrogen area on CV compared with sample B (Fig. 1.5). Despite the relatively large size of the NPs (Table 1.1) $ECSA_0$-values of these catalysts were respectively 55 and 100 $m^2/g(Pt)$.

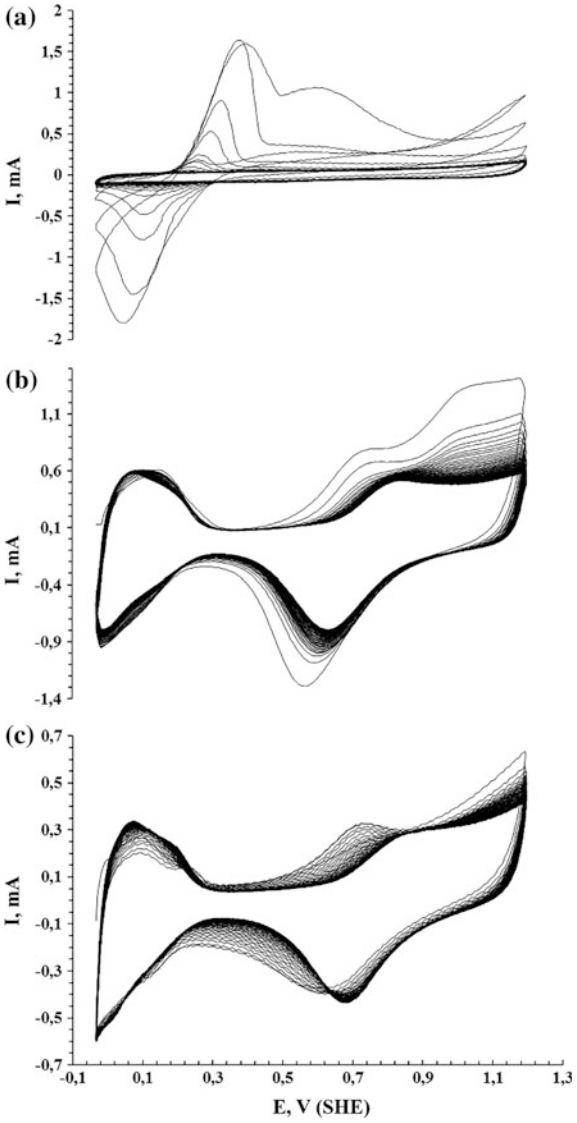

Fig. 1.4 The cyclic voltammograms at the stage of standardization: **a** sample Cu/C—A_1 (initial cores), **b** sample Cu@Pt/C—A (combined synthesis method), **c** sample Cu@Pt/C—B (chemical reduction method). De-aerated 0.1 $MHClO_4$, room temperature. Scan rate —200 mV/s

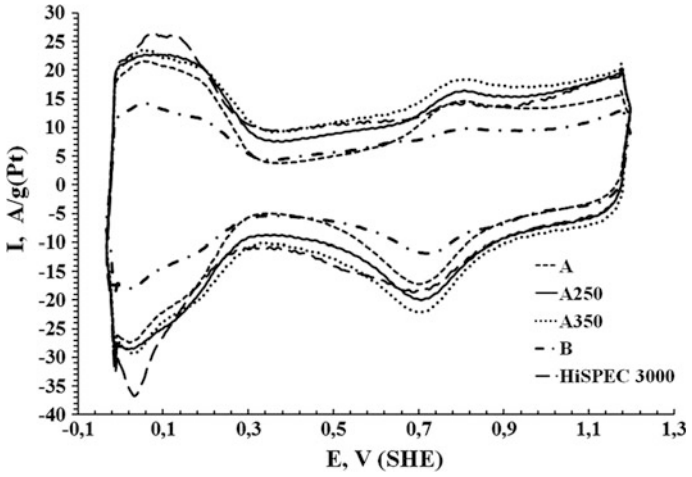

Fig. 1.5 CV curves of Cu@Pt/C and commercial Pt/C electrocatalysts. Ar-saturated 0.1 M $HClO_4$, room temperature, sweep rate: 20 mV/s

Note that so high value of $ECSA_0$ for materials with medium-sized NPs may be caused by the presence of a significant proportion of particles with the core-shell structure in these catalysts. The fact is that in the case of the material with core-shell structure of NPs, S is determined not so much by their size, but mostly by the thickness of the shell.

For the thermo-treated samples A_{250} and A_{350} was found a $ECSA_0$ reduction effect from 100 to 80 and 89 $m^2/g(Pt)$ respectively compared to the initial material A (Table 1.1). This effect may be associated with an increase in the average crystallite size (Fig. 1.5; Table 1.1), due to coalescence of the smallest of them with one another or with larger NPs. In addition, copper oxide formation (Fig. 1.2, curves 2 and 3) can result in lower value of S. The comparison of voltammograms for the samples A, A_{250} and A_{350} (Fig. 1.5) shows that the decrease of $ECSA_0$ for the thermo-treated samples does not lead to lower currents in the hydrogen CV area but increases the current in double-layer region. This effect may be associated with the changing composition of functional groups and the development of the carbon support surface [21]. However, even after the thermo-treatment, the values of S_0 for series A samples remain high enough—about the same as the commercial catalyst HiSPEC 3000, and significantly higher than S_0 for sample B.

Thermal post-treatment increases the mass activity of Cu@Pt/C electrocatalysts in ORR: for A_{250} and A_{350} samples ORR begins at higher potentials (Fig. 1.6). Current values in the diffusion-kinetic region of the polarization curve (0.7–0.9 V) are higher than values of current for catalysts A, HiSPEC 3000 and B (Fig. 1.6).

As a result of the stress test obtained Cu@Pt/C electrocatalysts showed high stability, not inferior to (A, A_{350}) or exceeding (B, A_{250}) stability of the commercial

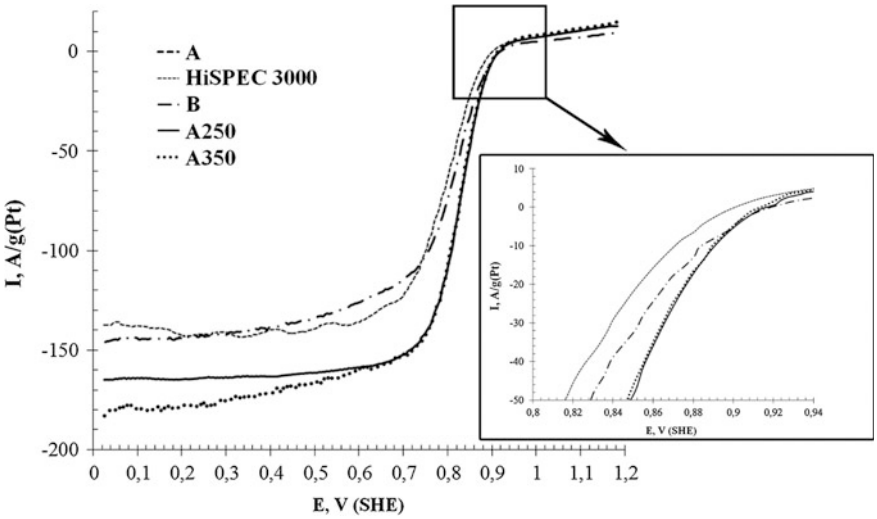

Fig. 1.6 LSV curves of Cu@Pt/C and commercial Pt/C electrocatalysts. O_2-saturated 0.1 M $HClO_4$, room temperature, sweep rate: 20 mV/s, rotation speed: 1600 rpm

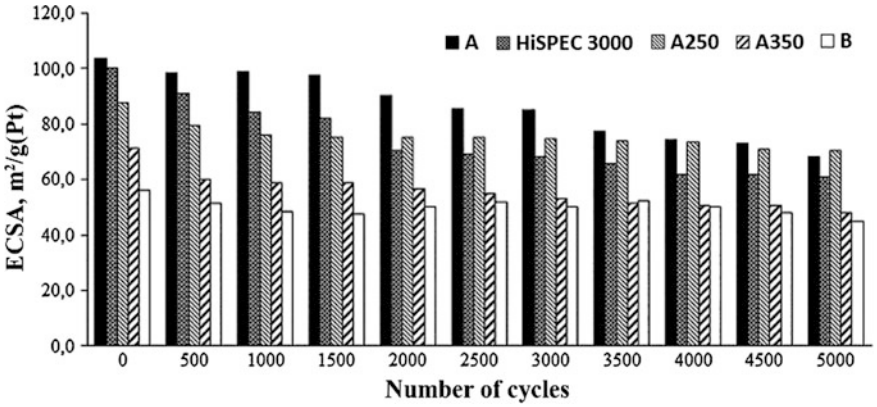

Fig. 1.7 Dependence of the ECSA on the number of cycles for Cu@Pt/C and commercial Pt/C samples

catalyst HiSPEC 3000 (Table 1.1). The absolute values of S and the nature of their changes over 5000 cycles (Fig. 1.7) are important along with the value of the degradation degree of the active surface of the catalyst after completion of the stress test (Table 1.1).

The highest values of ECSA in the process of testing retained sample A, which was obtained by the combined method—GR + ChR (Fig. 1.7). It is known that the stability of Pt/C electrocatalysts is the greater, the higher average size of the NPs,

bigger mass fraction of Pt in the catalyst and lower $ECSA_0$ value other conditions being equal [9, 29]. Sample B, characterized by the lowest value $ECSA_0$, and, unexpectedly, the sample A_{250}, which retained fairly high absolute values of ECSA in the testing process (Fig. 1.7), have been the most stable among studied materials. A similar effect of improving the behavior of the electrocatalyst after thermo-treatment, apparently associated with the ordering of the structure for the core-shell Co@Pt nanoparticles, was observed in [20, 21, 23]. A further increase of temperature during post-treatment of Cu@Pt/C catalyst to 350 °C led to reduction of its stability (samle A_{350}) (Table 1.1; Fig. 1.7). Therefore, thermo-treatment of Cu@Pt/C catalysts can lead to increased catalyst activity and stability, however, for each material is necessary to select the optimum treatment temperature and duration.

Thus, a sample A_{250}, obtained by the combined method and thermo-treated at 250 °C, has shown the best mass-activity and stability among studied materials. Combined synthesis methods of materials described in this study is perspective for obtaining high-active cathode catalysts for use in low temperature fuel cells.

1.4 Conclusions

$Cu@Pt_{0.8}/C$ electrocatalysts, containing NPs of core-shell structure and characterized by low (about 15 wt%) content of Pt, have been prepared by chemical reduction of Cu^{2+} and Pt(IV) (sample B), as well as by combining galvanic replacement of copper on platinum and chemical reduction of Pt(IV) (sample A). The electrochemically active surface area of the platinum in A electrocatalyst was about 100 $m^2/g(Pt)$. This is significantly higher than that in the commercial Pt/C electrocatalyst HiSPEC 3000 (81 $m^2/g(Pt)$).

Catalysts A_{250} and A_{350}, obtained by thermo-treatment of $Cu@Pt_{0.8}/C$ (sample A), showed improved ORR activity in comparison with HiSPEC 3000 and «as-prepared» $Cu@Pt_{0.8}/C$ materials (A and B). The increased stability during long cycling is a remarkable characteristic of A_{250} and B samples in comparison with other studied catalysts (HiSPEC 3000, A, A_{350}). Apparently, the thermo-treatment at 250 °C improves strength characteristics of the platinum shell, without leading to disruption of the complex architecture of bimetallic nanoparticles.

Optimization methods for the synthesis of electrocatalysts, containing Pt-M NPs with core-shell architecture, have a considerable interest. The combined synthesis method that includes galvanic replacement and chemical reduction is a promising tool for Cu@Pt/C catalysts development. This method is characterized by low content of Pt, high values of S_0, good activity in the ORR and corrosion-morphological stability.

The results of this research indicate that electrocatalysts containing bimetallic NPs with shell-core architecture are promising objects for testing in low-temperature hydrogen-air fuel cell.

Acknowledgements The studies of structural and electrochemical characteristics of Pt/C and Cu@Pt/C catalysts were carried out at financial support of Russian Foundation for Basic Research (grant No. 14-29-04041). Development of the combined method of synthesis of Cu@Pt/C catalysts was performed in the framework of Russian Foundation for Basic Research grant No. 16-38-80061.

References

1. A.B. Yaroslavtsev, Y.A. Dobrovolsky, N.S. Shaglaeva, L.A. Frolova, E.V. Gerasimova, E.A. Sanginov, Russ. Chem. Rev. **81**, 191 (2012)
2. D. Thompsett, Catalysts for the proton exchange membrane fuel cell, in *Handbook of Fuel Cells. Fundamentals, Technology and Applications*, vol. 3, p. 1 (2003)
3. H. Yang, Angew. Chem. Int. Ed. **50**, 2674 (2011)
4. Q. Lv, J. Chang, W. Xing, Ch. Liu, RSC Adv. **4**, 32997 (2014)
5. C. Xu, Y. Liu, J. Wang, H. Geng, H. Qiu, ACS Appl. Mater. Interfaces **3**, 4626 (2011)
6. M. Oezaslan, F. Hasche, P. Strasser, J. Phys. Chem. Lett. **4**, 3273 (2013)
7. L. Ou, Comput. Theor. Chem. **1047**, 69 (2014)
8. R.N. Singh, R. Awasthi, C.S. Sharma, Int. J. Electrochem. Sci. **9**, 5607 (2014)
9. V.E. Guterman, S.V. Belenov, A.Y. Pakharev, M. Min, N.Y. Tabachkova, E.B. Mikheykina, L.L. Vysochina, T.A. Lastovina, Int. J. Hydrogen Energy **41**, 1609 (2016)
10. H. Zhu, X. Li, F. Wang, Int. J. Hydrogen Energy **36**, 9151 (2011)
11. B.I. Podlovchenkoz, T.D. Gladysheva, A.Y. Filatov, L.V. Yashina, Russ. J. Electrochem. **46**, 1272 (2010)
12. J. Georgieva, E. Valova, I. Mintsouli, S. Sotiropoulos, S. Armyanov, A. Kakaroglou, A. Hubin, O. MiSteenhaut, J. Dille, J. Appl. Electrochem. **44**, 215 (2014)
13. A. Sarkar, A. Manthiram, J. Phys. Chem. C **114**, 4725 (2010)
14. M. Ji, Y. Zhang, J. Liu, J. Zhang, H. Zhu, Nano Res. **8**, 271 (2015)
15. M. Mohl, D. Dobo, A. Kukovecz, Z. Konya, K. Kordas, J. Wei, R. Vajtai, P.M. Ajayan, J. Phys. Chem. C **115**, 9403 (2011)
16. E. Sutter, K. Jungjohann, S. Bliznakov, A. Courty, E. Maisonhaute, S. Tenney, P. Sutter, Nat. Commun. **5**, 4946 (2014)
17. Z. Li, Ch. He, V. Cai, Sh Kang, P.K. Shen, Int. J. Hydrogen Energy **37**, 14152 (2012)
18. X. Xia, Y. Wang, A. Ruditskiy, Y. Xia, Adv. Mater. **25**, 6313 (2013)
19. M. Tsuji, M. Hamasaki, A. Yajima, M. Hattori, T. Tsuji, H. Kawazum, Mater. Lett. **121**, 113 (2014)
20. R. Lin, T. Zhao, M. Shang, J. Wang, W. Tang, V. Guterman, J. Ma, J. Power Sources **293**, 274 (2015)
21. C.W.B. Bezerra, L. Zhang, H. Liu, K. Lee, A.L.B. Marques, E.P. Marques, H. Wang, J. Zhang, J. Power Sources **173**, 891 (2007)
22. V.E. Guterman, S.V. Belenov, V.V. Krikov, L.L. Vysochina, W. Yohannes, N.Y. Tabachkova, E.N. Balakshina, J. Phys. Chem. C **118**, 23835 (2014)
23. A.N. Valisi, T. Maiyalagan, L. Khotseng, V. Linkov, S. Pasupathi, Electrocatalysis **3**, 108 (2012)
24. H.H. Ingelsten, R. Bagwe, A. Palmqvist, M. Skoglundh, Ch. Svanberg, K. Holmberg, D.O. Shah, J. Colloid Interface Sci. **241**, 104 (2001)
25. J. Qing-lai, P. Zhong-dong, X. Xiao-feng, D. Ke, H. Guo-rong, L. Ye-xiang, Trans. Nonferrous Met. Soc. China **21**, 127 (2011)

26. R.A. Soomro, S.T.H. Sherazi, N.M. Sirajuddin, M.R. Shah, N.H. Kalwar, K.R. Hallam, A. Shah, Adv. Mater. Lett. **4**, 191 (2014)
27. S.A. Kirakosyan, A.A. Alekseenko, V.E. Guterman, V.A. Volochaev, N.Y. Tabachkova, Nanotechnol. Russ. **11**, 287 (2016)
28. V.E. Guterman, A.Y. Pakharev, N.Y. Tabachkova, Appl. Catal. A **453**, 113 (2013)
29. V.E. Guterman, T.A. Lastovina, S.V. Belenov, N.Y. Tabachkova, V.G. Vlasenko, I.I. Khodos, E.N. Balakshina, J. Solid State Electrochem. **18**, 1307 (2014)

Chapter 2
Fluorine-Doped Titanium Dioxide: Synthesis, Structure, Morphology, Size and Photocatalytic Activity

Ekaterina M. Bayan, Timofey G. Lupeiko, Ekaterina V. Kolupaeva, Larisa E. Pustovaya and Aleksey G. Fedorenko

Abstract In this study, we analyzed the effect of fluoride ions on photocatalytic activity of titanium dioxide. Synthesized and calcined F-doped materials exhibit photocatalytic activity in the both UV and visible light range. The photocatalytic activity induced by UV exposure is higher than that of commercial material Degussa P25, which is pure titanium dioxide. Also the research on influence of fluoride ions on anatase-to-rutile phase transition was carried out by X-ray powder diffraction. The introduction of fluoride ions was found to increase the thermal stability of anatase modification of titanium dioxide.

2.1 Introduction

Recently, the issue concerning the purification of wastewater from organic pollutants have attracted much attention. The method based on photocatalytic degradation of organic substances is the most viable approach, since the reaction results in mineralization of organics to CO_2, H_2O and inorganic acids [1, 2]. Although various semiconductors can be used as photocatalysts [3], the most promising material is titanium dioxide (TiO_2) due to its high photocatalytic activity, photochemical and

E.M. Bayan (✉) · T.G. Lupeiko · E.V. Kolupaeva
Southern Federal University, 7, Zorge str., Rostov-on-Don 344090, Russia
e-mail: ekbayan@sfedu.ru

T.G. Lupeiko
e-mail: lupeiko@sfedu.ru

L.E. Pustovaya
Don State Technical University, 1, Gagarin Square, Rostov-on-Don 344090, Russia
e-mail: lapus1@yandex.ru

A.G. Fedorenko
Southern Scientific Center of Russian Academy of Sciences, 41 Chekhov Street, Rostov-on-don 344006, Russia

I.A. Parinov et al. (eds.), *Advanced Materials*, Springer Proceedings in Physics 193, DOI 10.1007/978-3-319-56062-5_2

thermal stability, low cost, nontoxicity, and biocompatibility [4–6]. To increase the efficiency of heterogeneous photocatalytic process, nanosized titanium dioxide with a large total surface area is applied. TiO_2 has three polymorphs: rutile, anatase and brookite [7]. Rutile is the most stable form of TiO_2, anatase and brookite convert to rutile upon heating above 600 °C. With a particle size of less than 14 nm, anatase is known to be more thermodynamically stable than rutile [8]. Anatase is considered the most photocatalytic active modification.

The application of TiO_2 as a photocatalyst is limited by its large band gap of 3.2 eV, due to which the activation of titanium dioxide requires UV radiation, thereby hindering the use of visible light [9]. To achieve the photocatalytic response of TiO_2 in the visible light range, the metal and nonmetal dopants are successfully employed [2, 9–11].

Nonmetals are used more often because it is believed that although metals decrease the band gap they are not always successfully introduced into the structure of titanium dioxide and the remaining metals on the surface of TiO_2 shelter photoreaction sites [12].

As for nonmetal dopants, the various ways to introduce nitrogen and subsequent characterization of resulting compounds are under intensive consideration [9, 13, 14]; the doping with sulfur, boron and halogens is also described in the literature [2, 9–11].

The introduction of fluorine is of interest, since the fluoride dopants increase the surface acidity and cause the formation of reduced ions Ti^{3+} due to the charge compensation between Ti^{4+} and F^-. Thus, the charge separation and enhancement of photoinduced processes can be achieved, whilst avoiding enlargement of band gap. The introduction of fluoride ions also enhances adsorptivity of molecules and increases the temperature of anatase-to-rutile phase transition [9]. The synthesized F-doped TiO_2 flower-like nanomaterials possess good crystallinity and exhibit high photoelectrochemical activity for water-splitting and photodegradation of organic pollutants compared with P-25, which is currently considered to be one of the best commercial TiO_2 photocatalysts [15]. The doping with fluoride ions increases thermostability, and the morphological features of F-doped titanium dioxide aggregates offer high photocatalytic activity of powders in a wide range of processing temperatures including 900–1000 °C. Additionally, the modified powders remain highly photocatalytically active being involved in cyclic photocatalytic process, while the activity of unmodified material drops from cycle to cycle [16].

In this paper, we report on soft chemistry synthesis of nanocrystalline powder based on titanium dioxide doped with fluoride ions and discuss its properties, including photocatalytic activity in the visible light range.

2.2 Experimental Methods

2.2.1 Materials

All reagents used were commercially obtained and used without any further purification. All solutions were prepared using deionized water.

2.2.2 Photocatalyst Preparation

TiO_2 nanocrystallites were synthesized from aqueous solutions of titanium chloride (pure $TiCl_4$ liquid was carefully diluted with ice water to a transparent colorless aqueous solution) with concentration $[Ti^{4+}] = 0.1$ M. Ammonia solution (10%) was added to these solutions drop wise until white precipitates (gels) were obtained and the pH = 7. The precipitates were washed with deionized water until chlorine ions were not detected. After the gel was filtered, hydrofluoric acid was introduced with the following molar ratios: 1 mol% (material 1), 5 mol% (material 2), or sodium fluoride (1, 3, 5 mol% for materials 3, 4, 5 respectively). Then the gels were dried and calcined for 120 min at different temperatures selected in accordance with DTA/TG-analysis and results of previous studies [17].

The materials 1, 2, 3, 4, 5 were calcined for 2 h at 500 °C (resulting materials 1.1, 2.1, 3.1, 4.1, 5.1), 600 °C (materials 1.2, 2.2, 3.2, 4.2, 5.2), 800 °C (materials 1.3, 2.3, 3.3, 4.3, 5.3), 900 °C (materials 1.4, 2.4, 3.4, 4.4, 5.4), and 1000 °C (materials 1.5, 2.5, 3.5, 4.5, 5.5). Degussa P25 (P25) was used as a reference for comparison.

2.2.3 Materials Characterization

X-ray powder diffraction (XRD) analysis was carried out using an ARL X'TRA diffractometer equipped with a high-intensity Kα1 irradiation ($\lambda = 1.540562$ Å) operated at 40 kV and 30 mA. Typical scans were performed in a wide range of Bragg angle ($20° \leq 2\theta \leq 60°$). The XRD patterns were analyzed using the standard JCPDS files. Qualitative analysis of phase composition was performed using PDF-2 database and PCPDFWIN software.

Coherent scattering region was calculated from the X-ray line broadening, according to the Debye-Scherrer equation.

Thermogravimetry (TGA) and Differential Thermal Analysis (DTA) were carried out using a thermal analyzer (STA 449-S/4G Jupiter Jupted) at a heating rate of 10 °C/min.

The morphological characteristics were analyzed with transmission electron microscopy utilizing a TEM Tecnai G^2 Spirit Bio TWIN operating at 120 kV.

2.2.4 *Photocatalytic Activity Measurements*

The photocatalytic activity of the prepared samples in the aqueous media was evaluated through monitoring of the discoloration of organic azo dye methylene blue (MB, $C_{16}H_{18}N_3SCl$). In a typical measurement TiO_2 power (1 g/l) was suspended in MB aqueous solution (20 mg/l) by stirring. Experiments were carried out at room temperature in quartz glass beakers. 125 W medium pressure mercury lamp was used as the UV light source. For modeling the photodegradation in the visible light range, a fluorescent light lamp was used (6400 K, 40 W). Residual concentration of the MB solutions was analyzed by mass spectrometry (Spectrophotometer UNICO 1201). Recycling test was subsequently performed three times.

2.3 Results and Discussion

As evidenced by XRD analysis, the titanium dioxide gel obtained from the diluted solutions of inorganic precursors at low temperatures is X-ray amorphous. After thermal exposure, the XRD patterns showed the peaks of anatase and/or rutile phase (Figs. 2.1 and 2.2). However, the anatase modification remain unchanged in all F-doped materials processed for 2 h at temperatures up to 800 °C (Fig. 2.2). When the materials were processed at 900 °C for 2 h, we observed a mixture of anatase and rutile phases, and at 1000 °C the anatase modification had fully converted to the rutile phase. It is worth noting that, for pure titanium dioxide, the anatase-to-rutile phase transition starts at temperatures of above 700 °C under the same synthesis conditions. Consequently, the introduction of fluoride ions into TiO_2-based materials offers the stabilization of anatase modification of titanium dioxide. This is consistent with the results reported in the literature [16].

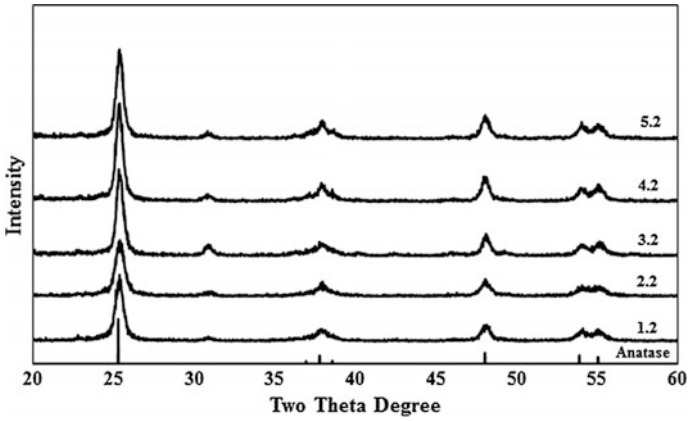

Fig. 2.1 XRD patterns of the F-doped TiO_2 materials calcined at 600 °C with different concentrations of fluoride ions; anatase profile from the PDF-2 database

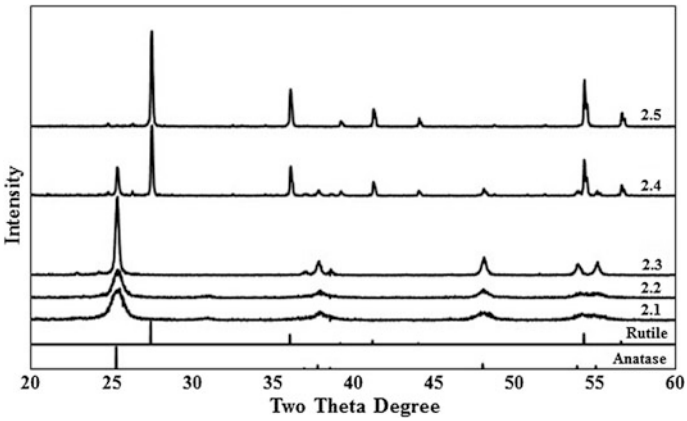

Fig. 2.2 XRD patterns of the F-doped TiO_2 materials calcined at different temperatures; rutile and anatase profiles from the PDF-2 database

Transmission electron microscopy revealed that all materials synthesized through this method contain nanoparticles. The characteristic particle shape is close to spherical, an average particle size is of about 10–30 nm, depending on the synthesis conditions (Fig. 2.3). The TEM data on average crystallite size coincide with the average size of corresponding coherent scattering areas calculated by the Debye-Scherrer equation. Among the factors influencing the crystallite size are the synthesis conditions for titanium hydroxide precursor phase, temperature and processing time for titanium dioxide. Thus, the crystallite size grows with increasing processing temperature and time.

Photocatalytic activity was studied both in the UV and visible light range. The photodegradation of standard methylene blue dye under UV radiation was carried out first. Among the materials containing 5 mol% fluoride ions, the material 2.2 calcined at 600 °C exhibits the best photocatalytic activity (Fig. 2.4). The same pattern was observed both for materials of other series containing a smaller amount of fluoride ions and pure TiO_2 obtained through this method. Therefore, this temperature was optimal for fabrication of F-doped TiO_2 photocatalytic materials. There is a general trend towards an increase in particle size and decrease in total surface area with increasing temperature. At lower processing temperatures, the particles of the material are poorly crystallized and do not show photocatalytic activity, even though the particle size is small and the total surface area is large.

All the synthesized materials that were calcined at 600 °C exhibit better photocatalytic activity than commercial Degussa P25 (Fig. 2.5). It is worth noting that amount of fluoride ions in a range of 1–5 mol% practically has no effect on the photocatalytic properties of obtained materials in the UV range.

The F-doped materials show high photocatalytic response not only under UV exposure but also in the visible light range (Fig. 2.6). The coverage of the visible light range offers significant increase in capacity of TiO_2-based materials as

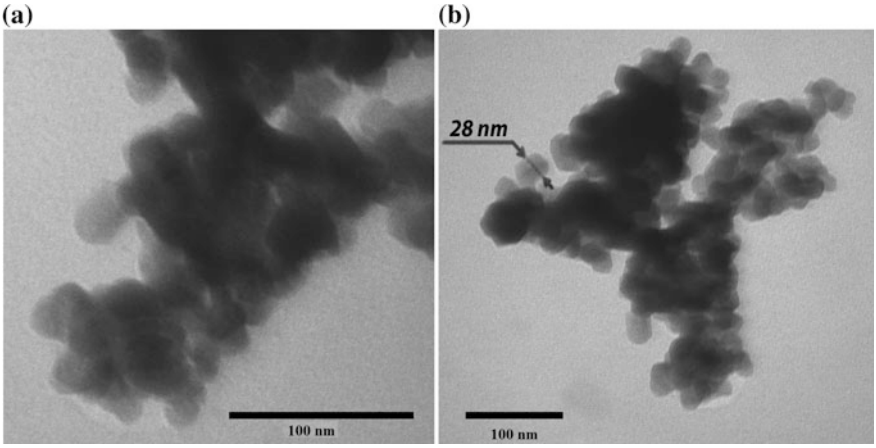

Fig. 2.3 TEM microphotographs of F-doped TiO_2 materials: 1.1 (**a**), 2.2 (**b**)

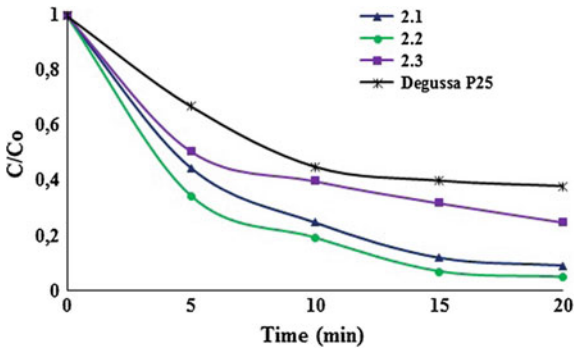

Fig. 2.4 The photodegradation of MB in aqueous solution by F-doped TiO_2 materials 2.1, 2.2, 2.3 and Degussa P25

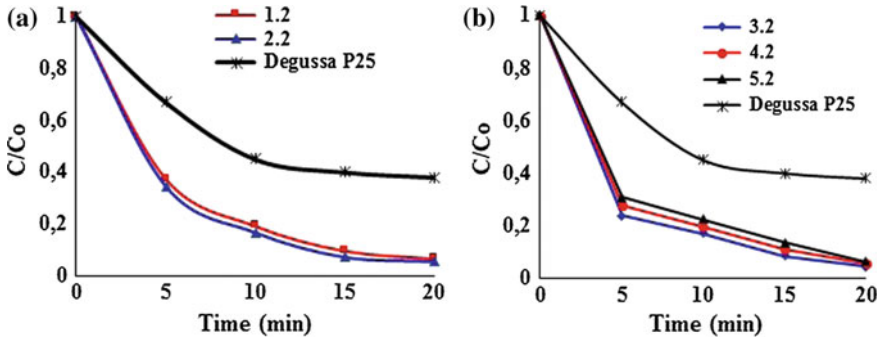

Fig. 2.5 The photodegradation of MB in aqueous solution by F-doped TiO_2 materials 1.2, 2.2 (**a**), 3.2, 4.2, 5.2 (**b**) and Degussa P25

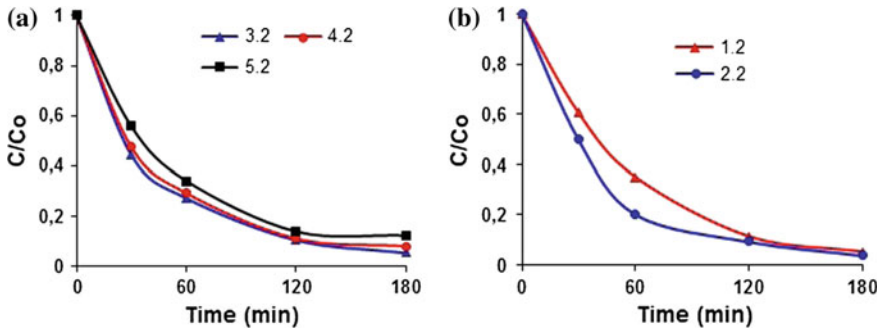

Fig. 2.6 The photodegradation of MB in aqueous solution by F-doped TiO_2 materials 3.2, 4.2, 5.2 (**a**) and 1.2, 2.2 (**b**) under visible light

photocatalysts. The reference sample, pure titanium dioxide synthesized through the same method under the same conditions, shows no photocatalytic activity in the visible light range.

2.4 Conclusions

The synthesized F-doped materials calcined at 600 °C exhibit photocatalytic activity in the both UV and visible light range. The photocatalytic activity induced by UV exposure is higher than that of commercial material Degussa P25, which is pure titanium dioxide. The introduction of fluoride ions was found to increase the thermal stability of anatase modification of titanium dioxide.

Acknowledgements This research was supported by the Project Part of the State Assignment for Research (Ref. No.: 4.2592.2014/K).

References

1. V. Etacheri, C. Di Valentin, J. Schneider, D. Bahnemann, S.C. Pillai, J. Photochem. Photobiol. C: Photochem. Rev. **25**, 1 (2015)
2. M. Pelaez, N.T. Nolan, S.C. Pillai et al., Appl. Catal. B **125**, 331 (2012)
3. M.R. Hoffmann, S.T. Martin, W. Choi et al., Chem. Rev. **95**(1), 69 (1995)
4. C. Wang, H. Liu, Y. Qu, J. Nanomaterials **1**, 2013 (2013)
5. A. Buthiyappan, A. Aziz, A. Raman, W. Daud, W.M. Ashri, Rev. Chem. Eng. **32**(1), 1 (2016)
6. Q. Guo, C. Zhou, Z. Ma, Z. Ren, H. Fan, X. Yang, Chem. Soc. Rev. **45**(13), 3701 (2016)
7. U. Diebold, Surf. Sci. Rep. **48**(5), 53 (2003)
8. J. Banfield, J. Mater. Chem. **8**(9), 2073 (1998)
9. L.G. Devi, R. Kavitha, Appl. Catal. B **140**, 559 (2013)
10. M. Hamadanian, S. Karimzadeh, V. Jabbari, D. Villagrán, Mater. Sci. Semicond. Process. **41**, 168 (2016)

11. N. Karanasios, J. Georgieva, E. Valova, S. Armyanov, G. Litsardakis, S. Sotiropoulos, Curr. Org. Chem. **19**(6), 512 (2015)
12. R. Fagan, D.E. MacCormack, D.D. Dionysiou, S.C. Pillai, Mater. Sci. Semicond. Process. **42**, 2 (2016)
13. S.A. Bakar, C. Ribeiro, J. Photochem. Photobiol., C **27**, 1 (2016)
14. S.A. Ansari, M.M. Khan, M.O. Ansari, M.H. Cho, New J. Chem. **40**(4), 3000 (2016)
15. G. Wu, J. Wang, D.F. Thomas, A. Chen, Langmuir **24**(7), 3503 (2008)
16. T.A. Sednieva, E.P. Lokshin, A.T. Belyaev, V.T. Kalinnikov, Adv. Mater. **6**, 49 (2007)
17. E.M. Bayan, T.G. Lupeiko, L.E. Pustovaya, A.G. Fedorenko, in, *Advanced Materials Manufacturing, Physics, Mechanics and Applications. Springer Proceedings in Physics*, vol. 175, eds. by I.A. Parinov, S.-H. Chang, V.Y. Topolov (Springer, Heidelberg, 2016), p. 51

Chapter 3
Obtaining, Crystal and Grain Structure, Macroresponses of the Binary System Solid Solutions $(1 - x)BiFeO_3$-$xPbTiO_3$

Nikita A. Boldyrev, Anatoly V. Pavlenko, Lidia A. Shilkina, Georgy M. Konstantinov, Anatoly V. Turik, Evgeniy I. Sitalo, Abdulkarim A. Amirov, Valeria V. Rodionova, Ksenia A. Chichay and Larisa A. Reznichenko

Abstract We obtained almost clean samples of binary system solid solutions $(1 - x)BiFeO_3$-$xPbTiO_3$ ($0.1 \leq x \leq 0.5$, $\Delta x = 0.1$) using the solid-state reaction technique with further sintering according to common ceramic technology. We studied the formation patterns of their crystalline structure, microstructure, dielectric and magnetic characteristics in a wide range of temperatures and frequencies. This research suggests an explanation for the observed effects.

3.1 Introduction

Multiferroics, with coexisting electric and magnetic order in a wide range of temperatures above room temperature, are currently being considered as the basis of magnetoelectric structures [1]. Bismuth ferrite, $BiFeO_3$ (BFO) is representative for this class of objects (Curie temperature, T_C—1123 K, Neel temperature, T_N—643 K) [1]. However, the critical dependence of its phase composition and characteristics

N.A. Boldyrev (✉) · L.A. Shilkina · G.M. Konstantinov · A.V. Turik · E.I. Sitalo · L.A. Reznichenko
Research Institute of Physics, Southern Federal University, 194 Stachki Avenue, Rostov-on-Don 344090, Russia
e-mail: nboldyrev@sfedu.ru

A.V. Pavlenko
Southern Scientific Center of the Russian Academy of Science, 41 Chekhov Avenue, Rostov-on-Don 344006, Russia

A.A. Amirov
Amirhanov Institute of Physics, Dagestan Scientific Center of the Russian Academy of Science, 94, M. Yaragsky Street, Makhachkala 367003, Russia

V.V. Rodionova · K.A. Chichay
Laboratory of Novel Magnetic Materials, Immanuel Kant Baltic Federal University, 14 Alexander Nevsky Street, Kaliningrad 236041, Russia

I.A. Parinov et al. (eds.), *Advanced Materials*, Springer Proceedings in Physics 193, DOI 10.1007/978-3-319-56062-5_3

from preparation conditions, high electrical conductivity and, as a consequence, impossibility of creating a polarized state, do not allow the use of this material in engineering. This has led to a great deal of attention to the creation of solid solutions on a BFO basis and the study of their properties, resulting in a range of materials with high T_C and T_N and locked the stable piezoelectric characteristics [2], magnetodielectric and magnetoelectric effects [3], etc.

This work focuses on the structure and properties of the binary system solid solutions $(1 - x)BiFeO_3$-$xPbTiO_3$, with $PbTiO_3$ as the second component. $PbTiO_3$ is a high-temperature ferroelectric compound with a perovskite-type structure, which is the main component of a number of industrially used ferro-piezoelectric materials. This system was studied for the first time in the 60–70s [4]. However, in spite of more than a half century of studies, the literature contains quite contradicting data on its properties [5, 6]. Considering the potential of this system for practical use, continuing to research it is very important.

3.2 Methods of Obtaining and Examination of Samples

Binary system solid solutions $(1 - x)BiFeO_3$-$xPbTiO_3$ ($0.1 \leq x \leq 0.5$, $\Delta x = 0.1$) were manufactured in two steps: by solid-state reaction technique, with further sintering and intermediate grinding at temperatures $T_1 = 1073$ K, $T_2 = 1123$ K and holding times $\tau_1 = 8$ h, $\tau_2 = 10$ h, respectively. The sintering of the ceramic templates was performed at $T_{sin} = (1193–1283)$ K during $\tau_{sin} = (1.5–2.5)$ h, depending on the composition.

X-ray studies were conducted using a diffraction meter DRON-3 (Bragg-Brentano focusing, filtered $Co_{K\alpha}$-radiation). Calculations of the cell parameters (*a, b, c*,—linear, α—angular, V_{exp}—volume) were performed according to the standard technique [7]. The accuracy of the measurements of structural parameters in single-phase solid solutions were the following: $\Delta a = \Delta b = \Delta c = \pm(0.002–0.004)$ Å, $\Delta\alpha = \pm 0.05°$, $\Delta V = \pm 0.05$ Å^3. In the morphotropic area (MA) of the studied system, the diffraction lines were very broad, hence the average cell parameters were calculated. The theoretical volume of the perovskite cell (V_{theor}) was calculated for substitutional solid solution in positions A and B according to the formula [8]:

$$V_{theor} = (\overline{\alpha}_{theor})^3,$$

$$\overline{\alpha}_{theor} = \frac{\sqrt{2}[(1-x)n_{Bi}L_{BiO} + xn_{Pb}L_{PbO}] + 2[(1-0.5x)n_{Fe}L_{FeO} + 0.5xn_{Nb}L_{NbO}]}{(1-x)\cdot n_{Bi} + x\cdot n_{Pb} + (1-0.5x)n_{Fe} + 0.5xn_{Nb}}, \quad (3.1)$$

Where L is the length of the unstrained bond "cation-oxygen" with consideration of the cation's coordination number towards oxygen (Belov-Bokiy ionic radii were used for calculations [9]), n = valency of cations.

The study of the microstructure of surfaces and chips of sintered ceramic samples were carried out on an electronic scanning microscope "Hitachi TM-1000". Temperature dependencies of relative complex dielectric permittivity $\varepsilon^*/\varepsilon_0 = \varepsilon'/\varepsilon_0 - i\varepsilon''/\varepsilon_0$($\varepsilon'/\varepsilon_0$ and $\varepsilon''/\varepsilon_0$ are the real and imaginary parts of $\varepsilon^*/\varepsilon_0$, respectively; ε_0—dielectric constant) at T = (300–1000) in the frequency range f = (102–106) Hz were obtained using impedance analyzer Agilent 4980.

Magnetic characteristics of solid solutions $0.7BiFeO_3$-$0.3PbTiO_3$ were studied using vibration magnetometer LakeShore7400. Samples weight was determined using thermobalance NETZSCH TG 209 F3 Tarsus for calculating specific magnetization.

3.3 Results and Discussion

The X-ray diffraction analysis showed that $BiFeO_3$ contains small quantity of $Bi_{25}FeO_{40}$ and $Bi_2Fe_4O_9$ compounds. Their relative line intensities do not exceed 5%. Traces of impurity phases were visible on the X-ray diffraction pattern of solid solutions with x = 0.1 and x = 0.2, while solid solutions with x = 0.3–0.5 represent a pure phase of the perovskite type. The appearance of $Bi_{25}FeO_{40}$ and $Bi_2Fe_4O_9$ compounds in ceramics is due to a narrow concentration interval of the existence phase of $BiFeO_3$ on the state diagram of Bi_2O_3 and Fe_2O_3; wide crystallization areas of $Bi_2Fe_4O_9$ and $Bi_{25}FeO_{39}$ compounds [10–12]; Bi_2O_3 volatility [13]; and complexity of the reactions in an equimolar mixture Bi_2O_3 and Fe_2O_3. The analysis of X-ray diffraction patterns showed that increasing of x results in a phase transition from rhombohedral (Re) phase, correspond to the pure $BiFeO_3$ transition into tetragonal (T) phase. The Re phase exists in the interval $0 \leq x < 0.5$, T phase—in the interval $0.2 \leq x < 0.5$, the area of phase existence is situated in the interval $0.2 \leq x < 0.5$. Figure 3.1a contains X-ray diffraction patterns of single-phase solid solutions close to morphotropic area (MA) from both sides and two-phase solid solution with x = 0.3 and x = 0.4 from MA. One can see that the phase appeared in sample with x = 0.3 has a very imperfect structure, it becomes more homogeneous at x = 0.4 and its quantity increases.

There are fragments of X-ray diffraction patterns on Fig. 3.1b including diffraction reflections $(200)_c$ of all solid solutions. One can see on a fragment of sample with x = 0.4 that the angle interval of 2θ = 48–52 contains 3 weak peaks corresponding to reflection 002, one of which (peak 3) gives parameter c close to the parameter c of the $PbTiO_3$ system. Since parameter a also matches the parameter a of $PbTiO_3$, it is possible to assume that the formation of the latter indicates the formation of tetragonal phase by analogy with the $PbZr_{1-x}Ti_xO_3$ system [14], with further dissolution of bismuth ferrite in it. Figure 3.1c shows diffraction reflection 200 of solid solution with x = 0.2 and symmetrically arranged satellites c^- and c^+. The corresponding modulation wavelength along [100] direction is equal to ≈160 Å, which is 40.2 cells. The appearance of satellites signalizes phase transition, because it indicates the formation regularly located local areas with

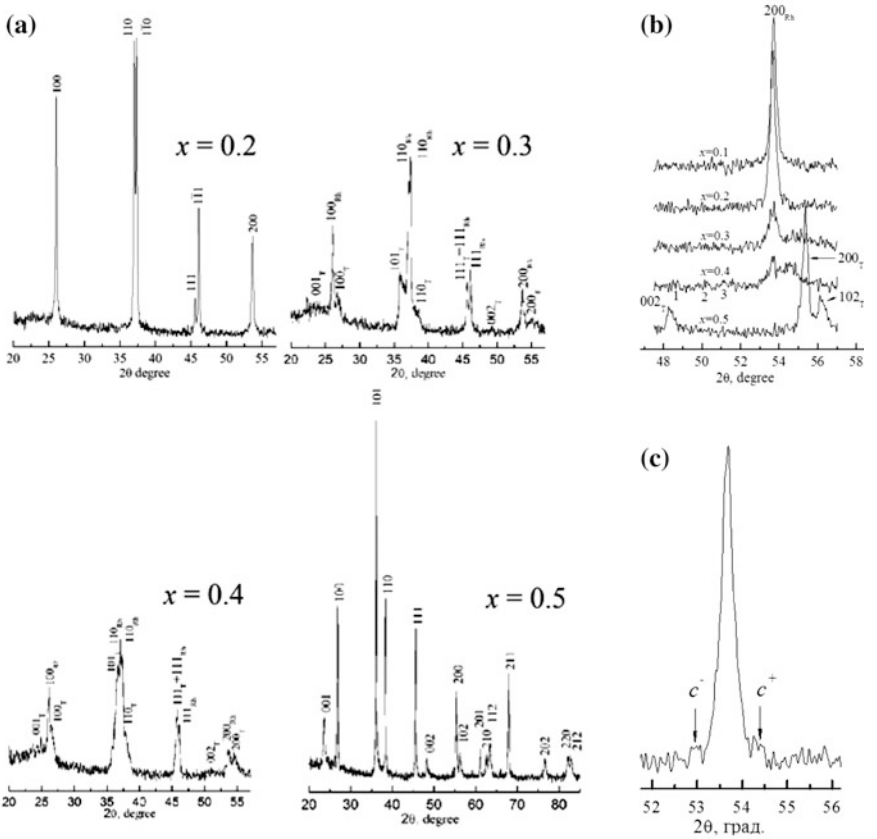

Fig. 3.1 **a** Fragments of X-ray diffraction patterns of the studied system solutions: x = 0.2—Re phase, x = 0.3, 0.4—mixture of Re and T phases, x = 0.5—T phase; **b** fragments of X-ray diffraction patterns including diffraction reflections $(200)_k$ of solid solutions; **c** diffraction reflection 200 with composition satellites

a different chemical composition. The large concentration step did not allow to establish more accurate boundaries.

Figure 3.2 shows the parameters of concentration dependencies of the studied elementary system at room temperature.

A decrease of the cell volume V along with an increase of x in the interval $0 \leq x < 0.1$ is associated with the crystal chemistry of the $BiFeO_3$ structure that is similar to the $PbTiO_3$ structure (Bi^{+3} and Pb^{+2} ions are isoelectric ions, both form inner solid solution taking A and B positions in compounds with a perovskite structure) [15]. Further increase of x leads to substantial changes in the experimental and theoretical cell volumes, the angle α also increases. T cell parameters have a completely different behavior. Non-monotonous changes of all characteristics along with drastic decrease of *V, c, c/a* and increase of *a* indicate that sample with

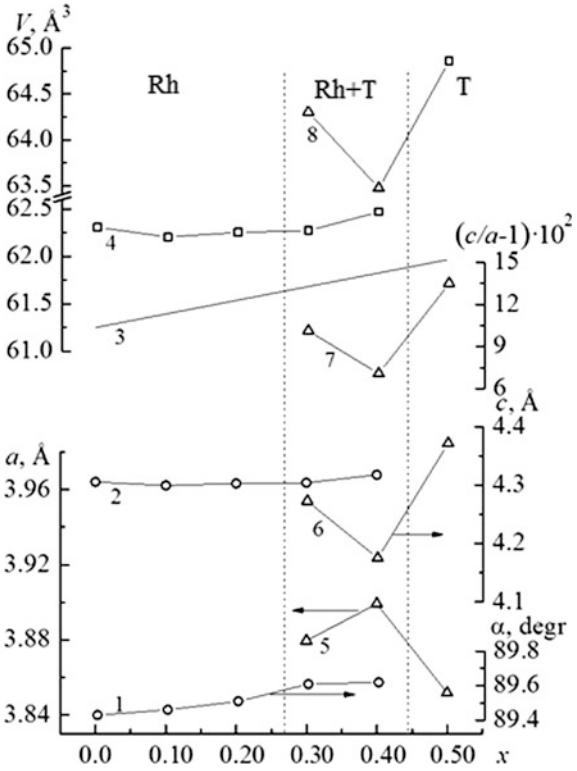

Fig. 3.2 Parameter dependencies, experimental and theoretical cell volumes of solid solutions of the studied system: rhombohedral —α *(1) a (2),* V_{theor} *(3),* V_{exp} *(4),* tetragonal—*a (5), c (6), c/a (7),* V_{exp} *(8), dotted lines* show the system's phase diagram

T symmetry is formed discretely in the interval $0.2 < x < 0.5$, that is, several tetragonal solid solutions with different lead content appear at first, then they mutually dissolve, which is confirmed by Fig. 3.1b (see above).

The patterns established above also appeared during the investigation of object's grained structure, the results are presented in Fig. 3.3. It is possible to distinguish three types of grains in $BiFeO_3$ ceramics (Fig. 3.3a): I—large, blocky shape, measuring 12–20 μm; II—medium, cubic shape, measuring 6–10 μm; III—small, rounded and measuring 2–5 μm, localized at joints of large grains and forming separate conglomerates. Intercrystalline spaces contained dark "fluxes" measuring up to 9 μm (Fig. 3.3a—LP-I) unequally distributed grain-framing intercrystalline layers with a thickness of ~1 μm (Fig. 3.3a—LP-II). Their presence in $BiFeO_3$ ceramics is probably connected with appearance of liquid phases of eutectic origin during synthesis and sintering of material [16]. Proceeding from the fact that the fluxes LP-II frame are mainly large grain type I and II, it is reasonable to assume that they act as a transport medium, favoring mass transition and diffusion during recrystallization sintering [16]. On the other hand, LP-I fluxes are mainly localized at joints of grains type I or II and contain small inclusions of main phase crystallites, indicating "cementing" role of this kind of LP [16]. The introduction of 10% of $PbTiO_3$ (Fig. 3.3b) leads to a decrease in the degree of microstructure heterogeneity,

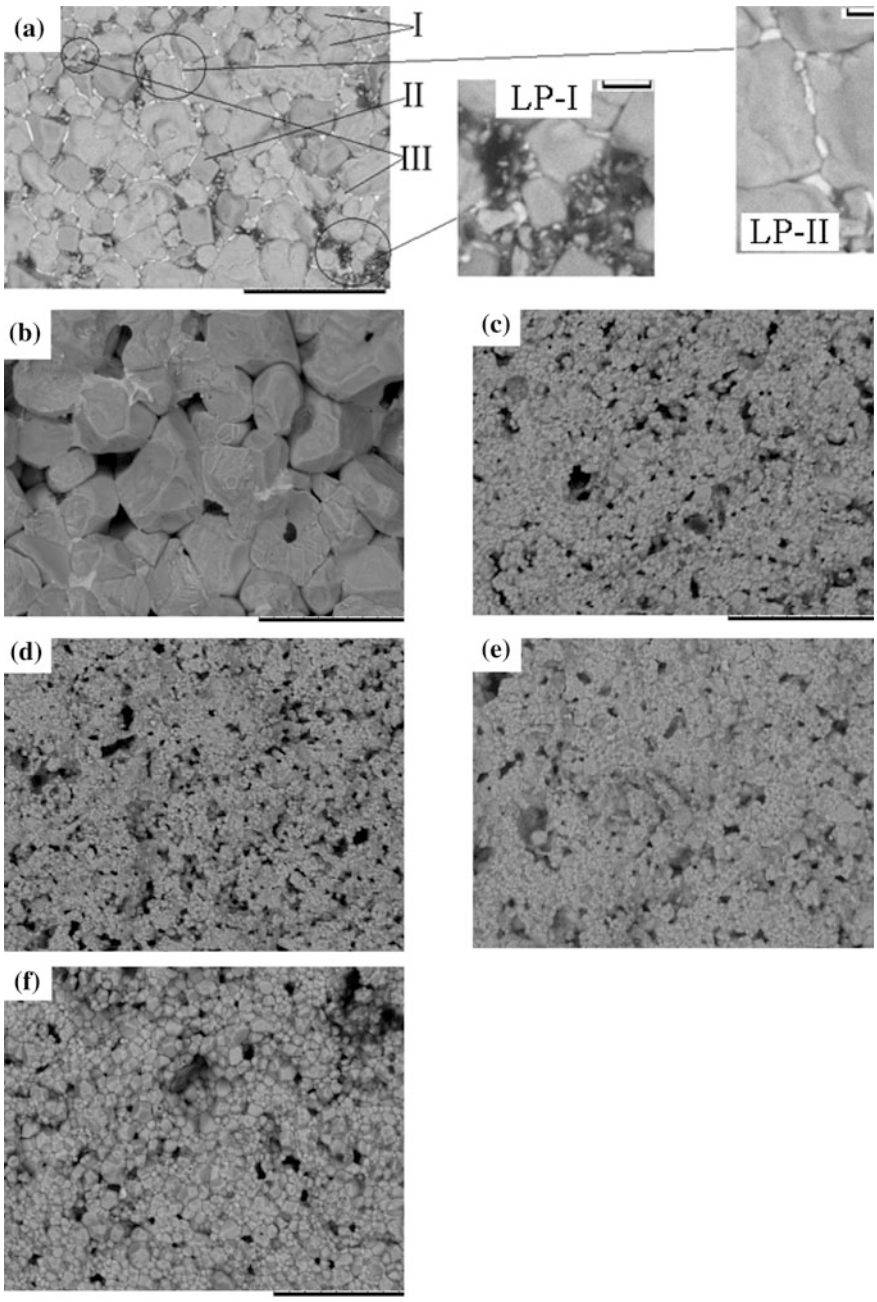

Fig. 3.3 Image fragments of chips of studied ceramics (**a** x = 0, **b** x = 0.1, and **c** x = 0.2, **d** x = 0.3, **e** x = 0.4, **f** x = 0.5). Markers—30 μm

sharp enlargement of grains (up to 30 μm), disappearance of LP-I and decrease LP-II fraction. This suggests that the introduction of $PbTiO_3$, on the one hand, leads to the stabilization of the object's perovskite phase (as a consequence, there is almost a complete disappearance of impurity phases), and on the other hand, it excludes the possibility of the appearance of LP-I alone that contributes to the observed evolution of the structure and microstructure. The nature of the mechanic chip in ceramics with $x = 0.1$, indicating the proximity of the strength characteristics of the grains and their boundaries, enabled to observe sufficiently strong intra-granular heterogeneity in the object, in some cases—pores measured up to 3 μm. Further increase in concentration of $PbTiO_3$ in the range $0.2 \leq x \leq 0.4$ leads to crushing and loosening of grained structure of objects, which is associated with increased complexity of the object's phase composition. In sample with $x = 0.5$ the uniformity of grained landscape recovers, grains become more clear cut, and have a polyhedral shape that measure 3–9 μm with flat borders.

Figure 3.4 shows $\varepsilon'/\varepsilon_0$ and tgδ temperature dependencies in a wide range of temperatures and frequencies for the $BiFeO_3$-$PbTiO_3$ composition. The graph shows (at $x > 0.1$) that dependencies contain three temperature intervals with abnormalities. Increasing the concentration of lead titanate in the temperature interval (450–700) K leads to all investigated compositions forming weak frequency-dependent maxima shifting into the area of high temperatures. One should note that intensity of these maxima highs also depends on the concentration of the introduced $PbTiO_3$—the higher the content is, the less they are expressed. Another group of weak maxima with great frequency dispersion, which decreases with increasing of lead titanate concentration, is observed in the interval (700–850) K (all compositions except pure BFO and $0.5BiFeO_3$-$0.5PbTiO_3$ solid solution). All of the ceramics studied form maximum on the $\varepsilon'/\varepsilon_0$ (T) dependencies at temperatures above 800 K. This is likely associated with a phase transition from the rhombohedral (or tetragonal—depending on the composition) phase to the cubic phase. The temperature corresponding to this maximum, (T_C), shifts to the area of low temperatures with as *x* increases, but increases again in compositions with $x = 0.5$. It should be noted that, despite the heterovalent cation substitution in A ($Pb^{2+} \rightarrow Bi^{3+}$) and B ($Ti^{4+} \rightarrow Fe^{3+}$) positions, manifestation of relaxation properties in objects near ferro-paraelectric phase transition has not been fixed Past the Curie point, all studied ceramics demonstrate strong growth of the relative permittivity accompanied by great frequency dispersion due to an increase in conductivity.

Behavior of all parameters listed in Fig. 3.5 correlates well with the phase diagram of the system. In particular, the values of $\varepsilon'/\varepsilon_0$ ($T = 300$ K) and tgδ($T = 300$ K) smoothly grow with increasing x and become maximum in solid solution with $x = 0.4$, which is most likely due to the great mobility of the domain structure in samples from MA. Dependence $T_C(x)$ has a flat characteristic and passes through minimum in MA on the border of the morphotropic phase transition Ph + T → T, that is typical for the systems based on both $BiFeO_3$ [2] and $PbTiO_3$ [7].

The giant negative infralow-frequency dielectric permittivity was found by us in $0.5BiFeO_3$-$0.5PbTiO_3$ ceramic samples in the high temperature range. Similar phenomena have been discussed previously [17–19]. But very high ratio between the conductivity and permittivity made one unable to measure the real part of the complex

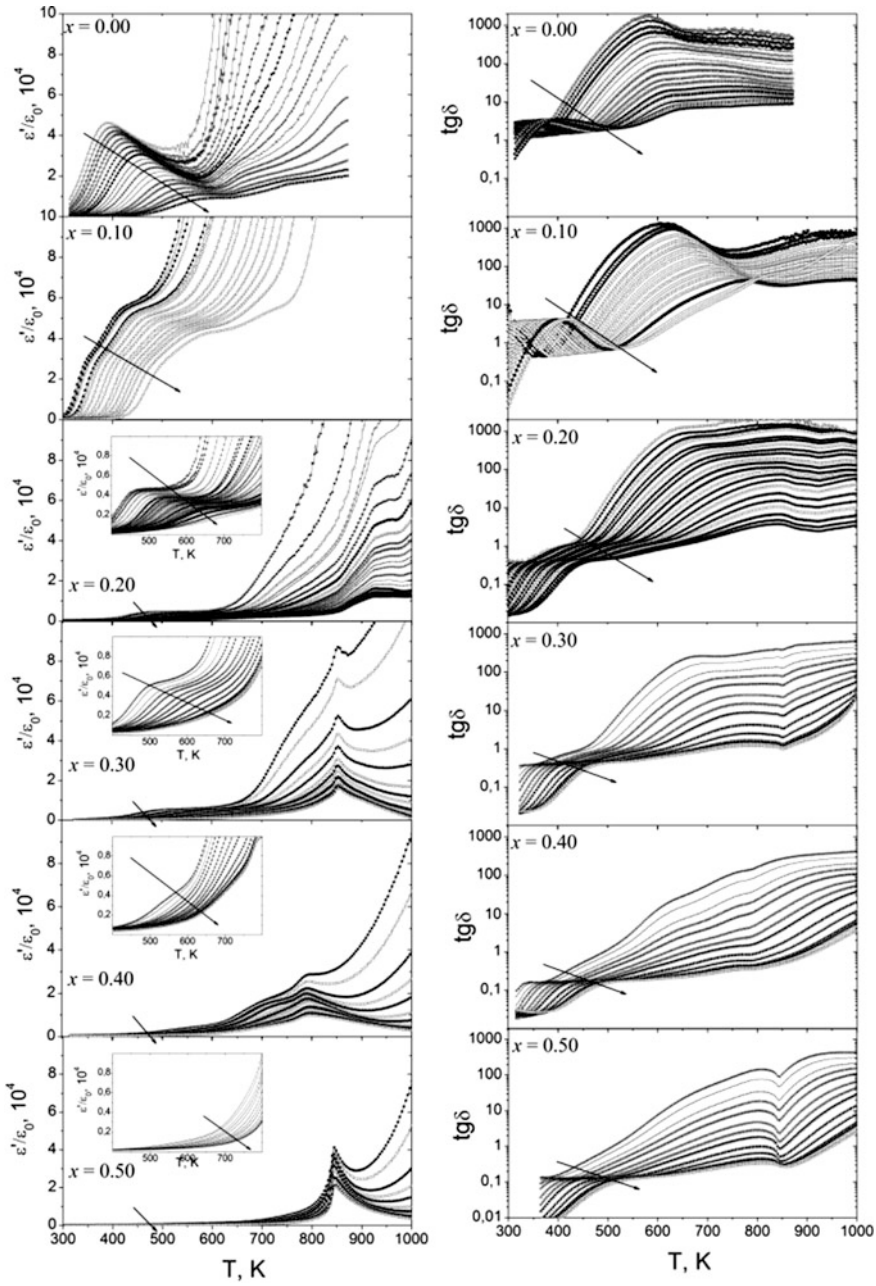

Fig. 3.4 Temperature dependences of $\varepsilon'/\varepsilon_0$ and tgδ in range of temperatures (300–1000) K and frequencies (10^2–2×10^6) Hz. *Arrows* indicate frequency increase

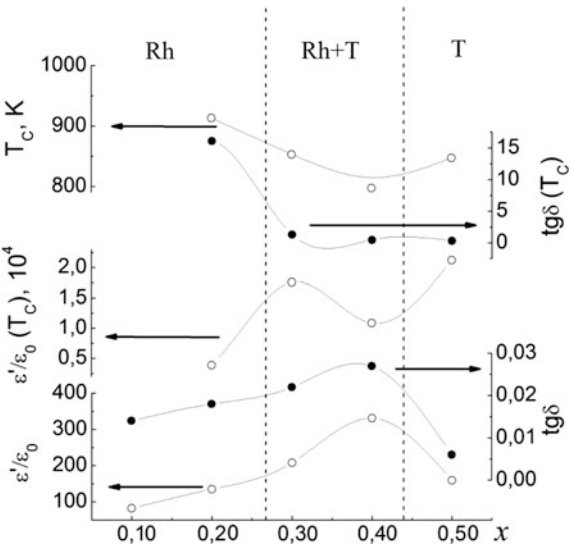

Fig. 3.5 Concentration dependencies $\varepsilon'/\varepsilon_0$ (T = 300 K), tgδ (T = 300 K), T_C, $\varepsilon'/\varepsilon_0$ (T = T_C) and tgδ(T = T_C) of ceramics of the studied systems at a frequency of 10^6 Hz (T_C was defined according to $\varepsilon'/\varepsilon_0$ (T) maximum)

dielectric permittivity. Negative dielectric permittivity was also found in [20] in the $CaCu_3Ti_40_{12}$ ceramics. In [21] for explanation this phenomenon model based on applying parallel connection circuit of capacity C (having only real part) and complex conductivity $G = 1/R = (G_1 - iG_2)$ has been used. For describing observed in $0.5BiFeO_3$-$0.5PbTiO_3$ ceramic phenomena we used that technique too. According to [21] admittance Y and complex capacity C^* of the circuit will be equal to:

$$\begin{aligned} Y &= \frac{1}{R} + i\omega C = G_1 - iG_2 + i\omega C, \\ C^* &= C - \frac{G_2}{\omega} - i\frac{G_1}{\omega} \end{aligned} \tag{3.2}$$

respectively. Accordingly, the real $\varepsilon^{*\prime}$ and imaginary $\varepsilon^{*\prime\prime}$ parts of the permittivity are linked with the imaginary γ'' and real γ' parts of the conductivity as

$$\varepsilon^{*\prime} = \varepsilon' - \frac{\gamma''}{\omega\varepsilon_0}, \quad \varepsilon^{*\prime\prime} = \frac{\gamma'}{\omega\varepsilon_0}, \tag{3.3}$$

where parameters of ceramics were marked by symbols with an asterisk, and parameters of the component of the equivalent circuit were marked by symbols without asterisk.

Figure 3.6 shows, that (1) and (2) formula calculations correlate with the experimental data. Character of the dependencies of the real and imaginary parts of the complex permittivity on the frequency is the result of hopping conductivity. Authors of [21] explain the observed phenomena (namely passing ε^* trough zero and existence of negative values of $\varepsilon^{*\prime}$) by mutual compensation of contributions of

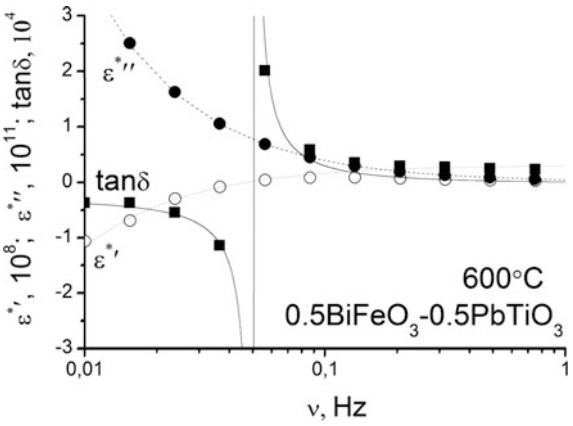

Fig. 3.6 Experimental (points) and calculated according to the formulas (3.1) and (3.2) (*lines*) dielectric spectra of $0.5BiFeO_3$-$0.5PbTiO_3$ ceramics at 600 °C

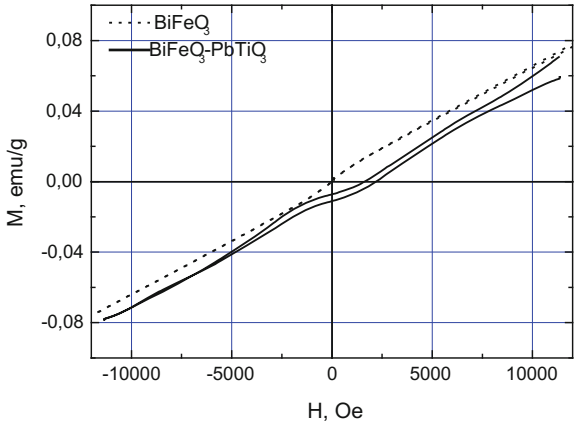

Fig. 3.7 Magnetization curves of $0.7BiFeO_3$-$0.3PbTiO_3$ and pure bismuth ferrite ceramics

the capacity and hopping conductivity to the formation of the real part of the complex permittivity, that most likely takes place in current case too.

Figure 3.7 shows the magnetization curves of $0.7BiFeO_3$-$0.3PbTiO_3$ and pure bismuth ferrite ceramics. As can be seen, pure bismuth ferrite shows the typical antiferromagnetic behavior. Magnetization increases linearly with increasing magnetic field that is in agreement with published data [22]. Studied object selection (x = 0.3) was caused by the fact that ceramics with similar component concentration has a maximum magnetic properties. According to published data further increase of x leads to the weakening of the magnetic properties [23–25]. For studied objects fairly weak ferromagnetic contribution is observed. Its observation may be associated with changes in the conditions of antiferromagnetic exchange interactions Fe-O-Fe because of substitution of Bi^{+3} ions by Pb^{+2} and Fe^{+3} ions by Ti^{+4}.

Obtained results shows complex phase transformations occurring in the system $(1 - x)BiFeO_3$-$xPbTiO_3$ and leading to significant changes in grain and crystal

structure, dielectric and magnetic characteristics that must be considered in the development of functional materials based on this system.

Acknowledgements This work was financially supported by the Ministry of Education and Science of the Russian Federation: themes № 1927, 213.01-2014/012-VG and 3.1246.2014/K (the basic and project parts of the state task). Scholarship of President of Russian Federation № SP-3197.2016.3. The work performed on equipment of Collective use center "Electromagnetic, electromechanical and thermal properties of solids" Southern Federal University.

References

1. A.P. Pyatakov, A.K. Zvezdin, Phys. Usp. **55**(6), 557 (2012)
2. L. Fan, J. Chen, S. Li, H. Kang, L. Liu, L. Fang, X. Xing, Appl. Phys. Lett. **37**(2), 022905 (2013)
3. K. Manish, S. Shankar, O.P. Thakur, A.K. Ghosh, J. Mater. Sci.: Mater. Electron. **26**, 1427 (2015)
4. Y.Y. Tomashpol'skii, Y.N. Venevtsev, Crystallogr. Rep. **6**(16), 1037 (1971)
5. D.I. Woodward, I.M. Reaney, R.E. Eitel, C.A. Randall, J. Appl. Phys **5**(94), 3313 (2003)
6. T.L. Burnett, T.P. Comyn, A.J. Bell, E. Condliffe, G. Lloyd, J. Phys: Conf. Ser. **26**, 239 (2006)
7. E.G. Fesenko, *Perovskite family and ferroelectricity* (Atomizdat, Moscow, 1972)
8. N.V. Dergunova, V.P. Sakhnenko, E.G. Fesenko, Crystallogr. Rep. **1**(23), 94 (1978)
9. G.B. Bokii, *Vvedenie v Kristallokhimiyu (Introduction to Crystal Chemistry)* (MSU Publ, Moscow, 1954)
10. T.T. Carvalho, P.B. Tavares, Mater. Lett. **62**, 3984 (2008)
11. S. Phapale, R. Mishra, D. Das, J. Nucl. Mater. **373**, 137 (2008)
12. R. Palai, R.S. Katiyar, H. Schmid, P. Tissot, S.J. Clark, J. Robertson, S.A.T. Redferm, G. Catalan, J.F. Scott, Phys. Rev. **77**, 014110 (2008)
13. M.S. Kartavtseva, O.Y. Gorbenko, A.R. Kaul, S.A. Savinov, J. Surface Inv **2**(1), 1 (2008)
14. I.N. Andryushina, L.A. Reznichenko, L.A. Shilkina, K.P. Andryushin, S.I. Dudkina, Ceram. Int. **39**(2), 1285 (2013)
15. S.V. Titov, L.A. Shilkina, O.N. Razumovskaya, L.A. Reznichenko, V.G. Vlasenko, A.T. Shuvajev, S.I. Dudkina, A.N. Klevtsov, Inorg. Mater. **37**, 849 (2001)
16. A.V. Pavlenko, N.A. Boldyrev, L.A. Reznichenko, I.A. Verbenko, G.M. Konstantinov, L.A. Shilkina, Inorg. Mater. **50**(7), 806 (2014)
17. O.V. Dolgov, D.A. Kirzhnits, E.G. Maksimov, Rev. Mod. Phys. **53**, 81 (1981)
18. H.L. Kwok, Solid-State Electron. **47**, 1089 (2003)
19. H.L. Kwok, Phys. Stat. Sol. (c) **5**(2), 638 (2008)
20. Yu. Kabirov, V. Gavrilyachenko, E. Panchenko, E. Milov, A. Klenushkin, Adv. Mater. Res. **705**, 52 (2013)
21. A.V. Turik, A.S. Bogatin, Funct. Mater. Lett. **8**(4), 1550035 (2015)
22. A.A. Amirov, I.K. Kamilov, A.B. Batdalov, I.A. Verbenko, O.N. Razumovskaya, L.A. Reznichenko, L.A. Silkina, Appl. Phys. Lett. **34**(17), 72 (2008)
23. S. Vura, P.S. Anil Kumar, A. Senyshyn, R. Ranjan, J. Mag. Magnetic Mater. **365**, 76 (2014)
24. A.M. Gotardo, D.S.F. Viana, M. Olzon-Dionysio, S.D. Souza et al., J. Appl. Phys. **112**, 104112 (2012)
25. K. Singh, N.S. Negi, R.K. Kotnala, M. Singh, Solid State Commun. **148**, 18 (2008)

Chapter 4
Non-thermal Effect of High-Voltage Nanosecond Pulses on Kimberlite Rock-Forming Minerals Processing

Igor Zh. Bunin, Valentine A. Chanturiya, Nataliya E. Anashkina, Maria V. Ryazantseva and Elizaveta V. Koporulina

Abstract In the present paper, we attempted to substantiate the efficiency of non-thermal high-power (high-voltage) nanosecond electromagnetic pulses for the directional change of phase (chemical and functional) composition and technological properties of kimberlite rock-forming minerals (olivine, calcite and serpentine) investigated using a complex of physical and chemical methods (XPS, DRIFTS, analytical electron microscopy, atomic-force microscopy, microhardness measurement—Vickers indentation method, and the method of acid-base indicators adsorption). According to XPS, DRIFTS, SEM-EDX and microhardness testing data, the effect of high-voltage nanosecond pulses leads to damage the surface microstructure of dielectric minerals with the subsequent formation of traces of surface breakdowns and microcracks, softening of rock-forming minerals, and reducing their microhardness by 40–66% overall.

4.1 Introduction

The current technology for mining and processing diamonds from primary deposits in Russia damages the diamond crystals at a rate of 25–75%, leading to an average weight loss of 12% [1, 2]. Diamonds are usually damaged during the autogeneous grinding of kimberlites (in mills of wet autogeneous grinding), and up to 29% of all diamonds disintegrate [1, 2]. Therefore, in processing of diamond-bearing kimberlites the actual problem of prime importance is development of new effective processes feasible to provide a higher grade concentrates due to softening of kimberlite, to preserve diamond crystal safety in autogenous ore grinding circuits, and to enhance difference of hydrophobic, lipophobic, luminescent properties of diamonds and rock minerals [3, 4].

I.Zh. Bunin (✉) · V.A. Chanturiya · N.E. Anashkina · M.V. Ryazantseva · E.V. Koporulina
Institute of Comprehensive Exploitation of Mineral Resources of the Russian Academy of Science (IPKON RAS), Moscow, Russia
e-mail: bunin_i@mail.ru

I.A. Parinov et al. (eds.), *Advanced Materials*, Springer Proceedings in Physics 193, DOI 10.1007/978-3-319-56062-5_4

The authors of papers [5, 6] uphold the view that the thermal disintegration of rocks by a powerful microwave oscillator shows great promise in processing of diamond-bearing ores. It is proved experimentally that heating of kimberlite (depth of skin layer $\delta \sim 60$ cm) by a microwave emitter of 600 W ($f = 2.45$ GHz) up to 300–400 °C for a few seconds resulted in a series of explosions with a failure of test specimens [5]. The efficiency of kimberlite rock disintegration by short-run microwave heating is appreciably raised thanks to preliminary exposure of test specimens in a vapor bath. Approximately ~5% water content in a rock can cause failure of test material because of speedy evaporation of moisture with resultant sharp increase in the saturated-steam pressure in pores and micro-cavities in rocks. The mechanical stresses arising in this process can exceed the yield limit of a geomaterial [5, 6].

In [7–20] we first established the conditions for realization of disintegration mechanisms for fine-disseminated mineral media under short electromagnetic pulses of ~1–10 ns and high electric field intensity $E \sim 10^7$ V/m. This type of energy effects referred to so-called non-thermal effects, as energy of a single pulse is not capable to alter total temperature of the whole specimen. In [21], the conditions and specific characteristics of the non-thermal action of high-power nanosecond electromagnetic pulses (HPEMP) on different natural and artificial media were established: (i) temperature T of a medium as a whole, as well as temperature of its relatively homogeneous constituents do not actually change, T_{mean} (before interaction) $\sim$ T_{mean} (after interaction); (ii) amplitude of the electric field intensity (field strength) per a pulse E is much higher than amplitude of static breakdown of a medium, $E_{\text{max imp.}} \gg E_{\text{stat. break}}$; (iii) pulse duration Δt is much less than that of thermal relaxation of a medium, $\Delta t \ll \Delta t_{\text{therm relax}}$. Together with that, during time much less as compared to time of typical identification of thermal and physical properties of material constituents of the medium, the high local temperature can be gained during a pulsed action.

In this chapter, we present new experimental data on changes in the structure, chemical composition of surface atoms, and microhardness of rock-forming minerals (olivine, calcite and serpentine) in Yakut kimberlites (Russia) in the result of non-thermal action produced by high-voltage nanosecond pulses. The effect of HPEMP-irradiation on phase composition and quantum (chemical) state of atoms in surface layers of dielectric minerals (calcite and serpentine) has been studied using X-ray photoelectron spectroscopy (XPS) analysis.

The spectroscopic results were justified by the microhardness testing data: it was found by Vickers' method that the effect of high-power pulsed fields leads to reduction in microhardness of rock-forming dielectric minerals, in total, by 40–66%, owning to the disturbance of microstructure of surface layers, new-formed defects at different structural levels (dislocation, microcracks, incomplete surface electric break-ups), disordering and amorphisation of the mineral surface.

4.2 Experimental

4.2.1 Materials and Research Technique

We spent the experiments on mineral specimens ground down to −100 + 63 μm and polished sections 1 × 1 × 0.45 cm in size. By using simultaneously a Varian VistaCCD, ICP-AES device and inductively coupled plasma, we employed atomic emission spectroscopy to determine the gross contents of elements in each sample of the mineral (see Table 4.1; the content of minor impurities is not given).

Olivine. By the results of optical microscopy (microscope Olympus SZ61) and confocal laser scanning microscopy (microscope Keyence VK-9700) olivine specimen $(Mg, Fe)_2[SiO_4]$ mainly consists of 0.5–3 mm forsterite grains with minor impurity of magnetite. Olivine specimens are characterized with different roundness of grains: 40% of 2–3 mm well-rounded grains, 35% of 1–2 mm medium-rounded grains and 25% of below 1 mm fine olivine spills. Olivine color varied from brownish-green to yellow-green and almost colorless; all grains were transparent. The mineral hardness in Mohs' scale is high (Mohs' hardness is equal to 6.5–7), mineral cleavage is moderate in a single direction. Some moderately-rounded grains (less than 5%) are covered with magnetite "shirt". Magnetite is used to form both coverings on surface of olivine grains and separate small (less than 1 mm) grains of irregular shape. This mineral was black in color with metallic luster, opaque, with strong magnetic properties. Mohs' hardness is 5.5 with none mineral cleavage.

Calcite ($CaCO_3$) specimens were presented with pop-offs along mineral cleavage (up to 1 × 1 cm in size) of calcite crystal (Iceland spar; element composition and impurity content in calcite specimen, % in mass: Ca—40.68, F—0.85, Si—0.11, Fe—0.10, Al—0.05, Mg—0.03, Ba—0.02, Sr—0.01). The mineral is colorless, transparent, with glass luster and stepped break-line. Calcite exhibits perfect mineral cleavage in rhomb directions. Mohs' hardness equal to 3.

Serpentine ($X_{(2-3)}Si_2O_5(OH)_4$, where X = Mg, Fe_{2+}, Fe_{3+}, Ni, Al, Zn, Mn) is a dense aggregate consisting of microcryptocrystalline mass. Serpentine specimen (lizardite—$Mg_3SiO_5(OH)_4$, antigorite—$(Mg, Fe)_3Si_2O_5(OH)_4$) is dark-green in color with greasy luster and Mohs' hardness 2.5–4. The microinclusions of sulfides (presumably, millerite NiS) and oxides (like chromite $FeCr_2O_4$, magnesiochromite $MgCr_2O_4$) of less than 0.01 mm in size were detected at surface of polished mineral sections.

Table 4.1 Phase and chemical composition of olivine and serpentine specimen, wt %

Specimen	MgO	SiO_2	Fe_2O_3	CaO	Al_2O_3	S	Ni	Cr	Br
Olivine $(Mg, Fe)_2[SiO_4]$	46.04	39.60	11.10	0.68	0.28	0.17	0.37	0.01	0.13
Serpentine (Mg, Al, Fe) $Si_4O_{10}(OH)_8$	36.56	41.12	5.57	0.18	0.83	0.24	0.37	0.26	–

Kimberlite rock specimens (dense porphyritic kimberlites of gray and greenish-gray in color) were flat-polished sections of 1 × 1 × 0.45 cm in size. By OM data the serpentized (from strongly altered to completely replaced by serpentine) olivine was dominating in disseminated inclusions along with random pyroxene grains of 0.5–0.7 mm, and ilmenite of mainly 0.2–0.3 mm in size and uncommonly up to 0.6 mm, and shpinels (0.1 mm). Calcite fills cavities and fractures in rocks, forming irregular-shaped nestles up to 2 mm.

4.2.2 The HPEMP Treatment Conditions and Analysis Techniques

We conducted the treatment of powdered mineral specimens and polished sections with high-voltage nanosecond video-pulses (HPEMP [7–21]). Pulse duration was no longer than 10 ns, the strength of the electric component of the field was $\sim 10^7$ V/m, the energy in each pulse was 0.1 J, the pulse repetition frequency was 10 Hz, and the range of varying the treatment time t_{tr} was 5–50 s (the dose of the electromagnetic pulsed radiation was $N_{pulses} = 5 \times 10^2 - 10^4$ pulses). Before treatment, the samples were wetted with distilled water in an S:L ratio of 5:1 to increase the efficiency of the electromagnetic pulse impact [8, 17] and simulated conditions approaching those of actual production processes.

We used X-ray photoelectron spectroscopy (XPES) and Diffuse reflectance infrared Fourier transform spectroscopy (DRIFTS) to analyze the phase composition of the surfaces of mineral particles. To acquire the X-ray photoelectron (XPE) spectra, we used a Kratos Axis Ultra DLD spectrometer with a monochromatic AlK_α X-ray radiation source. The IR-spectra of the diffuse reflection of mineral powders were recorded over a 400–4000 cm^{-1} range of varying wave numbers with a resolution of 4 cm^{-1} using an IRAffinity-1 IR spectrometer (Shimadzu) equipped with a DRS-8000 diffuse-reflection attachment.

We studied the morphological and structural-chemical properties of mineral surface modified by nanosecond electromagnetic pulses using analytical electronic microscopy (SEM/EDX, scanning electronic microscope LEO 1420VP with energy-dispersion microanalyzer Oxford INCA Energy 350). Features of mineral surface relief on meso(nano)-scale (Z—coordinate was less than 100 nm) have been studied by atomic force microscopy (AFM, INTEGRA Prima, NT-MDT) in semi-contact mode. We performed the mineral surface morphology measurements in ambient air and at standard conditions. The cantilever (NSG10/Au) has a resonance frequency of 240 kHz and a force constant of 11.8 N/m; tip curvature radius was $\sim$35 nm. Both the cantilever and tip are made from n-type single crystal Si (n-Si) and antimony (Sb) doped. Cantilever has Au reflective side coating to increase laser signal.

The change in the functional chemical composition (acid-base properties) of the minerals surface during HPEMP action was studied via the adsorption of Gammet indicators from aqueous media [22, 23]. The set of acid-base indicators, the values of constant pK_α of protolytic equilibrium, the working concentrations of the solutions, and the wavelengths corresponding to the maximum optical absorption in the spectrum we published in [24]. We measured the optical density of the initial aqueous solution of the indicator with constant concentration D_0 (the control sample) using spectrophotometry (Shimazdu UV 1700). The optical density of a similar indicator solution was also measured after adsorption–desorption equilibrium was established with mineral sample D_1. Finally, the optical density of a solution of an indicator solution added to distilled water decanted after the mineral under study came into contact with sample D_2 was measured. We determined the contents of the active sites with respective values of on a mineral surface using the following formula [25]: $q(pK_\alpha) = \left|\frac{|D_0-D_1|}{m_1} \pm \frac{|D_0-D_2|}{m_2}\right| \cdot C_{ind} \cdot V_{ind}/D_0$, where C_{ind} is the concentration of indicator in the solution (μmol/g), V_{ind} is the volume of the indicator solution (ml); and m_1 and m_2 are the mass (g) of weighed quantities of the sample in the trial and control experiments, respectively. The positive sign in the formula corresponds to the multidirectional change in D_1 and D_2 relative to D_0; the negative sign, to the unidirectional change.

We estimated the microhardness of rock-forming minerals in the initial state and after treatment with nanosecond HPEMP of polished mineral sections using Vickers' method (*HV*, MPa; under ISO 6507-1: 2005) at PMT-3M microhardness tester, equipped with photoelectric ocular micrometer FOM-2. Vickers' microhardness value was calculated using standard equation: $HV = (0.189P/d^2) \times 10^6$, where P is the normal load applied to diamond tip, N; d is the arithmetic average lengths of both indent diagonals, μm. Experimental procedure runs as follows: microhardness of serpentine, calcite, and kimberlite rock was measured before and after HPEMP treatment at flat-parallel polished plates (sections) in middle and peripheral areas (angles and/or edges) of sections under experimental loads (P, g) on an indenter (calcite—50 g, serpentine—200 g, kimberlite rock—100 g; loading time was 10–15 s). In every test, approximately ten microhardness measurements were made in each of five selected section-surface areas and for every mineral surface state under examination.

In experiments, the olivine grains we pressed into "blocks" of 2.5 cm in diameter with plane-parallel polished surfaces (edges). Microhardness of three grains in five spots of every grain was determined under 200 g load on an indenter and 10–15 s loading exposure time for every block. After high-power electromagnetic pulse treatment the olivine microhardness was measured on the same grains and in the same areas for every of test modes. In all tests on mineral microhardness measurements, the difference in the diagonal lengths of indents formed after pressing a diamond tip into specimen surface did not exceed 3%.

4.3 Results and Discussions

4.3.1 *Disintegration of Mineral Media Owing to Electrical Breakdown Effect*

We determined in [7–17] the main mechanisms of disintegration of mineral particles by the following physical processes occurring when an electromagnetic pulse with high electric field strength (E) acts on the mineral medium being processed (Table 4.2). In cases, where the strength of the electromagnetic field acting on a solid dielectric medium is greater than the so-called electric strength (E_{st}) of the material being tested (for example, E_{st} of quartz is approximately (2–3)× 10 MV/m), electric breakdown develops in the medium, with electric current arising in a narrow channel, forming a so-called current filament. Inasmuch as the medium exposed to electromagnetic pulses consists of "free", essentially separate particles, it may happen that the bulk of breakdown discharge current would flow through air gaps between mineral grains without entering them. To prevent this unwanted effect, there is reason to use pulses with short leading edge duration τ_1 ($\sim$1 ns) and amplitude E_A significantly exceeding E_{st} of the material being tested in a static electric field. With these pulse parameters, the parasitic breakdown through intergranular air gaps fails to develop because of comparatively long time τ_2 required for gas (air) ionization in narrow, strongly curved channels between the particles, such that breakdown of solid dielectric grains becomes the main current channel, being the least sluggish one.

The development of a current filament is accompanied by rapid energy dissipation. During the initial stage of current filamentation (approximately 1–50 ns), the process can be treated as adiabatic, with thermal energy dissipation giving rise

Table 4.2 The action of high-power electromagnetic pulses and possible mechanisms of disintegration of mineral particles

Modes and parameters of pulse action	Physical processes in the materials
$E_A > E_{st}$, ($E_A \geq 10^7$ V/m) $\tau_1 < \tau_2$, ($\tau_1 \sim$ 1–5 ns) $t_{puls} \ll t_{heat}$, ($t_{puls} \sim$ 5–20 ns)	Electric breakdown with current filamentation: – local evaporation of the material – local increase of pressure – formation of a through breakdown channel along local heterogeneities to each other and to sample surface, i.e., loosening of the mineral matrix
Action of a series of pulses	Formation of numerous breakdown channels and microcracks
$E_A \geq E_{st}$ $\tau_1 < \tau_2$ $t_{puls} \approx t_{heat}$, [$10^{-3}$ s]	Electrothermal breakdown due to heat redistribution in the bulk of the material: – overheating – fusion and sintering of particles – closure of breakdown channels
$E_A \leq E_{st}$, $\tau_1 \geq \tau_2$, [10^{-6} s]	Spark discharge in air gap between electrodes

to evaporation of the material, sharp increase of pressure and, finally, disintegration of the material and formation of a thorough breakdown channel. Maintaining the discharge further would result in redistribution of heat in the bulk of the test sample. This may cause unwanted effects (Table 4.2), such as overheating, sintering of particles, fusion of particle surfaces and closure of as-formed microdamages and microcracks.

4.3.2 Transformation of Morphological and Structural-Chemical Properties of Kimberlite Rock-Forming Mineral Surface Under HPEMP-Irradiation

4.3.2.1 Fourier Transform IR-Spectroscopy

We assessed the structural and chemical variations in surfaces of olivine and serpentine after HPEMP treatment used the data of IR spectroscopy of diffusive reflection (DRIFTS). Bands relating to valence, deformation and torsional oscillations of silicium-oxygen tetrahedron [SiO_4] appeared in IR-spectrum of *olivine* (Fig. 4.1a). The basic spectrum band ~800–1000 cm^{-1} is due to splitting of

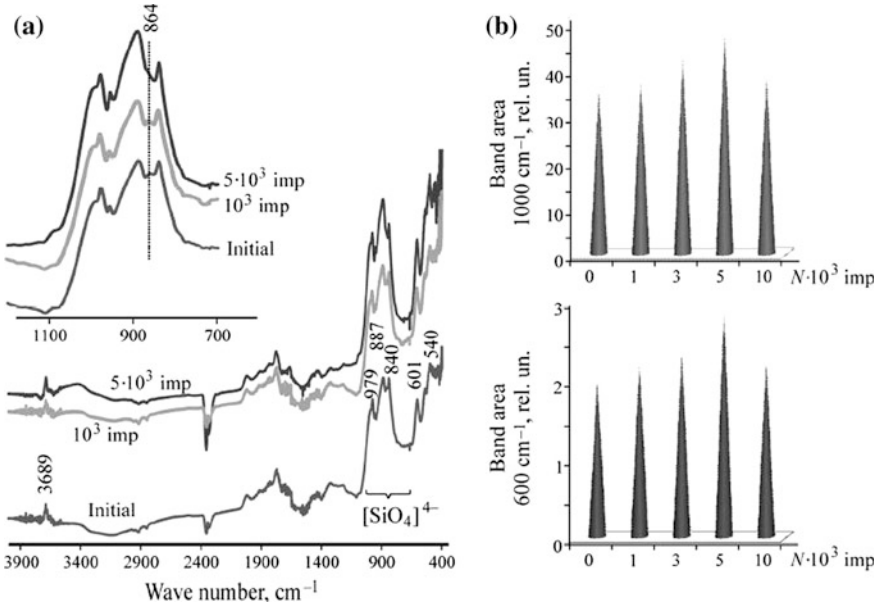

Fig. 4.1 **a** IR-spectra of olivine before and after HPEMP irradiation; **b** influence of pulsed effect on spectral integral characteristics

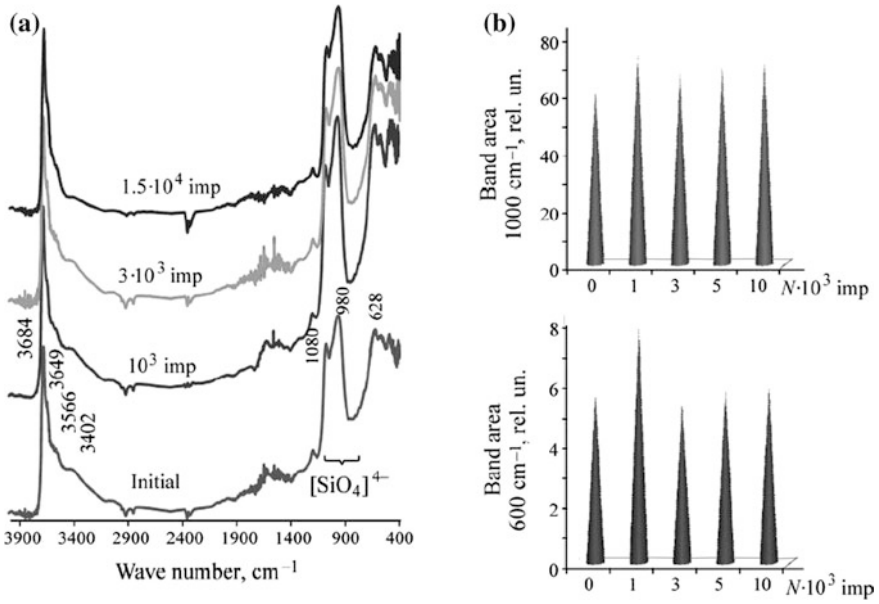

Fig. 4.2 **a** IR-spectra of serpentine before and after HPEMP irradiation; **b** influence of pulsed effect on spectral integral characteristics

degenerated asymmetric oscillation v_3 in Si–O bond. Bands of spectrum interval 400–600 cm^{-1} can be explained by splitting of asymmetric deformation oscillation v_4 of Si–O bond. Narrow band at 3689 cm^{-1} refers to OH–groups adsorbed at surface. Thereto, the analysis of IR-spectrum profile allowed conclusion that a test olivine specimen is presented with forsterite (Mg_2, Fe)SiO_4, which content was at least 88% in the test specimen in compliance with [26].

In IR-spectrum of *serpentine* we identified four bands: 3684, 3650, 3566, 3400 cm^{-1} were identified in the area of valence oscillations of O–H bond (3700–3400 cm^{-1}), Fig. 4.2a. The bond at 3684 cm^{-1} can be referred to valence oscillations of O–H bond in hydroxyl groups, coordinated with three magnesium atoms in octahedral layer; the rest bands (3650, 3566, 3400 cm^{-1}) are associated with oscillations of hydroxyl groups linked with octahedral layer cations (with Fe in our case), being magnesium substitutes in the mineral. Bands at 628, 980, and 1080 (1077) cm^{-1}, relating to valence oscillations of bonds Si–O and Si–O–Mg, were detected in spectral interval 400–1200 cm^{-1}. The analysis of specific characteristics of the mineral spectrum profile makes it possible to suppose that the test serpentine specimen is presented with antigorite [27].

HPEMP-treatment of powdered specimens caused appreciable alterations in spectra of minerals (Figs. 4.1 and 4.2). Alterations in IR-spectrum of olivine (Fig. 4.1a) concerned with the increasing intensity (area) of absorption bands 750–1100 cm^{-1} and dissipation of a weak band at 864 cm^{-1} as a result of $t_{tr} \sim 50$ s of nanosecond pulses treatment (Fig. 4.1a, b). Calculated integral characteristics

of serpentine spectra (Fig. 4.2a) indicated that the area of band (850–1150 cm^{-1}) pertaining to oscillations of silicium–oxygen bond in tetrahedral mineral structure increased 1.1–1.2 times in the result of a pulsed action (Fig. 4.2b).

Established variations in spectral characteristics may be caused by disturbance of microstructure of the surface minerals layers and deal with such processes, as formation, transition and interaction of defects (dislocations, microfractures, etc.) at different structural levels, as well as softening, and amorphization of the surface under pulsed high-intensity electric fields.

4.3.2.2 Analyzing of the XPES Data

To analyze in detail the chemical (valent) state of atoms of silicon and oxygen contained in the composition of serpentine surface layers, we investigated the X-ray photoelectron spectra of the Si 2*p* and O 1 *s* electron levels (the Mg 2 *s* spectrum is weakly sensitive to the chemical state of magnesium and was not analyzed in detail) and for the atoms of calcium, carbon, and oxygen in the composition of the calcite surface layers (Ca 2*p*, C 1 *s* and O 1 *s*).

Serpentine. Two components with binding energies of 102.4 and 103.4 eV that correspond to three-coordinate silicon Si^{3+} and silicon Si^{4+} were identified in the electron spectrum of the Si 2*p*-level [28]. The spectrum of the O 1 *s* level was decomposed with respect to three states: bridge oxygen Si–O–Si (E_{bond} = 532.51 eV), oxygen with bonds of Si–O–Mg (E_{bond} = 531.61 eV) [29], and oxygen bound with magnesium Mg–O (E_{bond} = 530.8 eV) [30]. Analysis of the XPS data showed (Table 4.3) that pulse actions during $t_{tr} \leq 10$ s with ($N_{pulse} \sim 10^3$) reduced fraction (at %) of trivalent silicon Si^{3+} and raised the atomic concentration of quadrivalent silicon Si^{4+}. This could have been due to the emission of electrons at the valent level of the atom under the action of HPEMP [15] and/or interaction between the mineral surface and the active products of the radiolytic decomposition of water [31].

In contrast, increasing the duration of pulse action to 100 s ($N_{pulse} \sim 10^4$) simultaneously reduced the atomic concentration of silicon Si^{4+} and the surface atomic concentration of oxygen bound in the state Si–O–Mg. These results indicate breaking of the bonds between the layers of magnesium–oxygen octahedrons and silicon tetrahedrons, resulting in disorder in the surface structure due to the octahedral layer escaping from its initial bound state. At the same time, triple valent

Table 4.3 Effect of HPEMP on the phase composition of the serpentine surface, according to the XPS data (at %)

HPEMP number, 10^3	Si 2*p*		O 1 *s*		
	Si^{3+}	Si^{4+}	Si–O–Si	Si–O–Mg	O–Mg
0	88.4	11.7	8.5	69.1	22.4
1	76.9	23.1	8.8	70.3	20.9
10	82.3	17.7	8.1	63.7	28.2

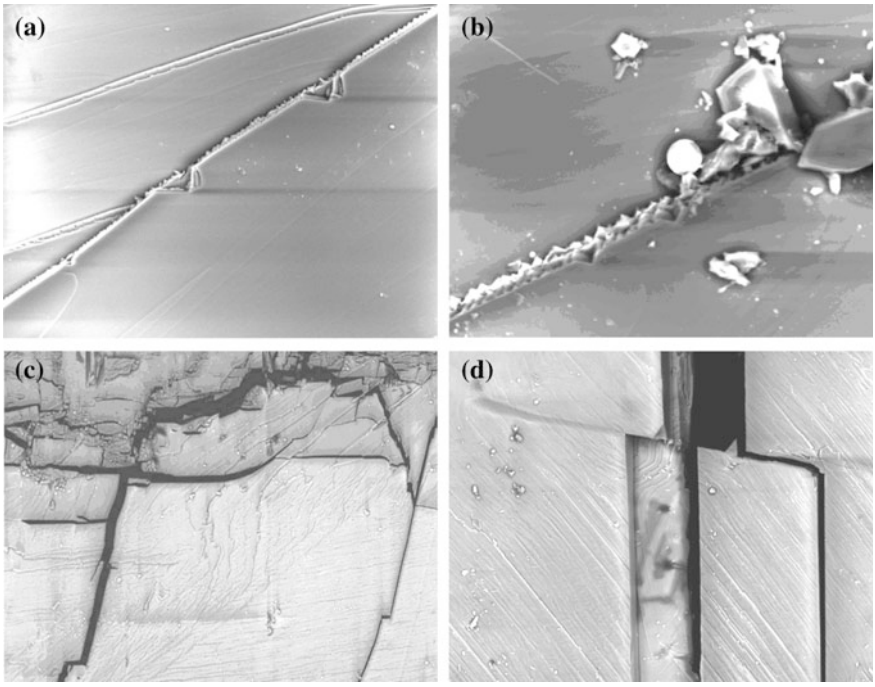

Fig. 4.3 SEM-image of calcite surface after high-voltage nanosecond electromagnetic pulse irradiation. Treatment time (t_{tr}) is 30 s (**a**, **b**) and 50 s (**c**, **d**); magnification are 1200 (**a**), 1700 (**b**), 200 (**c**), 550 (**d**)

silicon Si^{3+} was likely formed as a result of one electron from an oxygen ion O^{2-} being captured at the summit of the silicon tetrahedron [32].

In this investigation, we studied the high-voltage nanosecond pulses modification of dielectric mineral surface by measuring the change in the content of adsorption sites (active surface centers; $q(pK_\alpha)$, μmol/g) featuring with the following pK_α values: −4.4; 1.3; 4.1; 8.8; 12.8. The study of surface functionality by adsorption of acid-base indicators showed that content of adsorption sites on the serpentine surface for all values of pK_α have not changed under HPEMP-irradiation.

The initial surface of the olivine particles contains a large amount of the Brønsted base sites with $pK_\alpha = 12.8$; $q(pK_\alpha) = 31.8 \times 10^{-3}$ μmol/g (Fig. 4.4a). High-voltage nanosecond pulses processing ($t_{tr} \geq 50$ s) of olivine samples leads to a drastic decrease of the Brønsted base sites content with the simultaneous substantial increase in the content of Brønsted base sites with $pK_\alpha = 8.8$ and insignificant change in the content of Brønsted acid sites with $pK_\alpha = 4.1$ (Fig. 4.4a).

Calcite. Analysis of the XPS data [33] showed that the action of nanosecond HPEMPs in the range of change in the radiation dose (N_{pulse}) from 10^3 ($t_{tr} \sim 10$ s) to 3×10^4 (5 min) had no appreciable effect on the surface phase composition of the calcite particles. A gradual process of selective disintegration of the mineral was the

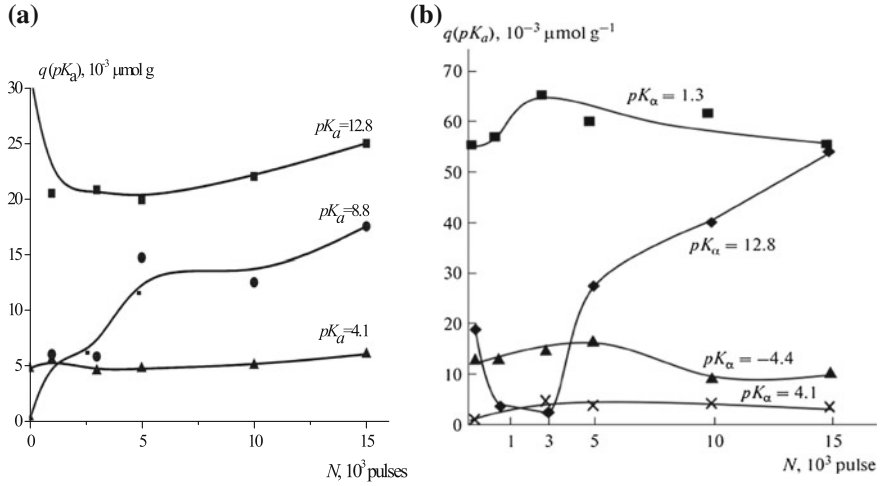

Fig. 4.4 Evolution (content) of the active adsorption sites with $pK_\alpha = -4.4$; 1.3; 4.1; and 12.8 on the olivine (**a**) and calcite (**b**) surface as function of the dose (N_{pulse}) of high-voltage nanosecond pulse irradiation

main mechanism behind the dissipation of energy in a high-voltage pulse electric field, namely, the opening (softening) of intercrystalline boundaries, the formation and propagation of cracks along the cleavage surfaces, and the formation of microcrystal fragments upon extending the pulse action to $t_{tr} \geq 50$ s (Fig. 4.3).

The adsorption of acid-base indicators showed that the Brønsted acid site predominated in the initial state on the calcite surface, $pK_\alpha = 1.3$, $q(pK_\alpha) = 55.4 \times 10^{-3}$ μmol/g; the number of the sites with $pK_\alpha = 4.1$ and 6.4 was an order of magnitude smaller. We also discovered the electron donating sites of the Lewis base type: $pK_\alpha = -4.4$, $q(pK_\alpha) = 13.4 \times 10^{-3}$ μmol/g and Brønsted base $pK_\alpha = 12.8$, $q(pK_\alpha) = 19.3 \times 10^{-3}$ μmol/g. In the result of HPEMP pretreatment for $t_{tr} \sim 10$ s, the mineral's surface dehydroxilated (the content of the Brønsted base sites with $q(pK_\alpha) = 12.8$ fell by a factor of more than six (Fig. 4.4b). There was also an increase in the concentration of Lewis-type aprotonic electron donating sites with $pK_\alpha = -4.4$ by a factor of ~ 1.3, along with proton-donating sites of the Brønsted type with $pK_\alpha = 1.3$ and $pK_\alpha = 4.1$. We observed the opposite effect when the duration of pulse treatment was increased to $t_{tr} \sim 100-150$ s: the calcite surface hydroxilated (the content of Brønsted base type with $pK_\alpha = 12.8$ grew by a factor of 4.6–9.3 (Fig. 4.4b)), and the concentration of both Lewis base and Brønsted acid sites fell.

4.3.2.3 Analytical Electronic (SEM/EDX) and Atomic-Force (AFM) Microscopy

According to the scanning electron microscopy (SEM/EDX) data, there were traces of surface break-downs on the polished sections of serpentine as a result of

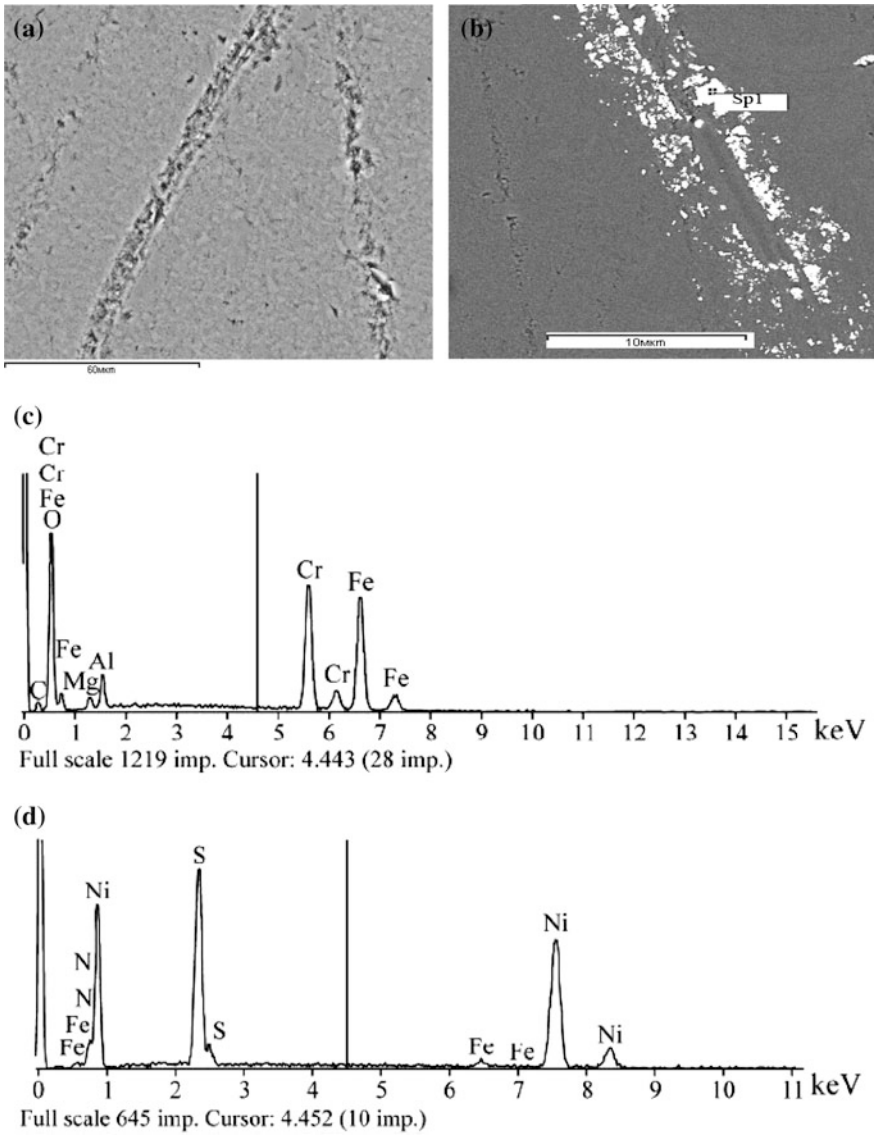

Fig. 4.5 SEM images (**a**, **b**) of the serpentine surface after HPEMP treatment (t_{tr} ~ 50 s), and EDX-spectra from the localization regions of microinclusions (**c**, **d**). The scale bars are 60 μm (**a**) and 10 μm (**b**)

electromagnetic pulse treatment for t_{tr} ~10–100 s, the surface layer of the mineral showed a picture of overall "loosening" (Fig. 4.5a, b). Traces of surface breakdowns formed at the sites of the localization of oxide microinclusions (possibly chromite $FeCr_2O_4$ (Fig. 4.5c) and/or magnesium–chromite $MgCr_2O_4$), sulfides (possibly milleritre NiS (Fig. 4.5b, d)), and other metal–containing microphases.

Using atomic-force microscopy (AFM), we revealed one morphological type of neoformations on olivine, calcite and serpentine surface corresponding to the processes of superficial structural and chemical transformations of the kimberlite rock-forming minerals due to the HPEMP-irradiation. This surface phase, represented by fine-disseminated spherical formations with sizes of 1 μm and lower (Fig. 4.6), is found mainly near the surface heterogeneity regions (surface scratch, crystallite boundaries). Single small formations are observed on the olivine surface (Fig. 4.6a). The surface of the calcite and serpentine was uniformly covered with neoformations (Fig. 4.6b–d); and for the serpentine we observed the self-similar nature of the particles distribution on the mineral surface (Fig. 4.6c, d).

Using special software package for nano- and microscale image processing SPIP™ 6.4.4 (Image Metrology), we estimated the alteration of surface roughness parameters (S_a and S_q), caused by HPEMP-irradiation. For example, the roughness average (S_a) of calcite surface increased by 1.2 times, and root mean square parameter (S_q) increased by a factor of 1.3.

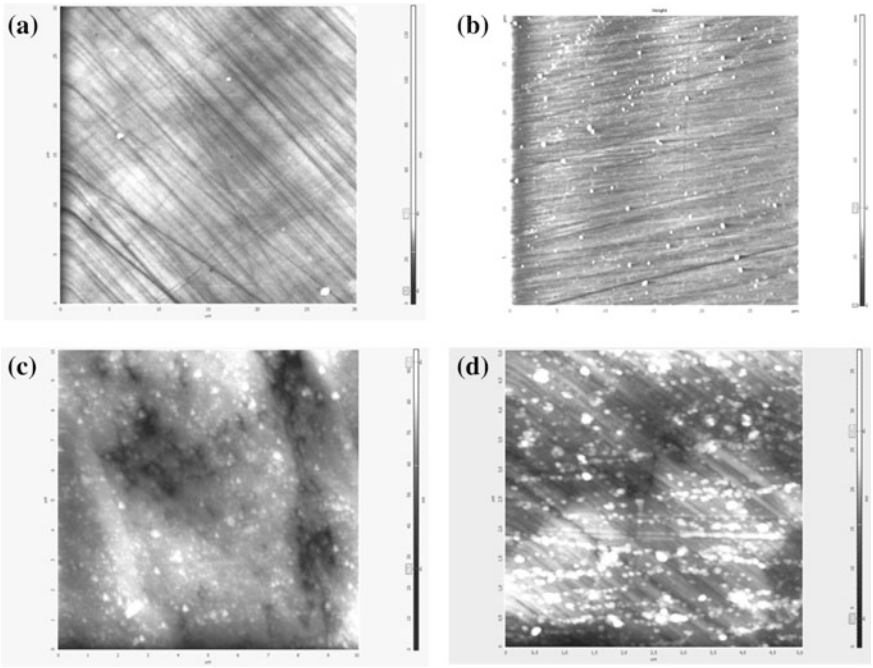

Fig. 4.6 Neoformations on olivine (**a**), calcite (**b**) and serpentine (**c**, **d**) surface as a result of HPEMP-irradiation; AFM, scanning fields: 30 × 30 μm^2, height $Z \sim 100$ nm (**a**, **b**); 10 × 10 μm^2, height $Z \sim 80$ nm (**c**), 5.0 × 5.0 μm^2, height $Z \sim 40$ nm (**d**)

4.3.3 *Effect of HPEMP-Irradiation on Microhardness of Kimberlite Rock-Forming Mineral*

Hardness is a well-recognized term for a property characterizing the ability of a surface layer of a solid body (material) to resist elastic and plastic deformation when other more solid body (an indenter) is intruding into it [34]. Hardness is not a physical constant; it is a complex characteristic depending on elastic (elastic-plastic) properties, brittleness (resistance to fracturing), microstructure of surface material layer, and test procedure. Nevertheless, hardness is "one of properties determined by general laws of a chemical bond in a substance" and variations in it are "conditioned by alteration of inter-atom bond forces, ion polarization and distance between lattice sites" [35].

Figure 4.7 presents the relationships (histograms) between relative variations in microhardness of minerals under HPEMP-irradiation *versus* the pulsed treatment time t_{tr} : $(HV_{0i} - HV_i)/HV_{0i}, \%$, where HV_{0i} is the microhardness of *i*th specimen in initial state; HV_i is the microhardness of *i*th specimen after electric pulse treatment.

The olivine microhardness (Mohs' hardness, 6.5–7) fell monotonically from 4250 MPa (the average *HV* of the samples in the initial state) to 1560 MPa after

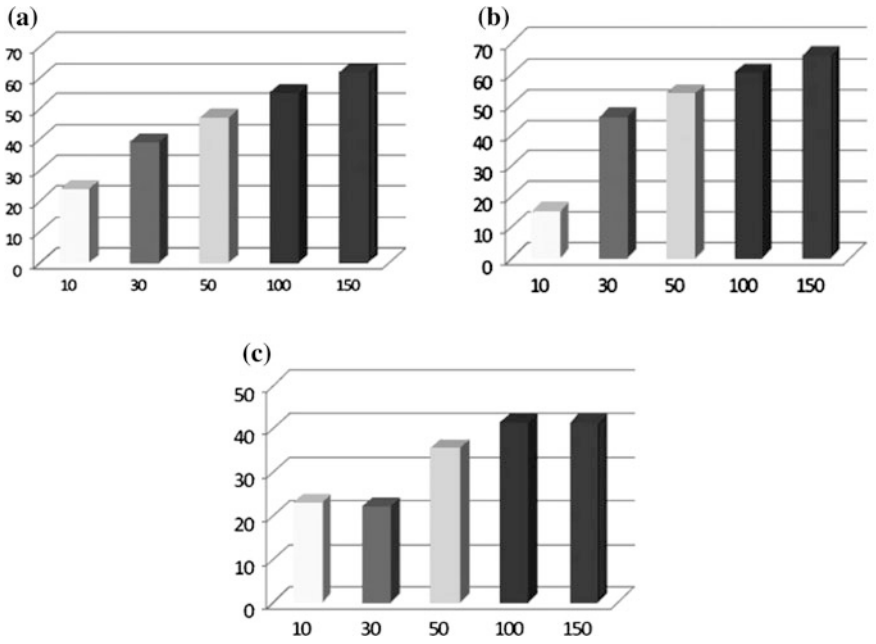

Fig. 4.7 Relative variation in microhardness ($\Delta HV_i/HV_{0i}$, %) olivine (**a**); calcite (**b**), serpentine (**c**) *versus* HPEMP treatment time (t_{tr}, s)

HPEMP treatment as the time of pulse treatment was increased to $t_{tr} \sim 150$ s; the maximum relative change in *HV* was approximately 63% (Fig. 4.7a).

The maximum relative drop in calcite (Mohs' hardness, 3) microhardness to 66% (from 790 MPa down to 265 MPa) was observed in the result of the HPEMP action for 100–150 s (Fig. 4.7b). In contrast to olivine, there was a substantial reduction in the microhardness of the calcite samples (by 45%) for the first 10–30 s of electric-pulse treatment, demonstrating the effectiveness of short pulse energy actions for minerals with relatively low levels of hardness according to Mohs' scale.

The serpentine microhardness (Mohs' hardness, 2.5–4) fell from 430 MPa (*HV* in the initial state) to 260 MPa after HPEMP action for 50–150 s after increasing the duration of pulse treatment. The maximum relative change in the microhardness ΔH, % was 42% (Fig. 4.7c). The increased duration of pulse treatment $t_{tr} \geq 50-150$ s did not substantially alter the mineral *HV*.

With increasing in time electric pulse treatment, the successive reduction in microhardness of binding mass of kimberlite rock was observed from 360 to 200 MPa ($t_{tr} \approx 100 - 150$ s); the relative reduction in *HV* was approximately 44%.

The experimental data obtained in the present research work show the softening of rock-forming mineral-dielectrics under high-voltage nanosecond electromagnetic pulse irradiation. The experimental data on microhardness variations for rock-forming minerals correspond to the results of our spectroscopic investigations. Apart from other factors, the rate of microhardness variation is determined by mineral Mohs'hardness (nature, energy, chemical bonds, and valence) and is maximal at small doses of electromagnetic pulsed radiation for minerals with relatively low hardness level.

In this way, the experimental results proved applicability of the pulsed energy effect to stimulate softening of rock-forming minerals of diamond-bearing kimberlites and to preserve the wholeness (integrity) of diamond crystals in ore-grinding circuits due to reduced time of kimberlite rock processing in autogenous mills.

4.4 Conclusions

In the result of spectroscopic investigations, we established the mechanism and stages of structural-chemical transformations of rock-forming kimberlite minerals surface under high-voltage nanosecond electromagnetic pulses irradiation. According to XPS data, at the initial stage of pulsed serpentine treatment during $t_{tr} \leq 10$ s, it was observed the reduction in portion (at. %) of trivalent silicium Si^{3+} and increase in atomic concentration of silicium in four-valent state Si^{4+} in near-surface layers of the mineral.

At the next stage, $t_{tr} \approx 100$ s, the atomic concentration of silicium Si^{4+} declined with concurrent reduction in surface concentration oxygen atoms bound in

Si–O–Mg state. These results indicate rapture of the bond between layers of magnesium-oxygen octahedral and silicium tetrahedral, followed disordering of the surface structure because of a "shear" of octahedral layer from its initial location. The concurrent formation of trivalent silicium Si^{3+} is supposed as a result of capture of one of electrons, belonging to oxygen ion O^{2-} in apex of silicium tetrahedral.

The microhardness test data confirmed the results of spectroscopic investigations: we found using Vickers' method that the effect of high-intensity pulsed fields leads to reduction in microhardness of rockforming minerals, in total, by 40–66%. The softening effect of natural dielectric minerals is mainly connected with the "disturbance" (damage) of microstructure of surface layers, new-formed defects at different structural levels (dislocations, microcracks, incomplete surface break-ups), disordering and amorphisation of the mineral surface. The rate of variations in microhardness of minerals relates to their hardness and reaches the maximum at low doses of electromagnetic pulsed radiation for minerals with relatively low Mohs' hardness level.

Acknowledgements This work was supported by the RF President's grant for the state support of leading scientific schools of the Russian Federation, Academician V.A. Chanturia's School NSh-7608.2016.5.

References

1. V.A. Chanturiya, K.V. Godun, Y.G. Zhelyabovskii, B.E. Goryachev, Gornyi Zhurnal **3**, 67 (2015) (in Russian)
2. V.A. Chanturiya, B.E. Goryachev, *Modern Technologies of Complex Processing of Mineral Raw Materials* (Ore & Metals, Moscow, 2008), p. 151 (in Russian)
3. A.I. Kaplin, *Intensification of Wet Autogenous Kimberlite Grinding Based on Electrochemical Conditioning of Aqueous Systems*. Cand. Tech. Sci. Thesis, IPKON RAN, Moscow (2010) (in Russian)
4. V.A. Chanturiya, G.P. Dvoichenkova, I.Zh. Bunin et al., J. Min. Sci. **37**(6), 151 (2014)
5. A.N. Didenko, B.V. Zverev, A.V. Prokopenko, Trans. (Doklady) Russian Akad. Sci. **403**(2), 19 (2005)
6. A.N. Didenko, *Microwave Energetic: Theory and Practice* (Nauka, Moscow, 2003) (in Russian)
7. V.A. Chanturia, Y.V. Gulyaev, V.D. Lunin, I.Zh. Bunin, V.A. Cherepenin, V.A. Vdovin, A. V. Korzhenevsky, Trans. (Doklady) Russian Akad. Sci. **366**(5), 680 (1999)
8. V.A. Chanturia, Y.V. Gulyaev, I.Zh. Bunin, V.A. Vdovin, A.V. Korzhenevsky, V.D. Lunin, V.A. Cherepenin, Trans. (Doklady) Russian Akad. Sci. 379(3), 372 (2001)
9. V.A. Chanturiya, Y.V. Gulyaev, I.Zh. Bunin et al., J. Min. Sci. **37**(4), 427 (2001)
10. I.Zh. Bunin, N.S. Bunina, V.A. Vdovin, P.S. Voronov, Y.V. Gulyaev, A.V. Korzhenevsky, V.D. Lunin, V.A. Chanturia, V.A. Cherepenin, Bull. Russian Acad. Sci.: Phys. **65**(12), 1950 (2001)
11. V.A. Chanturiya, I.Zh. Bunin, A.T. Kovalev, Bull. Russian Acad. Sci.: Phys. **68**(5), 629 (2004)
12. V.A.Chanturiya, I.Zh. Bunin, A.T. Kovalev, Bull. Russian Acad. Sci.: Phys. **69**(7), 1058 (2005)

13. V.A. Chanturiya, K.N. Trubetskoy, S.D. Viktorov, I.Zh. Bunin, *Nanoparticles in Geological Materials Destruction and Extraction Processes* (IPKON RAS, Moscow, 2006). (in Russian)
14. V.A. Chanturiya, I.Zh. Bunin, Min. Sci. **43**(3), 311 (2007)
15. V.A. Chanturiya, I.Zh. Bunin, A.T. Kovalev, Bull. Russian Acad. Sci. Phys. **71**(5), 646 (2007)
16. V.A. Chanturiya, I.Zh. Bunin, in *Proceedings TMS 2006 135th Annual Meeting and Exhibition, Supplemental Proceeding: Materials Characterization, Computation and Modeling*, TMS, San Antonio, USA (2006), p. 93
17. I.Zh. Bunin, *Theoretical Fundamentals of Nanosecond Electromagnetic Impulse Effects on Disintegration and Exposure of Finely Dispersed Mineral Complexes and Precious Metal Recovery from Ores*, Dr. Tech. Sci. Thesis, (Moscow, 2009) (in Russian)
18. V.A. Chanturiya, I.Zh. Bunin, M.V. Ryazantseva, L.O. Filippov, Miner. Process. Extr. Metall. Rev. **32**(2), 105 (2011)
19. V.A. Chanturiya, I.Zh. Bunin, *Nanobiotechnology in Energy, Environment and Electronics: Methods and Applications. Pan Stanford Series on Nanobiotechnology* (Pan Stanford Publishing Pte. Ltd., CRC Press, USA, 2015)
20. I.Zh. Bunin, V.A. Chanturiya, M.V. Ryazantseva, I.A. Khabarova, E.V. Koporulina, A.T. Kovalev, in *Advanced Materials—Manufacturing, Physics, Mechanics and Applications. Springer Proceedings in Physics,* vol. 175, eds. by I.A. Parinov, S.-H. Chang, V.Y. Topolov (Springer, Heidelberg, 2016), p. 3
21. V.A. Cherepenin, Phys. Usp. **49**(10), 1097 (2006)
22. L.P. Hammett, *Physical Organic Chemistry. Reaction Rates, Equilibria and Mechanisms* (McGraw-Hill Book Company, New York, 1970)
23. K. Tanabe, *Solid Acids and Bases. Their Catalytic Properties* (Academic Press, Kodansha, 1970)
24. M.V. Ryazantseva, I.Zh. Bunin, J. Min. Sci. **51**(5), 140 (2015)
25. I.V. Vasiljeva, S.V. Mjakin, A.V. Makarov, A.N. Krasovsky, A.V. Varlamov, Appl. Surf. Sci. **252**(24), 8768 (2006)
26. V.E. Hamilton, Chemie der Erde – Geochemistry **70**(1), 7 (2010)
27. V.C. Farmer, *The Infrared Spectra of Minerals* (Mineralogical Society, London, 1974)
28. S. Mohammadnejad, J.L. Provis, J.S.J. van Deventer, Miner. Eng. **52**, 31 (2013)
29. V.P. Zakaznova-Herzog, H.W. Nesbitt, G.M. Bancroft, J.S. Tse, Geochim. Cosmochim. Acta **72**(1), 69 (2008)
30. C.D. Wagner, A.V. Naumkin, A. Kraut-Vass, et al., *NIST X-ray Photoelectron Spectroscopy Database*. http://srdata.nist.gov/xps
31. A.K. Pikaev, *Modern Radiation Chemistry. Radiolysis of Gases and Liquids* (Nauka, Moscow, 1986) (in Russian)
32. S.M. Kacmarek, W. Chen, G. Boulon, Crystal Res. Thechnol. **41**(1), 41 (2006)
33. V.A. Chanturiya, I.Zh. Bunin, M.V. Ryazantseva, I.A. Khabarova, E.V. Koporulina, N.E. Anashkina, J. Min. Sci. **50**(3), 573 (2014)
34. N.P. Yushkin, *Mechanical Properties of Minerals* (Nauka, Leningrad, 1971). (in Russian)
35. RSh Shafeev, V.A. Chanturiya, V.P. Yakushkin, *Ionization Radiation Effect onto Flotation Process* (Nauka, Moscow, 1973). (in Russian)

Chapter 5
Properties of In_2O_3 Films, Deposited by dc-Magnetron Sputtering on Al_2O_3 Substrates with Different Temperatures

Vladimir A. Gritskikh, Igor V. Zhikharev, Svetlana V. Kara-Murza, Nataliya V. Korchikova, Tatyana V. Krasnyakova, Yuri M. Nikolaenko, Alexandr A. Tikhii, Anatoly V. Pavlenko and Yuriy I. Yurasov

Abstract The In_2O_3 films were deposited by dc-magnetron sputtering on substrates of Al_2O_3 (012) at different temperatures (20–600 °C). Ellipsometric and optical transmission measurements were used to investigate the effect of substrate temperature and annealing on the properties of the films. The profiles of refraction index, direct and "indirect" band gap were determined. The annealing naturally results in unification of the properties of the explored films: the refraction index grows, the degree of homogeneity on a thickness increases and the thickness of the disturbed layer on the surface of films decreases, i.e. film material is compact. Also the annealing reduces the energies of band-to-band transitions. This can be explained by a decrease of influence of barriers in the annealed films. However, the width of direct band gap changes more than "indirect" one. It seems that this is related to the mechanism of indirect transitions: phonon participation facilitates the interband transitions, even if they are hampered by the presence of extra barriers caused by grain boundary. The last result may indirectly evidence of the existence of indirect transitions in this material.

V.A. Gritskikh · S.V. Kara-Murza · N.V. Korchikova · T.V. Krasnyakova · A.A. Tikhii (✉)
Lugansk Taras Shevchenko University, 2, Oboronnaya Street, Lugansk 91011, Ukraine
e-mail: ea0000ffff@mail.ru

I.V. Zhikharev · Y.M. Nikolaenko · A.A. Tikhii
Donetsk Institute for Physics and Engineering Named After A.A. Galkin, 72, R. Luxembourg Street, Donetsk 83114, Ukraine

T.V. Krasnyakova
Institute of Physical Organic and Coal Chemistry, 70, R. Luxembourg Street, Donetsk 83114, Ukraine

A.V. Pavlenko · Y.I. Yurasov
Research Institute of Physics, Southern Federal University, 105/42, Bolshaya Sadovaya Street, Rostov-on-Don 344006, Russia

A.V. Pavlenko · Y.I. Yurasov
South Scientific Centre RAS, 41, Chehov Street, Rostov-on-Don 344006, Russia

I.A. Parinov et al. (eds.), *Advanced Materials*, Springer Proceedings in Physics 193, DOI 10.1007/978-3-319-56062-5_5

5.1 Introduction

Semiconductor of In_2O_3 is known enough and quite studied material. Nevertheless, interest of researchers does not weaken to films of this material, based on a number of their unique properties. In_2O_3 films are optically transparent, high conductive, very sensible to composition of ambient atmosphere. Thus, conductivity changes depending on composition of gas environment have quick-response and reversible character. Films of In_2O_3 already found wide application as transparent contacts and gas sensors. Doping of In_2O_3 by different dopants can widely change properties of films, especially, its conductivity, sensitiveness to the environments of gases of different composition and other.

5.2 Objects and Methods of Researches

We researched optical properties of In_2O_3 films, deposited by dc-magnetron sputtering [1] on substrates of Al_2O_3 (012). The composition of the target was controlled using X-ray diffractometer DRON-3. Its diffraction pattern is fully matched to the one of stoichiometric composition of In_2O_3 (Fig. 5.1). Sputtering was performed in an argon-oxygen atmosphere at the temperatures of substrates 600, 300, and 20 °C during 1 h; the working current was 50 mA, and voltage was 300 V. Optical properties were studied by the methods of spectrophotometry in the range of wavelengths from 190 to 1100 nm (photon energies 1–6 eV) and reflecting multiangular ellipsometry on the wavelength of helium-neon laser (632.8 nm). Ellipsometric measuring was performed with the purpose of researching the structure of films; spectrophotometric measurements were conducted with the purpose of determining the character of band-to-band transitions and the band gap widths according the analysis of fundamental absorption edge in the spectra of optical transmission.

5.3 Ellipsometric Research

Ellipsometric angles Δ and Ψ, determined by wavelength of probe radiation, angle of incidence φ, refraction indices of transparent film n and substrate n_0 (it is possible to neglect anisotropy of substrate) and thickness of film d, were measured. The results of measuring of Δ and Ψ for the surfaces with complex structure were interpreted by our method, based on modification of the method of Malin-Vedam [2] and uses physically infinitely thin layers with the fixed thickness and certain optical parameters changing on the laws set in advance [3].

The method defines that films sputtered on substrates with the temperature of 300 °C and more (“hot”) are homogeneous on a thickness, but have disturbed

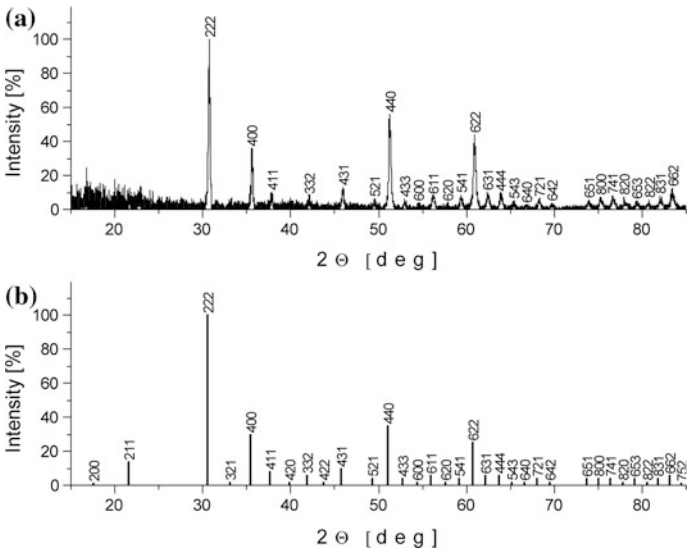

Fig. 5.1 X-ray diffraction pattern of In_2O_3 target (**a**) versus PDF2 card number: 6-416 (**b**)

surface layer. At the same time, the thickness of the film and the disturbed layer decrease with increase of the substrate temperature. The refraction index increased with increase the substrate temperature contrariwise.

The results for the films on the "hot" (300 and 600 °C) substrates are illustrated with profiles of the refractive index with the corresponding thickness in Fig. 5.2. The dependencies of the experimental and calculated ellipsometric angles Δ and Ψ on angle of incidence of the elliptically polarized light are present in Fig. 5.3. They show a good agreement of experiment with the results of calculations. These dependencies of properties of In_2O_3 films, presented in Fig. 5.2, are enough obvious: the higher substrate temperature during deposition leads to the greater density and therefore film material is less defective.

The results of processing of data of the ellipsometric measuring of film of In_2O_3, deposited on "cold" (20 °C) substrate of Al_2O_3 are present in Fig. 5.4a, b. As seen from the figure, the refraction index of layer of the actually explored material at first increases from 1.9 at the substrate-film interface, and then decreases from 2 to 1.8 in the disturbed layer. Material of film is "friable", thus, its general thickness more than one in cases considered before; the disturbed layer is also characterized by the larger value of thickness. The obtained results are in accordance with the foregoing consideration. It should be noted, that the registered growth of refraction index in the base material of film, presumably, is caused by the increase of temperature of the depositing material in the direction to the surface when sputtering.

The thicknesses of all annealed films are near to 400 nm, the refraction index approaches 2, thickness of the disturbed layer is 21 nm. It should be noted, that

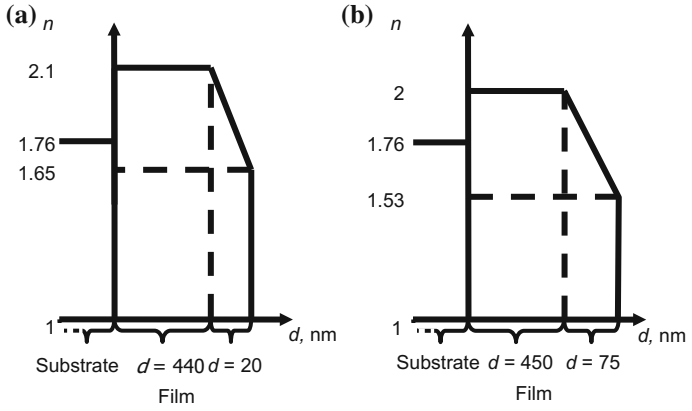

Fig. 5.2 Profiles of the refractive index of the films deposited on substrates with temperature 600 °C (**a**) and 300 °C (**b**)

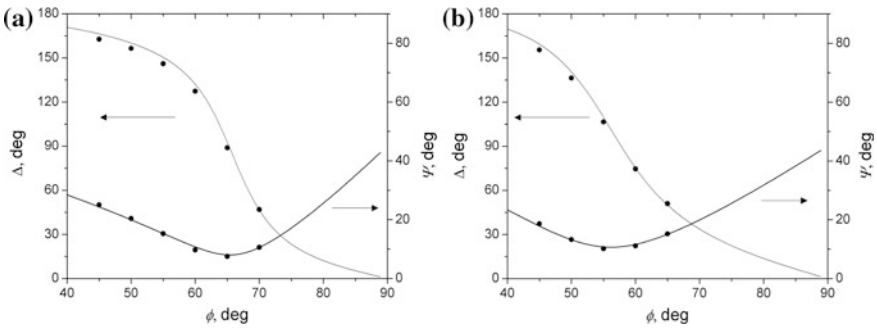

Fig. 5.3 Calculated and experimental dependencies of the ellipsometric angles Δ and Ψ on the incidence angle φ for the films deposited on substrates with temperature 600 °C (**a**) and 300 °C (**b**)

annealing had the most forming influence on the film deposited on substrate at 20 °C. The influence of annealing on two other films is slight.

5.4 Study of the Fundamental Absorption Edge

This is a particular interest to study the fundamental absorption edge, depending on the substrate temperature during the deposition of In_2O_3 films. It is related to the discussion about the nature of interband transitions in these materials [4, 5]. The observed absorption spectra [6, 7] suggest the presence of transitions with energy $E_g^{\text{indir}} = 2.62-2.69$ eV, interpreted as the "indirect" band-to-band transitions, and

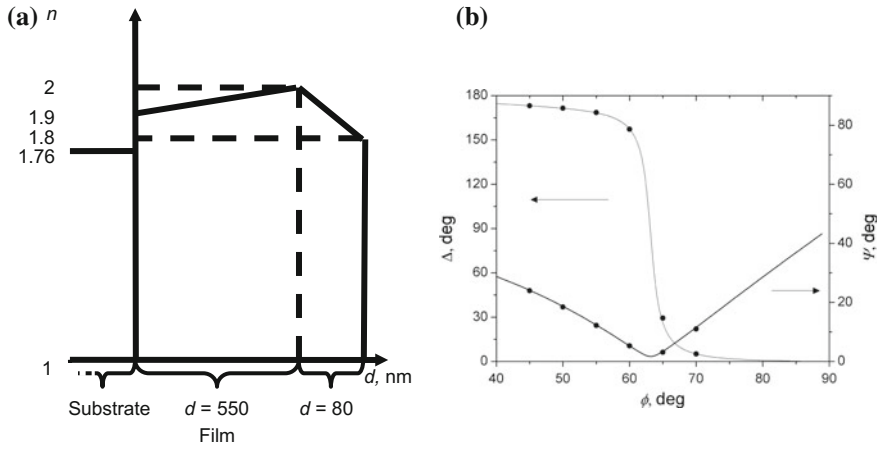

Fig. 5.4 Results of ellipsometric measurements of In_2O_3 films deposited on the substrate with the temperature 20 °C: **a** profile of the refractive index, **b** calculated and experimental dependencies of the ellipsometric angles Δ and Ψ on the incidence angle φ

direct transitions with energy $E_g^{\Gamma} = 3.56-3.75$ eV. However, based on calculations of the electronic structure of the defect-free indium oxide, the authors of [4, 5] concluded that the difference in direct and "indirect" transitions energies is less than 50 meV, and the observed "indirect" transitions are associated with the imperfections of the material structure. As the experimental confirmation, the authors refer to the boundary effects and the associated depleted layers found in indium oxide (characteristic activation energy is 2.2−3.5 eV) [5, 8, 9]. In this view, the experiments, aimed at the study of the fundamental absorption edge of In_2O_3 films depending on the degree of their imperfection, are important.

The spectral dependence of the absorption coefficient α was calculated from the optical transmission spectra according to the equation:

$$T = (1 - R)^2 e^{-\alpha d}.$$

Here T is the energy transmission coefficient, R is the energy reflection coefficient from system film-substrate, d is the film thickness.

Figure 5.5 shows the fragments of the optical transmission spectra corresponding to the fundamental absorption edge for films sputtered on substrates with different temperatures before and after annealing. Each curve on the graphs normalized to the maximum transmission of the corresponding sample in the wavelength range of 190–1100 nm. The alternating maxima and minima on these curves in the clear area are due to interference effects in the film.

It is known that zones are spherically symmetric, the transition from the valence band to the conduction band are direct. In this case, the band gap E_g^{Γ} is associated with the intrinsic absorption coefficient near fundamental absorption edge by ratio:

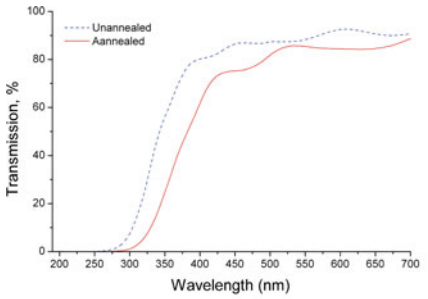

(a) Deposition temperature of substrate is 20 °C

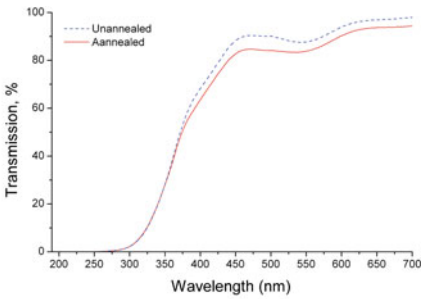

(b) Deposition temperature of substrate is 300 °C

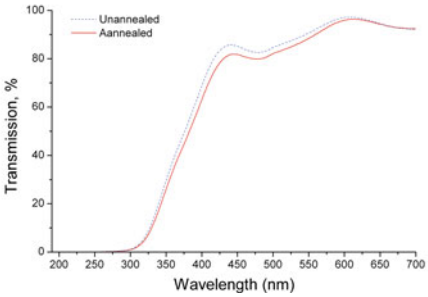

(c) Deposition temperature of substrate is 600 °C

Fig. 5.5 Fundamental absorption edge of the films before and after annealing

$$\alpha \sim \left(h\nu - E_g^{\Gamma}\right)^{1/2}, \quad \text{when } h\nu \geq E_g^{\Gamma}.$$

If zones are not spherically symmetric, indirect transitions become possible, which are implemented in the absorption or emission of phonons. In this case, the band gap is related to the absorption coefficient α near the fundamental absorption edge by ratios:

$$\alpha \sim \left(h\nu - E_g^{\text{indir}} + h\nu_P\right)^2, \quad \text{when } h\nu \geq E_g^{\text{indir}} - h\nu_P$$

and

$$\alpha \sim \left(h\nu - E_g^{\text{indir}} - h\nu_P\right)^2, \quad \text{when } h\nu \geq E_g^{\text{indir}} + h\nu_P.$$

Here $h\nu$ is the photon energy, $h\nu_P$ is the phonon energy.

We estimated the band gap for direct E_g^{Γ} and "indirect" E_g^{indir} band-to-band transitions basing on the fundamental absorption edge. Figure 5.6a, b shows the

corresponding dependence of the absorption coefficient α^2 and $\alpha^{0.5}$ versus the photon energy near the fundamental absorption edge for the "cold" and "hot" films. The obtained values of energies are shown in Table 5.1. This table also shows the difference between E_g^{Γ} and E_g^{indir} before and after annealing:

$$\Delta E = E_g^{\Gamma} - E_g^{indir}.$$

As seen from Fig. 5.6a, b, as well as from Table 5.1, the band gap of unannealed films is smaller at higher substrate temperature during film deposition. Annealing leads films to unification in the band gap (Fig. 5.7), and, as expected, has a normalizing effect mainly on the film deposited on the "cold" substrate. The difference between the energies of the direct and "indirect" transitions ΔE is virtually independent of the annealing of the films deposited on the "hot" substrate. This difference is slightly higher for the films, deposited on "cold" substrates. Should be noted that the difference $\Delta E \approx 1$ eV is consistent with the data in the short introduction [10, 11].

To clarify the nature of the reduction of ΔE in the result of annealing the film deposited on the "cold" substrate, we examined the difference between band gap energy of the direct transition $\Delta E_g^{\Gamma} = E_{g,\,unan}^{\Gamma} - E_{g,an}^{\Gamma}$ and "indirect" $\Delta E_g^{indir} = E_{g,unan}^{indir} - E_{g,an}^{indir}$ transitions before and after annealing (Table 5.2).

From the data presented in Table 5.2, it is seen that annealing has better impact on energy of direct transitions. It seems that this effect is related to the mechanism of indirect transitions—phonon participation facilitates the interband transitions, even if they are hampered by the presence of extra barriers caused by grain boundary.

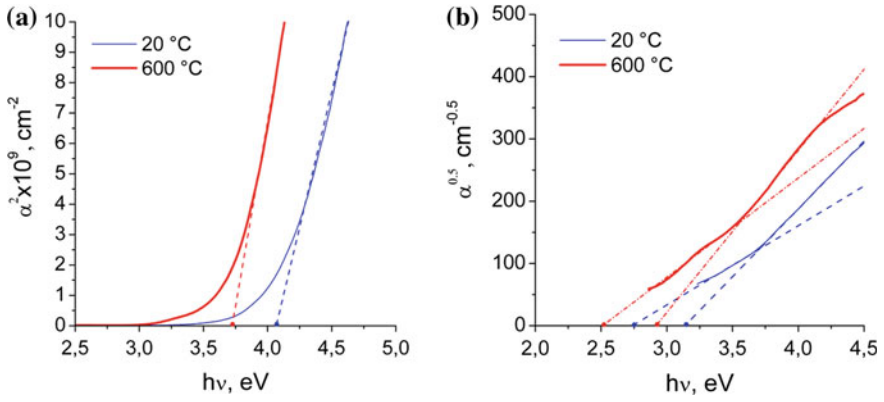

Fig. 5.6 The dependences of the absorption coefficient α^2 (**a**) and $\alpha^{1/2}$ (**b**) on photons energy for two films deposited on "hot" and "cold" substrates before annealing

Table 5.1 Widths of direct and "indirect" band gaps

Substrate temperature (°C)	Before annealing			After annealing		
	E_g^{Γ} (eV)	E_g^{indir} (eV)	ΔE (eV)	E_g^{Γ} (eV)	E_g^{indir} (eV)	ΔE (eV)
20	4.07	2.94	1.13	3.71	2.69	1.02
600	3.72	2.72	1	3.71	2.67	1.04

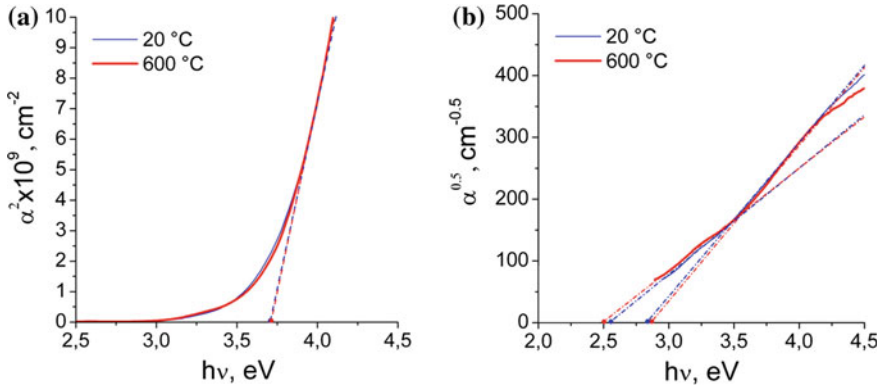

Fig. 5.7 Dependencies of the absorption coefficient α^2 (**a**) and $\alpha^{1/2}$ (**b**) on photons energy for two films deposited on "hot" and "cold" substrates after annealing

Table 5.2 Change of the band gap width for direct and indirect transitions in the film sputtered at substrate with temperature 20 °C

E_g^{Γ} (eV)		ΔE_g^{Γ} (eV)	E_g^{indir} (eV)		ΔE_g^{indir} (eV)
Before annealing	After annealing		Before annealing	After annealing	
4.07	3.71	0.36	2.94	2.69	0.25

5.5 Conclusion

The ellipsometric study showed that the annealing results in unification of the profiles of refraction index of the explored films: the refraction index grows, the degree of homogeneity on a thickness increases and the thickness of the disturbed layer on the surface of films decreases, i.e. film material is compact.

Obvious effect of annealing is the elimination of structural defects and increase of the grain size. Therefore, reducing the energies corresponding to the band-to-band transitions can be explained by a decrease of influence of barriers in the annealed films. A smaller effect of annealing on the energy of indirect transitions is due to the fact, that phonons, which participate in the indirect transitions, have any values of the wave vectors and different energies. The last result may

indirectly evidence of the existence of indirect transitions and demonstrates the need for further research to establish the nature of band-to-band electronic transitions in the indium oxide.

Acknowledgements This work was financially supported by the Ministry of Education and Science of the Russian Federation: themes Nos. 1927, 213.01-2014/012-VG and 3.1246.2014/K (the basic and project parts of the state task), and performed on equipment of the collective use center "Electromagnetic, Electromechanical and Thermal Properties of Solids" of the Institute of Physics, Southern Federal University.

References

1. Y.M. Nikolaenko, A.B. Mukhin, V.A. Chaika, V.V. Burkhovetskii, Tech. Phys. **80**(8), 1189 (2010)
2. A.A. Tikhii, V.A. Gritskikh, S.V. Kara-Murza, Y.M. Nikolaenko, I.V. Zhikharev, Opt. Spectrosc. **112**(2), 300 (2012)
3. A.A. Tikhii, V.A. Gritskikh, S.V. Kara-Murza, N.V. Korchikova, Y.M. Nikolaenko, V.V. Faraponov, I.V. Zhikharev, Opt. Spectrosc. **119**(2), 268 (2015)
4. P. Erhart, A. Klean, R.G. Egdell, K. Albe, Phys. Rev. B **75**, 153205 (2007)
5. A. Klein, Appl. Phys. Lett. **77**, 2009 (2000)
6. G.B. Gonzalez, J.B. Cohen, J.H. Hwang, T.O. Mason, J. Appl. Phys. **89**, 2550 (2001)
7. D.R. Lide (ed.), *Handbook of Chemistry and Physics*, 85th edn. (CRC Press, Boca Raton, FL, 2004)
8. Y. Gassenbauer, R. Schafranek, A. Klein, S. Zafeiratos, M. Hävecker, A. Knop-Gericke, R. Schlögl, Phys. Rev. B **73**, 245312 (2006)
9. S.P. Harvey, T.O. Mason, Y. Gassenbauer, R. Schafranek, A. Klein, J. Phys. D Appl. Phys. **39**, 3959 (2006)
10. R.A. Pollak, S. Kowalczyk, L. Ley, D.A. Shirley, Phys. Rev. Lett. **29**, 274 (1972)
11. T. Kendelewicz, P.H. Mahowald, K.A. Bertness, C.E. McCants, I. Lindau, W.E. Spicer, Phys. Rev. B **36**, 6543 (1987)

Chapter 6
Interaction of Elements of the Sixth Period with Grain Surfaces in Steel

Yuri F. Migal and Vladimir I. Kolesnikov

Abstract Interaction between atoms of impurity and alloying elements of the sixth period and grain surfaces in iron was investigated by quantum chemical methods based on the DFT approach. We used a two-periodic slab model within which a boundary between grains is simulated by a system consisting of a few monoatomic layers of iron and a single layer of impurity (or alloying) atoms in the middle of them. Grain surfaces corresponding to the Miller indices (100) and (110) were considered. We calculated the energy required for disintegration (decohesion) of the system into two parts. It is shown that dependence of disintegration energy of the system on atomic number of impurity and alloying atoms is of the same type for the models with different Miller indices. The compatibility of impurity elements with iron at grain boundaries in steel was estimated. It is consistent with known experimental and theoretical data and conforming to Mendeleev periodic law. The dependences discovered can be applied for predicting wear resistance and strength properties of steel containing impurity and alloying elements of the sixth period.

6.1 Introduction

Strength of polycrystalline materials is known to be determined in many respects by properties of intercrystalline interfaces (grain boundaries) whose thickness is comparable to the size of atoms. Grain boundaries play a particularly important role in deformation and fracture processes at elevated temperatures. One of the reasons of strength reduction of polycrystalline materials, often referred to in literature, is grain boundary segregation. This phenomenon is caused by transition of impurity and alloying elements from the bulk of grains to the boundaries between them [1–6]. Another variant of the appearance of impurity atoms at grain boundaries is

Y.F. Migal (✉) · V.I. Kolesnikov
Rostov State Transport University, 2, pl. Rostovskogo Strelkovogo Polka Narodnogo Opolcheniya, Rostov-on-Don 344038, Russia
e-mail: ymigal@mail.ru

I.A. Parinov et al. (eds.), *Advanced Materials*, Springer Proceedings in Physics 193, DOI 10.1007/978-3-319-56062-5_6

intergranular diffusion. As a result of such processes the bond between grains can weaken, and mechanical properties of materials can deteriorate.

Until now, ones of the most significant works on the role of grain boundary segregation in metal strength remain Seah's works published in the 80s of the last century (see, e.g., [1, 2]). In these works, by simple estimates it was shown that the ability of segregated atoms to weaken or strengthen grain boundaries is largely determined by the magnitude of the binding energy of the atoms per unit area. In these estimates that are consistent with known experimental facts, data only on sublimation enthalpy and sizes of atoms of investigated elements were used. These estimates that generally correspond to known experimental facts were made by using the data for only sublimation enthalpy and atom sizes of studied elements. Obviously, because of the assumptions underlying such estimates, the findings need further experimental and theoretical studies. In such studies, methods of quantum chemistry should play a greater role, because the process of grain boundary segregation significantly depends on characteristics of interatomic bonds, which are extremely difficult to measure experimentally.

Unfortunately, a sufficiently detailed theoretical analysis of changes in chemical bonding in polycrystals caused by grain boundary segregation, as far as we know, has not been performed yet. The vast majority of publications of the last decades on the problem of segregation have an experimental character, and in them a considerable success has been achieved in the study of grain boundaries properties (see, e.g., [3–5]). However, the chemical bond and the possibility to form purposefully any atomic structures at grain boundaries were not studied practically in these works. Investigations in which quantum chemical methods are used to establish a link between the phenomenon of grain boundary segregation and the problem of fracture and wear resistance of metals, are still rare in the world literature (see, e.g., [7–13]). They deal with segregation only of some selected elements (H, B, C, S, P, Mn, V, etc.).

In our opinion, for deeper understanding of the problem it is necessary to carry out more systematic analysis with use of a big group of segregated elements. In particular, it is important to find out why values of sublimation enthalpy (the phenomenon occurring at free surfaces of substances) were useful at Seah's research of grain boundary segregation (the phenomenon going on at internal surfaces).

For the first time in the world literature a comparative research of atomic interactions at grain boundaries in iron with participation of atoms of the whole periods of Mendeleev's table was begun in our group [14–17]. By using various models (cluster and slab models) within the DFT approach the investigation of a chemical bond of atoms of elements of the first five periods of Mendeleev's table with a surface of iron grains has been carried out. It was shown that there is a noticeable correlation between binding energies of the elements on external and internal surfaces in iron. This fact allows us to understand why Seah was successful in estimating the ability of segregated atoms to weaken or strengthen grain boundaries.

In these conditions, it is natural to accept that existence of atoms X on grain boundaries in iron, whose energy of a chemical bond with iron atoms ($|E_{Fe-X}|$) is larger or comparable with binding energy of iron atoms among themselves ($|E_{Fe-Fe}|$), can lead to strengthening of boundaries. In the opposite case, when $|E_{Fe-X}|$ is significantly smaller than $|E_{Fe-Fe}|$, it is followed by weakening of boundaries. It has been found, for example, that binding energies of boron and vanadium with iron on grain boundaries in steel exceed binding energy $|E_{Fe-Fe}|$, and for this reason boron and vanadium strongly sew together iron grains. On the contrary, atoms of sulfur and phosphorus, for which $|E_{Fe-X}| < |E_{Fe-Fe}|$, weaken grain boundaries. These results are in consent with the known experimental facts.

In this work we continue our research and consider elements of the sixth period (except for lanthanides).

6.2 Choice of Model and Methods of Calculation

For imitation of a grain boundary, as well as in the previous work [17], we used a two-periodic slab model in which the boundary is imitated by a set of the parallel monoatomic planes including several layers of iron atoms and one (intermediate) layer of atoms of impurity elements (Fig. 6.1). In this model, a part of the boundary of the minimum (one atomic) thickness of the impurity layer is considered. Such a model, certainly, does not reproduce the real grain boundary with its significantly

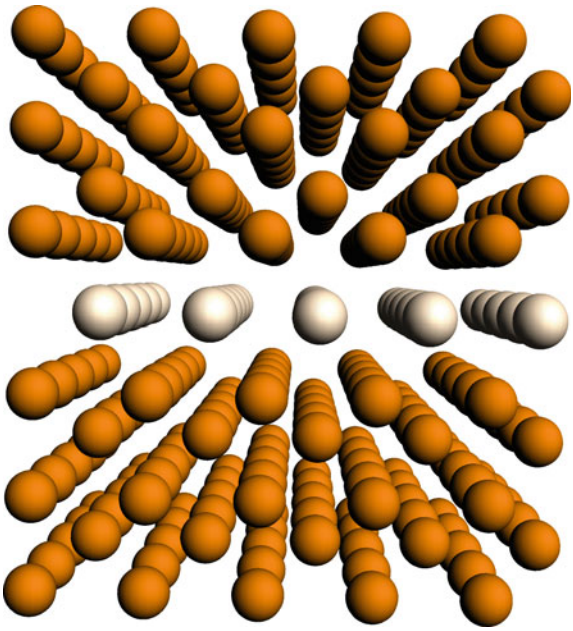

Fig. 6.1 Grain boundary model with (100) surface. The *upper* and *lower* parts of the model consist of iron atoms, and the intermediate does of impurity or alloying atoms

irregular atomic arrangement (see, e.g., [18]). Besides, this model does not assume a research of stability of the system consisting of impurity atoms and atoms of the matrix. It is supposed that such stability is caused by additional factors. Nevertheless, within this model it is possible, to some extent, to reflect the short-range order in arrangement of the interacting atoms, different types of mutual coordination of matrix and impurity atoms. The long-range order, which is absent in reality but used in the model, allows us to consider influence of far located atoms by means of effective methods of solid-state zonal calculations.

The basic purpose of the model is to estimate approximately the magnitude of a chemical bond energy E_{Fe-X} between iron atoms and impurity atoms X on grain boundaries and investigate dependence of this energy on atomic number of impurity elements. Since, as shown in [2], the binding energy is the magnitude significantly determining the boundary strength, we hope to make the approach used in [2] more precise, and to have as a result an opportunity to classify chemical elements more exactly according to how these elements strengthen grain boundaries.

In the calculations performed, grain boundaries were chosen along iron surfaces with Miller's indexes (100) and (110). In case of surface (100) (Fig. 6.1) the cell size is equal to 2.87 × 2.87 $Å^2$, n value (the total number of atomic layers) is equal to 11. In case of surface (110) (Fig. 6.2) the cell size is 4.06 × 2.87 $Å^2$, n = 5. The total number of atoms in a cell is approximately identical in both cases: for (100) surface this number is equal to 11, and for (110) surface it is equal to 10.

Use of different variants of grain boundaries makes the following sense: it allows us to see the dependence of binding energy of impurity elements with an iron surface on distribution of atoms at surfaces. In our previous works, where elements of the first five periods were investigated, along with slab model also cluster model was used within which only the nearest environment of impurity atoms was considered.

It has been shown that the dependence of energy of a chemical bond of impurity atoms with iron surface on atomic number of impurity is of the same type for

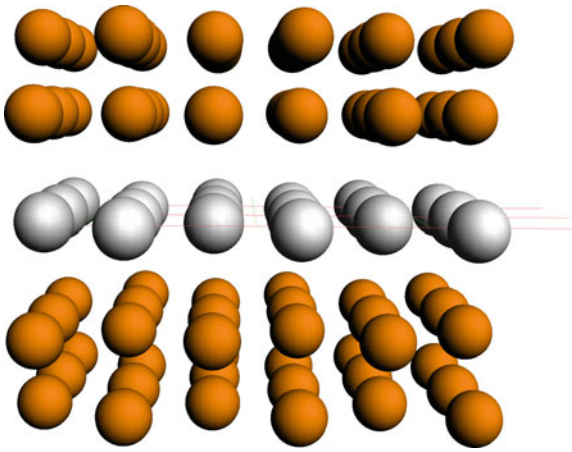

Fig. 6.2 Grain boundary model with (110) surface

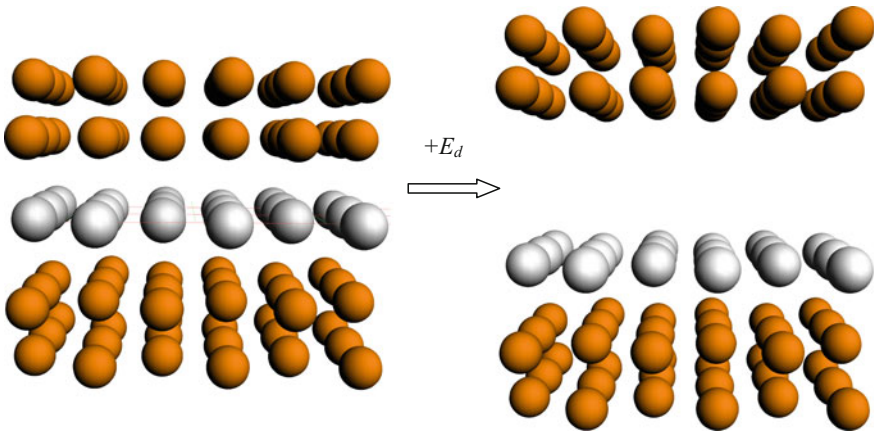

Fig. 6.3 Decohesion of a model segregation complex into two parts

different models and, respectively, for different types of environments. This fact allows us to hope to develop some general classification of chemical elements based on strengthening of grain boundaries by these elements.

Boundary strength was estimated in the work as follows. It was supposed that at mechanical action the general model system (a segregation complex) disintegrates into two parts, one of which consists only of iron atoms (imitation of iron grain surface), and the second includes impurity atoms as well (an adsorption complex) (Fig. 6.3).

In our previous calculations it was shown that such variant of decohesion on local sites of a boundary is most probable. Although in experimental works it is noted that at intercrystalline destruction the segregated atoms appear on both surfaces of disintegration, it is necessary to take into account that in ordinary experiments the distribution of atoms is observed at large sites of grain surfaces consisting of a set of alternating local sites.

The energy E_d needed for decohesion of a segregation complex was calculated (relating to one cell) by equation

$$E_d = \left|E_s - E_g - E_a\right|,$$

where E_s is the binding energy of a segregation complex, E_g and E_a are the binding energies of its disintegrating parts. All energies were calculated for one cell (energy of infinitely extended complexes is obviously equal to infinity).

The binding energies E_s, E_g and E_a were calculated by means of the ADF package [19] based on the DFT approach. The merit of this package is that the basic decompositions of wave functions used in it are adjusted for transition elements, and it is important at research of iron compounds. The main characteristics to be calculated were the binding energy of model complexes and interatomic distances.

Modulo binding energy of a complex is approximately the energy which should be expended in order to divide a complex in the ground state into individual atoms.

It is known that the results of energy calculations strongly depend on the selected approximation. Therefore, the calculations for all the objects under investigation were carried out uniformly. In the calculation we used the basis of TZ2P and the "frozen" core orbitals (the option "Small", see [19]). As a method of energy calculation, the non-local approximation GGA BLYP [20] was chosen.

6.3 Results of Calculations

Results of calculations of E_a, E_s and E_d values for complexes containing atoms of elements of the sixth period (excepting lanthanides) are presented in Tables 6.1, 6.2, 6.3, 6.4, 6.5 and 6.6 (For complexes with cesium results have not been received because, as it turned out, such complexes are unstable.). Data for slab model with (100) surface are presented in Tables 6.1, 6.2 and 6.3. In Tables 6.4, 6.5 and 6.6 there are data for the model with (110) surface.

Table 6.1 Binding energy E_a (eV) of adsorption complexes in slab model with (100) surface

	I	II	III	IV	V	VI	VII	VIII			0
6	Cs −34.7	Ba −37.0	La −41.6	Hf −42.8	Ta −44.4	W −45.5	Re −46.2	Os −46.4	Ir −45.9	Pt −41.5	
	Au −39.0	Hg −37.2	Tl −38.6	Pb −39.2	Bi −38.6	Po −37.0	At −34.8				Rn *

Table 6.2 Binding energy E_a (eV) of segregation complexes in slab model with (100) surface

	I	II	III	IV	V	VI	VII	VIII			0
6	Cs ?	Ba −74.5	La −79.5	Hf −81.7	Ta −83.4	W −84.9	Re −85.2	Os −84.8	Ir −84.2	Pt −79.5	
	Au −76.0	Hg −74.4	Tl −76.8	Pb −76.4	Bi −75.4	Po −73.8	At −71.3				Rn *

Table 6.3 Decohesion energy E_d (eV) of segregation complexes in slab model with (100) surface

	I	II	III	IV	V	VI	VII	VIII			0
6	Cs ?	Ba 0.8	La 1.3	Hf 2.4	Ta 2.4	W 2.8	Re 2.4	Os 1.9	Ir 1.6	Pt 1.4	
	Au 0.4	Hg 0.6	Tl 1.6	Pb 0.6	Bi 0.2	Po 0.1	At 0.1				Rn 0.

Table 6.4 Binding energy E_a (eV) of adsorption complexes in slab model with (110) surface

	I	II	III	IV	V	VI	VII	VIII			0
6	Cs ?	Ba −18.0	La −30.0	Hf −36.9	Ta −42.8	W −45.8	Re −46.8	Os −45.8	Ir −44.1	Pt −34.6	
	Au −28.2	Hg −23.9	Tl −23.4	Pb −22.3	Bi −20.4	Po −16.8	At −10.8				Rn *

Table 6.5 Binding energy E_a (eV) of segregation complexes in slab model with (110) surface

	I	II	III	IV	V	VI	VII	VIII			0
6	Cs ?	Ba −46.5	La −58.7	Hf −67.1	Ta −73.1	W −75.9	Re −76.4	Os −75.1	Ir −73.2	Pt −63.1	
	Au −56.6	Hg −52.0	Tl −51.6	Pb −50.4	Bi −48.4	Po −44.5	At −38.6				Rn *

Table 6.6 Decohesion energy E_d (eV) of segregation complexes in slab model with (110) surface

	I	II	III	IV	V	VI	VII	VIII			0
6	Cs ?	Ba 0.9	La 1.1	Hf 2.6	Ta 2.7	W 2.4	Re 2.1	Os 1.7	Ir 1.5	Pt 1.0	
	Au 0.8	Hg 0.5	Tl 0.5	Pb 0.4	Bi 0.4	Po 0.1	At 0.2				Rn 0.

The binding energy E_g of pure iron complexes, necessary for calculations of E_d value, has the following values: −36.6 eV for (100) surface and −27.6 eV for (110) surface.

6.4 Discussion of Results

In this section, the received results for greater visibility are presented in graphic form. By means of these graphs we will be convinced that the conclusions received earlier for elements of the 1–5 periods are qualitatively valid also for elements of the sixth period. Binding energies of model segregation and adsorption complexes are presented in Figs. 6.4 and 6.5. Note that atomic numbers from 58 to 71 are absent on the abscissa axis. Elements with such numbers (lanthanides) are not considered in this work.

From the presented graphs it follows, in particular, that dependence of binding energy on atomic number of elements is similar for the both types of complexes. If a segregation complex with some element has modulo larger binding energy, also an adsorption complex with the same element has modulo larger binding energy. This fact, in particular, allows us to understand why estimates of Seah who used data on sublimation enthalpy (the phenomenon where the adsorption states appear) are valid also in case where the segregation states are apparent.

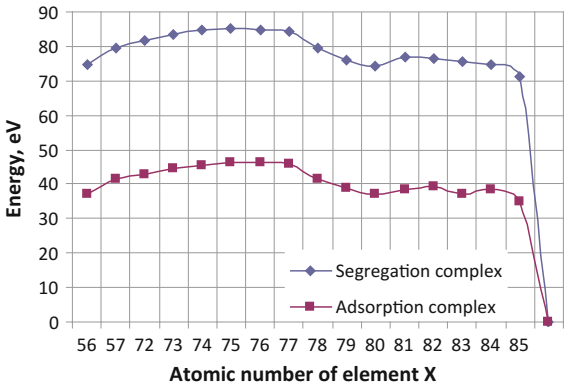

Fig. 6.4 Modulo binding energy of segregation and adsorption complexes with (100) surface

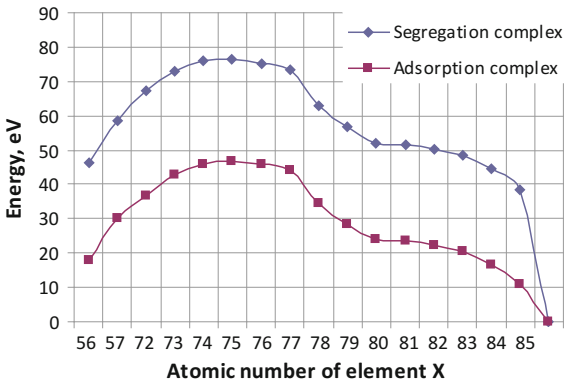

Fig. 6.5 Modulo binding energy of segregation and adsorption complexes with (110) surface

In Fig. 6.6 data on decohesion energy E_d of segregation complexes with (100) and (110) surfaces are presented. Comparing dependences of E_d on atomic number of impurity elements, we come to the conclusion that these dependences are also similar for both types of surfaces.

Besides, we can see that decohesion energy E_d satisfies the same regularity as in case of elements of the first five periods [17]. Namely, for elements from the beginning of the sixth period this quantity is rather small, then, as atomic number increases, it also increases and decreases further again. (Violation of this regularity is observed for thallium in case of (110) surface. For the present we cannot explain sharp increase in decohesion energy for this element.) According to calculations, complexes containing hafnium, tantalum and tungsten possess the greatest decohesion energy. It is possible to expect that presence of these elements on grain boundaries promotes hardening of steel.

Let us adduce also the generalized graph of dependence of decohesion energy of segregation complexes on atomic number for all elements from the first six periods of Mendeleev's table (Fig. 6.7). Here, along with the results received in this work also results from [17] relating to the first five periods are used.

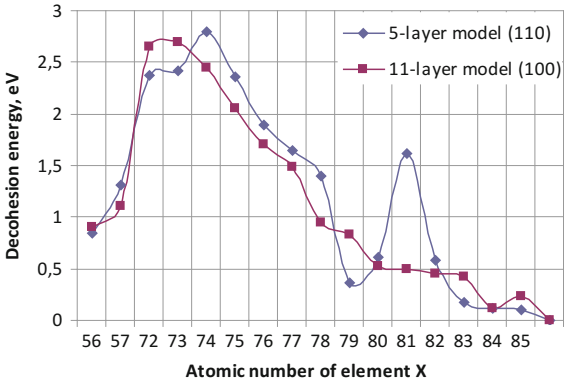

Fig. 6.6 Decohesion energy of segregation complexes with (100) and (110) surfaces

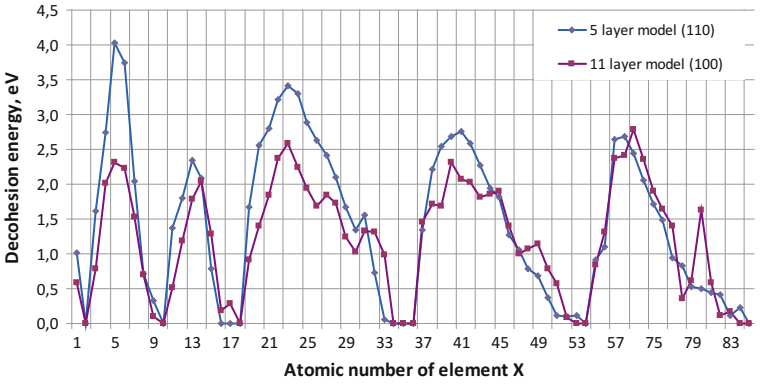

Fig. 6.7 Decohesion energy of segregation complexes with (100) and (110) surfaces for the first six periods of Mendeleev's table

The periodic dependence of decohesion energy of segregation complexes on atomic number of elements is obvious from this graph. This result, certainly, is not in essence new, because it follows from the Periodic law. For us it is very important that our results do not contradict the known common principles, and this fact in addition can testify to legitimacy of our approach.

6.5 Comparison with Results of Other Authors

Let us compare our results with data which are known from practical experience or received by other authors. In particular, some estimates for relatively heavy elements from the sixth period were received by Seah [2]. These data are shown in

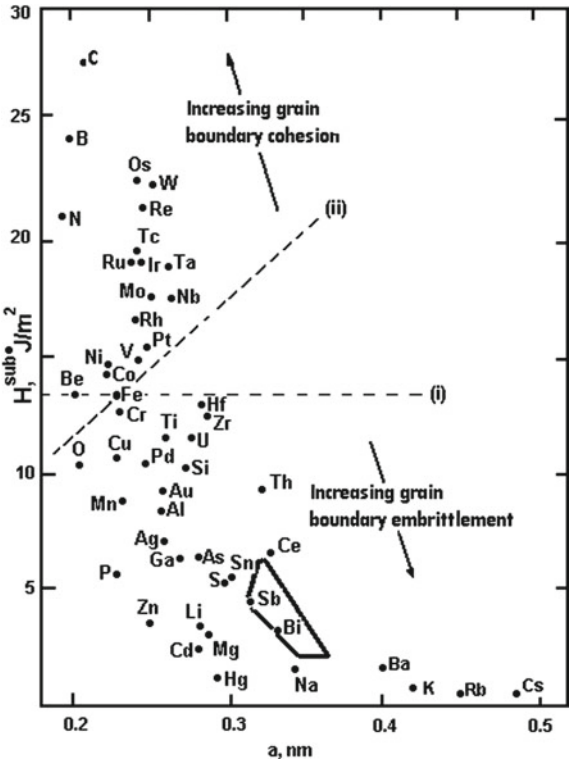

Fig. 6.8 Graph of grain boundary embrittlement, built according to the data from [2]

Fig. 6.8. Here the elements strengthening grain boundaries are located above dashed lines. Osmium, tungsten, rhenium, tantalum, iridium, platinum belong to such elements. The elements weakening grain boundaries are located below the dashed lines. Cesium, barium, hydrargyrum, bismuth concern to them.

To compare our results with Seah's data let us draw up Table 6.7. We accept that if decohesion energy E_d in Table 6.6 for some impurity element is larger than 2.2 eV, then this element has high energy of binding with iron surface and it can strengthen grains (in the table this element is marked by a sign ++). (Decohesion energy of a segregation complex from pure iron within the accepted model is equal to 2.6 eV [17].) If $E_d \leq 0.5$ eV, then we assume that the corresponding element has low binding energy and it is capable to weaken grains (such element is marked by a sign − −). Elements with intermediate E_d values are marked by signs +, 0 and −, depending on the value of E_d.

As it is seen from Table 6.7, in the most cases our results correlate with Seah's data. The greatest discrepancy is observed in case of osmium and iridium. According to Seah' estimate these elements significantly strengthen grain boundaries, but accordingly our evaluation their binding with iron is weak.

From experimental works relating to elements of the sixth period we can mention Barmin's work [21] in which it is shown that grain boundary segregation

Table 6.7 Strengthening and non-strengthening elements of the sixth period

Element	Our result	Seah [2]
55 Cs	− −	− −
56 Ba	−	− −
57 La	0	
72 Hf	++	+
73 Ta	++	++
74 W	++	++
75 Re	+	++
76 Os	0	++
77 Ir	0	++
78 Pt	0	+
79 Au	−	−
80 Hg	− −	− −
81 Tl	− −	
82 Pb	+	
83 Bi	− −	− −
84 Po	− −	
85 At	− −	
86 Rn	− −	

of tungsten in iron matrix leads to decrease in energy of boundaries of iron grains, thereby increasing strength of boundaries. This statement, apparently, agrees with our results. In [22] the high thermal strength of tungsten compounds is noted.

6.6 Conclusion

The received results allow us to state that the conclusions relating to dependence of energy of binding of atoms of various elements with iron surface and decohesion energy of segregation complexes on atomic number of elements, in case of elements of the sixth period are similar to the conclusions made for elements of the first five periods. The most important of them are the following.

1. Comparing characteristics of atoms in adsorbed and segregated states, we can conclude that if atoms of some elements are weakly interacting with a free iron surface, they also weakly bonded with iron at grain boundaries. It follows from this that the strength of binding is a quantity depending first of all on the type of atoms bonded directly rather than on location and number of atoms in the near environment. In spite of the fact that there is a certain dependence of the bond on the near environment, this circumstance does not influence essentially on the strength properties of steel.
2. If atoms of elements, whose binding energy with iron is noticeably lower than Fe–Fe binding energy, appear at grain boundaries, it leads to decreasing strength

properties of steel. The appearance of these atoms at grain boundaries in the surface layer of steel, due to their weak bond with iron atoms, results in decreasing wear resistance of this layer.

Acknowledgements This work was supported by the Russian Scientific Foundation (RSCF) (grant No. 16-19-10467 provided to the Rostov State Transport University).

References

1. D. Briggs, M.P. Seah, *Practical Surface Analysis by Auger and X-ray Photoelectron Spectroscopy* (Wiley, Chichester, 1990)
2. M.P. Seah, Acta Metall. **28**, 955 (1980)
3. M. Herbig, D. Raabe, Y.J. Li, P. Choi, S. Zaefferer, S. Goto, Phys. Rev. Lett. **112**, 126103 (2014)
4. P. Lejcek, *Grain Boundary Segregation in Metals* (Springer series in materials science, book 136) (Springer, Berlin, 2010)
5. B.S. Bokstein, A.O. Rodin, B.B. Straumal (eds.), Grain boundary diffusion, stresses and segregation. Selected, Peer Reviewed Papers from the International Conference on Grain Boundary Diffusion, Stresses and Segregation, DSS 2010, Held in Moscow, Russia, 1–4 June 2010 (2011)
6. Y.F. Migal, Theoretical modeling of friction and wear processes at atomic level. in *Anti-Abrasive Nanocoatings: Current and Future Applications*, ed. By M. Aliofkhazarei (Woodhead Publishing Ltd., 2015), p. 385 (Chapter 15)
7. G.S. Painter, F.W. Averill, Phys. Rev. Lett. **58**, 234 (1987)
8. R. Yang, R.Z. Huang, Y.M. Wang, H.Q. Ye, C.Y. Wang, J. Phys. Condens. Matter **15**, 8339 (2003)
9. Braithwaite J. Spencer, Rez Peter, Acta Mater. **53**, 2715 (2005)
10. S.B. Gesari, M.E. Pronsato, A. Juan, Appl. Surf. Sci. **253**, 5939 (2007)
11. M. Zhang, K. Yang, Z. Chen, Y. Wang, J. Zhang, Rare Metal Mater Eng **42**(7), 1531 (2013)
12. D. Raabe, M. Herbig, S. Sandlobes, Y. Li, D. Tytko, M. Kuzmina, D. Ponge, P.-P. Choi, Curr. Opin. Solid State Mater. Sci. **18**, 253 (2014)
13. M. Rajagopalan, M.A. Tschopp, K.N. Solanki, JOM **66**, 129 (2014)
14. V.I. Kolesnikov, A.T. Kozakov, Y.F. Migal, J. Frict. Wear. **31**, 11 (2010)
15. Y.F. Migal, V.I. Kolesnikov, V.N. Doronkin, E.S. Novikov, Adv. Mater. Phys. Chem. **2**(4), 201 (2012)
16. Y.F. Migal, V.I. Kolesnikov, E.S. Novikov, in *Advanced Nano- and Piezoelectric Materials and their Applications*, ed. by I.A. Parinov (Nova Science Publishers, Hauppauge, NY, USA, 2014), p. 1
17. Y.F. Migal, V.I. Kolesnikov, I.V. Kolesnikov, Comput. Mater. Sci. **111**, 503 (2016)
18. L. Priester, *Grain Boundaries from Theory to Engineering* (Springer series in materials science, book 172) (Springer, Berlin, 2013)
19. G. te Velde, F.M. Bickelhaupt, S.J.A. van Gisbergen, C.F. Guerra, E.J. Baerends, J.G. Snijders, T. Ziegler, J. Comp. Chem. **22**, 931 (2001)
20. J.P. Perdew, K. Burke, M. Ernzerhof, Phys. Rev. Lett. **77**, 3865 (1996)
21. A.E. Barmin. http://repository.kpi.kharkov.ua/bitstream/KhPI-Press/14362/3/2012_Barmin_Vliyanie_volframa.pdf (2012)
22. R. Tanaka, Y. Tobo. https://www.jstage.jst.go.jp/article/tetsutohagane1955/57/3/57_3_547/_pdf (1970)

Chapter 7
The Effect of Electroless Plating on Aluminum Metal Matrix Composite Reinforcement Bottom Ash on the Density and Porosity for Propeller Applications

Budi Prastio, Harjo Seputro and Muslimin Abdulrahim

Abstract The composite is a combination of two or more different materials with condition of the bonding surface between the two materials. One type of composites that attracts a great attention is metal matrix composites (MMC). In this study, we investigated the influence of variations of Mg and temperature of oxidation on the density and porosity of the composite reinforcement. This composite underwent to a process of electroless plating with variations (% by weight) of magnesium (0.005, 0.010, and 0.015%) and variations in temperature oxidation (100, 200 and 300 °C) at hold for 3 h, with following processing the composite by stir casting method. Based on the average chart, we show that increasing the value of (% by weight) of magnesium and oxidation temperature (°C), the density values further decrease. This is caused by the imbalance between the weight of magnesium particles moistened (coal bottom ash) during the electroless plating process. Based on the results of testing, the value of the highest density is achieved at a temperature of 300 °C to oxidation at 0.005% Mg and is equal to 2.609 g/cm^3. The value of the lowest density is achieved at a temperature of 200 °C to oxidation at 0.010% Mg and is equal to 2.406 g/cm^3.

7.1 Introduction

Metal matrix composites are combined of two or more materials, when metal is a matrix and ceramic is the reinforcement. Very often aluminum is selected as the matrix because it is cheap, light in weight and has good fabrication properties. With

B. Prastio · H. Seputro (✉)
Mechanical Engineering Department, University of 17 Agustus 1945 Surabaya, Surabaya, Indonesia
e-mail: harjoseputra@untag-sby.ac.id

M. Abdulrahim
Industrial Engineering Department, University of 17 Agustus 1945 Surabaya, Surabaya, Indonesia

I.A. Parinov et al. (eds.), *Advanced Materials*, Springer Proceedings in Physics 193, DOI 10.1007/978-3-319-56062-5_7

the development of composite, aluminum can be combined with ceramics to get better physical and mechanical properties [1].

Main function of the reinforcement in composites is bearing an applied load and its distribution to another section of matrix. The kind of reinforcement can be influenced by material properties, moreover the particle size of bearing an applied load, because the applied load will be redistributed to all of reinforcements. Coal bottom ash is one of oxide ceramic materials, whose composition includes 70% of Al_2O_3, SiO_2 and Fe_2O_3. They have high hardness and a melting point above 2000 °C.

The main problem of fabrication of composites or reinforced ceramic material is wettability. So, for facilitate wettability at the board of coal bottom ash, we can add Mg at electroless platting process and the process can increase wettability for Al_2O_3 with formed spinel phase ($MgAl_2O_4$).

Adding Mg at electroless platting process to coal bottom ash particles can influence the density and porosity of the composite at casting [2]. The main problem of composite with ceramic reinforcement Al_2O_3/Al is difficulties of aluminum infiltration for Al_2O_3, because formed passive film at the aluminum by adding Mg can increase capillarity penetration at oxide film and make easier formation of interfaces, influence strain and decrease contact angle.

7.1.1 Research Purpose

We study effect of variation (%wt) Mg and oxidation temperature at electroless platting process of coal bottom ash on density and porosity of the propeller of composite Al-coal bottom ash.

7.1.2 Research Scope

At this study, we consider the following circumscriptions of the problem:

- The material is Al-coal bottom ash composite
- Density and porosity testing
- T6 heat treatment: at 535 °C for 4 h
- Artificial ageing: 225 °C for 5 h
- Variation of oxide temperatures: 100, 200 and 300 °C
- Variation of Mg (%wt): 0.005, 0.010 and 0.015%
- Time of oxidation: 3 h.

7.2 Research Method

Firstly, we prepared the Mg, coal bottom ash, SiO_2, $HNO_{3(L)}$ 65%, and Al–Cu. Coal bottom ash with particle size 100 Mesh was obtained from PT. SMART, Tbk. Rungkut-Surabaya. Electroless platting process included the following procedures: (i) we washed the coal bottom ash with 97% Alcohol using magnetic stirrer, (ii) the ash was dried with oven at 100 °C for 3 h, (iii) we performed the electroless platting with different variations of Mg (%wt), and then varying oxidation temperature during 3 h.

We fabricated the composite by using stir casting method. T6 heat treatment was carried out for this material to increase physical and mechanical properties. After that, density and porosity tests were performed on the materials.

7.3 Result and Discussion

From the test results, obtained on aluminum-coal bottom ash composite, is known the effect of adding Mg (%wt) and oxidation temperature at electroless platting. Table 7.1 shows the results of density and porosity tests.

7.3.1 Effect of Adding Mg (%wt) on Composite Density

Figure 7.1a, b shows that by increasing Mg (%wt) content the value of density decreases. This is due to the imbalance between the content of magnesium and

Table 7.1 Test results of density and porosity

No	Variation of magnesium (%wt) and oxidation temperature	Actual density (g/cm^3)	Theoretical density (g/cm^3)	Porosity (%)
1	0.005% Mg; oxidation at 100 °C	2.507	2.675	6.27
2	0.005% Mg; oxidation at 200 °C	2.597	2.680	3.09
3	0.005% Mg; oxidation at 300 °C	2.609	2.682	2.73
4	0.010% Mg; oxidation at 100 °C	2.486	2.682	7.28
5	0.010% Mg; oxidation at 200 °C	2.406	2.679	10.21
6	0.010% Mg; oxidation at 300 °C	2.453	2.670	8.12
7	0.015% Mg; oxidation at 100 °C	2.495	2.679	6.87
8	0.015% Mg; oxidation at 200 °C	2.543	2.680	5.11
9	0.015% Mg; oxidation at 300 °C	2.420	2.681	9.72

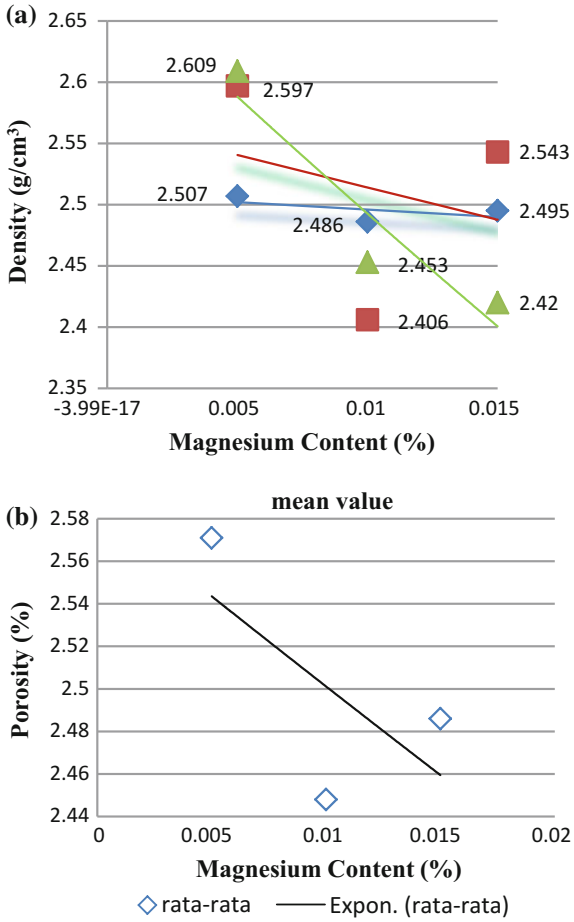

Fig. 7.1 **a** Effect of Mg on composite density; **b** averaged Mg effect on composite porosity

particles wetted at electroless platting process. Because the particles are not wetted, it is hard for aluminum to infiltrate to coal bottom ash.

7.3.2 Effect of Adding Mg (%wt) on Composite Porosity

Figure 7.2a, b shows that increasing Mg content increases the porosity value; this takes place because aluminum does not entirely infiltrate to the reinforcement. It results to cracking occurring around particles, which eventually will form porosity defects.

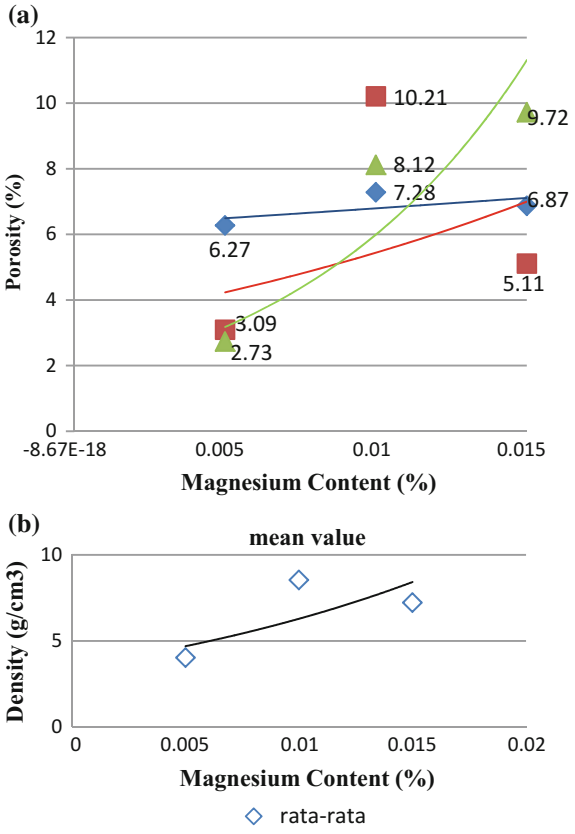

Fig. 7.2 **a** Effect of Mg on composite porosity, **b** averaged Mg effect on composite density

7.3.3 *Effect of Oxidation Temperature on Composite Density*

Figure 7.3a, b shows that increasing oxidation temperature decreases the value of composite density. Basically the higher oxidation temperature leads to that the particles (coal bottom ash) become more dense and uniform; it can facilitate infiltration of aluminium. In this study, inversely, it causes the value of the magnesium addition is so small for wetting the particles and their disposition between particles moistened do not lead to significant differences in density.

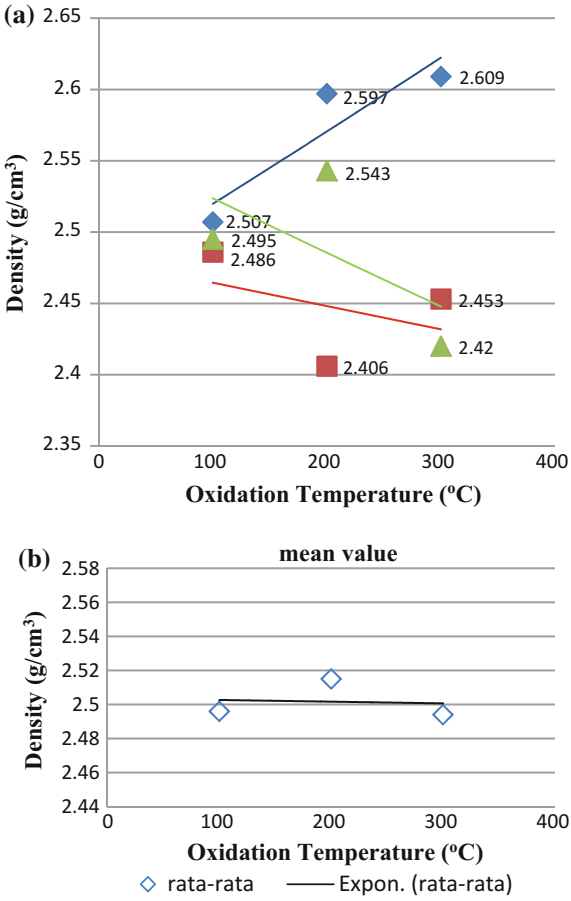

Fig. 7.3 **a** Effect of oxidation temperature (°C) on composite density, **b** averaged oxidation temperature (°C) effect on composite density

7.3.4 *Effect of Oxidation Temperature on Composite Porosity*

Figure 7.4a, b shows that increasing the oxidation temperature leads to increasing the value of porosity. It is caused by that the value of the magnesium addition is so small for wetting the particles and disposition between particles moistened. So, it is difficult for aluminum to be infiltrated by the all particles, that eventually will form porosity defects.

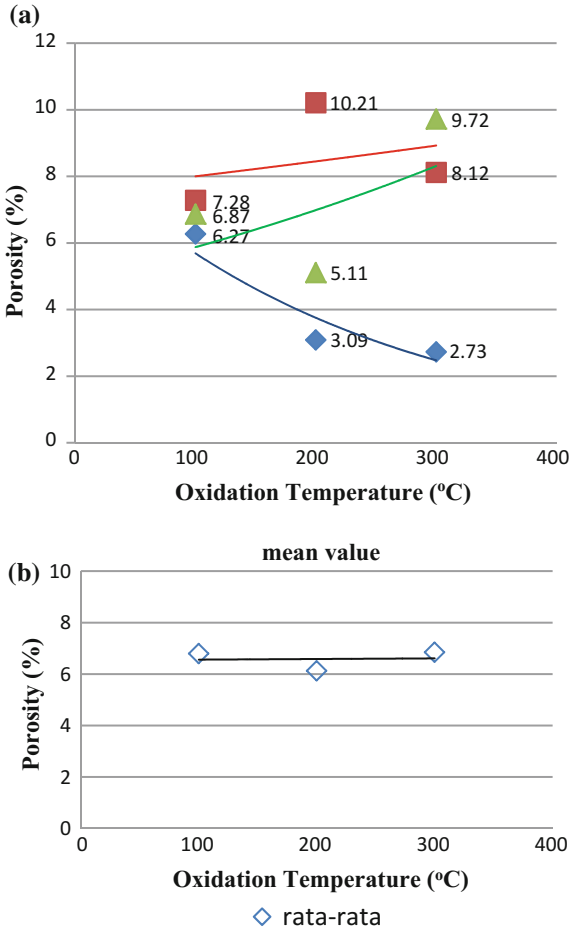

Fig. 7.4 **a** Effect of oxidation temperature (°C) on composite porosity, **b** averaged oxidation temperature (°C) effect on composite porosity

7.4 Conclusion

The increasing percentage of magnesium and oxidation temperature decreases the value of the average density, while the value of porosity increases. This is due to the imbalance between the content of magnesium particles, which are wetted (coal bottom ash) during the process of electroless plating. So the rest of the base coal ash particles that are not coated by Mg will be difficult to be infiltrated by aluminum. The highest density (2.609 g/cm^3) is achieved at 300 °C oxidation temperature with 0.005 %wt Mg. The lowest density (2.406 g/cm^3) is attained at 200 °C oxidation temperature with 0.010 %wt Mg. From these result, it is obvious that variations in the magnesium addition and in the temperature oxidation (°C) do not significantly influence on the density, this is due to the addition of magnesium is very small, and cannot cause significant differences in density values.

Acknowledgements This research was performed into framework of financing the ministry RISTEKDIKTI under agreement number 001/SP2H/P/K7/KM/2015.

References

1. J. Mulyanti, in *Pengaruh Temperatur Proses Aging Terhadap Karakteristik Material Komposit Logam Al–SiC Hasil Stir Casting* (Jurusan Teknik Mesin Fakultas Teknik Universitas Janabadra) (2011)
2. G.N. Anastasia Sahari, A. Zulfia, D.E.S. Siradj, in *Pengaruh Mg Terhadap Kekerasan Komposit Matrik Keramik Al_2O_3/Al* (Departemen Metalurgi dan Material Fakultas Teknik Universitas Indonesia, Depok dan Jurusan Mesin Fakultas Teknik Universitas Kristen Indonesia Paulus (UKIP) Makasar) (2009)

Chapter 8
The Effect of Composition and Particle Size of Mixed Briquettes Making Process on Temperature Combustion and Calorific Value

Muhyin and Asfiah Mahdiani

Abstract This research was motivated by the fact that the price of fuel, both gas and oil is expensive. In order to overcome the high price of fuel, it is necessary to develop an alternative energy. Producing alternative fuel consisting of a mixture of rice husks and coal is important as this fuel is cheaper and the materials are abundant. Some steps must be undertaken to make mixed briquettes. First, rice husk is the main material, processed into charcoal. The next step is the preparation of materials from particles of different sizes and compositions using the congestion pressure (compacting) of constant briquettes. The particle sizes used are 40 mesh (I), 60 mesh (II) and 80 mesh (III), with the following compositions: (I) coal—65%, rice husk—25%, starch—10%; (II) coal—55%, rice husk—35%, starch—10%; and (III) coal—45%, rice husk—45%, tapioca starch—10%; the compressive pressure for processing briquettes was 78 kg/cm^2. After that, it was performed the sintering at 100 °C for 30 min. The analysis, test and trials show the highest calorific value of fuel was equal to 4790.78 kcal/kg and the combustion temperature of 365 °C is for the 40-mesh particles with a composition of 65% coal, 25% rice husks, and 10% tapioca flour, at pressure of 78 kg/cm^2. The highest burning time was in briquettes with the particle size of 80 mesh, and a composition of 65% coal 25% rice husks and 10% tapioca, obtained at initial flame temperature of 390 °C during 4 min, and the final flame temperature was equal to 310 °C during 29 min. The highest compressive strength and density (bulk density) can be found in the briquettes with particle size of 80 mesh, and a composition of 65% coal, 25% rice husks and 10% tapioca flour, at pressure of 78 kg/cm^2, the compressive strength of 2.11 kg/cm^2 and a density value (bulk density) was 0.89 g/cm^3.

Muhyin (✉)
Department of Mechanical Engineering, University of 17 Agustus 1945 Surabaya, Surabaya, Indonesia
e-mail: muhyin@untag-sby.ac.id

A. Mahdiani
Department of Informatics, University of 17 Agustus 1945 Surabaya, Surabaya, Indonesia
e-mail: amahdiani@yahoo.com

I.A. Parinov et al. (eds.), *Advanced Materials*, Springer Proceedings in Physics 193, DOI 10.1007/978-3-319-56062-5_8

8.1 Introduction

Briquette is a solid fuel with specific size and shape, which is composed of granules of coal and materials used to dilute it (such as organic waste, clay, rice husks, etc.); it consists of two materials or more and is processed with a specific press power, to make the material easier to handle and has more value in its utilization. (Source: Centre for Research and Development of Mineral and Coal Technology)

Briquettes are generally composed of two major parts of the base material, a matrix and a filler. The requirement to make the briquettes is the surface bonding of matrix and filler. Matrix is engineering materials whose aim to improve the basic properties, and filler can be regarded as materials engineer.

The requirements to energy in these days increases steadily together with the progress in technology, as well as the rapid growth of the world population. Currently, Indonesia is facing problems of energy supply due to the increasing need of national energy every year. Meanwhile, the oil reserves in Indonesia are dwindling and will be running out of oil within 10 years [1].

8.2 Review of Related Literature

8.2.1 Briquettes

Coal is a combustible organic mineral, formed from remains ancient plant, which further deformed due to physical and chemical processes that took place over millions of years. Therefore, coal is included in the category of fossil fuels [2]. It can also be called as a solid hydrocarbon fuels formed from plants in an oxygen-free environment and exposed to the effect of heat and pressure that lasts longer [3].

Chemical Compositions of briquettes, used for this study, were obtained from Limited Company Coal Mine Hill Acids Gresik, East Java Indonesia. The chemical composition of the briquettes is present in Table 8.1.

Table 8.1 Chemical composition of coal used

Parameter	Unit	Element value
Total moisture	%	28
Inherent moisture	%	15.0
Ash content	%	8.0
Volatile matter	%	40
Fixed carbon	%	37.0
Total sulfur	%	0.8
Gross calorific value	kcal/kg	5800

Source Limited Company Coal Mine Hill Acids Gresik, East Java Indonesia

8.2.2 Rice Husk

Rice husk is produced from rice milling process. As waste, husks often cause problems. In fact, it has a great potential as cheap raw materials for the source of alternative energy. The chemical composition of rice husk can be seen in Table 8.2.

The husk is the outer portion of the grain that is a byproduct during the rice milling process. The weight of Rice consists of approximately 20–30% rice husk and more than 15% of it (husk) is ash. The moment of energy crisis like today is the right time to promote the husk as a source of alternative energy. Utilization of rice husks will provide choices to the public regarding the fulfillment of the energy source that is economical and advantageous, because the products of coal combustion can be utilized as mix materials in the manufacture of hydraulic cement, pressed brick, and the rubber processing.

One of the materials used in processing the briquettes is rice husk, which has been charred before proceeding to the next stage. The making of husk charcoal is intended to improve the physical properties of it. If the husk is used directly as a thermal energy source, it will cause smoke when burned. In addition to air pollution, the produced smoke can also change whiff and color of the dried material. The process of charcoaling is done by heating the chaff in the drum. The process ends, if the chaff becomes dark as burned (Erliza Hambali et al., Bioenergy Technology). The analysis can be seen from Table 8.3.

8.2.3 Adhesive

Adhesive is a material that has the ability to unit similar or unsimilar objects through bonding surface. The addition aims is to increase the adhesive strength of the produced briquettes [4].

The use and choice of adhesive material is carried on the base of some criteria such as good absorption of the water, relatively inexpensive and easy to obtain. The

Table 8.2 Chemical composition of rice husk

Component	Content (%)
Water content	9.02
Protein rough	3.03
Fiber rough	35.68
Ash	17.71
Carbohydrates rough	33.71
Hydrogen	1.54
Oxygen	33.64
Silica (SiO_2)	16.98

Source Research Institute of Post Harvest 2006

Table 8.3 Results of the analysis of the composition of rice husks already charred

Parameter	Unit	Analysis results	Method
Moisture content	%	5.35	ASTM. D 3302-97
Volatil matter	%	22.42	ASTM. D 3175-89
Ash content	%	8.35	ASTM. D 3174-97
Fixed carbon	%	63.88	By different
Heating value	kcal/kg	3734.38	ASTM. D 1989-97

Source Laboratory tests. Team Consulting Industry and Technology Institute of Sepuluh Nopember Indonesia affiliates, August 12, 2008

selection of adhesive materials affects the quality of briquettes [4]. Adhesives can be distinguished by the original material, i.e. organic and synthesis.

Tapioca is organic adhesive material, which is cheap and easy to obtain. Tapioca starch composition of the raw material briquettes are as much as 5% of the weight of briquettes itself. Starch and gluten are nonperishable because of the influence of fermentation.

8.2.4 Briquetting Process

According to [4], briquetting a material consists of several stages, presented below.

8.2.4.1 Enrichment and Weighing

Enrichment and weighing process is essential before doing the next step, due to determining the sizes and distribution of particles. This process is important to obtain the homogeneous materials.

8.2.4.2 Mixing

The mixing process serves to bind so that it will increase the strength of the briquettes. There are two methods can be used, namely:

(i) *Wet Mixing*.

Wet mixing is a mixing process, in which the powder matrix and filler mixed first with the solvent. This method is used, when the materials (matrix and filler) are susceptible to oxidation. The purpose of adding the solvent is to simplify the process of mixing the materials and to coat the surfaces of materials to protect the material from air and to prevent oxidation of the used materials.

(ii) *Dry Mixing.*

Dry mixing is a mixing process without using a solvent to dissolve and is done outdoor. This method is used, when the materials (matrix and filler) are not easily oxidized.

The mixing speed, the length of mixing time and the mixed particle size determine the homogeneity of particle distribution. The greater of mixing speed, the longer mixing time and the mixed smaller sizes cause the more homogeneous particle distribution. The homogeneity of mixing affects the process of compacting, since the compressive force is given at the time of compacting will be distributed evenly. So the quality of the bond between the particles is better.

8.2.4.3 Compaction

Compaction is the process of compacting powders into a sample. There are two methods used, namely:

(i) *Cold Compressing* is performed at room temperature. This method is used, when applied materials are easily oxidized.
(ii) *Hot Compressing* is performed at temperatures above room temperature. This method is used, when applied materials are not easily oxidized.

8.2.4.4 Sintering

The drying process can be defined as a process for separating water from the material. Drying can also be used for the preservation process. When the water content is reduced to lower 10%, the microorganisms cannot exist [5]. Based on the research, conducted by Widyaningsih [5], drying the briquettes can also determine the calorific fuel value. These results follow of Table 8.4.

8.3 Procedures of the Research

The material used in this experiment was a mixture of coal, rice whaff and organic adhesive, the composition can be seen as follows:

Table 8.4 Effect of drying method on calorific value of fuel [5]

Drying method	Calorific value (cal/g)
Heating the oven	2435.24
Direct solar heating	2425.95
Indirect solar heating	2425.85

(i) 65% coal, 25% rice husk, 10% tapioca flour
(ii) 55% coal, 35% rice husk, 10% tapioca flour
(iii) 45% coal, 45% rice husk, 10% tapioca flour

The first step is to pulverizing coal and charcoal powder of rice whaff with sizes of 40, 60 and 80 mesh, with a pressure of 78 kg/cm^2. Each sample consists of 5 pieces. Furthermore, all of the samples are pressured under 78 kg/cm^2, and sintered at 100 °C for 30 min. The next step is testing on compressive strength, density, calorific value and combustion temperature [6–10]. The scheme of performed experiments is present in Fig. 8.1.

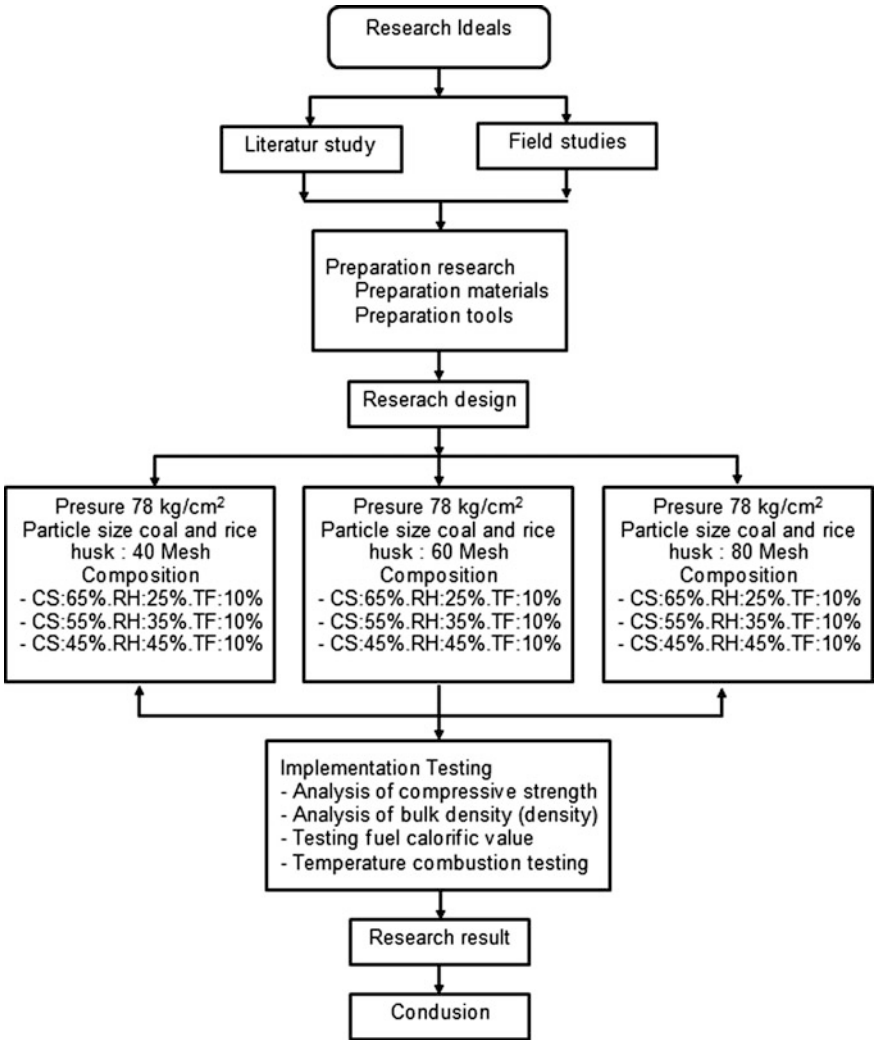

Fig. 8.1 Flowchart of research methods

8.4 Results and Discussion

After undertaking the tests and data analysis, the results can be presented in the form of graphs presented in Figs. 8.2, 8.3, 8.4, 8.5, 8.6, 8.7 and 8.8.

Figure 8.2 indicated in the analysis of compressive strength in the process of briquetting the mixture of coal and rice husk, that the highest value is attained in the briquettes with a particle size of 80 mesh, and the composition of 65% coal, 25% rice husk and 10% tapioca at the pressure of 78 kg/cm^2; this compressive strength is equal to 2.11 kg/cm^2. At the same time, the lowest value of compressive strength is occurred for briquettes particle size of 40 mesh, and the composition of 45% coal, 45% rice husk and 10% tapioca at the pressure of 78 kg/cm^2; this compressive strength is equal to 1.21 kg/cm^2. The briquette compressive strength can be affected by the level of particle fineness and fraction of matrix (coal) composition. When the particle size is finer, the bonds between the particles are more dense compared to the larger particle sizes. So the existing compressive strength of briquettes will affect bulk density.

Figure 8.3 shows the effect of composition and particle size in the process of briquetting the mixture of coal and rice husk on the values of bulk density. This figure demonstrates the value of the highest density occurs in briquettes with a particle size of 80 mesh, and the composition of 65% coal, 25% rice husk and 10% starch at the pressure of 78 kg/cm^2; this value of bulk density of briquettes is 0.89 g/cm^3. The lowest value of bulk density found in briquettes with a particle size of 40 mesh, the composition of coal is 45%, of rice husk 45%, tapioca 10%, pressure of 78 kg/cm^2 with a value of bulk density of briquettes is 0.78 g/cm^3. The value of the bulk density of briquettes is influenced by the fineness of the grain particles and the fraction of the matrix (coal). When the bonding matrix grains (coal) is higher, then the value of density (bulk density) is also greater.

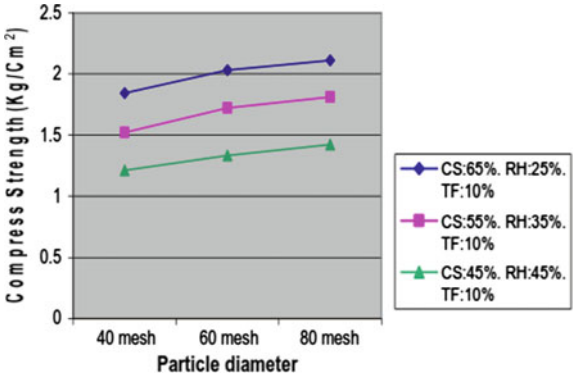

Fig. 8.2 Effects of the composition and size of briquettes particles on compressive strength

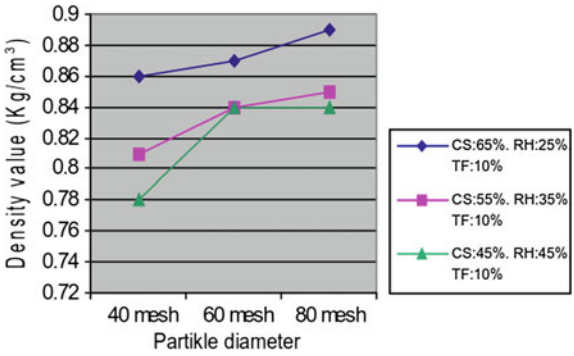

Fig. 8.3 Effects of the composition and diameter of briquettes particles on density

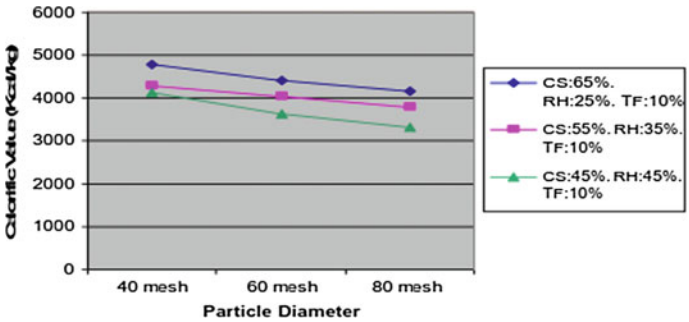

Fig. 8.4 Effects of the composition and diameter of briquettes particles on calorific value of burned briquettes

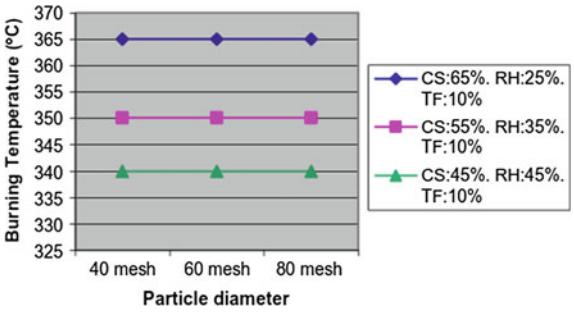

Fig. 8.5 Effects of the composition and diameter of briquettes particles on briquette combustion temperature

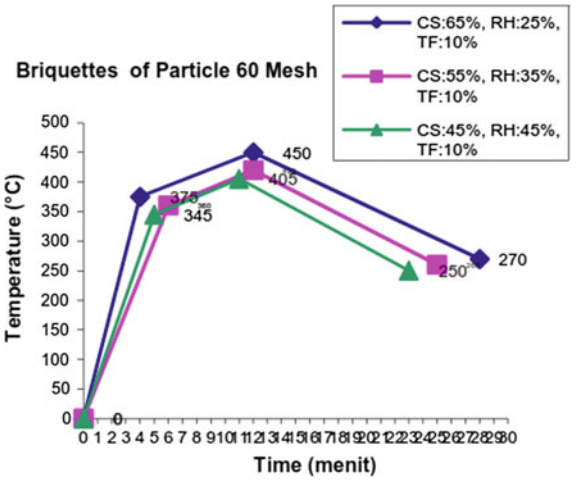

Fig. 8.6 Effect of burning rate on the mixture of coal briquettes and rice husk with particle sizes of 40 mesh

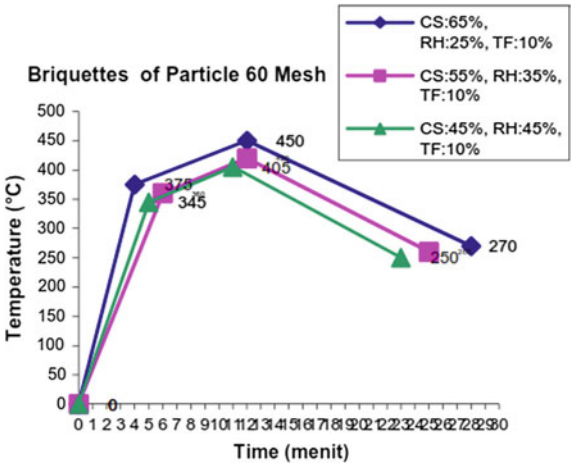

Fig. 8.7 Effect of burning rate on the mixture of coal briquettes and rice husk with particle sizes of 60 mesh

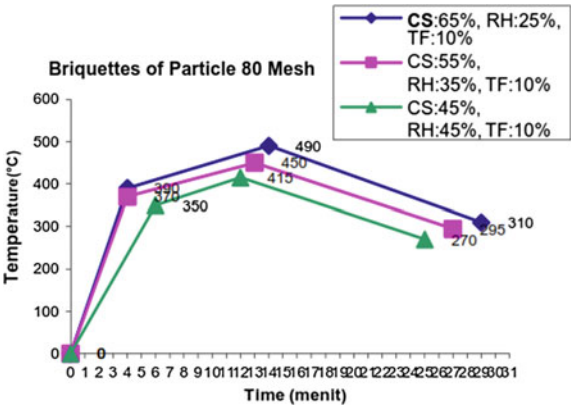

Fig. 8.8 Effect of burning rate on the mixture of coal briquettes and rice husk with particle sizes of 80 mesh

8.5 Conclusion

From the analysis conducted in this study, we made the following conclusions:

1. By comparing of different compositions and particle sizes in the process of briquetting the mix of coal and rice husk, we stated effects of these parameters on the compressive strength of briquettes and bulk density.
2. By comparing of different compositions and particle sizes in the process of briquetting the mix of coal and rice husk, we stated effects of these parameters on the calorific fuel value. However, the temperature of the burning briquettes was only influenced by the composition, while the size of the particles did not affect the value of briquettes combustion temperature.
3. From the performed analysis, we obtained:
   (i) the highest value of compressive strength in the process of briquetting of coal and rice husk was equal to 2.11 kg/cm^2, for the particle size of 80 mesh, at the composition of 65% coal, 25% rice husk and 10% tapioca and pressure of 78 kg/cm^2;
   (ii) the highest value of bulk density in the process of briquetting the mixture of coal and rice husk was equal to 0.89 g/cm^3 and occurred at the composition 65% coal, 25% rice husks and 10% tapioca flour, for the particle size of 80 mesh, and pressure of 78 kg/cm^2.
4. From the tests, we obtained:
   (i) the highest value of the calorific fuel in the process of briquetting the mixture of coal and rice husk was 4790.78 kcal/kg and occurred in the composition of 65% coal, 25% rice husk and 10% tapioca flour, for the particle size of 40 mesh, and pressure of 78 kg/cm^2;
   (ii) the highest temperature of combustion in the process of briquetting the mixture of coal and rice husk was 365 °C and occurred in the composition of 65% coal, 25% rice husks and 10% tapioca flour, while the particle size has no effect on the combustion temperature

References

1. Anonymous. *Solar Husk Replaces So Can Modified Source Diesel Power Center* (2003). www.mediaindonesia.com
2. Rahardjo. *Thesis: UCG Technology Management Sustainable Coal*, ed. by D. Fitriani (Graduate University of Sriwijaya Indonesia, 2006)
3. L.H. Kepmen. *Thesis: UCG Technology Management Sustainable Coal*, ed. by D. Fitriani (Graduate University of Sriwijaya Indonesia, 2003)
4. A.S. Budhi, *Charcoal Briquette Making of Faeces Cattle and Coconut Shell as an Alternative Energy Source* (Environmental Engineering Department of Civil Engineering Faculty, Institute Technology of Sepuluh Nopember, Surabaya, Indonesia, 2003)

5. A. Widyaningsih. *How Drying, Briquette Making, and Testing of Organic Solid Waste Heat* (Environmental Engineering Department, Institute Technology of Sepuluh Nopember, Surabaya, Indonesia, 1997)
6. Anonymous. *Japan—Indonesia Model Project for Clean Coal Technology of Coal Briquette (Carbonized) Manufacturing Technology* (Bukit Asam Coal Briquette Factory, Gresik, Indonesia, 2005) www.mediaindonesia.com
7. Anonymous. *Overcome Energy Deficit Can Use Biomass Waste*, Bukit Asam Coal Briquette Factory, Gresik, Indonesia (2004) www.mediaindonesia.com
8. B.J.M. Beumer. *Metal Materials Science*. *Volume I* (Translators: Bs. Anwir, Matondang. Bhratara Work Literacy, Jakarta, 1985)
9. A.W. Culp Jr. *Principles of Energy Conversion* (Translators: Darwin Sitompul. Erland, Jakarta, 1991)
10. O. De Lorenzi. *Combustion Engineering* (Combustion Engineering, Inc., 1957)

Part II
Physics of Advanced Materials

Chapter 9
Investigations of the Capability to Heavy Metals Adsorption Humic Acids: Correlation Between Structure and Absorption Properties

A.I. Chechevatov, Y.S. Miroshnichenko, T.N. Myasoyedova, Yu. V. Popov and G.E. Yalovega

Abstract In this chapter, we present the studies of the surface morphology and concentrations of microelements for water-soluble and insoluble humates. The features of the humates structure were studied by means of IR-spectroscopy. The changes in IR-spectra are observed after interaction of humates with Cu^{2+} ions. It was found that the saturation of humates by metal ions leads to changes in the infrared spectrum due to the copper ions binding. It was established that humates can effectively clean solution with a concentration of copper ions and lead ions equals to 0.3 g/l, which allows them to be used as sorbents for purification of waste water and mining engineering plants. Sorption capacity of humates is estimated.

9.1 Introduction

One of the most frequent found types of pollution is a supply of heavy metals to various areas of environment. Heavy metals are a notable source of pollution both in the aquatic and soil environments. Largely, their presence derives from industrial wastewater effluents [1–5]. The discharge of wastewater containing high concentrations of heavy metals to receiving water bodies has serious adverse environmental effects. Cleaning of soils, waters and the atmosphere from heavy metals is an

A.I. Chechevatov · G.E. Yalovega (✉)
Faculty of Physics, Southern Federal University,
Zorge str. 5, Rostov-on-Don 344006, Russia
e-mail: yalovega1968@mail.ru

Y.S. Miroshnichenko · T.N. Myasoyedova
Institute of Nanotechnologies, Electronics and Equipment Engineering,
Southern Federal University, Chehov str. 2, Taganrog 347900, Russia

Yu.V. Popov
Institute of Earth Sciences, Southern Federal University,
Zorge str. 40, Rostov-on-Don 344090, Russia

I.A. Parinov et al. (eds.), *Advanced Materials*, Springer Proceedings
in Physics 193, DOI 10.1007/978-3-319-56062-5_9

actual problem of environment protection against technological influences. In order to remove dissolved heavy metals ions from various environments, conventional techniques including chemical precipitation, ion exchange, reverse osmosis, membrane separation, electrochemical treatments, solvent extraction processes and sorption are widely used. The simplest in hardware design, low cost, performing deep-water purification is sorption method. Application of sorbents allows cleaning wastewaters without secondary pollution and provides reliability in fluctuating volumes and composition of wastewater. One of sorption method is usage of the natural adsorbing substances—humic substances (or humates). Humic substances are generally seen as important soil and natural water components. Humic substances are a mixture of resistant to biodegradation and high molecular weight naturally occurring organic compounds formed by decomposition of plant and animal residues by microorganisms and abiotic environmental factors [6].

Humic substances are a mixture of complex organic compounds that are usually separated into three fractions: humic acids, fulvic acids and humates [7–10]. The sorbents can be manufactured from humic substances of brown coal wastes, peat and sapropel [10] by alkali extraction in ammonia, potassium hydroxide or sodium hydroxide solutions. Such treatment converts them into water-soluble salts—potassium or sodium humate possessing high biological activity [11]. An alternative way involves the mechanical crushing of brown coal with a solid alkali, resulting in a solid, water-soluble potassium and sodium humate [9, 12]. A large number of works are devoted to application of humic substances as sorbents for the detoxification of soil.

Humic acids form strong bonds with metal ions. In the soil, they are able to bind radionuclides, polyaromatic hydrocarbons, pesticides, chlorinated hydrocarbons, petroleum products and heavy metals [10]. A lack of studies is devoted to water purification with humic substances. In water, they form stable complexes with radionuclides, polyaromatic hydrocarbons, pesticides, chlorinated hydrocarbons, petroleum products [10], phenols, mineral oils [12], heavy metals [11–13].

Usually, the elemental composition of humic acid composition means their organic part formed by comparable amounts of carbon, hydrogen and oxygen. A mandatory element is nitrogen, almost all determined drugs and sulfur. However, in addition to the organic part of the all selected products, humic acid also includes inorganic part. It consists of mineral elements (mainly, metal ions, silicon oxide and aluminum) and the hygroscopic moisture with content equals to 10%. Therefore, in general terms the gross formula of humic acids can be written as follows [14]: $C_xH_yN_zO_pS_qM_r(Al_2O_3)_l(SiO_2)_m(H_2O)_n$, where M is the metal ion, x, y, z, p, q, l, m, n are stoichiometric constants. In [15], it was established that humic acids consist of 45–60% carbon, 30–35% oxygen, 3–7% hydrogen, 3–5% nitrogen, 1–3% sulfur and metal ions (depends on formation source).

Humic compounds have complex structure. There are central and peripheral parts in the structure. First of them, central part, is formed by condensed and carbon bridges of aromatic and heteroaromatic rings with different functional groups. Aliphatic, polysaccharide and polypeptide chains form the second one. These humic substances structural features determine their chemical, physico-chemical

and biological properties. Some of the mentioned chemical groups such as carboxyl, carbonyl and phenolic hydroxyl in combination with aromatic structures, provide the ability of humic acids to the ion and the donor-acceptor interaction. Humic acids are actively involved to the sorption and oxidation—reduction processes [16, 17]. Thus, these facts demonstrate that humic acids have complexly, the stochastic structure of molecules and are able to take part in different reactions of condensation and various oxidation-hydrolytic cleavage. Oxidation—reduction properties of humic acids are explained by the presence of hydroquinone fragments in their structure [18]. Summing up, the complexity of the structure of humic acids, the presence of a large number of functional groups, the ability to form intermolecular and intramolecular bonds causes a wide range of interactions, which may come in humic acids.

Studies on complexes of heavy metals and humic substances showed that carboxyl and hydroxyl groups play the main role in interaction processes. These groups have several important characteristics. First, they have affinity for water, which provides dissolving of humic acids molecules. Second, carboxyl and hydroxyl groups substitute hydrogen atoms for heavy metals ions. However, chemical structure and fractional composition of humic substances depend on the methods of selection, modification, and source. As for humic acid salts—potassium and sodium humates, there are too many questions concerning their interaction with heavy metals ions. During producing humic acid salts, substitution of hydrogen atoms for potassium and sodium ions occurs and then there is the question of the mechanism of sorption of "humates—heavy metal ions". In addition, it is necessary to find optimal conditions for sorption of different heavy metals ions with humates. It is known, some works reported such results [11, 12, 19] but still there are some moot questions. This situation determines the relevance of organizing systematic research on the structure of humates, their properties due to which humates play a crucial role in the processes of binding detoxifiers, as well as the study of the influence of various factors on the sorption capacity.

Due to structural features to determine elemental composition and to establish correlations between structure of humic acids and their ecotoxicological properties is possible only with complex physical and chemical analysis methods [20]. At the present stage, are used different research methods GC: spectroscopy methods in the UV, visible, IR, nuclear magnetic (NMR) and electron paramagnetic (EPR) resonance fluorescence analysis, electron microscopy techniques, chromatography, thermal analysis and others [21–30].

In the present work, we study surface morphology, concentrations of microelements and composition of functional groups of a number of humic substances using electron microscopy, IR-spectroscopy and EDX analysis. Sorption capacity of different types of humates to copper (II) and lead (II) ions was also one of our research purposes.

9.2 Materials and Methods

9.2.1 Materials

The humates, obtained from brown coal wastes in the LLC "Agrarniye technologii" (Irkutsk, Russia), were used in experiment. There were three types of humates: water-soluble humates «Baikal» and «Humat-80» (were matched as PH and SH, respectively), and insoluble "dry" humates «Humat-GK» (were matched as DH). Copper (II) sulfate, lead (II) nitrate, formic acid were purchased from Aquatest, Russia. The pH was adjusted by sulphuric acid and nitric acid also obtained from Aquatest.

9.2.2 SEM and EDS Methods

The method of the scanning electronic microscopy (SEM) allows one to define morphology of a humic substances surface of molecules. The energy-dispersive spectroscopy reflects microelement structure of the studied humates, as well as supplies information about differences between the concentrations of microelements in the each sample. The morphology of the samples surfaces and chemical analysis were carried out using complex analytic device based on scanning electron microscope VEGA II LMU with operating voltage at 20 kV and system of the microanalysis INCA ENERGY 450/XT with X-Act DDD detector and energy dispersive X-ray (EDX) analyzer (Oxford Instruments).

9.2.3 Infrared Analysis

IR spectral analysis was performed on an ALPHA IR Fourier spectrometer (Bruker Optik GmbH, Germany) by the method of frustrated total internal reflection. Spectra were recorded in the mid-IR range from 500 to 4000 cm^{-1} using the OPUS software. IR spectra were measured using an ALPHA-E module with the following parameters: resolution of 2 cm^{-1} and spectrum recording time of 50 scans.

9.2.4 Sorption Experiments

Potentiometer method was used to analyze Cu^{2+} and Pb^{2+} ions in the solution. The hydrogen ion concentration of different solutions was measured by means of using pH-meter (Ekotest-2000, Russia). The demanded doses of humates and other reagents were weighted on analytical balance. A series of copper and lead solutions,

50 ml each, at different concentrations (0.3, 0.5, 0.8, 1.0 g/L) and pH values, 2 and 6, were treated with humates. PH and SH samples were dissolved in distilled water in order to achieve concentration of 1.0 g/L. Copper and lead solutions (50 ml) were mixed with different volumes of PH and SH solutions for sorption experiments. Humates concentration was recalculated to the volume of treated solution and mass of dry sample, using for preparation of water solution, was in the range of 0.4–4.6 g/L. DH sample were added into dry solutions. Sorption was carried out in static conditions for 15 min. As reported in [24], it leads to formation of strong coordination compounds, which were deposited by centrifugation for 30 min. The amount of extracted metal (extraction ability) can be calculated with the following equation: $\frac{C_0 - C}{C_0} \times 100\%$, where C_0 is the initial metal ion concentration (g/L), C is the equilibrium metal ion concentration (g/L).

9.3 Results and Discussion

9.3.1 SEM and Elemental Analysis

The energy dispersive X-ray analysis (EDX) apparatus that can work simultaneously to SEM which combines elemental and structural analysis of compounds with mapping techniques gave us the morphology of the sample surfaces, elemental and percentage composition of initial DH, PH, SH humates (see Figs. 9.1, 9.2 and 9.3).

As shown in Figs. 9.1, 9.2 and 9.3, all samples have a multiphase structure radically different for various types of humates. While DH humates are monolithic structure with small metal inclusions, soluble SH humates are loose needle-like structure. At the same time, PH humates combine structure with the presence of both solid and loose areas. Elemental mapping in various points of samples showed different elemental composition that indicates that formed structures have different compositions. Normalized to 100% of the elemental composition analysis of the DH, SH and PH samples is shown in Tables 9.1, 9.2 and 9.3, respectively. It should be noted that the composition of the data are 100% non-carbon accounting, water and "small" elements (i.e., the comparative data reflect rather than quantitative value). The detection limits of elements make up is 0.1–0.5% by weight.

All test phases for DH sample are characterized by a high content of sodium and calcium. Analysis of the silicon and aluminum percentage changes during the transition from one phase to another suggests the presence of aluminosilicate in the composition of the sample. For water-soluble humates, it is characterized by decrease in calcium content compared with humates for dry application, the high content of silicon and iron. An open question remains the high sodium content in both water-soluble samples.

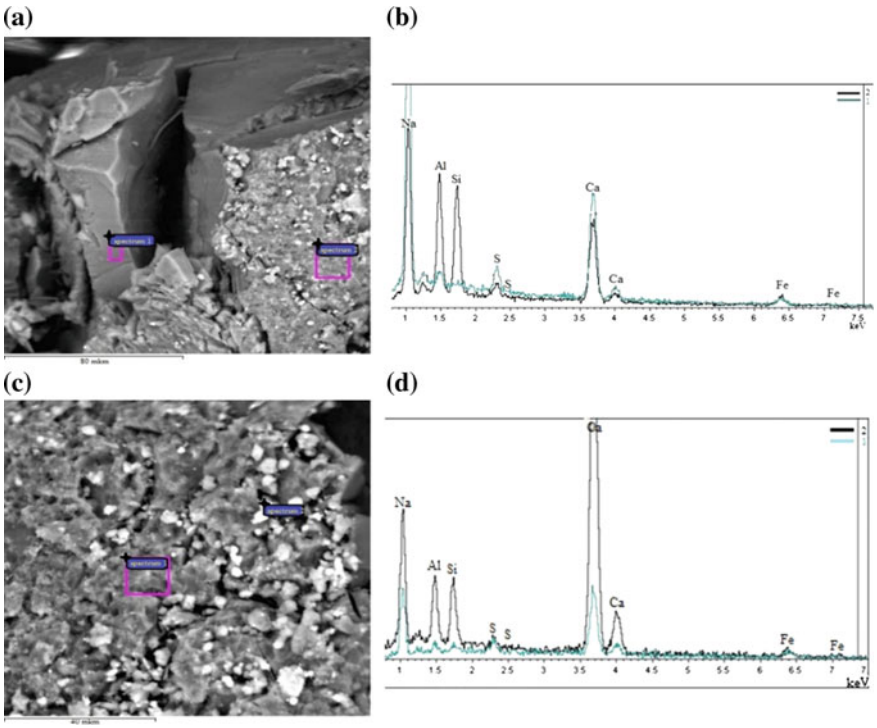

Fig. 9.1 SEM images (**a**, **c**) and EDX results (**b**, **d**) of DH humates

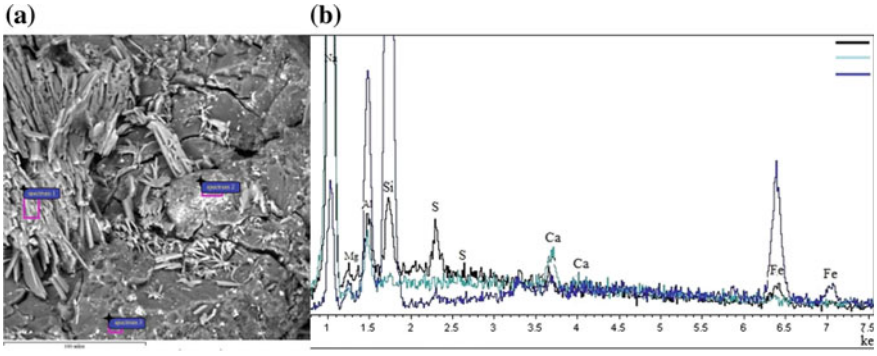

Fig. 9.2 SEM images (**a**) and EDX results (**b**) of PH humates

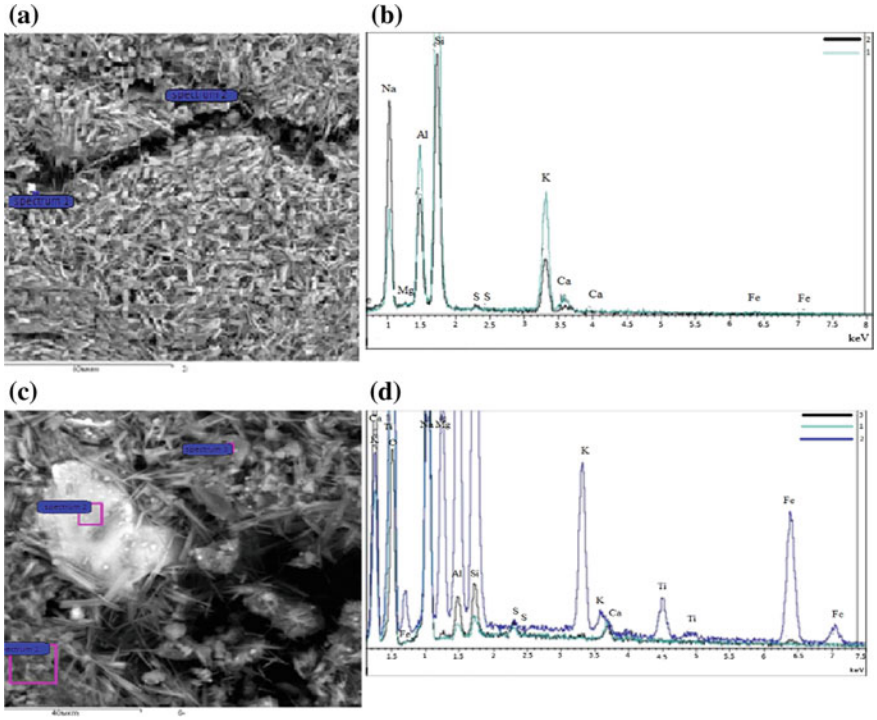

Fig. 9.3 SEM images (**a**, **c**) and EDX results (**b**, **d**) of SH humates

Table 9.1 Elemental composition of DH humates in various points of EDX analysis

Weight (%). Normalized to 100%. The error of ~20%									
Figure 1	Spectrum	O	Na	Mg	Al	Si	S	Ca	Fe
a	1	61.0	26.6	0.9	0.8	0.0	1.3	8.3	1.2
a	2	56.7	16.7	0.9	7.6	7.4	0.8	7.8	2.2
c	1	54.5	20.3	0.0	1.8	0.8	2.0	16.5	4.2
c	2	62.6	9.8	0.0	2.8	2.5	0.4	20.9	1.0

Table 9.2 Elemental composition of SH humates in various points of EDX analysis

Weight (%). Normalized to 100%. The error of ~20%										
Figure 2	Spectrum	O	Na	Mg	Al	Si	S	K	Ca	Fe
a	1	54.5	42.9	0.1	1.1	0.2	0.1	–	0.9	0.2
a	2	26.2	7.5	1.0	8.2	35.9	0.3	0.6	0.6	19.7
a	3	38.7	46.5	1.0	3.4	3.7	2.1	0.5	0.8	3.2

Table 9.3 Elemental composition of PH humates in various points of EDX analysis

Weight (%). Normalized to 100%. The error of ~20%										
Figure 3	Spectrum	O	Na	Mg	Al	Si	S	K	Ca	Fe
a	1	39.9	8.9	0.1	9.7	28.9	0.2	12.1	0.2	0.2
a	2	51.4	18.6	0.1	7.2	16.7	0.4	5.1	0.4	0.2
c	1	48.8	46.9	–	1.0	1.2	0.5	–	1.5	0.2
c	2	44.8	9.0	5.8	9.0	14.1	0.1	4.6	0.4	10.6
c	3	40.0	45.5	–	4.6	5.2	1.4	–	1.7	1.6

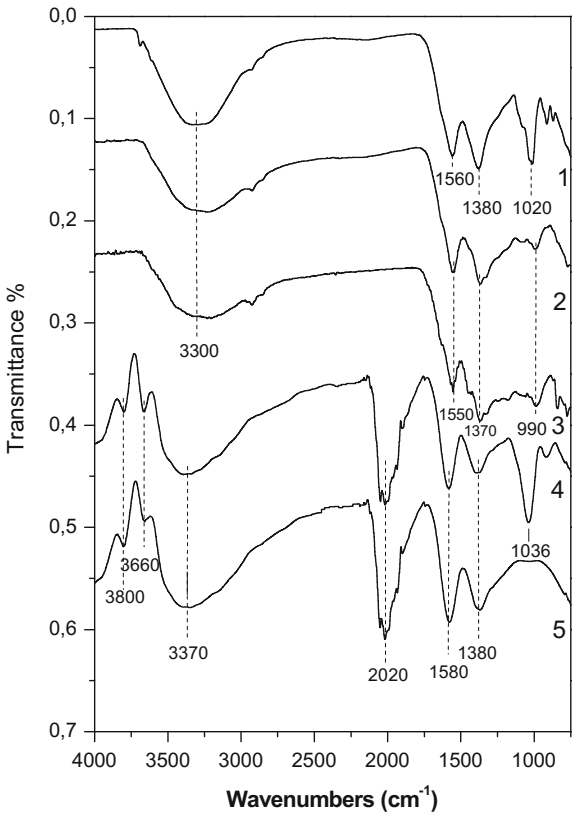

Fig. 9.4 *1* DH sample, *2* PH sample, *3* SH sample, *4* PH sample + Cu^{2+}, *5* DH sample + Cu^{2+}

9.3.2 IR-Spectroscopy

In order to get information about changes in structure of various humates, FTIR spectra were measured for the DH, PH and SH humates as well as humates after Cu^{2+} and Pb^{2+} extraction (Fig. 9.4). The study of humates by IR spectrometry revealed the presence of the aromatic core portion, benzenoid structure, primary and

secondary amines. The presence of alcohol, the methyl terminal groups, carboxyl groups and carbohydrate groups is also observed. CH, CH_2, CH_3 groups and the C–CH_3 groups were identified.

The presence of bands in the spectra of vibrations bonds C=C aromatic ring (near 1610 cm^{-1}) indicates presence of the aromatic framework portion in humic substances, benzoid structures correspond to 1510–1500 cm^{-1}, 1390–1400 cm^{-1}. The bands in the 1050–1150 cm^{-1} range correspond to the vibrations of C–O alcohol groups. The slight absorption band at 2920 cm^{-1} refers to the long methylene chains and at 2860 cm^{-1} to the terminal methyl groups. The absorption bands at wavelengths 1225 cm^{-1} correspond to OH-groups in the carboxylic groups, 1025 cm^{-1} relates to OH-groups of carbohydrate. The absorption band of 3000–2750 cm^{-1} (low-intensity stretching vibrations) was identified and corresponds to CH, CH_2, and CH_3 groups. The deformation vibrations of 1460–1380 cm^{-1} correspond to C–CH_3; bending vibrations to N–H connection of primary and secondary amines (1650–1550 cm^{-1}, 1650–1580 cm^{-1}); CH bond to purine and pyrimidine cycles (1000–960 cm^{-1}, 825–775 cm^{-1}); double bonds (995–985 cm^{-1}), oxygen heterocycles (800–740 cm^{-1}, 840–800 cm^{-1}). Figure 9.4 reveals reduction of peak intensity in the range of 3600–2500 cm^{-1} and 1750–750 cm^{-1} for humates containing Cu^{2+} ions, that means binding between copper ions and functional groups in the mentioned frequency range (Table 9.4).

Table 9.4 Attributions of the main infrared peaks of the humic substances [31]

Frequency (cm^{-1})	Assignment
3400–3300	O–H stretching, N–H stretching (trace)
2940–2840	Aliphatic C–H stretching
1725–1718	C=O stretching of COOH and ketones (trace)
1660–1630	C=O stretching of amide groups (amide I band), quinone C=O and/or C=O of H-bonded conjugated ketones
1620–1600	Aromatic C=C, strongly H-bonded C=O of conjugated ketones
1600–1585	C=C stretching within the ring
1590–1520	COO^- symmetric stretching, N–H bending, C=N stretching (amide II band)
1500–1400	C=C stretching within the ring
1400–1390	OH deformation and C–O stretching of phenolic OH, C–H deformation of CH_2 and CH_3 groups, COO^- antisymmetric stretching
1280–1200	C–O stretching and OH deformation of COOH
1170–950	C–O stretching of polysaccharide or polysaccharide-like substances, Si–O of silicate impurities

9.3.3 Extraction Ability

Figures 9.5 and 9.6 show effect of humates concentration to the extraction ability of Cu^{2+} and Pb^{2+} ions for the DH, PH and SH samples. The all experiments were carried out at pH = 6, initial metal ion concentration was 0.3 g/L, extraction time was 1 h, extraction was performed at room temperature. Figure 9.5 presents extraction ability of the DH samples to Cu^{2+} and Pb^{2+} ions. It is shown that removal of Pb^{2+} ions is better, than of Cu^{2+} ones. The maximum extraction ability of Pb^{2+} ions is 78%, while it reaches only 44% for Cu^{2+} ions at DH concentration 2 g/L. Maximum extraction ability of Cu^{2+} ions is 89% at humates concentration 4.6 g/L. Figure 9.6 shows the comparative study on extraction ability of PH and SH samples to Cu^{2+} and Pb^{2+} ions.

These results demonstrate that aqueous humates as dry humates application bind lead ions better than copper ones. For the sorption of lead ions soluble SH and PH humates are equally effective. For the adsorption of copper ions, aqueous SH is more effective than the aqueous PH at the same concentration. This is due to the ion sorption capacity is strongly dependent on the ion radius and the charge density. A comparison of two ions with the same charge shows that larger sorption capacity exhibits ion with a larger radius. This phenomenon is explained by the following: ions with larger radius are more polarized and attract to the charged sorbent surface better. At the same time, ions with smaller radius are more prone to hydration and hydration shell formation, which reduces such electrostatic interaction. Since the lead has a greater ionic radius (0.126 nm) in comparison with copper ions (0.080 nm), the sorption capacity of the sorbents with respect to the lead ions must be higher than with respect to copper ions, that is confirmed by experimental data. Figure 9.6 shows the comparative study on extraction ability of PH and SH samples to Cu^{2+} and Pb^{2+} ions.

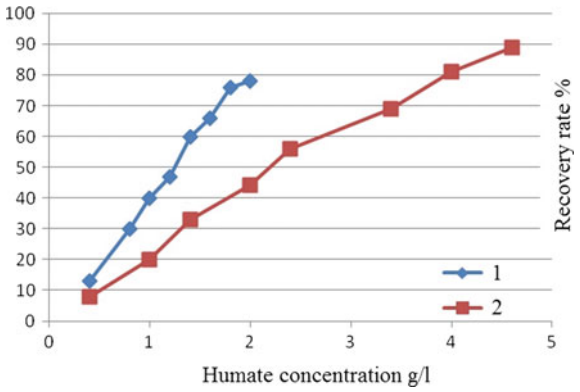

Fig. 9.5 Extraction ability of DH samples to Cu^{2+} and Pb^{2+} ions (pH = 6, initial metal ion concentration is 0.3 g/L, extraction time is 1 h, extraction at room temperature). *1* DH sample + Cu^{2+}, *2* DH sample + Pb^{2+}

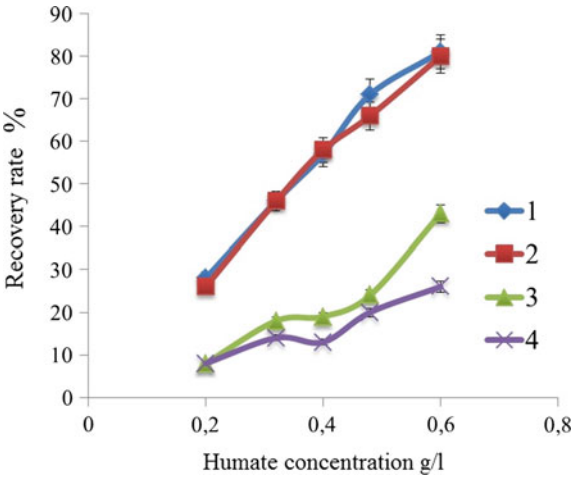

Fig. 9.6 Extraction ability of SH and PH samples to Cu^{2+} and Pb^{2+} ions (pH = 6, initial metal ion concentration is 0.3 g/L, extraction time is 1 h, extraction at room temperature). *1* SH sample + Pb^{2+}, *2* PH sample + Pb^{2+}, *3* SH sample + Cu^{2+}, *4* PH sample + Cu^{2+}

9.4 Conclusions

The studies of the surface morphology and concentrations of microelements for water-soluble PH and SH humates as well as insoluble "dry" humates were performed. The DH humates are monolithic structure with small metal inclusions, soluble SH are loose needle-like structure. At the same time, PH is combined structure with the presence of both solid and loose areas. Elemental mapping in various points of samples showed different elemental composition that indicates that formed structures have different composition. In the study of humate by IR spectrometry, revealed the presence of the aromatic core portion, benzenoid structure, primary and secondary amines is observed the presence of alcohol, the methyl terminal groups, carboxyl groups and carbohydrate groups. CH, CH_2, CH_3 and C–CH_3 groups were identified. It was also found that the saturation of humates by metal ions leads to changes in the infrared spectrum due to the copper ions binding. It was established that humates could effectively clean solution with a concentration of copper ions and lead ions equals to 0.3 g/l, which allows them to be used as sorbents for purification of wastewater and mining engineering plants. For the water sorption of lead ions SH and PH humates are equally effective. Thus, due to the internal structure and ease of production humic substances are great to eliminate the consequences of the environmental disasters and pollution have emerged in the course of an active human industrial activities.

Acknowledgements We would like to thank "Center for Research of Mineral Recourses and Environment" (Southern Federal University, Russia) for provided EDX measurements and Dr. G. Lazorenko for valuable discussions.

References

1. N.T. Abdel-Ghani, G.A. El-Chaghaby, IJLRST **3**(1), 24 (2014)
2. G. Gyananath, D.K. Balhal, Cell. Chem. Technol. **46**(1–2), 121 (2012)
3. L.V.A. Gurgel, L.F. Gil, Carbohyd. Polym. **77**(1), 142 (2009)
4. T.J.K. Ideriah, S. David-Omiema, D.N. Ogbonna, Resour. Environ. **2**(1), 33 (2012)
5. S. Ivana, Hem. Ind. **67**(5), 773 (2013)
6. F.J. Stevenson, in *Humus Chemistry: Genesis, Composition, Reactions* (1982), p. 443
7. P. Zuman, E.B. Rupp, in *Humic Acids—Are They Natural Products?* (2005)
8. I.V. Perminova, N.A. Kulikova, D.M. Zhilin, *Viable Methods of Soil* (2006), p. 249
9. E.M. Peña-Méndez, J. Havel, J. Patočka, J. Appl. Biomed. **3**, 13 (2005)
10. I.V. Perminova, K. Hatfield, in *Use of Humic Substances to Remediate Polluted Environments: From Theory to Practice*, vol. 3 (2005)
11. S. Sumayya, J. Basic Appl. Sci. **1**(2), 101–103 (2005)
12. J. Kochany, in *WM'01 Conference* (2001)
13. Y. Zheng, S. Hua, A. Wang, Desalination **263**, 170 (2010)
14. D.S. Orlov, *Humic Acids of Soils and General Theory of Hymification* (1990), p. 325 [in Russian]
15. G. Ricca, Structural investigations of humic acids from leonardite by spectroscopic methods and thermal analysis. Geoderma **57**(3), 263–274 (1993)
16. L.P. Komissarov, in *10th International Peat Congress*, vol. 2, (1996), p. 52 [in Russian]
17. F.D. Kopinke, Environ. Sci. Technol. **29**, 941 (1995)
18. A.A. Nozdrunova, Chem. Plant Raw Mater. **4**, 141 (2008)
19. S. Erdogan, Polish J. Environ. Stud. **16**, 671 (2007)
20. I.A. Savchenko, I.N. Korneeva, D.S. Goncharov, E.A. Luksha, *Modern Problems of Science and Education,* vol. 2 (2014) [in Russian]
21. A.V. Vasiliev, E.V. Grinenko, A.O. Shchukin, T.G. Fedulina, *Infrared Spectroscopy of Organic and Natural Products: Textbook for Students* (SPb.: SPbGLTA, 2007), p. 54 [in Russian]
22. G.A. Kalabin, L.V. Kanitskaya, D.F. Kushnarev, Quantitative NMR spectroscopy of natural organic raw materials and by- products (M.: Chemistry, 2000) p. 408 [in Russian]
23. A.A. Stepanov, L.V. Zharkova, E.A. Stepanova, Pedology **2**, 173–177 (1997). [in Russian]
24. N.V. Shpinova, M.P. Sartakov, Bull. YugraSU **4**(19), 88 (2010)
25. R.J. Abraham, P. Loftus, J. Chem. Educ. **230** (1978)
26. F. Adani, P. Genevini, F. Tambone, E. Montoneri, Chemosphere **65**, 1414 (2006)
27. J.A. Chromatogr, J. Chromatogr. A **1112**(1–2), 31 (2006)
28. P. Conte, R. Spaccini, A. Piccolo, Progr. Nucl. Magn. Res. Spect. **44**, 215 (2004)
29. V. Kholodov, A. Konstantinov, A. Kudryavtsev, I. Perminova, Eurasian Soil Sci. **44**(9), 976 (2011)
30. H.B. Yu, B.D. Xi, W.C. Ma, D.L. Li, Soil Sci. Soc. Am. J. **75**(4), 1385 (2011)
31. M. Giovanela, E. Parlanti, E.-J. Soriano-Sierra, M.S. Soldi, M.M.D. Sierra, Geochem. J. **38**, 255 (2004)

Chapter 10
Nanosized Effects in $BaTiO_3$

A. Surahman, N. Kofanova, Yu. Kuprina, A.G. Rudskaya and M.F. Kupriyanov

Abstract In this paper we report results of analysis of nanosized effects in $BaTiO_3$ and description of unit cells volume changes as effects of "negative pressure".

10.1 Introduction

The development of nanocrystalline ferroelectric materials (with ideality regions less than 100 nm in size) for nanoelectronic applications is confronted with a number of fundamental problems. The structure and ferroelectric properties of many nanocrystalline oxide materials differ drastically from those of bulk ferroelectrics (ideality regions more than 100 nm in size). In particular, the ferroelectric transition temperature of nanocrystalline materials decreases with decreasing crystallite size [1, 2]. The impact of particle size on the ferroelectric perovskites state undergoes increased attention. Examples of structural changes related to size effects in oxides of other structural types are given in [1–6]. We can distinguish the following most reliably determined structure changes and ferroelectric properties of perovskite-type oxides ABO_3 occurring with decreasing particle size: (i) reducing the spontaneous deformation of the unit cells at room temperature; it corresponds to a reduction of the phase transition temperature from ferroelectric to paraelectric phase; (ii) increasing the volume of the unit cell (or an average lattice parameter pseudocubic phase); (iii) observed loosening structure, resulting in reconstructive phase

A. Surahman (✉) · N. Kofanova · Y. Kuprina · A.G. Rudskaya · M.F. Kupriyanov
Department of Physics, Southern Federal University, 344090 Rostov-on-Don, Russia
e-mail: surakhman@mail.ru

A.G. Rudskaya
e-mail: arudskaya@yandex.ru

A. Surahman
University of Lampung, 35145 Bandar-Lampung, Indonesia

I.A. Parinov et al. (eds.), *Advanced Materials*, Springer Proceedings in Physics 193, DOI 10.1007/978-3-319-56062-5_10

transitions. Noteworthy is the increase in all cases, the unit cell volume and the decrease in the values of the spontaneous deformation with increasing temperature, with increasing number of radiation-induced defects and decreasing the size of crystals. Obviously, depending on the parameters from the crystallization temperature, $BaTiO_3$ cells also reflect the size effect: with increasing crystallization temperature, the crystallites grow larger. It is clear that in all these cases, the structure effects decrease $BaTiO_3$ correlation radius of the interatomic interaction.

In this work, we considered dependence of changes in the volume of the unit cells of barium titanate on both positive and negative pressure. In our opinion, nanocrystallinity should be taken into account for the state of crystals in which the size of regions with an ideal structure, rather than the crystallite size, is less than the critical one. Indeed, the most reports on nanomaterials deal with the size of coherently scattering regions (CSDs) (ideality regions) determined by *X*-ray diffraction (XRD) techniques. From this viewpoint, nanosized effects may take place in crystals containing high densities of various defects.

Figure 10.1 shows the dependence of the parameters of the $BaTiO_3$ cell at room temperature on the particle sizes (a), on neutron irradiation dose (b) as well as on temperature (c) [7]. We can see that with a decrease of crystallite size (Fig. 10.1a)

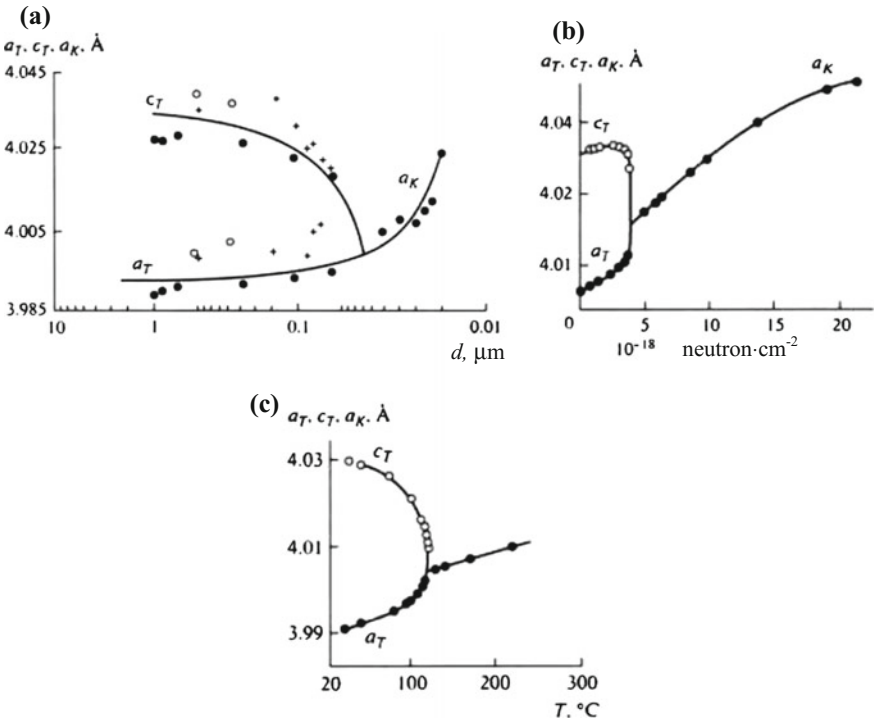

Fig. 10.1 Dependence of $BaTiO_3$ cell parameters on the crystallite size (**a**) on the dose of neutron irradiation (**b**) and on the temperature (**c**)

and an increase in the dose of neutron irradiation (Fig. 10.1b), phase transitions from the tetragonal to cubic phases are observed at room temperature in $BaTiO_3$. The parameters of the cells increase in cubic phases. For comparison, Fig. 10.1 shows the dependence of the similar cell parameters on temperature.

10.2 Method of Analysis

In our work, we consider the dependence of the parameters of the $BaTiO_3$ cells in the cubic phase on the crystallite size at room temperature. As the base state, we selected cell volume of cubic phase with a minimum size of the crystallites in accordance with [1]. The increase of crystallite size corresponds to a decrease of $\frac{V}{V_0}$ $\left(\frac{V}{V_0} < 1\right)$. This dependence is similar to dependence $\frac{V}{V_0}$ at increasing external (thoroughly) pressure. It is obvious that if in an initial state to select a point of the phase transition between the cubic and tetragonal phases, the reduction of crystallite sizes $BaTiO_3$ will match the increase of $\frac{V}{V_0}$ $\left(\frac{V}{V_0} > 1\right)$. Such dependence $\frac{V}{V_0}$ (<*D*>) can be compared with the dependence of the negative pressure. This approach to the analysis of changes in the parameters of the cubic $BaTiO_3$ cells of the crystallite size allows us to describe the observed changes, depending on the positive or negative pressure.

Consideration of nanosized effects in $BaTiO_3$ can be properly carried out for the cubic phase as for the tetragonal phase; it presents lists for additional changes $\frac{V}{V_0}$ associated with spontaneous deformation. Reference [8] shows the options to describe the effect of pressure in a number of nanomaterials, using the equation of state is most often used:

$$P = B_0\left(1 - \frac{V}{V_0}\right) + \frac{B_0\left(B_0' + 1\right)}{2}\left(1 - \frac{V}{V_0}\right)^2.$$

Figure 10.2 shows the relationship $\frac{V}{V_0}$ in $BaTiO_3$ of both positive and negative pressure ($\frac{V}{V_0} = 1$ at $P = 0$). Depending on the impact of $\frac{V}{V_0} = f(P)$, the quantities B_0 and B_0' are shown in Fig. 10.3. It can be seen that different values of B_0 correspond to different slopes. The lower values of B_0 characterize steeper $\frac{V}{V_0}(P)$ [9].

Analysis of the relationship $\frac{V}{V_0}$ (<*D*>) selects the highest value of the volume cell of $BaTiO_3$ ($\frac{V}{V_0} = 1$ at $D = 0.019$ μm) (Fig. 10.4) and shows that the nanosized effects are characterized by two regions of dependence $\frac{V}{V_0}(P)$ with $B_0 = 100$ GPa ($D < 0.035$ μm) and $B_0 = 200$ GPa ($D > 0.035$ μm). This fact means that there is critical value $D_c = 0.035$ μm in $BaTiO_3$ nanocrystallites. At a lower D, modulus of elasticity corresponds to a soft structure and when $D > D_c$ it corresponds to a rigid structure.

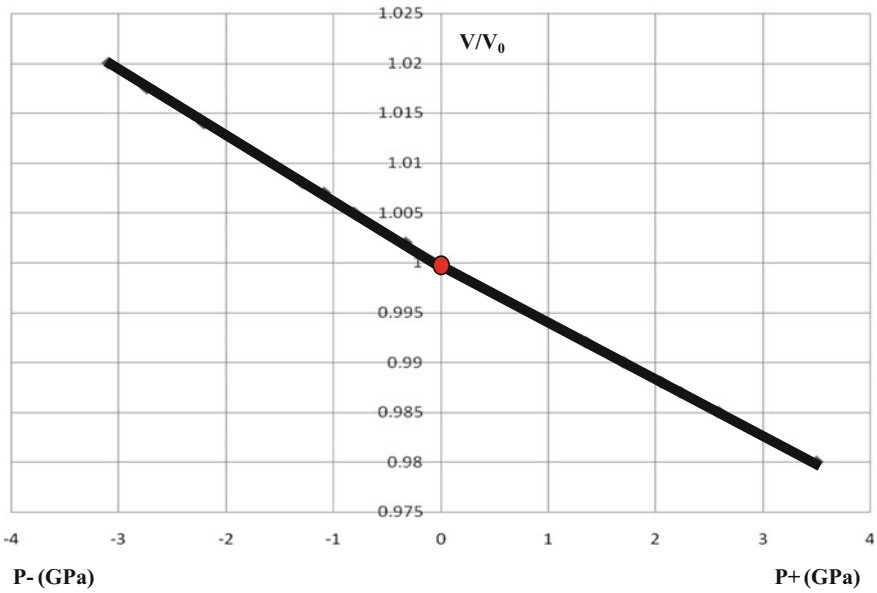

Fig. 10.2 Volume expansion $\frac{V}{V_o}$ as a function of both positive and negative pressure P for nanosized $BaTiO_3$ (B_0 = 165 GPa, $B_0{}'$ = 5)

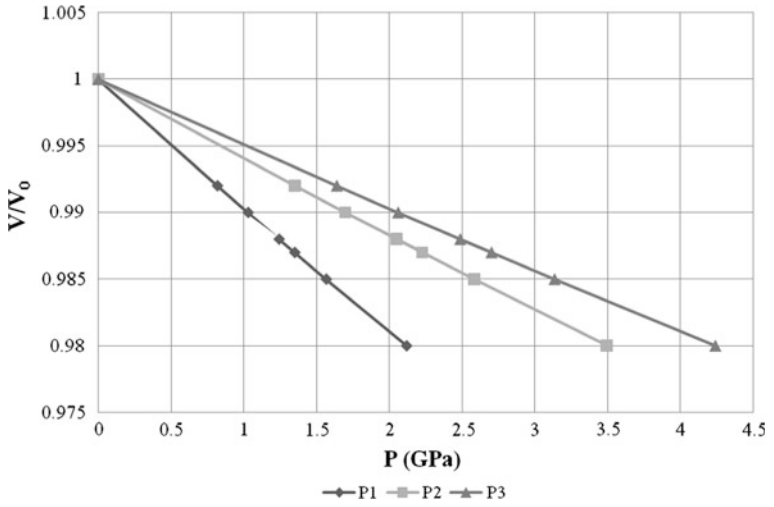

Fig. 10.3 Volume expansion $\frac{V}{V_0}$ as function of pressure P for nanosized $BaTiO_3$ ($P1$ at B_0 = 100 GPa, $B_0{}'$ = 5; $P2$ at B_0 = 165 GPa, $B_0{}'$ = 5; $P3$ at B_0 = 200 GPa, $B_0{}'$ = 5)

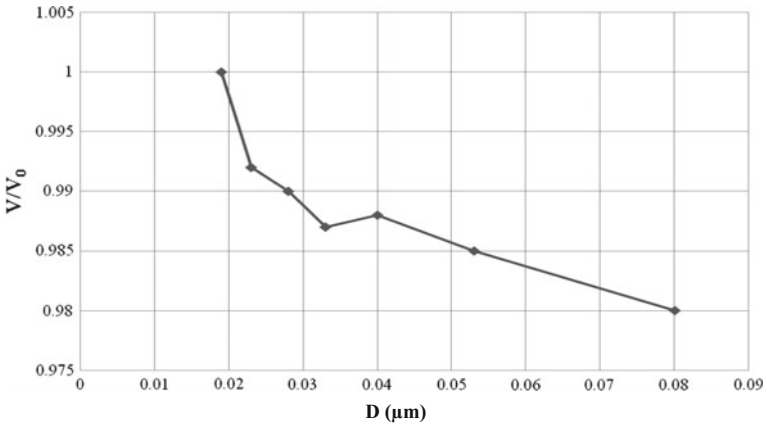

Fig. 10.4 Volume expansion $\frac{V}{V_0}$ as function of the crystallite size for nanosized $BaTiO_3$ at cubic phase

10.3 Conclusion

The first considered dependence of the parameters of $BaTiO_3$ nanocrystalline cubic cells in scale depends on how positive or negative pressure. It is found a critical crystallite size of $BaTiO_3$ (D_c = 0.035 μm), i.e. if the crystallite size is lesser than the critical value, then the elastic modulus corresponds to the soft state.

Acknowledgements This work was financially supported by the Ministry of Education and Science of the Russian Federation: themes Nos. 1927, 213.01-2014/012-VG and 3.1246.2014/K (the basic and project parts of the state task) and performed on equipment of the Collective Use Center "Electromagnetic, Electromechanical and Thermal Properties of Solids" of the Research Institute of Physics, Southern Federal University.

References

1. G. Caboche, F. Chaput, J.P. Boilot et al., Mater. Sci. Forum **133–136**(2), 801 (1993)
2. S. Chattopadhyay, P. Ayyub, V.P. Palkar, M. Multani, Phys. Rev. B **52**(18), 13177 (1995)
3. O. Hauser, M. Schenk, Phys. St. Sol. **18**, 547 (1966)
4. N. Nuraje, K. Su, Nanoscale **5**, 8752 (2013)
5. Y. Yoshimura, M. Morioka, A. Kojimab, N. Tokunaga, T. Koganezawa, K. Tozaki, Phys. Lett. A **367**, 394 (2007)
6. J.J. Wang, P.P. Wu, X.Q. Ma, L.Q. Chen, J. Appl. Phys. **108**, 114105 (2010)
7. N.B. Kofanova, YuA Kuprina, M.F. Kupriyanov, Izvestiya Akademii Nauk. Ser. Fizicheskaya **66**(6), 839 (2002)
8. M. Singh, S. Tlali, H. Narayan, Nanosci. Nanotechnol. **2**(6), 201 (2012)
9. A.S. Verma, A. Kumar, J. Alloy. Compd. **541**, 210 (2012)

Chapter 11
Dielectric and Thermal Properties of Multiferroic Bismuth Ferrite Doped with Praseodymium and Neodymium

S.V. Khasbulatov, A.A. Pavelko, Larisa A. Reznichenko, L. A. Shilkina, G.G. Gadjiev, A.G. Bakmaev, Z.M. Omarov and V.A. Aleshin

Abstract The paper presents the results of a comprehensive study of the crystal structure, grain structure, dielectric and thermal properties of high-temperature multiferroics $Bi_{1-x}(Nd, Pr)_xFeO_3$ (concentration interval x = 0.00–0.50). The regularities of the formation of the phase and grain structure, electrical and dielectric properties of objects at room temperature were established. The assumptions about the nature of the observed phenomena were suggested.

11.1 Introduction

Bismuth ferrite, and a number of solid solutions based on it have been studied deeply enough to the end of the twentieth century. A feature of bismuth ferrite is that its ferroelectric properties are combined with antiferromagnetic ones over a wide temperature range. In addition, the Curie temperature (1083 K) and antiferromagnetic Neel point (643 K) of bismuth ferrite are relatively high. At room temperature it has the R3c space group. The crystal structure of $BiFeO_3$ is characterized by rhombohedrally (Rh) distorted perovskite cell, very close to the cubic [1]. The message about the discovery of the giant magnetoelectric effect at room temperature [2] caused a new round of research in this field. It is considered that a necessary condition for the emergence of the magnetoelectric effect in $BiFeO_3$ is the destruction of its space-modulated spin structure. Such an effect can be achieved, in particular, by substitution of bismuth by rare-earth ions (REE).

S.V. Khasbulatov (✉) · A.A. Pavelko · L.A. Reznichenko · L.A. Shilkina · V.A. Aleshin
Research Institute of Physics, Southern Federal University,
Rostov-on-Don 344090, Russia
e-mail: said_vahaevich@mail.ru

G.G. Gadjiev · A.G. Bakmaev · Z.M. Omarov
Daghestan Scientific Center, H.I. Amirkhanov Institute of Physics,
Russian Academy of Sciences, Makhachkala 367010, Russia

I.A. Parinov et al. (eds.), *Advanced Materials*, Springer Proceedings
in Physics 193, DOI 10.1007/978-3-319-56062-5_11

The aim of the present work is to continue the initiated research [3, 4] and to extend the knowledge in the study of the crystal structure, grain structure, dielectric and thermophysical properties of high temperature multiferroic bismuth ferrite modified with rare earth elements Nd and Pr.

11.2 Objects and Methods

The objects become $Bi_{1-x}A_xFeO_3$ ceramics (where A = Nd, Pr; x = 0.00–0.50, Δx = 0.025–0.10). Samples obtained by two-stage solid-phase synthesis followed by sintering by conventional ceramic technology at T_{1synt} = 1143 K, T_{2synt} = 1163 K, $\tau_{1,2synt}$ = 10 h, T_{synt} = 1293 K, τ = 2 h (for Nd); and at T_{1synt} = 1073 K, T_{2synt} = 109 3 K, $\tau_{1,2synt}$ = 6 h, T_{synt} = 1123 K, τ = 2 h (for Pr).

X-ray study of the objects held by powder diffraction method using a DRON-3 diffractometer (CoKα-radiation, Bragg-Brentano focusing scheme). X-ray spectra smoothing algorithm and the corresponding software were used in the article contributed by Kovtun [5]. Symmetry and parameters of perovskite cell (for the convenience of the structural characteristics of the various phases comparison), microstrains, X-ray, experimental and relative densities of ceramics were calculated. Cell parameters were calculated by the standard technique [6]. Microstrains were calculated analytically by approximation of two X-ray lines 100 and 200, which represent two different order of reflection from a plane [7]. Microstrain $\Delta d/d$ calculations were conducted only in the Rh-phase up to x = 0.13, at higher x line broadening is largely due to different phase reflections overlapping.

Experimental (ρ_{exp}) density of the samples was measured by hydrostatic weighing in octane; X-ray density (ρ_{XRD}) was calculated according to the formula: $\rho_{XRD} = 1.66 \times M/V$, where M is the weight of formula unit in grams; the relative density (ρ_{rel}) was calculated by the formula (ρ_{exp}/ρ_{XRD}) × 100%.

Investigation of polycrystalline (grain) structure of the samples performed in reflected light on an optical microscope Neophot 21 and on the inverted high-precision microscope Leica DMI 5000M.

Temperature dependencies of relative dielectric permittivity, $\varepsilon/\varepsilon_0$, at frequencies $25 - 2 \cdot 10^6$ Hz were investigated in the range 300–900 K at the special setup with use of precision LCR meter Agilent E4980A. Thermal conductivity (λ) and thermal diffusivity (χ) were measured at the facility LFA-457 "MicroFlash" (NEZSCH), a heat capacity (C_p) defined by means of the differential scanning calorimeter DSC-204 F1 (NEZSCH).

11.3 Results and Discussion

In the result of X-ray diffraction studies of $Bi_{1-x}Nd_xFeO_3$ solid solutions, it was found that the Rh phase maintained until x = 0.1; in the range of $0.10 < x < 0.20$, the transition from the Rh phase to the $PbZrO_3$-type rhombic one (R_1) occurs; at

$x = 0.15$, Rh and R_1 phases co-exist; R_1 phase locates in the range of $0.15 < x \leq 0.20$ (Table 11.1). Our results differ from the data presented in [8], where at $0.05 \leq x < 0.17$, the solid solutions had triclinic symmetry.

XRD analysis showed that in the solid solutions with $x = 0.30$, traces of $Bi_2Fe_4O_9$ phase are visible, the remaining objects represent pure perovskite phase. Figure 11.1 shows the diffractogram of solid solutions with $x = 0.3$ (a), 0.4 (b), 0.5 (c) in the range of 2θ angles 25°–70°. Diffractogram of solid solution with $x = 0.3$ contains R_1 phase lines and weak peaks corresponding to the $GdFeO_3$-type rhombic phase (R_2). Objects with $x = 0.4$ and $x = 0.5$ have a pure R_2 phase. Thus, $Bi_{1-x}Nd_xFeO_3$ system in the range of $0.0 < x < 0.5$ has two phase transitions: Rh → R_1, and R_1 → R_2; with phase localization: Rh − $0.00 \leq x < 0.15$, Rh + R_1 − $0.15 \leq x < 0.20$, R_1 − $0.15 < x \leq 0.20$, R_1 + R_2 − $0.20 < x \leq 0.30$, R_2 − $0.30 < x \leq 0.50$. Figure 11.2 shows dependencies of the parameters of the Rh phase perovskite cell and of the rhombic phases unit cells on x. For ease comparison, here are given dependencies of the experimental (V_{exp}) and theoretical (V_{XRD}) volumes of all the phases perovskite cells on x.

Figure 11.2 shows that the Rh → R_1 transition is accompanied by a decrease in cell volume by the amount of $\Delta V = 0.58$ Å^3 (∼1%), exceeding significantly the measurement error. At R_1 → R_2 transition, V_{exp} decreases by 1.46 Å^3 (2%). The figure shows that V_{exp} decreases with increasing x as consistent with V_{XRD} only in the $0.05 \leq x \leq 0.10$ interval, in other intervals V_{exp} decreases very slightly or remains constant or even increases with increasing x. Constancy of V_{exp} at $x = 0$–0.05 is due to the shortage of A-positions arising in ABO_3 structure with crystallographic shear—planar defect characteristic of the oxygen octahedral ReO_3-type compounds containing elements with variable valence in the B-position [9, 10].

In [11] the authors called it structural non-stoichiometry, γ, in [12] it was found that the γ is not less than 3% in bismuth ferrite. It is clear that the structural non-stoichiometry prevents formation of substitutional solid solutions in A-position as long as the amount of A-cation eliminated from the matrix compound will not exceed γ. That is why the cell volume not change in $0.0 \leq x \leq 0.05$ range. Decrease of V_{exp} with increasing x as consistent with V_{XRD} in interval $0.05 < x \leq 0.10$ indicate the substitutional solid solutions to form there. When $x > 0.1$ structure of objects becomes unstable, probably due to the large difference in electronegativity of Bi and Nd atoms (2.02 and 1.14 by Pauling, respectively) [13], and therefore it undergoes a series of phase transitions. Increase of V_{XRD} in $0.3 < x \leq 0.4$ range may be associated with the substitution of some Fe ions with Bi or Nd ones. The latter, as is known, forms a $FeNdO_3$ compound [14], whose perovskite cell volume more than $NdFeO_3$ one at 0.27 Å^3.

XRD analysis $Bi_{1-x}Pr_xFeO_3$ ceramics showed that pure solid solutions formed only at a concentration of Pr, $x \geq 0.12$. With smaller x, samples contain a small amount of $Bi_{25}FeO_{40}$ and $Bi_2Fe_4O_9$ compounds (Table 11.2). Analysis of the diffraction peaks reveals 5 specific areas of concentration with different phase composition: in the range of $0.00 \leq x \leq 0.05$, only Rh phase exists; in the range of $0.05 < x \leq 0.075$, a region of coexistence of Rh phase and two rhombic phases R_1 ($PbZrO_3$-type) and R_2 ($GdFeO_3$-type) are located, the content of R_1 and R_2

Table 11.1 Parameters of the Rh phase perovskite cell

x	Impurity phase composition	Symmetry	a (Å)	b (Å)	c (Å)	α/β (°)	V_{exp} (Å^3)	V_{XRD} (Å^3)	ρ_{exp} (g/cm^3)	ρ_{XRD} (g/cm^3)	ρ_{rel} (%)
0	6 (25-1-40) 5 (2-4-9)	Rh	3.9644	–	–	89.43	62.308	61.257	–	–	–
0.05	8 (25-1-40) 11 (2-4-9)	Rh	3.9630	–	–	89.47	62.238	60.870	–	–	–
0.10	2 (25-1-40) 2 (2-4-9)	Rh	3.9534	–	–	89.58	61.789	60.485	7.32	8.283	88.37
0.15	Pure	Rh + R_1	3.9513 7.806	11.208	5.588	89.63	61.691 61.110	60.101	7.26	8.194	88.60
0.20	Pure	R_1	7.801	11.201	5.595	–	61.111	59.719	7.24	8.195	88.35
0.30	$Bi_2Fe_4O_9$ traces	R_1 R_2	7.812 5.448	11.181 5.613	5.591 7.793	–	61.045 59.584	–	7.36	8.027	91.69
0.40	Pure	R_2	5.4393	5.6377	7.8163	–	59.922	–	7.43	7.996	92.92
0.50	Pure	R_2	5.4529	5.6138	7.8116	–	59.78	57.462	7.046	7.834	95.22

R_1 and R_2 phases unit cell; perovskite cells volumes V_{exp} and V_{XRD} of all phases; ρ_{exp}, ρ_{XRD}, and ρ_{rel} of the $Bi_{1-x}Nd_xFeO_3$ ceramics
(25-1-40) impurity $Bi_{25}FeO_{40}$; (2-4-9) impurity $Bi_2Fe_4O_9$; R_1 $PbZrO_3$-type rhombic phase; R_2 $GdFeO_3$-type rhombic phase

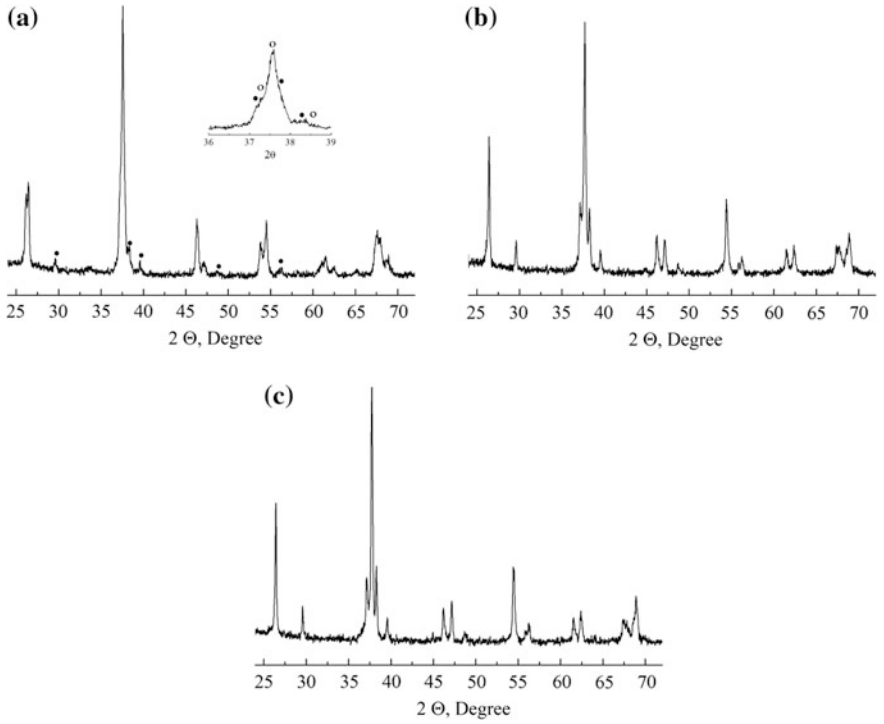

Fig. 11.1 Diffractograms of solid solutions **a** $Bi_{0.7}Nd_{0.3}FeO_3$ **b** $Bi_{0.6}Nd_{0.4}FeO_3$, and **c** $Bi_{0.5}Nd_{0.5}FeO_3$. The *inset* shows $(110)_C$ multiplet, where the R_1 phase lines are marked with *empty circles*, *black circles* denote the R_2 phase lines

phases does not exceed 10–15%. At $0.075 < x \leq 0.10$ range, a clean Rh phase reappears, and in the range of $0.10 < x \leq 0.20$, three phases Rh, R_1 and R_2 coexist again with a clear predominance of Rh one. In the $0.20 < x \leq 0.30$ interval, Rh phase disappears and two phases R_1 and R_2 coexist up to $x = 0.50$.

Appearance of Rh phase within the area of coexistence of R_1 and R_2 phases with increasing x at room temperature has not yet been reported. Similar behaviour was observed at high-temperature studies of $Bi_{1-x}La_xFeO_3$ [15] and $Bi_{1-x}Pr_xFeO_3$ [16] solid solutions. In [15], in objects with $x = 0.16$ and 0.185, phase transitions $Rh + R_1 \rightarrow R_2 \rightarrow Rh$ were detected with increasing temperature; Rh phase in the first one exists in interval 350–530 °C, the second one exists in the range of 450–500 °C.

In [16], a decrease in the amount of R_1 phase with increasing temperature in two-phase ($Rh + R_1$) solid solution with $x = 0.125$ is indicated. And in a narrow temperature range of 380–410 °C, three-phase $Rh + R_1 + R_2$ state was found. The presented phase diagram (PD) of $Bi_{1-x}Pr_xFeO_3$ system differs significantly from the PD given in [17, 18]. Despite the fact that specimens manufactured by various methods (sol-gel in [17] and by the method of solid-phase reactions in [18]), PD of the systems are almost identical and contain 3 monophase regions Rh ($0.00 \leq$

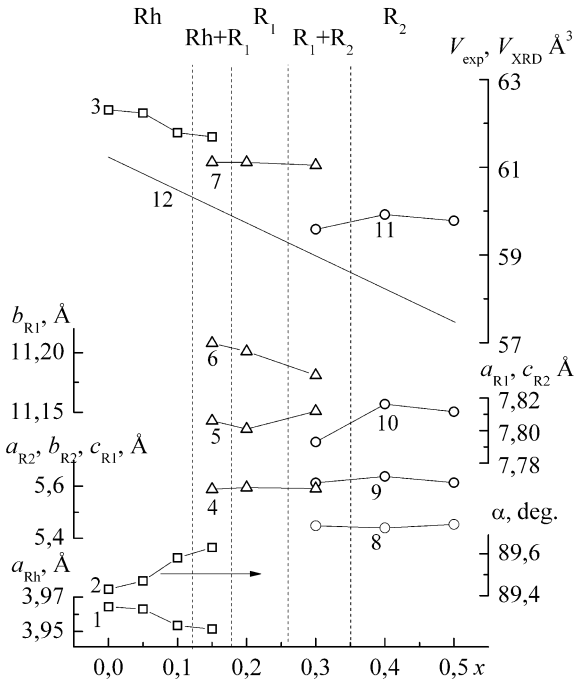

Fig. 11.2 Dependencies of the structural parameters of the $Bi_{1-x}Nd_xFeO_3$ solid solutions on *x*: *1*, *2*, *3 a* parameter, alpha angle, and V_{exp} of the Rh phase perovskite cell, respectively; *4*, *5*, *6 c*, *a*, and *b* parameters of an unit cell, respectively; *7* V_{exp} of R_1 phase perovskite cell; *8*, *9*, *10 a*, *b*, *c* parameters of an unit cell; *11* V_{exp} of the R_2 phase perovskite cell; *12* V_{XRD} of a perovskite cell

$x \leq 0.125$), R_1 ($0.15 \leq x \leq 0.25$), R_2 ($0.25 < x \leq 0.50$), and two relatively narrow morphotropic areas (MA) Rh → R_1 in $0.125 < x < 0.150$ range and R_1 → R_2 in $0.25 < x < 0.30$ range. The authors in [17] argue that all samples have no impurity phases, but in [18] the presence/absence of the impurities are not reported. The difference with the data [18], possibly relates to the different time of samples firing: 15–70 h in [18], and 2–6 h in our work. Figure 11.3 shows diffractograms of solid solutions with $x = 0.3$, 0.4, 0.5, which show a gradual transition from antipolar R_1 phase to nonpolar R_2 phase.

Figure 11.4a shows the dependencies of the structural parameters of the perovskite cell of all phases and $\Delta d/d$ on *x*. Figure 11.4b presents dependencies of densities ρ_{exp}, ρ_{XRD}, ρ_{rel} of objects on *x*. The $V(x)$ dependence has a form typical for solid solutions experiencing morphotropic phase transition (in the MA, $V(x) = \text{const}$). The jump in volume during the Rh → R_1 transition is 0.39 Å^3, at R_1 → R_2 transition, it is 1.55 Å^3. Dependence $\Delta d/d(x)$ has two maxima at $x = 0.09$ and $x = 0.12$, and two minima at $x = 0.10$ and $x = 0.14$. The maximum at $x = 0.12$ corresponds to the phase of pre-extraction of R_1 and R_2 phase clusters from coherently related Rh phase, and the followed by minimum corresponds to the state where these clusters are already separated from the matrix. The first weak maximum can be interpreted as a wedging of phase coexistence region in which the contents of R_1 and R_2 do not exceed 10–15% in Rh phase. A further increase of $\Delta d/d$ is already associated with the approach to morphotropic phase boundary between the three-phase and two-phase regions, where Rh cluster that originated in the depths of

Table 11.2 Phase composition, symmetry and cell parameters of $Bi_{1-x}Pr_xFeO_3$ perovskite solid solutions

x	Impurity phase composition	Symmetry	a (Å)	α/β (°)	V_{exp} (Å^3)	$\Delta d/d \times 10^3$	ρ_{exp} (g/cm^3)	ρ_{XRD} (g/cm^3)	ρ_{rel} (%)
0	9 (25-1-40) 8 (2-4-9)	Rh	3.9641	89.43	62.308	0.6	7.55	8.37	91.21
0.025	25(25-1-40) 8 (2-4-9)	Rh	3.9599	89.52	62.095	1.31	7.08	8.37	84.61
0.05	10(25-1-40) 10(2-4-9)	Rh	3.9585	89.51	62.027	0.68	7.32	8.33	87.87
0.075	2(25-1-40) 3 (2-4-9)	80Rh + 10R_1+ 10R_2	3.9569	89.51	61.953	1.46	7.24	8.29	87.28
0.09	2 (2-4-9)	Rh	3.9569	89.55	61.955	1.56	7.27	8.27	87.94
0.10	6 (25-1-40) 6 (2-4-9)	Rh	3.9572	89.56	61.966	1.37	7.35	8.25	89.12
0.11	9 (25-1-40) 8 (2-4-9)	70Rh + 10 R_1 + 20R_2	3.9569	89.55	61.956	2.09	7.44	8.23	90.40
0.12	7(25-1-40) 9 (2-4-9)	70Rh + 10R_1 + 20R_2	3.9553	89.55	61.878	2.22	7.36	8.22	89.51
0.13	Pure	80Rh + 10R_1 + 10R_2	3.9534	89.61	61.79	1.41	7.37	8.20	89.84
0.14	Pure	85Rh + 10R_1 + 5R_2	3.9530	89.61	61.770	1.39	7.45	8.20	90.85
0.15	Pure	75Rh + 15R_1 + 10R_2	3.9529	89.63	61.764	1.62	7.19	8.18	87.87
0.175	Pure	65Rh + 20R_1 + 15R_2	3.9523	89.62	61.741	1.9	7.53	8.14	92.51
0.2	Pure	56Rh+ 24R_1+ 20R_2	3.9521 3.9601 –	89.64 c = 3.9112 –	61.731 61.338 –	2.20	7.12	8.09	87.96
0.30	Pure	74R_1+26R_2	3.9601 3.9110	−91.19	61.282 59.736	c = 3.9077 b = 3.9061	7.48	8.02	93.26
0.40	Pure	50R_1+50R_2	3.9555 3.9119	−91.20	61.099 59.709	c = 3.9050 b = 3.9026	7.22	7.896	91.44
0.50	Pure	38R_1+62R_2	3.9528 3.9111	– 91.14	61.109 59.762	c = 3.9110 b = 3.9076	7.00	7.724	90.62

(25-1-40) impurity $Bi_{25}FeO_{40}$; (2-4-9) impurity $Bi_2Fe_4O_9$; R_1 $PbZrO_3$-type rhombic phase; R_2 $GdFeO_3$-type rhombic phase

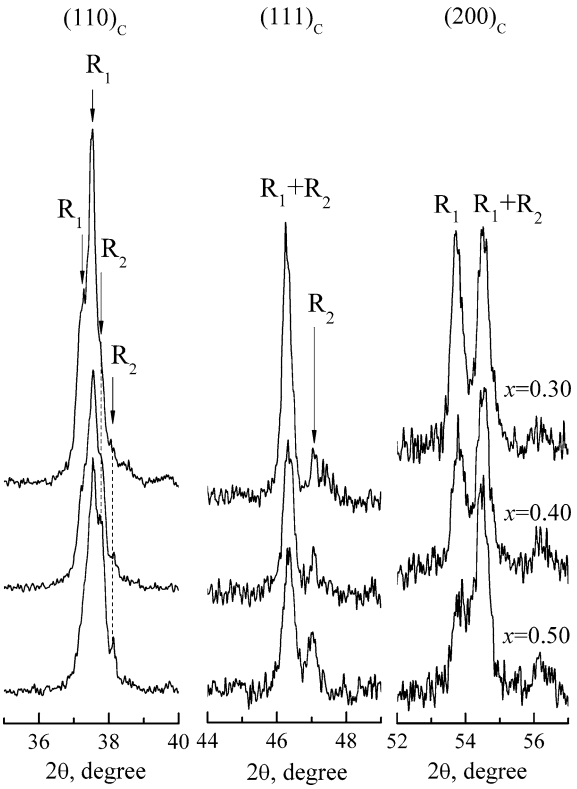

Fig. 11.3 Diffraction reflections $(110)_C$, $(111)_C$, and $(200)_C$ of $Bi_{1-x}Pr_xFeO_3$ solid solutions with $x = 0.30$, 0.40, 0.50 consist of two phases: $PbZrO_3$-type R_1 phase and $GdFeO_3$-type R_2 phase. It can be seen that as x increases the intensity of R_2 phase reflections increases and those of R_1 phase reflections decreases in accordance with their concentration to change in the solid solution

the rhombic phase is expected to separate from the matrix. Dependencies of ρ_{exp} and ρ_{rel} on x (Fig. 11.4b) have a maximum in the range of $0.075 < x < 0.150$, where the three-phase area locates, which has heightened imperfection due to its complex composition.

Figure 11.5 shows photographs of a microstructure of studied objects. Black rounded and irregular shape areas are pores. They are distributed inhomogeneously over the surface. Etching revealed crystallite boundaries: closed dark lines around the lighter areas (ceramic grains). Bright grains present the main "light" phase. Darker grains show the second "gray" phase. A certain amount of etching products are found to exist.

Microstructure of $Bi_{1-x}Nd_xFeO_3$ solid solutions (Fig. 11.5) has the following features. When $x = 0.00$, there is a large amount of grains that differ significantly from each other in morphological characters: there are large grains of irregular shape—"light" phase (grain size ~10 μm), and smaller grains—"gray" phase (grain size of about 4 μm). It is evident that the admixture of "gray" phase in unmodified bismuth ferrite ceramics is maximum. With rise of x to 0.05 the number of "gray" phase is reduced, and the size of grains of "light" phase remains virtually unchanged (grain size of about 8 μm). Non-core "gray" phase grains are captured

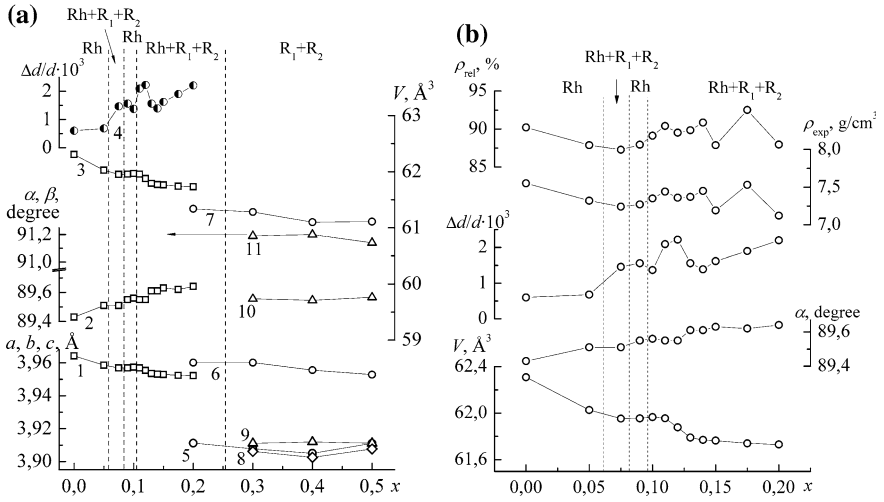

Fig. 11.4 **a** Dependencies of parameters, perovskite cell volume, and microstrain, $\Delta d/d$, of $Bi_{1-x}Pr_xFeO_3$ solid solutions on *x*: *1*, *2*, *3* *a*, *α* parameters and *V* of Rh cell; *5*, *6*, and *7* *a*, *c* parameters and *V* of pseudotetragonal cell (R_1 phase); *8*, *9*, *10*, *11* *b*, *a*, *β* parameters and *V* of monoclinic cell (R_2 phase), respectively; *4* $\Delta d/d$. The *dashed lines* show the PD of the system; **b** dependencies of the ρ_{exp}, ρ_{XRD}, ρ_{rel} of $Bi_{1-x}Pr_xFeO_3$ ceramic solid solutions on *x*

by the "light" phase grains while those exhibit rapid growth during recrystallization process. For $x = 0.10$, "gray" phase completely disappears, which is accompanied by a sharp increase in the size of grains of "light" phase (grain size $\sim$30 μm). With the further *x* increase the degree of heterogeneity of the microstructure increases as well, resulting in a sharp decrease in grain size with $x = 0.15$ (grain size about 4 μm) and with $x = 0.20$ (1–2 μm).

Figure 11.6 shows the photos of the most typical microstructure of the $Bi_{1-x}Pr_xFeO_3$ solid solutions. After thermal etching crystallite boundaries, image occurs in both the main "light" and in the impurity phases, represented on the surface by fine dark lines closed around the grains. It should be noted that the etching rate of boundaries are somewhat inhomogeneous. The microstructure of the studied ceramics represented by pores and three crystalline phases ("light" main phase and two non-core phases: a lighter impurity phase and a "gray" one). Thermal etching does not increase the observed porosity, but in some cases there is the appearance of a small amount of etching products that are similar to a pore in contrast and form. Grains of basic light phases have curved borders. "Grey" phase consists of crystallites with more regular shape. The dimensions of "gray" grains are always smaller than those of the main phase crystallites. In some cases, all of them form clusters with a wide range of scale. The microstructure of some samples (in their area) are extremely heterogeneous (Fig. 11.7) both in terms of grain size, as well as in the percentage of two crystalline phases. In some cases, the "gray"

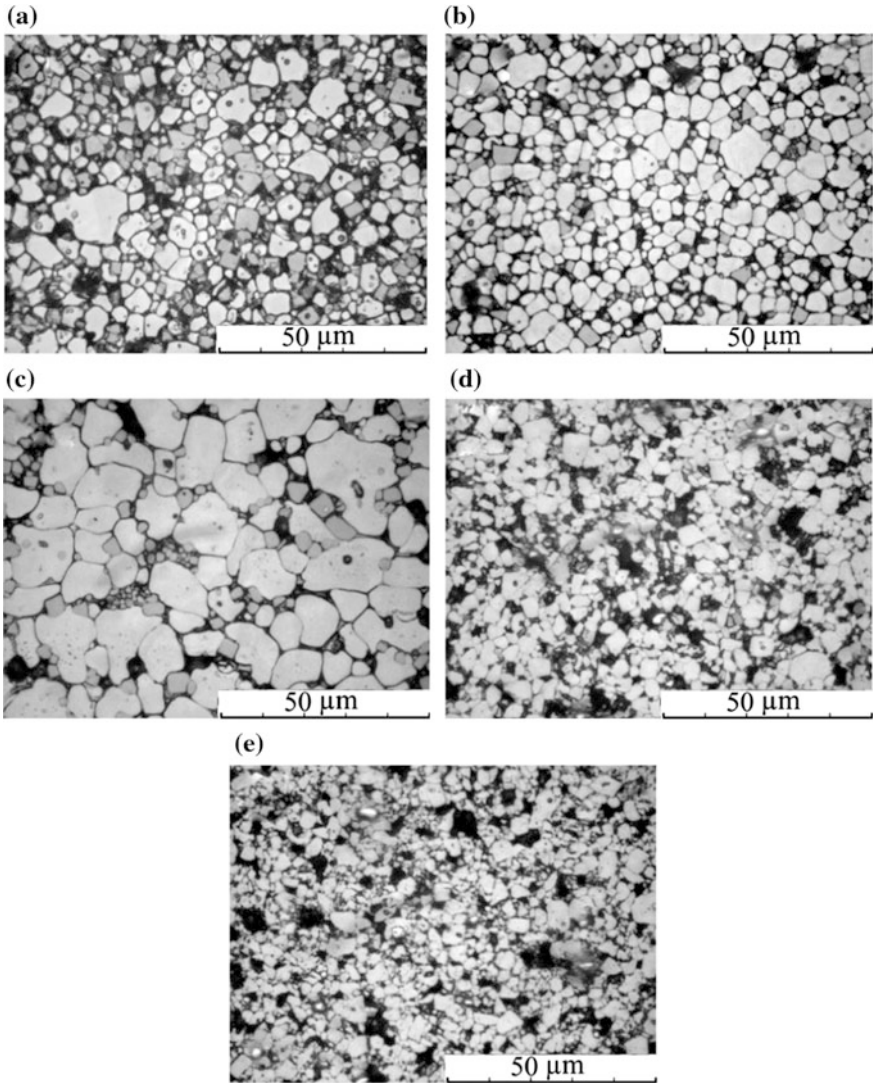

Fig. 11.5 The microstructure of the $BiFeO_3$ ceramics (**a**) and of the $Bi_{1-x}Nd_xFeO_3$ solid solutions with x = 0.05 (**b**); 0.1 (**c**); 0.15 (**d**); 0.2 (**e**)

phase crystallites are captured by grains of the main phase (in addition to this, a pore capturing may occurs).

Figure 11.8 shows the dependence of the real ($\varepsilon'/\varepsilon_0$) and imaginary ($\varepsilon''/\varepsilon_0$) parts of the dielectric constant and dielectric loss tangent ($tg\delta$) of the $Bi_{1-x}Nd_xFeO_3$ ceramic solid solutions on the temperature and measurement field frequency. As can be seen from the figure, for all Nd concentrations a nonlinear increase in $\varepsilon'/\varepsilon_0$

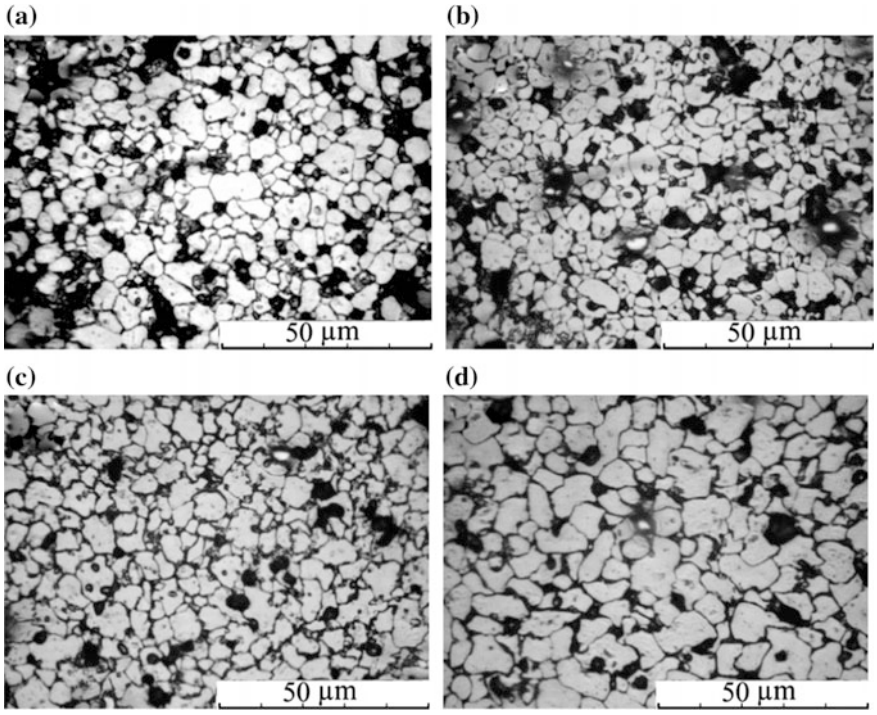

Fig. 11.6 Microstructures of $Bi_{1-x}Pr_xFeO_3$ ceramic samples, $x = 0.05$ (**a**), 0.10 (**b**), 0.15 (**c**), 0.20 (**d**)

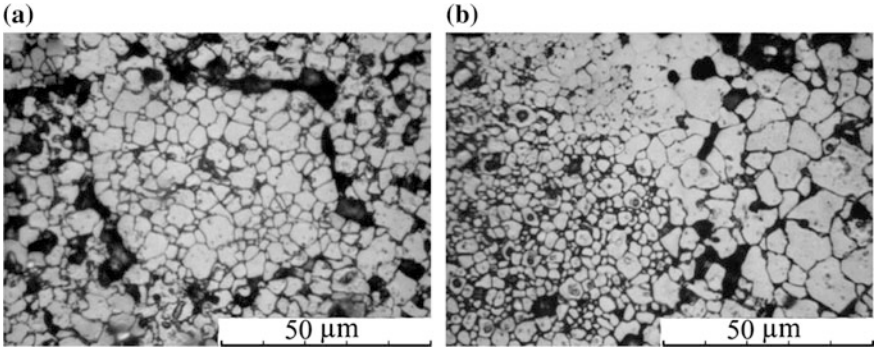

Fig. 11.7 Microstructure variations in surface of $Bi_{1-x}Pr_xFeO_3$ ceramic samples, **a** $x = 0.15$, **b** $x = 0.20$

occures with increasing temperature. The latter passes through several local maxima, the temperature of which vary widely while the measurement field frequency is increased. Offset of the observed $\varepsilon'/\varepsilon_0$ temperature anomalies probably associated with the increased of ceramics' conductivity, which is confirmed by high values and

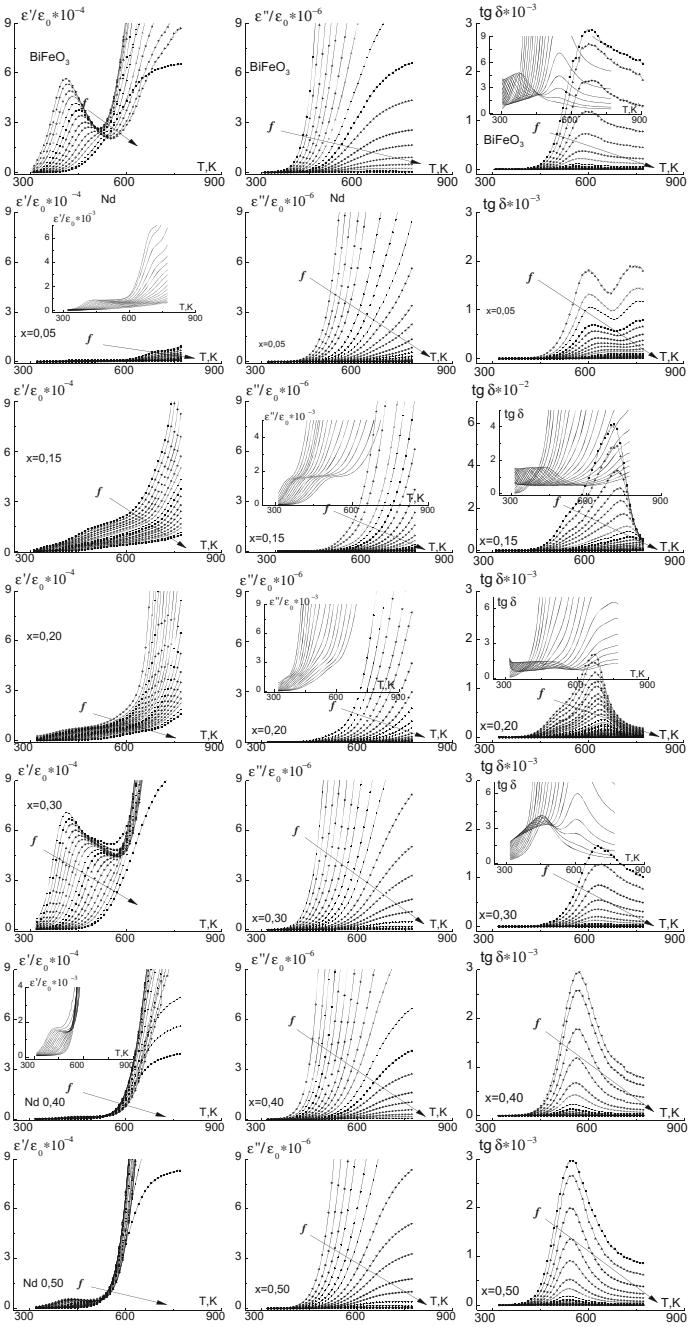

Fig. 11.8 Dependencies of $\varepsilon'/\varepsilon_0$, $\varepsilon''/\varepsilon_0$, and tg$\delta$ of $Bi_{1-x}Nd_xFeO_3$ ceramic samples on temperature in the range of frequencies $f = 25 - 1.2 \times 10^6$ Hz (frequency growth is indicated by the *arrows*)

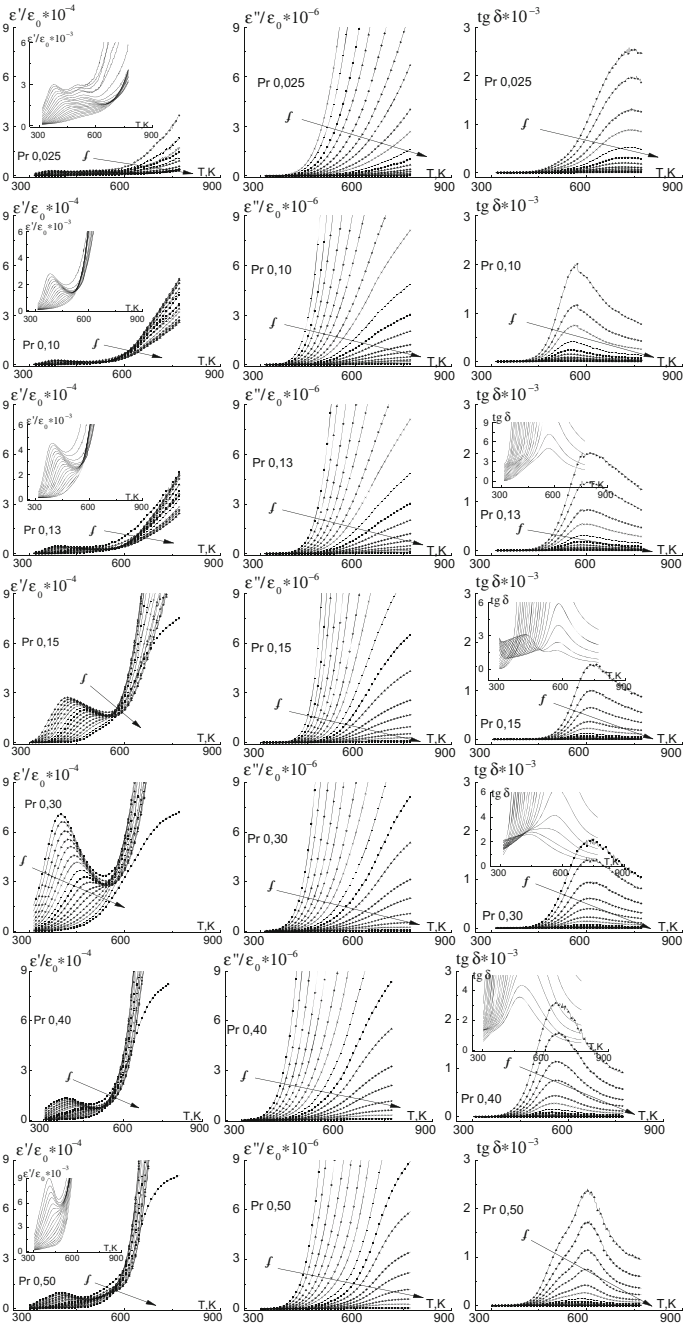

Fig. 11.9 Dependencies of $\varepsilon'/\varepsilon_0$, $\varepsilon''/\varepsilon_0$, and tg$\delta$ of $Bi_{1-x}Pr_xFeO_3$ ceramic samples on temperature in the range of frequencies $f = 25 - 1.2 \times 10^6$ Hz (frequency growth is indicated by the *arrows*)

characteristic forms of $\varepsilon''/\varepsilon_0(T)$ dependencies. Such phenomena known as Maxwell-Wagner relaxation observed previously in [19, 20] and have been associated with the accumulation of free charges at the interface surfaces of the components on the background of the interlayer, and interfacial intraphase rearrangements. The complexity of the curves indicates the presence of a large number of structural rearrangements, but high-temperature X-ray diffraction studies of the objects are required to determine a nature of those and to clarify the temperature ranges of those existence.

Figure 11.9 shows the dielectric spectra of $Bi_{1-x}Pr_xFeO_3$ solid solutions. Analysis of the obtained results showed that the dependencies under consideration experience two types of anomalies. The first one locates in the 300–450 K temperature range, and belongs to the $\varepsilon'/\varepsilon_0(T)$ dependences; the second one disposes in the 500–650 K range, and belongs to the tgδ curves. Both of them are of the form of strong dispersion maxima having relaxation character. The increase in Pr concentration leads to complication of recorded dielectric spectra (their displacement, diffusion, enhance of the dispersion, the formation of additional anomalies).

Dependencies of thermal characteristics of all studied objects on temperature (Fig. 11.10) are traditional with minima and maxima [21, 22] near the Neel temperature ($T_N \sim 643$ K) [1].

11.4 Conclusions

The phase diagram of the $Bi_{1-x}Nd_xFeO_3$ system in the range of $0.0 < x < 0.5$ has two phase transitions: Rh $\rightarrow$ R_1, and $R_1 \rightarrow R_2$; with phase localization: Rh $-$ $0.00 \leq x < 0.15$, Rh + R_1 $-$ $0.15 \leq x < 0.20$, R_1 $-$ $0.15 < x \leq 0.20$, R_1 + R_2 $-$ $0.20 < x \leq 0.30$, R_2 $-$ $0.30 < x \leq 0.50$.

The phase diagram of the $Bi_{1-x}Pr_xFeO_3$ systems contain 3 monophase regions Rh ($0.00 \leq x \leq 0.125$), R_1 ($0.15 \leq x \leq 0.25$), R_2 ($0.25 < x \leq 0.50$), and two relatively narrow morphotropic areas Rh $\rightarrow$ R_1 in $0.125 < x < 0.150$ range and $R_1 \rightarrow R_2$ in $0.25 < x < 0.30$ range. Appearance of Rh phase clusters within the area of coexistence of R_1 and R_2 phases with increasing x at room temperature has been first established.

Ceramics of $Bi_{1-x}A_xFeO_3$ (A = Nd, Pr) multiferroics are a multicomponent microstructures of "pores—the basic coherent matrix—the minor local phases" type, and correspond to complex conglomerate of crystallites undergoing specific changes in a space of technology and concentrational parameters. Differences in the nature of the evolution of microstructures with an increase in the content of Nd or Pr is correlated with the XRD data (absence or presence of a phase transition). The behavior of the microstructure of these materials with variations in the concentrations of modifiers is very complex due to the eccentricity of their phase composition and crystalline phases behavior. An additional experiments are obviously required to identify the detected phases.

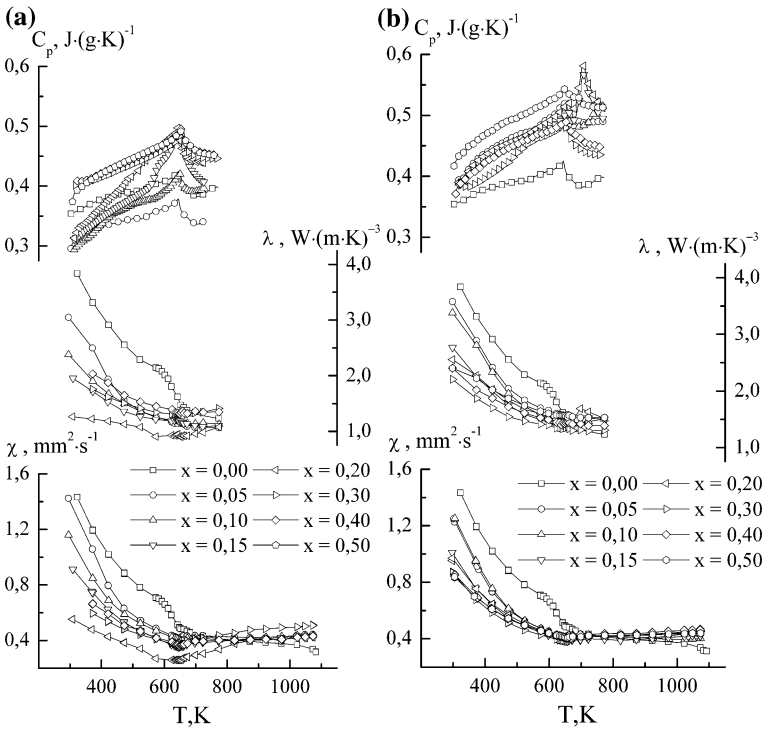

Fig. 11.10 Dependence of C_p, χ, λ of **a** $Bi_{1-x}Nd_xFeO_3$ and **b** $Bi_{1-x}Pr_xFeO_3$ ceramic solid solutions on temperature

The results should be used in the development of high-temperature multiferroic type $BiFeO_3$.

Acknowledgements This work has been done on equipment of the Collective use center "Electromagnetic, Electromechanical and Thermal Properties of Solids" of the Institute of Physics, Southern Federal University. This work was financially supported by the Ministry of Education and Science of the Russian Federation: grant of the President of the Russian Federation No. MK-3232.2015.2; themes Nos. 1927, 213.01-2014/012-VG and 3.1246.2014/K (the basic and project parts of the state task).

References

1. G.A. Smolenskii, I.E. Chupis, Sov. Phys. Usp. **25**, 475 (1982)
2. A.K. Zvezdin, A.P. Pyatakov, Sov. Phys. Usp. **47**, 416 (2004)
3. I.A. Verbenko et al., Bull. Russ. Acad. Sci. Phys. **74**(8), 1141 (2010)
4. K.P. Andryushin, A.A. Pavelko, A.V. Pavlenko, I.A. Verbenko, L.A. Shilkina, S.P. Kubrin, L.A. Reznichenko, Tech. Phys. Lett. **37**(7), 617 (2011)

5. S.P. Zinchenko, A.P. Kovtun, G.N. Tolmachev, Technical physics. Russ. J. Appl. Phys. **54**, 1689 (2009)
6. E.G. Fesenko, *Perovskite Family and Ferroelectricity* (Atomizdat, Moscow, 1972). (In Russian)
7. V.P. Nagornov, Analytical determination of the parameters of the substructure of the deformed polycrystalline X-ray method of approximation using Cauchy functions. "*Engineering". Apparatus and methods for X-ray analysis, Leningrad* (1982) (In Russian)
8. G.L. Yuan, S.W. Ora, H.L.W. Chan, J. Appl. Phys. **101**, 064101 (2007)
9. A.G. Petrenko, V.V. Prisedsky, Structural defects in a ferroelectric material. *Teaching study on higher education at the Ministry of Higher Education of the Ukrainian SSR*, *Kiev* (1989) (In Russian)
10. C.N.R. Rao, J. Gopalakrishnan, *New Direction in Solids State Chemistry* (Cambridge University Press, Cambridge, 1997)
11. L.A. Reznichenko, L.A. Shilkina, E.S. Gagarina, YuI Yuzyuk, O.N. Razumovskaya, A.V. Kozinkin, Crystallogr. Rep. **49**(5), 820 (2004)
12. A.G. Abubakarov, L.A. Shilkina, I.A. Verbenko, L.A. Reznichenko, S.I. Dudkina, Bull. Russ. Acad. Sci. Phys. **78**(8), 713 (2014)
13. V.S. Urusov, *Theory of Isomorphic Miscibility* (Nauka, Moscow, 1977). (In Russian)
14. *Powder Diffraction File. Data Card. Inorganic Section*. Set 25, card 1149. (JCPDS. Swarthmore, Pennsylvania, USA, 1948)
15. D.V. Karpinsky, I.O. Troyanchuk, O.S. Mantytskaja, G.M. Chobot, V.V. Sikolenko, V. Efimov, M. Tovar, Phys. Solid State **56**(4), 701 (2014)
16. D.V. Karpinsky, I.O. Troyanchuk, V.V. Sikolenko, V. Efimov, E. Efimova, M.V. Silibin, G. M. Chobot, E. Willinger, Phys. Solid State **56**(11), 2263 (2014)
17. J. Zhang, Y.-J. Wu, X.-J. Chen, J. Magn. Magn. Mater. **382**, 1 (2015)
18. D.V. Karpinsky, I.O. Troyanchukb, O.S. Mantytskaya, V.A. Khomchenko, A.L. Kholkin, Solid State Commun. **151**, 1686 (2011)
19. P. Lin et al., J. Alloy. Compd. **600**, 118 (2014)
20. E. Palaimiene et al., Appl. Phys. Lett. **106**(1), 012906 (2015)
21. B. Magomedov Ya, G.G. Hajiyev, *TVT*. **28**, 185 (1990) (In Russian)
22. M.-R.M. Magomedov, I.K. Kamilov, Z.M. Omarov et al., Instrum. Exp. Tech. **4**, 165 (2007). (In Russian)

Chapter 12
Phase Transitions in $BiFeO_3$–$ANbO_3$ (A = Na, K) Solid Solutions

P. Teslenko, Anatoly V. Pavlenko, Larisa A. Reznichenko, A.G. Rudskaya, N. Kofanova, Y. Kabirov, E. Chebanova, S. Chagovets, A. Shevchuk, E. Ananyeva and M.F. Kupriyanov

Abstract The structures of $(1 - x)BiFeO_3$–$xKNbO_3$ and $(1 - x)BiFeO_3$–$NaNbO_3$ (x = 0.3, 0.5, 0.7) solid solutions have been studied by means of X-ray diffraction and dielectric spectroscopy methods. It was established that in the compounds of $(1 - x)BiFeO_3$–$xKNbO_3$ system the $Pbnm$ (x = 0.3), $P4mm$ (x = 0.5) and $Amm2$ (x = 0.7) phases are observed at room temperature. Results revealed that in the compounds of $(1 - x)BiFeO_3$–$NaNbO_3$ system the $R3c$ (x = 0.3), $Pbnm$ (x = 0.5) and $P4/mbm$ (x = 0.7) phases take place at room temperature. The symmetry of the phases, unit cell parameters, positional atomic parameters as well as the temperatures of phase transitions in the 20 °C < T < 500 °C temperature range have been determined. It was found that the peculiarities of temperature and frequency dependencies of dielectric parameters correspond to structural phase transitions.

12.1 Introduction

The main problems of solid solutions studying are associated with: (i) choosing the optimal preparation conditions, (ii) determining regularities in concentration changes of the structural parameters, (iii) establishing correlations between changes both in structure and physical properties in the wide range of concentration variations of the components in solid solutions as well as temperature and pressure and

P. Teslenko · A.G. Rudskaya (✉) · N. Kofanova · Y. Kabirov · S. Chagovets · A. Shevchuk · E. Ananyeva · M.F. Kupriyanov
Department of Physics, Southern Federal University, Rostov-on-Don, Russia
e-mail: arudskaya@yandex.ru

A.V. Pavlenko
Southern Scientific Center of Russian Academy of Sciences, Rostov-on-Don, Russia

L.A. Reznichenko
Research Institute of Physics, Southern Federal University, Rostov-on-Don, Russia

E. Chebanova
Don State Technical University, Rostov-on-Don, Russia

I.A. Parinov et al. (eds.), *Advanced Materials*, Springer Proceedings in Physics 193, DOI 10.1007/978-3-319-56062-5_12

(iv) developing phenomenological and microscopic models that describe the established correlations. Solving the above-mentioned problems, it is necessary to take into account the possible effects of the crystalochemical order-disorder, especially in the vicinities of such concentration ratios of components, as 1:1, 1:2, 1:3, etc. It was found that the compounds of numerous solid solutions with concentration ratio 1:2 (or 2:1) are the most effective ones [1, 2]. Moreover, the most effective compounds of solid solutions are those relating to morphotropic phase boundaries (MPBs) which is observed in the PZT system [3]. $BiFeO_3$ (BFO) has been found to have a combination of ferroelectric, ferroelastic, magnetic and other properties, which makes it an ideal basis for many solid solutions [4–9].

The results of solid $0.5BiFeO_3$–$0.5LiNbO_3$ solution investigation were recently published [10]. This compound is solid solution between perovskite-type (BFO) and ilmenite-type ($LiNbO_3$) structures. It should be noted that the authors of [10] incorrectly interpreted the structure of the formed solid solution, as a tetragonal phase with lattice parameters $a = 6.8962(24)$, $c = 14.15(24)$ Å. The simple analysis shows that XRD pattern corresponds a pyrochlore-type structure (the cubic phase of $Fd\,\bar{3}m$ (sp. gr. 227) with $a = 10.47$ Å) [11].

The results of several compounds of $(1 - x)BiFeO_3$–$xNaNbO_3$ (BFNNO) solid solutions studies are given in [12–17]. In [12, 13], temperature dependencies of dielectric permittivities maxima (T_m) were studied. In [14, 15], the compounds with $0.25 \leq x \leq 0.90$ at the room temperature were characterized by a cubic phase, and the compounds close to pure BFO ($x < 0.25$) and $NaNbO_3$ (NNO) ($x > 0.9$) were with rhombohedral and orthorhombic structures, respectively. Following temperature dependencies of dielectric permittivity $\varepsilon'(T)$, there were revealed the effects of ferroelectric relaxation. In [16], two dielectric relaxations were observed in the temperature ranges of 550–600 and 650–710 K in 0.9BFO–0.1NNO. In [17], it was established that with increase in concentration of NNO ($0.1 < x < 0.3$), there was structural transformation from the rhombohedral to the tetragonal phase. The dielectric constant and dielectric loss of samples increase with increasing in temperature. It is found that with increase of concentration of NNO in the solid solution, dielectric loss is greatly reduced.

Preparation and properties of a number of solid solutions system compounds $(1 - x)BiFeO_3$–$xKNbO_3$ (BFKNO) are described in [18]. Structural researches at the room temperature have shown that compounds with $x = 0$ and 0.1 were characterized by a rhombohedral cell, and the structures of compounds $x \geq 0.2$ were defined as pseudo-cubic. Frequency dependencies of dielectric permittivity, dielectric loss in compounds with $0.1 \leq x \leq 0.3$ revealed only insignificant monotonous changes. In compounds with $x = 0.1$ and 0.2 dielectric hysteresis loops were observed. A loop *M-H* revealed a weak antiferromagnetism.

In this paper we present the research results of the structural phase transitions and temperature-frequency changes of dielectric parameters in the solid solutions of BFKNO and BFNNO with the concentration ratios of components close to 2:1 ($x = 0.3$), 1:2 ($x = 0.7$) and equal to 1:1 ($x = 0.5$).

12.2 Materials and Methods

12.2.1 Sample Preparation

The samples were prepared by the solid-phase synthesis method by using stoichiometric mixtures of Bi_2O_3, Fe_2O_3, $KNbO_3$ (KNO) and NNO (KNO and NNO pre-synthesized). Mixtures were annealed successively at temperatures of T_1 = 800 °C for 10 h and T_2 = 900 °C for 5 h.

12.2.2 Phase Composition and Structural Characterization

Compositions of the samples were confirmed by X-ray analysis using a RFS-001 spectrometer (Fig. 12.1). Structure phase transitions in BFKNO and BFNNO solid solutions were studied on DRON-3M diffractometer (CuK_α-radiation with Ni-filter) by heating samples in the temperature range of 20 °C < T < 500 °C. The phase symmetries, unit cell parameters, positional atomic parameters were determined by using the PowderCell 2.4 program [19]. The profile of R_p-factor was used as a criterion to refine the structural parameters. The microstructures of the samples were recorded by the FE-SEMZeiss SUPRA 25 scanning electron microscope (Fig. 12.2).

12.2.3 Dielectric Spectroscopy

Temperature dependencies of relative complex dielectric permittivities $\varepsilon^*/\varepsilon_0 = \varepsilon'/\varepsilon_0 - i\varepsilon''/\varepsilon_0$ ($\varepsilon'/\varepsilon_0$ and $\varepsilon''/\varepsilon_0$ are the real and imaginary parts of $\varepsilon^*/\varepsilon_0$, respectively; ε_0 is an electric constant) were studied by using Agilent E4980A LCR meter at T = (30–500) °C in the range of frequencies $f = (20 - 2 \times 10^5)$ Hz.

12.3 Results and Discussion

12.3.1 Phase Composition and Structural Data

The results of the preliminary investigation of (x, T) phase diagrams for BFKNO and BFNNO systems are presented in [20, 21]. The structural parameters of the compounds with x = 0.3; 0.5; 0.7 studied at room temperature are given in Tables 12.1 and 12.2.

The compounds of BFKNO system at room temperature are characterized by the following phases: BFKNO-0.3 (x = 0.3)—*Pbnm*, BFKNO-0.5 (x = 0.5)—*P*4*mm*

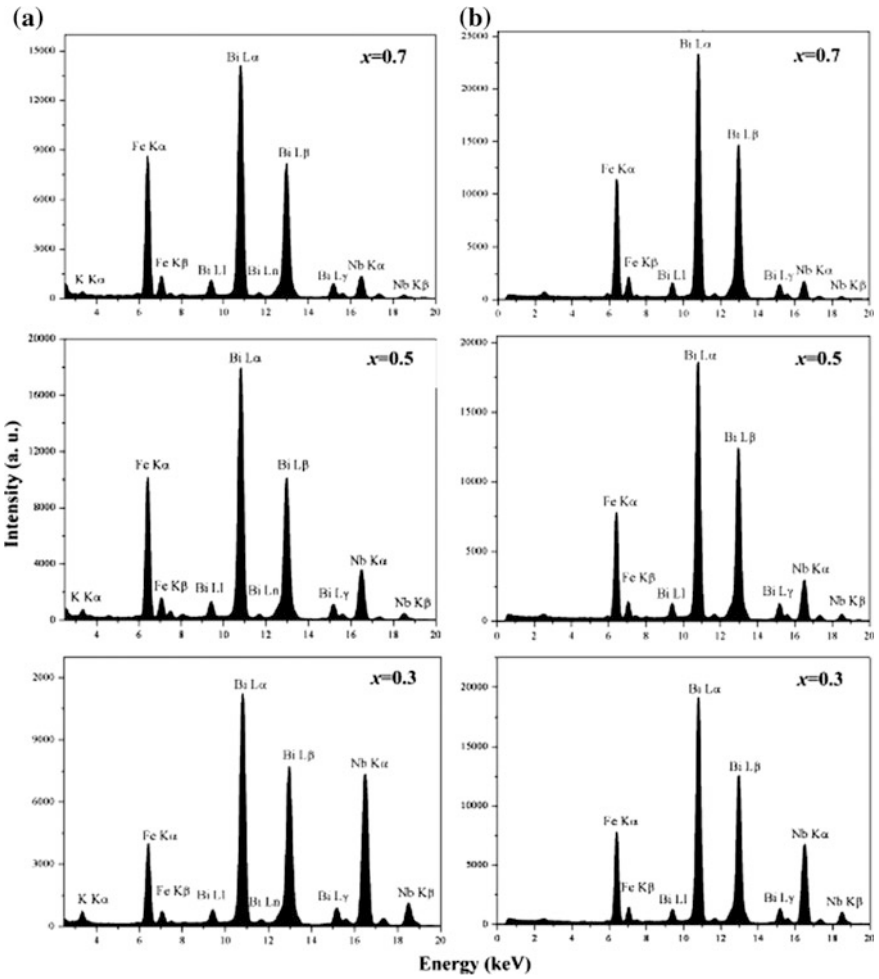

Fig. 12.1 *X*-ray fluorescence spectrum of the ceramics: **a** $(1 - x)BiFeO_3$–$xKNbO_3$ and **b** $(1 - x)$ $BiFeO_3$–$xNaNbO_3$ for $x = 0.3$; 0.5; 0.7

and BFKNO-0.7 ($x = 0.7$)—*Amm*2. The *Pbnm* phase is the high-temperature phase of pure BFO [22]. In the BFKNO-0.3 compound this phase at room temperature is a result of the structural disorder in the arrangement of different types of atoms (Bi and K; Fe and Nb) in identical positions of perovskite-type structure (*A* and *B* type, respectively). In the BFKNO-0.5 compound the high temperature tetragonal *P*4*mm* phase of pure KNO ($T_{PT} = 220$ °C) is observed at room temperature. In the

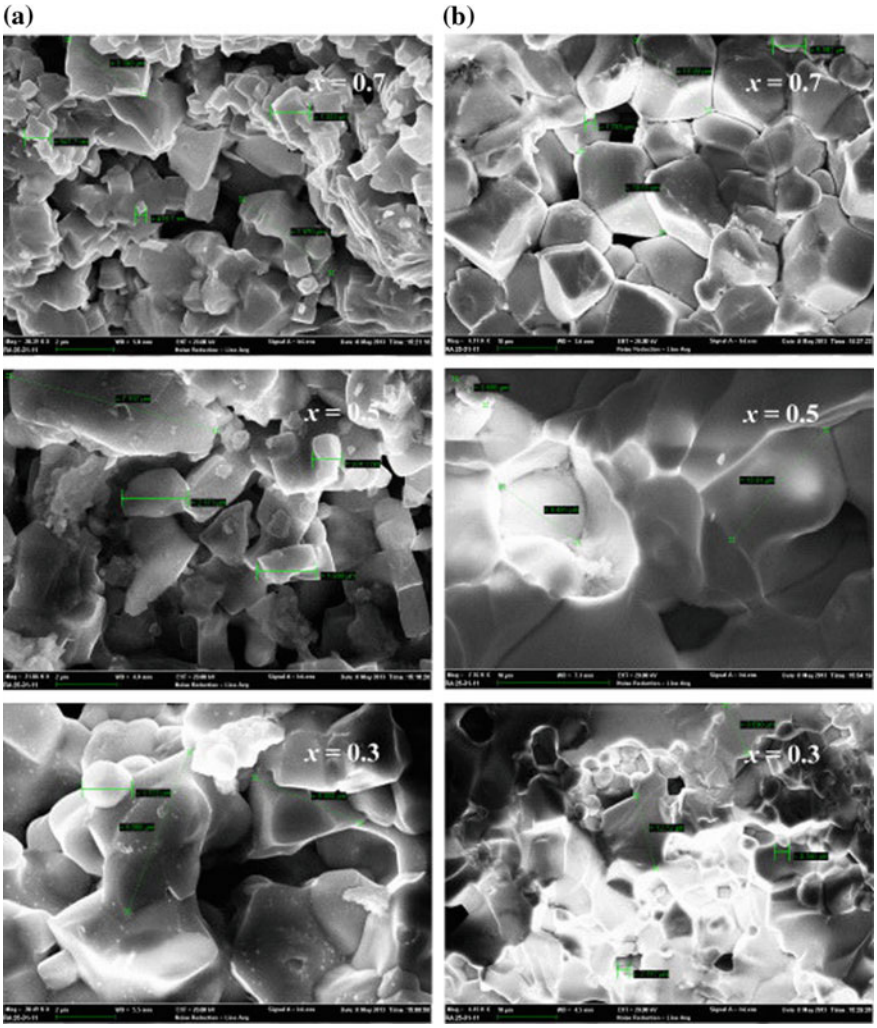

Fig. 12.2 SEM images showing morphology of the samples: **a** $(1 - x)BiFeO_3$–$xKNbO_3$ and **b** $(1 - x)BiFeO_3$–$xNaNbO_3$ for x = 0.3; 0.5; 0.7

BFKNO-0.7 compound the *Amm*2 phase taking place at room temperature in pure KNO is observed as well.

For the compounds of BFNNO solid solutions at room temperature the following three phases are observed: (i) the ferroelectric *R*3*c* phase (BFNNO-0.3), (ii) the orthorhombic *Pbnm* phase (BFNNO-0.5)—high-temperature phase of pure BFO and (iii) the tetragonal *P*4/*mbm* phase (BFNNO-0.7)—high-temperature phase of pure NNO.

Table 12.1 Structural parameters of BFKNO compounds at room temperature

Phase composition	Atom	Wyck	*x*/*a*	*y*/*b*	z/*c*
BFKNO-0.3					
Orthorhombic *Pbnm* (N 62) *a* = 5.633(1) Å *b* = 5.678(1) Å *c* = 7.981(1) Å R_p = 0.035	*A*	4*b* (*x*, *y*, 1/4)	0.973(2)	0.018(2)	0.25
	B	4*c* (1/2, 0, 0)	0.5	0	0
	O(1)	4*b* (*x*, *y*, 1/4)	0.070(2)	0.480(2)	0.25
	O(2)	8*d* (*x*, *y*, *z*)	0.710(2)	0.289(2)	0.030(2)
BFKNO-0.5					
Tetragonal *P*4*mm* (N 99) *a* = 3.999(1) Å *c* = 4.014(1) Å R_p = 0.048	*A*	1*a* (0, 0, *z*)	0	0	0.943(2)
	B	1*b* (1/2, 1/2, *z*)	0.5	0.5	0.489(2)
	O(1)	1*b* (1/2, 1/2, *z*)	0.5	0.5	0.044(2)
	O(2)	2*c* (1/2, 0, *z*)	0.5	0	0.540(2)
BFKNO-0.7					
Orthorhombic *Amm*2 (N 38) *a* = 3.990(1) Å *b* = 5.658(1) Å *c* = 5.682(1) Å R_p = 0.043	*A*	2*b* (0, 0, *z*)	0	0	0.014(2)
	B	2*a* (1/2, 0, 1/2)	0.5	0	0.5
	O(1)	2*b* (0, 0, *z*)	0	0	0.536(2)
	O(2)	4*e* (1/2, *y*, *z*)	0.5	0.248(2)	0.284(2)

Table 12.2 Structural parameters of BFNNO compounds at room temperature

Phase composition	Atom	Wyck	*x*/*a*	*y*/*b*	z/*c*
BFNNO-0.3					
Rhombohedral *R*3*c* (N 161) *a* = 5.577(1) Å *c* = 13.785(3) Å R_p = 0.043	*A*	6*a* (0, 0, *z*)	0	0	0.998(2)
	B	6*a* (0, 0, *z*)	0	0	0.222(2)
	O(1)	18*b* (*x*, *y*, *z*)	0.443(2)	0.012(2)	0.954(2)
BFNNO-0.5					
Orthorhombic *Pbnm* (N 62) *a* = 5.557(1) Å *b* = 5.601(1) Å *c* = 7.879(1) Å R_p = 0.032	*A*	4*b* (*x*, *y*, 1/4)	0.977(2)	0.022(2)	0.25
	B	4*c* (1/2, 0, 0)	0.5	0	0
	O(1)	4*b* (*x*, *y*, 1/4)	0.430(2)	0.980(2)	0.25
	O(2)	8*d* (*x*, *y*, *z*)	0.710(2)	0.289(2)	0.030(2)
BFNNO-0.7					
Tetragonal *P*4/*mbm* (N 127) *a* = 5.565(1) Å *c* = 3.979(1) Å R_p = 0.044	*A*	2*a* (0, 0, 0)	0	0	0
	B	2*c* (0, 1/2, 1/2)	0	0.5	0.5
	O(1)	2*b* (0, 0, 1/2)	0	0	0.5
	O(2)	4*g* (*x*, *y*, 0)	0.320(2)	0.820(2)	0

12.3.2 Temperature Phase Transitions

The temperature studies of phase transitions in the compounds of solid solutions allowed us to determine the peculiarities of structural changes in the 20 °C < T < 500 °C temperature range. Figures 12.3 and 12.4 show the temperature dependencies of the perovskite subcell parameters of BFKNO (Fig. 12.3) and BFNNO (Fig. 12.4).

In the BFKNO-0.3, before the main transition in the cubic phase takes place, the following changes in the ratio of the monoclinic perovskite subcell parameters are observed: $b_p/a_p < 1$ at $T < 190$ °C, and $b_p/a_p > 1$ at $T > 190$ °C. Such an isostructural phase transition in the *Pbnm* orthorhombic phase corresponds to the one between the *O* and *O′* phases as described by Goodenough in [23]. It should be noted that the volume of the perovskite subcell reduces with the increase in temperature to 200 °C and starts to grow when the temperature increase.

In the BFKNO-0.5 (Fig. 12.3b) the tetragonal to cubic phase transition at 280 °C is similar to the high-temperature phase transition in pure KNO (T_C = 420 °C). From the Fig. 12.3b, it is clear that the volume of the perovskite subcell decreases with increase in temperature to 100 °C and then increase above 100 °C.

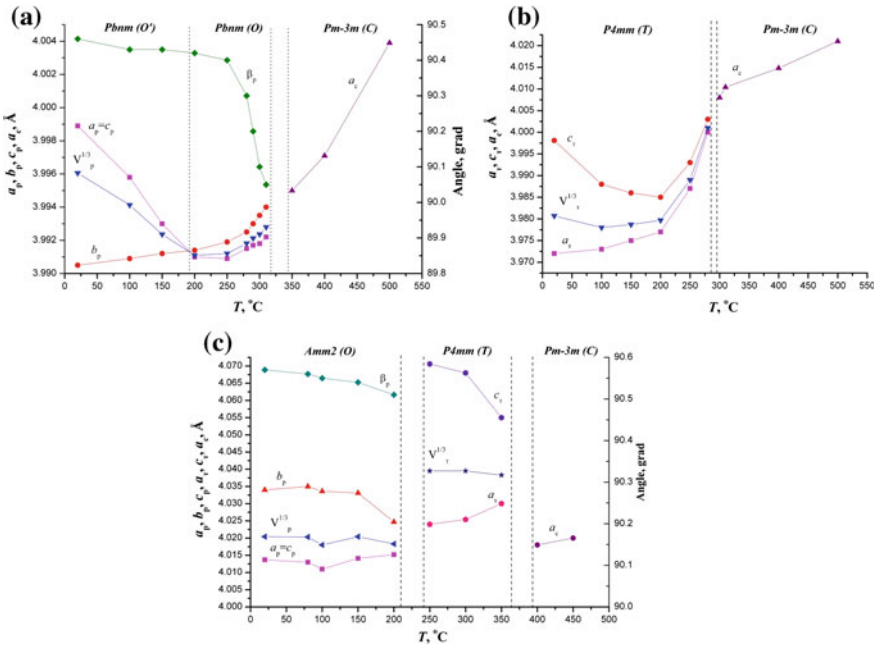

Fig. 12.3 **a** Temperature dependencies of structural parameters of BFKNO-03. **b** Temperature dependencies of structural parameters of BFKNO-05. **c** Temperature dependencies of structural parameters of BFKNO-07

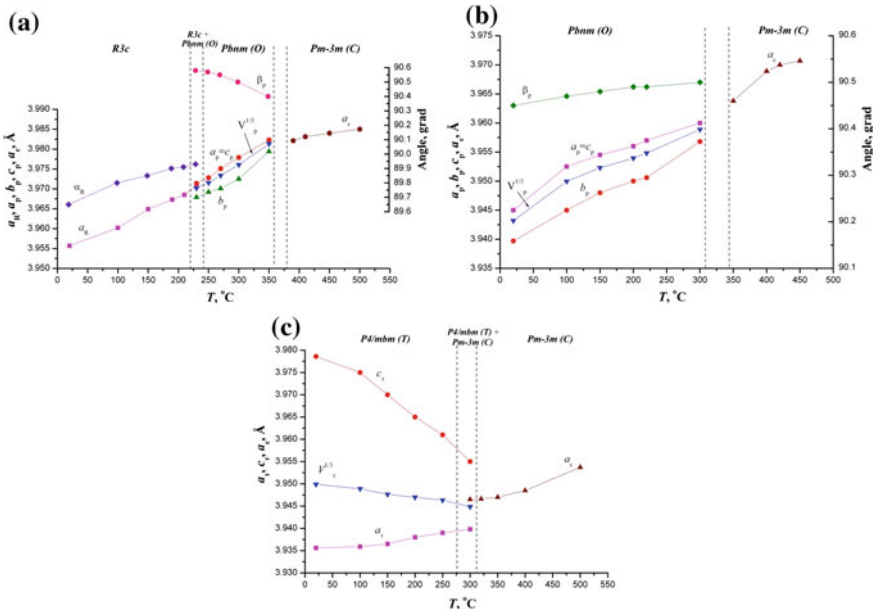

Fig. 12.4 **a** Temperature dependencies of structural parameters of BFNNO-03. **b** Temperature dependencies of structural parameters of BFNNO-05. **c** Temperature dependencies of structural parameters of BFKNO-07

The peculiarity of phase transitions in the BFKNO-0.7 (Fig. 12.3c) is that they repeat the sequence of the pure KNO phase transitions. But if the phase transition from the orthorhombic *Amm*2 phase into the tetragonal *P*4*mm* phase occurs at the same temperature as in pure KNO, then the tetragonal to cubic phase transition takes place at a lower temperature (T_C = 380 °C).

The phase transitions in the BFNNO-0.3 (Fig. 12.4a) are similar to those in the pure BFO, but the phase transition temperatures are significantly below, in particular, the phase transition from the rhombohedral into the orthorhombic phase occurs at 230 °C (at 820 °C in the pure BFO) and the orthorhombic-cubic phase transition take place at 370 °C (at 920 °C in the pure BFO). Note that the volume expansion coefficient does not change up to 350 °C ($\beta = 5.9 \times 10^5$ grad^{-1}) and decreases after the phase transition at 370 °C ($\beta = 2.0 \times 10^5$ grad^{-1}).

The nature of the structural changes in the BFNNO-0.5 (Fig. 12.4b) is similar to the character of changes at the orthorhombic—cubic phase transition as observed in the BFNNO-0.3. The difference is that at room temperature this compound is already characterized by the orthorhombic phase while the *Pbnm* to *Pm*3*m* phase transition occurs at 325 °C.

In the BFNNO-0.7 (Fig. 12.4c), the phase transition from the tetragonal to the cubic phase is similar to high-temperature phase transition in pure NNO, however, in this case the phase transition temperature is significantly below 300 °C. The behaviors of lattice parameters and the volume of perovskite subcell in tetragonal

phase indicate that the observed transition corresponds to either ferroelectric relaxor transition or phase transition observed in $PbTiO_3$, since in this phase the perovskite subcell volume becomes smaller with the increase in temperature up to the temperature of phase transition.

12.3.3 *Effects of Relaxation Polarization*

In Figs. 12.5 and 12.6, there are presented temperature and frequency dependencies of dielectric constants ε' and ε'' of studied BFKNO and BFNNO. Such dispersive

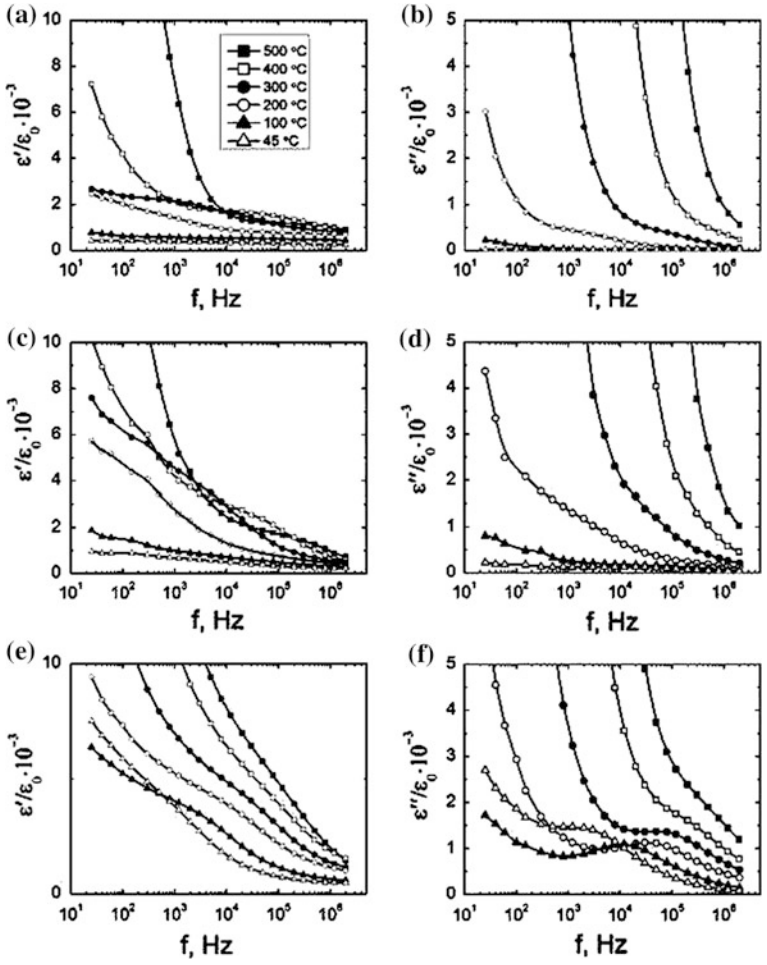

Fig. 12.5 Frequency dependencies of dielectric constants (ε' and ε'') at different temperatures of BFKNO: **a**, **b** BFKNO-03; **c**, **d** BFKNO-05; **e**, **f** BFKNO-07

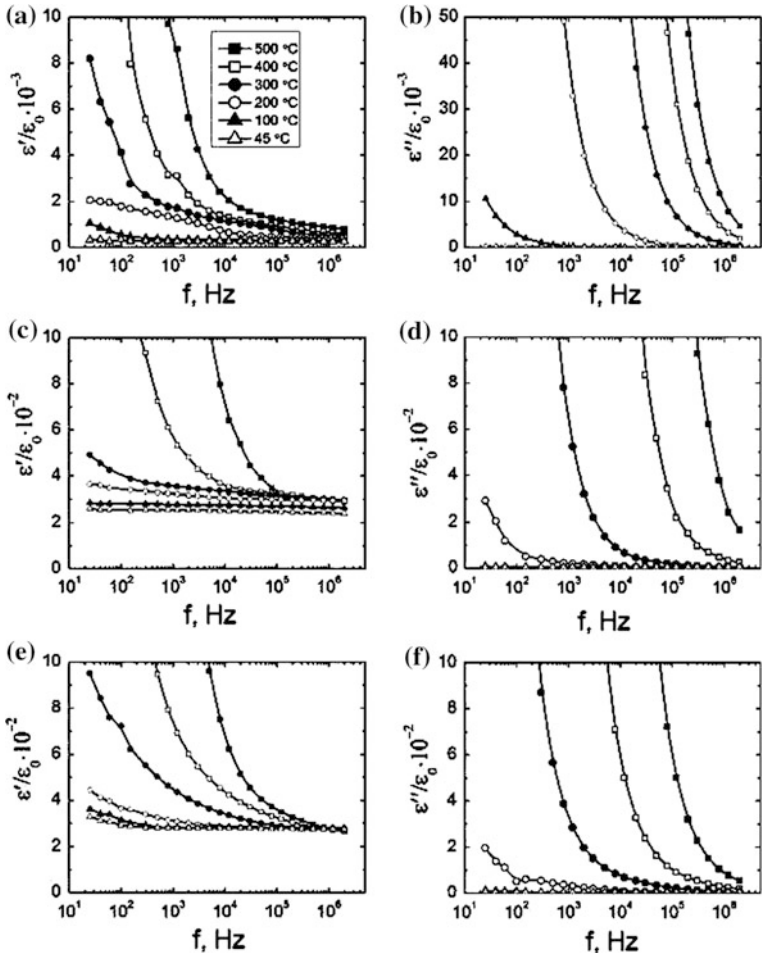

Fig. 12.6 Frequency dependencies of dielectric constants (ε' and ε'') at different temperatures of BFNNO: **a**, **b** BFNNO-03; **c**, **d** BFNNO-05; **e**, **f** BFNNO-07

dependencies are typical for dielectrics with the relaxation polarization with addition of prevailing conductivity effects [24–26].

Observed features of dependencies $\varepsilon'(f)$ in various areas of frequencies in the samples of BFNNO system are connected with changes of polarization mechanisms at phase transitions. They are revealed at abrupt increase ε' of the BFNNO-0.3 compound in the area of frequencies from 20 to 200 Hz after the transition from the ferroelectric *R*3*c* phase to the ferroelastic *Pbnm* phase. In the BFNNO-0.7 compound, abrupt increase ε' is observed at the transition from the ferroelectric *P*4/*mbm* phase to the paraelectric *Pm*3*m* phase in the area of frequencies from 0.02 to 2 kHz. In the BFNNO-0.5 compound frequency changes ε' at the phase transition from the

ferroelastic *Pbnm* phase to the paraelectric *Pm*3*m* phase are less pronounced. The analysis of frequency dependencies ε'' at various temperatures makes it clear that thermally activated dispersion, leading to the significant contributions to ε'' prevailing conductivity, dominates in BFNNO.

In the BFKNO, the dielectric dispersion is not very sensitive to structural phase transitions. Frequency dependencies ε' in all the compounds are typical for dielectrics with weak relaxation processes. In the BFKNO-0.3 compound there is revealed weak sensitivity of ε' to temperature and frequency changes at the transition from the ferroelastic *Pbnm* (*O*′) phase to the *Pbnm* (*O*) phase [23]. In the BFKNO-0.5 compound the ε' dispersion is more revealed and corresponds to the usual phase transition from the ferroelectric *P*4*mm* phase to *Pm*3*m* paraelectric phase. In the BFKNO-0.7 compound the ε' dispersion reflects the transition between two ferroelectric phases: *Amm*2 (at $T < 200$ °C) and *P*4*mm* (at $T > 200$ °C). This transition is the most evident in temperature and frequency dependencies of ε''. It may be seen (Fig. 12.5f) that in the area of frequencies from 0.02 to 10 kHz abrupt changes ε'' take place, meaning the interaction of different relaxation polarization' mechanisms, connected with internal heterogeneities, which lead to variations of local conductivities and dielectric permittivities.

12.4 Conclusions

In the compounds of $(1 - x)BiFeO_3$–$xKNbO_3$ and $(1 - x)BiFeO_3$–$NaNbO_3$ (x = 0.3, 0.5, 0.7) systems of solid solutions, the structural parameters and their changes in the 20 °C < T < 500 °C temperature range was determined. The sequence of symmetry changes of structures, unit cell parameters, atomic positional parameters and the phase transition temperatures of the phase states was found. By measurements of temperature and frequency dependencies of dielectric constants ε' and ε'', it is stated that changes of relaxation polarization correspond to structural phase transitions. There are revealed the correlations of these changes with transitions of the type: ferroelectric–ferroelastic, ferroelectric–paraelectric and ferroelectric–paraelectric.

The structural peculiarities of $(1 - x)BiFeO_3$–$xANbO_3$ compounds of solid solutions with the concentration ratios of components equal to 1:1 on the first hand are of particular interest being structural analogs of well-known ferroelectrics-relaxors ($Bi_{0.5}Na_{0.5}TiO_3$ and $Bi_{0.5}K_{0.5}TiO_3$ [27]). On the other hand, these compounds are very similar to the classical $PbFe_{0.5}Nb_{0.5}O_3$–multiferroic [28].

Acknowledgements This work was financially supported by the Ministry of Education and Science of the Russian Federation: themes Nos. 1927, 213.01-2014/012-VG and 3.1246.2014/K (the basic and project parts of the state task) and performed on equipment of the Collective use center "Electromagnetic, Electromechanical and Thermal Properties of Solids" of the Research Institute of Physics, Southern Federal University.

References

1. D.I. Khomskii, J. Magn. Magn. Mater. **306**, 1 (2006)
2. A. KhomchenkoV, I.O. Troyanchuk, M.V. Bushinsky, O.S. Mantytskaya, V. Sikolenko, J.A. Paixao, Mater. Lett. **65**, 1970 (2011)
3. B. Jaffe, W.R. Cook Jr., H. Jaffe, *Piezoelectric Ceramics* (Academic Press, London, New-York, 1971)
4. R.T. Smith, G.D. Achenbach, R. Gerson, W.J. James, J. Appl. Phys. **39**, 70 (1968)
5. K.K. Mishra, V. Sivasubramanian, R.M. Sarguna, T.R. Ravindran, A.K. Arora, J. Solid State Chem. **184**, 2381 (2011)
6. V.A. Khomchenko, D.A. Kiselev, M. Kopcewicz, M. Maglione, V.V. Shvartsman, P. Borisov et al., J. Magn. Magn. Mater. **321**, 1692 (2009)
7. I.O. Troyanchuk, M.V. Bushinsky, A.N. Chobot, O.S. Mantytskaya, N.V. Pushkarev, R. Szymczak, J. Exp. Theor. Phys. **107**(2), 245 (2008)
8. D. Kan, L. Palova, V. Anbusathaiah, C.J. Cheng, S. Fujino, V. Nagarajan, K.M. Rabe, I. Takeuchi, Adv. Funct. Mater. **20**, 1108 (2010)
9. J. Silva, A. Reayes, H. Sparza, H. Camacho, L. Fuentes, Integr. Ferroelectr. **126**, 47 (2011)
10. S. Dash, R. Padhee, R. Piyush, P.R. Das, R.N.P. Choudhary, Phase Transit. (2013). doi:10.1080/01411594.2013.812214
11. E.V. Satulova, V. Kabirov Yu, A.G. Rudskaya, M.F. Kupriyanov, in *Proceedings of International Symposium "Phys of Lead Free Piezo- and Relative Mater"*, 2–6 Sept 2015; Rostov-on-Don; vol. 2, p. 197 (2015) (in Russian)
12. I.P. Raevski, Ferroelectrics **299**, 95 (2004)
13. I.P. Raevski, S.A. Prosandeev, J. Phys. Chem. Solids **63**, 1939 (2002)
14. I.P. Raevski, S.P. Kubrin, J.L. Dellis, S.I. Raevskaya, D.A. Sarychev, V.G. Smotrakov, V.V. Eremkin, M.A. Seredkina, Ferroelectrics **371**, 113 (2008)
15. I.P. Raevski, S.P. Kubrin, S.I. Raevskaya, V.V. Stashenko, D.A. Sarychev, M.A. Malitskaya, I.N. Zakharchenko, V.G. Smotrakov, V.V. Eremkin, Ferroelectrics **373**, 121 (2008)
16. M. Ya, X.M. Chen, J. Appl. Phys. **105**, 054107 (2009)
17. S. Dash, R. Padhee, P.R. Das, R.N.P. Choudhary, J. Mater. Sci.: Mater. Electron. (2013). doi:10.1007/s10854-013-1249-4
18. Nakashima Yo., Shimura T., Sakamoto W., Yogo T. *Ferroelectrics*, **356**, 180 (2007)
19. W. Kraus, Nolze G. J. Appl. Cryst. **29**, 301 (1996)
20. P. Teslenko, A. Pavlenko, L. Reznichenko, O. Razumovskaya, Y. Kabirov, Acta Cryst. **A67**, 243 (2011)
21. P. Teslenko, A. Nazarenko, L. Reznichenko, Y. Kabirov, M. Kupriyanov, Acta Cryst. **A68**, 241 (2012)
22. R. Palai, R.S. Katiyar, H. Schmid, P. Tissot, S.J. Clark, J. Robertson, S.A. Redfern, G. Catalan, J.F. Scott, Phys. Rev. B. **77**, 014110 (2008)
23. J.B. Goodenough, Phys. Rev. **100**, 564 (1955)
24. V.A. Isupov, Ferroelectrics **315**, 123 (2005)
25. A.A. Bokov, Z.G. Ye, J. Mater. Sci. **41**, 31 (2006)
26. L.E. Cross, Ferroelectrics **151**, 305 (1994)
27. J.A. Samara, J. Phys. Condens. Matter **15**, R367 (2003)
28. A.S. Bogatin, A.V. Turik, S.A. Kovrigina, V.N. Bogatina, E.V. Andreev, Ferroelectrics **413** (1), 266 (2011)

Chapter 13
Crystal Structure, Phase and Elemental Composition and Chemical Bonding in $Bi_{1-X}A_XFeO_{3\pm Y}$ Systems (A = Sr, Ca; $0 \leq X \leq 1$) from X-ray Diffraction, Mössbauer, and X-ray Photoelectron Spectra

A.T. Kozakov, A.G. Kochur, V.I. Torgashev, S.P. Kubrin, V.G. Trotsenko, A.A. Bush and A.V. Nikolskii

Abstract An integrated study of samples of $Bi_{1-x}A_xFeO_{3\pm y}$ (A = Sr, Ca) systems for $0 \leq x \leq 1$ (step 0.1) is performed using X-ray diffraction (XRD), Mössbauer spectroscopy (MS), and X-ray photoelectron spectroscopy (XPS). Considerable deviations of actual elemental compositions from nominal ones in the samples of both systems are discovered. Both Fe^{3+} and Fe^{4+} ions are found to be present in the samples of the $Bi_{1-x}Sr_xFeO_{3\pm y}$ system with $x > 0$. No Fe^{4+} ions are discovered upon substitution of Bi^{3+} by Ca^{2+} in $Bi_{1-x}Ca_xFeO_{3\pm y}$, neither by Mössbauer spectroscopy, nor by XPS. Charge compensation in $Bi_{1-x}Ca_xFeO_{3\pm y}$ takes place mostly via creation of oxygen vacancies.

A.T. Kozakov · S.P. Kubrin (✉) · A.V. Nikolskii
Scientific Research Institute of Physics, Southern Federal University, 194 Stachki Avenue, Rostov-on-Don 344090, Russia
e-mail: stasskp@gmail.com

A.G. Kochur
Rostov State Transport University, 2, Narodnogo Opolcheniya Square, Rostov-on-Don 344038, Russia

V.I. Torgashev · V.G. Trotsenko
Faculty of Physics, Southern Federal University, Rostov-on-Don 344006, Russia

V.G. Trotsenko
Laboratory of Condensed Matter Physics, University of Picardy, Amiens 80039, France

A.A. Bush
Moscow State Technical University of Radio Engineering, Electronics and Automation, Moscow 119454, Russia

I.A. Parinov et al. (eds.), *Advanced Materials*, Springer Proceedings in Physics 193, DOI 10.1007/978-3-319-56062-5_13

13.1 Introduction

Bismuth ferrite $BiFeO_3$ is a well-known multiferroic [1] having simultaneously ferroelectric and magnetic properties, the latter being dependent to certain extent on the valence of the Fe-ions. Various practical applications require either a simultaneous existence of ferroelectric and magnetic properties, or selection of one of them. To this end, the initial compound $BiFeO_3$ is doped by the ions of other atoms, which are soluble in the initial matrix. In particular, in order to give the material a weak ferromagnetism, $BiFeO_3$ is doped by bivalent metal ions such as Pb, Ba, Sr, Ca [2]. Crystal structure and phase composition of the $Bi_{1-x}A_xFeO_{3\pm y}$ (A = Sr, Ca) samples have been studied in [2–4], however, only a small number of works [5–7] were addressed studying the valence state of the Fe-ions and their role in charge compensation mechanism.

This work's aim is in the analysis of similarities and differences in the effect of Sr^{2+} and Ca^{2+} on elemental and phase composition, crystal structure and valence state of the Fe-ions in solid solutions $Bi_{1-x}A_xFeO_{3\pm y}$ (A = Sr, Ca).

13.2 Methods

Synthesis of samples. All the ceramic samples of $Bi_{1-x}Sr_xFeO_{3\pm y}$ and $Bi_{1-x}Ca_xFeO_{3\pm y}$ systems were obtained with the solid-state reaction method within usual ceramic technology in air. Synthesis details are given in [6, 7].

X-ray phase analysis is performed on an automated DRON-4 (λCuK_α or λCoK_α radiation); germanium powder was used as an internal standard.

Mössbauer spectra were taken with the MS1104Em spectrometer designed and built in the Scientific Research Institute of Physics at the Southern Federal University. Moving-source geometry is employed. The source of the γ-quanta was ^{57}Co in a chromium matrix for $Bi_{1-x}Ca_xFeO_{3\pm y}$ samples, and ^{57}Co in a rhodium matrix, for $Bi_{1-x}Sr_xFeO_{3\pm y}$ samples. Isomer shifts are calculated with respect to the metallic α-Fe. Experimental spectra were fitted using the SpectrRelax software [6–8].

X-ray photoelectron spectra of ceramic solid solutions were taken at room temperature with X-ray photoelectron microprobe ESCALAB 250. The spectra were excited with a monochromatized Al$K\alpha$-radiation. Absolute energy resolution is 0.6 eV; it was determined from the Ag$3d_{5/2}$ line profile. The diameter of the X-ray spot on a sample surface was 500 μm. Flow of slow electrons was used to counteract the charging of samples. Clean surfaces of samples were obtained by a diamond file scribing in vacuum in a sample preparation chamber at a pressure of about 1×10^{-7} mbar. The state of the surfaces was monitored with the C1s line, which was very weak. C1s line binding energy was taken to be 285 eV.

Elemental compositions of the samples were determined via the XPS method using a standard routine and spectrometer's software package. Relative intensities

of Bi4f, Sr2p, Ca2p, Fe2p, and O1s lines were used for the analysis. Actual elemental compositions differ significantly from the intended ones. Still, we shall use nominal Sr and Ca contents x for labeling the samples for the sake of brevity.

13.3 Crystal Structure from X-ray Diffraction

It was found that the samples of the $Bi_{1-x}Sr_xFeO_{3\pm y}$ system are single-phased at $0.2 < x < 0.8$; they have a cubic symmetry with the lattice parameter $a \sim 3.95$ Å. Measured density of the ceramics made 70–85% of the XRD-data-based one. The symmetry of the $Bi_{1-x}Sr_xFeO_{3\pm y}$ solid solutions depends on x. For example, the symmetries of the samples with nominal Sr content x of 0, 0.5, and 1 are $R3c$, $Pm\bar{3}m$, and $P4mm$, respectively. Unit cell parameters are also x-dependent. The lattice compresses upon the increase of x. X-ray phase analysis does not show any traces of secondary phases, however one cannot exclude minor presence of Fe_2O_3, Bi_2O_3, $Bi_2Fe_4O_9$, etc. (not more than 4 mol%).

Crystal structure and phase composition of the $Bi_{1-x}Ca_xFeO_{3\pm y}$ samples are more diverse than in the $Bi_{1-x}Sr_xFeO_{3\pm y}$ case. X-ray phase analysis of $Bi_{1-x}Ca_xFeO_{3\pm y}$ samples has shown that the formation of solid solutions $Bi_{1-x}Ca_xFeO_{3\pm y}$ of perovskite structure occurs up to $x = 0.9$. Measured parameters of the rhombohedral cell in hexagonal setting for $BiFeO_3$ sample are $a = \sqrt{2}\, a_p = 5.601$ Å, $c = 2\sqrt{3}\, a_p = 13.718$ Å (where $a_p = 3.965$ Å is a pseudo-cubic cell parameter). The diffraction pattern of $BiFeO_3$ has reflections from impurity phases $Bi_2Fe_4O_9$ and $Bi_{25}FeO_{39}$ having relative intensities of less than 5%. The samples with $0.1 \leq x$ 0.4 are single-phased within the accuracy of the XRD method. Thorough analysis of the data on $x = 0.5$, 0.6, and 0.7 samples has shown the presence of Fe_2O_3 making 10, 5, and 5%, respectively. The samples with $0.7 \leq x < 1$ contained an impurity phase $CaFe_2O_4$, whose amount increases with the increase of x to 0.9.

The $x = 1$ sample consisted mainly of the $Ca_2Fe_2O_5$ phase with brownmillerite structure [7]. The diffraction pattern of this sample also has reflections from an impurity phase $CaFe_2O_4$ ($\sim$ 50%). The parameters of orthorhombic unit cells for phases $Ca_2Fe_2O_5$ and $CaFe_2O_4$, determined on indexing of the $x = 1$ Å sample diffraction pattern, are, respectively: $a = 5.421(1)$ Å, $b = 14.774(5)$, $c = 5.599(1)$ Å (space group *Pnma*) and $a = 3.020(1)$ Å, $b = 9.234(2)$ Å, $c = 10.699(2)$ Å (space group *Pnma*). Some changes in the size of the latter phase's elementary cell are apparently due to partial substitution of Ca atoms by Bi atoms with the formation of solid solutions (Ca, Bi)Fe_2O_4.

The dependencies of the unit cell parameters on x are similar in $Bi_{1-x}Ca_xFeO_{3\pm y}$ and $Bi_{1-x}Sr_xFeO_{3\pm y}$ solid solutions. In the $0 \leq x \leq 0.2$ range, the solid solutions are characterized by a rhombohedral symmetry apparently similar to that of the $BiFeO_3$ structure. The increase of Ca content in solid solutions decreases the parameter a, indicating that the Ca ions are incorporated in the unit cell, which keeps the perovskite structure. Reduction of size can be caused by the fact that the

ionic radius of Ca^{2+}(VI), 1.00 Å, is smaller than that of Bi^{3+}(VI), 1.03 Å [9]. In $Bi_{1-x}Ca_xFeO_{3\pm y}$, within the $0.3 \leq x \leq 0.9$ interval, a pseudo-cubic unit cell size decreases in a near-linear fashion upon the increase of the Ca content.

13.4 Ceramics Elemental Composition

Measured atomic concentrations of bismuth, strontium, calcium, iron, and oxygen in $Bi_{1-x}A_xFeO_{3\pm y}$ (A = Ca, Sr) ceramics are presented in Fig. 13.1 as functions of the nominal content of x in Sr and Ca. In a stoichiometric case, the concentration of oxygen is expected to be 60 at.%, iron 20 at.%, while bismuth and strontium (or calcium) should make 20 at.% combined. Upon linear increase of the nominal Sr (Ca) content x, linear decrease of the Bi concentration is expected (dot lines in Fig. 13.1a, b). One can see from Fig. 13.1 that the actual measured atomic concentrations follow this tendency rather poorly. For example, in $Bi_{1-x}Sr_xFeO_{3\pm y}$, up to $x = 0.4$, and in the $0.5 < x < 0.7$ region, the samples are Bi-rich and Sr-poor (Fig. 13.1a, c). In the $0.7 \leq x \leq 0.8$ region, Sr deficit is seen while the content of Bi is nominal. Only for $x = 0.4$ the Bi-Sr relative content is close to nominal.

In the case of $Bi_{1-x}Ca_xFeO_{3\pm y}$ system (see Fig. 13.1b, d), the measured concentrations of Bi and Ca deviate from the nominal ones as well. One may note an excess of bismuth for most values of x, and calcium deficiency for $0.1 \leq x \leq 0.6$.

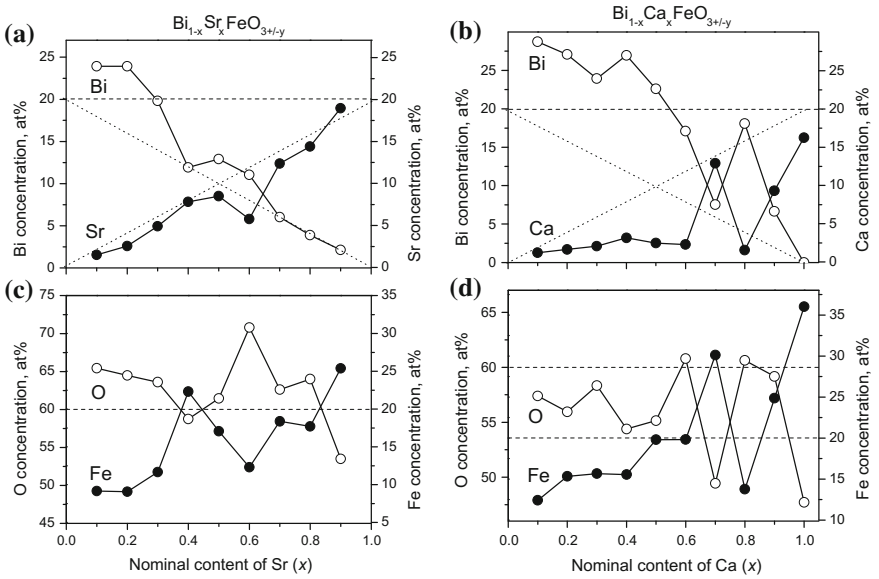

Fig. 13.1 Measured atomic concentrations of Bi, Sr, Ca Fe, and O in ceramic samples: **a**, **c** $Bi_{1-x}Sr_xFeO_{3\pm y}$; **b**, **d** $Bi_{1-x}Ca_xFeO_{3\pm y}$

Starting from $x = 0.6$, an opposite-slope correlation is seen between the concentrations of Bi and Ca. In the samples of the $Bi_{1-x}Ca_xFeO_{3\pm y}$ system one cannot observe the regions with constant or weakly varying Bi concentrations as it was the case for the $Bi_{1-x}Sr_xFeO_{3\pm y}$ system.

As of the variation of the concentrations of Fe and O, their variations are correlated, as seen from Fig. 13.1c, d. Concentrations of iron and oxygen change in an opposite-slope manner. At first glance, this seems to be rather strange, as if iron replaced oxygen in the lattice, and vice versa. In fact, such behavior can be explained by the presence of oxygen vacancies around the Fe^{3+} ions. According to generally accepted conception [6, 7], the lack of positive charge produced by the substitution of Bi^{3+} by Sr^{2+} or Ca^{2+} can be compensated either by the increase of the iron ion valence (at x close to 1 in the $Bi_{1-x}Sr_xFeO_{3\pm y}$ case) or by the appearance of the oxygenic vacancies near Fe^{3+} ions. According to [5–7], in the case of the $Bi_{1-x}Sr_xFeO_{3\pm y}$ system, the increase of x up to 0.5 does not lead to the increase of valence, instead, oxygen vacancies appear. Their number increases together with the increase of the Sr content. Therefore, the change of the number of Fe^{3+} ions in a sample must be accompanied by an opposite-slope variation of the number of oxygen atoms.

The presence of Fe^{4+} ions means the presence of octahedral oxygenic environment. That would cause same-slope variation of Fe and O concentrations. Generally, the opposite-slope behavior of Fe and O concentrations may mean that the materials of the system under study contain mostly Fe^{3+} ions. As seen from Fig. 13.3b, d, in the $Bi_{1-x}Ca_xFeO_{3\pm y}$ $Bi_{1-x}Ca_xFeO_{3\pm y}$ case, even sharper opposite-slope correlation between Fe and O concentration than in $Bi_{1-x}Sr_xFeO_{3\pm y}$ is observed.

13.5 Estimate of Iron Ions Valence State from Mössbauer Spectra

For both systems, one may expect the presence of the Fe^{4+} ions at close-to-terminal greater x. In Fig. 13.2, the $x = 0.9$ spectra of $Bi_{1-x}A_xFeO_{3\pm y}$ (A = Ca, Sr) are compared. Isomer shifts of Mössbauer spectra and their fine structure are sensible to the valence of iron ions, and to their nearest-neighbor environment. One can see that the two spectra differ significantly from each other.

Mössbauer spectrum of $Bi_{0.1}Sr_{0.9}FeO_{3\pm y}$ (left panel of Fig. 13.2) is a superposition of a singlet and two doublets. The doublet with an isomer shift $\delta = 0.48$ mm/s corresponds to Fe^{3+} ions within oxygenic octahedrons with coordination number (CN) equal to 6 [9]. Another doublet ($\delta = 0.21$ mm/s) comes from Fe^{3+} ions in polyhedral environment with CN = 5. The singlet component ($\delta = -0.06$ mm/s) reflects Fe^{4+} ions in octahedral oxygenic environment. The areas of the components give approximate concentrations of ions in different ionic states mentioned above. The presence of oxygenic polyhedrons with different CN may be caused by the presence of oxygenic vacancies.

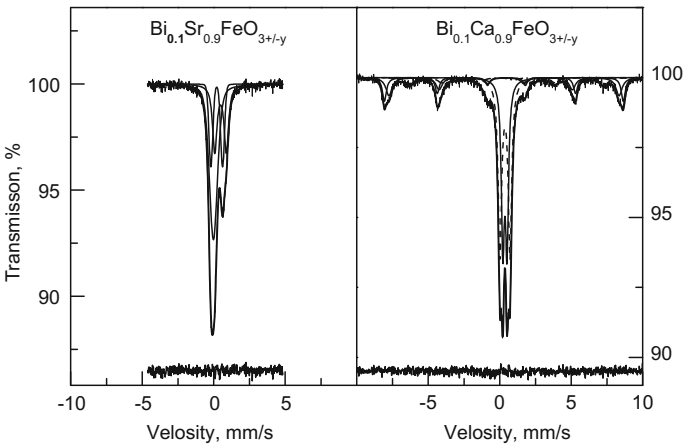

Fig. 13.2 Mössbauer spectra of ceramic samples $Bi_{1-x}Sr_xFeO_{3\pm y}$ and $Bi_{1-x}Ca_xFeO_{3\pm y}$ at $x = 0.9$ taken at room temperature

The spectrum of $Bi_{0.1}Ca_{0.9}FeO_{3\pm y}$ (right panel of Fig. 13.2) is a superposition of two doublets and three sextets. The isomer shifts of all components are characteristic of Fe^{3+} ions [10], at that, one sextet, and two doublets correspond to octahedral oxygen environment while another sextet – to tetrahedral environment. The two sextets' parameters match the compound $Ca_2Fe_2O_5$ [11], and the parameters of the doublets match $CaFe_2O_4$ [12]. The third sextet refers to α-Fe_2O_3. It follows then that the $Bi_{0.1}Ca_{0.9}FeO_{3\pm y}$ sample does not have any Fe^{4+} ions, in contrast to the $Bi_{0.1}Sr_{0.9}FeO_{3\pm y}$ case. According to Mössbauer spectra, all other samples of both systems contain only Fe^{3+} ions in different oxygenic environments. Mössbauer spectra are discussed in more detail in [6, 7].

It follows then that the Mössbauer spectroscopy detects the Fe^{4+} ions only in the $Bi_{0.1}Sr_{0.9}FeO_{3\pm y}$ sample; estimated portion of Fe^{4+} is equal to 0.45.

13.6 Estimate of Iron Ions Valence State from Fe2p XPS

Valence state of iron in $Bi_{1-x}A_xFeO_{3\pm y}$ (A = Sr, Ca) has been a subject of most of the studies on these systems, see, for example, [5–7]. Energy position and fine structure of Fe2p XPS are known to be sensitive to the valence of Fe.

Figure 13.3 shows the Fe2p-spectra of two samples, $Bi_{0.2}A_{0.8}FeO_{3\pm y}$ (A = Sr, Ca) in a x-region, where a strongly opposite-slope behavior of Fe and O concentrations is seen for the samples of the $Bi_{1-x}Ca_xFeO_{3\pm y}$ $Bi_{1-x}Ca_xFeO_{3\pm y}$ system. The spectra are placed so that their principal $Fe2p_{3/2}$ (A) maxima have the same energy position. It is seen from Fig. 13.3 that in this case, all other features of the spectra (B, C, D) have also the same positions. Peaks A and B reflect $Fe2p_{3/2}$ and $Fe2p_{1/2}$

levels, respectively. Features B and D come from the charge transfer satellites; their positions and intensities are characteristic of the spectra of a trivalent iron. The analysis of the overall profiles of the Fe2p-spectra does not then make it possible to see if there are contributions from the Fe^{4+} ions in the spectra.

More detailed analysis of the spectra [6] showed, that in the $Bi_{1-x}Sr_xFeO_{3\pm y}$ system, there are correlations between the position of the $Fe2p_{3/2}$ peak ($E_{3/2}$) and its full width at half maximum (FWHM) $\Gamma_{3/2}$ (Fig. 13.3c), and between $\Gamma_{3/2}$ and the spin-doublet energy separation $\Delta E_{2p} = E(Fe2p_{1/2}) - E(Fe2p_{3/2})$, Fig. 13.3d.

We calculated ΔE_{2p} and $\Gamma_{3/2}$ for various ions of iron. Calculations are performed in an isolated ion approximation, they are described in detail in [6]; the results are present in Fig. 13.3e. The isolated ion approximation does not allow calculating absolute binding energies, however it is known that $Fe2p_{3/2}$-peak binding energy is 711.2 eV in a trivalent iron in single crystal $BiFeO_3$, is equal to 710.5 in ceramic $BiFeO_3$ sample, and equals 709.3 eV in quadrivalent iron. It is seen from Fig. 13.3e that the width of the $Fe2p_{3/2}$ peak $\Gamma_{3/2}$ decreases when going from Fe^{3+} to Fe^{4+}. Since upon going from Fe^{3+} to Fe^{4+} Fe2p binding energy decreases, we expect same-slope variations in $E_{3/2}$ and $\Gamma_{3/2}$ upon the change of valence. This is, generally, indeed the case, see Fig. 13.3c. Non-monotonic character of these variations means non-monotonic change of the valence of iron between 3+ and 4+ in the $0 \leq x \leq 1$ interval.

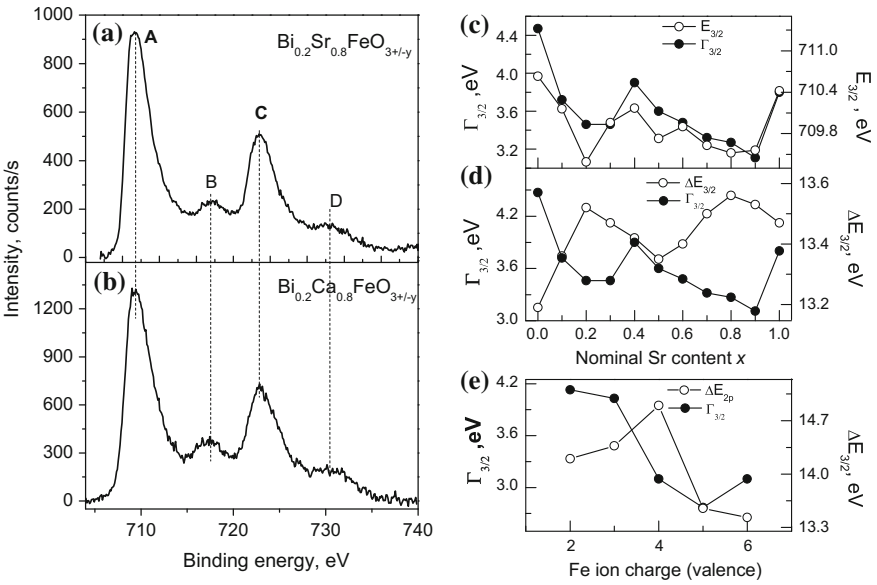

Fig. 13.3 **a** Fe2p XPS of $Bi_{0.2}Sr_{0.8}FeO_{3\pm y}$; **b** Fe2p XPS $Bi_{0.2}Ca_{0.8}FeO_{3\pm y}$; **c** measured binding energies ($E_{3/2}$) and FWHM ($\Gamma_{3/2}$) of $Fe2p_{3/2}$ peaks in $Bi_{1-x}Sr_xFeO_{3\pm y}$; **d** measured FWHM of $Fe2p_{3/2}$ peaks ($\Gamma_{3/2}$) and spin-doublet separation (ΔE_{2p}) in $Bi_{1-x}Sr_xFeO_{3\pm y}$; **e** calculated FWHM of $Fe2p_{3/2}$ peaks ($\Gamma_{3/2}$) and spin-doublet separation (ΔE_{2p}) for various Fe ions

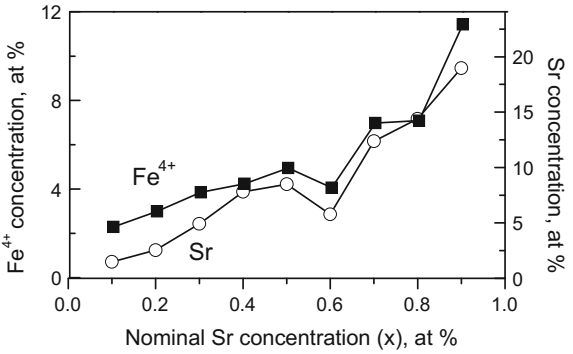

Fig. 13.4 Concentrations of Sr and Fe^{4+} in $Bi_{1-x}Sr_xFeO_{3\pm y}$ as functions of nominal Sr concentration [6]

The calculated spin-doublet energy separation ΔE_{2p} increases upon going from Fe^{3+} to Fe^{4+} (Fig. 13.3e). It means that upon the change of valence, $Fe2p_{3/2}$ binding energies $E_{3/2}$ and Fe2p peak energy separation ΔE_{2p} must vary in an opposite-slope manner. Figure 13.3d shows that this is in fact like this. Opposite-slope variation of ΔE_{2p} and $\Gamma_{3/2}$ upon the change of valence between 3+ and 4+, predicted by calculation, is clearly seen in the experiment, see Fig. 13.3d. In a very crude approximation, one can consider the x-dependencies of the $Fe2p_{3/2}$ peak width $\Gamma_{3/2}$ in Fig. 13.3c, d as a calibration curve reflecting the variation of relative Fe^{3+}/Fe^{4+} abundances—the less the width is, the more Fe^{4+} ions there are. Suggesting that there is no Fe^{4+} ions in the $x = 0$ sample, and that the content of Fe^{4+} is 0.45 at $x = 0.9$ as determined from the Mössbauer spectrum, one can estimate relative abundances of Fe^{3+} and Fe^{4+} ions in the whole $Bi_{1-x}Sr_xFeO_{3\pm y}$ series. Concentration of Fe^{4+} ions in a sample can be obtained by multiplying the concentration of Fe (see Fig. 13.1c) by the relative content of Fe^{4+} [6].

In Fig. 13.4, the measured concentration of Fe^{4+} ions in $Bi_{1-x}Sr_xFeO_{3\pm y}$ ceramics is compared with measured concentrations of Sr at various nominal concentrations x of Sr. As expected, these two values correlate with each other. Fe2p XPS of the $Bi_{1-x}Ca_xFeO_{3\pm y}$, in contrast to the samples of the $Bi_{1-x}Sr_xFeO_{3\pm y}$ system, did not change neither their energy position, nor any other parameters discussed above. By their profile and energy position, they can be assigned to Fe^{3+} ions for all the samples.

13.7 Conclusions

The samples of the $Bi_{1-x}Ca_xFeO_{3\pm y}$ contain only Fe^{3+} ions on the whole interval of $0 \leq x \leq 1$. Both Fe^{3+} and Fe^{4+} ions are discovered in the $Bi_{1-x}Sr_xFeO_{3\pm y}$ system; the Fe^{4+}/Fe^{3+} ratio grows with the increase of x. It follows then that in $Bi_{1-x}Ca_xFeO_{3\pm y}$ the charge compensation takes place only via creation of oxygen vacancies. In $Bi_{1-x}Sr_xFeO_{3\pm y}$, both vacation-creation and valence-change mechanisms are present; the latter becomes more important with the growth of x.

Acknowledgements This study was supported by the Ministry of Education and Science of Russian Federation (grants Nos. 3.6105.2017/BCh, 3.5346.2017/BCh, and RFMEFI60714X0110).

References

1. J. Li, Y. Duan, H. He, D. Song, J. Alloys Compd. **315**, 259 (2001)
2. V.A. Khomchenko, D.A. Kiselev, J.M. Vieira, A.L. Kholkin, M.A. Sa, Y.G. Pogorelov, Appl. Phys. Lett. **90**, 242901 (2007)
3. J. Schiemer, R. Withers, L. Noren, Y. Liu, L. Bourgeois, G. Stewart, Chem. Mater. **21**, 4223 (2009)
4. K. Sardar, J. Hong, G. Catalan, P.K. Biswas, M.R. Lees, R.I. Walton, J.F. Scott, S.A.T. Redfern, J. Phys. Condens. Matter **24**, 045905 (2012)
5. E. Folcke, J.M. Le Breton, Y. Breard, A. Maignan, Solid State Sci. **12**, 1387 (2010)
6. A.T. Kozakov, A.G. Kochur, V.I. Torgashev, A.A. Bush, V.Y. Shkuratov, S.P. Kurbin, A.V. Nikolskii, K.A. Googlev, J. Electron Spectrosc. **189**, 106 (2013)
7. A.T. Kozakov, A.G. Kochur, V.I. Torgashev, K.A. Googlev, S.P. Kubrin, V.G. Trotsenko, A. A. Bush, A.V. Nikolskii, J. Alloys Compd. **664**, 392 (2016)
8. M.E. Matsnev, V.S. Rusakov, Conf. Proc. **1489**, 178 (2012)
9. R.D. Shannon, Acta Cryst. A **32**, 751 (1976)
10. F. Menil, J. Phys. Chem. Solids **46**(7), 763 (1985)
11. E.V. Tsipis, Y.V. Pivak, J.C. Waerenborgh, V.A. Kolotygin, A.P. Viskup, V.V. Kharton, Solid State Ionics **178**, 1428 (2007)
12. R. Lin, Y. Qian, Z. Chen, Ch. Zhu, G. Wang, Yu. Zhang, Mater. Sci. Eng. B **13**, 133 (1992)

Chapter 14
Mössbauer Study of the Effect of Mechanical Activation on the Magnetic Properties of $PbFe_{0.5}Nb_{0.5}O_3$

S.P. Kubrin, I.P. Raevski, V.V. Stashenko, A.A. Gusev, V.P. Isupov, H. Chen, C.-C. Chou, D.A. Sarychev, V.V. Titov and S.I. Raevskaya

Abstract Mössbauer studies of $PbFe_{0.5}Nb_{0.5}O_3$ samples prepared by mechanical activation of PbO, Fe_2O_3 and Nb_2O_5 mixture and subsequent sintering at various temperatures T_S were performed. The room temperature Mössbauer spectra consist of two doublets (D1 and D2) for the samples with $T_S < 800$ °C and one doublet (D1) for the samples with $T_S > 800$ °C. The parameters of the doublet D1 correspond to Fe^{3+} in the octahedron environment. Doublet D2 has a lower isomer shift corresponding to Fe^{3+} with the coordination number 5 that indicates the presence of oxygen vacancies. Dependence of the temperature T_N of magnetic phase transition on T_S has a maximum at $T_S \approx 700$ °C. The effect of Fe^{3+}/Nb^{5+} ordering degree and oxygen deficiency on T_N is discussed.

14.1 Introduction

Ternary perovskite oxide $PbFe_{0.5}Nb_{0.5}O_3$ and its solid solutions exhibit high dielectric, piezoelectric, pyroelectric, electrostrictive responses [1–4]. Ceramics of these materials may be sintered at rather low temperatures (1050–1100 °C), and are prospective for many applications. As PFN contains a magnetic ion (Fe^{3+}) it

S.P. Kubrin · I.P. Raevski (✉) · V.V. Stashenko · D.A. Sarychev · V.V. Titov · S.I. Raevskaya
Faculty of Physics, Research Institute of Physics,
Southern Federal University, Rostov-on-Don, Russia
e-mail: igorraevsky@gmail.com

A.A. Gusev · V.P. Isupov
Institute of Solid State Chemistry and Mechanochemistry SB RAS,
Novosibirsk, Russia

H. Chen
University of Macau, Macau, China

C.-C. Chou
National Taiwan University of Science and Technology,
Taipei, Taiwan, China

I.A. Parinov et al. (eds.), *Advanced Materials*, Springer Proceedings in Physics 193, DOI 10.1007/978-3-319-56062-5_14

belongs to the currently very actively studied family of multiferroics. These materials possess simultaneously ferroelectric and magnetic orders [5–7]. On cooling PFN undergoes phase transitions from a cubic paraelectric phase to a tetragonal ferroelectric phase at $T_{CT} \approx 380$ K, then to a rhombohedral [8] (or monoclinic [9, 10]) ferroelectric phase at $T_{TR} \approx 360$ K and finally to a G-type antiferromagnetic (AFM) phase at $T_N \approx 150$ K [5, 6, 10]. In several works, magnetization loops were reported for ceramics and thin films of PFN and its analog $PbFe_{0.5}Ta_{0.5}O_3$ (PFT) as well as for their solid solutions with PZT [7, 11, 12]. As the T_N values of PFN, PFT and their solid solutions with $PbTiO_3$ (PT) and $PbZrO_3$ (PZ) are well below the room temperature [13–16] a possible origin of these room-temperature magnetic properties was supposed to be the formation of super-paramagnetic clusters [6, 7] and/or Fe spin clustering [11]. However in PFN-PT single crystals the super-antiferromagnetic and/or super-paramagnetic clusters were observed up to rather high temperatures well above the T_N, while the magnetization loops were observed only below ≈50 K [13]. Another possible explanation of these room-temperature magnetic properties is the presence of some small admixture of the ferromagnetic or ferrimagnetic phase, e.g. $PbFe_{12}O_{19}$, however its amount is below the detection limit of X-ray diffraction and Mössbauer spectroscopy [16, 17].

Until recently, there had been a belief that Fe and Nb in PFN are distributed over the lattice in a random fashion, but several observations now indicate that the Fe ions might segregate at the nanoscale level. Studies of ^{57}Fe Mössbauer spectra [18], as well as ^{93}Nb and ^{17}O NMR spectra [19] and magnetization [6] have led to the conclusion that PFN is a chemically inhomogeneous system and that long range AFM order forms in Fe-rich-Nb-poor regions while, a magnetic relaxor spin-glass like state below $T \approx 20$ K can arise from the Fe-poor-Nb-rich regions [6, 19]. These data are reinforced by the results of first principles calculations showing that Fe^{3+} and Nb^{5+} ions are distributed in the PFN lattice not randomly, but that they exhibit clustering [18]. Such clustering is actually a sort of local ordering changing the number of the nearest-neighbor Fe^{3+} ions and this fact, in particular, explains why the experimental values of T_N, for both PFN and PFT (≈150 K) are much lower than the calculated values of T_N for the case of random distribution of Fe^{3+} and Nb^{5+} (Ta^{5+}) ions in the lattice ($T_N \approx 300$ K) [20].

Such self-organization would be of great interest for applications if one could control it. Previously Li- doping was successfully used to change the compositional ordering degree of B-site cations in $PbB^{3+}_{0.5}B^{3+}_{0.5}O_3$ perovskites with B^{3+} = Sc, Yb; B^{5+} = Nb, Ta, [21]. Such ordering should decrease T_N as the number of the nearest-neighbor Fe^{3+} ions decreases. Indeed Li-doping was reported to decrease T_N value of PFN and PFT ceramics by ≈50 K [22].

However much more important is to increase T_N values, preferably up to room temperatures. Though linear-quadratic paramagnetoelectric effect in PFN ceramics is observed at room temperature and up to the ferroelectric Curie temperature $T_{CT} \approx$ 380 K, the value of this effect is several orders of magnitude lower that in the magnetic phase [23].

Some years ago there appeared a report that T_N value of the epitaxial PFN nanofilm is more than 50 K higher than that of the bulk samples [12]. Moreover in this film a remnant magnetization was observed up to room temperature, while in the bulk PFN single crystals it vanishes above ≈10–15 K [13]. These intriguing properties of PFN nanofilms seem to be due to the effect of epitaxial strain on the degree of Fe^{3+} and Nb^{5+} ions ordering. First-principles calculations support such possibility [24].

Recently we found out that T_N values of both PFN and PFT powders can be increased by 50–70 K by means of high-energy mechanical activation [25–27]. Such treatment is known to increase disorder of *B*-site cations in $PbB^{3+}_{0.5}B^{5+}_{0.5}O_3$ perovskites [28]. However the origin of the observed increase of T_N in mechanically activated multiferroics is not well understood yet.

The aim of the present study was a thorough study of Mössbauer spectra of mechanically activated PFN powders annealed at different temperatures in order to elucidate a correlation between T_N values and the environment of magnetic Fe^{3+} ions.

14.2 Experimental

PFN samples were fabricated from a stoichiometric mixture of high purity PbO, Fe_2O_3 and Nb_2O_5 powders. Mechanical activation was carried out using the high-energy planetary-centrifugal ball mill AGO-2 under a ball acceleration of 40 g. A mixture of powdered reagents (10 g) was placed into a steel cylinder together with 200 grams of steel balls, 8 mm in diameter. Activation was carried out for 15 min. After each five minutes of activation, the mill was stopped, the cylinders were opened, the powder was taken out and mixed, then it was put back into the cylinders for further mechanical activation. Besides the described above one-stage activation, the second batch of the powders was prepared by two-stage activation. At the first stage only Fe_2O_3 and Nb_2O_5 powders were activated for 15 min. At the second stage PbO was added and the resulting mixture was activated for 15 min. The samples for subsequent sintering were pressed at 1000 kg/cm^2 without a plasticizer. Sintering of the samples, placed into a closed alumina crucible, was carried out in an electric oven at different temperatures for 2 h. X-ray diffraction (XRD) studies were performed using DRON-3 diffractometer and Cu-K_α radiation. Transmission Mössbauer spectra of ^{57}Fe were measured with the aid of MS-1104EM rapid spectrometer and analyzed using the computer program SpectrRelax [29]. Mössbauer studies were carried out in the 12–320 K range using the closed-cycle helium cryostat-refrigerator Janis Ccs-850 (Cryogenics).

14.3 Results and Discussion

Figure 14.1 shows XRD patterns of mechanically activated stoichiometric mixture of PbO, Fe_2O_3 and Nb_2O_5 just after one-stage (a) and two-stage (b) activation. XRD patterns of both samples are very similar. One can see that using of AGO-2 high-energy planetary-centrifugal ball mill enables one to obtain practically pure perovskite phase of PFN after only 15 min of activation. It is worth noting that in the case of usual planetary or vibrating mills pure perovskite phase of PFN forms only after 20–30 h of activation [28, 30]. The diffraction reflexes of as-synthesized PFN are somewhat diffused, which seems to be caused by the small size of the particles formed. The mean size D of X-ray coherent scattering blocks, estimated using the Scherrer formula, appeared to be about 15–20 nm. Increase of the sintering temperature T_S leads to the sharpening of the diffraction reflexes (Fig. 14.1a, b, curves 2). This sharpening correlates with the increase of the D values up to ≈40 nm at T_S = 800 °C and 50–55 nm at higher sintering temperatures. However in the sample obtained by one-stage activation and sintered at 800 °C there is a substantial admixture of the parasitic pyrochlore phase (Fig. 14.1a, curve 2).

Figure 14.2 shows Mössbauer spectra of the same two samples. Both spectra are superposition of doublet and sextet. The doublet and sextet parameters are listed in Table 14.1. Parameters of sextet correspond to α-Fe_2O_3. The doublet is related to perovskite phase of PFN with admixture of $FeNbO_4$. The areas of doublet and sextet give the concentration of Fe ions in corresponding phases. Thus 25% of Fe^{3+} ions are related to PFN/$FeNbO_4$ phase in the sample (A). Similar ratio of the Fe_2O_3 and PFN/$FeNbO_4$ phases was reported for the stoichiometric mixture of PbO, Fe_2O_3 and Nb_2O_5 activated in SPEX 8000D vibrating mill for 20 h [30]. The doublet isomer shifts value correspond to Fe^{3+} state with coordination number 5 [31] and is lower than that for PFN single crystal (0.4 mm/s) [32]. The coordination number of Fe^{3+} ions in perovskites is 6. The reduction of coordination number is

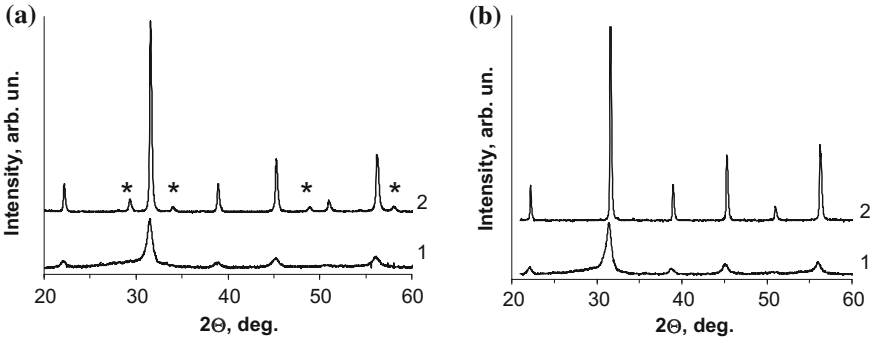

Fig. 14.1 X-ray diffraction patterns of mechanically activated stoichiometric mixture of PbO, Fe_2O_3 and Nb_2O_5 just after activation (*1*) and after sintering at 800 °C for 2 h (*2*): **a** one-stage activation; **b** two-stage activation; *asterisks mark* reflexes of the pyrochlore phase

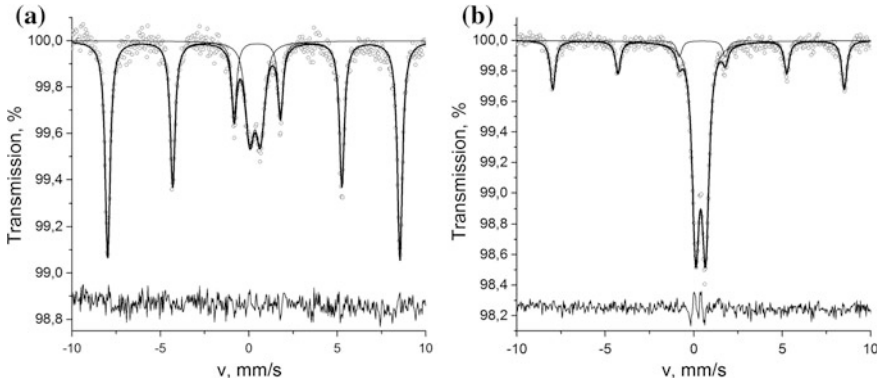

Fig. 14.2 Room-temperature ^{57}Fe Mossbauer spectra of mechanically activated stoichiometric mixture of PbO, Fe_2O_3 and Nb_2O_5. **a** One-stage activation. **b** Two-stage activation

Table 14.1 Parameters of room-temperature ^{57}Fe Mossbauer spectra of mechanically activated stoichiometric mixtures of PbO, Fe_2O_3 and Nb_2O_5

Preparation method	Spectrum component	$\delta \pm 0.02$, mm/s	$\Delta/\varepsilon \pm 0.02$, mm/s	$S \pm 2$, %	$H \pm 5$, kOe	$G \pm 0.02$, mm/s	χ^2
One-stage activation (Fig. 1a)	D	0.34	0.60	25		0.60	1.342
	S	0.37	−0.2	75	512	0.34	
Two-stage activation (Fig. 1b)	D	0.39	0.56	73		0.47	1.497
	S	0.38	−0.2	27	511	0.34	

D doublet, *S* sextet, δ isomer shift, Δ quadrupole splitting for paramagnetic component (doublet), ε quadrupole shift for sextet, *H* effective magnetic field on ^{57}Fe, *S* component area, *G* linewidth, χ^2 pearson's criterion

probably related to oxygen vacancies, which appear during mechanical activation. In addition, the quadrupole splitting value is higher than that for PFN single crystal (0.4 mm/s) because of high dispersion of the investigated mixture [33]. The doublet isomer shift value of the sample (B) is close to that for PFN single crystal and also corresponds to Fe^{3+} ions in the octahedron. The doublet quadrupole splitting value for sample (B) is lower than that for the sample (A). This fact may indicate the increase of the particle size. For further studies, the samples sintered from the powders fabricated by two-stage mechanical activation were used.

Mössbauer spectra of PFN samples sintered at different temperatures T_S from mechanically activated powders are present in Fig. 14.3. The spectra consist of one or two paramagnetic doublets. Their parameters are listed in Table 14.2. For some spectra, a Zeeman sextet is observed as well. The sextet parameters correspond to α-Fe_2O_3 admixture.

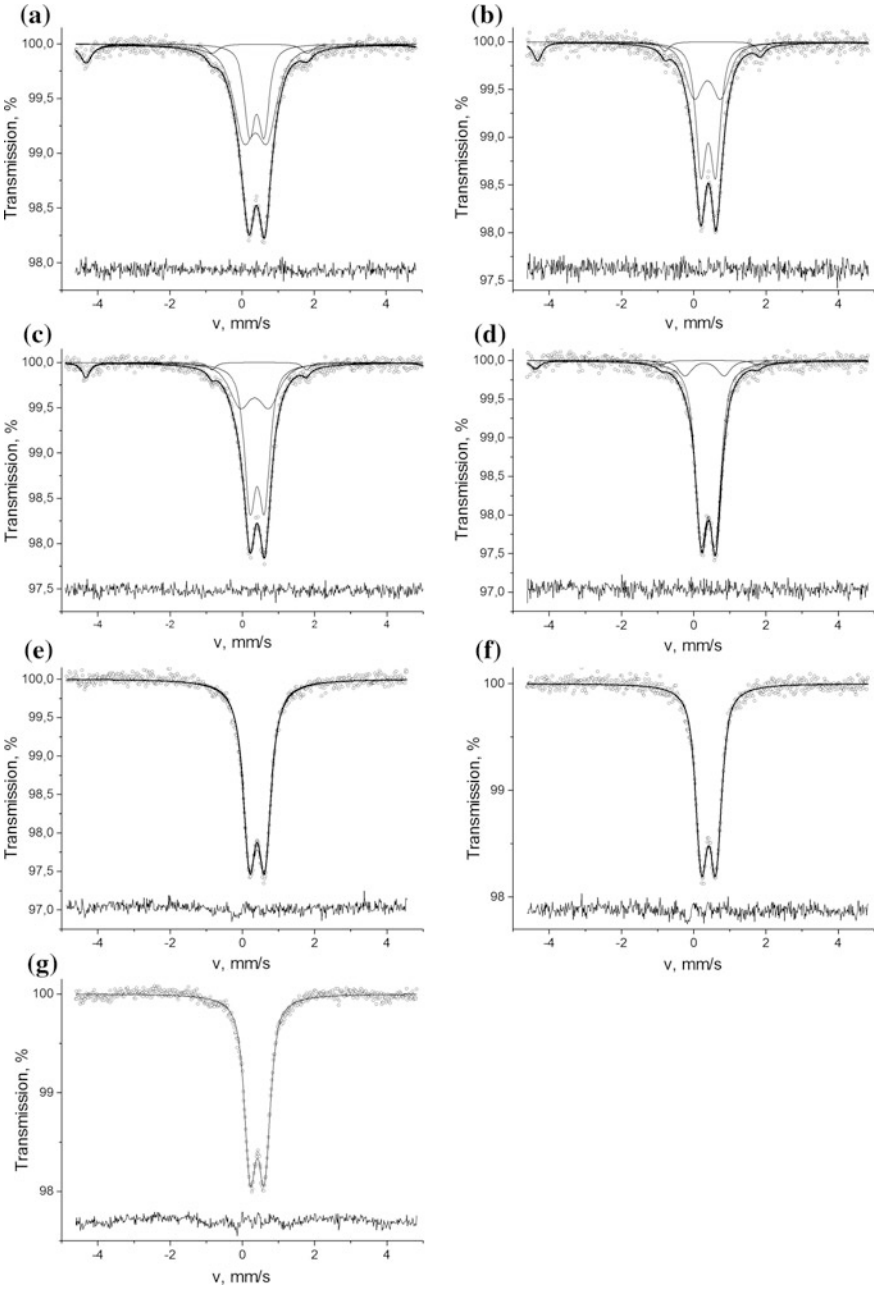

Fig. 14.3 Room temperature Mössbauer spectra of PFN samples sintered from mechanically activated powders at different temperatures: **a** T_s = 400 °C, **b** T_s = 500 °C, **c** T_s = 600 °C, **d** T_s = 700 °C, **e** T_s = 800 °C, **f** T_s = 1000 °C, **g** T_s = 1100 °C

Table 14.2 Parameters of room temperature Mössbauer spectra of PFN samples sintered from mechanically activated powders at different temperatures T_S

T_S, °C	Spectrum component	$\delta \pm 0.2$, mm/s	$\Delta/\varepsilon \pm 0.2$, mm/s	$A \pm 2$, %	$H \pm 5$, kOe	$G \pm 0.2$, mm/s	χ^2
400	D1	0.41	0.42	31		0.37	1.016
	D2	0.37	0.65	48		0.71	
	S1	0.30	−0.38	21	508	0.39	
500	D1	0.41	0.41	48		0.31	1.087
	D2	0.37	0.73	32		0.59	
	S1	0.30	−0.40	20	510	0.3	
600	D1	0.42	0.40	50		0.37	0.953
	D2	0.34	0.72	36		0.72	
	S1	0.30	−0.34	14	508	0.3	
700	D1	0.41	0.39	73		0.37	1.121
	D2	0.36	0.86	17		0.66	
	S1	0.30	−0.26	10	509	0.3	
800	D1	0.41	0.42	100		0.42	1.463
1000	D1	0.41	0.40	100		0.39	1.150
1100	D1	0.41	0.39	100		0.39	1.809

D doublet, *S* sextet, δ isomer shift, Δ quadrupole splitting for paramagnetic component (doublet), ε quadrupole shift for sextet, *H* effective magnetic field on ^{57}Fe, *A* component area, *G* linewidth, χ^2 Pearson's criterion

The spectra of the samples with T_S = 400–700 °C are a superposition of two doublets D1 and D2. The D1 parametres correspond to Fe^{3+} ions in octahedron and are close to parametres of PFN synthesized by conventional solid-phase reactions route [18]. The doublet D1 is present in the spectra of all the samples. The quadruple splitting is a consequence of the composition disorder in *B*-sublattice of PFN. In contrast to this, Mössbauer spectrum of the highly ordered (in the rock-salt manner) $PbFe_{1/2}Sb_{1/2}O_3$ perovskite appears to be a singlet at room temperature [34]. The second doublet D2 has an isomer shift value ≈0.36–0.37 mm/s that is lower than that for D1. The reduction of the isomer shift value indicates the lowering of coordination number due to the presence of oxygen vacancies. The doublet D2 quadruple splitting value is higher than that of D1, showing the presence of large crystallographic distortions in close environment of Fe^{3+} ions. The oxygen vacancies and distortions are probably related to the appearance of crystallographic shear planes during mechanical activation. The line broadening of D2 may be also due to the inhomogeneity of the environment of Fe^{3+} ions.

Figure 14.4 shows the dependence of the Mössbauer spectra component's area on T_S. The D2 area decreases as T_S grows. Thus the oxygen vacancies concentration decreases with the increase of T_S. In addition, the α-Fe_2O_3 impurity disappears when T_S exceeds 700 °C. The isomer shift and quadrupole splitting dependencies on T_S are present in Figs. 14.5 and 14.6. One can see that the isomer shift does not

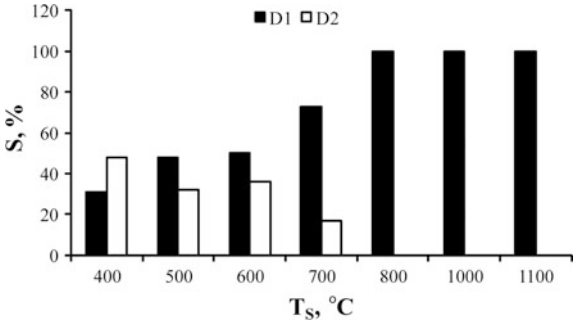

Fig. 14.4 Dependence of Mössbauer spectra doublets' area S on T_S for PFN samples sintered from mechanically activated powders at different temperatures T_S

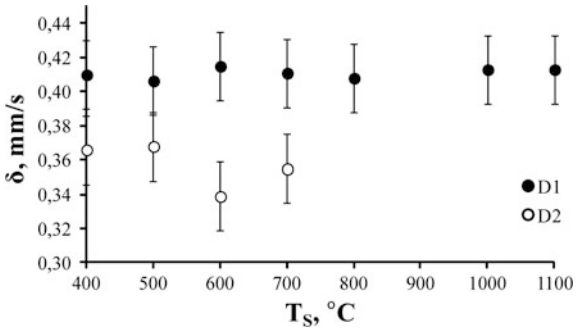

Fig. 14.5 Dependence of Mössbauer spectra isomer shifts on T_S for PFN samples sintered from mechanically activated powders at different temperatures T_S

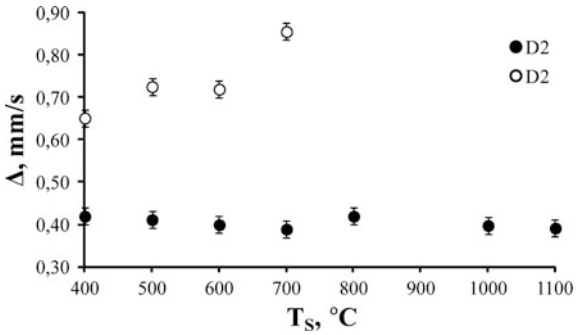

Fig. 14.6 Dependence of Mössbauer spectra quadruple splitting on T_S for PFN samples sintered from mechanically activated powders at different temperatures T_S

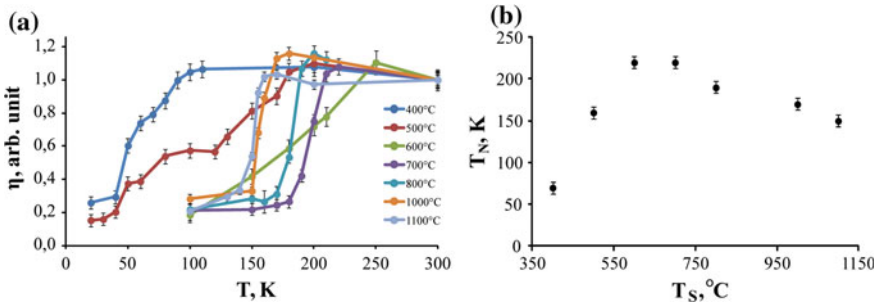

Fig. 14.7 **a** Temperature dependencies of η-maximal intensity of doublet in Mössbauer spectrum related to its value at 300 K for PFN samples, sintered from mechanically activated powders at different temperatures T_S; **b** magnetic phase transition temperature dependence on T_S for PFN samples sintered from mechanically activated powders at different temperatures T_S

change as T_S increases. The quadrupole splitting of D2 increases with T_S indicating the growth of crystallography distortions around Fe^{3+} ions corresponding to D2.

For estimation of magnetic phase transition temperature T_N, the method of temperature scanning was used. The essence of temperature scanning is measuring of Mössbauer spectrum line intensity in the course of sequential decreasing of the temperature. When magnetic ordering appears, the paramagnetic doublet transforms into Zeeman sextet, which is accompanied by a dramatic decrease of the line intensity. The temperature dependencies of Mössbauer spectrum intensity η, related to its value at 300 K for PFN ceramic samples, sintered at different temperatures from mechanically activated powders, are present in Fig. 14.7a. The abrupt drop of $\eta(T)$ curve corresponds to T_N value.

One can see from Fig. 14.7a that the samples sintered at T_s = 400–600 °C have diffused magnetic phase transitions in a wide temperature range. For the samples sintered at higher T_S, magnetic phase transitions temperature range is much more narrower. This may come from the lowering of inhomogeneity in the environment of Fe^{3+} ions and growth of grain size. Figure 14.7b shows the T_N versus T_S dependence for PFN samples studied. The T_N value grows up to ≈220 K as T_S increases from 400 up to 700 °C and on further increase of sintering temperature T_N gradually lowers down to ≈150 K, i.e. to the value typical of PFN single crystal. The uprising part of $T_N(T_S)$ dependence corresponds to T_S range, where the D2 area decreases.

The magnetic structure in perovskites comes from 180° superexchange between Fe^{3+} ions. So the T_N value is determined by the number of Fe^{3+}–O^2–Fe^{3+} links [35]. This number depends on the degree of compositional ordering of Fe^{3+} and Nb^{5+} ions. Namely, the Fe^{3+}–O^2–Fe^{3+} links number increases, when the compositional ordering degree lowers. In addition, oxygen vacancies also reduce the number of Fe^{3+}–O^2–Fe^{3+} links. Thus, the T_N growth with T_S in the 400–600 °C range coincides with decrease of oxygen vacancies' concentration. The largest values of T_N in the samples sintered in the 650–800 °C range are probably explained by growing of grain size as well as by compositional disorder stimulated by mechanical activation.

Decrease of T_N values in the samples sintered at $T_S > 800$ °C comes from appearing of the regions with local compositional ordering of Fe^{3+} and Nb^{5+}.

14.4 Summary

In PFN ceramics sintered from mechanically activated powders dependence of the temperature T_N of magnetic phase transition on sintering temperature T_S has a maximum at $T_S \approx 700$ °C. The low T_N value of the samples having lower T_S is likely to be connected with a small size of $PbFe_{0.5}Nb_{0.5}O_3$ particles, presence of $FeNbO_4$ admixture as well as with oxygen deficiency. In the samples, sintered at 600–700 °C, T_N achieves the maximal value and slowly decreases to 150 K in the samples with higher T_S. The T_N value in oxides depends on the number of Fe–O–Fe links, which in turn correlates with Fe^{3+}/Nb^{5+} cation ordering degree and oxygen deficiency. Thus, it seems that in the samples with $T_S \leq 700$ °C, the clusters with low cation ordering degree are present. The oxygen deficiency in such samples is probably related to the appearance of crystallographic shear planes during mechanical activation.

Acknowledgements This work was partially supported by Ministry of Education and Science of the Russian Federation (Research project No. 3.5346.2017/BP), Russian Foundation for Basic Research (project 17–03–01293_a) and Research Committee of the University of Macau under Research & Development Grant for Chair Professor No RDG007/FST-CHD/2012.

References

1. I.P. Raevskii, S.T. Kirillov, M.A. Malitskaya, V.P. Filippenko, S.M. Zaitsev, L.G. Kolomin, Inorg. Mater. **24**, 217 (1988)
2. YuN Zakharov, S.I. Raevskaya, A.G. Lutokhin, V.V. Titov, I.P. Raevski, V.G. Smotrakov, V. V. Eremkin, A.S. Emelyanov, A.A. Pavelko, Ferroelectrics **399**, 20 (2010)
3. D. Bochenek, P. Kruk, R. Skulski, P. Wawrzała, J. Electroceram. **26**, 8 (2011)
4. E.I. Sitalo, I.P. Raevski, A.G. Lutokhin, A.V. Blazhevich, S.P. Kubrin, S.I. Raevskaya, Y.N. Zakharov, M.A. Malitskaya, V.V. Titov, I.N. Zakharchenko, IEEE Trans. Ultrason. Ferroelectr. Freq. Contr. **58**, 1914 (2011)
5. D.I. Khomskii, J. Magn. Magn. Mater. **306**, 1 (2006)
6. W. Kleemann, V.V. Shvartsman, P. Borisov, A. Kania, Phys. Rev. Lett. **105**, 257202 (2010)
7. R. Blinc, P. Cevc, A. Zorko, J. Holc, M. Kosec, Z. Trontelj, J. Pirnat, N. Dalal, V. Ramachandran, J. Krzystek, J. Appl. Phys. **101**, 033901 (2007)
8. K.H. Ehses, H.Z. Schmid, Kristallography **162**, 64 (1983)
9. W. Bonny, M. Bonin, Ph Sciau, K.J. Schenk, G. Chapuis, Solid State Commun. **102**, 347 (1997)
10. S.P. Singh, S.M. Yusuf, S. Yoon, S. Baik, N. Shin, D. Pandey, Acta Mater. **58**, 5381 (2010)
11. D.A. Sanchez, N. Ortega, A. Kumar, G. Sreenivasulu, R.S. Katiyar, J.F. Scott, D.M. Evans, M. Arredondo-Arechavala, A. Schilling, J.M. Gregg, J. Appl. Phys. **113**, 074105 (2013)
12. W. Peng, N. Lemee, M. Karkut, B. Dkhil, V. Shvartsman, P. Borisov, W. Kleemann, J. Holc, M. Kosec, R. Blinc, Appl. Phys. Lett. **94**, 012509 (2009)

13. V.V. Laguta, M.D. Glinchuk, M. Maryško, R.O. Kuzian, S.A. Prosandeev, S.I. Raevskaya, V. G. Smotrakov, V.V. Eremkin, I.P. Raevski, Phys. Rev. B. **87**, 064403 (2013)
14. I.P. Raevski, S.P. Kubrin, S.I. Raevskaya, S.A. Prosandeev, M.A. Malitskaya, V.V. Titov, D. A. Sarychev, A.V. Blazhevich, I.N. Zakharchenko, IEEE Trans. Ultrason. Ferroelectr. Freq. Contr. **59**, 1872 (2012)
15. I.P. Raevski, S.P. Kubrin, V.V. Laguta, M. Marysko, H. Chen, S.I. Raevskaya, V.V. Titov, C.-C. Chou, A.V. Blazhevich, E.I. Sitalo, D.A. Sarychev, T.A. Minasyan, A.G. Lutokhin, YuN Zakharov, L.E. Pustovaya, I.N. Zakharchenko, M.A. Malitskaya, Ferroelectrics **475**, 20 (2015)
16. I.P. Raevski, V.V. Titov, M.A. Malitskaya, E.V. Eremin, S.P. Kubrin, A.V. Blazhevich, H. Chen, C.-C. Chou, S.I. Raevskaya, I.N. Zakharchenko, D.A. Sarychev, S.I. Shevtsova, J. Mater. Sci. **49**, 6459 (2014)
17. A.A. Gusev, S.I. Raevskaya, V.V. Titov, V.P. Isupov, E.G. Avvakumov, I.P. Raevski, H. Chen, C.-C. Chou, S.P. Kubrin, S.V. Titov, M.A. Malitskaya, D.A. Sarychev, V.V. Stashenko, S.I. Shevtsova, Ferroelectrics **496**, 231 (2016)
18. I.P. Raevski, S.P. Kubrin, S.I. Raevskaya, D.A. Sarychev, S.A. Prosandeev, M.A. Malitskaya, Phys. Rev. B. **85**, 224412 (2012)
19. V.V. Laguta, J. Rosa, L. Jastrabik, R. Blinc, P. Cevc, M. Zalar, B. Remskar, S.I. Raevskaya, I. P. Raevski, Mater. Res. Bull. **45**, 1720 (2010)
20. S. Nomura, H. Takabayashi, T. Nakagawa, Jpn. J. Appl. Phys. **7**, 600 (1968)
21. I.P. Raevski, VYu. Shonov, M.A. Malitskaya, E.S. Gagarina, V.G. Smotrakov, V.V. Eremkin, Ferroelectrics **235**, 205 (1999)
22. I.P. Raevski, S.P. Kubrin, S.I. Raevskaya, V.V. Stashenko, D.A. Sarychev, M.A. Malitskaya, M.A. Seredkina, V.G. Smotrakov, I.N. Zakharchenko, V.V. Eremkin, Ferroelectrics **373**, 121 (2008)
23. V.V. Laguta, A.N. Morozovska, E.I. Eliseev, I.P. Raevski, S.I. Raevskaya, E.I. Sitalo, S.A. Prosandeev, L. Bellaiche, J. Mater. Sci. **51**, 5330 (2016)
24. S.A. Prosandeev, I.P. Raevski, S.I. Raevskaya, H. Chen, Phys. Rev. B. **92**, 220419(R) (2015)
25. A.A. Gusev, S.I. Raevskaya, V.V. Titov, E.G. Avvakumov, V.P. Isupov, I.P. Raevski, H. Chen, C.-C. Chou, S.P. Kubrin, S.V. Titov, M.A. Malitskaya, A.V. Blazhevich, D.A. Sarychev, V.V. Stashenko, S.I. Shevtsova, Ferroelectrics **475**, 41 (2015)
26. A.A. Gusev, S.I. Raevskaya, V.V. Titov, V.P. Isupov, E.G. Avvakumov, I.P. Raevski, H. Chen, C.-C. Chou, S.P. Kubrin, S.V. Titov, M.A. Malitskaya, D.A. Sarychev, V.V. Stashenko, S.I. Shevtsova, Ferroelectrics **496**, 231 (2016)
27. A.A. Gusev, S.I. Raevskaya, I.P. Raevski, V.P. Isupov, E.G. Avvakumov, S.P. Kubrin, H. Chen, V.V. Titov, T.A. Minasyan, C.-C. Chou, S.V. Titov, M.A. Malitskaya, Ferroelectrics **496**, 250 (2016)
28. X. Gao, J. Xue, J. Wang, Mater. Sci. Eng. B **99**, 63 (2003)
29. M.E. Matsnev, V.S. Rusakov, AIP Conf. Proc. **1489**, 178 (2012)
30. D. Bochenek, G. Dercz, D. Oleszak, Arch. Metall. Mater. A. **56**, 1015 (2011)
31. F. Menil, J. Phys. Chem. Solids **46**, 763 (1985)
32. S.P. Kubrin, S.I. Raevskaya, S.A. Kuropatkina, D.A. Sarychev, I.P. Raevski, Ferroelectrics **340**, 155 (2006)
33. W. Kundig, H. Bommel, G. Constabaris, R.H. Lindquist, Phys. Rev. **142**, 327 (1966)
34. I.P. Raevski, N.M. Olekhnovich, A.V. Pushkarev, Y.V. Radyush, S.P. Kubrin, S.I. Raevskaya, M.A. Malitskaya, V.V. Titov, V.V. Stashenko, Ferroelectrics **444**, 47 (2013)
35. J.B. Goodenough, *Magnetism and Chemical Bond.* (Interscience Publisher, a division of Wiley, New York, London, 1963), 393 pp

Chapter 15
Polarization Switching Dynamics in $PbFe_{1/2}Nb_{1/2}O_3$ Ceramics as Seen via the Frequency Dependence of Hysteresis Loops

A.N. Pavlov, I.P. Raevski, T.A. Minasyan, S.I. Raevskaya, M.A. Malitskaya, V.V. Titov, D. Pandey and A.A. Bokov

Abstract Our studies have shown that both the shape of hysteresis loops and the value of the remnant polarization P_r of highly-resistive Li-doped $PbFe_{1/2}Nb_{1/2}O_3$ (PFN) ceramics, depend substantially on the frequency of the measuring field. With decreasing of the field frequency, the value of P_r increases. We propose a model explaining this phenomenon, taking into account the relaxation of the charge localized at the grain-boundary surface states. In polycrystalline ferroelectrics-semiconductors, Schottky-type depletion layers are formed at the grain boundaries. The presence of such barrier layers in the PFN ceramics is evidenced by a small positive temperature coefficient of resistivity anomaly near the Curie temperature. Electric field in the Schottky layer is very large and it usually determines the direction of polarization P_{gb} in the layer. This direction may be opposite to the direction of polarization P_g in the bulk of the grain. If the measuring electric field changes sinusoidally with time, the temporal changes of P_{gb} are determined by the relaxation time τ of the charge redistribution in the Schottky layers. For high enough values of the external field frequency ($\upsilon \sim 70$ Hz), this charge has not enough time to relax and spontaneous polarization in the part of the grain adjacent to the grain boundary does not manage to switch. Computer simulations have shown that this model gives rather good agreement with experiment for different frequencies of the external field.

A.N. Pavlov
Rostov State Technical University, 344022 Rostov-on-Don, Russia

I.P. Raevski · T.A. Minasyan (✉) · S.I. Raevskaya · M.A. Malitskaya · V.V. Titov
Research Institute of Physics and Physics Department, Southern Federal University, 344090 Rostov-on-Don, Russia
e-mail: min.tigran@gmail.com

D. Pandey
School of Materials Science & Technology, Institute of Technology, Banaras Hindu University, Varanasi 221005, India

A.A. Bokov
4D LABS, Department of Chemistry, Simon Fraser University, Burnaby, BC V5A 1S6, Canada

I.A. Parinov et al. (eds.), *Advanced Materials*, Springer Proceedings in Physics 193, DOI 10.1007/978-3-319-56062-5_15

15.1 Introduction

One of the application areas of ferroelectric materials, are devices based on polarization switching, such as, non-volatile memory cells, the shift registers and so on [1–4]. Study of the dependence of ferroelectric materials' characteristics on frequency is an important task for determining the performance of future devices [5–7], as well as from the fundamental point of view. Regularities of the frequency dependencies of remnant polarization and coercive field can be the key for understanding the dynamics of polarization switching in certain material. It is well known that the shape of the *P*–*E* hysteresis loop depends on the frequency of the external electric field, consequently frequency dependencies of some important parameters of ferroelectrics can be obtained by studying loops at different frequencies. For a better understanding of the issue, it is useful to pay attention to the frequency dependencies of the shape of the dielectric hysteresis loops of well-studied ferroelectric material $Pb(Zr,Ti)O_3$ (PZT) and its various modifications.

The authors of [8] and [9] managed to obtain well saturated hysteresis loop, for high quality 100 nm-thick epitaxial PZT films, grown on $SrRuO_3/SrTiO_3$ (001) substrates, by pulsed laser deposition. The studies of frequency dependencies of characteristics have shown the increase of the coercive field E_c by approximately 2 times as frequency increased from 1 to 100 kHz [8] and 80% increase of the E_c as frequency increased from 50 to 2000 Hz [9]. The square-like shape of the loop, measured at 50 Hz, becomes rounded and slanted at 2000 Hz. Changes in remnant P_r and spontaneous P_s polarizations with increasing of frequency in [8] and [9] were not noticed.

However, studies of the frequency dependencies of *P*–*E* hysteresis loops for PZT ceramic samples by different authors have shown a decrease in both the remnant P_r and spontaneous P_s polarization values with increasing of the external field frequency [10–12].

Reference [10] presents an investigation of frequency dependencies of the shape of *P*–*E* hysteresis loops for different external electric field amplitudes E_{max} (14–56 kV/cm) for PZT ceramics. It was found out that for E_{max} values lower than E_c ($\sim$34 kV/cm), the frequency dependence of hysteresis loops is rather small. For $E_{max} \sim E_c$, frequency dependence of P_r and P_s becomes strong, with the increase of the field frequency from 1 to 100 Hz. At $E_{max} = 30$ kV/cm ($\sim E_c$), values of both P_r and P_s decrease approximately by 76% and E_c decreases approximately by 20%. At $E_{max} = 40$ kV/cm (1.2 E_c), both P_r and P_s decrease approximately by 35%, while E_c increases approximately by 21%. For $E_{max} > E_c$, frequency dependence of P_r and P_s starts to weaken and at $E_{max} = 56$ kV/cm (1.6 E_c), both P_r and P_s decrease by approximately 2% while the value of E_c increases by approximately 30% [10].

Studies of $Pb(Mn_{1/3}Nb_{2/3})O_3$–$PbTiO_3$–$PbZrO_3$ ceramic samples have shown that for $E_{max} = 40$ kV/cm (~ 4 E_c) an increase of the applied field frequency from 10 mHz to 20 Hz leads to 55% decrease of P_r and 10% decrease of E_c [11].

PZT ceramic samples doped by either donors Nb_2O_5 (PZTN) or acceptors Fe_2O_3 (PZTF) were investigated in [12]. Dielectric hysteresis loops shown by the authors

were obtained at the amplitude of the external field E_{max} = 25 kV/cm ($\sim$2.5 E_c) while the frequency increased from 1 mHz to 1 Hz. In the case of donor-doped PZTN remnant polarization P_r, decreased by about 14%, the coercive field E_c increased by 28%, while in the case of acceptor-doped PZTF P_r decreased by 17%, whereas E_c did not change.

Lead iron niobate $PbFe_{1/2}Nb_{1/2}O_3$ (PFN) is a widely investigated ferroelectric with perovskite structure, which has promising properties as a multiferroic. However, there are only a few reports about PFN hysteresis loops investigations due to the difficulty of obtaining highly resistive PFN ceramics.

There are several works, which provide PFN hysteresis loops for different frequencies of the external field [13–15]. However, they do not present a systematic study of the frequency characteristics of PFN and it is not efficient to identify the frequency dependence of characteristics of PFN ceramics from the different works, because of the different conditions of ceramics fabrication or measurement of the hysteresis loops by various authors. One more negative factor is the inconsistency of the data in different studies. The main reason for these contradictions is a relatively large value of conductivity of PFN samples, which prevents the effective poling of ceramics and obtaining of saturated hysteresis loops. Reference [16] is one of rare reports on the systematic investigation of the frequency dependencies of some characteristics of PFN. The authors report that as frequency increases from 10^{-4} to 10^2 Hz, P_s decreases by approximately 30% and E_c decreases by approximately 45%.

From a theoretical point of view, the frequency dependence of the shape of ferroelectric hysteresis loops is often explained by the difference of the applied field impact time, in other words, a longer exposure time of the electric field, in the case of small frequencies. Longer exposure time allows one to achieve a better distribution of the domains in the electric field, while at high frequencies, the electric field is removed quickly and domains generally return to their equilibrium positions faster and do not manage to orient along the field direction. Some studies analyze the dynamics of domain wall motion and propose models that take into account the potential, which forms in the ferroelectric due to the existence of domain boundaries [9, 17]. This approach is consistent with the experimental data, for single-crystal structures, but does not provide reliable results for the ceramics. To obtain more realistic results for ceramic samples, one should take into account additional effects, which arise due to the complex grain structure of the ceramic.

We provide a systematic study of the frequency dependencies of characteristics of highly-resistive ($\rho \sim 10^8$ Ω m) ceramics of both PFN and PFN–$PbTiO_3$ (PFN–xPT) solid solution compositions PFN + 0.06$PbTiO_3$ and PFN + 0.15$PbTiO_3$. The study was carried out by measuring the hysteresis loops and analyzing their parameters for different frequencies of the external field. An attempt has been made to explain the nature of the frequency dependence of the shape of the hysteresis loops using a model, which is based on the classical approach [9, 17] but also takes into account the effects related to the grain boundaries.

15.2 Experiment

Ceramic samples of PFN and PFN–*x*PT solid solutions (x = 0.06 and 0.15) were obtained by solid-state reaction route using high-purity Fe_2O_3, Nb_2O_5, TiO_2, and PbO oxides. These oxides were batched in stoichiometric proportions, and then 1 wt% Li_2CO_3 was added to the batch. This addition promotes the formation of the perovskite modification of PFN and reduces its conductivity [14, 18–20]. The synthesis was carried out at 900 °C for 2 h. The final sintering was performed at 1020–1070 °C for 2 h in a closed alumina crucible. Weight losses from PbO evaporation did not exceed 1 wt%. The density of the ceramics obtained was about 93–96% of the theoretical density. The electrodes for measurements were deposited on the grinded disks (9 mm in diameter, 0.9 mm in height) by firing the silver paste at 500 °C. X-ray diffraction studies have shown that all the investigated compositions were single-phase and had a structure of the perovskite type [20].

The polarization versus electric field (P–E) hysteresis loops were studied at room temperature and at different frequencies of applied field with the help of RT-66A (Radiant Technologies) setup with a high voltage supply.

15.3 Model Description

To describe the observed frequency dependence of the shapes of hysteresis loops we propose a model, taking into account the presence of areas depleted of free electric charges, near grain boundaries of ceramics. The proof of the existence of such areas in ceramic ferroelectrics, may be the presence of the effect of positive temperature coefficient of resistance (effect of PTCR or posistor effect) [21–23], which is an increase of the electrical resistance in the course of heating in the region of the ferroelectric phase transition (the Curie point, T_c). Such PTCR anomaly is observed even in Li-doped PFN ceramics with low dc-conductivity (Fig. 15.1).

To explain the occurrence of the posistor effect in [24], semiconductive $BaTiO_3$ single crystals were investigated in which this effect was not observed. However, in ceramic samples, prepared from the powder of the same crushed single crystals, posistor effect was observed. Though some papers reported about the existence of posistor effect in single crystals [25–27], further studies have shown that the effect is stronger in the thin single-crystal samples (67 μm [27]) and with the increase of thickness it weakened significantly. Such behavior was explained by an important role of the single crystal's surface in posistor effect. The thinner the sample is, the greater is the role of the surface layer and the posistor effect is more noticeable. Usually posistor effect is observed in electrically inhomogeneous materials in which resistivity of the grain boundaries is several orders of value higher than that of the grain bulk [22, 28]. Further, it was concluded that there are electrical charges localized at the grain boundaries, which create "dead" or dielectric layers in the

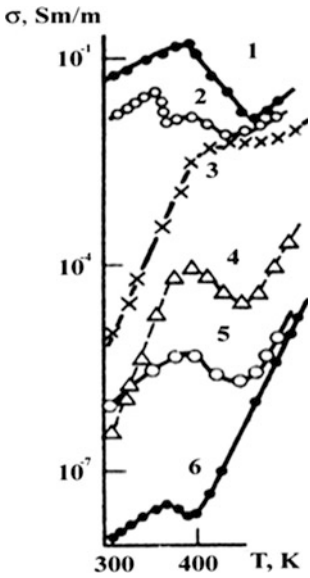

Fig. 15.1 Temperature dependencies of dc-conductivity for undoped PFN ceramics sintered at different temperatures (*curves 1–4*) and PFN ceramics doped with 0.1 wt% of Li_2CO_3 (*curve 5*) and 1 wt% of Li_2CO_3 (*curve 6*)

grain-boundary areas, which are the cause of the posistor effect in polycrystalline ferroelectrics [23, 29].

Although our samples have high resistance, they exhibit the posistor effect (Fig. 15.1), suggesting that there are bound, electric charges on the grain boundaries of ceramic.

The grain boundaries in PFN are charged negatively due to the bound surface charges caused by the filling of the surface acceptor states. Consequently, the grain boundaries behave like potential barriers for free electric charges (Fig. 15.2). Under the action of the field of the bound negative grain boundary charges, redistribution of the free charges takes place in the grains and the areas of positive space charge (Schottky layers), depleted of free charges, are being formed near the grains boundaries. Negatively charged grain boundaries, are being screened both by the Schottky layers, and by the part of polarization of grains. From the equation of electrical neutrality (1), it is possible to estimate the linear dimensions of the Schottky layers,

$$qn_s = ql_1N_D + ql_2N_D. \tag{15.1}$$

Here N_s is the density of the populated localized states at the crystallite boundaries, N_D is the donor density of the space charge, l_1, l_2 are the thicknesses of the Schottky layers from different sides of the boundary between two grains (Fig. 15.2).

Part of the grain's polarization, which is spent on screening of grain boundary charges is stabilized. Due to this the switching of this part of polarization by the external electric field is hampered and it requires a certain relaxation time τ, which is spent for charge redistribution in the Schottky layers and on the grain boundaries

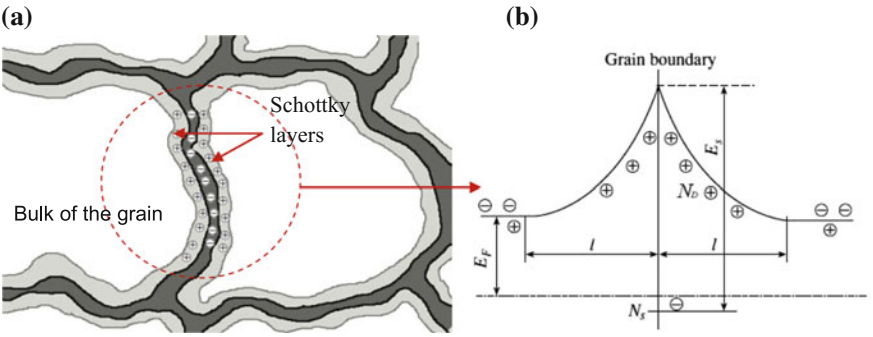

Fig. 15.2 **a** Schematic picture of grain boundaries and Schottky layers, **b** energy diagram near the grain boundary in the absence of an external electric field; E_S is the activation energy of localized states at the grain boundaries, E_F is the Fermi energy

surface states. Taking this into account, the remnant polarization P_{rem} in the proposed model is described by an expression:

$$P_{rem} = P_g + \Delta P_{gb}, \tag{15.2}$$

where P_g is the contribution of grain areas in which the polarization electric field is not stabilized, ΔP_{gb} is near-boundary stabilized part of polarization. Let us assume that external electric field varies sinusoidally with time with a frequency v. It is possible to consider three different relations between τ and the duration of the one switching of polarization, i.e. the half of the period of external alternating field T. For small values of v, $\tau \ll v^{-1} = T/2$, relaxation processes manage to occur completely during $T/2$ and the hampering influence of the charge relaxation, does not affect the behavior of the polarization of ceramics:

$$P_{rem1} = P_g(T/2) + P_{gb}. \tag{15.3}$$

Here P_{gb} is the maximum (peak) value of the stabilized polarization.

If $\tau \gg T/2$, relaxation processes do not manage to occur and stabilized part of the polarization does not switch, $\Delta P_{gb2} = 0$. In this case, the remnant polarization is smaller

$$P_{rem2} = P_g(T/2). \tag{15.4}$$

If $\tau \sim T/2$, relaxation processes take place throughout the time that one switching of polarization takes, and the stabilized part of the polarization can be obtained from the expression:

$$\Delta P_{gb3} = P_{gb}[1 - \exp(t/\tau)] \tag{15.5}$$

and the remnant polarization:

$$P_{rem3} = P_g(T/2) + \Delta P_{gb3} = P_g(T/2) + P_{gb}[1 - \exp(t/\tau)]. \tag{15.6}$$

Theoretically, the relaxation time τ can be described in terms of *RC*-circuit model according to which each grain is considered as a set of resistors R and capacitors C. In this model, the charged surface states at the grain boundaries provide dielectric layers with capacity C_{gb} and resistance R_{gb}, the parameters of the bulk of the grain are C_g and R_g (Fig. 15.3). In the proposed model, τ can be described by the following expression:

$$\tau = \frac{C_{gb} + C_g}{1/R_{gb} + 1/R_g} = \varepsilon_0 \frac{\varepsilon_{gb}/l_{gb} + \varepsilon_g/l_g}{(1/\rho_{gb}l_g + 1/\rho_{gb}l_g)}. \tag{15.7}$$

Here ρ_g, l_g and ε_g are resistivity, linear dimensions and permittivity of the bulk of the grain, respectively; ρ_{gb}, l_{gb} and ε_{gb} are resistivity, thickness and permittivity of Schottky layers, respectively, ε_0 is the electric constant.

The frequency dependence of conductivity σ in the terms of *R*-circuit model is described by expression:

$$\sigma = \frac{L(1 + bv^2)}{l_{gb}\rho_{gb}\sqrt{[1 + a(1 + bv^2)]^2 + bv^2}}, \tag{15.8}$$

where L is the thickness of the grain, $a = \frac{R_g}{R_{gb}} = \frac{\rho_g l_g}{\rho_{gb} l_{gb}}$, $b = (2\pi R_{gb} C_{gb})^2 = (2\pi\rho_{gb}\varepsilon_{gb}\varepsilon_0)^2$.

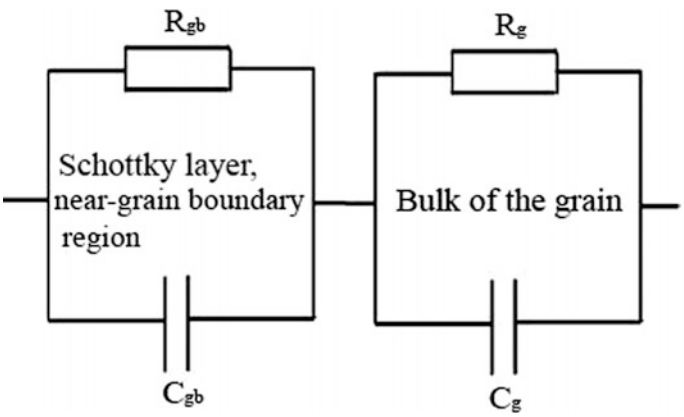

Fig. 15.3 Equivalent RC-circuit of the grain

For the range of frequencies used, the expression (15.8) can be simplified as follows:

$$\sigma = \frac{2\pi\varepsilon_{gb}\varepsilon_0 L}{l_{gb}} v \tag{15.9}$$

15.4 Results and Discussion

Figures 15.4, 15.5, and 15.6a present experimental dielectric hysteresis loops, measured at different frequencies of the external field for ceramics of PFN and solid solution compositions PFN + 0.06$PbTiO_3$ and PFN + 0.15$PbTiO_3$, respectively. The change of the shapes of the loops with frequency is clearly visible.

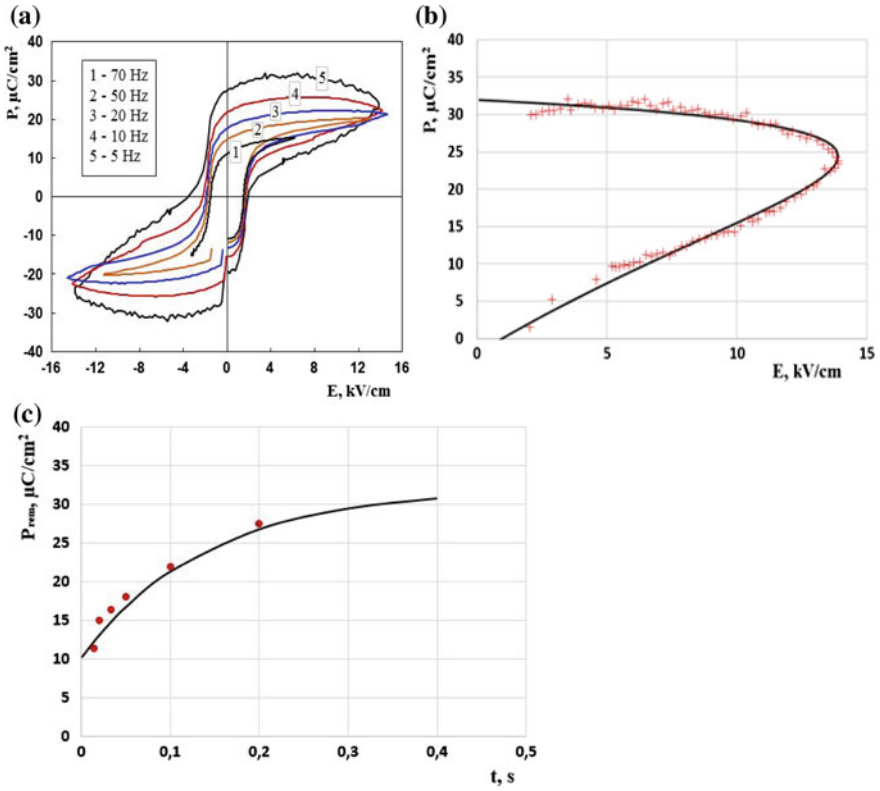

Fig. 15.4 **a** Experimental polarization versus electric field (*P–E*) hysteresis loops for PFN ceramics, at different frequencies of external field; **b** *P*(*E*)-dependence for PFN ceramics, at the frequency 5 Hz, for the half of the period of external alternating field (*T*/2), *solid line* calculations in the frame of the model used (relaxation time τ = 0.2 s); *symbols* experimental data; **c** dependence of P_{rem} on the exposure time of external electric field for PFN, *points* experiment, *solid line* calculations in the frame of the model used

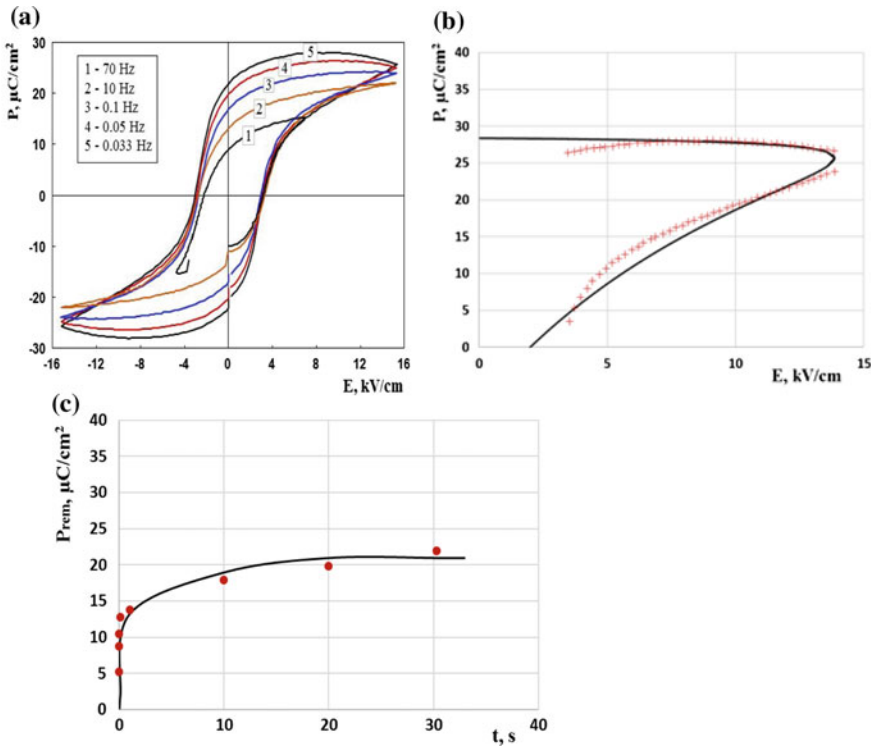

Fig. 15.5 **a** Experimental polarization versus electric field (*P–E*) hysteresis loops for solid solution ceramics PFN + 0.06$PbTiO_3$ at different frequencies of external field; **b** *P*(*E*) dependence for solid solution PFN + 0.06$PbTiO_3$, at the frequency 0.033 Hz, for the half of the period of external alternating field (*T*/2), *solid line* calculations in the frame of the model used (relaxation time $\tau = 0.02$ s); *symbols* experimental data; **c** dependence of P_{rem} on the exposure time of external electric field for PFN + 0.06$PbTiO_3$, *points* experiment, *solid line* calculations in the frame of the model used

The character of frequency dependence of the loops is qualitatively similar for all three compounds (Fig. 15.4, 15.5, and 15.6a): as the external field frequency increases the remnant P_{rem} and spontaneous P_s polarizations decrease. It is important to note that, despite the fact that in the case of all three samples $E_{max} \sim 4.5\ E_c$, the frequency dependencies of P_{rem} and P_s are not weak.

For the sample that does not contain Ti (Fig. 15.4a), P_{rem} and P_s decrease by approximately 44% as the frequency increases from 5 to 50 Hz. For solid solution composition PFN + 0.06PT (Fig. 15.5a), P_{rem} and P_s decrease by approximately 42% as the frequency increases from 0.033 to 10 Hz, and for solid solution composition PFN + 0.15PPT (Fig. 15.6a), P_{rem} and P_s decrease by approximately 47% as the frequency increases from 0.33 to 20 Hz. These results allow us to conclude that similar to PZT, ferroelectric ceramics based on PFN exhibit a clearly expressed frequency dependence of P_{rem} and P_s.

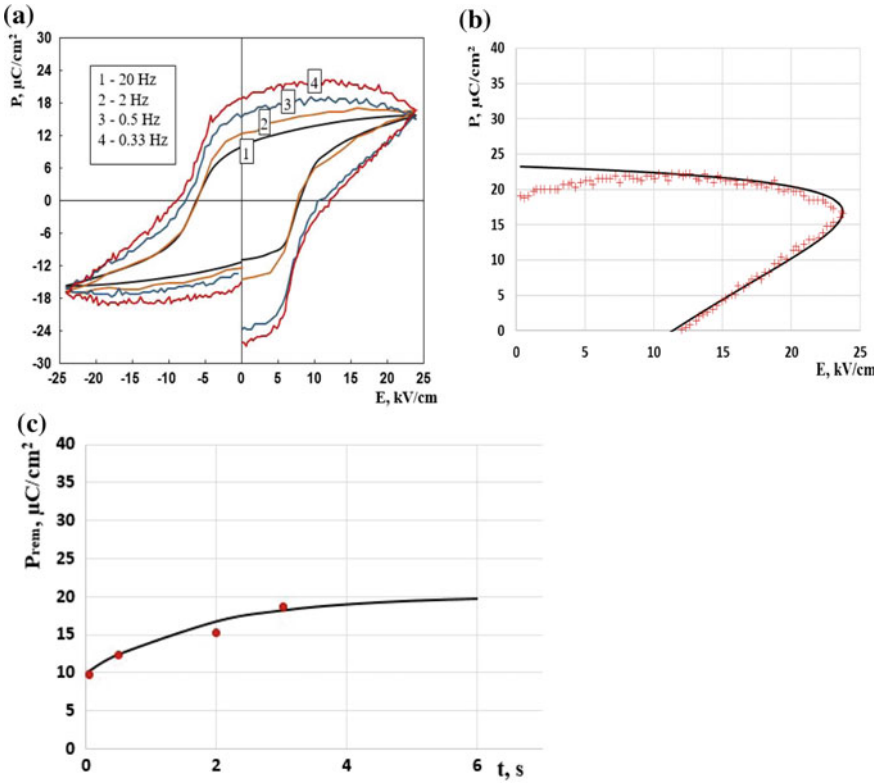

Fig. 15.6 **a** Experimental polarization versus electric field (*P–E*) hysteresis loops for solid solution PFN + 0.15$PbTiO_3$ ceramics at different frequencies of external field; **b** *P*(*E*) dependence for solid solution PFN + 0.15$PbTiO_3$ ceramics at the frequency 0.33 Hz, for the half of the period of external alternating field (*T*/2), *solid line* calculations in the frame of the model used (relaxation time $\tau = 0.03$ s); *symbols* experimental data; **c** dependence of P_{rem} on the exposure time of external electric field for PFN + 0.15$PbTiO_3$, *points* experiment, *line* calculations in the frame of the model used

Figures 15.4, 15.5, and 15.6b present combination of theoretical and experimental data for the half of the period of external alternating field (*T*/2). The theoretical curves were plotted using the results of the calculations made in the frame of the model described above. This model takes into account the time τ of the charge relaxation in the vicinity of the grain boundaries and the grain boundaries surface states.

Dependencies of P_{rem} on the applied field exposure time for the samples studied are present in Figs. 15.4, 15.5, and 15.6c. For the values of $L = 3 \cdot 10^{-4}$ cm, $l_{gb} = 10^{-6}$ cm, the calculations using expression (15.9) give the solid line in Fig. 15.7.

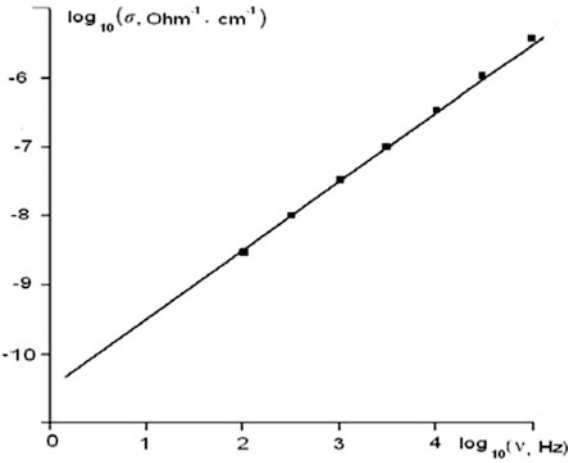

Fig. 15.7 Frequency dependence of conductivity σ for PFN ceramics; *points* experiment, *solid line* calculations in the frame of the model used

Good agreement between the experimental and theoretical data seen in Figs. 15.4, 15.5, 15.6b and 15.7 confirms the importance of considering the grain boundaries effect on polarization switching dynamics in polycrystalline ferroelectrics.

Acknowledgements This work was partially supported by the Ministry of Education and Science of the Russian Federation (Research project No. 3.1649.2017/PP) and by the Southern Federal University (Grant No. 213.01-2014/012VG).

References

1. H.M. Duiker, P.D. Beale, J.F. Scott, J.F. Scott, C.A. Paz de Araujo, B.M. Melnick, J.D. Cuchiaro, L.D. McMillan, J. Appl. Phys. **68**, 5783 (1990)
2. J.F. Scott, Science **315**, 954 (2007)
3. V. Garcia, S. Fusil, K. Bouzehouane, S. Enouz-Vedrenne, N.D. Mathur, A. Barthélémy, M. Bibes, Nature **460**, 81 (2009)
4. Y. Yongbo, T.J. Reece, S. Pankaj, S. Poddar, S. Ducharme, A. Gruverman, Y. Yang, J. Huang, Nat. Mater. **10**, 296 (2011)
5. S.M. Yang, J.G. Yoon, T.W. Noh, Curr. Appl. Phys. **11**, 1111 (2011)
6. J. Li, B. Nagaraj, H. Liang, W. Cao, H. Lee Chi, W. Cao, H. Lee Chi, R. Ramesh, Appl. Phys. Lett. **84**, 1174 (2004)
7. T.N. Christopher, G. Peng, J.R. Jokisaari, C. Heikes, C. Adamo, A. Melville, B. Seung-Hyub, C.M. Folkman, B. Winchester, Y. Gu, L. Yuanming, K. Zhang, E. Wang, J. Li, C. Long-Qing, E. Chang-Beom, D.G. Schlom, X. Pan, Science **334**, 968 (2011)
8. Y.W. So, D.J. Kim, T.W. Noh, T.W. Noh, J.-G. Yoon, T.K. Song, Appl. Phys. Lett. **86**, 092905 (2005)
9. S.M. Yang, J.Y. Jo, T.H. Kim, J.-G. Yoon, T.K. Song, H.N. Lee, Z. Marton, S. Park, Y. Jo, T. W. Noh, Phys. Rev. Lett. **82**, 174125 (2010)
10. X. Chen, X. Dong, F. Cao, J. Wang, G. Wang, J. Am. Ceram. Soc. **97**, 213 (2014)
11. B.S. Li, G.R. Li, Q.R. Yin, Z.G. Zhu, A.L. Ding, W.W. Cao, J. Phys. D: Appl. Phys. **38**, 8 (2005)

12. M.H. Lente, A. Picinin, J.P. Rino, J.A. Eiras, J. Appl. Phys. **95**, 2646 (2004)
13. D. Bochenek, P. Kruk, R. Skulski, P. Wawrzała, J. Electroceram. **26**, 1 (2011)
14. I.P. Raevski, S.T. Kirillov, M.A. Malitskaya, V.P. Filippenko, S.M. Zaitsev, L.G. Kolomin, Inorg. Mater. **24**, 217 (1988)
15. O. Raymond, R. Font, J. Portelles, J.M. Siqueiros, J. Appl. Phys. **109**, 094106 (2011)
16. J. Rossignol, A. Simon, J. Ravez, P. Hagenmuller, Revue de Chimie Minerale **22**, 577 (1985)
17. J. Li, F. Li, S. Zhang, Am. Cer. Soc. **97**, 1 (2014)
18. A.A. Bokov, L.A. Shpak, I.P. Rayevsky, J. Phys. Chem. Solids **54**, 495 (1993)
19. I.P. Raevski, S.P. Kubrin, S.A. Kovrigina, S.I. Raevskaya, V.V. Titov, A.S. Emelyanov, M.A. Malitskaya, I.N. Zakharchenko, Ferroelectrics **397**, 96 (2010)
20. E.I. Sitalo, I.P. Raevski, A.G. Lutokhin, A.V. Blazhevich, S.P. Kubrin, S.I. Raevskaya, Y.N. Zakharov, M.A. Malitskaya, V.V. Titov, I.N. Zakharchenko, IEEE Trans. Ultrason. Ferroelectr. Freq. Contr. **58**, 1914 (2011)
21. L.A. Belova, Y.I. Golcov, O.I. Prokopalo, I.P. Rayevsky, Inorg. Mater. **22**, 1004 (1986)
22. I.P. Raevski, O.I. Prokopalo, A.E. Panich, E.I. Bondarenko, A.N. Pavlov, *Electrical Conductivity and Posistor Effect in Oxides of the Perovskite Family* (SKNC VSh Press, Rostov-on-Don, 2002), 280 p. (In Russian)
23. W. Heywang, J. Am. Ceram. Soc. **47**, 484 (1964)
24. G. Goodman, J. Am. Ceram. Soc. **46**, 48 (1963)
25. F. Brown, G.E. Taylor, J. Appl. Phys. **35**, 2554 (1964)
26. T. Takeda, A. Watanabe, H. Sasaki, J. Phys. Soc. Jpn. **21**, 2414 (1966)
27. K. Kawabe, Y. Inuishi, Jpn. J. Appl. Phys. **2**, 590 (1963)
28. C.G. Koops, Phys. Rev. **83**, 121 (1951)
29. W.T. Peria, W.R. Bratschun, R.D. Fenity, J. Am. Ceram. Soc. **44**, 249 (1961)

Chapter 16
Structure, Grains Structure and Dielectric Responses of the Ternary System Solid Solutions $(Bi_{1-X-Y}Pb_{x+Y})(Fe_{1-X/2-Y}Ti_yNb_{x/2})O_3$

E.V. Glazunova, N.A. Boldyrev, L.A. Shilkina, Larisa A. Reznichenko, A.V. Nagaenko and I.N. Andryushina

Abstract Samples of the ternary system $(Bi_{1-x-y}Pb_{x+y})(Fe_{1-x/2-y}Ti_yNb_{x/2})O_3$ (sections $y = 0.10$ with $0.175 \leq x \leq 0.325$ and $x = 0.05$ with $0.175 \leq y$ 0.325) were obtained by the solid-phase reactions method with following conventional ceramic technology sintering. Optimal regulations of synthesis and sintering of these materials were determined. It is shown that the obtained objects have a complex phase structure affecting both on microstructure and on macroresponses of studied samples. For one of the studied section were measured dielectric properties in a wide temperature and frequency ranges. Explanation of the observed effects from the viewpoint of crystal-chemical disorder and morphotropic areas evolution in the ceramic structures was proposed.

16.1 Introduction

Currently, great attention is paid to study of multiferroics (materials combining magnetic and electrical properties). It is associated with the discovery in the beginning of 21st century a gigantic magnetoelectric effect, that led to the possibility of the practical application of these materials in the field of information and energy saving technologies. Multiferroic materials also can be used in the microwave devices and global security systems.

E.V. Glazunova (✉) · N.A. Boldyrev · L.A. Shilkina · L.A. Reznichenko · I.N. Andryushina
Research Institute of Physics, Southern Federal University, Rostov-on-Don, Russia
e-mail: kate93g@mail.ru

A.V. Nagaenko
Scientific Design and Technology Bureau "Piezopribor", Southern Federal University, Rostov-on-Don, Russia

I.A. Parinov et al. (eds.), *Advanced Materials*, Springer Proceedings in Physics 193, DOI 10.1007/978-3-319-56062-5_16

Binary and ternary solid solutions based on multiferroics, at present, are one of the most promising basis for the creation of multifunctional materials. They have high temperatures of magnetic and ferroelectric phase transitions and enough low conductivity (in contrast to the pure compounds) not blocking the formation of the piezoelectric response.

Previously, we studied the binary system $(1 - x)BiFeO_3$–$xPbTiO_3$. Its elements are high-temperature multiferroic bismuth ferrite and ferroelectric lead titanate widely used in the piezoceramics industry. It was shown that coexistence of several phases (morphotropic region) at room temperature was observed in objects with optimum characteristics [1]. Since in multicomponent systems the probability of occurrence of such areas is above, it seems relevant to research the regularities of the formation of structure, microstructure and dielectric properties of complex systems. In this case, the object of the study was a ternary system $(Bi_{1-x-y}Pb_{x+y})(Fe_{1-x/2-y}Ti_yNb_{x/2})O_3$, which also contains a high-temperature magnetoelectric lead iron niobate.

16.2 Objects: Methods of Preparation and Examination of Samples

The objects of investigation were ceramic samples of the ternary system solid solutions $(Bi_{1-x-y}Pb_{x+y})(Fe_{1-x/2-y}Ti_yNb_{x/2})O_3$. Ternary system was investigated using seven quasi-binary sections (Fig. 16.1). This article shows the results obtained for the two of them ($y = 0.10$ with $0.175 \leq x \leq 0.325$, $\Delta x = 0.025$, and $x = 0.05$ with $0.175 \leq y \leq 0.325$, $\Delta \mathbf{y} = 0.025$). Samples were obtained by double solid-phase synthesis at $T_1 = 1093$ K $\tau_1 = 10$ h, $T_2 = 1143$ K $\tau_2 = 10$ h (for the first section $y = 0.05$) и $T_1 = 1173$ K $\tau_1 = 10$ h, $T_2 = 1223$ K $\tau_2 = 10$ h (for the second section $y = 0.10$) with following conventional ceramic technology sintering [2] at temperature T_S equal to 1273 K for $\tau_S = 2$ h and equal to (1323–1353) K for $\tau_S = 2$ h (respectively, for the first and second sections). The starting reagents were Bi_2O_3 (analytical grade), Fe_2O_3 (analytical grade), PbO (very pure), TiO_2 (pure), Nb_2O_5 (pure). Samples were discs Ø = 10 and $h = 1$ mm with following machining and deposition on the flat surface a silver paste (by stepwise calcination with isothermal exposures at 473 K for 20 min, at 773 K for 30 min, and at 1073 K for 20 min with following cooling in the furnace to room temperature).

X-ray research was performed by powder diffraction technique on diffractometer DRON-3 (focusing Bragg–Brentano) using radiation $Co_{K\alpha}$. Cell parameters were calculated by the standard procedure [3], parameter measurement errors are $\Delta a = \pm 0.003$ Å, $\Delta\alpha = 0.05^o$, $\Delta V = \pm 0.05$ Å^3, where, α is a parameter, V is the volume of the rhombohedral cell.

The microstructure of sintered ceramics was studied by scanning electron microscope JSM-6390L. The temperature dependencies of the relative complex permittivity $\varepsilon^*/\varepsilon_0 = \varepsilon'/\varepsilon_0 - i\varepsilon''/\varepsilon_0$ ($\varepsilon'/\varepsilon_0$ and $\varepsilon''/\varepsilon_0$ are the real and imaginary parts of $\varepsilon^*/\varepsilon_0$, respectively; ε_0 is the electric constant in the temperature and frequency

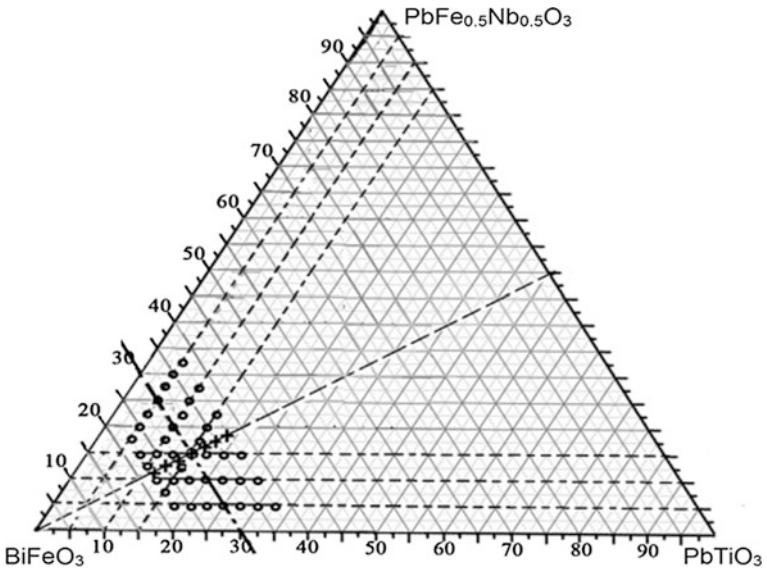

Fig. 16.1 Triangle of Gibbs of analyzed system with applied research sections and experimental points

ranges (300–900) K and $f = (25 - 2 \times 10^6)$ Hz were obtained by using the measuring set-up based on LCR-meter Agilent 4980A.

16.3 Experimental Results: Discussion

X-ray diffraction analysis of objects in the first section shows that all samples have a perovskite structure and do not contain foreign phases, except solid solutions with $x = 0.250$ and $x = 0.275$. These both solid solutions contain a small amount of the impurity phase, presumably $PbNb_2O_6$ (relative intensity of the strongest line in the first sample is 2%, relative intensity in the second sample is 13%). All solid solutions have a rhombohedral (Rh) perovskite cell. Solid solutions with $x = 0.175$ and $x = 0.200$ have R3c space group of bismuth ferrite. Superstructure reflections indicating this space group disappear at large x, and phase transition R3c → R3m occurs in the range $0.200 < x < 0.225$.

The cell parameters of solid solution with $x = 0.175$ in the hexagonal system are $a = 5.605$ Å, $c = 13.862$ Å, $V = 374.5$ Å^3, for solid solution with $x = 0.200$, we have $a = 5.610$ Å, $c = 13.859$ Å, $V = 375.2$ Å^3, parameters of $BiFeO_3$ are equal to $a = 5.577$ Å, $c = 13.862$ Å, $V = 373.4$ Å^3 [4]. In Fig. 16.2, fragments of radiographs including diffraction reflections $(111)_K$ and $(200)_K$ are present. Asterisks denote superstructure reflections indicating space group R3c. Figure 16.3 shows the concentration dependencies of the angle α, the experimental volume, V, of the Rh cell, X-ray and relative densities of studied solid solutions.

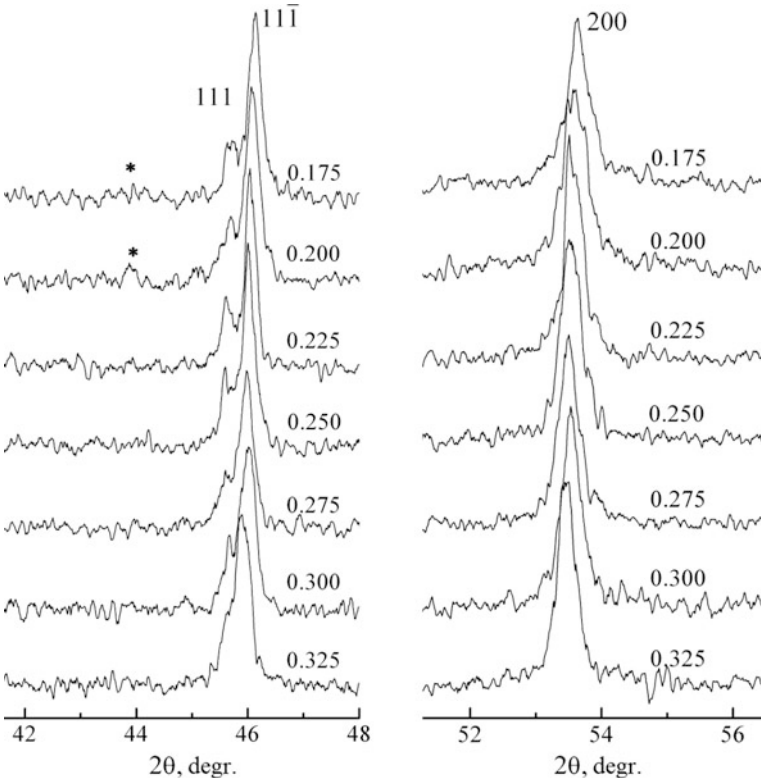

Fig. 16.2 Fragments of radiographs of solid solutions $(0.95 - x)BiFeO_3$–$0.05PbTiO_3$–$xPbFe_{1/2}Nb_{1/2}O_3$, comprising reflection diffractions $(111)_K$ and $(200)_K$. *Asterisks* denotes a superstructure reflections, pointing to the space group R3c

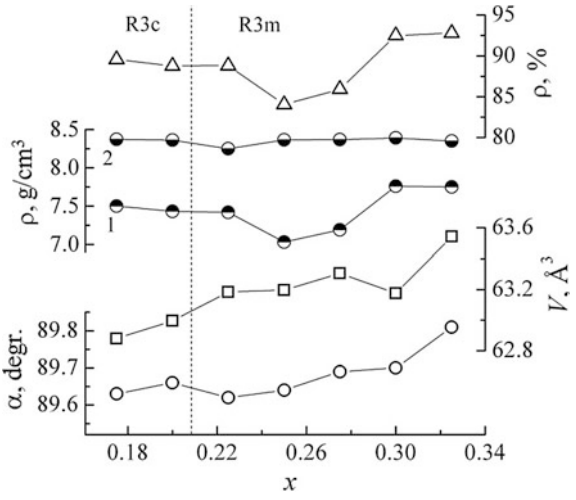

Fig. 16.3 Dependencies of the angular parameter α, the experimental volume *V* of the Rh cell, X-ray (*1*) and relative (*2*) densities of ceramics solid solutions $(0.95 - x)BiFeO_3$–$0.05PbTiO_3$–$xPbFe_{1/2}Nb_{1/2}O_3$ on *x*

Figure 16.3 shows that the transition R3c → R3m in the range $0.200 < x < 0.225$ is accompanied by a decrease of the angle α while the volume of the cell grows with increasing x. The angle α increases in the range $0.225 \leq x \leq 0.250$, and cell volume becomes constant (the invar effect) indicating a continuation of the restructuring of the structure, which is now most likely related to changes in defected structure. In [5], we have shown that the structure of $PbFe_{1/2}Nb_{1/2}O_3$ is characterized by multiwave modulation caused by the ordering fields of structure with high content of Nb or Fe. Furthermore in regions of structure with increased content of Nb planar defects appeared. These defects are crystallographic shear planes representing Nb_2O_5 structure defects [6, 7]. Also, crystalline lattice of $PbFe_{1/2}Nb_{1/2}O_3$ can has isolated crystallographic shear planes. Their number and length depend on the number of oxygen vacancies. It is safe to say that in these solid solutions, similar structural features also exist, which is confirmed by the results of X-ray studies. Figure 16.2 shows that the profile of the X-ray line 200 of all solid solutions is a superposition of the main lines and satellites located very close to it. Solid solution with $x = 0.225$ has the least distorted profile 200 and therefore lesser defect structure; profile of solid solution with $x = 0.250$ is the most distorted and has the most defect structure. Figure 16.2 shows that on the diffractogram of solid solution with $x = 0.325$ background at the base of the lines (111) and (200) has the form of a halo especially well noticeable on the last line. It is a sign of the emergence of new phase clusters coherently coupled to the matrix on planes {100} [8]. Therefore solid solutions with $x = 0.325$ can be attributed to the morphotropic region in which the rhombohedral and "pseudocubic" (because its symmetry is not known) Psc phases coexist.

Figure 16.3 shows non-monotonic changes of measured and related densities ρ_{mes} and ρ_{rel} with increase of x and minima of these characteristics at $0.25 \leq x \leq 0.275$. This concentration range locates near a phase transition R3c → R3m inside one-axis symmetry rhombohedral field. Considering the analogy with the effect of Hedval (increased reactivity of solids, as a result, of polymorphic transformations), this area is characterized by the intensification of diffusion processes initiated by the high mobility of the lattice components during its restructuring [9]. It is typical the case of morphotropic transitions that leads to compaction and improvement of prepared environments grain structure [10]. However, when the formation of solid solutions is associated with the impurity phases appearance possibility (for example in solid solution based on $BiFeO_3$ [11]) during the phase transition (where any violation of specified stoichiometry leads to a noticeable change in the phase pattern, structure and macroproperties), appearance of spurious (ballast) phases loosening the structure can becomes a priority process. We observe these phenomena in studied objects.

Other cause of the decreasing ρ_{mes} and ρ_{rel} in the aforementioned concentration range can be clustering structure (the formation of nuclei of new phases [8, 13] at the left and right sides of the area of decompression. This area locates in the center between the first morphotropic region R3c + R3m (we do not see it because of the small concentration research step) and second (Rh + Psc) region discussed above.

Figure 16.4 shows fragments of this section of solid solution microstructure. It is shown that the compositions with low value of x have a dense structure consisting of small crystallites densely adjacent to each other. With increasing concentration of

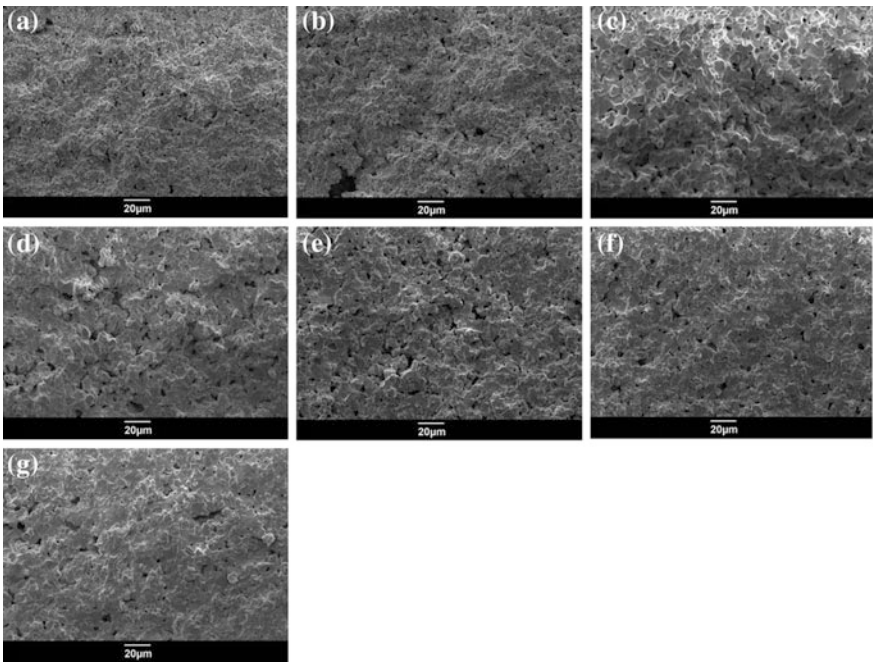

Fig. 16.4 Fragments of investigated ceramic microstructure (**a** $x = 0.175$, **b** $x = 0.20$, **c** $x = 0.225$, **d** $x = 0.25$, **e** $x = 0.275$, **f** $x = 0.30$, **g** $x = 0.325$) panoramic view at low magnification

lead iron niobate, the microstructure of the samples loosens. Large number of pores appears (Fig. 16.4d, e), that reflects on the relative density of the studied ceramics.

Figure 16.5 shows fragments of the grain structure of objects. It is shown that samples with $x = 0.225$ have the most homogeneous grain structure with large (up to 15 m) firmly attached to each other crystallites. At $x < 0.225$, the microstructure is presented by relatively small grains of irregular shape. At $x > 0.225$, the microstructure heterogeneity intensifies, that manifests in the presence of two types of grains, namely large crystallites (10–15 μm) in the form of irregular polyhedra and small (up to 5 μm) grains localized in small groups mainly near the pores. The observed effects can be explained by the possibility of appearance of ballast phases during ceramic preparation. It is confirmed by the fact that the objects with the most heterogeneous microstructure (Fig. 16.5d–g) locate in the concentration range having morphotropic areas and clusters of new phases, as we wrote above.

During obtaining objects from the second section ($x = 0.05$ with $0.175 \leq y$ 0.325, $\Delta y = 0.025$), we have paid attention to the self-destruction phenomenon in the samples of composition $(Bi_{0.675}Pb_{0.325})(Fe_{0.70}Ti_{0.275}Nb_{0.025})O_3$ at T_S, equal to 1050 °C which is close to optimal $T_{S.opt}$ for other samples. Analysis of structural (Fig. 16.6a, b) and microstructural (Figs. 16.6 and 16.7) data revealed the extreme behavior of these characteristics with increasing T_S with maxima of tetragonal degree ($c/a - 1$), the number of T-phase (χ), the average grain size ($\bar{d}$) (dotted was

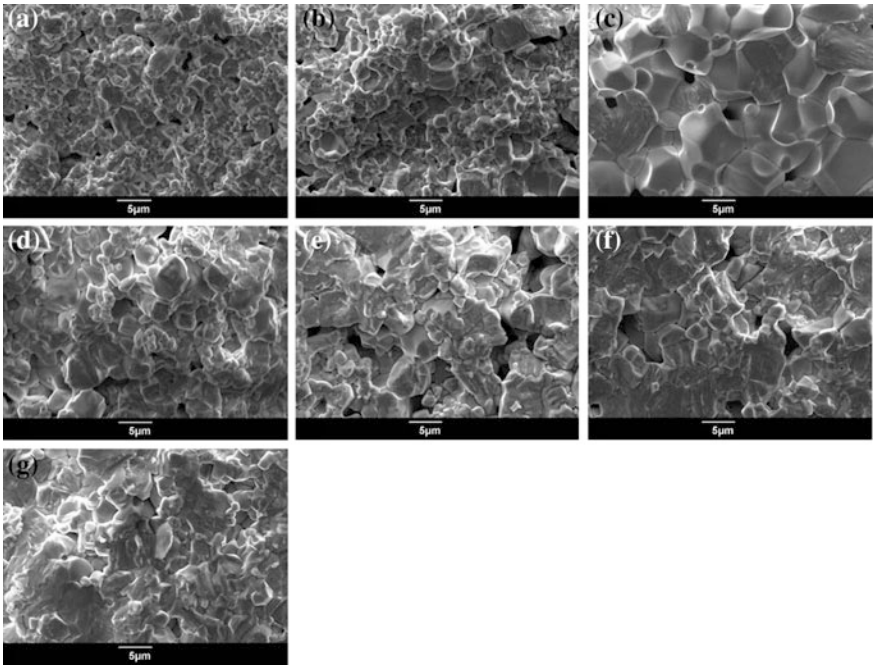

Fig. 16.5 Fragments of the grain structure of ceramics (**a** $x = 0.175$, **b** $x = 0.20$, **c** $x = 0.225$, **d** $x = 0.25$, **e** $x = 0.275$, **f** $x = 0.30$, **g** $x = 0.325$)

reconstructed alleged curves $d(T_S)$, $\rho_{mes.}(T_{S.})$, $\rho_{rel.}(T_{sp.})$). It is associated with unit cell deformation increase with growth of tetragonality degree, substantial enlargement of the grains, decrease of the surface area of their boundaries and, as consequence, their weakening contributing to the destruction of objects [14].

In [15], we installed an inverse dependence $\bar{d}$ on the magnitude of uniform strain parameter, δ, equal to $2/3(c/a - 1)$ for T-phase at change of cationic quantitative composition of solid solution. Note that the smaller size of the crystallite is observed in compositions with larger δ. That can be explained by the increase of internal stress in the piezoceramic with increasing spontaneous deformation. These strain deformations inhibit the growth of crystallites.

This situation occurs in our case at low T_S (1273–1298) K. The further behavior of $\bar{d}$ changes symbiotically with values of $(c/a - 1)$, that we also observed earlier [16]. This phenomenon is associated with the intensification of mass transfer and diffusion processes at higher T_S (in the temperature range 1298–1373 K), which play the prevailing roles in the formation of the grains landscape. Hindering the normal development of ceramic compaction and recrystallization (Fig. 16.6b —ρ_{mes}, ρ_{rel} reduction), defects formation at very high (limit for the considered solid solution) T_S (above 1373 K) also influences on grain structure.

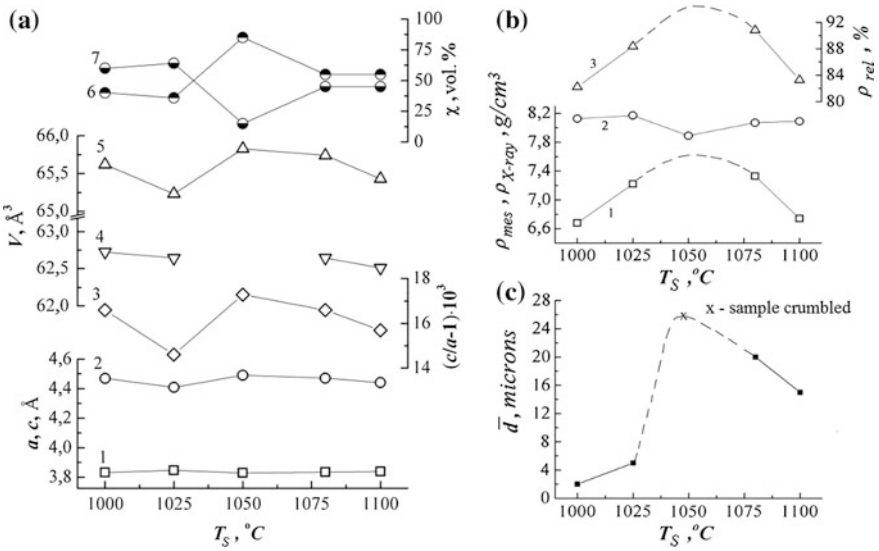

Fig. 16.6 **a** Sintering temperature dependencies of parameters *a* (*1*), *c* (*2*), of tetragonality degree, $(c/a - 1)$ (*3*), volume *V* of the tetragonal cell (*5*), volume *V* of rhombohedral cell (*4*) of the solid solution $(Bi_{0.675}Pb_{0.325})(Fe_{0.70}Ti_{0.275}Nb_{0.025})O_3$ and content, *χ*, tetragonal (*6*) and the rhombohedral (*7*) phases; **b** sintering temperature dependencies of ceramic densities: measured (*1*), X-ray (*2*) and relative (*3*) of the solid solution with composition $(Bi_{0.675}Pb_{0.325})(Fe_{0.70}Ti_{0.275}Nb_{0.025})O_3$ (the sample crumbled at 1050 °C); **c** dependence of average grain size, $\bar{d}$, on the sintering temperature

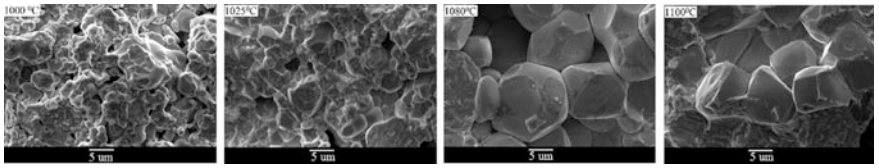

Fig. 16.7 Fragments of the grain structure of solid solutions $(Bi_{0.675}Pb_{0.325})(Fe_{0.70}Ti_{0.275}Nb_{0.025})O_3$

Figure 16.8 shows the temperature dependence of the real part of the complex permittivity $\varepsilon'/\varepsilon_0$ and dielectric loss tangent $tg\delta$ at frequencies $(25 - 2 \times 10^6)$ Hz for the objects from the first section. Figure 16.8 shows that compositions with a high content of bismuth ferrite $(0.175 \leq x \leq 0.2)$ at the temperature range (500–700) K demonstrate abnormal behavior of $\varepsilon'/\varepsilon_0$ manifested in the appearance of the points of inflection which shift to area of high temperatures during frequency increasing. These anomalies can be associated with the effects of Maxwell–Wagner relaxation which is more clearly visible on the temperature dependences of $\varepsilon'/\varepsilon_0$ in pure bismuth ferrite. Majority samples are characterized by presence of strongly blurred relaxing $\varepsilon'/\varepsilon_0$ peaks shifted to the high-temperature region with increasing frequency.

Despite the fact that accurate definition the temperature of phase transition in most of the samples is difficult, it is possible to observe a common tendency to decrease of the Curie temperature with increase of concentration of lead iron niobate. Increase of blurring ferroelectric → paraelectric (FE → PE) transition and T_C reduction may be associated with growth of crystal-chemical disorder. This disorder can be caused by embedding variable valence metal ions (Fe, Nb) into crystal structure of the base compound (BFO in this case), possibility of their incorporation in irregular positions and intergranular layers and complex phase content of the objects, that was already mentioned. Temperatures of FE → PE phase transitions

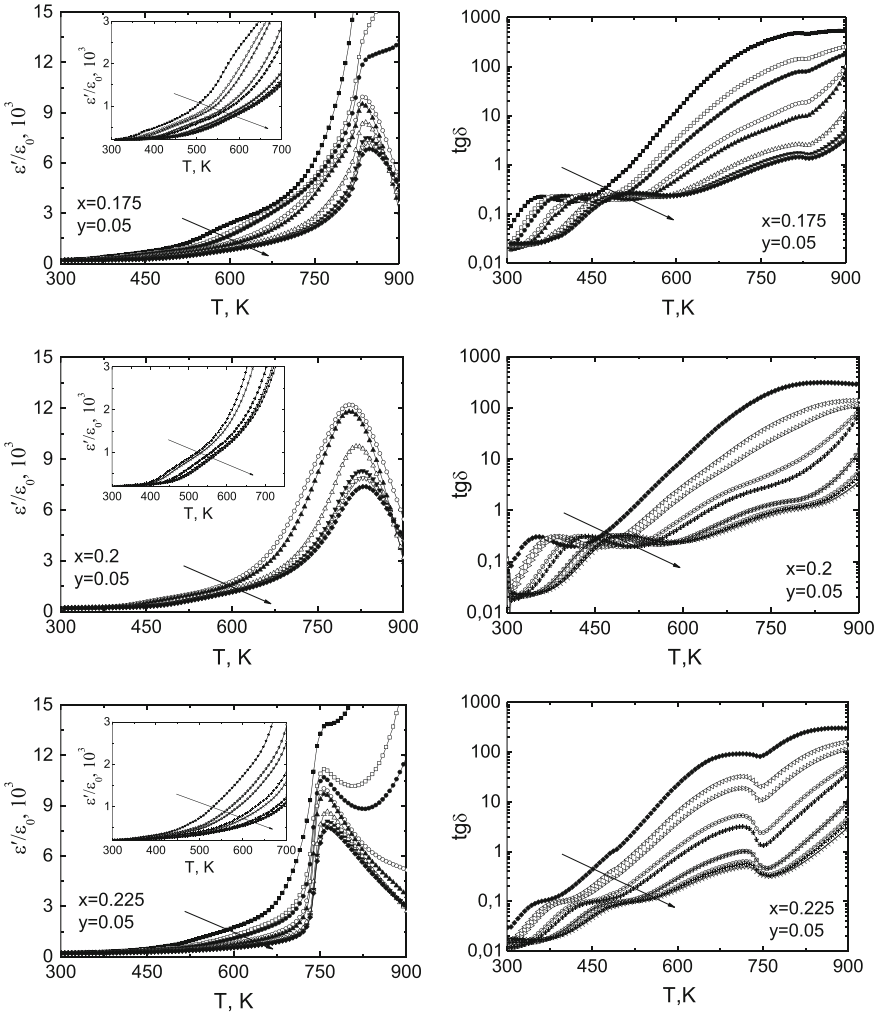

Fig. 16.8 Temperature dependencies of $\varepsilon'/\varepsilon_0$ and $tg\delta$ in the frequency range $(25 - 2 \times 10^6)$ Hz and in the temperature range (300–900) K; *arrows* show frequency growth direction

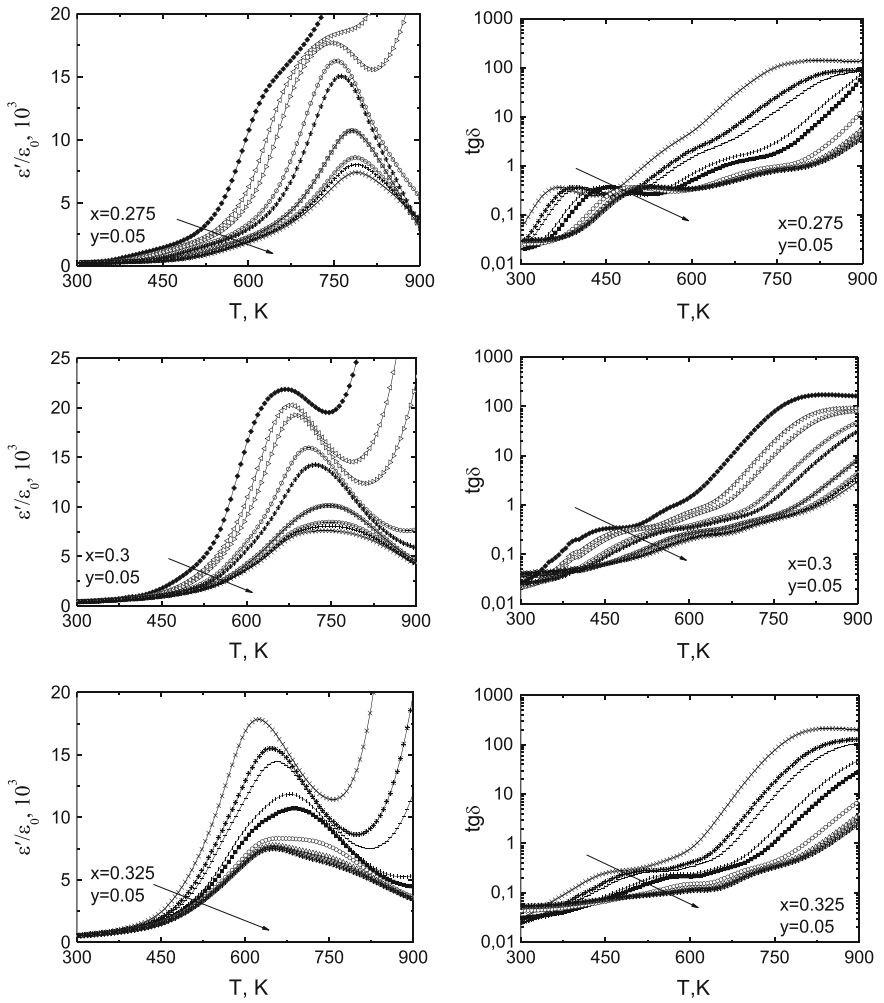

Fig. 16.8 (continued)

were determined only in two samples ($x = 0.175$ and $x = 0.225$), where the maxima on the $\varepsilon'/\varepsilon_0$ curves have shape similar to classical ferroelectrics. The difference between the temperature dependencies of these two compositions and the other dependencies having strong relaxation character can be explained by the fact that phase formation effects in these objects do not play strong role in the dielectric response formation or completely absent. For example, at $x = 0.175$ concentration transition R3c → R3m could even not begin, and at $x = 0.225$ the same transition could be fully completed before appearance the clusters of Psc phase. It should also be noted that in the compositions with $0.3 \leq x \leq 0.325$ on the dependencies of ε'

ε_0 were found high frequency anomalies at $T > T_C$. Their appearance may be associated with formation of new (Psc) phase, that we described above.

16.4 Conclusions

The obtained results may be used to create new multifunctional materials based on multiferroics.

Acknowledgements The work was supported by the Ministry of Education of the Russian Federation: the themes Nos. 1927, 213.01-2014/012-IG and 3.1246.2014/K. It was used equipment of CCU "Electromagnetic, Electromechanical and Thermal Properties of Solids" of the Physics Research Institute, Southern Federal University.

References

1. N.A. Boldyrev, A.V. Pavlenko, L.A. Shilkina, L.A. Reznichenko, A.I. Miller, Bull. Russ. Acad. Sci. Phys. **80**(6), 733 (2016)
2. K. Okazaki, *Ceramic Engineering for Dielectrics*. Tokio, 340 p. (1969)
3. E.G. Fesenko, *Perovskite Family and Ferroelectricity* (Atomizdat, Moscow, 1972), 248 p (In Russian)
4. I. Sosnowska, R. Przenioslo, P. Fischer, V.A. Murashov, J. Magn. Magn. Mater. 384 (1996)
5. A.V. Pavlenko, L.A. Shilkina, L.A. Reznichenko, Crystallogr. Rep. **57**(1), 118 (2012)
6. Y.D. Tretyakov, *Chemistry of the Nonstoichiometric Oxides* (MSU Press, Moscow, 1974), 364 p. (In Russian)
7. C.N.R. Rao, J. Gopalakrishnan, *New Directions in Solid State Chemistry* (Cambridge University Press, Cambridge, 1997), 549 p
8. S.V. Titov, L.A. Shilkina, L.A. Reznichenko, S.I. Dudkina, O.N. Razumovskaya, S.I. Shevtsova, E.M. Kuznetsova, JETP Lett. **26**(18), 9 (2000) (In Russian)
9. E.M. Kuznetsova, L.A. Reznichenko, O.N. Razumovskaya, L.A. Shilkina, JETP Lett. **27**(5), 36 (2001) (In Russian)
10. I.N. Andryushina, L.A. Reznichenko, V.A. Alyoshin, L.A. Shilkina, S.V. Titov, V.V. Titov, K.P. Andryushin, S.I. Dudkina, Ceram. Int. **39**(1), 753 (2013)
11. K.P. Andrushin, A.A. Pavelko, I.A. Verbenko, O.N. Razumovskaya, L.A. Shilkina, V.A. Aleshin, L.A. Reznichenko, Bull. Russ. Acad. Sci. Phys. **75**(8), 1082 (2011)
12. L.A. Reznichenko, A.Y. Dantsiger, S.I. Dudkina, L.A. Shilkina, O.N. Razumovskaya, V.A. Servuli, I.V. Pozdnyakova, Tech. Phys. **45**(9), 1207 (2000).
13. Shilkina L.A., Grin' P.G., Reznichenko L.A., Dudkina S.I., Yurasov Yu.I., Razumovskaya O. N. *Physics of the Solid State*. **58**(3), 537 (2016)
14. E.I. Bondarenko, V.D. Komarov, L.A. Reznichenko, V.A. Chernyshkov, Tech. Phys. **58**(9), 1771 (1988) (In Russian)
15. L.A. Reznichenko, A.Y. Dantsiger, O.N. Razumovskaya, L.S. Ivanova, S.I. Dudkina, L.A. Silkina, V.A. Servuli, V.P. Sakhnenko, *Proceedings of the International Scientific-Practical Conference "Fundamental Problems of the Pezoelectronics" ("Piezotehnika-95")*, vol 2, p. 13 (1995) (In Russian)
16. A.Y. Dantsiger, L.A. Reznitchenko, S.I. Dudkina, O.N. Razumovskaya, L.A. Shilkina, Ferroelectrics. **214**, 255 (1998)

Chapter 17
Structure Disorder and Photorefractive Properties of $LiNbO_3$:Zn and $LiNbO_3$:B Crystals

Nikolay V. Sidorov, Mikhail N. Palatnikov, Natalya A. Teplyakova, Alexander A. Yanichev and Roman A. Titov

Abstract Due to the Raman spectra, structure changes were searched in a $LiNbO_3$:Zn (0.04–5.84 mol%) and $LiNbO_3$:B (0.08–0.18 mol%) single crystals series with the varying of the dopant concentration. Optical homogeneity and photorefractive properties were researched by photoinduced light scattering.

17.1 Introduction

Researches aimed at optimization of structure and properties of optically nonlinear lithium niobate ($LiNbO_3$) single crystals are highly actual. It is important to obtain optically perfect single crystals with the possible lowest photorefractive effect and coercive field [1–11]. Papers [4, 11–13] claim that photorefraction and coercive field decrease abruptly when the dopant concentration exceeds the "threshold". This is true for the "non-photorefractive" dopants such as Zn^{2+}, Mg^{2+}, Gd^{3+} etc. Structure and many physical parameters anomalies are observed in the crystals around concentration thresholds [4, 6, 7, 11, 12, 14]. Crystal $LiNbO_3$:Zn possesses two characteristic thresholds: at ~4.0 [6, 7, 14] (~3.0 mol% ZnO [4, 11, 12]) and ~7.0 mol% ZnO in the melt [4, 6, 7, 11, 12, 14]. But at zink concentration in the melt >7.0 mol% (higher than the highest threshold) $LiNbO_3$:Zn single crystals have low optical quality, are compositionally inhomogeneous and often two-phased [6, 7]. At the same time crystals grown from the melt containing from ~4.0 to ~7.0 mol% ZnO are compositionally and optically homogeneous [6, 7]. At varying of the single crystals composition within the homogeneous area predominantly the secondary structure of the $LiNbO_3$ changes. Researches of the changes in the secondary structure of $LiNbO_3$ single crystals that occur due to varying of the

N.V. Sidorov (✉) · M.N. Palatnikov · N.A. Teplyakova · A.A. Yanichev · R.A. Titov
Kola Science Center, I.V. Tananaev Institute of Chemistry and Technology of Rare Elements and Mineral Raw Materials, Russian Academy of Sciences, 26 a, Akademgorodok, Apatity, Murmansk Region 184209, Russia
e-mail: sidorov@chemy.kolasc.net.ru

I.A. Parinov et al. (eds.), *Advanced Materials*, Springer Proceedings in Physics 193, DOI 10.1007/978-3-319-56062-5_17

composition is of high interest because it mostly determines the characteristics of photorefractive, optically nonlinear and other properties of the crystal [15].

Changes of the secondary structure in a series of $LiNbO_3$:Zn (0.04–5.84 mol%) and $LiNbO_3$:B (0.08–0.18 mol%) single crystals are investigated by Raman spectroscopy and photoinduced light scattering (PILS). The obtained results for crystals doped by Zn^{2+} and B^{3+}, were compared with the identical data on nominally pure stoichiometric (Li/Nb = 1) and congruent (Li/Nb = 0.946) single crystals ($LiNbO_{3stoich}$ and $LiNbO_{3cong}$ correspondingly). $LiNbO_3$:Zn (0.04–5.84 mol%) single crystals are interesting as optical materials for conversion of laser radiation on periodically poled domain structures due to high resistivity to optical damage and low coercive field. $LiNbO_3$:B (0.55–1.24 mol%) single crystals are interesting as electro optical modulators.

$LiNbO_3$:Zn crystals were previously researched in papers [1–4, 6–13, 15–20]. The researches of the doped crystals with small concentration step of the Zn^{2+} dopant in the wide range of concentrations were performed in works [6, 7]. Influence of doping of the single crystals by B^{3+} cations are investigated in the literature quite poorly (except paper [21]). Doping by B^{3+} cations is different from doping by other metallic "non-photorefractive" cations. This is caused by very low coefficient of embedding of the cations to the octahedral gaps in the crystal structure. Due to our data at 1.2 mol% B_2O_3 in the melt crystals will contain only $\sim 4 \times 10^{-4}$ mol% B_2O_3, which is more characteristic for the uncontrolled impurities in the $LiNbO_3$ crystal [9, 13, 20]. But crystals $LiNbO_3$:B have high optical and structure homogeneity and low photorefractive effect [20, 22]. This is also confirmed by birefringence clearly observed when laser beam in the crystals is directed perpendicular to the polar axis Z [23]. In more disordered crystals with higher value of photorefractive effect birefringence is blurred by disordering effects and photorefraction and it is difficult to observe it. Thus investigation of the reasons for such a good optical quality in $LiNbO_3$:B single crystals is of great interest.

17.2 Method

Nominally pure congruent $LiNbO_3$, $LiNbO_3$:Zn (0.04–5.84 mol%) and $LiNbO_3$:B (0.55–1.24 mol%) crystals were grown from congruent melt. $LiNbO_3$:Zn crystals were obtained by direct doping: pure ZnO was added to granulated charge, and thoroughly mixed before fusing of the crucible.

$LiNbO_3$:B crystals were obtained by homogeneous doping: dopant was added to the reextract during obtaining of the niobium oxide. Boric acid was added to the niobium reextract during extractional obtaining of the pure niobium hydroxide. 0.08–0.15 wt% boric acid was added in ratio with niobium (as oxide) in the reextract. Part of the acid bound fluorine to HBF_4 that was also taken into consideration. Niobium hydroxide was precipitated and neutralized by the ammonia water to pH = 8–9. Washed by deionized water hydroxide was heated till doped

oxide was obtained. The doped oxide was used to obtain lithium niobate charge from which the single crystals were grown.

$LiNbO_3$ single crystals were grown from stoichiometric melt with 58.6 mol% Li_2O.

For growing of congruent $LiNbO_3$ single crystals a granulated charge synthesized in ICTREMRM was used. The charge allowed growing of water white nominally pure $LiNbO_3$ single crystals [24]. Impurities concentration was less than 5×10^{-4} wt%. All crystals were grown in air atmosphere at the equipment "Crystal-2". Charge preparation and crystal growth methods are described in detail in [5, 7, 24].

All grown single crystals were turned to single domains by high-temperature electro-diffuse annealing. DC was applied to crystals cooled 20 grades per hour from 1240 to 880 °C. Single domain state was confirmed by analysis of the frequency dependence of the electrical impedance and detection of static piezo modulus (d_{33st}) of the crystal boule.

Samples for research of Raman spectra and PILS were cut in the shape of the cuboids ($\sim 7 \times 6 \times 5$ mm^3) with the edges coinciding with the crystallographic axis *X, Y, Z* (*Z* is the polar axis of the crystal). Faces of the samples were thoroughly polished.

Raman spectra were excited by the 514.5 nm band of the argon laser by Spectra Physics (model 2018-RM) and registered by spectrograph T64000 by Horiba Jobin Yvon with the confocal microscope. To decrease the photorefraction effect influence on the Raman scattering, the spectra were excited by low power radiation (not higher than 3 mW under the microscope). Spectra were detected with the resolution 1.0 cm^{-1}. Spectra were treated by software Horiba LabSpec 5.0 and Origin 8.1. Detection errors for frequencies, bandwidths and band intensities were ± 1.0, ± 3.0 cm^{-1} and 5%, respectively. PILS detection method was described in detail in [25, 26]. PILS was excited by Nd:YAG (MLL-100) laser with the wavelength 532 nm, power density $p \sim 6.3$ W/cm^2.

17.3 Results and Discussion

Figure 17.1 reveals Raman spectra of single crystals $LiNbO_{3stoich}$, $LiNbO_{3cong}$, $LiNbO_3$:Zn (0.03–5.84 mol%), $LiNbO_3$:B (0.55–1.24 mol%) that correspond to the fundamental vibrations of the crystal lattice in the scattering geometries $Y(ZX)\bar{Y}$ and $Y(ZZ)\bar{Y}$. Band frequencies stayed the same within the error. This indicates little influence of the changes in the secondary structure on the quasielastic lattice constants of $LiNbO_3$ crystal.

Figure 17.1 reveals that at change of $LiNbO_3$:Zn and $LiNbO_3$:B crystals compound behavior of widths and intensities of spectral bands are observed in the whole spectra: two-particle states of acoustic phonons (100–150 cm^{-1}), vibrations of the cations located in the oxygen octahedrons BO_6 (*B* = Nb, Li, doping cation) (200–300 cm^{-1}), vibrations of the oxygen in octahedrons (500–900 cm^{-1}). The

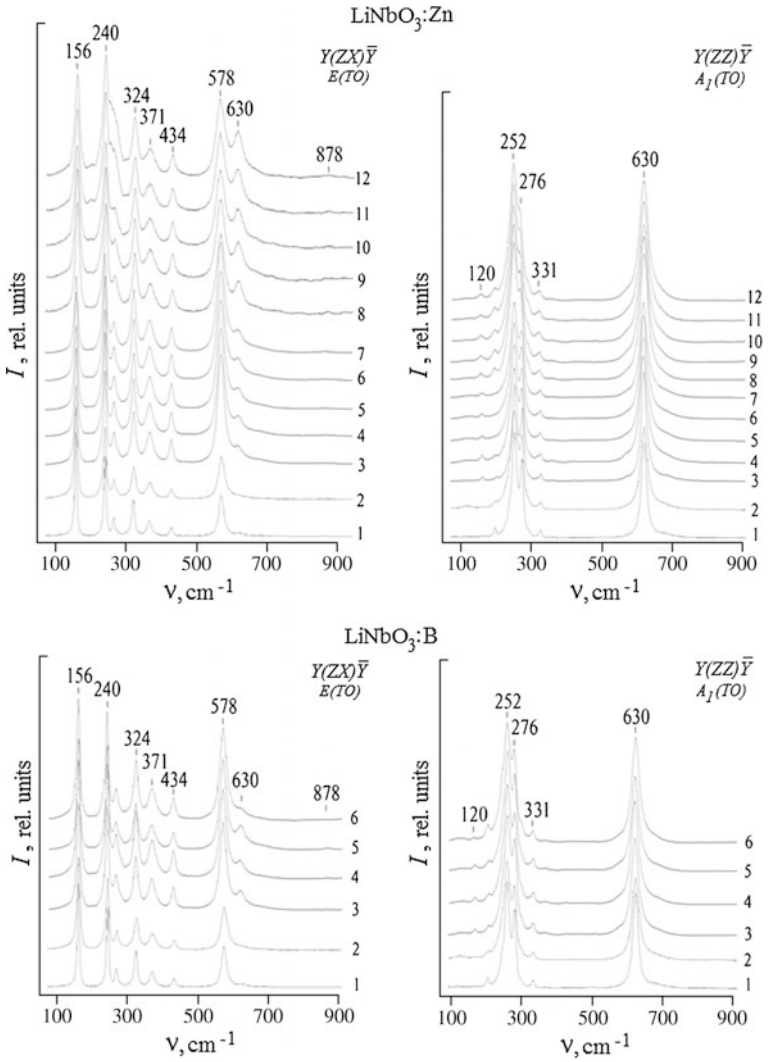

Fig. 17.1 Raman spectra of crystals: $LiNbO_{3stoich}$ (*1*), $LiNbO_{3cong}$ (*2*), $LiNbO_3$:Zn (0.04 (*3*), 0.07 (*4*), 1.19 (*5*), 1.39 (*6*), 2.01 (*7*), 3.43 (*8*), 3.95 (*9*), 5.19 (*10*, *11*), 5.84 (*12*) mol% ZnO) and $LiNbO_3$:B (0.55 (*3*), 0.69 (*4*), 0.83 (*5*), 1.24 (*6*) mol% B_2O_3) in scattering geometrics $Y(ZX)\bar{Y}$ and $Y(ZZ)\bar{Y}$

data indicate that the change in the crystal compound leads to change in the order of alternation of main, doping cations and vacancies along the polar axis, distortion of the BO_6 octahedrons, shift of the resonance interaction between fundamental vibrations and two-particle states of acoustic phonons.

Due to the selection rules [11, 27], scattering geometry $Y(ZX)\bar{Y}$ should contain only $E(TO)$ symmetry type vibrations and $Y(ZZ)\bar{Y}$–$A_1(TO)$ symmetry type

vibrations. But photorefractive effect produces forbidden in the $Y(ZX)\bar{Y}$ geometry $A_1(TO)$ symmetry type vibrations with intensities proportional to the photorefractive effect value [11]. The most suitable analytical band for evaluation of the photorefractive effect value in [11, 28] was agreed 630 cm^{-1} band that corresponds to vibration of oxygen atoms in the octahedrons O_6. Due to the fact that 580 cm^{-1} ($E(TO)$)) band does not change at varying of photorefractive effect value at least for crystals with low photorefraction, relative intensity $I_{отн} = (I_{630}/I_{580}) \times 100\%$ is a convenient value [9, 10, 13, 28].

Disordering of structure contributes to the rise in the Raman bandwidth at constant temperature [11, 27]. Figure 17.1 reveals a minima around 0.05 × 0.94 mol% ZnO on concentration dependences of the widths of several bands. This confirmes conclusions of papers [19, 20] about existence of highly ordered state of lattice units in this Zn^{2+} concentration area. Disordering of the structure and photorefractive effect contribute to changes of band intensities [11, 27]. In this research Raman spectra were on purpose excited by low power radiation thus the influence of photorefractive effect could be neglected (at least for crystals with low photorefractive effect).

630 cm^{-1} band relative intensity has the smallest value for $LiNbO_{3stoich}$ and $LiNbO_{3cong}$ crystals and the biggest value for $LiNbO_3$:Zn (5.84 mol% ZnO) and $LiNbO_3$:B (0.55–0.83 mol%) crystals. Meanwhile the intensity of the band rises with the rise in dopant concentration for the whole researched ZnO concentrations (0.04–5.84 mol%) in the lithium niobate single crystals.

As Fig. 17.1 reveals, concentration dependence of intensities has a sharp jump (a break) around 2.01–3.43 mol% ZnO. It is perhaps caused by transient phenomena that occur near the concentration threshold at 5.38 mol% ZnO. Intensity of 630 cm^{-1} band in a series of $LiNbO_3$:B crystals first increases and then increases with the rise in dopant concentration, Fig. 17.1.

Increase in the forbidden band 630 cm^{-1} $A_1(TO)$ intensity cannot be explained by increase in the photorefractive effect value in $LiNbO_3$:Zn single crystals. It was discovered [4, 8, 11, 13, 16] that with the rise in Zn^{2+} concentration photorefractive effect decreases. Decrease of the photorefractive effect value in $LiNbO_3$:Zn is also confirmed by decrease of the angle of PILS indicatrix opening θ with the rise in Zn^{2+} concentration, Fig. 17.2. Thus only disordering of the crystal lattice units leads to increase in 630 cm^{-1} $A_1(TO)$ band intensity.

The bands with frequencies 630 and 876 cm^{-1} correspond to vibrations of oxygen atoms in oxygen octahedrons of $A_1(TO)$ symmetry type and stretching bridge vibrations of oxygen atoms of $A_1(LO)$ symmetry type [11, 29]. In the Raman spectra of crystals $LiNbO_3$:Zn their widths dependence on concentration is the strongest (in comparison with the widths of other bands) and they have the sharpest jumps (Fig. 17.1; Table 17.1). We believe such a behavior of the bandwidths to be caused by anisotropic expansion of oxygen octahedrons mostly along the polar axis due to the fact that ion radius of Zn^{2+} cations (0.74 Å) is bigger than that of the main cations Li^+ and Nb^{5+} (0.68 and 0.68 Å, respectively) [11]. The jumps on the concentration dependencies could be caused by changes in the mechanism of incorporation of doping Zn^{2+} cations to the cation sublattice of the crystal around the

threshold concentrations. This might also cause redistribution of main cations, doping cations and vacancies in oxygen octahedrons. Our data are confirmed by the data on X-ray structure analysis that revealed anisotropic expansion of oxygen octahedrons mostly along the polar axis of the $LiNbO_3$:Zn crystals at rise in Zn^{2+} concentration [2, 4, 11, 12]. But the number of jumps on the concentration dependence of 630 cm^{-1} $A_1(TO)$ and 876 cm^{-1} $A_1(LO)$ bands (five, Fig. 17.1; Table 17.1) exceeds the number of known from literature concentration thresholds [4, 6, 7]. PILS confirm greater number of jumps at change of composition of crystals $LiNbO_3$:Zn, Fig. 17.2. Figure 17.2 demonstrates that speckle-structure of PILS indicatrix of all crystals changes drastically and abruptly with the rise in dopant concentration.

Table 17.1 shows basic parameters of bands revealed in the Raman spectra of $LiNbO_3$:Zn (3.43–5.84 mol%) crystals in comparison with $LiNbO_{3stoich}$ and $LiNbO_{3cong}$ single crystals. $LiNbO_3$ single crystals containing ZnO between the threshold concentrations ~4.0 and ~7.0 mol% ZnO in the melt are compositionally and optically homogeneous [6, 7]. Due to [4], at Zn concentration in the lithium niobate crystal ~3 mol%, there is a threshold with anomalies of a number of crystal properties. For example, at this concentration of the dopant concentrational dependence of linear electro-optic effect has a minimum [11]. This is explained by substitution of Nb_{Li} (Nb^{5+} ions in the Li^+ site) by Zn cations and minimization of Li-vacancies at this concentration of the dopant. Decrease of Li-vacancies decreases the possibility to distort oxygen octahedrons due to rise in the lattice stiffness [4]. Due to [30, 31] electro-optic properties of $LiNbO_3$ single crystals are determined by deformation and polarizability of $Nb(Li)O_6$ clusters. The bands from area 500–900 cm^{-1} of Raman spectra are the narrowest for the crystal $LiNbO_3$:Zn (3.43 mol%) among the searched crystals, Table 17.1. Paper [4] explains increase in the electro-optic coefficients at 3–7.6 mol% ZnO by increase in Li-vacancies and sharp decrease at [ZnO] > 7.69 mol% by disappearance of the Li-vacancies.

Thus due to the Raman spectra and XRD analysis [32] could be concluded that $LiNbO_3$ single crystals structure in the ZnO concentration area ~3.95–4.54 mol% is the most ordered and close to the $LiNbO_{3\ stoich}$ crystal and free of Nb_{Li} defects.

The further increase of Zn concentration (4.76–5.19 mol%) leads to appearance of Nb_{Li} defects due to XRD, although $LiNbO_3$:Zn (4.76–5.19 mol%) crystals are free of Li-vacancies [32]. Defects in the structure of these crystals are described by the formula $[Li_{0.94}Zn_{0.04}Nb_{0.01}]NbO_3$. The interatomic distances Nb-O, Li-O, Nb-Zn coincide within error with the ones for the crystal $LiNbO_3$:Zn (4.54 mol%) and interatomic distance Nb2-O coincides with the one for the crystal $LiNbO_{3cong}$ [32]. Figure 17.3 reveals bonds between octahedrons and shows approximate values of distance metal-oxygen for the congruent crystal. Lengths of the bonds of the three oxygen atoms connecting LiO_6 and $Nb1O_6$ octahedrons are identical and they are longer than lengths of other three oxygens, Fig. 17.3.

The disappearance of the Li-vacancies from the $LiNbO_3$:Zn crystal is observed at much smaller ZnO concentration (4.76 mol%) thus the gradual increase in electro-optical coefficients at 3–7.6 mol% ZnO should be connected with something else in the lithium niobate crystals. Full-profile XRD analysis showed

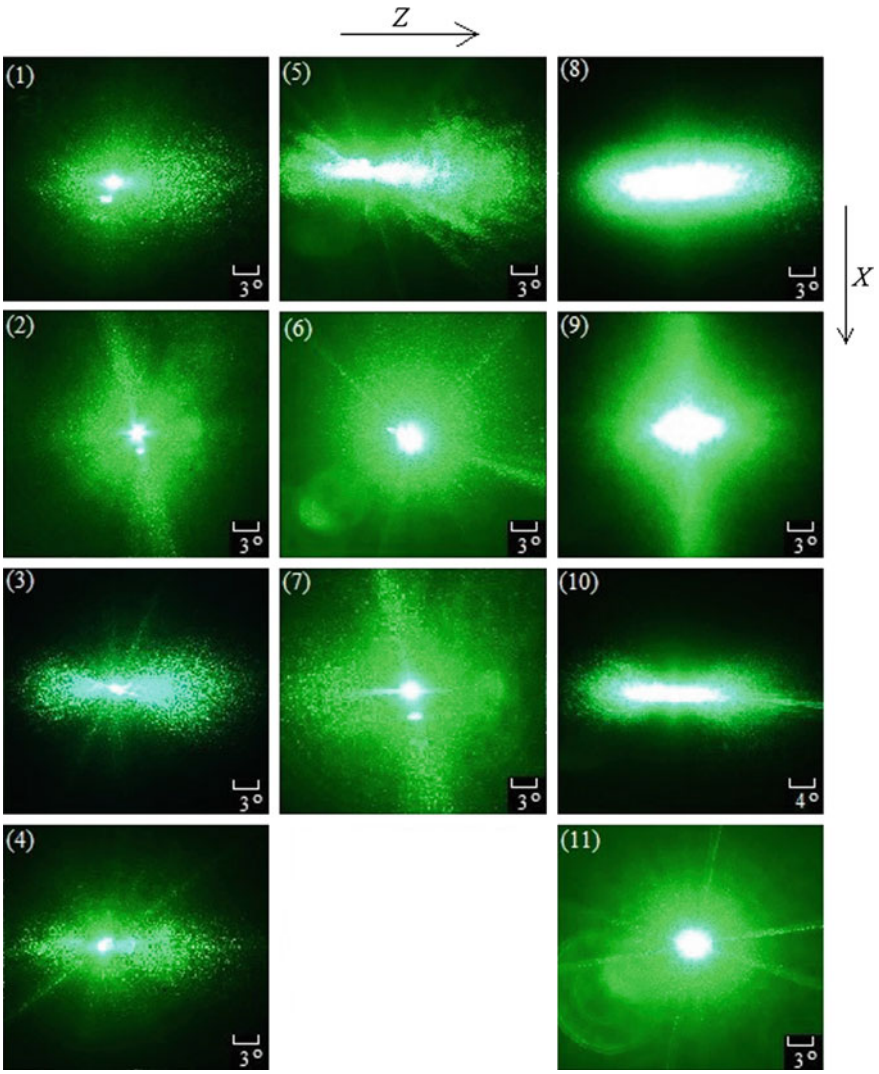

Fig. 17.2 Speckle-structure of PILS ($p \sim 6.3$ W/cm^2) of crystals $LiNbO_3$:Zn (0.04 (*1*), 0.07 (*2*), 1.19 (*3*), 1.39 (*4*), 2.01 (*5*), 5.19 (*6*), 5.84 (*7*) mol% ZnO) and $LiNbO_3$:B (0.55 (*8*), 0.69 (*9*), 0.83 (*10*), 1.24 (*11*) mol% B_2O_3). Time of the total PILS indicatrix opening for all researched crystals is 60 s

decrease of the *a* and *c* unit cell parameters with the rise of Zn concentration in the lithium niobate crystals to 4.76 mol% which also means decrease of the unit cell volume [32]. Increase in Zn concentration in the lithium niobate crystals to 5.19 mol% leads to increase in constants and volume of the unit cell [32]. However oxygen frame distortions are not observed at increase in Zn concentration,

Table 17.1 Values of the frequencies (v) and widths (S) of the bands, corresponding to the fundamental vibrations, observed in the Raman spectra of $LiNbO_{3stoich}$, $LiNbO_{3cong}$ and $LiNbO_3$:ZnO (3.43–5.84 mol%) crystals in scattering geometries $Y(ZX)\bar{Y}$ and $Y(ZZ)\bar{Y}$

$LiNbO_{3stoich}$		$LiNbO_{3cong}$		$LiNbO_3$:ZnO							
				[Zn] = 3.43		[Zn] = 3.95		[Zn] = 5.19		[Zn] = 5.84	
ν	*S*	ν	*S*	ν	*S*	ν	*S*	ν	*S*	ν	*S*
$A_1(TO)$											
253	14	252	29.7	254	27.6	254	28.2	253	29.3	253	29.4
275	9.4	275	12.1	273	15.5	275	15.6	275	16.2	275	16.4
333	7.7	332	11	332	12.5	332	12.9	332	12.2	332	12.8
632	19.7	631	26.2	633	30	632	31.1	632	33.6	632	33.8
$E(TO)$											
156	7	156	12	154	14	154	15	155	18	155	16
240	9	240	11	239	14	239	15	239	16	238	17
268	10	268	14	267	24	267	30	266	27	267	30
324	10	324	13	325	17	326	18	326	18	326	18
371	17	371	23	371	28	371	29	371	28	371	28
434	10	434	14	436	15	437	15	438	16	437	15
578	16	578	15	580	28	580	30	579	31	579	33
630	20	629	25	632	30	632	38	631	39	632	34
876	20	876	30	878	25	879	26	878	39	878	48

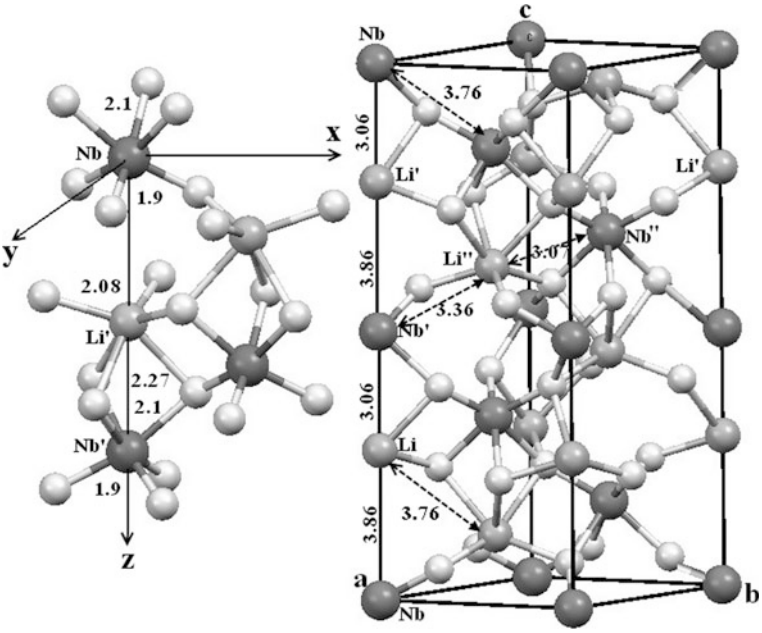

Fig. 17.3 Type of octahedron connection and atom locations in the lithium niobate unit cell. Alternation of short and long Nb-Li (Zn, Nb_2) distances is demonstrated

Table 17.1. Oxygen atoms coordinates do not change and interatomic distances in octahedrons LiO_6 and Nb_2O_6 are almost equal to the ones of the congruent crystal. Zn atoms distort lithium sublattice the same way atoms Nb_2 do in congruent crystals. Coordinates of Zn and Nb_2 atoms coincide and differ from the ones of the lithium in the oxygen octahedrons [32].

The changes in the width of Raman bands of the crystals $LiNbO_3$:Zn (3.43–5.84 mol%) are not observed except 876 cm^{-1} band. This band corresponds to the stretching bridge vibrations of the oxygen atoms in the octahedrons. Increase of Zn concentration in crystals $LiNbO_3$:Zn (3.43–5.84 mol%) does not lead to distortion of the cation and oxygen sublattices although leads to change of the bridge *B*-O-*B* (*B* = Nb, Li, Zn) character. Perhaps change of ion contribution to this bond explains a gradual increase in electro-optic coefficients at 3–7.6 mol% ZnO in lithium niobate crystals.

Doping of congruent $LiNbO_3$ crystal by the boron has some particularities. By the mass spectrometry, the B^{3+} cations were shown do not incorporate to structure, but to change the properties of the melt. Sobol and Voronko [33–35] proved stable clusters in the lithium niobate melt. Structure and size of the clusters depend on the melt compound and thermal history. Crystallization occurs by adding of the whole clusters to the growing crystal. Perhaps concentration of the boron influences structure and the size of the clusters in the melt. Thus, melts containing different concentrations of the boron will crystallize differently. This leads to different secondary structure,[1] different optical quality and structure characteristics of the grown crystals.

It is known that complexes (clusters) with the highest electrochemical activity have an advantage in crystallization during growth of crystals in isothermal conditions [36]. These complexes provide optical, structural and chemical characteristics corresponding to this compound of the melt. At change of the melt compound, other complexes might obtain advantage and thus the secondary structure and other properties of the single crystals will be different. This particularity is what we observe when $LiNbO_3$:B crystals are grown from melts with different concentrations of the boron.

The single crystals, grown from melt with a different structure (at doping by low concentrations of the boron), has higher optical and structural homogeneity than nominally pure congruent crystal [21]. The nature of this highly interesting and potentially highly beneficial fact is still researched. This is obviously connected with the changes of viscosity and structure of lithium niobate melt containing admixture of the boron but the mechanism is yet unclear. High optical homogeneity of crystals $LiNbO_3$:B (0.55–1.24 mol% B_2O_3 in the charge) was confirmed by PILS

[1]Primary structure of the crystal is the one detected by XRD methods: neutron scattering and X-ray analysis. Primary structure is described by theories based on the Fedorov space groups of symmetry. However, real crystals could be conformed to the theory only by accepting of the secondary structure. It consists of microstructures, clusters etc. $<10^{-6}$ m in diameter. Physical properties of crystals can also be formed by the cluster boundaries because they are sources of defects with localized electrons. Diffusion of the substance and charge transport occurs due to such defects thus they play huge role in the forming of the photorefractive effect.

pictures, Fig. 17.2. The lowest photorefractive effect was detected in the crystal $LiNbO_3$:B (1.24 mol% B_2O_3 in charge), Fig. 17.2. PILS indicatrix of this crystal did not open even at high laser beam intensity 160 mW, Fig. 17.2.

Figures 17.1 and 17.4 reveal that doping by small amount of boron leads to decrease in one part of the Raman bands widths and increase in the other. This indicates anisotropic influence of the dopant on the crystal structure. Bands from the area of oxygen octahedrons vibrations (500–900 cm^{-1}) have the strongest dependence on the boron concentration 576 ($E(TO)$) and 630 ($A_1(TO)$) cm^{-1} bandwidths increase with rise in dopant concentration up to 0.83 mol% boron in charge. At the same time width of 876 cm^{-1} ($A_1(LO)$) band that corresponds to the stretching bridge vibrations of oxygen atoms decreases with the rise in dopant concentration, Fig. 17.1. The data reveal distortion of crystals $LiNbO_3$:B (0.55, 0.69, 0.83 mol% B_2O_3 in charge) oxygen octahedrons at doping of the melt by boron. Meanwhile these bands in the Raman spectra of the crystal $LiNbO_3$:B (1.24 mol% B_2O_3 in charge) are much narrower thus the distortions of the octahedrons of the structure are absent. The general behavior of the width of the forbidden 630 ($A_1(TO)$) cm^{-1} band of crystals $LiNbO_3$:B (0.55–1.24 mol% B_2O_3 in charge) correlate with the behavior of its intensity and angle θ of PILS indicatrix opening, Figs. 17.2 and 17.4.

Raman spectra of nominally pure and doped $LiNbO_3$ crystals contain low intensive 120 cm^{-1} band. It corresponds to two-particle state of acoustic phonons with sum wave vector equal to zero [11],[2] Fig. 4. In the spectra of structurally homogeneous $LiNbO_{3cong}$ crystals, due to the improvement of the selection rules for wave vector of the total acoustic phonons of A_1 symmetry type [11, 37–39], this band splits into two bands of 105 and 118 cm^{-1}, Fig. 17.4. It is well known [11, 38, 39] that Raman spectra of structurally perfect crystals $LiNbO_{3stoich}$ do not contain this band, Fig. 17.4. Intensity of this band first decreases then increases with the rise of boron concentration in the charge, Fig. 17.4. Decrease of this band intensity also confirms existence of the area of higher order of the structure units at doping of $LiNbO_3$ crystals by ions with radii close to the one of the Nb^{5+} and Li^+ ions [11, 39]. This band is split into two (with frequencies 112 and 123 cm^{-1} (Fig. 17.4)) in the crystal $LiNbO_3$:B (1.24 mol% B_2O_3 in charge) that indicates high structure homogeneity of this crystal. Decrease of 120 cm^{-1} band intensity at doping of lithium niobate by boron also indicates decrease in Nb_{Li} defects concentration and decrease of resonance inharmonic interaction of fundamental $A_1(TO)$ vibrations of the lowest frequencies with two-particle acoustic $A_1(TO)$ excitations which is considered in [40]. Meanwhile depending on the magnitude of these interactions the mixing of single-phonon and multi-phonon $A_1(TO)$ states can be varied as well as the character of Raman specter around 120 cm^{-1}. The 120 cm^{-1} band was found [41] to be sensitive towards changes of acoustic Q factor of $LiNbO_3$ crystals. The

[2]Due to paper [37], low intensive 120 cm^{-1} band could correspond to the mode of the pseudo-scalar of A_2 type forbidden by the selection rules for the group C_{3v}. The vibration can occur at local decrease of the point symmetry from C_{3v} to C_3 due to turn of O_3 triangle because real crystals contain impurities [37].

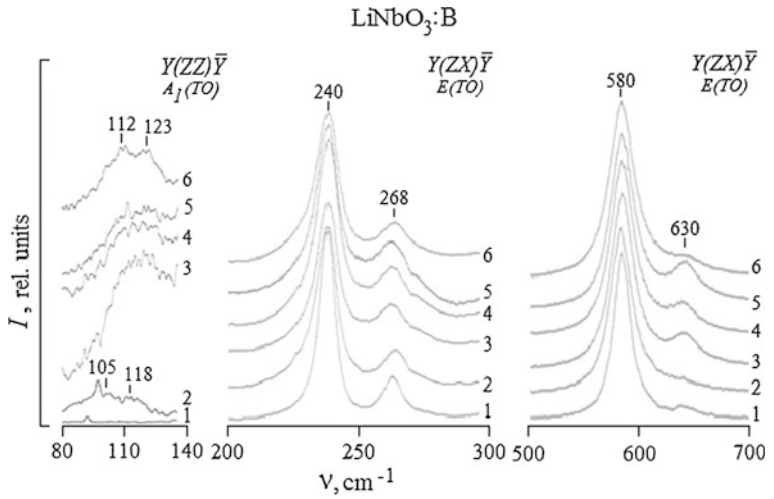

Fig. 17.4 Fragment of the Raman spectra of the crystals $LiNbO_{3stoich}$ (*1*), $LiNbO_{3cong}$ (*2*), $LiNbO_3$:B (0.55 (*3*), 0.69 (*4*), 0.83 (*5*), 1.24 (*6*) mol% B_2O_3 in the charge) in scattering geometries $Y(ZX)\bar{Y}$ and $Y(ZZ)\bar{Y}$

higher the acoustic Q factor is the lesser 120 cm^{-1} band intensity is. This can be explained by increase in the structure perfection of the crystal due to decrease of Nb_{Li} defects concentration.

17.4 Conclusion

Raman spectra of $LiNbO_3$:Zn and $LiNbO_3$:B crystals revealed changes in two-particle state of acoustic phonons (100–150 cm^{-1}) with total wave vector equal to zero. It concerns Raman bands in the area of vibrations of the cations located in the oxygen octahedrons BO_6 (B = Nb, Li, doping cation) (200–300 cm^{-1}), vibrations of the oxygen in octahedrons (500–900 cm^{-1}). The data indicate that the change in the crystal compound leads to change in the order of alternation of main, doping cations and vacancies along the polar axis, distortion of the BO_6 octahedrons. The concentration dependencies of the widths and intensities of the bands revealed changes in the mechanism of incorporation of doping Zn^{2+} cations to the cation sublattice of the $LiNbO_3$ crystal that leads to abrupt anisotropic expansion of oxygen octahedrons mostly along the polar axis at increase of the dopant concentration. The number of jumps on the concentration dependence of 630 cm^{-1} $A_1(TO)$ and 876 cm^{-1} $A_1(LO)$ bandwidths (five) exceeds the number of known from literature concentration thresholds (2). Doping of $LiNbO_3$ crystal by Zn^{2+} and B^{3+} cations decreases concentration of Nb_{Li} defects and photorefractive effect. The Raman spectra and PILS indicatrix opening angle confirmed that with rise in the Zn^{2+} and B^{3+} cations concentration photorefractive effect changes nonlinearly.

Distortion of the oxygen octahedrons was not detected for the concentration range 3.43–5.84 mol% ZnO. At the same time, alteration of cation sublattice units and bridge *B*-O-*B* (*B* = Nb, Li, Zn, vacancy) bond change. The latter reveals as increases the width of 876 cm^{-1} band that corresponds to stretching bridge vibrations of $A_1(TO)$ symmetry. Perhaps change of ion contribution to this bond explains a gradual increase in electro-optic coefficients at 3–7.6 mol% ZnO in lithium niobate crystals detected in papers [4, 31].

$LiNbO_3$ single crystals structure in the ZnO concentration area ~3.95–4.54 mol% is free of Nb_{Li} defects. The further increase of Zn concentration (4.76–5.19 mol%) leads to appearance of Nb_{Li} defects, although $LiNbO_3$:Zn (4.76–5.19 mol%) crystals are free of Li-vacancies.

By the mass spectrometry, the B^{3+} cations were shown to incorporate to structure of the single crystals in the trace amounts. Meanwhile change of B_2O_3 concentration in the charge (0.55–1.24 mol% B_2O_3) leads to change in photorefractive effect in the grown crystals, which is easily detected by the Raman spectra. Thus boron dopant does not incorporate to $LiNbO_3$ single crystals structure therefore influences structure and physical characteristics of the melt and the secondary structure of the grown crystals. The boron dopant decreases concentration of Nb_{Li} defects and photorefractive effect by increasing of the structure homogeneity. The further researches aimed at revealing the mechanism of this phenomenon is of high interest.

Acknowledgements Authors appreciate L.A. Aljoshina and A.V. Kadetova for data on full profile X-ray analysis of crystals $LiNbO_3$:Zn.

References

1. M. Aillerie, P. Bourson, M. Mostefa, F. Abdi, M.D. Fontana, J. Phys Conf. Ser. **416**, 012001 (2013)
2. L. Zhao, X. Wang, W. Wen, T.Y. Zhang, Appl. Phys. B **78**(6), 769 (2004)
3. Y. Zhang, Y.H. Xu, Y.Q. Zhao, J. Cryst. Growth **233**, 537 (2001)
4. T.S. Chernaya, T.R. Volk, I.A. Verin, V.I. Simonov, Cryst. Rep. **53**(4), 6121 (2008)
5. M.N. Palatnikov, I.V. Biryukova, S.M. Masloboeva, O.V. Makarova, D.V. Manukovskaya, N.V. Sidorov, J. Cryst. Growth **386**, 113 (2014)
6. M.N. Palatnikov, I.V. Biryukova, O.V. Makarova, N.V. Sidorov, V.V. Efremov, I.N. Efremov, N.A. Teplyakova, D.V. Manukovskaya, Chapter 7: research of concentration conditions for growth of strongly doped $LiNbO_3$:Zn single crystals. In: *Advanced Materials—Manufacturing, Physics, Mechanics and Applications*, ed. By I.A. Parinov, S.-H. Chang, V.Y. Topolov, vol 175 (Springer, Heidelberg, 2016), p. 87
7. M.N. Palatnikov, I.V. Biryukova, O.V. Makarova, V.V. Efremov, O.E. Kravchenko, V.I. Skiba, N.V. Sidorov, I.N. Efremov, Inorg. Mater. **51**(4), 428 (2015)
8. N.V. Sidorov, M.N. Palatnikov, N.A. Teplyakova, A.A. Gabain, I.N. Efremov, Inorg. Mater. Appl. Res. **7**(2), 170(2016)
9. N.V. Sidorov, OYu. Picoul, A.A. Kruk, N.A. Teplyakova, A.A. Yanichev, M.N. Palatnikov, Opt. Spectrosc. **118**(2), 273 (2015)
10. N.V. Sidorov, A.A. Kruk, P.O. Yu., M.N. Palatnikov, N.A. Teplyakova, A.A. Yanichev, O.V. Makarova, Optik Int. J. Light Electron. Opt. **126**(11–12), 1081 (2015)

11. N.V. Sidorov, T.R. Volk, B.N. Mavrin, V.T. Kalinnikov, *Lithium Niobate: Defects, Photorefraction, Vibrational Spectra* (Polaritons, Nauka, Moscow, 2003). (In Russian)
12. T.S. Chernaya, B.A. Maksimov, T.R. Volk, N.M. Rubinina, V.I. Simonov, JETP Lett. **73**(2), 110 (2003)
13. N.V. Sidorov, A.A. Yanichev, M.N. Palatnikov, A.A. Gabain, OYu. Picoul, Opt. Spectrosc. **117**(1), 76 (2014)
14. N.V. Sidorov, M.N. Palatnikov, N.A. Teplyakova, A.A. Gabain, I.N. Efremov, Opt. Spectrosc. **120**(4), 668 (2016)
15. N.V. Sidorov, M.N. Palatnikov, V.T. Kalinnikov, *Influence of the Secondary Structure on Optical Properties of Ferroelectric Crystals of Lithium Niobate with Low Photorefractive Effect.* Proceedings KSC RAS. Chemistry and Materials. Apatity (2015) (In Russian)
16. A.V. Syui, N.V. Sidorov, M.N. Palatnikov, D.S. Shtarev, E.A. Antonycheva, AYu. Gaponov, K.A. Chekchonin, Opt. J. **82**(5), 71 (2015)
17. M.-L. Sun, C.-T. Chia, M.-L. Hu, J.Y. Chang, W.-S. Tse, Z.P. Yang, H.H. Cheng, Appl. Phys. **78**(3), 355 (2004)
18. M. Quintanilla, M. Rodriguez, E. Cantelar, F. Cusso, C. Domingo, Opt. Express **18**(6), 5449 (2010)
19. N.V. Sidorov, M.N. Palatnikov, A.A. Yanichev, A.A. Gabain, A.A. Kruk, V.T. Kalinnikov, Dokl. Phys. Chem. **452**(5), 529 (2013)
20. N.V. Sidorov, A.A. Yanichev, M.N. Palatnikov, A.A. Gabain, Opt. Spectrosc. **116**(2), 281 (2014)
21. N.V. Sidorov, YuA Serebryakov, Ferroelectrics **160**, 191 (1994)
22. M.N. Palatnikov, N.V. Sidorov, V.T. Kalinnikov, Nonferrous Met. **10**, 54 (2000)
23. N.V. Sidorov, A.A. Kruk, A.A. Yanichev, M.N. Palatnikov, V.T. Kalinnikov, Dokl. Phys. Chem. **459**(1), 58 (2014)
24. M.N. Palatnikov, N.V. Sidorov, I.V. Biryukova, O.B. Shcherbina, V.T. Kalinnikov, Perspekt. Mater. **2**, 93 (2011)
25. V.A. Maksimenko, A.V. Syui, YuM Karpets, *Photoinduced Processes in Lithium Niobate Crystals* (Fizmatlit, Moscow, 2008). (In Russian)
26. A.V. Syui, N.V. Sidorov, E.A. Antonycheva, *Photorefractive Properties and Peculiarities of the Structure of Optically Nonlinear Lithium Niobate Crystals* (DVGUPS, Khabarovsk, 2011). (In Russian)
27. N.V. Sidorov, B.N. Mavrin, P.G. Chufyrev, M.N. Palatnikov, in *Phonon Spectra of Lithium Niobate Single Crystals,* ed. By V.T. Kalinnikov. KSC RAS Publ. Apatity (2012) (In Russian)
28. A.A. Kruk, N.V. Sidorov, A.A. Yanichev, M.N. Palatnikov, J. Appl. Spectr. **81**(1), 5 (2014)
29. M.D. Fontana, P. Bourson, Appl. Phys. Rev. **2**, 046002 (2015)
30. M. Fontana, K. Laabidi, B. Jannot et al., Solid State Commun. **92**, 827 (1994)
31. F. Abdi, M. Aillerie, P. Bourson et al., J. Appl. Phys. B **84**, 2251 (1998)
32. N.V. Sidorov, N.A. Teplyakova, A.A. Yanichev, M.N. Palatnikov, O.V. Makarova, L.A. Alyoshina, A.V. Kadetova, Inorg. Mater. (2016, in print)
33. Y.K. Voronko, A.B. Kudrjavtsev, V.V. Osiko, A.A. Sobol, E.V. Sorokin, Phys. Solid State **29** (5), 1348 (1987)
34. Y.K. Voronko, A.B. Kudrjavtsev, A.A. Sobol, E.V. Sorokin, Bull. GPI RAS **29**, 50 (1991)
35. Y.K. Voronko, A.B. Kudrjavtsev, V.V. Osiko, A.A. Sobol, E.V. Sorokin, Bull. Lebedev Phys. Inst. **2**, 34 (1987)
36. H. Kimura, H. Koizumi, T. Uchidab, S. Uda, J. of Cryst. Growth **311**, 1553 (2009)
37. V.S. Gorelik, P.P. Sverbil', Inorg. Mater. **51**(11), 1104 (2015)
38. N.V. Sidorov, M.N. Palatnikov, V.T. Kalinnikov, Opt. Spectrosc. **82**(1), 32 (1997)
39. A.A. Anikjev, N.V. Sidorov, YuA Serebryakov, J. Appl. Spectr. **56**(4), 670 (1992)
40. A.A. Anikjev, Eng. J. Sci. Innov. **19**(7), 50 (2013) (In Russian)
41. M. Umarov, V. Gruzienko, A. Vtjurin, A. Hodgabaev, Componen. Technol. **107**(6), 138 (2010)

Chapter 18
Method of Experimental Determining of the Microwave Absorbing Properties of Composite Materials

A.G. Abubakarov, J.A. Reyzenkind, A.M. Lerer, A.B. Kleshenkov, M.B. Manuilov and Anatoly V. Pavlenko

Abstract The method for characterization of radar absorbing properties of materials and the possibility of measuring complex dielectric and magnetic permeability of the material in a broad frequency range by using coaxial lines and a vector network analyzer is studied. The formulae of rating calculation of microwave absorption materials is proposed.

18.1 Introduction

18.1.1 Analysis of the Problem Current Status

Functional materials offering highly efficient absorption of ultra-high frequency (UHF) electromagnetic radiation become increasingly important. Currently, materials offering such property are widely used in microwave technology (phase shifters, filters, switches) [1, 2] and as various radar absorbing coatings [3–5]. The use of UHF absorbing materials is quite relevant not only for parts of various devices, design of radioelectronic equipment and microelectronics, protection of communications equipment from the external electro-magnetic interference, but also for personnel protection from radiation during working with powerful microwave devices as well. It should be noted that application of radar-absorbing materials and coatings for improvement of radar systems performance has a

A.G. Abubakarov (✉) · J.A. Reyzenkind · A.V. Pavlenko
Research Institute of Physics, Southern Federal University,
344090 Rostov-on-Don, Russia
e-mail: abubakarov12@mail.ru

A.M. Lerer · A.B. Kleshenkov · M.B. Manuilov
Faculty of Physics, Southern Federal University,
344090 Rostov-on-Don, Russia

A.V. Pavlenko
Southern Scientific Center of the Russian Academy of Sciences,
344006 Rostov-on-Don, Russia

I.A. Parinov et al. (eds.), *Advanced Materials*, Springer Proceedings in Physics 193, DOI 10.1007/978-3-319-56062-5_18

potential. In particular, it provides the required law of reflected signal distribution over the reflector antenna aperture by installing radar absorbing elements, distributed over the aperture in a certain way, as well as eliminates the impact of multipath electromagnetic wave interference (to eliminate "false" echo). In addition, range of work on reduction of visibility of special equipment of all kinds has been recently expanded as soon as modern strategically important objects are characterized by a large number of telltale features, which include large dimensions, specific outlines, differences in spectral-response coating characteristics and reflecting radar signals [6]. Such materials can be used for radio-camouflage of any surface facilities and aircraft, which can significantly reduce detection and destruction probability.

Such radar-absorbing materials and coatings as electrically conductive particulates (carbon black, graphite, metal particles), fiber (carbon, metal and metallized polymer) and magnetic (sintered ferrite sheets, ferrite powders, iron and carbonyl iron oxides) filling materials are used as electromagnetic wave absorbers. They can be used both singularly and jointly [5]. Main types of such materials are specified in the cited literature [7–12]. We will introduce only the most common groups, such as ferrite powders [13–17], composites [18–30] and various (generally carbonic) nanostructures [31–39].

Sometimes (quite rarely) along with the above listed materials, dielectrics and ferroelectrics are used as absorbing materials. For example, radar-absorbing material based on Zr-containing powders has been developed in Germany, and, in Japan; they use ceramics consisting of $Pb(Zr_{0.53}Ti_{0.47})O_3$ as a material absorbing energy in centimeter and millimeter range of wave lengths. Also, as an example, there are projects [40–47] where PZT-composites and solid solutions with ferroelectric behaviour had been used as electromagnetic radiation absorbing material.

Analysis of the literature testified that currently the achieved reproducible level of UHF absorption in passing regarding the composite materials is about L = 20–30 dB. At the same time, the most of the developed materials are passive media (absorbing EMR only).

In a number of studies [48–57], we revealed advantages of radar-absorbing media based on heterogeneous structures belonging to morphotropic areas with appropriate phase states of different symmetric properties. The examined UHF absorption had been associated with specific morphotropic phase changes, such as bond opening, formation and development of defective situation, variety of domain and interphase boundaries, promoting the effective UHF absorption. The objects were ferrielectric solid solutions of numerous binary and more complex systems with different compositions.

Taking into consideration the current common trend of creating multifunctional structures, we investigated large groups of multiferroic materials, which combine electric and magnetic subsystems, primarily based on bismuth ferrite, due to its high temperature of ferroelectric ($T_C \sim 1083$ K) and magnetic ($T_N \sim 643$ K) orderings. Peculiarly interesting were the media with bismuth ferrite doped with rare

earth elements (REE), which, on top of everything else, boost piezoelectric response in ferroelectric host materials and magnetoelectric effect in ferromagnetic materials. In [58] we found another interesting feature of REE impact on matrix compounds, which is non-monotonic (cyclic) dependence of their dielectric and piezoelectric properties on crystal-chemical REE characteristics (secondary periodicity of properties), providing opportunity for predicting properties of the objects initially. It was testified that dielectric properties vary in waves with increase of REE ionic radius in the range from La to Lu with sequentially alternate maximum and minimum of corresponding characteristics. Such an effect is related to the specific electronic REE structure, which is sequential filling of 4*f*-level, half in the first subgroup in regard to the large elements (Ce, Pr, Nd, Pm, Sm, Eu, Gd), and fully in the second subgroup (with "small" elements: Tb, Dy, Ho, Er, Tm, Yb, Lu). Similar behaviour of dispersive properties was not observed. However, preliminary studies with use of latest generation equipment testified implementation of such critical dissipative characteristic dependence on REE radius with maximum of UHF absorption in $BiFeO_3$/Ho. Currently, nature of the described phenomena is not evident and in the future, high values of formation mechanisms of the dissipative characteristics in the composition are expected to determine. We also suppose that the current level of microwave absorption can be further enhanced by topochemical nanotexturing (texture placement) of the object by use of highly oriented laminar Bi- and Fe-containing nanoparticles, prepared according to the special technology, during $BiFeO_3$/Ho synthesis. This will change isotropic grain structure of matrix host material into anisotropic with needle-shaped grains, which will lead to increase of the absorbing properties (2.5–3) times or more in comparison with the achieved level of microwave absorption of international standard. Thus, at this stage of the study, we shall determine fundamental rules of formation of extensive microwave absorption in multiferroic media and, at the level of further applied studies, we shall develop physical principles of generation of the functional shielding (radar-absorbing) materials, corresponding to the RF critical technology: production and processing of functional nanomaterials.

Currently, there is no common method [59–77] of measuring and evaluating the radar-absorbing properties, in this respect, the aim of this study is determine a single common method of measuring the radar-absorbing properties.

18.2 Routine of Experiment

18.2.1 UHF Absorption Parameters

At present time, electrodynamic modelling programme is used for development of various microwave devices. To use such programmes, it is necessary to have parameters of the medium, complex dielectric and magnetic permeabilty, in particular. Therefore, current development level of microwave devices design methods

requires knowledge of these two variables. Their direct definition is difficult in the microwave range. There are many different devices of that range, which allow measuring vector characteristics, i.e. complex elements and coefficient modules of dispersion matrix ($|S_{11}|^2$ и $|S_{21}|^2$). As is clear from the above, it is necessary to identify four actual parameters ε', ε'', μ' and μ'' at a fixed frequency. Provided that we use vector network analyzers measuring two complex characteristics at a fixed frequency of a device containing the test material, the complex reflection coefficient S_{11} and complex transmission coefficient S_{21}, i.e. four actual values, as well.

Therefore, the methods based on usage of vector network analyzer, measuring these particular values, are preferred. Having two complex parameters S_{11} and S_{12} (or four real values), it is necessary to identify four real parameters ε', ε'', μ' and μ'', i.e. technically there are four implicit equations for determination of four unknowns. In general, these are the preferred particular methods.

Consider the next existing approaches from the described perspective.

18.2.2 Common Research Methods

18.2.2.1 Condenser-Type Methods

Condenser-type methods are used for measuring dielectric constant of liquid and solid dielectrics flat in the low part of the EMR range. The applied modern device Precision LCR Meter Agilent E4980A [1], which uses a bridge measuring diagram, provides sufficient accuracy and can measure the complex dielectric constant and magnetic permeabilty of the laminar samples, where radius of the sample is much larger than thickness. Operating frequency range of the unit is 20 Hz–2 MHz. The measurements are carried out by replacement method, when the diagram balance adjustment is performed without the sample first, and with the sample after. Sample cell schematic representation for measuring complex dielectric constant of flat solid samples is shown in Fig. 18.1.

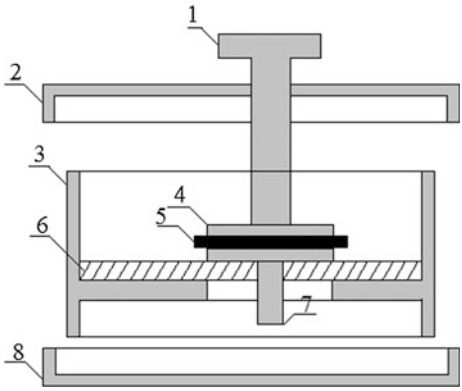

Fig. 18.1 Sample cell design [59]: *1* clamp screw; *2* upper cell cover; *3* cell body; *4* upper (removable) capacitor sheet; *5* test sample; *6* insulator; *7* lower (fixed) capacitor sheet; *8* lower cell cover

Such method is not appropriate for the purposes set out herein, since the measurements are carried out in a low frequency range and only dielectric constant can be measured, which is insufficient for characterization of radar-absorbing materials and devices.

18.2.2.2 Cavity Method

Common advantages of cavity measuring method provide their popularity, when choosing facilities for measuring electromagnetic characteristics [67–76]. Shape and design of resonator cavity depend on the physical state of matter, sample shape and values of complex dielectric constant and magnetic permeabilty. Long rods are tested in a rectangular resonator cavity [67, 68], disks in a rounded resonator [69–71], plates in a non-repetitive microstrip [72–74], strip-type cavity [76] and large-sized plates in open cavities [69, 76, 77].

18.2.2.3 Resonator Cavity Perturbation Method

Resonator cavity perturbation method requires extra small-sized samples in order to cause only a small perturbation of the fields, leading to a change of the measured resonant frequency value and cavity Q-factor (Fig. 18.2).

Calculation of constitutive parameters is conducted through the complex elements of dispersion matrix ($|S_{11}|^2$ and $|S_{21}|^2$), such a method does not allow measuring complex elements of dispersion matrix in a wide frequency range, as soon as the waveguide with inserted sample is associated with the principle wave frequency range.

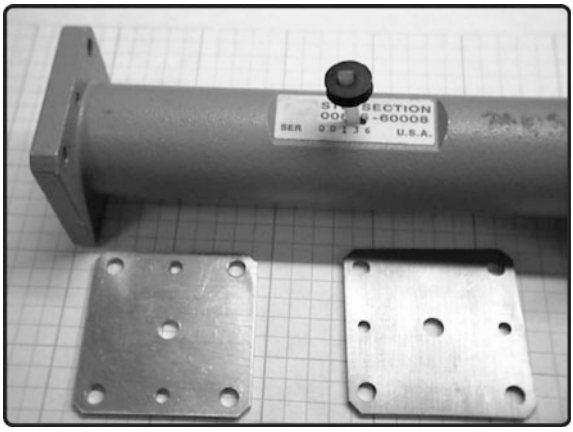

Fig. 18.2 Parts of frequency range resonator cavity from 8.2 to 12.4 GHz, and the inserted sample

18.2.2.4 Quasi-Optic Method

It is convenient to apply quasi-optic approach [77], which combine methods with use of horn converters [78–80] in order to study the local and integral electromagnetic characteristics. Horn techniques are relatively simple, therefore became widely used. For the purposes of measuring they use "passing" method (Fig. 18.3), when the horn converters are located on both sides of the sample, or "reflection" method, when the transmitting and receiving antennas are located on one side of the examined sample.

In some cases, they use a single horn converter as a receiving and transmitting device. Usually, horn converters are separated from the samples by some distance. However, while studying small-sized samples, the tested materials are directly located on the aperture of the horn (Fig. 18.4).

Lens antennas are gained widespread currency in antenna-equipment of microwave range [81, 82]. They consist of an electromagnetic lens and primary feed, the phase centre of which is aligned with the lens focus. Electromagnetic lens is a radio-transparent corpus bounded by two surfaces: the lightened surface of curved profile and flat surface of aperture. The lens should meet the following basic requirements: they should have low heat losses and be well aligned with the

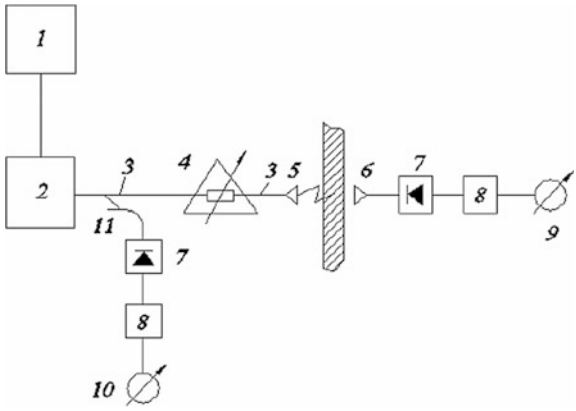

Fig. 18.3 "Passing" diagram of the inspection unit [79]: *1* power supply unit; *2* generator; *3* wave-guide duct; *4* attenuator; *5*, *6* transmitting and receiving antenna; *7* detector; *8* amplifier; *9*, *10* recording devices

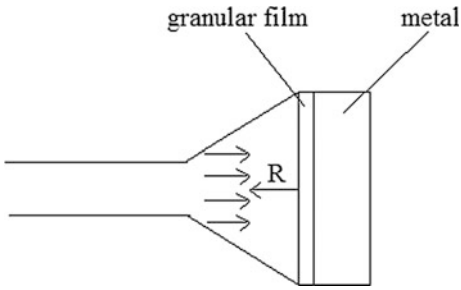

Fig. 18.4 Horn method for measuring in 3–80 GHz frequency ranges [73]

environment. The primary feed is designed for the required amplitude distribution at the lens aperture. It should have a single-point phase centre and provide the required polarization of the radiation field. Such weakly directional antennas as horn antennas, open-ended waveguides, vibrator with reflecting curtain etc., are used as primary feed.

Unlike in optical region, the lens can be both retarding and accelerating in the radio region. In practice, dielectric (retarding) and metal plate (accelerating) lens are the most commonly used. Lens antennas aperture sizes are usually large in comparison with the wavelength therefore they are highly directional antennas and designed for narrow beams.

The lens antennas operating principle is borrowed from optics and involves transformation of angular-spread beam from the low-directivity source into a parallel light beam or transformation of spherical wave front of the primary feed into a flat wave front at the output of the lens. Thus, it is possible to get a flat in-phase aperture of the required size and create a narrow beam.

18.2.2.5 Microstrip Line Method

Currently, microstrip transmission line is widely used in UHF and EHF technology [83]. A microstrip transmission line (MTL) is a rectangular-sectioned ribbon-type conductor (strip) installed on a substrate with high dielectric permittivity, which has a grounded metal plane (screen) on the reverse side. Figures 18.5 and 18.6 illustrate a E8363B measuring unit, its principle diagram, MTL and location of the examined sample. The sample is placed on a 50 Ω microstrip line at the point where the high-frequency electric field has maximum value. MTL section with the sample can be considered as a linear reciprocal (reversible) symmetrical four-terminal device [84–86].

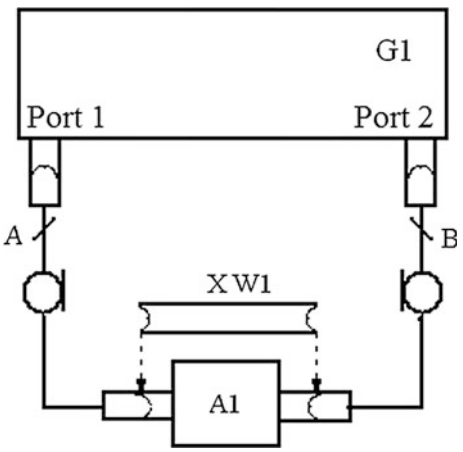

Fig. 18.5 Principle diagram of the E8363B measuring unit

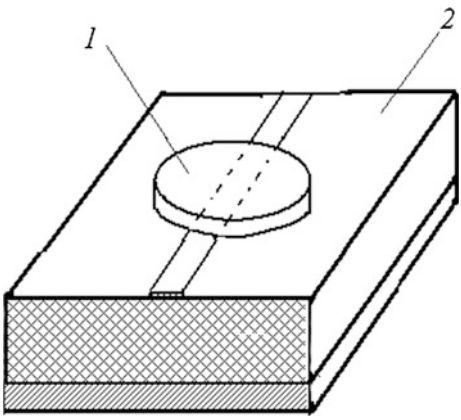

Fig. 18.6 Examined sample on the MTL (*1* examined sample; *2* MTL)

The main parameter characterizing microwave absorption by the EMR research objects is an element of the dispersion matrix (S_{21}), which is specifically introduced for the analysis of microwave circuits [87]. Method of its determination is based on presentation of MTL as a four-terminal [88], where, to determine the $\dot{S}_{11}$ element, it is necessary to measure module and phase of the reflection coefficient from the input of the examined four-terminal, when switching, in output of its reflection absorbing termination: $\dot{S}_{11} = \left|\dot{S}_{11}\right| e^{j\phi_{.11}}$. The $\dot{S}_{22}$ element is determined in a similar way but at the reverse switching of the four-terminal device: $\dot{S}_{22} = \left|\dot{S}_{22}\right| e^{j\phi_{22}}$. For determining $\dot{S}_{21}$ and $\dot{S}_{12}$ elements, it is necessary to measure complex transfer coefficients of the four-terminal at the direct and reverse switching and their phases as well.

18.2.2.6 Waveguide Slotted Line

Wave guide methods [60] are applied for measuring dielectric permittivity of liquid crystals [61], ferroelectrics [62], composites based on hexaferrite and carbon nanostructures [63, 64], ferromagnetic fluids (FMF) (Fig. 18.7) [65].

Such units allow us to examine materials with heavy losses and wide frequency range. Currently, they use circuits with measuring line [66] and modern scalar and vector network analyzers of home [63] and foreign manufacture [64]. Broad-bandness is provided by a set of sample cells of different standards. Waveguide slotted lines complicate automation of the measurements and significantly reduce measurement accuracy.

Waveguide measurement methods are limited to the frequency range, which emerges difficulties with production of samples and increases inaccuracy in determining the standing wave ratio according upon voltage and change of the minimum value.

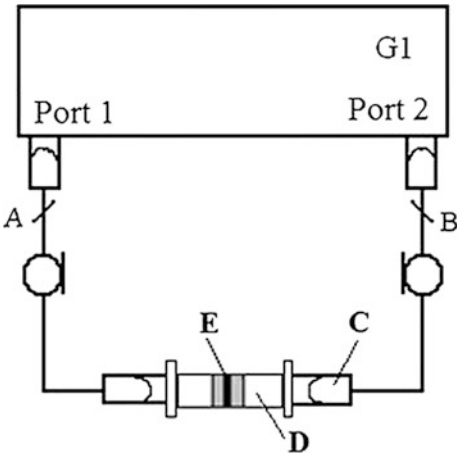

Fig. 18.7 Flow diagram of the waveguide line installation [65]: *A, B* connecting cables (coaxial), *C* adapter from the coaxial cable to the waveguide line, *D* waveguide line, *E* examined sample

In general, the upper limit of the waveguide method extends up to 60 GHz, however, at the frequency of about 25–30 GHz, there are difficulties associated with small sizes of waveguides. There are common problems of sample preparation, fitting them into the sample cell for electrical contact of the sample and wave guide, arising during examination of solid materials.

18.2.2.7 Coaxial Line

Coaxial line method includes placing material inside the closed part of the coaxial air line (Fig. 18.8). Dielectric and magnetic permeability of the medium is calculated of the reflected (S_{11}) and transmitted signal (S_{21}) measurement results.

Coaxial transmission lines cover a wide frequency range, extend up to millimeter-wave frequencies and simplify the sample processing. A typical

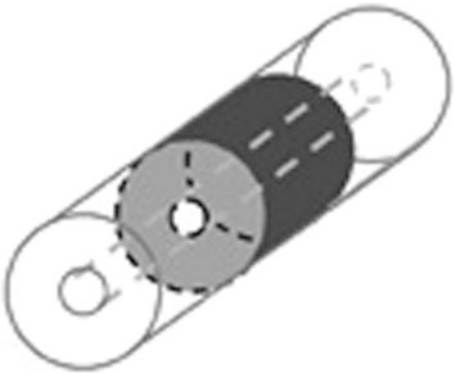

Fig. 18.8 Coaxial transmission line method

measuring system involving the coaxial transmission line method comprises a vector network analyzer, a coaxial air-line and an external computer.

It is necessary to determine four actual parameters ε', ε'', μ' and μ'', calculated of the reflected (S_{11}) and transmitted signal (S_{21}) measurement results. Prior to measurements, it is necessary to calibrate the measuring line, as soon as calibration significantly reduces measurement failures. After calibration, we use the measuring line for measurement of the reflected (S_{11}) and transmitted (S_{21}) signals without the sample.

Samples are tightly placed into the coaxial line. Using a vector network analyzer (P4M-18, Micran), we carry out measurements in a wide frequency range of module and phase, S_{11} and S_{21}. Complex dielectric and magnetic permeability is identified by minimizing the sum of squared deviations of the measured and calculated S_{11} and S_{21}. Calculations are performed by commercial software CST MicrowaveStudio. This task is multivariable as soon as ε and μ depend on frequency.

The second approach for solving the problem is measurement of S_{11} and S_{21} at a given frequency in different positions of the sample in the waveguide. The values of ε and μ are determined by comparison of experimental and calculated data. Numerical implementation of this approach is simpler. It is possible to combine these two methods.

We used the following parameters as additional in order to characterise microwave absorption in the materials. In generator linear modulation mode, we measured reflection (S_{11}) and transmission (S_{21}) coefficients of microwave radiation for the measuring line without the sample, record and save the data as a *prn file. Thereupon, we measured frequency dependences of $|S_{21}|$ and $|S_{11}|$ modules of the measurement line with the sample. In the absence of dissipative losses, energy conservation principle provides the following relationship between the modules of dispersion matrix coefficients: $S_{11}^2 + S_{21}^2 = 1; S_{12}^2 + S_{22}^2 = 1$. Hereafter we performed calculations according to the following formulae.

If matrix elements of the measuring line without the sample are S_{ij}^0, and dispersion matrix elements of the measuring line with the sample are S_{ij}, then absorption of the measuring line without the sample; $L_0 = 1 - \left|S_{11}^0\right|^2 - \left|S_{21}^0\right|^2$; absorption of the measuring line with the sample: $L_1 = 1 - |S_{11}|^2 - |S_{21}|^2$; UHF absorption of the sample is calculated as $L = L_1 - L_0 = \left(1 - |S_{11}|^2 - |S_{21}|^2\right) - \left(1 - \left|S_{11}^0\right|^2 - \left|S_{21}^0\right|^2\right) = |S_{11}|^2 - |S_{21}|^2 - \left|S_{11}^0\right|^2 - \left|S_{21}^0\right|^2$; full absorption of the sample is $1 - L$.

Next transfer the UHF absorption L values into logarithmic scale using formula: $|L| = 10lg|L|^2 = 20|L|(\mathrm{dB})$. The logarithmic value transfer is performed for better visualization of graphic material.

18.3 Conclusions

Analysis of the existing approaches carries inference that, if it is necessary to determine complex dielectric and magnetic permeability, the most common measuring methods are wave guide and coaxial line. The wave guide method depends on frequency range of the principal wave and small size of the sample, which complicates the process of sample preparation and wave-guide line. Coaxial line allows to carry out measurements and calculations over a wide frequency range, using vector network analyzers of home and foreign production. It is reasonable to use this method for comprehensive characterization of microwave absorption in the materials.

Acknowledgements The study had been performed with equipment belonging to the "Electro-magnetic, Electromechanical and Thermal Properties of Solids" CUC, Research Institute of Physics, Southern Federal University, with support of Ministry of Education and Science of the Russian Federation: project No. 1927, 213.01-2014/012-VG and 3.1246.2014/K (basic and project parts of the state task), and the scholarship of the President of the Russian Federation SD—3330.2016.3, and also RFBR grant No. 16-32-60095 mol_a_dk.

References

1. OYu. Buslov, V.N. Keyes, A.B. Kozyrev, I.V. Kotelnikov, P.V. Kulik, Tech. Phys. **75**(9), 89 (2005)
2. A.B. Kozyrev, *Izvestiya SPbGETU «LETI»*, 115–122 (2002) (in Russian)
3. O.G. Vendik, M.A. Nicholas, M.S. Gashinova, Tech. Phys. Lett. **29**(4), 5 (2003)
4. N.N. Antonov, I.M. Buzin, O.G. Vendik et al., in *Ferroelectrics in Microwave Technology*, vol. 272, ed. by O.G.M. Vendice (Soviet Radio, Moscow) (1979) (in Russian)
5. V.S. Pirumov, A.G. Alekseev, B.V. Aizikovich, Foreign Electron. **4–5**, 2 (1994)
6. L.K. Mikhailovsky, Foreign radioelectronics. Success. Mod. Radio Electron. **9**, 21 (2000). (in Russian)
7. V.A. Nikitenko, A.S. Zubov, A.N. Bogolyubov, J. Radio Electron. **4**, 1 (2015)
8. V.G. Andreev, R.M. Mirgazov, S.B. Menshova, S.B. Bibikov, M.V. Prokof'ev, *Proceedings of Interanational Sci.-Tech. Conference on «INTERMATIC»,* Moscow 186, (2014) (in Russian)
9. R. Menezes, P.M. Souto, R.H.G.A. Kiminami, in *Sintering of Ceramics—New Emerging Techniques,* vol. 3 (2012)
10. A.N. Titov, S.B. Bibikov, K.A. Cherepanov, N.N. Evtikhiev, O.N. Smolnikova, M. Prokofiev, in *Methods and Devices for the Remote Sensing,* Is. 11, 224 (2009)
11. P. Saville, *Review of Radar Absorbing Materials*. DRDC Atlantic TM (2005) http://dtic.mil/dtic/tr/fulltext/u2/a436262.pdf
12. M.I. Bichurin, *Vestnik of Novgorod State University*. No. 19 (2001) (in Russian)
13. S. Wei, Y. Liu, H. Tian, H. Tong, Y. Liu, X. Binshi, J. Magn. Magn. Mater. **377**, 419 (2015)
14. Sameer Duggal, Gagan deep aul. Int. J. Eng. Adv. Technol. **3**(5), 12 (2014)
15. G. Vazquez-Victorio, *Ferromagnetic Resonance—Theory and Applications* (2013)
16. V.G. Kostishin, R.M. Mirgazov, V.G. Andreev, T.A. Marchenko, A.S. Komlev, A.N. Nikolaev, *Eng. J. Don*. **26**(3) (2013) (in Russian)
17. J. Song, L. Wang, X. Naicen, Q. Zhang, J. Mater. Sci. Technol. **26**(9), 787 (2010)
18. Y. Liu, X. Zhao, X. Tuo, *J. Textile Inst.* p. 1 (2015)

19. M. Gupta, S. Sankaranarayanan, in TMS2015 Annual Meeting Supplemental Proceedings, 187 (2015)
20. Z. Yu, Ph.D thesis. Southern Federal University Press, Rostov-on-Don (2014) (in Russian)
21. S. Qian, V.A. Bath, A.L. Samofalov, I.V. Semchenko, S.A. Khakhomov, *Prob. Phys. Math. Technol.* **4**(21), 40 (2014) (in Russian)
22. V.V.R. Repi, A. Manaf, B. Soegiono, Adv. Mater. Res. **896**, 440 (2014)
23. A. Aman, S. Majcherek, M.-P. Schmidt, S. Hirsch, Proc. Eng. **87**, 124 (2014)
24. W. Yang, Y. Shuhui, R. Sun, D. Ruxu, Ceram. Int. **38**, 3553 (2012)
25. V.A. Zhuravlev, V.I. Suslyaev, O.A. Dotsenko, A.N. Babinovich, Russ. Phys. J. **53**(8), 874 (2011)
26. Z. Ma, Y. Zhang, C.T. Cao, J. Yuan, Q.F. Liu, J.B. Wang, Phys. B **406**, 4620 (2011)
27. M.B. Shelar, R.N. Jadhav, V. Puri, Prog. Electromagnet. Res. C **17**, 55 (2010)
28. D.O. Smirnov, Ph.D thesis. Southern Federal University Press, Rostov-on-Don (2009) (in Russian)
29. S.M. Abbas, C. Mahesh, A. Verma, R. Chatterjee, T.C. Goel, Compos. A **37**, 2148 (2006)
30. L.M. Lynkov, V.A. Bogush, T.V. Borbotko, E.A. Ukrainets, N. Kolbun, *Reports BSUIR*, 152 (2004) (in Russian)
31. L.V. Kozhitov, A.P. Kuzmenko, D.G. Muratov, V.V. Rodionov, A.V. Popkov, E.V. Yakushko, Scientific Statement BSU. Ser. Math. Phys. **37**(125), 151 (2014). (In Russian)
32. Y. Sun, C. Feng, X. Liu, S.W. Or, C. Jin, Mater. Res. **17**(2), 477 (2014)
33. E.A. Zakharychev, S.A. Ryabov, V.L. Zefirov, D. Semchikov Yu, M.S. Belov, D.V. Kirpiche, A.A. Zuev, Inorg. Mater. Appl. Res. **5**(5), 405 (2013)
34. W.F. Liang, R.B. Yang, S.T. Choi, Ferroelectrics **434**, 100 (2012)
35. Z. Ma, C. Cao, J. Yuan, Q. Liu, J. Wang, Appl. Surf. Sci. **258**, 7556 (2012)
36. V. Petrov, G. Nikolaychuk, S. Yakovlev, L. Lucev, Components and Technology **10**, 147 (2008). (in Russian)
37. N.E. Kazantseva, N.G. Ryvkina, I.A. Chmutin, *Technol. Electron,* **48**(2), 196(2003) (in Russian)
38. A.S. Basaev, V.A. Labunov, V.V. Barkaline, I.A. Taratyn, A.M. Sagachenko, Abstr. Rep. Scientific Technol. Sect. **1**, 11 (2008). (in Russian)
39. V.A. Labunov, A.L. Danilyuk, E.L. Prudnikova, A.S. Basayev, V.N. Rodionov, MEPHI. *Minsk*, 1 (2011) (in Russian)
40. Patent CN 104211386 (2014)
41. Patent CN 104164708 (2014)
42. A. Mandal, D. Ghosh, A. Malas, P. Pal, C.K. Das, *J. Eng.* Article ID 391083, 8 pp (2013)
43. Z.J. Wanga, Y. Otsukab, Z. Caob, M.W. Zhua, N. Yoshikawab, H. Kokawa, Proc. of SPIE. **7267**, 726702-1 (2008)
44. H.Y. Chang, S.Y. Cheng, C.I. Sheu, Mater. Lett. **62**, 3620 (2008)
45. A.S. Yu, V.V. Gagulin, S.K. Korchagina, V.V. Ivanov, in *Proceedings of International Symposium on Order, Disorder and Properties of Oxides (ODPO-2003)*, p. 282 (2003) (in Russian)
46. P.K. Pramod, Z. Ounaies, V.V. Varadan, V.K. Varadan, Smart Mater. Struct. **10**, 878 (2001)
47. B. Vaidhyanathan, A.P. Singh, D.K. Aqraqwal, T.R. Shrout, R. Roy, J. Am. Ceram. Soc. **84** (6), 1197 (2001)
48. A.G. Abubakarov, H.A. Sadykov, L.A. Reznichenko, A.V. Pavlenko, M. Neuken Yu, M.B. Manuilov, Izv. Universities. Ser. Physics. **56**(8/2), 239 (2013)
49. A.G. Abubakarov, H.A. Sadykov, L.A. Reznichenko, A.V. Pavlenko, M. Neuken Yu, M.B. Manuilov, V.V. Gershenovich, S.V. Khasbulatov, Izv. Universities. Ser. Phys. **56**(8/2), 244 (2013)
50. A.G. Abubakarov, A.V. Pavlenko, L.A. Reznichenko, Y.M. Neuken, M.B. Manuilov, I.A. Verbenko, L.A. Shilkina, in *Proceedings of Second International Youth Symposium on "Physics of without Lead Piezoactive and Related Materials (Analysis of the Current State and Prospects of Development)" ("LFPM-2013").* Tuapse, vol. 1, p. 106 (2013) (in Russian)

51. A. Abubakarov, I.A. Verbenko, Y.M. Neuken, M.B. Manuilov, D.S. Kuznetsov, H.A. Sadykov, *Abstracts of XX All-Russian Conference on Physics of Ferroelectrics (VKS–XVIII)*, Krasnoyarsk, p. 93 (2014) (in Russian)
52. A.G. Abubakarov, M.B. Manuilov, Y.M. Neuken, A.V. Pavlenko, V.V. Gershenovich, I.A. Verbenko, L.A. Reznichenko, . *Proceedings of the IX International Symposium on fundamental and applied problems of science dedicated to the 90th anniversary from the birthday of academician V. P. Makeeva. Nepryakhino*, Moscow: Russian Academy of Sciences, *1*, 52 (2014). (In Russian)
53. A.G. Abubakarov, Y.M. Nonin, M.B. Manuilov, I.A. Verbenko, M.A. zakrieva, S.A. Zeilinger, H.A. Sadykov. in *Proceedings of International Scientific-Technical Conference "Fundamental Problems of Electronic Instrumentation" (INTERMATIC-2014)*, Moscow, p. 107 (2014) (in Russian)
54. A.G. Abubakarov, M.B. Manuilov, YuM Noyken, A.V. Pavlenko, V.V. Gershenovich, I.A. Verbenko, L.A. Reznichenko, Vestnik SSC RAS **11**(2), 17 (2015). (In Russian)
55. A.G. Abubakarov, M.B. Manuilov, M. Noyken Yu, L.A. Reznichenko, A.A. Matter, in *Proceedings of Fourth International Youth Symposium "Physics of Lead-Free Piezoactive and Related Materials (Analysis of the Current State and Prospects of Development)"* Rostov-on-Don, vol. 1, p. 44 (2015) (in Russian)
56. A.G. Abubakarov, A.A. Pavelko, L.A. Shilkina, M.B. Manuilov, J.M. Noykin, L.A. Reznichenko, S.A. Zeilinger, in *Proceerdings of Fourth International Youth Symposium "Physics of Lead-Free Piezoactive and Related Materials (Analysis of the Current State and Prospects of Development)"* Rostov-on-Don, vol. 1, p. 39 (2015) (in Russian)
57. A.G. Abubakarov, Y.M. Nonin, M.B. Manuilov, I.A. Verbenko, M.A. Zakrieva, S.A. Zeilinger, H.A. Sadykov, L.A. Shilkina, I.M. Aliyev, L.A. Reznichenko, in *Proceedings of IX Russian Conference of Young Scientists "Science and Sustainable Development"* (Kabardino-Balkarian regional branch of the Russian organization "Russian Union of Young Scientists", Nalchik), p. 9 (2015) (in Russian)
58. K.P. Andryushin, A.A. Pavelko, V.A. Pavlenko, I.A. Verbenko, L.A. Shilkina, S.P. Kubrin, L.A. Reznichenko, Tech. Phys. Lett. **37**(13), 54 (2011). (in Russian)
59. K.R. Zhdanov, A.I. Romanenko, G.M. Zharkova, V.I. Buslaev, V.A. Zhuravlev, News of higher educational institutions. Physics **56**(8), 48 (2013). (in Russian)
60. V.S. Solosin, *Reflectometry on the basis hollow metal-dielectric waveguides range*. Ph.D Thesis. Fryazino, p. 25 (2004) (in Russian)
61. V.A. Emelyanov, A.V. Shubin, Electronic journal "Bulletin of Moscow State Regional University". Physics and Mathematics **3**, 116 (2012). (in Russian)
62. Y.M. Poplavko, V.I. Molchanov, V.M. Pashkov, et al., *Appliances and Microwave Devices*, vol. 1, p. 39 (2010) (in Russian)
63. G.E. Kuleshov, V.I. Buslaev. in *Modern Problems of Radio Electronics: Collection of Scientific Works*, ed. by G.J. Shaydurova (SFU, Krasnoyarsk), p. 318 (2012) (in Russian)
64. EYu. Korovin, V.I. Buslaev, I.P. Klonowski, E.V. Chebotarev, News of higher educational institutions. Physics **55**(9/2), 247 (2012). (in Russian)
65. O.I. Kotov, V.N. Chernyshov, Vestnik Tomsk State Univ. Technol. **16**(2), 303 (2010). (in Russian)
66. I.V. Bychkov, D.V. Dubrovsky, I.S. Izotov, A.A. Fedi, Vestnik Chelyabinsk State University. Physics **9**(7), 7 (2011). (in Russian)
67. E.P. Found, V.I. Buslaev, A.V. Bir, J. Struct. Chem. **45**, 102 (2004)
68. V.A. Zhuravlev, V.I. Suslyaev, Russ. Phys. J. **49**(9), 1032 (2006)
69. V.I. Buslaev, G.E. Dunaevsky, E.V. Emelyanov, G.E. Kuleshov, News of higher educational institutions. Physics **54**(9), 53 (2011). (in Russian)
70. V.I. Buslaev, E.Y. Korovin, E.N. Sokolenko, *STO TSU 031-2009* (in Russian)
71. J. Krupka, J. Eur. Ceram. Soc. **23**, 2607 (2003)
72. G.E. Kuleshov, Ph.D. Thesis. Tomsk (2013) (in Russian)
73. O.A. Dotsenko, G.E. Kuleshov, V.I. Buslaev, News of higher educational institutions. *Physics*, **9/2**, 170 (2008) (in Russian)

74. G.E. Kuleshov, V.I. Buslaev, O. Dotsenko. News of higher educational institutions. *Physics*, **9/2**, 217 (2010) (in Russian)
75. A.S. Sovlukov, A.A. Maslov, V.V. Yatsenko, A.P. Vlasov, *Vestnik of The Moscow State Tech. Univ.* **12**(2), 271 (2009) (in Russian)
76. E.V. Emelyanov, G.E. Dunaevskii, V.I. Suslyaev, et al. News of higher educational institutions. *Physics*, **9/3**, 315 (2010) (in Russian)
77. G.E. Dunaevsky, NTL Press, Tomsk, p. 304 (2006) (in Russian)
78. S.V. Mishchenko, N. Malkov, Tambov State Technical University Press, p. 128 (2003) (in Russian)
79. V.A. Tabarin, S.D. Dementieva, *Oil and Gas Business* (2009) (in Russian)
80. V. Petrov, G. Nikolaichuk, S. Yakovlev, L. Lucev, Comp. Technol. **10**, 147 (2008). (in Russian)
81. O.A. Yurtsev, *Resonant Aperture Antenna. Part 2: Methodical Manual for the Course "Antennas and Microwave Device",* Issue 3 (Belarusian State University of Informativs and Radioelectronics, Minsk), p. 89 (2000) (in Russian)
82. V.N. Egorov, V.L. Masalov, A. Nefyodov Yu, A.F. Shevchun, M.R. Trunin, *Rev. Scientific Instrum.* **75**(11), 4423 (2004) (in Russian)
83. I.N. Filatov, et al., in *Microelectronic Microwave Devices*, ed. by L.A. Koledov (Higher School, Moscow), p. 94 (1987) (in Russian)
84. A.G. Abubakarov, Y.A. Reyzenkind, L.A. Reznichenko, M.B. Manuilov, L.A. Shilkina, I.A. Verbenko, Y.M. Noykin, V.A. Aleshin, A.A. Pavelko, Res. J. Pharm. Biol. Chem. Sci. **6**(1), 1731 (2015)
85. A.G. Abubakarov, H.A. Sadykov, A.V. Pavlenko, YuM Noykin, M.B. Manuilov, L.A. Reznichenko, News of higher educational institutions. Physics **55**(9/2), 253 (2012). (in Russian)
86. A.G. Abubakarov, M.B. Manuilov, M. Noyken Yu, A.V. Pavlenko, V.V. Gershenovich, I.A. Verbenko, L. A. Reznichenko, *Bull. Southern Scientific Center RAS*, **11**(2), 17 (2015) (in Russian)
87. A.S. Elizarov, *Automation of Measurements of Parameters of Linear Non-reciprocal Microwave Two-Port Networks* (Soviet Radio, Moscow, 1978). (in Russian)
88. A. Weissflog, in *Circuit Theory and Technique of Measurements in the Decimeter and Centimeter Ranges*, ed. by M.A. Silaeva (Soviet Radio, Moscow) (1961) (in Russian)

Chapter 19
Thermovoltaic Effect in Field Effect Metal–Dielectric–Semiconductor–Metal Structure

Gevork Ya Karapetyan, Ivan A. Parinov, Nikolay S. Runkevich and Guido Parchi

Abstract The chapter is devoted to research of thermoelectric converter based on metal-dielectric-semiconductor-metal (MDSM) structure that can work without creating a temperature difference. An overview of the studies on thermoelectric converters is presented. We present the experiments with field-effect transistors KP304 (2N4268), the structure of which is similar to the proposed structure.

19.1 Introduction

State of the art in the field of thermoelectric conversion is described in the reviews [1] and [2]. Although first review was written by 2008, and the second by 2010, in both reviews the principle of thermoelectric conversion is not questioned. This is the obligatory presence of the heater and the refrigerator. This principle of thermoelectric conversion implies that the presence of the thermal conductivity significantly decreases the efficiency of thermoelectric conversion, because a part of the heat passes from the hot end to the cold one, is not converted into electrical energy. The main parameter of thermoelectric conversion is the thermoelectric figure of merit $ZT = q\alpha^2/k$, where α is the Seebeck coefficient, q is the conductivity, k is the thermal conductivity of the thermoelectric material. For many decades until the end of the last century the properties of thermoelectric materials on dimensionless parameter quality ZT was at the level of ~ 1. It corresponds to the efficiency of about 5%, when is used in practical devices. It is not enough to compete with conventional generators and coolers. To be competitive, thermoelectric generator, of course, must match the settings available solutions, whose efficiency is not worse than 35–37%, and, in addition, operate at rather high temperatures. For

G.Y. Karapetyan (✉) · I.A. Parinov · N.S. Runkevich
I.I. Vorovich Institute of Mathematics, Mechanics and Computer Science,
Southern Federal University, 8a, Milchakov Street, Rostov-on-Don 344090, Russia
e-mail: gkarapetyan@sfedu.ru

G. Parchi
Prometeon srl, Via Santo Stefano, n.16, Bologna, Italy

I.A. Parinov et al. (eds.), *Advanced Materials*, Springer Proceedings in Physics 193, DOI 10.1007/978-3-319-56062-5_19

example, assume that the thermoelectric generator will run hot and cold temperatures 2000 K and 900 K, respectively. This equates to value of efficiency (Carnot efficiency) 0.55, which corresponds to the efficiency of conventional turbines of solid or liquid fuel. In this case, the efficiency of thermoelectric generators should be 0.64, and $ZT = 12$. So as in semiconductor materials, which are currently mainly used for thermoelectric converters, the higher the conductivity, the lesser the thermopower, the basic reserve to further increase the quality factor is a reduction in the thermal conductivity of the material. In this direction, in recent, there were the most active researches. Physically this means that in a solid body can create such a heterogeneity, which would be effective in scattering phonons, reducing their mean free path and, hence, thermal conductivity, and at the same time virtually no effect on the scattering of charge carriers, would not change their mobility and hence the conductivity. For materials with such a combination of properties in modern literature are adopted special terms: electron—crystal, phonon—glass. They meet the physical picture described above, i.e. the strong scattering of phonons in disordered structures of the type of glazing, and weak scattering of charge carriers, as in perfect crystals. The creation of materials with strong scatterers of phonons is based on the filling the interstices (micropores) of the initial crystal-matrix of heavy atoms, the effective radius which smaller than the radius of the micropores. It ensures their weak connection with the matrix and the emergence of large anharmonic state for local oscillation modes. This can improve conversion of heat flow into electrical energy in the manufacture of the thermoelement branches of *p*- and *n*-types in the form of solid solutions containing magnesium, silicon, lead and barium, as well as one or more additional alloying materials: $Ba_{2r}Mg_{2(1-r)}Si_{1-x}Pb_x$, where r, $(1 - r)$, $(1 - x)$ and x represent the atomic proportions of each of the elements: barium, magnesium, silicon and lead in the alloy, respectively, and in which the compound if necessary contains one or more additional alloying materials [3]. Due to careful selection of the parameters r and x in the formula components, it becomes possible to obtain compositions having an extremely low values of thermal conductivity, the minimum value which should be about 0.002 W cm^{-1} K^{-1}. Atomic or molecular proportion of the doping agent, or impurity, and the concentration of free charge carriers in the composition should preferably be in the range from 10^8 to 10^{-1} and from 1×10^{15} to 5×10^{20} carriers per cubic centimeter, respectively. Through careful control over the doping level and on the concentration of free charge carriers becomes possible to provide the maximum value of thermoelectric power factor S2, which, together with a minimum conductivity of approximately 0.002 W cm^{-1} K^{-1} is reasonably expected to lead to improved thermoelectric quality indicator *ZT* to about 3 at room temperature through use of the composition. To reduce heat conductivity due to the scattering of phonons, it was also suggested to make for semiconductors other composition, based on copper, zinc, tin and selenium [4]. Such crystals are proposed to call as the crystals with the structure of skutterudite. As noted in [1, 2], thermoelectric studies have only experienced a resurgence with the advent of new concepts and theories aimed at controlling the transfer of electrons and phonons in nanostructures and bulk materials. As in the quantum nanostructures and classic materials with size effects, control of electronic and

phonon transfers is based on the creation of special structures. Interest in the creation of structures with sizes of elements in the field of nanometers and high density of these elements was emerged in the 1990 s in connection with the discovery of quantum-size effects in such systems, on the base of which, at the present, it is possible to divide these patterns into the following types:

(i) quantum dots, whose dimensions in all three directions are several interatomic distances (depending on the scale of consideration, the structure is considered to be zero-dimensional or three dimensional);
(ii) quantum wire, the dimensions of which in two directions composed of several interatomic distances, and the size in the third direction is a macroscopic value;
(iii) quantum wall, otherwise quantum well structure, the size of which in one direction is a few interatomic distances, and the dimensions in the other two directions are of macroscopic size.

Reviews [1, 2] provide a large amount of references on nanostructured materials, but in recent years the number of works devoted to this subject is sufficiently large. For example, it was developed in [4, 5] a special measurement structure for measuring the parameters of nanowires from indium arsenide, allowing one to measure the thermopower and conductivity and the measurement of the above quantities. The same structure was discussed for silicon carbide in [6], and it was grown from bismuth nanowires with a diameter of 725 nm and a length of 2.7 mm in [6]. It is shown [6] that the nanowires can increase the indicator ZT up to 2.7. In [7, 8], it was shown theoretically that two-dimensional superlattice with quantum walls in semimetals can increase the thermoelectric figure of merit ZT up to 9, when the thickness of the quantum wall is no more than 2–3 nm. In [9], it is shown that the use of double quantum dots can be used in thermoelectric generators using different quantum dots as n- and p-branches. Quantum dots are also dedicated to the works [10, 11]. Thus, in [10], it was proposed to obtain self-organized quantum dots in InAs films on GaAs substrates. Another way to reduce the thermal conductivity of thermoelectric materials due to the strong scattering of phonons is the use nanoporous materials. For example, in [12], it is shown that the pore size of 20 nm in crystals of SiGe allows one to increase the ZT to 1.4, while the pore size of about 1 μm has almost no influence on the thermal conductivity of crystals. Reference [13] considers the nanoporous graphene, which can significantly reduce the thermal conductivity to 0.9 W/m K, i.e. reduce heat conductivity 5000 times. Reference [14] was succeeded in telluride bismuth through increasing the nanopore size from 30 to 60 nm to reduce the thermal conductivity to 0.24 W/m K. Since the parameter ZT depends linearly from $1/k$, and the Seebeck coefficient α of a quadratic dependence, a significant increase in the latter would make the long-expected leap in the development of thermoelectric devices. One of the possible implementations is associated with the creation of composite materials with tunnel junctions (TC) between particles or layers [15, 16]. These works deal with the materials consisting of microparticles, between which there are tunnel junctions, which

provide the electrical conductivity. According to calculations, carried out in these works, while the dimensions of tunneling junctions are about a share of nm, it is possible to achieve an increase in *ZT* to 5 and above. Recently appeared articles where the thermoelectric conversion occurs without the use of a temperature difference, and when the temperature of the sample varies with time. This allows one to tune the thermal conductivity of the crystal, because in this case, there is no heat flow from the hot end to the cold that allows one to increase conversion efficiency. For example, [17–20] demonstrated that by heating samples of samarium sulfide at temperatures of about 500 K, electromotive force (EMF) occurs. With the closure of the electrodes of the sample, there is a current in the circuit and the temperature of the sample reduces by several tens of degrees. When current ceases and the temperature of the sample again rises to 500 K, it is arisen a current and temperature decrease, i.e. a current pulse takes place. EMF can reach 2.5 V, and the efficiency can attain 28%. Completely get rid of the possibility of creating gradients of temperature or heating of the sample was proposed in [21]. The closest to the proposed by us converter is the converter described in [21], because it has two junctions, under different conditions: one edge locates in the magnetic field and the other edge–outside of it. According to the author of the invention [21], due to the circumstance, the different thermoelectric power will be on junctions. It would lead to greater absorption of heat at the junction in a magnetic field, compared to heat generation in the junction outside of magnetic field. But the author does not take into account that during the transition of charge carriers from a region in a magnetic field, where their energy is higher into a region without magnetic field, where their energy is lower, it will be arisen the excessive energy into crystal lattice. This will lead to heating of the semiconductor in the transition region, and the heating of the converter in a whole and, consequently, to break of absorption of environmental heat and its conversion into electrical energy. Finally, [22, 23] proposed the design of alternating current of the thermoelectric cooler, which has no hot end. It operates only on cooling. However, it can only operate at liquid helium temperatures, where aluminum is in the superconducting state, which is a significant drawback. Thus, the overview shows that currently all of the thermoelectric converters use either the temperature difference or the temperature change of samples in time (heating–cooling) and there is no way of thermoelectric conversion that can use the heat equilibrium of environment, i.e. to work without creating a temperature gradient or process “heating–cooling”. Therefore, the proposed thermoelectric converter based on MDSM structures has a significant novelty and can make a significant contribution to the scientific basis of thermoelectric conversion, not to mention a great practical application. We can say that the above thermoelectric capacitor, to some extent, simulates the situation, which takes place in the single-electron refrigerator with switches: switches create a situation, in which electrons carry heat from a semiconductor substrate during the charge–discharge cycle of thermoelectric capacitor.

19.2 MDSM Structure and Field-Effect Transistor

The aim of this work is to obtain thermoelectric power without creating a temperature gradient in the metal–dielectric–semiconductor–metal (MDSM) structures. As such structures, we investigated KP304 (2N4268) field-effect transistors, and the transistors KP305 (MFE3004). This effect was described in [24] by describing the work of the metal–dielectric–metal structure of field-effect transistor type operating at saturation mode instead of strong inversion. In the proposed converter (Fig. 19.1), by connecting a voltage between the gate and the bottom gate electrodes, barrier layer between the surface charge and metal electrodes disappears.

After charging the gate capacitor (the gate–dielectric–substrate), the current through the resistor R becomes zero and the electric potential difference at junction becomes a lot less than the difference at the junction between the bottom electrode and the substrate. This leads to the appearance of an electric potential difference between the connected in parallel drain–source and bottom electrode. With the closure of these electrodes, through a resistor r, there is a current flow I, which leads to the absorption of heat at the junction of the bottom electrode and the substrate, which is supported by this resulting potential difference. So this potential difference can be considered as the EMF, for which the non-electrical force supporting the potential difference is the kinetic (thermal) energy of the molecules of the

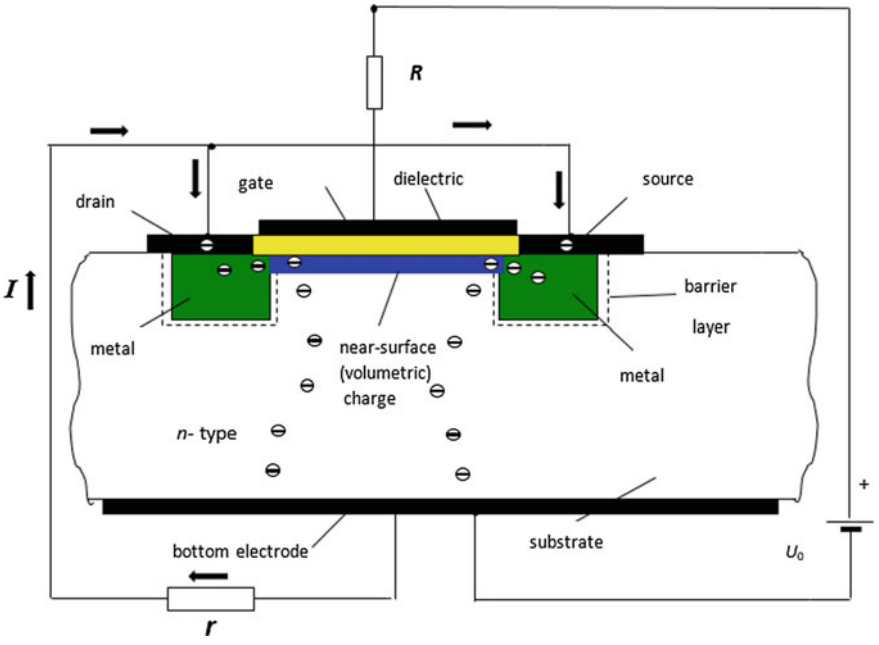

Fig. 19.1 Offered MDSM structure: ⊖ electrons, ***I*** current

environment, which force the electrons to overcome the electric potential barrier at the junction of the bottom electrode and the substrate (the Peltier effect). In this case, current flows only through the substrate, surface charge, and further through the metallic electrodes (drain–source). The electrons in this case do not need to overcome the barrier layer. They bypass it.

In a field-effect transistor (see Fig. 19.2), by connecting a voltage between the gate and the bottom gate electrodes, a barrier layer between the surface charge and metal electrodes disappears. After charging the gate capacitor (the gate–dielectric–substrate), the current through the resistor R becomes zero.

However, the isolation layer between the substrate, the surface charge and p-regions does not disappear. It just disappears between p-regions and near-surface charge so that, these regions, united together with surface charges, are isolated from the substrate by barrier layer. In this case, this layer forms near the parasitic capacitance (Fig. 19.3), which cannot be overcame by the electrons. Therefore, if

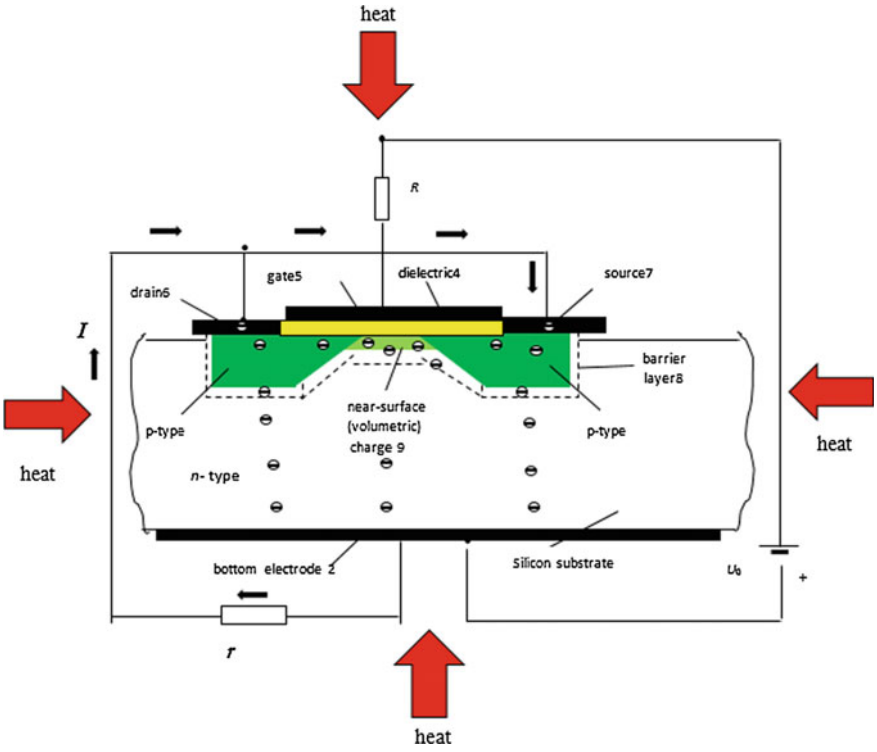

Fig. 19.2 Field-effect transistor

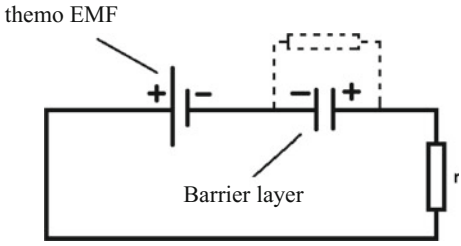

Fig. 19.3 Diagram explaining operation of shut-off layer

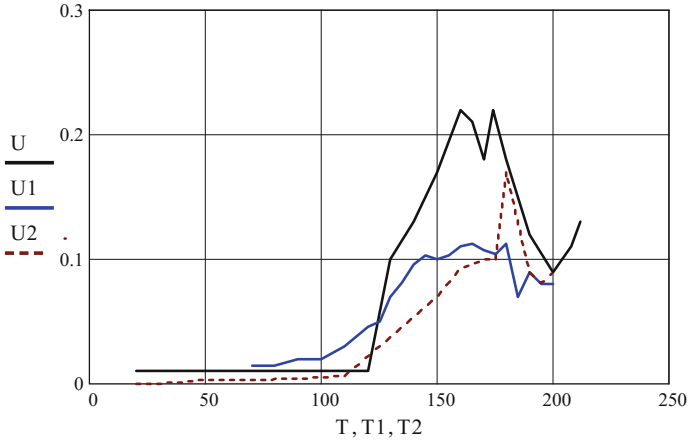

Fig. 19.4 Temperature dependence of voltage between the substrate and the connected in parallel drain–source: *1* heating in closed chamber (U2); *2* cooling in closed chamber (U1); *3* cooling in open chamber (U)

we reduce the resistance of the barrier layer in the field-effect transistor, so that there could not be formed a charge, which neutralize the thermopower, then thermopower can be seen. This can be performed by heating of the transistor.

Indeed, in the field-effect transistor KP304, uniformly (in the oven) heated to temperatures when the resistance of the gate layer is decreased to several tens of MΩ, it is appeared EMF, which at temperatures of 120–150 °C, reaches only 0.1–0.2 mV (Figs. 19.4 and 19.5) instead of 100 mV due to the reasons described above [24].

19.3 Conclusion

In the transistor KP305 with an embedded channel and a *p*-type substrate of finite conductivity, the shut-off layer was observed already at room temperature, which also led to the emergence of EMF in a fraction of mV. As follows from the

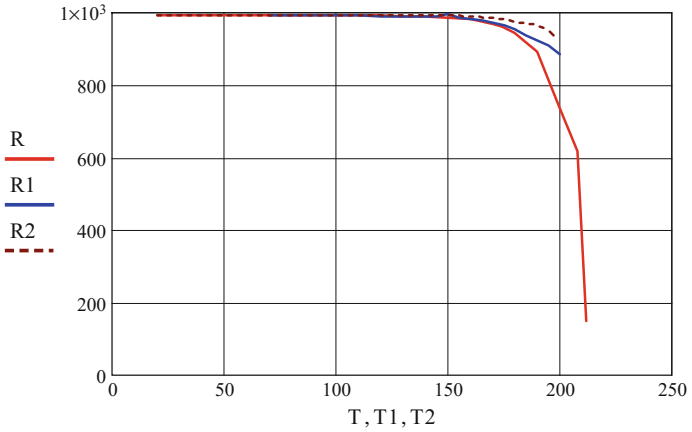

Fig. 19.5 Temperature dependence of the resistance *p-n*-junction, which is shunted by a resistance of 1 MΩ: *1* heating in closed chamber (R2); *2* cooling in closed chamber (R1); *3* cooling in open chamber (R)

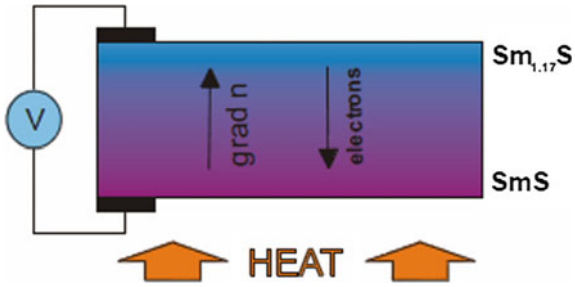

Fig. 19.6 Thermovoltaic effect in SmS

construction of field-effect transistor, it is impossible to get rid of the parasitic gate layer, which greatly reduces EMF. We can try to reduce its electric resistance at junction and the electric potential difference between bottom electrode and substrate using substrates with lower resistance, which can lead to a slight increase in EMF. However, it is better to use the design of the converter, shown in Fig. 19.1, instead of having to master the technology of manufacturing field-effect transistors using substrates with lower resistance. In this case, we can immediately obtain the EMF equal to tens or even hundreds of mV, and the manufacturing technology of the transducer, presented in Fig. 19.1, which differs little from the technology of manufacturing field-effect transistors.

Thermovoltaic effect was first observed in [17–20, 25], as mentioned in introduction, for crystals of samarium sulfide, which was created by the concentration gradient of samarium ions perpendicular to the electrodes (Fig. 19.6). However,

here EMF arises in the form of very narrow peaks with voltage amplitudes up to 6 V, which occur randomly and do not provide the ability to stack the voltages from individual samples and do not allow one to obtain output power greater than 500 μW. The source of electricity, based on the thermovoltaic effect in field-effect transistors, provides constant voltage, which allows one to summarize this voltage from different samples to obtain the necessary voltage and power.

Acknowledgements The study was supported by the RFBR Project No. 16-08-00740_a.

References

1. J.-C. Zheng, Front. Phys. China. **3**(3), 269 (2008)
2. A.V. Dmitriev, I.P. Zvyagin, Adv. Phys. Sci. **180**(8), 821 (2010)
3. K.M. Nicolau, (US) Patent of Russian Federation, No. 2295801, 06.09.2002 (2002)
4. V. Schmidt, F.J.M. Mensch, S.F. Karg, B. Gotsmann, P.D. Kanungo, H. Schmid, H. Riel, Appl. Phys. Lett. **104**, 012113 (2014)
5. L. Shi, J. Jiang, G. Zhang, B. Li, Appl. Phys. Lett. **101**, 233114 (2012)
6. L.A. Valentín, J. Betancourt, L.F. Fonseca, M.T. Pettes, L. Shi, M. Soszyński, A. Huczko, J. Appl. Phys. **116**, 174505 (2014)
7. L.D. Hicks, T.C. Harman, M.S. Dresselhaus, Appl. Phys. Lett. **63**, 3230 (1993)
8. A. Balandin, K.L. Wang, J. Appl. Phys. **84**, 6149 (1998)
9. S. Donsa, S. Andergassen, K. Held, arXiv:1308.4882 (2014)
10. D. Wasserman, S.A. Lyon, M. Hadjipanayi, A. Maciel, J.F. Ryan, Appl. Phys. Lett. **83**, 5050 (2003)
11. H.Z. Yu, X.Y. Liu, Y. Chen, J. Appl. Phys. **114**, 244308 (2013)
12. H. Lee, D. Vashaee, D.Z. Wang, M.S. Dresselhaus, Z.F. Ren, G. Chen, J. Appl. Phys. **107**, 094308 (2010)
13. Thiyagarajan Pradheep, M.W. Oh, J.C. Yoon, J.H. Jang, Appl. Phys. Lett. **105**, 033905 (2014)
14. M. Takashiri, S. Tanaka, H. Hagino, K. Miyazaki, J. Appl. Phys. **112**, 084315 (2012)
15. A.A. Snarski, A.K. Sarychev, I.V. Bezsudnov, A.N. Lagarkov, Phys. Tech. Semiconductors **46**(5), 677 (2012)
16. V.F. Kharlamov, J. Exp. Theor. Phys. **117**(1), 83 (2013)
17. M.M. Kazanin, V.V. Kaminski, S.M. Soloviov, Tech. Phys. **70**(5), 136 (2013)
18. V.V. Kaminski, V. Soloviov, Phys. Solids **43**(3), 423 (2013)
19. V.M. Egorov, V.V. Kaminski, M.M. Kazanin, S.M. Soloviev, A.V. Golubkov, Tech. Phys. Lett. **39**(1), 57 (2013)
20. V. Kaminsky, Tech. Phys. Lett. **39**(15), 12 (2013)
21. V.N. Kluchnik, The thermoelectric converter. Patent of the Russian Federation 2 388 105, 27.04.2010 (2010)
22. J.P. Pekola, F. Giazotto, O.P. Saira, Phys. Rev. Lett. **98**, 037201 (2007)
23. O.P. Saira, M. Meschke, F. Giazotto, A.M. Savin, M. Mottonen, J.P. Pekola, Phys. Rev. Lett. **99**, 027203 (2007)
24. L.S. Lunin, G.Y.A. Karapet'yan, V.G. Dneprovskii, V.F. Kataev, Tech. Phys. **58**(11), 1619 (2013)
25. V.V. Kaminskii, A.A. Molodykh, I.S. Polukhin, S.M. Solov'ev, K.V. Shuvaev, Tech. Phys. Lett. **40**(6), 453 (2014)

Chapter 20
Identification of Graphene Properties in the Framework of Molecular Dynamics

Arkadiy N. Soloviev, Roman U. Gruzdev, Alexander V. Derkun and Erkki Lahderanta

Abstract The chapter is devoted to the mathematical modeling of graphene-based structures in the framework of molecular dynamics. These structures are based on honey-comb crystal lattice. Simulations were performed in LAMMPS software with different interaction potentials and values of prescribed deformation. Results are given in tables.

20.1 Introduction

The graphene-based materials are promising for applications in solar panel industry and energy saving due to their unique properties (e.g. 1 photon makes graphene to produce more than 1 electron, excellent mechanical behavior, etc.). This chapter provides the reader with sufficient details of molecular dynamics (MD) method, details of computational experiment for elastic properties identification and importance of using up-to-date computational software for better precision of results.

A.N. Soloviev (✉)
Department of Theoretical and Applied Mechanics, Don State Technical University, Rostov-on-Don, Russia
e-mail: solovievarc@gmail.com

A.N. Soloviev · R.U. Gruzdev · A.V. Derkun
I.I. Vorovich Institute of Mathematics, Mechanics and Computer Science, Southern Federal University, Rostov-on-Don, Russia
e-mail: rgruzd91@gmail.com

A.V. Derkun
e-mail: derkun.santery.victory@yandex.ru

E. Lahderanta
Lappeenranta University of Technology, Lappeenranta, Finland
e-mail: Erkki.Lahderanta@lut.fi

I.A. Parinov et al. (eds.), *Advanced Materials*, Springer Proceedings in Physics 193, DOI 10.1007/978-3-319-56062-5_20

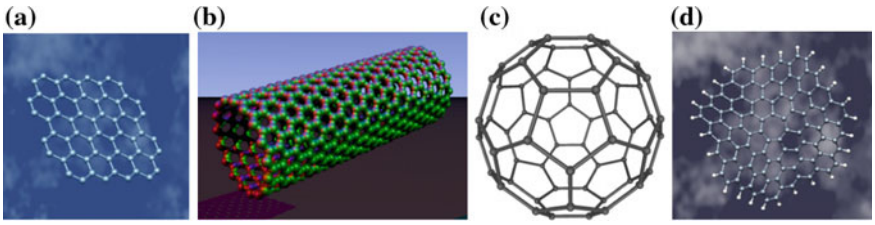

Fig. 20.1 Graphene structures: **a** ideal graphene sheet; **b** carbon nanotube; **c** fullerene (pentagonal defects); **d** sadle structure (heptagonal defects)

According to [1] there are next key issues in mathematical modeling:

(i) the principle of adequacy of information;
(ii) the principle of feasibility;
(iii) the principle of multiplicity of models;
(iv) the principle of aggregation;
(v) the principle of parameterization.

In order to satisfy these principles, in this Chapter first it will be defined the method, then material properties of graphene and numerical experiment explanation.

Graphene can be used as base for modern materials. Most common graphene structures are presented in Fig. 20.1.

This Chapter is devoted to the structures presented in Fig. 20.1a. Due to graphene properties, described in Sect. 20.3, these structures can be used as covering material for solar panels, increasing efficiency. Another advantage is symmetrical 2D structure, which is easy to model. By performing simulations with such materials, we can develop experimental base for further research of complex structures (nanoscale composites) [1–4].

20.2 Molecular Dynamics Framework

Details of MD method can be found in [5]. In general, different atomic systems are used for modeling. First of all, we should describe potentials, which are related to inter- and intramolecular degrees of freedom. In general case we have:

$$U = U_{intra} + U_{ang} + U_{tor} + U_{el} + U_{emp}, \tag{20.1}$$

where U_{intra} is the intramolecular bond potential, U_{ang} is the angular potential, U_{tor} is the torsion potential, U_{el} is the electrostatic potential, U_{emp} is the empirical part of the potential. In this study, an attention is given to the first kind of potential, U_{intra}.

For carbon modeling was used LCBOP potential, which is the part of LAMMPS software. This potential computes the long-range bond-order Los and Fasolino potential. This potential has been explored in [6]. The potential is defined as the sum of an angular and coordination dependent short-range part accounting for the strong covalent interactions and a radial long-range part describing the weak interactions responsible. The short-range part is a Brenner type of potential, with several modifications introduced to get an improved description of elastic properties and conjugation.

The *pair_style lcbop* command computes the long-range bond-order potential for carbon (LCBOP). The approach used by Los and Fasolino [6] is to represent potential as sum of long- and short-range parts. Total binding energy E_b is defined as

$$E_b = \frac{1}{2}\sum_{i,j}^{N} V_{ij}^{tot} = \frac{1}{2}\sum_{i,j}^{N}\left(f_{c,ij}V_{IJ}^{SR} + S_{ij}V_{ij}^{LR}\right), \tag{20.2}$$

where V_{ij}^{tot} is the sum of short- and long-range parts, $f_{c,ij}$ is the smooth cutoff function, S_{ij} is the switching function to exclude first neighbors.

To prove correctness of the model, we shall use some other interaction potentials. LAMMPS software provides us with the next efficient potentials: Charge-optimized many-body (COMB3) potential (described in [7–9]), Tersoff potential [10–12], Rebo potential [13–15]. The results of numerical experiments for this potential can be used in different researches (in dependence on specification of potential). Sufficient information on each potential can be found in [7–15].

20.3 Model of Graphene Structures

Sufficient introduction to graphene theory can be found in [2, 16]. Graphene is the 2D structure of carbon atoms. The crystal lattice is honey-comb hexagonal lattice with lattice constant 0.246 nm. Graphene got unique electronic properties due to its 2D structure. Carbon atom has 4 electrons for bonding, but in graphene each atom connected to 3 other atoms so one electron is freely available for electronic conduction (π-electrons). Another point of interest is that graphene's electrons and holes have zero effective mass (Dirac fermions, or Graphinos). Tests have shown that the electronic mobility of graphene is very high, with previously reported results above 15,000 $cm^2\ V^{-1}\ s^{-1}$ and theoretically potential limits of 200,000 $cm^2\ V^{-1}\ s^{-1}$.

This Chapter is devoted to another outstanding side of grapheme, its elastic properties and mechanical strength.

First we had built crystal lattice based on graphene's basis cell (Fig. 20.2). In LAMMPS software the basis cell is based on 3 vectors (2 in case of 2D problem). For simulation we used next vectors:

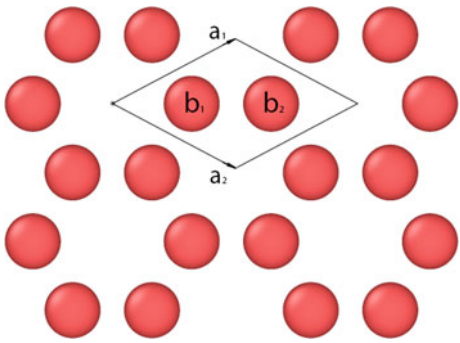

Fig. 20.2 Graphene basis cell

$$a_1 = \left[\frac{\sqrt{3}}{2}a, \frac{1}{2}a\right], a_2 = \left[\frac{\sqrt{3}}{2}a, -\frac{1}{2}a\right]. \tag{20.3}$$

Basis atoms are based on these vectors and have form:

$$b_1 = \left[\frac{1}{3}a_1, \frac{1}{3}a_2\right], b_1 = [\frac{2}{3}a_1, \frac{2}{3}a_2]. \tag{20.4}$$

20.4 Details of Simulation

Since graphene is 2D isotropic material, its elastic properties are described by Voigt notation matrix:

$$\begin{pmatrix} \lambda+2\mu & \lambda & 0 \\ \lambda & \lambda+2\mu & 0 \\ 0 & 0 & \mu \end{pmatrix}. \tag{20.5}$$

From (20.5), one can see that we have to determine only 2 constants: $C_{11} = C_{22} = \lambda + 2\mu$ and $C_{33} = \mu$. Full Voigt notation for (20.5) can be written as

$$\begin{pmatrix} \sigma_{11} \\ \sigma_{22} \\ \sigma_{12} \end{pmatrix} = \begin{pmatrix} C_{11} & C_{12} & 0 \\ C_{12} & C_{11} & 0 \\ 0 & 0 & C_{33} \end{pmatrix} \begin{pmatrix} \varepsilon_{11} \\ \varepsilon_{22} \\ 2\varepsilon_{12} \end{pmatrix}. \tag{20.6}$$

In [17], it can be found that:

$$v = \frac{\lambda}{(d-1)\lambda + 2\mu}; \tag{20.7}$$

$$E = \frac{2\mu(d\lambda + 2\mu)}{k + (d-1)\lambda + 2\mu}, \tag{20.8}$$

where $k = 0$ for isotropic material, d is the dimension. Graphene is the 2D structure, but even for 2D modeling, LAMMPS software uses three-dimensional computing, so $d = 3$.

The idea of computational experiments in current research is to apply axial loading over graphene sheet (see Fig. 20.3), as described in [18, 19].

Since graphene is 2D material, point of interest in this case is to identify in-plane stiffness E^{2D} instead of classical 3D Young's modulus (E^{3D}). These constants are coupled by

$$E^{2D} = \frac{1}{A_0}\left(\frac{\partial^2 E_s}{\partial \varepsilon_x^2}\right) = E^{3D} c_0, \tag{20.9}$$

where E_s, ε_x and A_0 correspond to the total energy, linear strain and equilibrium reference area of the 2D material, respectively, c_0 is the interlayer distance in graphene and is equal to 3.35 Å. After loading we had performed equilibration of sample and the equilibration reference area is the area of interest after this process.

For simulation, we got LAMMPS-based graphene sheet, presented in Fig. 20.4.

Deformed shape is not shown, because we use small deformations (see Sect. 20.5).

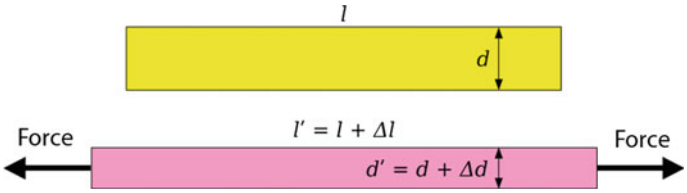

Fig. 20.3 Graphene sheet loading

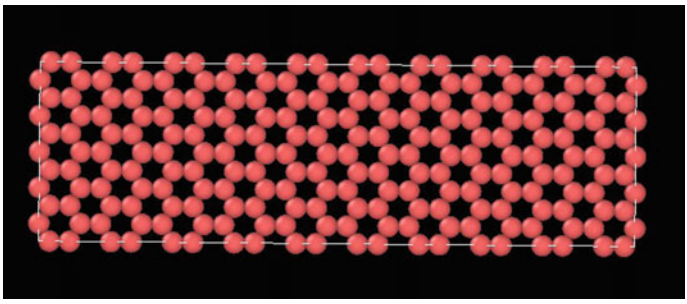

Fig. 20.4 LAMMPS-based graphene sheet

20.5 Results

By performing computational experiments using LCBOP, Tersoff, COMB3, Rebo potentials we obtained results shown in Table 20.1.

As reported in [18], theoretical study obtained value of E^{2D} = 3.41 TPa Å and this result is almost identical to that obtained for graphene. Full list of theoretical results (E^{2D}, E^{3D}, Poison ratios) can be found in [20]. In Tables 20.2 and 20.3, one can find some valuable results from [20]. During computational experiment using Tersoff potential, we obtained negative value of Poison ratio. This result is similar to the result of [21].

To confirm the correctness of the model, we explored three different samples. Details are given in Table 20.4.

Table 20.1 Numerical results

Potential	Poison ratio	E^{2D} (GPa Å)
LCBOP	0.18	3047
Tersoff	−0.18	3929
COMB3	0.33	1771
Rebo	0.26	2563

Table 20.2 Poison ratio as reported in different numerics and theoretical works [20]

Method	Poison ratio
Atomistic Monte Carlo	0.12
DFT	0.18
Brenner's potential	0.27
Multiple component correlation model	0.4
Continuum elasticity theory and tight-binding atomistic simulations	0.31

Table 20.3 Young's modulus E^{2D}, expressed in N/m, as reported in different computational and theoretical works

Method	Young's modulus E^{2D} (N/m)
Atomistic Monte Carlo	353
Brenner's potential	336
DFT	330
Tersoff-Brenner potential	235
Continuum elasticity theory and tight-binding atomistic simulations	312

Table 20.4 Sample parameters

Sample number	Size (Å)		Number of atoms
	Length	Width	
1	42	12	200
2	85	24	800
3	170	50	3200

LAMMPS software provides us with opportunity to change simulation box size by using *change_box command*. This command is used to apply a strain to the sample. We had used style "*delta*" of this command. It means that plus or minus changes in the box boundaries of a dimension are specified. This fact gives us opportunity for another verification of the correctness—results should be independent of values of size changes. Tables for different potentials are given below. Change of size is defined as

$$delta = kl_0, \tag{20.10}$$

where l_0 is the initial size in chosen dimension, k is the percentage of initial size. After each deformation, the command "minimize" is performed in order to adjust atom coordinates. After that LAMMPS software allows us to get the value of pressure that should be loaded for obtaining such deformation (Tables 20.5, 20.6, 20.7 and 20.8).

Table 20.5 LCBOP potential

Sample number	k	E^{2D} (GPa Å)	Poison ratio
1	1.0×10^{-6}	3047.24548	0.1811
	1.0×10^{-5}	3047.22544	0.1811
	1.0×10^{-4}	3047.02560	0.1811
2	1.0×10^{-6}	3047.24536	0.1811
	1.0×10^{-5}	3047.22550	0.1811
	1.0×10^{-4}	3047.02559	0.1811
3	1.0×10^{-6}	3047.24626	0.1811
	1.0×10^{-5}	3047.22541	0.1811
	1.0×10^{-4}	3047.02562	0.1811

Table 20.6 Tersoff potential

Sample number	k	E^{2D} (GPa Å)	Poison ratio
1	1.0×10^{-6}	3929.74576	−0.1877
	1.0×10^{-5}	3929.74576	−0.1877
	1.0×10^{-4}	3929.74602	−0.1877
2	1.0×10^{-6}	3929.74584	−0.1877
	1.0×10^{-5}	3929.74576	−0.1877
	1.0×10^{-4}	3929.74603	−0.1877
3	1.0×10^{-6}	3929.74585	−0.1877
	1.0×10^{-5}	3929.74569	−0.1877
	1.0×10^{-4}	3929.74603	−0.1877

Table 20.7 COMB3 potential

Sample number	k	E^{2D} (GPa Å)	Poison ratio
1	1.0×10^{-6}	1771.0508	0.3398
	1.0×10^{-5}	1771.0507	0.3398
	1.0×10^{-4}	1771.0505	0.3398
2	1.0×10^{-6}	1771.0507	0.3398
	1.0×10^{-5}	1771.0507	0.3398
	1.0×10^{-4}	1771.0505	0.3398
3	1.0×10^{-6}	1771.0520	0.3398
	1.0×10^{-5}	1771.0508	0.3398
	1.0×10^{-4}	1771.0520	0.3398

Table 20.8 Rebo potential

Sample number	k	E^{2D} (GPa Å)	Poison ratio
1	1.0×10^{-6}	2563.7052	0.2675
	1.0×10^{-5}	2563.9446	0.2675
	1.0×10^{-4}	2566.3340	0.2675
2	1.0×10^{-6}	2563.7052	0.2675
	1.0×10^{-5}	2563.9444	0.2675
	1.0×10^{-4}	2566.3341	0.2675
3	1.0×10^{-6}	2563.7066	0.2675
	1.0×10^{-5}	2563.9454	0.2675
	1.0×10^{-4}	2566.3340	0.2675

20.6 Conclusion

Today we have a new version of LCBOP available (LCBOPII), which got some improvements [3]. LCBOPII contains coordination dependent medium range term for bond distances between 1.7 and 4 Å, meant to reproduce the dissociation energy curves for single, double, and triple bonds and improve the reactive properties as well as the description of the liquid and low coordinated phases. Other features of LCBOPII are a coordination dependent angular correlation, a correction for anti-bonding states, and a conjugation dependent torsional interaction based on ab initio calculations of the torsional barriers for a set of molecular configurations.

Results obtained in current research are in accordance with results of other research. LCBOP potential provides us with best result as it was created for carbon modeling. With LCBOPII it can be already used for modeling of graphene structures. Further work can be done on fitting Tersoff, COMB3 and Rebo potentials for better results. Importance of COMB3 potential is possibility of creating polarizable models for solar panel industry [3, 4].

Acknowledgements This work is partly supported by Russian Foundation for Basic Research (RFBR), Project 16-58-52013 MNT_a.

References

1. K.K. Vasiliev, M.N. Sluzhivii, *Mathematical Modeling of Communication Systems* (UlSTU, Ulianovsk, 2008). (in Russian)
2. M.I. Katsnelson, *Graphene Carbon in Two Dimensions* (Cambridge University Press, New York, 2012)
3. A.N. Soloviev, R.U. Gruzdev, V.V. Naprasnikov, Y.-M. Liu, H.-C. Huang, in *Abstracts and Schedule of International Conference on "Physics and Mechanics of New Materials and Their Applications" (PHENMA 2015)* (SFedU Press, Azov, Russia) 19–22 May 2015, p. 228 (2015)
4. R. Gruzdev, A. Soloviev, in *Abstracts 8-th International Conference on Materials Structure and Micromechanics of Fracture* (VUTIUM Brno, Brno, Czech Republic), June 27–29 2016, p. 100 (2016)
5. D.C. Rapaport, *The Art of Molecular Dynamics Simulation* (Cambridge University Press, New York, 2004)
6. J.H. Los, A. Fasolino, Phys. Rev. B, **68** (2003)
7. T.-R. Shan, B.D. Devine, T.W. Kemper, S.B. Sinnott, S.R. Phillpot, Phys. Rev. B **81**, 125328 (2010)
8. T. Liang, T.-R. Shan, Y.-T. Cheng, B.D. Devine, M. Noordhoek, Y. Li, Z. Lu, S.R. Phillpot, S.B. Sinnott, Mat. Sci. Eng. R **74**, 255 (2013)
9. S.W. Rick, S.J. Stuart, B.J. Berne, J. Chem. Phys. **101**, 6141 (1994)
10. J. Tersoff, Phys. Rev. B **37**, 6991 (1988)
11. J. Nord, K. Albe, P. Erhart, K. Nordlund, J. Phys. Condens. Matter **15**, 5649 (2003)
12. J. Tersoff, Phys. Rev. B, **39**, 5566 (1989) (errata (*PRB* **41**, 3248))
13. S.J. Stuart, A.B. Tutein, J.A. Harrison, J. Chem. Phys., **112**, 6472 (2000)
14. B. Shenderova, H. Stuart, N. Sinnott, J. Phys. Condens. Matter **14**, 783 (2002)
15. T.C. O'Connor, et al., J. Chem. Phys. **142**, 024903 (2015)
16. *Graphene Properties*//Graphenea http://www.graphenea.com/pages/graphene-properties
17. I.E. Berinskiy, in *Theoretical Mechanics. The Thermal and Elastic Properties of the Ideal Crystal* (Saint-Petersburg State Polytechnic University Press, Saint-Petersburg), p. 136 (2009) (in Russian)
18. R. Faccioa, P.A. Denisc, H. Pardoa, C. Goyenolaa, Á.W. Mombrúa, J. Phys. Condens. Matter (2009). doi:10.1088/0953-8984/21/28/285304
19. C. Xu, T. Xue, J. Guo, Y. Kang, W. Qiu, H. Song, H. Xie, Mater. Lett. **161**, 755 (2015)
20. A. Politano, G. Chiarello, in *Nano Research* (Tsinghua University Press), p. 4 (2014)
21. E.S. Sergeeva, V.S. Zarubin, in *Youth Science and Technology Gazette* (Bauman Moscow State Technical University Press) (2015) (in Russian)

Chapter 21
System Research of Plane-Parallel Electrochemical Electrolytic Cell with Perforated Cathode

A.N. Gerasimenko, Yu Ya Gerasimenko, E. Yu Gerasimenko and R. Yu Gerasimenko

Abstract It is present mathematical modeling of plane-parallel electrochemical electrolyzes with a perforated cathode. It is performed mathematical modeling of plane-parallel electric and concentration fields of electrolyte in electrolyzes with planar electrodes, coinciding with boundary surfaces of opposite faces.

21.1 Introduction

It is considered the plane-parallel electric and concentration field electrolyte in the electrolyzer with planar electrodes. In the simulation of electrolyzer, we adopt the following physical assumptions [1]: (i) side electrolyzer is made of a dielectric; (ii) the electrical conductivity of the electrolyte is a constant value; (iii) the diffusion coefficient of an electrolyte is a constant value; (iv) the kinetics of electrode processes of electrolyzer at the diffusion stage is controlled in the electrolyte; (v) mass transfer in the electrolyte is described by the hyperbolic diffusion equation with a constant relaxation τ_r; (vi) electric field in the electrolyte is a potential; (vii) electric current density over the surfaces of all the electrodes are distributed evenly.

In viewpoint of the adopted assumptions, the task of mass transfer in the electrolyte can be represented in the form of the Laplace operator of the Fourier series. The expansion coefficients of this series are uniquely determined by the boundary conditions of the second kind, totally dependent on the electric current density in accordance with Faraday's law.

In accordance with the accepted assumptions, the scalar potential of the electric field is described by a differential equation of Laplace. Its solution can also be represented by a Fourier series with up to a constant operator.

A.N. Gerasimenko · Y.Y. Gerasimenko · E.Y. Gerasimenko · R.Y. Gerasimenko (✉)
Don State Technical University, 344010 Rostov-on-Don, Russia
e-mail: geralla79@mail.ru

I.A. Parinov et al. (eds.), *Advanced Materials*, Springer Proceedings in Physics 193, DOI 10.1007/978-3-319-56062-5_21

21.2 Methods

21.2.1 Objective

We consider plane-parallel electrolyte in electrolytic cell with planar electrodes, coinciding with the boundary surfaces of opposite faces. Cathode is made in the form of flat strips, lying in the same plane. By modeling the electrolytic cell with depth, a, we take the following physical assumptions [1–4]:

(i) electrolytic cell walls are made of dielectric (Fig. 21.1),
(ii) the electrical conductivity of the electrolyte is a constant,
(iii) the diffusion coefficient of the electrolyte is a constant,
(iv) the kinetics of electrode processes of electrolytic cell at diffusion stage is controlled in the electrolyte,
(v) mass-transfer in the electrolyte is described by the hyperbolic diffusion equation with a relaxation constant τ_r,
(vi) electric field in electrolyte is a potential,
(vii) electric current density on the surfaces of all electrodes is distributed uniformly.

21.2.2 Mathematical Modeling of Concentration Field of Electrolyte

Let us consider the following initial boundary-value problem for electrolyte:

$$\frac{\partial C(x;t)}{\partial t} + \tau_r \frac{\partial^2 C(x;t)}{\partial t^2} = D\left(\frac{\partial^2 C(x;t)}{\partial x^2} + \frac{\partial^2 C(x;t)}{\partial y^2}\right), \tag{21.1}$$

$$C(x;y;0) = C_0, \tag{21.2}$$

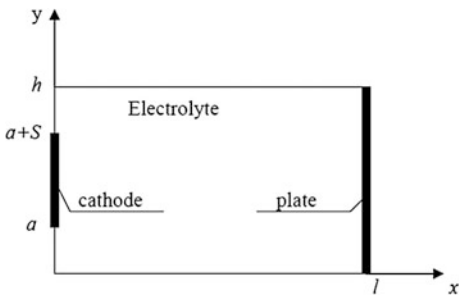

Fig. 21.1 Considered electrolyzer

$$\frac{\partial C}{\partial t}(x;y;0) = 0, \tag{21.3}$$

$$\frac{\partial C}{\partial y}(x;0;t) = 0, \tag{21.4}$$

$$\frac{\partial C}{\partial y}(x;h;t) = 0, \tag{21.5}$$

$$\frac{\partial C}{\partial x}(0;y;t) = \begin{cases} 0, & 0 \le y \le a \\ \frac{NI(t)}{sB}, & a < y < a+s \\ 0, & a+s \le y \le h. \end{cases} \tag{21.6}$$

$$\frac{\partial C}{\partial x}(l;y;t) = \frac{NI(t)}{hB}. \tag{21.7}$$

where τ_r is the relaxation constant, D is the diffusion coefficient, $N > 0$ is the electrode kinetic constant, c_0 is the initial concentration.

We shall solve this problem by using the Laplace operator method [5, 6]. We introduce the next compliances:

$$\begin{aligned} &C(x;y;t) \mathrel{\mathop{=}^{\circ}_{\circ}} \overset{\circ}{C}(x;y;p), I(t) \mathrel{\mathop{=}^{\circ}_{\circ}} \overset{\circ}{I}(p) \\ &\frac{\partial C}{\partial t}(x;y;t) \mathrel{\mathop{=}^{\circ}_{\circ}} p\,\overset{\circ}{C}(x;y;p) - C(x;y;0), \\ &\frac{\partial C}{\partial t}(x;y;t) \mathrel{\mathop{=}^{\circ}_{\circ}} p\,\overset{\circ}{C}(x;y;p) - C_0, \end{aligned} \tag{21.8}$$

$$\begin{aligned} &\frac{\partial^2 C}{\partial t^2}(x;y;t) \mathrel{\mathop{=}^{\circ}_{\circ}} p^2\,\overset{\circ}{C}(x;y;p) - pC_0 - \frac{\partial C}{\partial t}(x;y;0), \\ &\frac{\partial^2 C}{\partial t^2}(x;y;t) \mathrel{\mathop{=}^{\circ}_{\circ}} p^2\,\overset{\circ}{C}(x;y;p) - pC_0. \end{aligned} \tag{21.9}$$

$$p\,\overset{\circ}{C}(x;y;p) - C_0 + \tau_r\left(p^2\,\overset{\circ}{C}(x;y;p) - pC_0\right) = D\left(\frac{\partial^2\,\overset{\circ}{C}(x;y;p)}{\partial x^2} + \frac{\partial^2\,\overset{\circ}{C}(x;y;p)}{\partial y^2}\right), \tag{21.10}$$

$$D\left(\frac{\partial^2\,\overset{\circ}{C}(x;y;p)}{\partial x^2} + \frac{\partial^2\,\overset{\circ}{C}(x;y;p)}{\partial y^2}\right) - \tau_r p^2\,\overset{\circ}{C}(x;y;p) - p\,\overset{\circ}{C}(x;y;p) = -\tau_r pC_0 - C_0, \tag{21.11}$$

$$\frac{\partial^2\,\overset{\circ}{C}(x;y;p)}{\partial x^2} + \frac{\partial^2\,\overset{\circ}{C}(x;y;p)}{\partial y^2} - \frac{p(1+\tau_r p)}{D}\,\overset{\circ}{C}(x;y;p) = -\frac{(1+\tau_r p)C_0}{D}, \tag{21.12}$$

$$\frac{\partial \overset{\circ}{C}}{\partial y}(x;0;p) = 0, \tag{21.13}$$

$$\frac{\partial \overset{\circ}{C}}{\partial y}(x;h;p) = 0, \tag{21.14}$$

$$\frac{\partial \overset{\circ}{C}}{\partial x}(0;y;p) = \begin{cases} 0, & 0 \le y \le a \\ \frac{N\overset{\circ}{I}(p)}{sB}, & a < y < a+s \\ 0, & a+s \le y \le h. \end{cases}, \tag{21.15}$$

$$\frac{\partial \overset{\circ}{C}}{\partial x}(l;y;p) = \frac{N\overset{\circ}{I}(p)}{hB}. \tag{21.16}$$

We introduce new unknown function as follows:

$$\overset{\circ}{U}(x;y;p) = \overset{\circ}{C}(x;y;p) - \frac{C_0}{p}. \tag{21.17}$$

Relation (21.17) allows one to reduce problem (21.12)–(21.16) to the following one:

$$\frac{\partial^2 \overset{\circ}{U}(x;y;p)}{\partial x^2} + \frac{\partial^2 \overset{\circ}{U}(x;y;p)}{\partial y^2} - \frac{p(1+\tau_r p)}{D}\overset{\circ}{U}(x;y;p) = 0, \tag{21.18}$$

$$\frac{\partial \overset{\circ}{U}}{\partial y}(x;0;p) = 0, \tag{21.19}$$

$$\frac{\partial \overset{\circ}{U}}{\partial y}(x;h;p) = 0, \tag{21.20}$$

$$\frac{\partial \overset{\circ}{U}}{\partial x}(0;y;p) = \begin{cases} 0, & 0 \le y \le a \\ \frac{N\overset{\circ}{I}(p)}{sB}, & a < y < a+s \\ 0, & a+s \le y \le h. \end{cases} \tag{21.21}$$

$$\frac{\partial \overset{\circ}{U}}{\partial x}(l;y;p) = \frac{N\overset{\circ}{I}(p)}{hB}. \tag{21.22}$$

Differential equation (21.18) with similar boundary conditions (21.19), (21.20) allows one to define eigen-functions of problem (21.18)–(21.22) in the form:

$$Y_k(y) = \begin{cases} \frac{1}{\sqrt{h}}, k = 0 \\ \sqrt{\frac{2}{h}}\cos\frac{k\pi}{h}y, k = 1,2,\ldots \end{cases} \tag{21.23}$$

We present [7–9] a solution $\overset{\circ}{U}(x;y;p)$ of the problem (21.18)–(21.22) in the form of Fourier series on Eigen-functions (21.23):

$$\overset{\circ}{U}(x;y;p) = \beta_0(x;p)Y_0(y) + \sum_{k=1}^{\infty} \beta_k(x;p)Y_k(y), \tag{21.24}$$

$$\beta_0''(x;p) - \frac{p(1+\tau_r p)}{D}\beta_0(x;p) = 0, \tag{21.25}$$

$$\beta_k''(x;p) - \left(\frac{k^2\pi^2}{h^2} + \frac{p(1+\tau_r p)}{D}\right)\beta_k(x;p) = 0, \tag{21.26}$$

$$\beta_0(x;p) = M_0(p)sh\sqrt{\mu(p)}x + N_0(p)ch\sqrt{\mu(p)}x, \tag{21.27}$$

$$\beta_k(x;p) = M_k(p)sh\sqrt{\mu(p)}x + N_k(p)ch\sqrt{\mu(p)}x, \tag{21.28}$$

$$\mu_0(p) = \frac{p(1+\tau_r p)}{D}; \quad \mu_k(p) = \frac{k^2\pi^2}{h^2} + \frac{p(1+\tau_r p)}{D}.$$

The substitution (21.29) into (21.24) leads to the following representation:

$$\begin{aligned}\overset{\circ}{U}(x;y;p) = &\left(M_0(p)sh\sqrt{\mu_0(p)}x + N_0(p)ch\sqrt{\mu_0(p)}x\right)Y_0(y) \\ &+ \sum_{k=1}^{\infty}\left(M_k(p)sh\sqrt{\mu_k(p)}x + N_k(p)ch\sqrt{\mu_k(p)}x\right)Y_k(y).\end{aligned} \tag{21.29}$$

By differentiating $\overset{\circ}{U}(x;y;p)$ on x, we obtain

$$\begin{aligned}\frac{\partial \overset{\circ}{U}(x;y;p)}{\partial x} = &\sqrt{\mu_0(p)}\left(M_0(p)ch\sqrt{\mu_0(p)}x + N_0(p)sh\sqrt{\mu_0(p)}x\right)Y_0(y) \\ &+ \sum_{k=1}^{\infty}\sqrt{\mu_k(p)}\left(M_k(p)ch\sqrt{\mu_k(p)}x + N_k(p)sh\sqrt{\mu_k(p)}x\right)Y_k(y).\end{aligned} \tag{21.30}$$

For $x = 0$ we get from (21.30)

$$\frac{\partial \overset{\circ}{U}(x;y;p)}{\partial x} = \sqrt{\mu_0(p)}M_0(p)Y_0(y) + \sum_{k=1}^{\infty}\sqrt{\mu_k(p)}M_k(p)Y_k(y). \tag{21.31}$$

By comparing (21.21) with (21.31), we get:

$$\sqrt{\mu_0(p)}M_0(p)Y_0(y)+\sum_{k=1}^{\infty}\sqrt{\mu_k(p)}M_k(p)Y_k(y)=\begin{cases}0, & 0\le y\le a\\ \frac{\overset{\circ}{NI}(p)}{sB}, & a<y<a+s\\ 0, & a+s\le y\le h.\end{cases}$$

For $k = 0$, we have

$$M_0(p)=\frac{\overset{\circ}{NI}(p)}{B\sqrt{h}\sqrt{\mu_0(p)}}. \tag{21.32}$$

For $k \neq 0$, we have after simple transformations:

$$M_k(p)=\sqrt{\frac{2}{h}}\cdot\frac{\overset{\circ}{NI}(p)}{sB}\cdot\frac{h}{k\pi}\frac{\sin\frac{k\pi}{h}(a+s)-\sin\frac{k\pi}{h}a}{\sqrt{\mu_k(p)}}. \tag{21.33}$$

For $x = l$, we get from (21.30)

$$\begin{aligned}\frac{\partial\overset{\circ}{U}(l;p)}{\partial x}&=\sqrt{\mu_0(p)}\Big(M_0(p)ch\sqrt{\mu_0(p)}l+N_0(p)sh\sqrt{\mu_0(p)}l\Big)Y_0(y)\\&+\sum_{k=1}^{\infty}\sqrt{\mu_k(p)}\Big(M_k(p)ch\sqrt{\mu_k(p)}l+N_k(p)sh\sqrt{\mu_k(p)}l\Big)Y_k(y).\end{aligned} \tag{34}$$

By comparing (21.22) with (21.34), we get after simple transformations:

$$\begin{aligned}&\sqrt{\mu_0(p)}\Big(M_0(p)ch\sqrt{\mu_0(p)}l+N_0(p)sh\sqrt{\mu_0(p)}l\Big)Y_0(y)\\&+\sum_{k=1}^{\infty}\sqrt{\mu_k(p)}\Big(M_k(p)ch\sqrt{\mu_k(p)}l+N_k(p)sh\sqrt{\mu_k(p)}l\Big)Y_k(y)=\frac{\overset{\circ}{NI}(p)}{hB}.\end{aligned} \tag{21.35}$$

$$M_0(p)ch\sqrt{\mu_0(p)}l+N_0(p)sh\sqrt{\mu_0(p)}l=\frac{\overset{\circ}{NI}(p)}{\sqrt{h}B\sqrt{\mu_0(p)}}. \tag{21.36}$$

$$N_0(p)=\frac{-\overset{\circ}{NI}(p)sh\sqrt{\mu_0(p)}\frac{l}{2}}{\sqrt{h}B\sqrt{\mu_0(p)}ch\sqrt{\mu_0(p)}\frac{l}{2}} \tag{21.37}$$

We get expression for kth harmonic after simple transformations:

$$M_k(p)ch\sqrt{\mu_k(p)}l + N_k(p)sh\sqrt{\mu_k(p)}l = \frac{N\overset{\circ}{I}(p)}{sB}\sqrt{\frac{2}{h}}\cdot\frac{h}{k\pi}\frac{\sin\frac{k\pi}{h}(a+s)-\sin\frac{k\pi}{h}a}{\sqrt{\mu_k(p)}}. \tag{21.38}$$

$$N_k(p) = \frac{-N\overset{\circ}{I}(p)}{sB}\sqrt{\frac{2}{h}}\cdot\frac{h}{k\pi}\frac{\sin\frac{k\pi}{h}(a+s)-\sin\frac{k\pi}{h}a}{\sqrt{\mu_k(p)}}\cdot\frac{sh\sqrt{\mu_k(p)}\frac{l}{2}}{ch\sqrt{\mu_k(p)}\frac{l}{2}}. \tag{21.39}$$

Then finish expression for $\overset{\circ}{U}(p)$ takes the form:

$$\begin{aligned}\overset{\circ}{U}(x;y;p) = {} & \frac{N\overset{\circ}{I}(p)}{\sqrt{h}B\sqrt{\mu_0(p)}}\left(sh\sqrt{\mu_0(p)}x - \frac{sh\sqrt{\mu_0(p)}\frac{l}{2}\cdot ch\sqrt{\mu_0(p)}x}{ch\sqrt{\mu_0(p)}\frac{l}{2}}\right)Y_0(y)\\ & + \sum_{k=1}^{\infty}\frac{N\overset{\circ}{I}(p)}{sB}\sqrt{\frac{2}{h}}\cdot\frac{h}{k\pi}\cdot\frac{\sin\frac{k\pi}{h}(a+s)-\sin\frac{k\pi}{h}a}{\sqrt{\mu_k(p)}}\\ & \left(sh\sqrt{\mu_k(p)}x - \frac{sh\sqrt{\mu_k(p)}\frac{l}{2}\cdot ch\sqrt{\mu_k(p)}x}{ch\sqrt{\mu_k(p)}\frac{l}{2}}\right)Y_k(y).\end{aligned} \tag{21.40}$$

Finally, we get expression for $\overset{\circ}{C}(p)$ as

$$\begin{aligned}\overset{\circ}{C}(x;y;p) = {} & \frac{C_0}{p} + \frac{N\overset{\circ}{I}(p)}{\sqrt{h}B\sqrt{\mu_0(p)}}\cdot\frac{sh\sqrt{\mu_0(p)}\left(x-\frac{l}{2}\right)}{ch\sqrt{\mu_0(p)}\frac{l}{2}}Y_0(y)\\ & + \sum_{k=1}^{\infty}\frac{N\overset{\circ}{I}(p)}{sB}\sqrt{\frac{2}{h}}\cdot\frac{h}{k\pi}\cdot\frac{\sin\frac{k\pi}{h}(a+s)-\sin\frac{k\pi}{h}a}{\sqrt{\mu_k(p)}}\cdot\frac{sh\sqrt{\mu_k(p)}\left(x-\frac{l}{2}\right)}{ch\sqrt{\mu_k(p)}\frac{l}{2}}Y_k(y).\end{aligned} \tag{21.41}$$

21.2.3 Mathematical Modeling of the Electrical Field

Mathematical modeling of the electrical field is the second boundary problem for differential equation of Laplace.

$$\frac{\partial^2\varphi}{\partial x^2} + \frac{\partial^2\varphi}{\partial y^2} = 0, \tag{21.42}$$

$$\frac{\partial\varphi}{\partial y}(x;y;t) = 0, \tag{21.43}$$

$$\frac{\partial\varphi}{\partial y}(x;h;t) = 0, \tag{21.44}$$

$$\frac{\partial\varphi}{\partial x}(l;y;t)=\begin{cases}0, & 0<y\le a\\ \frac{I(t)}{sB\gamma}, & a<y\le a+s\\ 0, & a+s<y\lhd h.\end{cases} \tag{21.45}$$

$$\frac{\partial\varphi}{\partial y}(l;y;t)=\frac{I(t)}{hB\gamma}, \tag{21.46}$$

$$\frac{\partial^2\overset{\circ}{\varphi}}{\partial x^2}+\frac{\partial^2\overset{\circ}{\varphi}}{\partial y^2}=0 \tag{21.47}$$

$$\frac{\partial\overset{\circ}{\varphi}}{\partial y}(x;0;p)=0, \tag{21.48}$$

$$\frac{\partial\overset{\circ}{\varphi}}{\partial y}(x;h;p)=0. \tag{21.49}$$

$$\frac{\partial\varphi}{\partial x}(0;y;p)=\begin{cases}0, & 0<y\le a\\ \frac{\overset{\circ}{I}(p)}{sB\gamma}, & a<y\le a+s\\ 0, & a+s<y<h.\end{cases} \tag{21.50}$$

$$\frac{\partial\varphi}{\partial y}(l;y;p)=\frac{\overset{\circ}{I}(p)}{hB\gamma}. \tag{21.51}$$

We present [10] a solution $\varphi(x;y;p)$ of the problem (21.42)–(21.51) in Furies series:

$$\overset{\circ}{\varphi}(x;y;p)=X(x;p)Y(y)-\frac{X''}{X}=\frac{Y''}{Y}=-\lambda^2$$

or

$Y''+\lambda^2Y=0$ with boundary conditions: $Y'(0)=0$; $Y'(h)=0$, if $\lambda\neq 0$. Then we obtain

$$Y(y)=A\sin\lambda y+B\cos\lambda y;\ Y'(y)=\lambda A\cos\lambda y-\lambda B\sin\lambda y$$

$$Y'(0)=\lambda A=0\Rightarrow A=0\Rightarrow Y(y)=B\cos\lambda yY';\ (y)=-\lambda B\sin\lambda y.$$

$Y'(h)=\lambda B\sin\lambda h=0\Rightarrow\sin\lambda h=0\Rightarrow\lambda_k=\frac{k\pi}{h},\ k=1,2,3$ or $Y_k(y)=B_k\cos\frac{k\pi}{h}y$. If $\lambda=0$, then $Y''(0)=0\Rightarrow Y(y)=A_0y+B_0$; $Y''(y)=A_0\Rightarrow A_0=0$ or $Y_0(y)=B_0$.

Differential equation with similar boundary condition allows one to define Eigen-functions of the problem in the form:

$$Y_k(y) = \begin{cases} \frac{1}{\sqrt{h}}, & k = 0 \\ \sqrt{\frac{2}{h}} \cos \frac{k\pi}{h} y, & k = 1, 2, \ldots \end{cases}$$

We present a solution $\varphi(x; y; p)$ of the problem in the form of Furies series on Eigen-functions:

$$\overset{\circ}{\varphi}(x; y; p) = \beta_0(x; p) Y_0(y) + \sum_{k=1}^{\infty} \beta_k(x; p) Y_k(y).$$

We substitute last expression into (21.42) and obtain

$$\beta_0''(x; p) Y_0(y) + \sum_{k=1}^{\infty} \beta_k''(x; p) Y_k(y) - \sum_{k=1}^{\infty} \frac{k^2 \pi}{h^2} \beta_k''(x; p) Y_k(y) = 0.$$

The common solutions of the differential equation are:

$$\beta_0''(x; p) = 0 \Rightarrow \beta_0(x; p) = M_0(p)x + N_0; \beta_k(x; p) = M_k(p) sh \frac{k\pi}{h} x + N_k(p) ch \frac{k\pi}{h} x$$

$$\overset{\circ}{\varphi}(x; y; p) = (M_0(p)x + N_0) Y_0(y) + \sum_{k=1}^{\infty} \left(M_k(p) sh \frac{k\pi}{h} x + N_k(p) ch \frac{k\pi}{h} x \right) Y_k(y).$$

By differentiating $\varphi(x; y; p)$ on x, we obtain

$$\frac{\partial \overset{\circ}{\varphi}}{\partial x}(x; y; p) = M_0(p) Y_0(y) + \sum_{k=1}^{\infty} \frac{k\pi}{h} \left(M_k(p) ch \frac{k\pi}{h} x + N_k(p) sh \frac{k\pi}{h} x \right) Y_k(y).$$

For $x = 0$, we have

$$\frac{\partial \overset{\circ}{\varphi}}{\partial x}(0; y; p) = M_0(p) Y_0(y) + \sum_{k=1}^{\infty} \frac{k\pi}{h} M_k(p) Y_k(y).$$

$$M_0(p) Y_0(y) + \sum_{k=1}^{\infty} \frac{k\pi}{h} M_k(p) Y_k(y) = \begin{cases} 0, & 0 < y \le a \\ \frac{\overset{\circ}{I}(p)}{sB\gamma}, & a < y \le a + s \\ 0, & a + s < y < h \end{cases}$$

$$M_0(p) = \frac{\overset{\circ}{I}(p)}{B\gamma\sqrt{h}}; \frac{k\pi}{h} M_k(p) = \frac{\overset{\circ}{I}(p)}{sB\gamma} \sqrt{\frac{2}{h}} \cdot \frac{h^2}{k^2\pi^2} \left(\sin \frac{k\pi}{h}(a + s) - \sin \frac{k\pi}{h} a \right)$$

For $x = l$, we have

$$\frac{\partial \overset{\circ}{\varphi}}{\partial x}(l;y;p) = M_0(p)Y_0(y) + \sum_{k=1}^{\infty}\frac{k\pi}{h}\left(M_k(p)ch\frac{k\pi}{h}l + N_k(p)sh\frac{k\pi}{h}l\right)Y_k(y).$$

$$M_0(p)Y_0(y) + \sum_{k=1}^{\infty}\frac{k\pi}{h}\left(M_k(p)ch\frac{k\pi}{h}l + N_k(p)sh\frac{k\pi}{h}l\right)Y_k(y) = \frac{\overset{\circ}{I}(p)}{hB\gamma}.$$

$$\frac{k\pi}{h}\left(M_k(p)ch\frac{k\pi}{h}l + N_k(p)sh\frac{k\pi}{h}l\right) = 0,$$

$$N_k(p) = \frac{-\overset{\circ}{I}(p)}{sB\gamma}\sqrt{\frac{2}{h}}\cdot\frac{h^2}{k^2\pi^2}\left(\sin\frac{k\pi}{h}(a+s) - \sin\frac{k\pi}{h}a\right)\cdot\frac{ch\frac{k\pi}{h}l}{sh\frac{k\pi}{h}l}.$$

$$\begin{aligned}\overset{\circ}{\varphi}(x;y;p) = &\left(\frac{\overset{\circ}{I}(p)}{\sqrt{h}B\gamma}x + N_0(p)\right)Y_0(y)\\ &+ \sum_{k=1}^{\infty}\frac{\overset{\circ}{I}(p)}{sB\gamma}\sqrt{\frac{2}{h}}\cdot\frac{h^2}{k^2\pi^2}\left(\sin\frac{k\pi}{h}(a+s) - \sin\frac{k\pi}{h}a\right)\frac{ch\frac{k\pi}{h}(x-l)}{sh\frac{k\pi}{h}l}Y_k(y).\end{aligned}$$

21.2.4 Matching of Boundary Conditions on the Border of Separation of Phases

Voltage U at the electro-chemical device is calculated using the 2-nd Kirchhoff's Law

$$\overset{\circ}{U} = \overset{\circ}{u^+} - \overset{\circ}{u^-}, \tag{21.61}$$

Let, for example

$$\overset{\circ}{u^-} = 0. \tag{21.62}$$

Then expression (21.61) transforms to the form:

$$\overset{\circ}{U} = \overset{\circ}{u^+}. \tag{21.63}$$

The increments of potential on anode and cathode are calculated by using the following relationships, respectively:

$$\overset{\circ}{\Delta}{}^{+}(x;y;p) = \overset{\circ}{u}{}^{+} - \overset{\circ}{\varphi}{}^{+}_{\ni}(x;y;p), \tag{21.64}$$

$$\overset{\circ}{\Delta}{}^{-}(x;y;p) = \overset{\circ}{u}{}^{-} - \overset{\circ}{\varphi}{}^{-}_{\ni}(x;y;p), \tag{21.65}$$

The approximation of the Nernst equation gives the following increments:

$$\overset{\circ}{\Delta}{}^{+}(x;y;p) = E_0 - E_1\,\overset{\circ}{C}{}^{+}(x;y;p); \tag{21.66}$$

$$\overset{\circ}{\Delta}{}^{-}(x;y;p) = E_0 - E_1\,\overset{\circ}{C}{}^{-}(x;y;p), \tag{21.67}$$

where $E_0 = 0.799$ V, $E_1 = 0.25 \cdot 10^{-1}\,\mathrm{V}/\left(\mathrm{kmol}/\mathrm{m}^3\right)$.

From comparison of (21.64) with (21.66) and (21.65) with (21.67), we have for $u^- = 0$:

$$\overset{\circ}{\varphi}{}^{+}_{\ni}(x;y;p) = \overset{\circ}{U} - E_0 - E_1\,\overset{\circ}{C}{}^{+}(x;y;p);\ \overset{\circ}{\varphi}{}^{-}(x;y;p) = -E_0 - E_1\,\overset{\circ}{C}{}^{-}(x;y;p)$$

From here, we have

$$\overset{\circ}{U}(p) = E_1\left(\overset{\circ}{C}{}^{+}(x;y;p) - \overset{\circ}{C}{}^{-}(x;y;p)\right) + \overset{\circ}{\varphi}{}^{+}_{\ni}(x;y;p) - \overset{\circ}{\varphi}{}^{-}_{\ni}(x;y;p).$$

Then we calculate necessary expressions at $x = 0$, $x = l$, $y = a + \frac{s}{2}$:

$$\overset{\circ}{U}(p) = E_1\left(\overset{\circ}{C}\left(l;a+\frac{s}{2};p\right) - \overset{\circ}{C}\left(0;a+\frac{s}{2};p\right)\right) + \overset{\circ}{\varphi}\left(l;a+\frac{s}{2};p\right) - \overset{\circ}{\varphi}\left(0;a+\frac{s}{2};p\right),$$

$$\overset{\circ}{C}\left(l;a+\frac{s}{2};p\right) = \frac{C_0}{p} + \frac{N\overset{\circ}{I}(p)}{\sqrt{h}B\sqrt{\mu_0(p)}} \cdot \frac{sh\sqrt{\mu_0(p)}\frac{l}{2}}{ch\sqrt{\mu_0(p)}\frac{l}{2}} \cdot \frac{1}{\sqrt{h}} + \sum_{k=1}^{\infty} \frac{N\overset{\circ}{I}(p)}{sB}\sqrt{\frac{2}{h}} \cdot \frac{h}{k\pi} \cdot \frac{\sin\frac{k\pi}{h}(a+s) - \sin\frac{k\pi}{h}a}{\sqrt{\mu_k(p)}} \cdot \frac{sh\sqrt{\mu_k(p)}\frac{l}{2}}{ch\sqrt{\mu_k(p)}\frac{l}{2}}\sqrt{\frac{2}{h}}\cos\frac{k\pi}{2}.$$

$$\overset{\circ}{C}\left(0;a+\frac{s}{2};p\right) = \frac{C_0}{p} - \frac{N\overset{\circ}{I}(p)}{\sqrt{h}B\sqrt{\mu_0(p)}} \cdot \frac{sh\sqrt{\mu_0(p)}\frac{l}{2}}{ch\sqrt{\mu_0(p)}\frac{l}{2}} \cdot \frac{1}{\sqrt{h}} - \sum_{k=1}^{\infty} \frac{N\overset{\circ}{I}(p)}{sB}\sqrt{\frac{2}{h}} \cdot \frac{h}{k\pi} \cdot \frac{\sin\frac{k\pi}{h}(a+s) - \sin\frac{k\pi}{h}a}{\sqrt{\mu_k(p)}} \cdot \frac{sh\sqrt{\mu_k(p)}\frac{l}{2}}{ch\sqrt{\mu_k(p)}\frac{l}{2}}\sqrt{\frac{2}{h}}\cos\frac{k\pi}{2}.$$

$$\overset{\circ}{\varphi}\left(l;a+\frac{s}{2};p\right)=\left(\frac{\overset{\circ}{I}(p)}{\sqrt{h}B\gamma}+N_0(p)\right)\cdot\frac{1}{\sqrt{h}}$$
$$+\quad\sum_{k=1}^{\infty}\frac{\overset{\circ}{I}(p)}{sB\gamma}\sqrt{\frac{2}{h}}\cdot\frac{h^2}{k^2\pi^2}\left(\sin\frac{k\pi}{h}(a+s)-\sin\frac{k\pi}{h}a\right)\cdot\frac{1}{sh\frac{k\pi}{h}l}\sqrt{\frac{2}{h}}\cos\frac{k\pi}{2}.$$

$$\overset{\circ}{\varphi}\left(0;a+\frac{s}{2};p\right)=N_0(p)\cdot\frac{1}{\sqrt{h}}$$
$$-\quad\sum_{k=1}^{\infty}\frac{\overset{\circ}{I}(p)}{sB\gamma}\sqrt{\frac{2}{h}}\cdot\frac{h^2}{k^2\pi^2}\left(\sin\frac{k\pi}{h}(a+s)-\sin\frac{k\pi}{h}a\right)\cdot\frac{ch\frac{k\pi}{h}l}{sh\frac{k\pi}{h}l}\sqrt{\frac{2}{h}}\cos\frac{k\pi}{2}.$$

So the finish expression for $\overset{\circ}{U}(p)$ is defined as

$$\overset{\circ}{U}(p)=\frac{2E_1N\overset{\circ}{I}(p)}{\sqrt{h}B\sqrt{\mu_0(p)}}\cdot\frac{sh\sqrt{\mu_0(p)}\frac{l}{2}}{ch\sqrt{\mu_0(p)}\frac{l}{2}}\cdot\frac{1}{\sqrt{h}}$$
$$+\quad\sum_{k=1}^{\infty}\frac{2E_1N\overset{\circ}{I}(p)}{sB}\sqrt{\frac{2}{h}}\cdot\frac{\sin\frac{k\pi}{h}(a+s)-\sin\frac{k\pi}{h}a}{\sqrt{\mu_k(p)}}\cdot\frac{sh\sqrt{\mu_k(p)}\frac{l}{2}}{ch\sqrt{\mu_k(p)}\frac{l}{2}}\sqrt{\frac{2}{h}}\cos\frac{k\pi}{2}$$
$$+\quad\frac{\overset{\circ}{I}(p)}{hB\gamma}l+\sum_{k=1}^{\infty}\frac{\overset{\circ}{I}(p)}{sB\gamma}\sqrt{\frac{2}{h}}\cdot\frac{h^2}{k^2\pi^2}\left(\sin\frac{k\pi}{h}(a+s)-\sin\frac{k\pi}{h}a\right)\cdot\frac{sh\frac{k\pi}{h}\frac{l}{2}}{ch\frac{k\pi}{h}\frac{l}{2}}\cdot\sqrt{\frac{2}{h}}\cos\frac{k\pi}{2}.\tag{21.68}$$

21.3 Conclusions

1. If a scientific calculation is required for a transient current process with given input voltage, then calculation result is represented as a specific sum of an infinite series. The number of terms in specific sum of the series is found by a predetermined current calculation error. In engineering calculations of transient current, an electrochemical device with a finite number of parallel branches with reactive elements is used.
2. Numerical calculations of an electrochemical device are possible only in the case of a system with known physical fields (concentration and electrical ones).
3. Mathematical model of an electrochemical device as an element of an electric circuit can be constructed after calculation of operating voltage at the device electrodes.

References

1. Y.Y. Gerasimenko, in *Mathematical Modeling of Electrochemical Systems* (SRSTU Press, Novocherkassk), 314 p. (2009)
2. Y.Y. Gerasimenko, E.Y. Gerasimenko, in *IWK Information Technology and Electrical Engineering—Devices and Systems, Materials and Technology for the Future*, Germany, Ilmenau, 7–10 Sept. 2009, p. 391 (2009)
3. Y.Y. Gerasimenko, N.I. Tsygulev, A.N. Gerasimenko, E.Y. Gerasimenko, D.D. Fugarov, O. A. Purchina, Life Sci. J. **11**(12), 265 (2014)
4. Y.Y. Gerasimenko, E.Y. Gerasimenko. in *IWK Information Technology and Electrical Engineering—Devices and Systems, Materials and Technology for the Future*, Germany, Ilmenau, 7–10 Sept. 2009, p. 389 (2009)
5. W.H. Beyer, in *CRS Standard Mathematical Tables and Formulae* (CRS Press, Boca Raton), 609 p. (1991)
6. B. Davis, *Integral Transforms and Their Applications* (Springer, New York, 1978)
7. E. Butkcov, *Mathematical Physics* (Addison-Wesley, Reading, 1968)
8. D. Zwillinger, in *Handbook of Differential Equations* (Academic Press, Boston), 673 p. (1989)
9. S.J. Farlow, *Partial Differential Equations for Scientists and Engineers* (John, New York, 1982)
10. A.N. Gerasimenko, Y.Y. Gerasimenko, E.Y. Gerasimenko, A.I. Emelyanov, in *Proceedings of the 2015 International Conference on "Physics, Mechanics of New Materials and Their Applications", Devoted to the 100th Anniversary of the Southern Federal University*, ed. by I. A. Parinov, S.-H. Chang, V.Y. Topolov, p. 537 (2016)

Chapter 22
Thermal Properties of As-Cast Bottom Ash Reinforced Aluminum Metal Matrix Composite

Harjo Seputro, I. Made Kastiawan and Gatut Priyo Utomo

Abstract The purpose of this research is to study characteristics of composite Al 6061 + coal ash, namely: thermal conductivity, linear thermal expansion, and melting point, density, porosity and hardness. Before testing, we carried out T6 treatment of material, where the material solution underwent to sintering at 538 °C during 16 h, then quenching, and artificial ageing. We studied the following cases: for temperatures 200, 225, 250 °C and holding times 8, 12, 16 h. The thermal conductivity tests were performed by using DSC (Differential Scanning Calorimetry) and TDA (Thermal Dilatometry Analysis) for linear thermal expansion, for melting point were used trial and error tests, Archimedes principle was used for density test, and hardness testing by Brinell hardness test. In this study, a minimum value of thermal conductivity factor (5.703 W/m K) was obtained at a temperature 200 °C with holding time 8 h, and a maximum value (8.314 W/m K) was obtained at a temperature 225 °C with holding time 12 h. Minimum value of linear thermal expansion (4.6238×10^{-4}/°C) was obtained at a temperature 225 °C with holding time 16 h and maximum value (7.7312×10^{-4}/°C) was obtained at a temperature 200 °C with holding time 8 h. The result of test melting point is 700–1000 °C, the optimum value of test density is 2.4044 g/cm^3 at 250 °C with holding time 8 h. The optimum value of porosity is 2.8876% at 250 °C with 8 h holding time. The higher aging temperature leads to longer holding time for the material during aging, the diffusion which occurs will be greater so the shrinkage will be even bigger causing a reduction in the volume of large pores. The maximum hardness was attained for the sample at 250 °C and holding time 12 h; the minimum hardness was found for the sample at 200 °C, and holding time 8 h.

H. Seputro (✉) · I.M. Kastiawan · G.P. Utomo
Mechanical Engineering Department, University of 17 Agustus 1945 Surabaya, Kota Surabaya, Indonesia
e-mail: harjoseputra@untag-sby.ac.id

I.M. Kastiawan
e-mail: madekastiawan@untag-sby.ac.id

G.P. Utomo
e-mail: gatut_pu@untag-sby.ac.id

I.A. Parinov et al. (eds.), *Advanced Materials*, Springer Proceedings in Physics 193, DOI 10.1007/978-3-319-56062-5_22

22.1 Introduction

The composite material has many advantages compared to existing materials, in addition to high resistance to damage, it is also lighter. Based on this, composite materials are widely used in several industries, such as aerospace and automotive industries.

Material characteristics are very important. Because knowing them, we can apply these materials appropriately. The characteristics in question are thermal, physical and mechanical. Composite Al + ash coal as an alternative material has not been well-characterized. So the study to determine their characteristics is very important.

Composite Al + ash coal has been produced. To get good results, the material was underwent T6 heat treatment. There are many examples of the applications of Al-based metal matrix composites, for instance linear cylinder of Honda Motor Company with Al_2O_3 reinforcement having well wear-resistant properties and low thermal expansion values.

Thermal characteristics define physical changes when material is exposed to heat either directly or indirectly. Thermal characteristics include several types: thermal conductivity, melting point, coefficient of linier thermal expansion [1]. Some important mechanical characteristics include strength, strain, hardness, fracture toughness, modulus of elasticity etc. But in this study we tested only the mechanical characteristics of the hardness. At the same time, the physical characteristics tested were the density and porosity.

22.1.1 Effect of Material Reinforcement with Precipitation and Dispersion for Heat Characteristics

One that needs to be reviewed in the technology of composite materials is to improve strength. Treatment, in which the solute atoms are added beyond the solubility, to process a solid solution at high temperature, is called solution treatment. After this treatment, by heating at various temperatures, phase precipitates generally arise.

Precipitates differ in sizes ranging from very small, visible only under an electron microscope to a large size that can be seen under an optical microscope with a low magnification. Precipitates have many shapes, in particular they are like balls, plates or needles.

The precipitates are dispersed in solid solution, defining dispersion strengthening. The dispersion strengthening has been developed further to produce some materials that were reinforced by artificial powder mix, fiber and so on, becoming stronger effectively. The material is a composite material, when it, in particular, consists of polymer materials and ceramics.

For metal materials, one example is a heat-resistant material. The most well way to strengthen the solid solution is the use of super-powder at high temperatures with a dispersion that does not react with matrix. For this purpose, the dispersion phase used would has exceeded strength at high temperatures and a stable shape of oxides such as Al_2O_3.

The material is processed by using the powder metallurgy techniques at composition optimization or using other materials for thermal dispersion. The sample Al 6061 transforms to Al_2O_3 with a value of thermal conductivity k = 171 W/m K (ASM Handbook, Vol. 21, 2001) [2].

This process is expected to be able to improve the material properties, especially thermal characteristics. It should be noted that thermal is one of the form of energy, which can pass from one object to another one because of the temperature difference between the objects.

22.1.2 Thermal Conductivity (ASTM C372, Vol. 15.02)

This property is designated as the transport properties, defining the rate, with which energy is transferred by diffusion processes. Thermal conductivity depends on the structure of matter, atoms and molecules associated with the state of matter, important aspects of its behavior identification and show the value of typical properties. The temperature gradient at various points and any time is defined as the change in temperature T on the distance x along the body:

$$Temperature\,Gradient = \frac{dT}{dx}. \tag{22.1}$$

Thermal conductivity (k) of rod material is defined as the heat flow (negative) per unit area (A), which is perpendicular to the direction of flow, and temperature gradient unity:

$$k = -\frac{Q}{A(dT/dx)}. \tag{22.2}$$

The negative sign input in the definition, because Q is positive (a heat flows from left to right), when the temperature gradient is negative. So, k has a positive magnitude. The above equation can be written as

$$Q = -kA\frac{dT}{dx}. \tag{22.3}$$

In general, a substance expands when it is heated. Swelling may cause problems, but it can also be used. Benefits of the expansion include: metal plates on the hulls,

bimetallic thermostats, bimetallic thermometers, and so on. At the expansion of the solids heated which experience a long-time expansion, the expansion area, and volume expansion are defined as

$$\Delta L = \alpha L_0 \Delta T. \tag{22.4}$$

In this case we also discussed the importance of the expansion portion which is no proportional between the reinforcement and matrix. Of course, some things are hard to avoid in the composite, anyway, one can control the overall characteristics of the matrix and the reinforcement and expansion of the distributed reinforcement in the matrix.

Many researchers have proposed a model to predict the thermal expansion coefficient of composite, the coefficient is determined experimentally and analyzes thermal characteristics in common of metal matrix composites. Solid line presents the predictions of the Turner model expansion coefficient as follows:

$$\alpha = \frac{\alpha_m V_m K_m + \alpha_{p1} V_{p1} K_{p1} + \alpha_{p2} V_{p2} K_{p2}}{V_m K_m + V_{p1} K_{p1} + V_{p2} K_{p2}}. \tag{22.5}$$

Solid line in Fig. 22.1 symbolizes the Turner model predictions and the above equation seems to predict the value is sufficiently well for different particle-reinforced composite.

Thermal conductivity, tested with regard to heat, has great difference in the direction of location of carbon fibers in aluminum matrix and can have very high value along the direction of fibers.

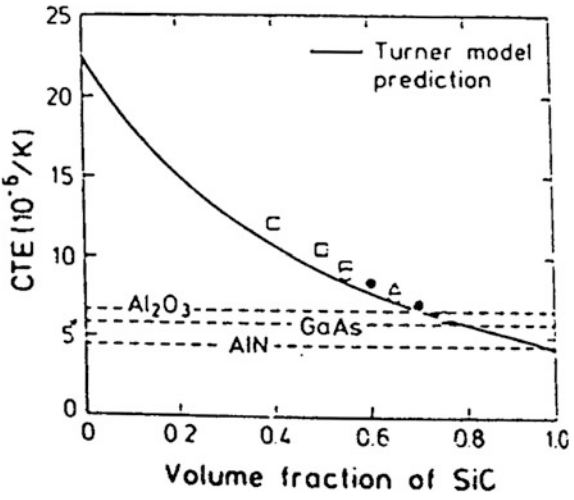

Fig. 22.1 Illustration of the Turner model prediction

22.1.3 Melting Point

Atomic energy prices in direct proportion to the melting point of the material. Comparison between actual temperature T and T_m, presenting the melting point (at fixed scale), give that their ratio for material must be less than 0.3:

$$\frac{T}{T_m} < 0.3 \tag{22.6}$$

One of the factors that should be considered in the design of materials a vicinity of melting point, especially for high-temperature applications. To achieve fuel efficiency and cleaner emissions, the engine needs to operate in the highest possible temperature. Because of their high melting point, ceramic material now are used and constantly tested as material applied for combustion chamber, such as in motor vehicles and aircraft [1].

22.1.4 Density and Porosity (ASTM C 20-92)

Density is a measurement of the weight of object per volume unit. Archimedes test is a testing process to get the dependence "density – porosity". The density (D) can be calculated as

$$D = \frac{W_d}{W_w - W_s}, \tag{22.7}$$

where D is the density (g/cm^3), W_d is the dry weight (g), W_w is the wet weight in air (g); W_s is the wet weight in water (g).

22.1.5 Brinell Hardness (ASTM E 384-89 Vol.05.02)

Principle of hardness testing is to determine the resistance of material to plastic deformation at the compression of material. Therefore, the hardness of a material is defined as material's resistance to applied force. Hardness testing is done by using a hardened steel ball with the load and indentation during certain time. The standard procedure requires testing by using steel ball with a diameter of 10 mm and a load of 3000 kg for testing ferrous metals, or 500 kg for non-ferrous materials; indentation time is usually about 30 s. Brinell hardness is defined as

$$\mathrm{BHN} = \frac{2p}{(\pi D)(D - \sqrt{D^2 - d^2})}, \tag{22.8}$$

where p is the load (kg), D is the diameter of indenter (mm), d is the diameter of trace (mm).

22.1.6 T6 Treatment

The heat treatment is a process to improve the properties of the material by heating the material to a certain temperature, and then cooling to a lower temperature. The heat treatment is carried out on castings for softening at low temperatures, annealing, normalizing, hardening and tempering. T6 heat process consists of three stages, namely:

(i) the process of dissolution (solution treatment);
(ii) the process of dyeing/rapid cooling (quenching);
(iii) the process of aging (artificial aging).

In the composite material, this process is performed at a temperature of 538 °C for 16 h [3]. The function of quenching is to maintain the soluble phase of saturated solution obtained from the process of solution. Dyeing interval is the time lost on the opening of a material to conduct heat into the cooling medium of immersed alloy. In this case, we use a tub filled with water + 10% sodium chloride during immersion range. The time must be reduced to a minimum and equal to 10–20 s.

Different processes deposition in the case of supersaturated solution are present in Fig. 22.2. Higher deposition temperatures can lead to grain-boundary precipitation and lower temperatures produce precipitation in the grain structure. After conducting the process of heating and quenching solution, the hardening can be achieved by heating precipitates due to artificial aging at temperature of 250 °C for 20 h [3]. In this case, the variables of artificial aging are the temperature and holding time (in our experiments these values are equal 200, 225, 250 °C for 8, 12, 16 h). For different temperatures and holding times, we can expect different processes and material characteristics.

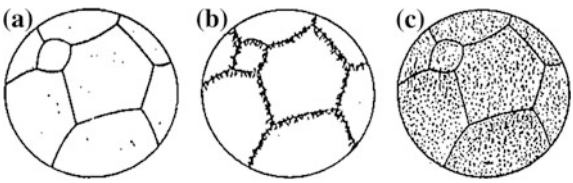

Fig. 22.2 **a** supersaturated solution, **b** deposition at the grain boundaries and **c** deposition in grain structure

22.2 Research Method

We study the test composite Al 6061 + coal ash under conditions of artificial aging at the different temperatures and holding times. We consider the following cases:

(A1) temperature 200 °C, holding time 8 h
(A2) temperature 200 °C, holding time 12 h
(A3) temperature 200 °C, holding time 16 h
(B1) temperature 225 °C, holding time of 8 h
(B2) temperature 225 °C, holding time 12 h
(B3) temperature 225 °C, holding time 16 h
(C1) temperature 250 °C, holding time of 8 h
(C2) temperature 250 °C, the holding time 12 h
(C3) temperature 250 °C, holding time 16 h.

22.3 Result and Discussion

22.3.1 Thermal Conductivity

The obtained results for thermal conductivity factor in various considered cases are present in Table 22.1 and Fig. 22.3.

Maximum value of thermal conductivity factor (8.313 W/m K) was attained at a temperature 225 °C. This increase in the value of the thermal conductivity factor is caused by the small value of the porosity, whereas the decreased value (5.703 W/m K) at a temperature of 200 °C is explained by the great value of porosity (see test results for density and porosity). These results are also consistent with the EDXA observation, where the content and the number of phases formed affect the thermal conductivity.

Table 22.1 Results for thermal conductivity factor

Specimen	k (W/m K)
A1	5.703
A2	7.843
A3	7.987
B1	8.147
B2	8.313
B3	8.147
C1	7.543
C2	7.686
C3	7.843

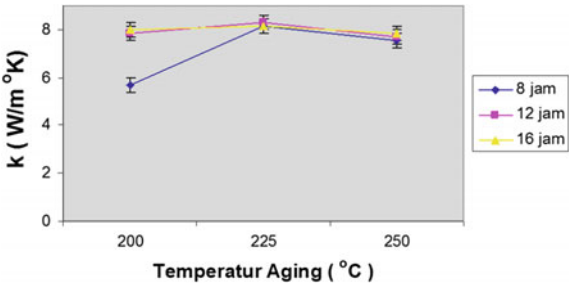

Fig. 22.3 Thermal conductivity factor versus aging temperature

22.3.2 Linear Heat Expansion

The obtained results for linear heat expansion factor in various considered cases are present in Fig. 22.4.

As it follows from Fig. 22.4, the values of linear heat expansion factor rise at temperatures of 200 °C from the value of $\alpha = 2.46/K$. This increase is caused by the large density and small porosity. The values decrease at the temperature of 250 °C and $\alpha = 1.77/K$. This result is explained by the small density and large porosity.

22.3.3 Melting Point

Test results (see Table 22.2) show that the melting point is the dominant factor, influenced by the type and fraction of reinforcement, can occur no effect, since the amount of reinforcement is small.

22.3.4 Brinell Hardness

Hardness tends to increase with increasing temperature (see Table 22.3 and Fig. 22.5). Hardness reached the maximum value for the sample with the temperature condition of 250 °C and holding time 12 h, and the minimum value with the temperature condition of 200 °C and holding time 8 h. The greater temperature increases the hardness value due to the formation of a growing number of precipitates.

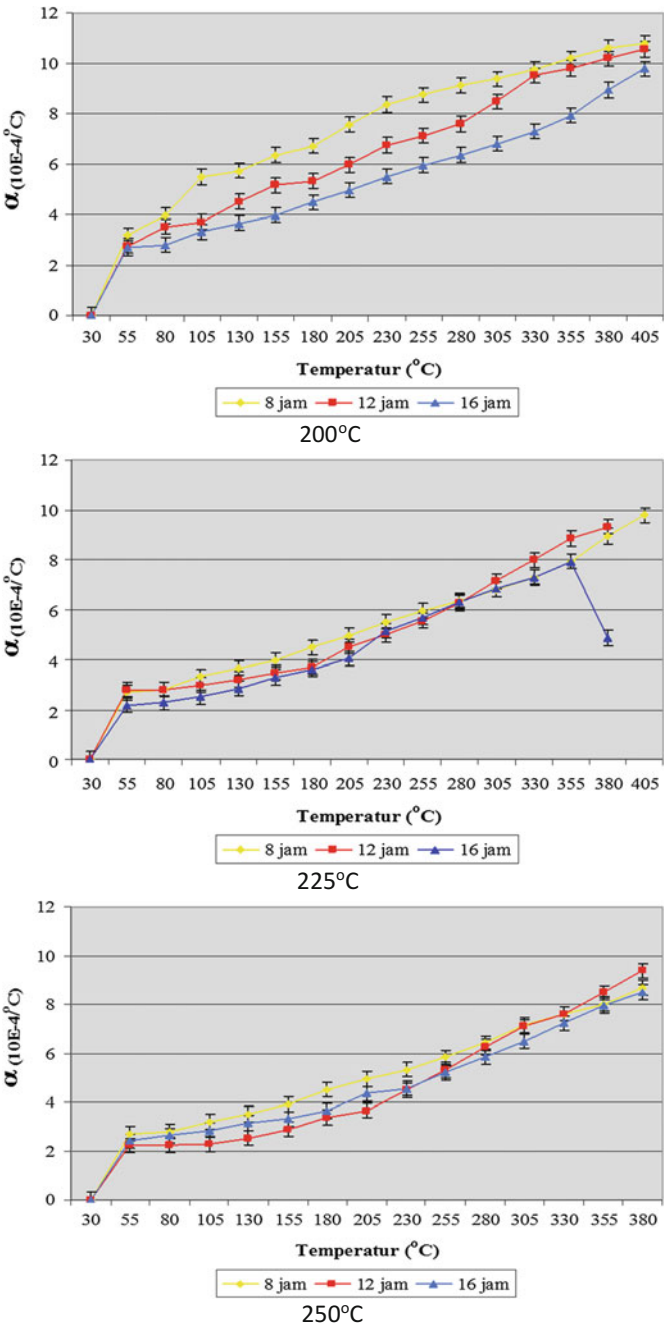

Fig. 22.4 Linear heat expansion factor versus temperature for different considered cases

Table 22.2 The melting point

Specimen	T_m (°C)
T6	700–1000
A1, A2, A3	700–1000
B1, B2, B3	700–1000
C1, C2, C3	700–1000

Table 22.3 Hardness reached the maximum value for the sample

Specimen	Indentation diameters (mm)			BHN (kg/mm^2)
	D_1	d_2	d average	
A_1	2.8	2.8	2.8	37.1
A_2	2.4	2.4	2.4	51.9
A_3	2.5	2.5	2.5	47.5
B_1	2.7	2.7	2.7	40.2
B_2	2.3	2.3	2.3	56.8
B_3	2.5	2.5	2.5	47.5
C_1	2.5	2.5	2.5	47.5
C_2	2.2	2.2	2.2	62.4
C_3	2.4	2.4	2.4	51.9

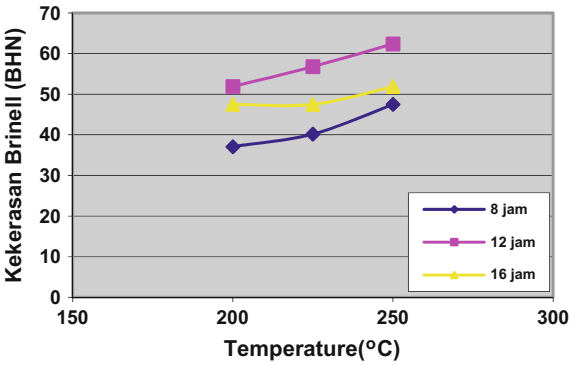

Fig. 22.5 Brinell hardness versus aging temperature

22.3.5 Density and Porosity

Increasingly high-temperature aging given for the composite material obtained has a tendency for percentage porosity first decrease and then increase. It is inversely proportional to the density values obtained. We obtained the following values of the porosity percentage for the composite material Al 6061–ash coal: 5.17, 3.25, and 4.33%, respectively for aging temperatures: 200, 225, and 250 °C.

The percentage value of porosity for composite material Al 6061–ash coal obtained at 200 °C aging is big enough (5.17%). This is due to the material is heated at a sufficiently low temperature of aging, so that the bonding exists between

the particles causing a small grain growth. So it ensures a little shrinkage and pore volume reduction.

In contrast, in the composite material with aging temperature of 225 °C, the percentage of porosity obtained much smaller (3.25%). The reason is the increasing aging temperature and holding time longer given to the material during aging. The existing diffusion will be greater so that the shrinkage that occurs also larger, reducing large pore volume.

The increase in porosity at a temperature of 250 °C backs to 4.33% due to the aging process is prolonged at the final stage, resulting in more grain growth that results in reduced grain boundary area and pore coarsening and it increases the percentage of porosity.

22.4 Conclusion

- Maximum heat conductivity was 7.03 W/m K in the composite obtained after T6-treatment at a temperature of 225 °C for 12 h holding time. At the same time, the minimum value (5.703 W/m K) was obtained in the composite after T6-treatment at a temperature of 200 °C for 8 h holding time.
- The higher temperature and the longer holding time after T6-treatment decrease linear thermal expansion. Its maximum value (2.46/K) is obtained at temperature of 200 °C aging. At the same time, the minimum value (1.77/K) is obtained at a temperature of aging 250 °C.
- The T6-treatment does not affect the value of the composite melting point. The values of melting point are in the temperature range of 700–1000 °C for all considered cases.
- The optimum value of density (2.4044 g/m^3) was achieved at a temperature of 250 °C and a holding time of 8 h. Increasing the final stage of the aging process and temperature cause excessive grain growth and coarsening of the pores, causing a decrease in the density from 2.73 g/cm^3 at a temperature of 225 °C to 2.40 g/cm^3 at a temperature of 250 °C
- Porosity testing optimum value achieved was 2.8876% at 250 °C aging temperature and holding time of 8 h. The higher aging temperature and longer holding time, given to the material during aging, ensure the greater diffusion and so the bigger shrinkage that leads to a reduction in the volume of large pores.
- The higher temperature provided the greater hardness for a time of 12 h-artificial aging and then decreased it at the 16 h holding time.
- The hardness reached its maximum with the temperature of 250 °C and 12 h holding time; its minimal value was observed at conditions of 200 °C and 8 h holding time.

References

1. L.P. Mangonon, in *The Principles of Materials Selection for Engineering Design* (Florida Institute of Technology Melbourne, Florida), p. 122 (1999)
2. M. Charles, et al., in *Composites* (*21st,* ASM Handbook Committee, Material Park), 840 pp (2001)
3. R.F. Christensen, in *Prosseding of IUTAM Symposiumon Mechanics of Composit Material* (Virginia Polytechnic Institute and State University, Blacksburg) (1982)
4. A.J. Hartomo, in *Komposit Metal* (Andi Offset, Yogyakarta), p. 15 (1992)
5. P. Malcom, in *Kimia Polimer* (PT Pradnya Paramita, Jakarta), p. 184 (1962)
6. R.W. Cahn et al., *Structure and Properties of Composites*, vol. 162 (VCH, New York, 1993)
7. S. Zemansky, in *Fisika Universitas* (Bina Cipta, Jakarta), pp. 368, 392 (1962)
8. R.E. Smallman, R.J. Bishop, D. Sriati, in *Metalurgi Fisik Modern dan Rekayasa Material* (Erlangga, Jakarta), p. 179 (2000)
9. Shinroku Saito dan Tata Surdia, in *Pengetahuan Bahan Teknik* (PT Pradnya Paramita, Jakarta), p. 47 (1985)
10. F.K. Thomas, A.J. James, in *Enginering Material Technology* (Prentice Hall), pp. 740 (1985)

Part III
Mechanics of Advanced Materials

Chapter 23
Elastic Wave Propagation in Anisotropic and Functionally Graded Layered Phononic Crystals: Band-Gaps, Pass-Bands and Low Transmission Pass-Bands

Mikhail V. Golub, Sergey I. Fomenko, Andrey A. Alexandrov, Chuanzeng Zhang, Yue-Sheng Wang and A-Li Chen

Abstract This paper describes a mathematical model of plane wave propagation in anisotropic and functionally graded layered phononic crystals with finite and infinite number of unit-cells. Classification of pass-bands and band-gaps is presented based on asymptotic analysis of the wave-fields in periodic layered structures. Two kinds of band-gaps where the transmission coefficient decays exponentially with the number of unit-cells are specified. The so-called low transmission pass-bands are introduced in order to identify frequency ranges in which the transmission is low enough for engineering applications, but it does not tend to zero exponentially with the number of unit-cells approaching infinity. The results of the numerical simulation are presented in order to demonstrate wave propagation phenomena. The influence of the anisotropy and functionally graded interlayers on the band-gaps and pass-bands is analysed.

M.V. Golub (✉) · S.I. Fomenko · A.A. Alexandrov
Institute for Mathematics, Mechanics and Informatics, Kuban State University, Stavropolskaya Str., 149, Krasnodar 350040, Russia
e-mail: m_golub@inbox.ru

S.I. Fomenko
e-mail: sfom@yandex.ru

C. Zhang
Chair of Structural Mechanics, Department of Civil Engineering, University of Siegen, Paul-Bonatz Strasse 9-11, 57076 Siegen, Germany

Y.-S. Wang · A.L. Chen
Institute of Engineering Mechanics, Beijing Jiaotong University, Beijing 100044, PR China

I.A. Parinov et al. (eds.), *Advanced Materials*, Springer Proceedings in Physics 193, DOI 10.1007/978-3-319-56062-5_23

23.1 Introduction

In recent years, there is a great deal of works on the analysis of the elastic wave propagation in phononic crystals [1]. Phononic crystals are functional materials composed of periodic arrays of two or more materials with different elastic moduli and mass densities. The effect of a complete reflection of time-harmonic waves by a periodic structure in certain frequency ranges is well-known as the band-gap or stop-band formation. Owing to the great advantages in a broad range of engineering applications, the wave propagation phenomena in structures with phononic crystals particularly play an important role in the design of new elastic and acoustic wave devices [2, 3]. Functionally graded materials are composites consisting of two or more material phases, characterized by a gradual variation in composition and structure in some spatial directions. In particular, blocking and resonance properties of phononic crystals can be strongly affected by the functionally graded variation of the material properties [4, 5].

The present study investigates the plane wave propagation in layered phononic crystals composed of anisotropic and functionally graded interlayers arisen from the solid diffusion of materials or due to manufacturing process. A classification of band-gaps in layered phononic crystals is proposed. The classification relies on the analysis of the eigenvalues of the transfer matrix for a unit-cell and the asymptotics for the transmission coefficient if the number of the unit cells tends to infinity. Two kinds of band-gaps, where the transmission coefficient decays exponentially with the number of unit-cells, are specified. The so-called low transmission pass-bands are introduced in order to identify frequency ranges where the wave transmission is very low for engineering applications, but it does not tend to zero exponentially as the number of the unit-cells tends to infinity. The dispersion equation and its relation to the pass-bands and band-gaps is also studied. It is demonstrated that either the P- or the S-wave propagates through the phononic crystal if the frequency belongs to a low transmission pass-band. A polyvalent analysis of the geometrical and physical parameters on band-gaps is presented.

23.2 Mathematical Statement

Let us consider a periodic layered structure which consists of N identical elastic unit-cells or one-dimensional (1D) phononic crystal between two elastic half-planes. The Cartesian coordinates (x, y, z) are introduced in such a way that the x-axis is parallel to the interfaces of the phononic crystal and the origin of the coordinate system is on the left boundary of the periodic structure (Fig. 23.1). Each of the N unit-cells is composed of two homogeneous elastic layers (A_0 and B_0) and two functionally graded (FG) interlayers between them so that the elastic properties of the whole unit-cell are continuous. The properties of the layers A and B are described the elastic constants $C_{ijmn,A}$ and $C_{ijmn,B}$, as well as, mass densities ρ_A and

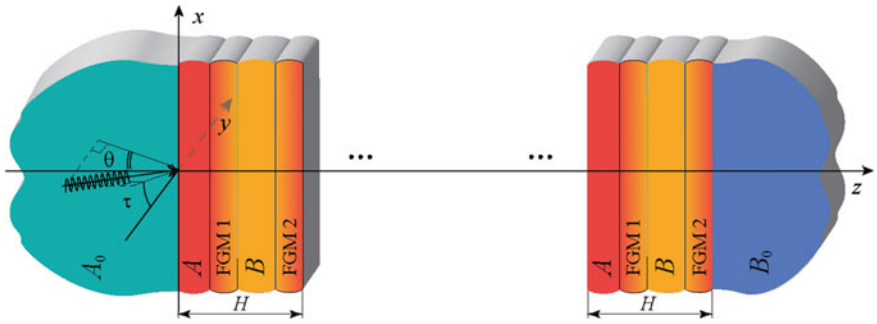

Fig. 23.1 Geometry of the problem

ρ_B, respectivelly. To describe the property variation in the local Cartesian coordinate system of the unit-cell of thickness H in the direction of the z-axis, two laws are used for the functionally graded interlayers. The function

$$P(z) = \begin{cases} P_A, & z \in [0, h_A], \\ (P_A - P_B)\left(\frac{z-h_A}{h_F}\right)^n, & z \in [h_A, h_A + h_F], \\ P_B, & z \in [h_A + h_F, h_A + h_F + h_B], \\ (P_B - P_A)\left(\frac{H-z}{h_{F'}}\right)^n & z \in [h_A + h_F + h_B, H] \end{cases} \tag{23.1}$$

provides a power law variation [4], while an exponential law is given by [5]

$$P(z) = \begin{cases} P_A, & z \in [0, h_A], \\ P_A \exp\left(\eta_A \frac{z-h_A}{h_F}\right), & z \in [h_A, h_A + h_F], \\ P_B, & z \in [h_A + h_F, h_A + h_F + h_B], \\ P_B \exp\left(\eta_B \frac{H-z}{h_{F'}}\right), & z \in [h_A + h_F + h_B, H] \end{cases} \tag{23.2}$$

with constant factors η_A and η_B. Here, P denotes an appropriate material property of the unit-cell materials that corresponds to a mass density or a component of the elasticity tensor, h_A and h_B are the thicknesses of the homogenous layers A and B, h_F and $h_{F'}$ are the thicknesses of two the FG interlayers such that $H = h_A + h_B + h_F + h_{F'}$. The entire periodic structure ($0 \le z \le NH$) is composed of N unit-cells with individual layers $a_{k-1} \le z \le a_k (a_k = a_{k-1} + H,\ k = 1, 2 \ldots, N)$.

For each unit-cell the partial differential equations of wave motion and the constitutive equations are given by

$$\begin{aligned} \sigma_{ij,j} &= \rho\, \ddot{u}_i, \\ \sigma_{ij} &= C_{ijmn} \varepsilon_{mn}. \end{aligned} \tag{23.3}$$

Here, σ_{ij} and $\varepsilon_{mn} = \frac{1}{2}(u_{m,n} + u_{n,m})$ are the stress and strain tensors, $\boldsymbol{u} = \{u_1, u_2, u_3\}$ is the displacement vector, $\rho(z)$ and $C_{ijmn}(z)$ are continuous functions of the forms (23.1) or (23.2).

The continuity conditions of the elastic displacements, normal (σ_{33}) and tangential (σ_{13}, σ_{23}) stresses at the internal interfaces $z = a_k$ can be written in terms of the state vector $\mathbf{v}(x, y, z) = \{u_1, u_2, u_3, \sigma_{13}, \sigma_{23}, \sigma_{33}\}$ as

$$\mathbf{v}(x, y, a_k - 0) = \mathbf{v}(x, y, a_k + 0). \tag{23.4}$$

The time-harmonic plane wave propagation is considered in this analysis. The incident plane wave $\mathbf{v_{inc}}$ with the angles of incidence θ and τ with respect to the z-axis (Fig. 23.1) and the wave filed $\mathbf{v}$ in the structure excited by the plane wave are given by

$$\mathbf{v}(x, y, z, t) = \mathrm{Re}\, \boldsymbol{V}(z) \exp(\mathrm{i}\, k_x x + \mathrm{i}\, k_y y - \mathrm{i}\, \omega t). \tag{23.5}$$

Here $\boldsymbol{V}$ is the vector of the complex amplitudes of the displacement and stress components, $k_x = k_0 \sin(\theta)$ and $k_y = -k_0 \sin(\tau)\cos(\theta)$ are the components of the wave propagation vector of the incident wave, k_0 is the wave number of the P- or S-waves in the half-space A_0, and ω is the circular frequency of the time-harmonic waves.

23.3 Solution of the Problem

23.3.1 Transfer Matrix of a Homogeneous Elastic Sub-layer

The governing (23.3) for an anisotropic elastic medium can be rewritten as the following system of ordinary differential equations in terms of the complex amplitude vector:

$$\frac{d\boldsymbol{V}}{dz} = K\boldsymbol{V}. \tag{23.6}$$

The matrix K can be expressed in terms of the elastic constants C_{ijmn}, the mass density ρ, the wavenumber k_0, the angles of incidence θ and τ, and the frequency ω.

The solution of (23.6) has the following matrix form:

$$\boldsymbol{V} = M\, E(z)\, \boldsymbol{c}, \tag{23.7}$$

where $\boldsymbol{c}$ is a vector of arbitrary constants. The matrix E is a diagonal matrix and depends on the position z.

The matrices E and M are composed of the eigenvalues and the eigenvectors of the matrix K in (23.6), and they have the following forms:

$$E = \mathrm{diag}\{e^{q_1 z}, e^{q_2 z}, \ldots, e^{q_6 z}\}, \quad M = (\boldsymbol{m}_1, \boldsymbol{m}_2, \ldots, \boldsymbol{m}_8),$$
$$(K - q_i I_6)\boldsymbol{m}_i = 0, \quad i = 1, 2, \ldots, 6.$$

The solution (23.7) provides the transfer matrix (T-matrix) relation as

$$\boldsymbol{V}_R = T_{layer}\, \boldsymbol{V}_L,$$

$$T_{layer} = M \cdot E(h) \cdot M^{-1}, \tag{23.8}$$

where h is the width of the layer, $\boldsymbol{V}_L$ and $\boldsymbol{V}_R$ are the values of $\boldsymbol{V}$ at the left and right interfaces of the layer. The correct branches should be chosen by using the principle of bounded energy absorption as

$$\mathrm{Re}\, q_s \geq 0, \ \mathrm{Im}\, q_s \geq 0, \quad s = 1, 2,$$

where $q_1 = \kappa_1 \cos\theta_1$ and $q_2 = \kappa_2 \cos\theta_2$.

For instance, in the case of an isotropic layer with wavenumbers κ_1 and κ_2 of P- and SV-waves, the matrix M is composed of four column-vectors as

$$M = \left(\boldsymbol{b}_1^+, \boldsymbol{b}_2^+, \boldsymbol{b}_1^-, \boldsymbol{b}_2^-\right), \tag{23.9}$$

$$\boldsymbol{b}_1^{\pm} = \{\mathrm{i}\kappa_1 \sin\theta_1, \pm\mathrm{i}\kappa_1 \cos\theta_1, \mp\mu\kappa_1^2 \sin 2\theta_1, -\mu\kappa_2^2 \cos 2\theta_2\}^T,$$
$$\boldsymbol{b}_2^{\pm} = \{\pm\mathrm{i}\kappa_2 \cos\theta_2, -\mathrm{i}\kappa_2 \sin\theta_2, -\mu\kappa_2^2 \cos 2\theta_2, \pm\mu\kappa_2^2 \sin 2\theta_2\}^T.$$

The matrix $E_k(z) = \mathrm{diag}\{e^{\mathrm{i}q_1 z}, e^{\mathrm{i}q_2 z}, e^{-\mathrm{i}q_1 z}, e^{-\mathrm{i}q_2 z}\}$ is a diagonal matrix composed of the exponentials. The angles θ_1 and θ_2 of the refracted P- and SV-waves satisfy following Snell's law in terms of the wavenumber and the angle of the incident plane wave [6]

$$\kappa_1 \sin\theta_1 = \kappa_2 \sin\theta_2 = \kappa_0 \sin\theta.$$

The angles θ_1 and θ_2 are the complex-valued and multivalent functions in general cases.

23.3.2 Transfer Matrix for a Layered Phononic Crystal

In order to simulate the plane wave scattering by a layered phononic crystal between two half-spaces, the transfer matrix method is used [7], where the total T-matrix for the whole layered periodic structure is composed of N T-matrices of the unit-cells, i.e., $T = T_{cell}^N$. If the unit-cell consists of L sub-layers then the transfer matrix $T_{cell} = T_L \cdot T_{L-1} \cdots T_1$ is a composition of the T-matrices for each sub-layer.

Using the Jordan basis of the matrix T_{cell}, the total T-matrix of the phononic crystal can be expressed as

$$T = G^{-1}\Lambda^N G, \tag{23.10}$$

where G is a change-of-basis matrix to the Jordan normal form $\Lambda = \mathrm{diag}(\{\lambda_1, \lambda_2, \ldots, \lambda_6\})$. The set of then eigenvalues λ_i $(i = 1, 2, \ldots, 6)$ is ordered by the rule $|\lambda_1| \geq |\lambda_2| \geq \cdots \geq |\lambda_6|$ for convenience.

The state vector for the half-spaces is represented by

$$\boldsymbol{V}_s(z) = M_s E_s(z - z_s)\boldsymbol{c}_s, \quad s = A, B,$$

in accordance with (23.7), where $z_A = 0$, $z_B = HN$. In the half-space A_0 the vector of the arbitrary constants $\boldsymbol{c}_A = \{\boldsymbol{d}_0, \boldsymbol{r}\}$ consists of two vectors, $\boldsymbol{d}_0$ is the displacement vector of the incident plane wave, and $\boldsymbol{r}$ is the vector of the amplitude reflection coefficients. The vector $\boldsymbol{c}_B = \{\boldsymbol{t}, \boldsymbol{0}\}$ is composed of the zero vector $\boldsymbol{0}$ and the transmission coefficients $\boldsymbol{t}$ describing the amplitudes of the plane waves in the half-space B_0. The lengths of these sub-vectors are the same. Using the T-matrix of the phononic crystal (23.10), the equation $\boldsymbol{V}_B(HN) = T\boldsymbol{V}_A(0)$ leads to the following equation to determine the transmission coefficients

$$A\,\boldsymbol{t} = \boldsymbol{d}_0, \quad A = (I_3 0_3) D (I_3 0_3)^{\mathrm{T}} \tag{23.11}$$

and the reflection coefficients

$$\boldsymbol{r} = B\boldsymbol{t}, \quad B = (0_3\, I_3) D (I_3 0_3)^{\mathrm{T}}. \tag{23.12}$$

Here, the matrices I_3 and 0_3 are three-by-three identity and zero matrices. So A and B are the top-left and the bottom-left blocks of the matrix $D = M_A^{-1} T^{-1} M_B$.

According to (23.10) the elements of the matrix A may have an exponential behaviour with increasing number N of the unit-cells. Application of the conventional numerical routines in order to solve the system (23.11) may lead to unstable results. However, it is possible to represent the transmission coefficients explicitly in terms of the eigenvalues λ_i $(i = 1, 2, \ldots, 6)$ as

$$\begin{aligned} t_s &= \frac{\Delta_s}{\Delta}, \quad \Delta_s = \sum_{i=1}^{5} \sum_{j=i+1}^{6} \beta_{s\,ij} \left(\frac{\lambda_i \lambda_j}{\lambda_1 \lambda_2 \lambda_3} \right)^N, \quad s = 1, 2, 3; \\ \Delta &= \sum_{i=1}^{4} \sum_{j=i+1}^{5} \sum_{k=j+1}^{6} \alpha_{ijk} \left(\frac{\lambda_i \lambda_j \lambda_k}{\lambda_1 \lambda_2 \lambda_3} \right)^N. \end{aligned} \tag{23.13}$$

The coefficients α_{ijk} and $\beta_{s\,ij}$ are the determinants of the matrices and not depend on λ_i and N, which can be written as

$$\alpha_{ijk} = \left|A(\boldsymbol{\eta}_{ijk})\right|, \quad \boldsymbol{\eta}_{ijk} = \{\eta_{6,ijk}, \eta_{5,ijk}, \ldots, \eta_{1,ijk}\}, \quad \eta_{m,ijk} = \max(\delta_{mi}, \delta_{mj}, \delta_{mk});$$
$$\beta_{s\,ij} = \left|A'_s(\boldsymbol{\tau}_{ij})\right|, \quad \boldsymbol{\tau}_{ij} = \{\tau_{6,ij}, \tau_{5,ij}, \ldots, \tau_{1,ij}\}, \quad \tau_{m,ij} = \max(\delta_{mi}, \delta_{mj}), \quad m = 1, 2 \ldots 6.$$

Here δ_{mi} is the Kronecker delta. The matrix function $A(\boldsymbol{\eta})$ depends on six components of a vector $\boldsymbol{\eta}$ as follows

$$A(\boldsymbol{\eta}) = (I_3 0_3) M_A^{-1} G^{-1} (\mathrm{diag}(\boldsymbol{\eta}))^{-N} G M_B (I_3 0_3)^{\mathrm{T}}. \tag{23.14}$$

The matrix function $A'_s(\boldsymbol{\eta})$ is formed via the replacement of the sth column of $A(\boldsymbol{\eta})$ by the column vector $\boldsymbol{d}_0$ in accordance with Cramer's rule.

The calculation of the transmission coefficients (23.13) is numerically stable since the denominator $\Delta = O(1)$ and Δ_s are composed of terms that cannot grow exponentially, if $N \to \infty$.

23.3.3 Transfer Matrix for Functionally Graded Phononic Crystals

The T-matrix method can be exploited for the analysis of FG phononic crystals in a similar manner to the procedure described above. Let us consider the unit-cell of a FG phononic crystal as described in Sect. 23.2. It is composed of the homogeneous layers A and B of the thicknesses h_A and h_B and two FG interlayers (AB and BA) of the thickness h_F. Thus, the T-matrix for the unit-cell is given by

$$T_{cell} = T_{BA} \cdot T_B \cdot T_{AB} \cdot T_A, \tag{23.15}$$

where T_A and T_B are the T-matrices of the homogeneous elastic layers (23.9). The T-matrices for the FG interlayers T_{AB} and T_{BA} have been evaluated numerically except some particular cases, e.g., exponential laws or special power laws for the material gradation [8].

A simple layer model (LM) for the FG layer is used further. According to the LM, the T-matrix of the FG layers are approximated by the product of the T-matrices $T_{AB,j}$ and $T_{BA,j}$ for the M sub-layers (Fig. 23.2b) as

$$T_{AB} \approx \prod_{j=M}^{1} T_{AB_j}, \quad T_{BA} \approx \prod_{j=M}^{1} T_{BA_j}. \tag{23.16}$$

Each sub-layer AB_j is limited by the planes $z = z_{j-1}$ and $z = z_j$, and it has the constant material properties $\rho_j = \rho(\bar{z}_j)$ and $C_{ikmn,j} = C_{ikmn}(\bar{z}_j)$, where

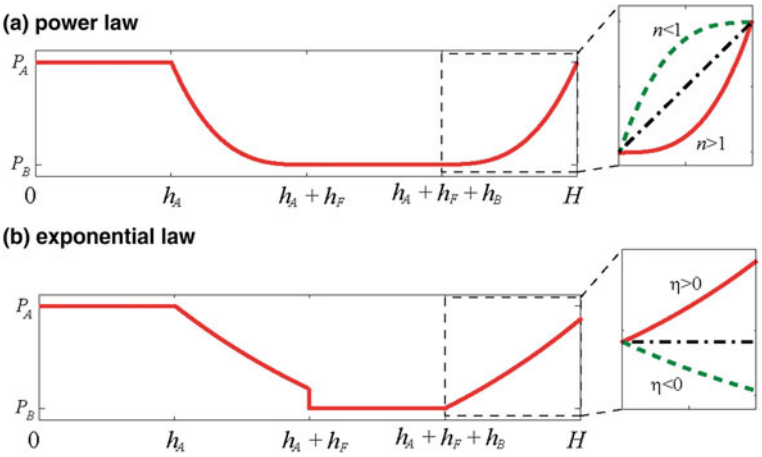

Fig. 23.2 Property variation in a unit-cell of an FG phononic crystal **a** power law, **b** exponential law

$$z_j = h_A + h_j(j-1),\ \bar{z}_j = h_A + h_j(j-\tfrac{1}{2}), j = 1,2,\ldots,M.$$

Similarly, the boundaries of the sub-layers BA_j are determined by

$$z_j = H - h_F + h_j(j-1), \bar{z}_j = H - h_F + h_j(j-\tfrac{1}{2}), \quad j = 1,2,\ldots,M.$$

The sub-layers have the same thickness $h_j = h_F/(M-1)$.

In the numerical calculations, normalized parameters are introduced for convenience. The length parameter equal to the thickness of the unit-cell H and the shear wave velocity $\boldsymbol{c}_A$ of the material A are used for the normalization. Accordingly, the normalized frequency is defined by $\Omega = \omega H/(2\pi c_A)$.

Our numerical studies have shown that with the increasing number of the sub-layers, the relative error in the calculated band-gaps decreases. In particular, our numerical experiments have demonstrated that $M = 200$ sub-layers are more than sufficient to achieve convergent results. An example of the convergence study of the calculated band-gaps for incident P- and SV-waves ($\theta = 40^\circ$) is shown in Fig. 3 for the phononic crystal composed of the isotropic materials Alumina and Aluminium with the same thickness ($h_A/h_B = 1$). The FG interlayers have the thickness $h_F/H = 0.5$, and the material parameters are described by (23.1) and (23.2) with $n = 3$. The parameters of the homogeneous layers are given in Table 23.1. The numerical results are visibly indistinguishable, if $M > 60$. In Fig. 23.3, the coloured and the dashed domains in the sub-plots are band-gaps and low transmission pass band, which will be discussed in Sect. 23.5 in details.

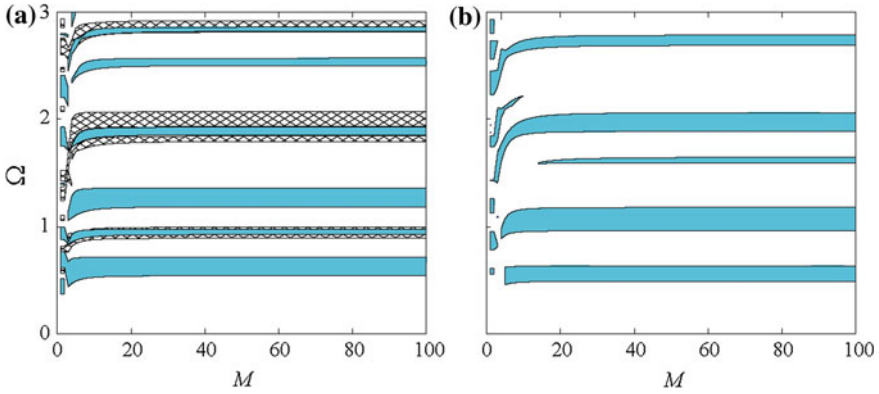

Fig. 23.3 Band-gap convergence with increasing number M of the homogeneous sub-layers to approximate the FG sub-layers for incident P-wave **a** and S-wave **b** at an incident angle $\theta = 40°$

Table 23.1 Material parameters

Notation	Materials	Density (kg/m^3)	Young's modulus (GPa)	Poison' ratio
Isotropic				
A	Alumina	4000	400	0.231
B	Aluminium	2700	70	0.33
Anisotropic				
A	Graphite/epoxy	1600	$C_{11} = C_{33} = 7.3802$ GPa, $C_{12} = C_{23} = 2.3121$ GPa, $C_{13} = 1.8682$ GPa, $C_{22} = 173.406$ GPa, $C_{44} = C_{66} = 3.445$ GPa, $C_{55} = 1.378$ GPa	

23.4 Pass-Bands and Band-Gaps in Layered Phononic Crystals

The most interesting phenomenon of phononic crystals is the existence of band-gaps or stop-bands. Band-gaps are frequency ranges, where the transmission of elastic waves or mechanical energy in the periodic structure is impossible. All other frequency ranges, in which a non-zero wave transmission is observed, are called pass-bands. In the present investigation, oblique wave incidence is also considered. Band-gaps valid for all incidence angles are often denoted as full or complete band-gaps. It should be noted here, that periodic structures with a finite and infinite number of unit-cells are considered here. The definition of band-gaps here differs slightly from the band-gap definition for infinite phononic crystals.

In phononic crystals with an infinite number of unit-cells, the special type of waves known as Floquet-Bloch waves can propagate through the periodic structure. At least one Floquet-Bloch wave propagates without attenuation at a given

frequency within the pass-band. The frequency range in which all Floquet-Bloch waves propagate with attenuation corresponds to a band-gap. Accordingly, the analysis of the band structure can be based on the dispersion equation:

$$|T_{cell} - \exp(\mathrm{i}\zeta H)I| = 0, \tag{23.17}$$

with respect to the wavenumber ζ_n of (23.17). The dispersion (23.17) has 6 complex roots in the strip: $-\pi \le \mathrm{Re}\zeta_n \le \pi$, the latter are closely related to the eigenvalues λ_n via the relation $\zeta_n = \frac{\mathrm{i}}{H} \ln \lambda_n$. The frequency dependence of ζ_n $(n = 1, 2, 3)$ forms the dispersion curves, and the corresponding analysis is a common way to study the pass-bands and band-gaps. In band-gaps, all of the solutions (23.17) have a non-zero imaginary part. Another characteristic to analyse the band-gaps is the localization factor. Floquet-Bloch waves at the frequencies laying within the band-gap have an exponential decay as $e^{-\gamma z}$. The coefficient $\gamma = \min \gamma_n$ is the localization factor, which is the minimum of the attenuation factor $\gamma_n = \mathrm{Im}\,\zeta_n \ge 0$. Within the pass-band at least one of ζ_n is purely real, therefore we have $\gamma = 0$.

The dispersion curves and the localization factors are also useful for the analysis of phononic crystals with a finite number of unit-cells between two half-spaces as considered in this study. However the primary factors are the amplitude transmission coefficients $\boldsymbol{t}$ or the energy transmission coefficient κ^+. They must decrease in the band-gaps exponentially with the increasing number of the unit-cells.

The convinience of the energy transmission coefficient is that κ^+ is the normalized factor due to the following energy conservation law:

$$\kappa^+ + \kappa^- = 1,$$

where κ^- is the energy reflection coefficient. The energy transmission and reflection coefficients are defined as the ratio of the energy amounts of the transmitted (E^+) and reflected (E^-) waves by the phononic crystal and the energy amount E_0 transferred by the incident wave [9], i.e.

$$\kappa^\pm = E^\pm / E_0.$$

For the plane wave propagation, the energy flow is proportional to the normal components of the Umov-Pointing vectors

$$E^\pm = C\mathrm{Im}(\boldsymbol{u}^\pm, \boldsymbol{\tau}^\pm), \quad E_0 = C\mathrm{Im}(\boldsymbol{u}_{inc}, \boldsymbol{\tau}_{inc}),$$

where C is a constant, $\boldsymbol{u}^\pm, \boldsymbol{\tau}^\pm$ are the wave field at the left $(-)$ and the right $(+)$ boundaries of the phononic crystal ($z = 0$ and $z = HN$, respectively), $\boldsymbol{u}_{inc}, \boldsymbol{\tau}_{inc}$ are the displacement and stress vectors of the incident plane wave on the left boundary of phononic crystal. The energy transmission coefficient is used for the estimation

Table 23.2 Band structure classification

Type of band	Condition	Localization factor γ
Pass-band (PB)	$h_B = h_{F'} = 0$	0
Band-gap of 1. kind (BG-I)	$(\forall n \in Y \gamma_n > 0) \wedge (\exists Y' \subset Y : (\forall k \in Y', \lvert\tilde{\boldsymbol{t}}_k\rvert > 0) \wedge (\forall j \in Y/Y', \lvert\tilde{\boldsymbol{t}}_j\rvert = 0))$	$\min_{k \in Y'} \gamma_k$
Band-gap of 2. kind (BG-II)	$\exists Y' \subset Y : (\forall k \in Y', \gamma_k > 0, \lvert\tilde{\boldsymbol{t}}_k\rvert > 0) \wedge (\forall j \in Y/Y', \gamma_j = 0, \lvert\tilde{\boldsymbol{t}}_j\rvert = 0)$	$\min_{k \in Y'} \gamma_k$
Low transmission pass-band (LTPB)	$\exists Y' \subset Y : (\forall k \in Y', \gamma_k > 0, \lvert\tilde{\boldsymbol{t}}_k\rvert \geq 0) \wedge (\forall j \in Y/Y', \gamma_j = 0, 0 < \lvert\tilde{\boldsymbol{t}}_j\rvert < \varepsilon < 1)$	0

Note Here $Y = \{1, 2, \ldots, L\}$, $L = 1$ for anti-plane and $L = 2$ for in-plane waves in isotropic PnCr, $L = 3$ for anisotropic PnCr

of the numerical convergence or when periodic defects are introduced into the phononic crystal [10, 11].

Another way to analyze the band structure is to use the derived semi-analytical expression (23.13) for the transmission coefficients. The asysmptotics of (23.13) at $N \to \infty$ has the following form

$$\boldsymbol{t} \sim \sum_{n=1}^{3} \tilde{\boldsymbol{t}}_n \exp(\mathrm{i}\, \zeta_n H N), \tag{23.18}$$

which provides the band-gap and pass-band classification as given in Table 23.2.

23.5 Numerical Analysis

23.5.1 Band-Gaps and Low Transmission Pass-Bands

Some numerical examples for the band-gaps are demonstrated in Fig. 23.4, where an FG phononic crystal with isortopic interlayers of Alumina and Aluminium is considered for $h_F = 0.1\,\mathrm{H}$ and $h_A/h_B = 1$. An incident SV-wave is considered for normal incidence ($\theta = 0°$) and oblique incidence at a very small angle ($\theta = 5 \cdot 10^{-4\,\circ}$), see left and right columns of the subplots. Remarkable changes of the energy transmission coefficient at some frequencies are observed, if the angle of wave incidence becomes non-zero, see Fig. 23.4a, b. The band-gaps of 1. kind (BG-I) retains, while the band-gaps of 2. kind (BG-II) are converted to low transmission pass-bands (LTPBs) if $\theta \neq 0°$. The frequency ranges are marked as follows: the BG-I are represented by blue rectangles, the BG-II are marked by purple dashed and the LTPBs are designated by yellow rectangles.

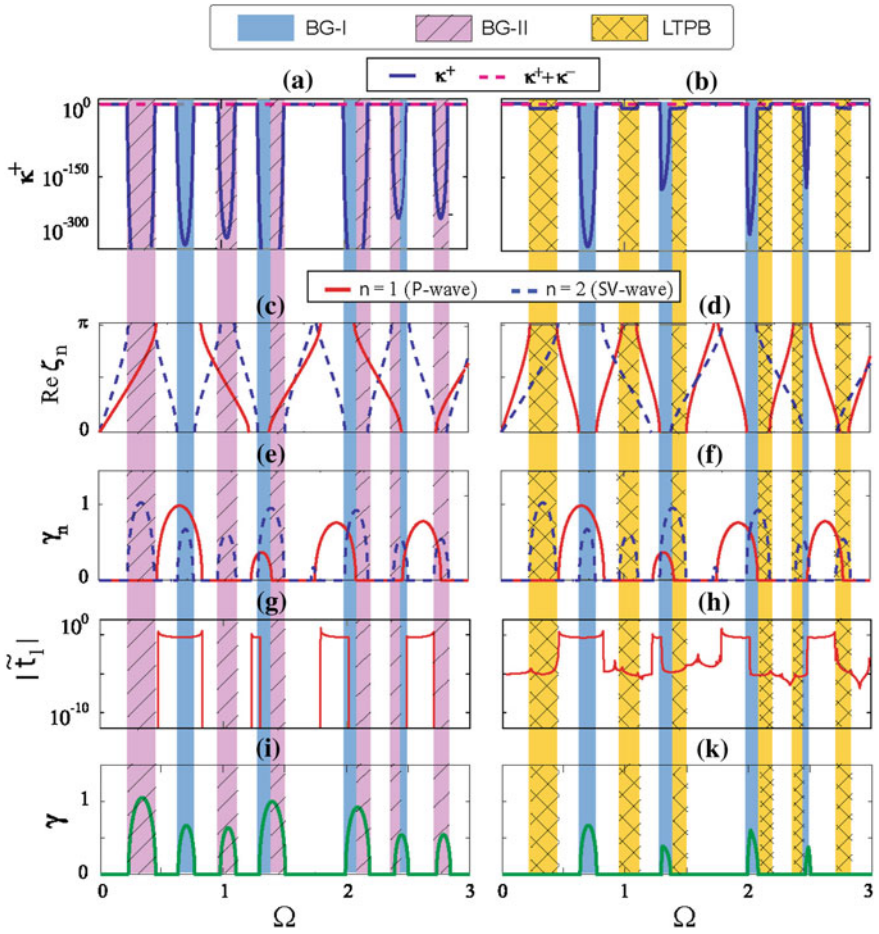

Fig. 23.4 Transition of BG-II for normally incident SV-wave with $\theta = 0°$ (**a**, **c**, **e**, **g**, **i**) to LTPB for an incidence angle $\theta = 5 \cdot 10^{-4}°$ (**b**, **d**, **f**, **h**, **k**) in isotropic FGM PnC. Frequency dependencies of transmission coefficient κ^+ (**a**, **b**), localization factor (**c**, **d**), real disperse curves of wavenumbers for Floquet-Bloch (pseudo-P, pseudo-SV) waves (**e**, **f**), its attenuation factors (**g**, **h**) and amplitude factor $\tilde{t}_1$ for pseudo-P-waves (**i**, **k**)

The sub-plots of Fig. 23.4 denoted by (e)–(h) show the dispersion curves of the Floquet-Bloch waves (in terms of the real and imaginary parts of the wavenumbers) in the case of an infinite number of unit-cells. Here, solid and dashed lines can be associated with pseudo-longitudinal and pseudo-transverse waves in the considered periodic structure of an infinite extent. Therefore the BG-II and LTBPs for the incident SV-wave are observed in the frequency ranges, where the pseudo S-wave is attenuated. For the considered phononic crystal with a finite number of unit-cells, the amplitude of the pseudo-P-wave is expressed via the factor $\tilde{\mathbf{t}}_1$ in (23.18). It can

be zero at the normal incidence, while it is usually non-zero for an oblique incidence, see Fig. 23.4i, k. In accordance with the classification criterions given in Table 23.2, the BG-II are observed for $\theta = 0°$, and they are converted to the LTPBs with the increase of the incidence angle θ. The localization factor is shown in Fig. 23.4c, d. The numerical analysis shows that the BG-II may appear only in the case of normally incident waves ($\theta = 0°$). In the case of anisotropic phononic crystals, the BG-II are observed if at least one of the angles θ and τ is equal to zero [12].

The LTPBs occur only if $\theta \neq 0°$ and they arise usually from the BG-II. The consideration of an arbitrary incidence angle like in the present investigation demands some comments and examples regarding the relation between the solutions for the normal incidence and the oblique incidence. The transition of the BG-II (purple ranges at left sub-plots) to the LTPBs (yellow ranges at right sub-plots) is demonstrated in Fig. 23.4. Though there is a jump in the localization factor from zero to a certain small non-zero value due to the special asymptotic behaviour, the other quantities of the solutions (the energy transmission coefficient κ^+, the eigenvalues λ_n, and $\tilde{t}_n$ etc.) are smooth functions of θ.

23.5.2 *Influences of Functionally Graded Interlayers on Band-Gaps*

In this section the influences of the thicknesses of the homogenous layers and FG interlayers in the unit-cell as well as the incident wave on the band-gaps are analyzed. The band-gap diagrams are used to show the variations of the band-gaps with the variation of the geometrical and material parameters. Different types of the band-gaps and pass-bands are marked in different ways in Figs. 23.5 and 23.6. Graded domains are the BG-I, the gradually coloured domains with light hatching are the BG-II, the LTPBs with a transmission coefficient $\kappa^+ < 0.1$ are designated by hatching only, and purely white domains correspond to pass-bands.

The color intensity for the BG-I and BG-II is given in accordance with the localization factor γ, which is non-zero within the band-gaps. The value of the localization factor is shown by a corresponding colour, and the last column in each figure shows the localization factor within the band-gaps. In some cases the width of the LTPB is very small and therefore such "point" band-gaps are marked by dashed lines.

Functionally graded interlayers may have significant influences on the elastic wave propagation in layered periodic phononic crystals. The dependence of the band structure on the relative thickness of the FG interlayers h_F/H for incident *P*-waves at different incidence angles θ is shown in Fig. 23.5. The band-gap diagrams for incident *SV*-waves at the same incidence angles are given in Fig. 23.6. Obviously, $h_F = 0$ corresponds to the case of a phononic crystal composed of homogenous elastic layers only. The band-gaps shift to higher frequencies with increasing h_F/H.

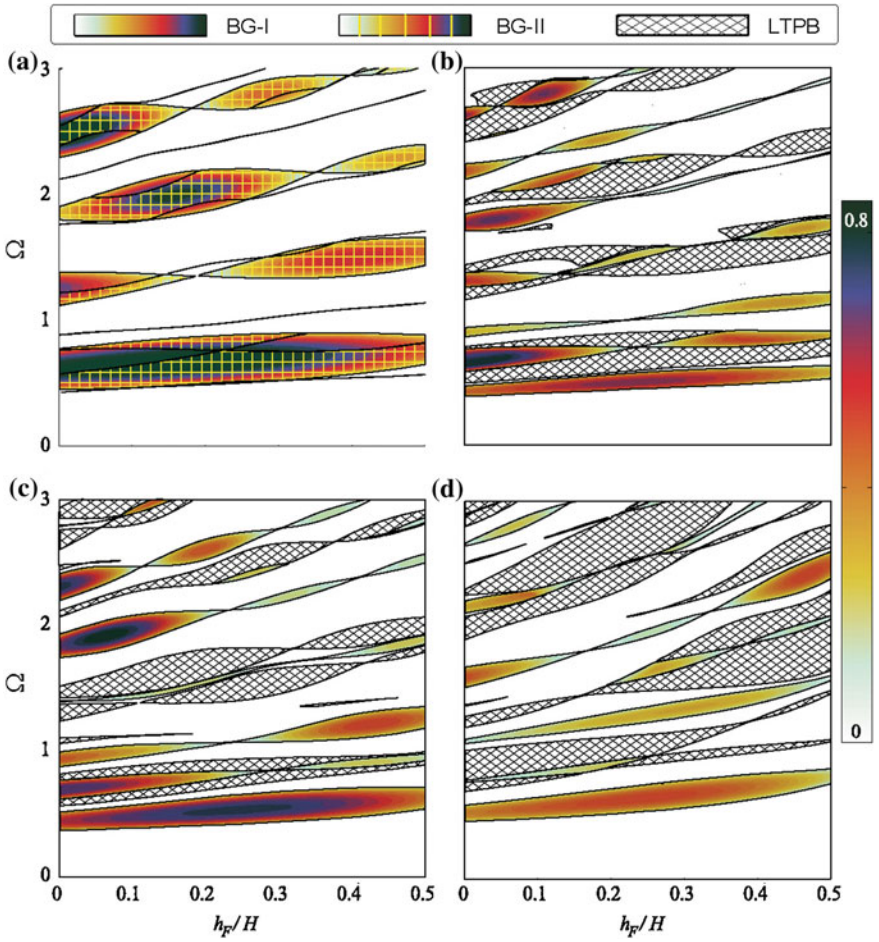

Fig. 23.5 Influence of the relative thickness of FG interlayers h_F/H on band-gaps for incident *P*-waves at angles $\theta = 0°$ (**a**), $\theta = 20°$ (**b**), $\theta = 40°$ (**c**) and $\theta = 80°$ (**d**), and for $h_A/h_B = 1$

Usually the width of the first band-gap at low frequencies (see for example Fig. 5a) depends only weakly on h_F/H, while the width of the high-frequency band-gaps changes more considerably with h_F/H and it may shrink to zero in certain cases.

Some point band-gaps are observed in these figures (see curves in Fig. 23.5a). The term "point band-gap" is used here for the case of an infinitesimally small width in the frequency domain for fixed parameters of the phononic crystal. The point stop-band is transformed to the conventional band-gap with increasing incidence angle.

If the incidence angle deviates from zero, then the BG-II are changed to the LTPBs as shown in Fig. 23.4. Therefore, two different kinds of band-gaps in Fig. 23.5b–d can be observed. Some BG-I exist in a consolidation with the LTPBs. This consolidation continuously changes with the variation of the relative thickness

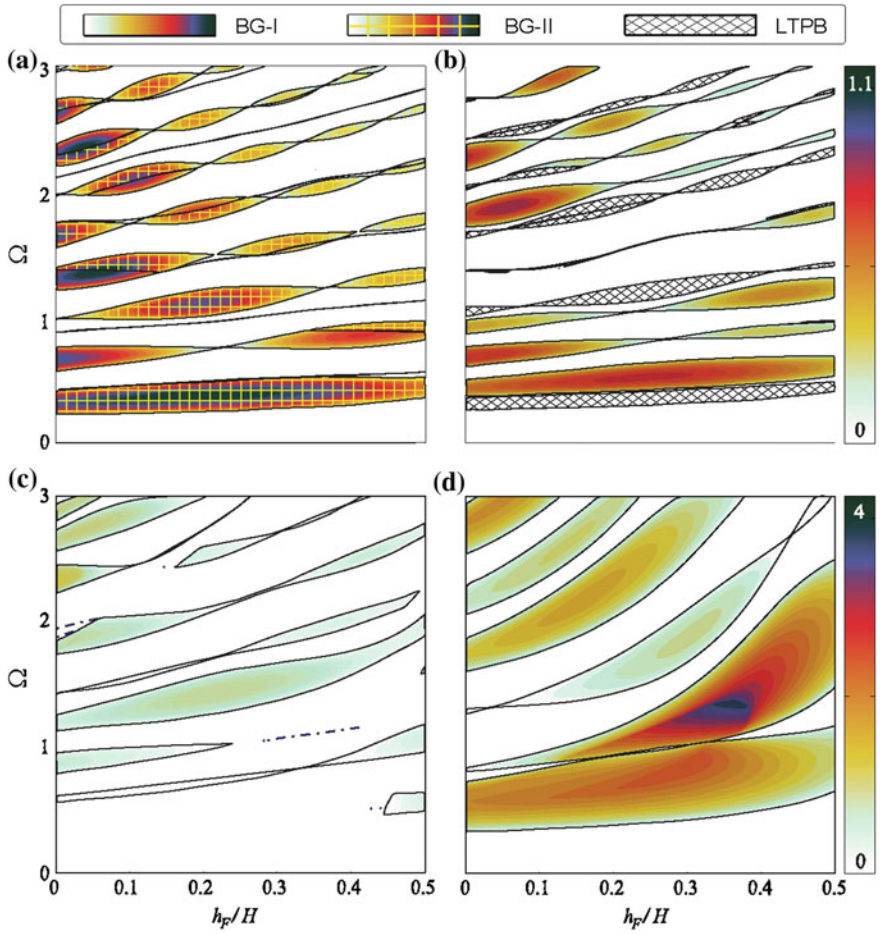

Fig. 23.6 Influence of the relative thickness of FG interlayers h_F/H on band-gaps for incident SV-waves at angles $\theta = 0°$ (**a**), $\theta = 20°$ (**b**), $\theta = 40°$ (**c**) and $\theta = 80°$ (**d**), and for $h_A/h_B = 1$

of the FG interlayers and the incidence angle. Furthermore, some BG-I appear only in the FG phononic crystals, e.g., the BG-I in the range of $2 < \Omega < 2.2$ for $0.05 < h_F/H < 0.2$ in Fig. 23.5b. However, these BG-I exist in a consolidation with the LTPBs. Other BG-I appear in the diagrams without contiguity to the LTPBs, e.g., the BG-I in Fig. 23.5b. Interestingly, the eigenvalue λ_1 is the complex conjugate of λ_2 within these zones, and the corresponding LTPBs evolve from the point BG arising at $\theta = 0°$ as shown in Fig. 23.5a.

The corresponding band-gaps for incident *SV*-waves are presented in Fig. 23.6. In contrast to incident *P*-waves, here the LTPBs disappear with increasing incidence angle. For example, the LTPBs become the point LTPBs at an incidence angle $\theta = 40°$ as shown in Fig. 23.6c by dashed lines. With further increasing

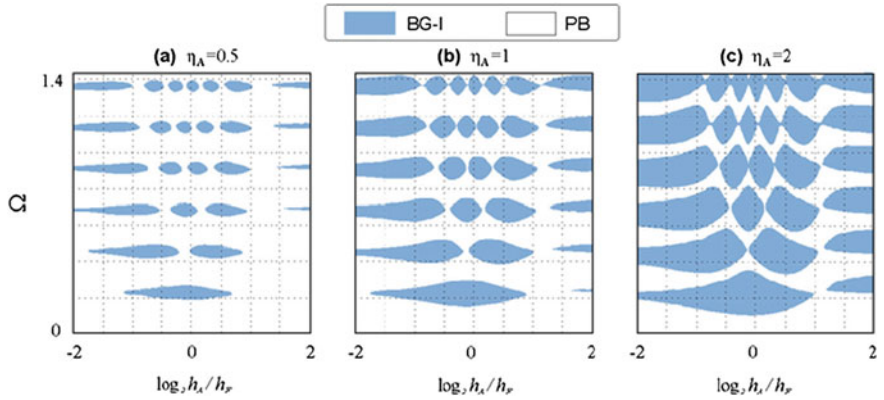

Fig. 23.7 Influences of $\log_2(h_A/h_F)$ on the band-gaps for phononic crystal with anisotropic FG interlayers for normally incident P-waves at the incidence angle $\theta = 0°$, $h_B = h_{F'} = 0$; **a** $\eta_A = 0.5$, **b** $\eta_A = 1$, **c** $\eta_A = 2$

incidence angle, the BG become wider, and the localization factor increases (see Fig. 23.6d).

In order to consider FG phononic crystals with an anisotropy, another law is used for the material gradation in contrast to isotropic case. The anisotropic phononic crystal is made of the graphite/epoxy layers of thickness h_A without gradation and the FG interlayer of thickness h_F with exponential factor η_A. Figure 23.7 shows the influence of the exponential factor η_A on the band-gap formation. It can be seen that with the increase of the material gradation, i.e. η_A, the band gaps become wider and denser.

23.6 Conclusions

Propagation of the time-harmonic plane waves in periodically laminated composites or layered phononic crystals composed of functionally graded isotropic and anisotropic interlayers is analyzed. The FG interlayers are approximated by using a multi-layer model, and the convergence of the method is demonstrated. The present investigation is mainly focused on the development of efficient and accurate methods for the calculation of the band-gap characteristics in 1D FG phononic crystals.

A classification of the band-gaps and pass-bands in layered phononic crystals is proposed. The classification relies on the analysis of the eigenvalues of the transfer matrix for a unit-cell and the asymptotics of the transmission coefficient. In particular, two kinds of band-gaps are specified as BG-I and BG-II. The transmission coefficient decays exponentially as the number of the unit-cells tends to infinity within the band-gaps. The term “low transmission pass band” (LTPB) is introduced

in order to identify frequency ranges where the transmission coefficient of the phononic crystals with a finite number of the unit-cells is not exactly zero but sufficiently small and negligible for practical engineering applications. The BG-II exist only in the case of normally incident elastic waves ($\theta = 0°$) and they are transformed into the LTPBs, when the incidence angle becomes larger than zero. The LTPBs are observed if the type of the incident wave does not coincide with the type of the wave propagating in an infinite phononic crystal.

Numerical results show that the width and the location of the band-gaps are strongly dependent on the relative thickness of the homogeneous layers, the thickness of the FG interlayers, the material properties, as well as the type and the incidence angle of the incident plane waves. It is revealed that the band-gaps are shifted to higher frequencies and the pass-bands become wider with the increasing thickness of the FG interlayers. The transition of the BG-II to LTPBs for different parameters of the phononic crystals are investigated.

Acknowledgements The work is supported by the Russian Foundation for Basic Research grants 16-41-230352, 16-51-53043 (joint RFBR-NSFC project 11611130017), the grant of the President of the Russian Federation (MK-7154.2015.1) and Ministry of Science and Education of Russian Federation (Project 1.189.2014K).

References

1. A. Khelif, A. Adibi, in *Phononic Crystals Fundamentals and Applications* (Springer New York), 245 p. (2016)
2. S. Alaie, D. Goettler, M. Su, Z. Leseman, C. Reinke, I. El-Kady, Nat. Commun. **6**, 7228 (2015)
3. M.P. Schmidt, A. Oseev, R. Lucklum, M. Zubtsov, S. Hirsch, Microsyst. Technol. **22**(7), 1593 (2015)
4. S.I. Fomenko, M.V. Golub, T.Q. Bui, Ch. Zhang, Y.-S. Wang, Int. J. Solids Struct. **51**(13), 2491 (2014)
5. F. Ramirez, P.R. Heyliger, E. Pan, Compos. B **37**, 10 (2006)
6. L.M. Brekhovskikh, O.A. Godin, *Acoustics of Layered Media I. Plane and Quasi-plane Waves* (Springer, Berlin, 1998)
7. F.-M. Li, Y.-S. Wang, Int. J. Solids Struct. **42**, 6457 (2005)
8. X. Han, G.R. Liu, Mech. Res. Commun. **29**(5), 327 (2002)
9. E. Glushkov, N. Glushkova, J. Comp. Acoust. **9**(3) (2001)
10. M.V. Golub, Ch. Zhang, J. Acoust. Soc. Am. **137**, 238 (2015)
11. C. Zhang, D. Gross, Int. J. Eng. Sci. **31**, 841 (1993)
12. S.I. Fomenko, M.V. Golub, A.A. Alexandrov, A.-L. Chen, Y.-S. Wang, Ch. Zhang, in *Proceedings of the International Conference Days on Diffraction*, pp. 149–154 (2016). http://ieeexplore.ieee.org/document/7756832/

Chapter 24
Advanced Characterization of Laminate Fiber-Reinforced Composite Materials with Elastic Guided Waves and Non-contact Measurement Techniques

Artem Eremin, Olga Miakisheva, Evgeny Glushkov, Natalia Glushkova and Rolf Lammering

Abstract Guided wave based nondestructive evaluation of elastic moduli of laminate fiber-reinforced composite materials is important for a permanent health monitoring of engineering structures in order to control their time-dependent degradation and failure prevention. For this purposes, the method of elastic modulus reconstruction via the minimization of discrepancy between the measured and calculated dispersion curves of the first fundamental symmetric and antisymmetric (S0 and A0) Lamb modes has been earlier developed and experimentally tested. It provided the values of all elastic parameters of the prepregs constituting a unidirectional or cross-ply composite plate; however, the Young modulus E_y was obtained with lower accuracy. To improve this point, the enhancement, based on the accounting for the zero group velocity effect, is proposed and experimentally validated.

24.1 Introduction

Laminate composite materials are becoming a preferred solution for a wide range of engineering structures in aerospace, civil and energy applications. Steady subjection to various static and dynamic loads and harsh environmental conditions, such as operation temperature and humidity changes, causes a time-dependent degradation

A. Eremin (✉) · O. Miakisheva · E. Glushkov · N. Glushkova
Institute for Mathematics, Mechanics and Informatics,
Kuban State University, Stavropolskaya Street, 149,
Krasnodar 350040, Russia
e-mail: eremin_a_87@mail.ru

E. Glushkov
e-mail: evg@math.kubsu.ru

R. Lammering
Institute of Mechanics, Helmut-Schmidt-University/University
of the Federal Armed Forces, Holstenhofweg, 85, 22043 Hamburg, Germany

I.A. Parinov et al. (eds.), *Advanced Materials*, Springer Proceedings
in Physics 193, DOI 10.1007/978-3-319-56062-5_24

of composite mechanical properties, resulting in increasing maintenance costs and possible structure failure. Therefore, any changes in mechanical properties, detected by a non-invasive technique, provide additional information on the construction condition that may be used for predicting its remaining operation time.

Among the approaches to non-destructive evaluation of the integrity of plate-like structures, ultrasonic guided waves (GWs) are recognized as an efficient solution, serving as a basis for in-situ structural health monitoring systems [1]. Along with the damage detection and localization, GWs are intensively utilized for the evaluation of elastic moduli of both isotropic materials and anisotropic composite structures. Usually, the experimentally acquired dispersion characteristics for wave numbers and phase or group velocities of the fundamental antisymmetric (A0) and symmetric (S0) normal modes or for their propagation angles serve as input data for the reconstruction approaches [2–5]. They rely on a stochastic-based minimization of an objective function, being a weighted discrepancy between the experimentally obtained data and corresponding theoretically calculated values, which are achieved in the course of elastic constant variation in the computational model.

Elastic properties of a typical fiber-reinforced polymer composite (FRPC) may be described by no less than five independent elastic constants. Five constants are enough if the laminate is fabricated from identical unidirectional plies (transversely isotropic material) with varying ply orientation. In order to guarantee a successful solution of a corresponding multi-parameter optimization problem, a sensitivity analysis should be performed beforehand to estimate sensitivity of the GW dispersion characteristics to changes in the elastic moduli. Recent results obtained for unidirectional samples show a considerable dependence of the A0 and S0 phase and group velocities on particular elastic constants, allowing almost one-to-one reconstruction strategies [4, 5]. The complication of lamination schemes leads to more sophisticated dependencies, when, for example, certain dispersion characteristic is influenced almost equally by several moduli [3, 4]. Therefore, further investigations involving higher normal modes are of particular interest, since they might exhibit unique sensitivity properties.

Among such potential candidates, there are so-called back-propagating modes. Together with their forward-propagating counterparts, they form dispersion curve branches with turning points, at which the group velocity of the mode becomes equal to zero while the phase velocity remains finite (so-called zero-group-velocity (ZGV) points) [6–8]. At a ZGV point, the wave energy supplied by the source of oscillation is localized in its vicinity. It results in a strong and easily detectable resonance of the plate. This behavior is commonly observed for the first symmetric Lamb wave S1. Being thoroughly investigated for materials with isotropic or cubic symmetry [6–11], ZGV modes are successfully used for the determination of Poisson's ratio [12], the plate thickness, and thickness profile [13].

In the current contribution, an attempt is made to understand how ZGV points of S1 mode may be utilized for the estimation and/or refinement of specific elastic moduli of composite laminate plates fabricated from identical FRP unidirectional transversally isotropic prepregs. In the next section, a brief description of the mathematical framework and experimental procedures, which are applied for the dispersion characteristic evaluation, is provided. It is followed by the numerical

results revealing the ZGV sensitivity extent to the variation of elastic constants. Finally, the obtained experimental data are discussed and some verification is provided.

24.2 Mathematical Framework and Experimental Setup

Time-harmonic oscillation $\mathbf{u}(\mathbf{x},\omega)\mathrm{e}^{-i\omega t}, \mathbf{u}=(u_x,u_y,u_z), \mathbf{x}=(x,y,z)$ of a free laminate anisotropic waveguide of thickness H excited by a surface load $\mathbf{q}(\mathbf{x},\omega)\mathrm{e}^{-i\omega t}$ localized at the top surface $z=0$ are considered (the time-harmonic factor $\mathrm{e}^{-i\omega t}$ is further omitted) (Fig. 24.1). It is assumed that the waveguide is fabricated from M identical transversely-isotropic prepregs ideally bonded with each other. Therefore, the mechanical properties of the considered composite structure are characterized by the density ρ, lamination scheme and five prepregs' independent elastic moduli (engineering constants), namely, two Young's moduli E_x, E_y, two shear moduli G_{yz}, G_{xy} and one Poisson coefficient v_{xy}. The direction of the axis Ox coincides with the fiber orientation in the upper layer.

The geometry of the problem allows one to apply the integral Fourier transform F_{xy} over the horizontal spatial variables x, y and to obtain the explicit solution in terms of inverse Fourier two-fold path integral:

$$\mathbf{u}(\mathbf{x})=\frac{1}{4\pi^2}\int\limits_{\Gamma_+}\int\limits_{0}^{2\pi}K(\alpha,\gamma,z)\mathbf{Q}(\alpha,\gamma)\mathrm{e}^{-i\alpha r\cos(\gamma-\varphi)}d\gamma\alpha d\alpha, \tag{24.1}$$

where the polar coordinates $(r,\ \varphi)$ and $(\alpha,\ \gamma)$: $x=r\cos\varphi, y=r\sin\varphi$, and $\alpha_1=\alpha\cos\varphi$, $\alpha_2=\alpha\sin\varphi$ are introduced; $K = F_{xy}[k]$ and $\mathbf{Q} = F_{xy}[\mathbf{q}]$ are Fourier symbols of the Green's matrix $k(\mathbf{x})$ for the corresponding boundary value problem and the contact stress vector $\mathbf{q}(x,\ y)$ (for more details see [14]). The integration path Γ_+ goes in the complex plane α along the real semi-axis Re $\alpha \geq 0$, Im $\alpha = 0$, bypassing real poles $\zeta_n=\zeta_n(\gamma)>0$ of the matrix K elements according to the principle of limiting absorption. These poles $\zeta_n(\gamma)$ are equal to the wave numbers of plane GWs propagating in direction γ. They serve as a starting point for the evaluation of wave number and phase/group velocity dispersion curves for the prescribed observation direction φ [15]. For the composite's principal axes, the

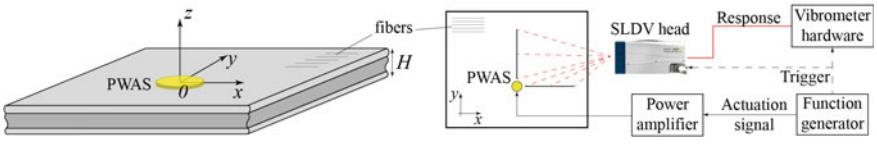

Fig. 24.1 Geometry of the problem (*left*) and the schematic representation of the experimental setup

angles of observation and plane wave propagation become equal making the calculation of dispersion characteristics rather straightforward.

Experimental investigations are performed for a cross-ply carbon FRP plate with the lay-up $[0_2^\circ, 90_2^\circ]_s$ fabricated from eight identical unidirectional prepregs. The dimensions of the specimen are 1000 × 1000 × 4.5 mm^3. The elastic properties of the prepregs, except the density ρ = 1522 kg/m^3, are initially unknown. Vertically polarized thin piezoelectric wafer active sensors (PWAS) of circular shape (6 mm diameter) adhesively bonded to the structure are utilized for guided wave excitation. The out-of-plane velocity field of propagating waves $\dot{u}_z(r,t)$ is measured on the plate surface by means of a Polytec PSV-500 one-dimensional scanning laser vibrometer. A sketch of the experimental setup is shown in Fig. 24.1.

The experimental frequency dependencies of wave numbers for fixed observation angles φ are obtained using double Fourier transform over spatial and time variables [16]. The latter is applied to the velocities $v_z = \dot{u}_z(r,t)$ measured along radius-vectors $r(\varphi)$ (straight black lines in the right subplot of Fig. 24.1):

$$H(k,f) = \int_{-\infty}^{\infty} \int_{-\infty}^{\infty} \dot{u}_z(r,t) e^{i(kr + 2\pi f t)} dr dt \tag{24.2}$$

Local maxima of $|H(k,f)|$ function form the traces in wave number-frequency domain (k,f) that coincide with partial segments of the wave-number dispersion curves.

24.3 Parametrical Analysis and Discussion

While for an isotropic waveguide, the location of ZGV points in the frequency-wave number plane does not depend on the propagation direction, in anisotropic materials such a dependence takes place [10]. In order to illustrate this phenomena for FRP composites, the branches of the first and second symmetric modes S1 and S2 are shown in Fig. 24.2 for the directions $\varphi = 0$ and $\varphi = \pi/2$

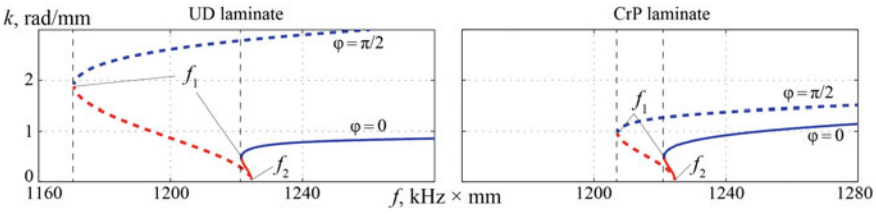

Fig. 24.2 Branches of S1 (*blue*) and S2 (*red*) Lamb wave dispersion curves with ZGV points for the UD (*left*) and CrP (*right*) laminates. *Solid lines* are for φ = 0, *dashed ones* stand for φ = π/2

along the principal axes of unidirectional (UD) $[0°]$ and cross-ply (CrP) $[0°, 90°]_s$ laminates fabricated from the prepregs of the following elastic properties: $\rho = 1578$ kg/m^3, $E_x = 127.6$ GPa, $E_y = 11.3$ GPa, $G_{yz} = 3.75$ GPa, $G_{xy} = 5.97$ GPa, and $v_{xy} = 0.3$. While the cut-off frequency of S2 mode (further denoted as f_2) does not depend neither on observation direction nor on lamination scheme, the ZGV point (frequency, at which it occurs, is denoted as f_1) exhibits strong sensitivity to both these parameters.

In order to understand how S1-S2 ZGV phenomena may be utilized for the estimation of elastic moduli, a sensitivity analysis is performed for both UD and CrP laminates. For this purpose, each elastic constant of the prepreg is varied from 80 to 120% of its initial value with all the other parameters fixed, and the frequencies f_1 and f_2 are recalculated as functions of the parameter $V = 100\% \times (P - P_0)/P_0$ (P_0 is the initial value of the varied elastic modulus, P denotes the current value in the range from $0.8P_0$ to $1.2P_0$). The results obtained for two observation directions $\varphi = 0$ and $\varphi = \pi/2$ are summarized in Figs. 24.3 and 24.4. It is readily noted from the plots that, for both lamination types, the ZGV-point frequency f_1 as well as its deviation from the S2 cut-off frequency f_2: $f_2 - f_1$, strongly depend only on the Young's modulus E_y and shear modulus G_{yz}, and the effect of the former is the strongest. The influence of the remaining three constants is insignificant: blue, magenta and black lines are almost parallel to the horizontal axis and virtually indistinguishable from each other, except in the right-bottom plot of Fig. 24.4.

Though in the case of UD laminate, E_y and G_{yz} constants may be determined from low and mid frequency parts of A0 and S0 dispersion curves, for CrP composites the influence of E_y is not pronounced complicating its reliable estimation.

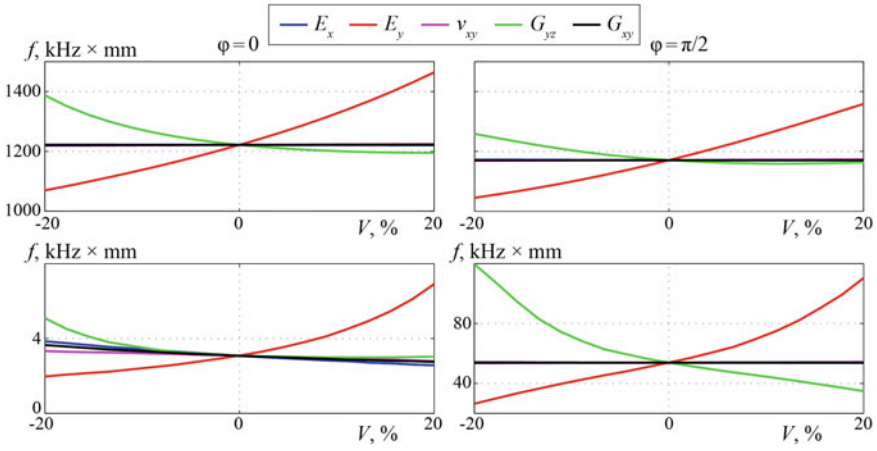

Fig. 24.3 Sensitivity of ZGV frequency to elastic modulus variation in the UD laminate. *Left subplots* are for $\varphi = 0$, *right* ones stand for $\varphi = \pi/2$. *Upper subplots* characterize the variation of ZGV frequency f_1, *lower* ones depict the difference $f_2 - f_1$

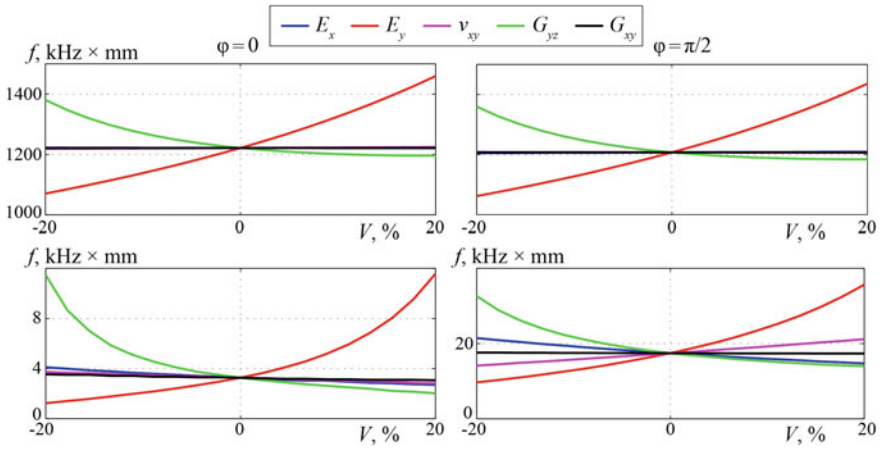

Fig. 24.4 Sensitivity of ZGV frequency to elastic modulus variation in the CrP laminate. *Left subplots* are for $\varphi = 0$, *right* ones stand for $\varphi = \pi/2$. *Upper subplots* characterize the variation of ZGV frequency f_1, *lower* ones depict the difference $f_2 - f_1$

Therefore, ZGV-point frequency, if being detected, would allow a refined reconstruction of this parameter.

In order to check this assumption, the CrP laminate described above has been investigated. At the first stage, the dispersion curves of A0 and S0 modes for the observation directions $\varphi = 0$ and $\varphi = \pi/2$ have been extracted from the broadband $|H(k,f)|$ data that served as an input for the elastic modulus reconstruction algorithm [4]. The following values of E_x, G_{yz}, G_{xy} elastic constants have been obtained: $E_x = 120.5$ GPa, $G_{yz} = 2.61$ GPa, $G_{xy} = 5.01$ GPa. The Young's modulus E_y has been also evaluated through the averaging of multiple algorithm runs yielding the value of 7.5 GPa. However, the deviations from this median value are sufficient.

Additionally, both Young's moduli have been determined through tensile tests: $E_x^T = 119.6$ GPa and $E_y^T = 8.04$ GPa. Assuming the obtained approximations for E_y, the locations of f_1 and f_2 frequencies are estimated numerically being in the frequency region from 250 to 330 kHz. At the second stage the PWAS is excited with a two-cycle sine-windowed sine signal with the central frequency $f_c = 300$ kHz, and new values of $|H(k,f)|$ are calculated (Fig. 24.5). The location of ZGV-points and S2 cut-off frequencies are clearly visible in these plots and the following values are obtained: $f_1^0 = 288$ kHz, $f_2^0 = 289$ kHz, $f_1^{\pi/2} = 284$ kHz, $f_2^{\pi/2} = 290$ kHz. With these data Young's modulus E_y is refined ($E_y = 7.82$ GPa) and corresponding wave number dispersion curves are computed and depicted with colored lines in Fig. 24.5 exhibiting good coincidence with the experimental data.

Since within the structural health monitoring concept, the amount of sensors is limited, it is of particular interest to figure out whether it is possible to detect

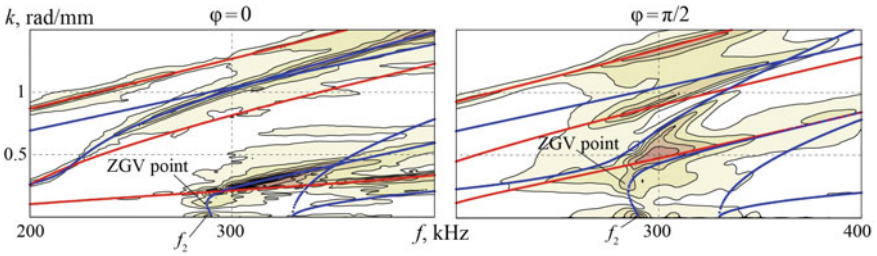

Fig. 24.5 Level lines of $|H(k, f)|$ function indicating propagating normal modes with ZGV and thickness-mode resonances; $\varphi = 0$ (*left*) and $\varphi = \pi/2$ (*right*). *Colored lines* stand for the dispersion curves computed with the reconstructed elastic moduli (antisymmetric GWs are shown by *red* while symmetric ones are *blue*)

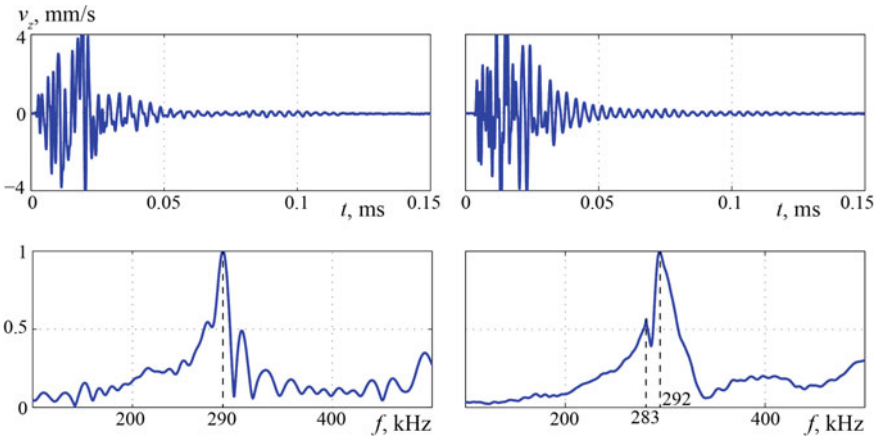

Fig. 24.6 Out-of-plane velocities measured in the source vicinity, indicating long-living and slowly decaying oscillations typical to ZGV and cut-off resonances (*top plots*); normalized spectra of these prolonged oscillations for $\varphi = 0$ (*left*) and $\varphi = \pi/2$ (*right*) (*bottom plots*)

ZGV-point frequencies using only few measurement locations. As an example, out-of-plane velocities $\dot{u}_z(\mathbf{x}, t)$ acquired 20 mm away from the PWAS center along the directions $\varphi = 0$ and $\varphi = \pi/2$ are shown in Fig. 24.6. The PWAS is excited with a broadband 1 μs square pulse. Prolonged oscillations typical to ZGV-point resonances [7, 11, 12] are visible after the main wave-package. Their Fourier transforms possess strong local maxima at the frequencies being close to the ones detected from the $|H(k, f)|$ plots (indicated by vertical dashed lines at bottom sub-plots). Though a slight discrepancy is present and the frequencies f_1 and f_2 are fused together for the direction $\varphi = 0$, the obtained data is also applicable for E_y refinement.

24.4 Conclusions

The method of reliable obtaining of the effective Young modulus E_y for the prepegs of a fiber-reinforced laminate composite plate has been developed and experimentally confirmed. It is based on the accounting for the change of the ZGV frequency depending on the elastic properties and direction of GW propagation. On this base, the previously developed method of non-destructive evaluation of effective elastic moduli of FRPC plates has been improved, making it possible to identify all elastic constants using experimentally acquired GW characteristics as input data.

Acknowledgements The work is supported by the Russian Foundation for Basic Research (RFBR) project together with the Administration of Krasnodar Region No. 16-41-230744 and the Ministry of Education and Science of the Russian Federation (agreements No. 1.189.2014K).

References

1. V. Giurgiutiu, *Structural Health Monitoring with Piezoelectric Wafer Active Sensors*, 2nd edn. (Elsevier Academic Press, New-York, 2014)
2. J. Vishnuvardhan, C.V. Krishnamurthy, K. Balasubramaniam, Smart Mater. Struct. **16**, 1650 (2007)
3. K. Lasn, A. Klauson, F. Chati, D. Dcultot, Mech. Compos. Mater. **47**, 446 (2011)
4. A.A. Eremin, E.V. Glushkov, N.V. Glushkova, R. Lammering, Compos. Struct. **125**, 458 (2015)
5. J. Zhao, J. Qiu, H. Ji, Compos. Sci. Technol. **126**, 34 (2016)
6. P.V. Burlii, I. Kucherov, Ya. JETP Lett. **26**(9), 492 (1977)
7. C. Prada, D. Clorennec, D. Royer, J. Acoust. Soc. Am. **124**(1), 212 (2008)
8. V.A. Babeshko, E.V. Glushkov, N.V. Glushkova, Wave Motion **16**, 192 (1992)
9. P.V. Burlii, P.P. Il'in, I.Ya. Kucherov, Acous. J. **43**(3), 314 (1997) (in Russian)
10. C. Prada, D. Clorennec, T.W. Murray, D. Royer, J. Acoust. Soc. Am. **126**(2), 625 (2009)
11. C.M. Gruensteidl, I.A. Veres, T.W. Murray, J. Acoust. Soc. Am. **138**(1), 250 (2015)
12. C.M. Gruensteidl, T.W. Murray, T. Berer, I.A. Veres, Ultrasonics **65**, 4 (2016)
13. D. Clorennec, C. Prada, D. Royer, IEEE Trans. Ultrason. Ferroelectr. Freq. Control **57**(5), 1132 (2010)
14. E. Glushkov, N. Glushkova, A. Eremin, J. Acoust. Soc. Am. **129**(5), 2934 (2011)
15. E. Glushkov, N. Glushkova, A. Eremin, R. Lammering, J. Acoust. Soc. Am. **135**(1), 154 (2014)
16. D. Alleyne, P.A. Cawley, J. Acoust. Soc. Am. **89**(3), 1168 (1991)

Chapter 25
Theoretical and Experimental Study of an Acoustically Active Material Containing a Doubly-Periodic System of Cylindrical Holes

Vitaly V. Popuzin, Vladimir M. Zotov and Mezhlum A. Sumbatyan

Abstract In the present work the problem on the propagation of the ultrasonic waves in the material with an interior periodic array of round holes is analyzed from both numerical and experimental points of view. The steel specimen with an array of small cylindrical drilling holes has been prepared in order to perform a full-scale ultrasonic simulation. This sample is scanned by the ultrasonic waves of different frequencies and the results presented are compared with the direct numerical and low-frequency analytical solutions. Numerical solution is constructed in frames of the Boundary Integral Equations (BIE) with further reduction to a discrete sytem by using the Boundary Element Method (BEM) and further solution via bi-conjugate gradients method.

25.1 Introduction

Acoustical meta-materials represent solids with inner periodic arrays of inclusions or voids. This special structure affects the propagation of the elastic waves through this media and, as a result, changes its behaviour in the media. Almost all properties, founded in electromagnetic fields for the metamaterials, take place also in acoustic fields: band gapping, filtering, inverse refraction, cloaking and others new properties can be seen in acoustic waves propagating in the metamaterials. The experimental and numerical study of this fields has become more intensive in the last 20 years [1–4]. However, all works which concerned the propagation of waves

V.V. Popuzin (✉) · V.M. Zotov · M.A. Sumbatyan
I.I. Vorovich Institute of Mathematics, Mechanics and Computer Science, Southern Federal University, 8a, Milchakov Street, Rostov-on-Don 344090, Russia
e-mail: popuzin@gmail.com

V.M. Zotov
e-mail: zot48@mail.ru

M.A. Sumbatyan
e-mail: sumbat@math.rsu.ru

I.A. Parinov et al. (eds.), *Advanced Materials*, Springer Proceedings in Physics 193, DOI 10.1007/978-3-319-56062-5_25

through periodic arrays of obstacles can also be considered as significant investigations in this branch of science [5–8].

The theoretical studies of such problems were performed for infinite arrays of inclusions based on some asymptotic assumptions, for example, for extremely high or low frequencies [8]. The numerical treatment permits consideration of the finite number of obstacles for any frequency, which is under the interest. However, the most part of numerical works in this field is performed with the help of the Finite Element Method. In the present work we use the Boundary Element Method (BEM) to test how this approach can be applied to such problems.

The mathematical model is constructed in frames of linear acoustics by the application of the Boundary Integral Equation (BIE) method. The theoretical approach permits investigation of various cross-sections of the holes, however in the present work we concern with the cylindrical shapes only. The reduction of the BIE to a discrete form is attained with the application of the uniform numerical grid over holes' boundaries; this leads to the Linear Algebraic System (LAS) with the dense matrix of a special structure. The diagonal blocks, which correspond to the nodes belonging to a certain chosen hole, in the case of cylindrical holes, are represented by circulant matrices. The additional periodicity arises in the system due to the periodic structure of the array of holes. Accepting the hypothesis that good precision can be attained by taking at least ten nodes per wavelength, the applied method requires operation with a huge number of nodes. This yields the LAS with the dense matrix of a big size. The implementation of the direct numerical algorithm with such matrices even on modern PC takes too much computer time. In the current work, an iterative bi-conjugate gradients method has been applied to solve this problem.

At last, we apply an approximate low-frequency analytical method based on our previous works, which allows us to construct explicit-form representations for the reflection and transmission coefficients versus frequency parameter. This shows a periodic behavior with the frequency increasing.

The comparison between the natural experiments and the theoretical results is demonstrated in numerous diagrams. The physical treatment shows that the doubly-periodic structure may behave as an acoustical filter, with certain frequency intervals of cut and passage of the ultrasonic signal.

25.2 Problem Formulation and Reduction to the Integral Equation

Let us consider a solid sample with N rows and M columns of cylindrical holes where we imply the normal falling of the longitudinal elastic wave on this array. In the case of plane or cylindrical wave and holes with equal cylindrical cross-sections, the problem can be modelled in the two-dimensional formulation, due to the symmetry.

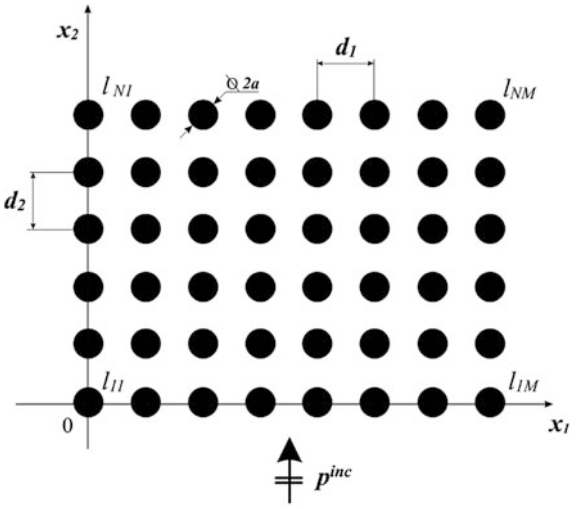

Fig. 25.1 Propagation of incident wave p^{inc} through a doubly periodic array of cylindrical holes

The matrix of the holes inside the solid is presented in Fig. 25.1. Here a is the radius of a hole and d_1, d_2 specify the horizontal and vertical distance between the centres of two nearest cylinders, respectively. The boundaries of the holes are denoted as l_{nm}, where first subscript $n = 1, .., N$ defines the number of the row and the second subscript $m = 1, .., M$ determines the number of the column inside the matrix. The longitudinal elastic wave p^{inc} propagates in the direction x_2 as shown in Fig. 25.1.

Considering harmonic oscillations of the pressure wave, the time-dependence component of the wave field can be presented by the exponential term in the full pressure $P = pe^{-iwt}$, where w is the angular frequency, i is the imaginary unit and t is the time. Then the wave equation can be reduced to the Helmholtz equation [9]

$$\Delta p + k^2 p = 0 \tag{25.1}$$

where k is the wave number and all quantities depend only upon spatial variables (x_1, x_2).

In terms of linear acoustics the full pressure field is represented as the sum of the incident and the scattered wave

$$p = p^{inc} + p^{sc} \tag{25.2}$$

where p^{sc} is the wave scattered by the obstacles.

From the mathematical viewpoint, the boundary condition for the cylindrical holes can be presented as for the acoustically hard boundary (Neumann-type condition):

$$v_n|_L = 0 \sim \left.\frac{\partial p}{\partial n}\right|_L = 0 \sim \left.\frac{\partial p^{inc}}{\partial n}\right|_L = -\left.\frac{\partial p^{sc}}{\partial n}\right|_L \tag{25.3}$$

where relation $v_n = 1/i\rho w * \partial p/\partial n$ has been used. The overall boundary contour L of all cylindrical obstacles is a sum of the contours of all circles in the solid: $L = \sum_{n=1}^{N}\sum_{m=1}^{M} l_{nm}$.

The Boundary Integral Equation approach reduces the system (25.1)–(25.3) to the Fredholm integral equation of the second kind over the boundary L:

$$\frac{p(y_0)}{2} - \int_L p(y)\frac{\partial \Phi(|y_0 - y|)}{\partial n_y} dL_y = p^{inc}(y_0) \tag{25.4}$$

where $y_0 \in L$.

Once (25.4) is solved, the scattered field at arbitrary point $z = (z_1, z_2), z \notin L$ can be obtained from the distribution of the full pressure on the boundary $p(y), y \in L$ by using the following integral relation:

$$p^{sc}(z) = \int_L p(y)\frac{\partial \Phi(|z - y|)}{\partial n_y} dL_y \tag{25.5}$$

Finally, full pressure is calculated by the use of (25.2) $p(z) = p^{inc}(z) + p^{sc}(z)$, where, for simplicity, in the dimensionless form, we use the plane incident wave with a unit amplitude in all our numerical experiments: $p^{inc}(z) = e^{ikz_2}$.

The Green function for the Helmholtz equation in the 2D case is represented by the Hankel function of the first kind $\Phi(\mathbf{r}) = i/4 * H_0^{(1)}(kr)$, where $\mathbf{r} = |r| = |y_0 - y|$ is the distance between two points.

Then the kernel of the integral (25.4) can be rewritten in the following form:

$$\frac{\partial \Phi(r)}{\partial n_y} = \frac{\partial \Phi(r)}{\partial r}\frac{\partial \mathbf{r}}{\partial n_y} = \frac{\partial \Phi(r)}{\partial r}\frac{(\vec{r}, n_y)}{r} = -\frac{i}{4}kH_1^{(1)}(kr)\frac{(\vec{r}, n_y)}{r} \tag{25.6}$$

In order to achieve explicit representation for the kernel, let us write out the representation of the "internal" and "external" variable in the polar coordinate system. For the points located on the boundary of a certain circle $\left(y^{nm} \in l_{nm}, y_0^{uw} \in l_{uw}\right)$ the following relations in the polar coordinate system are valid:

$$y^{nm} = \begin{cases} a\cos(\theta) + (m-1)d_1 \\ a\sin(\theta) + (n-1)d_2 \end{cases}, \quad y_0^{uw} = \begin{cases} a\cos(\phi) + (w-1)d_1 \\ a\sin(\phi) + (u-1)d_2 \end{cases} \tag{25.7}$$

where $0 \le \theta, \phi \le 2\pi$, $n, u = 1, \ldots, N$, $m, w = 1, \ldots, M$. Thus, the point with coordinates $\{(n-1)d_1, (m-1)d_2\}$ is the center of the circle with boundary l_{nm}.

It is clear, that the normal vector for the "inner" variable $\boldsymbol{y}$ inside (6) is identical for all circles, being equal to

$$\boldsymbol{n}_{\boldsymbol{y}}^{\boldsymbol{nm}} = \frac{\partial}{\partial \boldsymbol{\theta}} \left\{ \boldsymbol{y}_2^{\boldsymbol{nm}}, -\boldsymbol{y}_1^{\boldsymbol{nm}} \right\} = \{ \mathbf{cos}(\boldsymbol{\theta}), \mathbf{sin}(\boldsymbol{\theta}) \}. \tag{25.8}$$

The radius-vector between two points can be calculated as

$$\vec{\boldsymbol{r}} = \boldsymbol{y}_0^{\boldsymbol{uw}} - \boldsymbol{y}^{\boldsymbol{nm}} = \begin{cases} \boldsymbol{a}(\mathbf{cos}(\boldsymbol{\phi}) - \mathbf{cos}(\boldsymbol{\theta})) + (\boldsymbol{w} - \boldsymbol{m})\boldsymbol{d}_1 \\ \boldsymbol{a}(\mathbf{sin}(\boldsymbol{\phi}) - \mathbf{sin}(\boldsymbol{\theta})) + (\boldsymbol{u} - \boldsymbol{n})\boldsymbol{d}_2 \end{cases}, \tag{25.9}$$

which gives explicit representation for the scalar product in (25.6)

$$\left(\vec{\boldsymbol{r}}, \boldsymbol{n}_{\boldsymbol{y}}\right) = -2\boldsymbol{a}\,\mathbf{sin}^2\left(\frac{\boldsymbol{\phi} - \boldsymbol{\theta}}{2}\right) + \mathbf{cos}(\boldsymbol{\theta})(\boldsymbol{w} - \boldsymbol{m})\boldsymbol{d}_1 + \mathbf{sin}(\boldsymbol{\theta})(\boldsymbol{u} - \boldsymbol{n})\boldsymbol{d}_2 \tag{25.10}$$

The distance between two points is given by

$$\begin{aligned} \boldsymbol{r}^2 = {} & 2\boldsymbol{a}^2(1 - \mathbf{cos}(\boldsymbol{\phi} - \boldsymbol{\theta})) + (\boldsymbol{w} - \boldsymbol{m})^2\boldsymbol{d}_1^2 + (\boldsymbol{u} - \boldsymbol{n})^2\boldsymbol{d}_2^2 \\ & - 4\boldsymbol{a}\,\mathbf{sin}\left(\frac{\boldsymbol{\phi} - \boldsymbol{\theta}}{2}\right)\left[\mathbf{sin}\left(\frac{\boldsymbol{\phi} + \boldsymbol{\theta}}{2}\right)(\boldsymbol{w} - \boldsymbol{m})\boldsymbol{d}_1 - \mathbf{cos}\left(\frac{\boldsymbol{\phi} + \boldsymbol{\theta}}{2}\right)(\boldsymbol{u} - \boldsymbol{n})\boldsymbol{d}_2\right]. \end{aligned} \tag{25.11}$$

By using simple relation for the linear combination of sine waves of the same frequency but different phase shifts, one can reduce the term in square brackets in (25.11) to

$$\boldsymbol{r}^2 = 4\boldsymbol{a}^2\mathbf{sin}^2\left(\frac{\boldsymbol{\phi} - \boldsymbol{\theta}}{2}\right) - 4\boldsymbol{a}\,\mathbf{sin}\left(\frac{\boldsymbol{\phi} - \boldsymbol{\theta}}{2}\right) * \boldsymbol{R}\,\mathbf{sin}\left(\frac{\boldsymbol{\phi} + \boldsymbol{\theta}}{2} + \boldsymbol{\varphi}\right) + \boldsymbol{R}^2, \tag{25.12}$$

where

$$\boldsymbol{\varphi} : \begin{cases} \mathbf{tan}(\boldsymbol{\varphi}) = \frac{-(\boldsymbol{u} - \boldsymbol{n})\boldsymbol{d}_2}{(\boldsymbol{w} - \boldsymbol{m})\boldsymbol{d}_1}, & (\boldsymbol{w} - \boldsymbol{m})\boldsymbol{d}_1 \neq 0 \\ \boldsymbol{\varphi} = \boldsymbol{\pi}/2, & (\boldsymbol{w} - \boldsymbol{m})\boldsymbol{d}_1 = 0 \end{cases} \tag{25.13}$$

and $\boldsymbol{R} = \sqrt{(\boldsymbol{w} - \boldsymbol{m})^2\boldsymbol{d}_1^2 + (\boldsymbol{u} - \boldsymbol{n})^2\boldsymbol{d}_2^2}$ represents the distance between the centres of two respective circles.

25.3 Numerical Treatment

Let us divide the boundary of each cylinder to $\boldsymbol{v}$ equal arcs by putting the discrete set of nodes at angles $\boldsymbol{\theta}_{\boldsymbol{q}} = \boldsymbol{q} * \boldsymbol{h}, \boldsymbol{q} = 1, \ldots, \boldsymbol{v}$, with the constant step $\boldsymbol{h} = 2\boldsymbol{\pi}/\boldsymbol{v}$. Using the "co-location" approach we dispose "internal" variable $\boldsymbol{y}^{\boldsymbol{nm}}$ and "external"

variable y_0^{uw} at the same nodes: $y_q^{nm} = y^{nm}(\theta_q)$ and $y_{0_g}^{uw} = y_0^{uw}(\phi_g)$, $\phi_g = g * h$, $g = 1, \ldots, v$. It is clear, that the integral in (25.4) is equal to the sum of integrals over each elementary arc. Then, by using simple quadrature formula, we put the integrand approximately constant over each elementary arc and take it outside the integral sign. This leads to the following LAS for the (25.4)

$$\begin{aligned} &\frac{p(y_{0_g}^{nm})}{2} + \sum_{u=1}^{N}\sum_{w=1}^{M}\sum_{q=1}^{v} G\left(\left|y_{0_g}^{nm} - y_q^{uw}\right|\right) p\left(y_q^{uw}\right) = p^{inc}\left(y_{0_g}^{nm}\right), \\ &G\left(\left|y_{0_g}^{nm} - y_g^{nm}\right|\right) = \frac{1}{2}, \quad G\left(\left|y_{0_g}^{nm} - y_q^{uw}\right|\right) = ah\frac{ik}{4} H_1^{(1)}(kr)\frac{(\bar{r}, n)}{r} \end{aligned} \tag{25.14}$$

For diagonal elements $\left(y_{0_g}^{nm} = y_g^{nm}\right)$, the singular behavior appears in the argument of the Hankel function. This singularity can be treated separately with accurate computation of integral on the corresponding elementary arc. However, it can be shown, that the so obtained value is relatively small comparing to the value ½ of the first term in (25.4) and with the simplest approach it can be neglected.

To rewrite system (25.14) in the matrix-vector notation, a one-dimensional numbering is introduced. The right-hand side term p^{inc} and the unknown pressure p are collected in vectors in such a way that point $y_{0_g}^{nm}$ corresponds to the vector element with index $[g + (m - 1 + (n - 1) * M) * v]$ and point y_q^{uw} corresponds to element in the $[q + (w - 1 + (u - 1) * M) * v]$ cell, respectively. Thus, the former index gives the matrix row and the latter one denotes the matrix column. In the other words, index $[(m - 1 + (n - 1) * M) * v, (w - 1 + (u - 1) * M) * v]$ specifies the matrix block and indexes g, q mark the elements inside this block.

With this said, the matrix-vector notation of the system (25.14) can be written out as

$$Gp = p^{inc} \tag{25.15}$$

where matrix G has $(NM * v)^2$ elements, p and p^{inc} are vectors of size $NM * v$.

Application of the standard Gauss elimination technique to the system (25.15) requires $(NM * v)^3$ arithmetical operations. To achieve good computational precision, one should take at least ten nodes per one wavelength. In the high-frequency range it leads to a matrix of big size and, as a result, the computations require huge computer resource in memory and time. Instead of such a direct treatment, we apply an iterative approach, where the matrix-vector multiplication is known to be the most computationally expensive operation at each iteration step and it requires only $(NM * v)^2$ operations. As a result, if the solution is attained with $n_{it} < NM * v$ number of iterations, then the total number of arithmetical operations is $n_{it}(NM * v)^2$. This value can be further reduced by using a special fast matrix-vector multiplication technique for dense matrices as the well-known Fast Multipole Method or Hierarchical matrix approach [10–13].

Another advantage of the iterative approaches is the possibility of choosing a desired precision. In fact, the numerical computation even with double precision brings some inaccuracy to the solution process, so the absolute accuracy is impossible in discrete implementation. That is why we are always interested in the solution with some "working" precision and the iterative approach gives the possibility to attain it.

In our numerical treatmen we use the bi-conjugate gradients method (Bi-CG), since it is stable for non-symmetric matrices. The Bi-CG can be written out in simple recurrence relations:

$$\begin{aligned}
\boldsymbol{\alpha}_j &= \left(\hat{\boldsymbol{r}}_{j-1}, \boldsymbol{r}_{j-1}\right) / \left(\hat{\boldsymbol{z}}_j, \boldsymbol{G}\boldsymbol{z}_j\right), \\
\boldsymbol{p}_j &= \boldsymbol{p}_{j-1} + \boldsymbol{\alpha}_j \boldsymbol{z}_j, \\
\boldsymbol{r}_j &= \boldsymbol{r}_{j-1} - \boldsymbol{\alpha}_j \boldsymbol{G}\boldsymbol{z}_j, \\
\hat{\boldsymbol{r}}_j &= \hat{\boldsymbol{r}}_{j-1} - \boldsymbol{\alpha}_j \boldsymbol{G}^T \hat{\boldsymbol{z}}_j, \\
\boldsymbol{\beta}_j &= \left(\hat{\boldsymbol{r}}_j, \boldsymbol{r}_j\right) / \left(\hat{\boldsymbol{r}}_{j-1}, \boldsymbol{r}_{j-1}\right), \\
\boldsymbol{z}_{j+1} &= \boldsymbol{r}_j + \boldsymbol{\beta}_j \boldsymbol{z}_j, \\
\hat{\boldsymbol{z}}_{j+1} &= \hat{\boldsymbol{r}}_j + \boldsymbol{\beta}_j \hat{\boldsymbol{z}}_j.
\end{aligned} \tag{25.16}$$

where at the first iteration the initial residual vector is chosen in the form $\boldsymbol{r}_0 = \boldsymbol{p}^{inc} - \boldsymbol{G}\boldsymbol{p}_0$ and $\hat{\boldsymbol{r}}_0 = \hat{\boldsymbol{z}}_1 = \boldsymbol{z}_1 = \boldsymbol{r}_0$. The initial guess $\boldsymbol{p}_0$ can be set trivially zero or taken from some general assumption.

As follows from the results of the numerical experiments, the number of required iterations grows with frequency increasing (Fig. 25.2). However, this behaviour is not

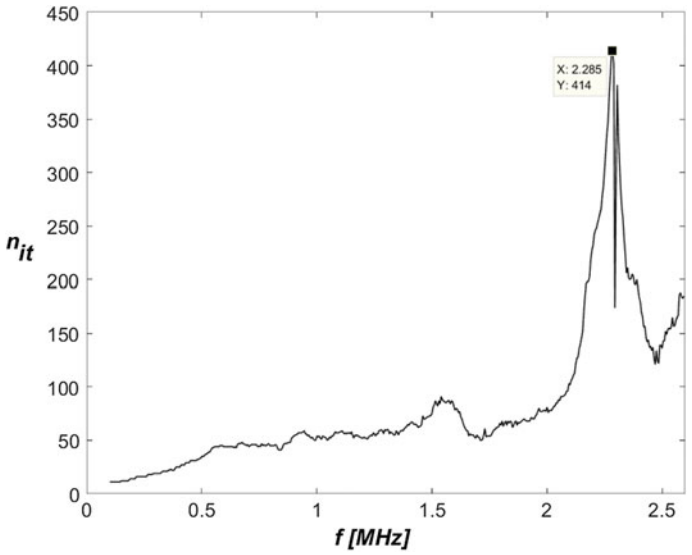

Fig. 25.2 Number of iterations in Bi-CG method versus frequency

linear and strongly depends on the complexity of the solution. As an example, the highest number of iterations corresponds to the frequency f = **2.285 MHz**, where some irregular resonance behaviour appears inside the material. Thus, the number of iterations in the iterative methods can be itself the starting point of the analysis.

25.4 Numerical Experiments

To provide the in-depth study of the acoustically active material, the number of numerical experiments were performed with varying frequency, receiver position and the structure of the periodic system in the media. All calculations below were implemented for the system with 8 column and 6 rows of cylindrical holes $(M = 8, N = 6)$ of radius $a = 1\,\mathbf{mm}$ with horizontal and vertical spacing equal to $d_1 = d_2 = 4a = 4\,\mathbf{mm}$. On each contour the discretization net with 2^6 nodes were used $(v = 64)$. Thus, the total matrix size in (25.15) is **3072 * 3072** elements. The main material of the media was considered to be made of steel with the velocity of propagation of longitudinal elastic wave equal to $c = 6000\,\mathbf{m/s}$.

As mentioned above, the solution of the main integral (25.4) gives the full pressure field $p(y), y \in L$ on the boundary of each cylinder. Detailed analysis shows, that in the range $k * a < 0.4$ only weak interaction between cylinders in the system takes place. However, even this small interaction just concentrates the energy of the wave inside the array and also create very slight drop of energy near left and right sides of the array. This "tunneling" effect becomes more apparent for highest frequencies. Two examples presented in Fig. 25.3 and example in Fig. 25.4 clearly demonstrate this behavior. At frequency 0.9 MHz denoted by the red line in Fig. 25.3, one can notice that full pressure is much higher at the parts of the boundary which oriented inside the system of holes. For the high ultrasonic frequency 7.22 MHz (blue line) almost all energy is concentrated in the first three rows of the array.

Once the distribution of the full pressure on the boundary is known, (25.5) can be used to calculate the scattered field at any point inside the media. In order to calculate the wave transmitted through the array, the scattered field at the points above the system $(x_2 = 0.023\,\mathbf{m}$ and $x_1 \in [-0.03, 0.06]\,\mathbf{m})$ is calculated and then (25.2) is applied to obtain the full pressure $p(x_1, x_2)$. The magnitude of the full pressure is demonstrated in Fig. 25.4, where the small black circles along the horizontal axis schematically denote the location of the array of holes in the material.

The "tunneling" effect of the concentration of wave energy above the array of holes and drop of the energy near left and right sides of it (at $x_1 \in [-0.01, -0.005] \cup [0.03, 0.035]\,\mathbf{m}$) can be clearly seen from this figure. The frequency 0.555 MHz shows a bright example of both these behaviours. At higher frequencies this geometric filtration of the transmitted wave becomes even more evident and for some frequencies the wave passes just between the cylindrical holes, as it is demonstrated in Fig. 25.5 for $f = 3.3\,\mathbf{MHz}$ and $f = 10.3\,\mathbf{MHz}$. It is clear from the physical viewpoint that the wave behaves similarly to the rays in the

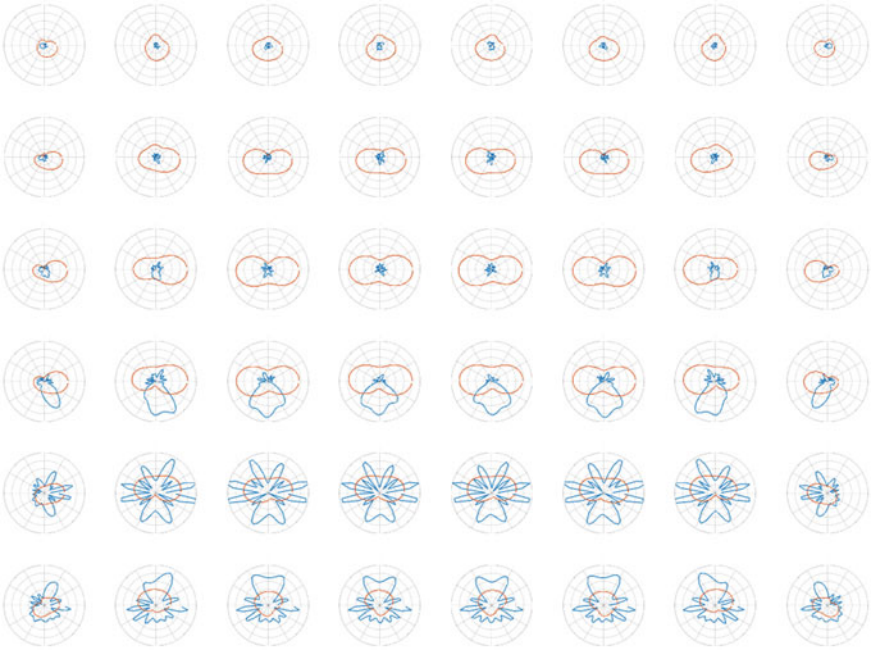

Fig. 25.3 Distribution of the full pressure magnitude $|\boldsymbol{p}(\boldsymbol{y}_1, \boldsymbol{y}_2)|$ on the boundary of each cylinder; *red line* 0.9 MHz, *blue line* 7.22 MHz

high-frequencies range. The reflected wave under the system of holes ($\boldsymbol{x}_2 = -0.003\,\mathbf{m}$) is also presented in these figures shown by the dotted lines. Notice, that in this case only the scattered wave should be taken into consideration without the summation with incident wave, which obviously does not reach the receiver placed below the source.

In order to calculate the transmission and reflection coefficients, the average value of $|\boldsymbol{p}(\boldsymbol{x}_1, 23{*}\boldsymbol{a})|$ and $|\boldsymbol{p}^{\boldsymbol{sc}}(\boldsymbol{x}_1, -3{*}\boldsymbol{a})|$, respectively, are calculated in the interval $\boldsymbol{x}_1 \in [-0.002, -0.03]\,\mathbf{m}$. These quantities are presented in Fig. 25.6 for the frequency range 0–11 MHz. It can be noticed, that the identity law $|\boldsymbol{T}|^2 + |\boldsymbol{R}|^2 = 1$ is valid in this calculation with a good precision. The product of the wavelength $\boldsymbol{k}$ by the radius of cylinder $\boldsymbol{a}$ is reflected on the upper bound of the graph. It can be concluded from this figure, that the band gapping property of such materials has an irregular character at higher frequencies.

In the theoretical work [7] there is shown for the periodic system of linear obstacles that the system where every second row of the array is shifted in the horizontal axis in the distance of obstacle's length, that the transmission and reflection coefficients behave like in the basic system without any shift. To study this behavior by the BEM approach, another series of numerical experiments has been performed for the system with a periodic shift of each even row.

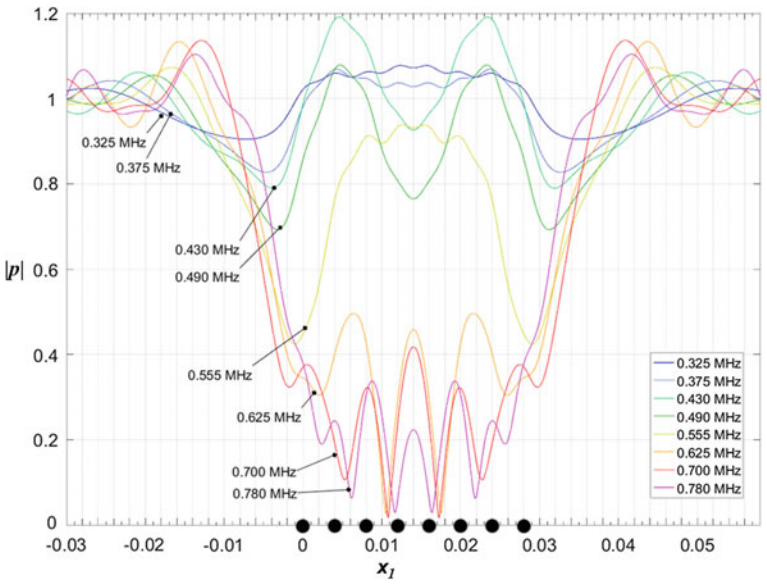

Fig. 25.4 Magnitude of the full pressure $|\boldsymbol{p}(\boldsymbol{x}_1, \boldsymbol{x}_2)|$ calculated above the system of cylinders ($\boldsymbol{x}_2 = 0.023\,\mathbf{m}$)

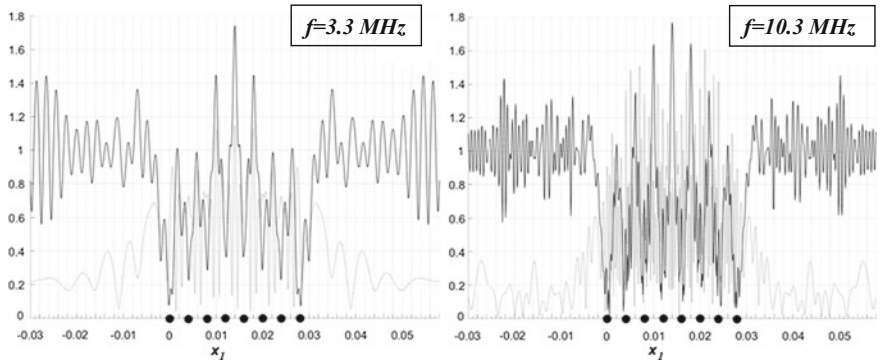

Fig. 25.5 Amplitude of the full pressure $|\boldsymbol{p}|$ calculated above the system of cylinders (*solid line*) and of the scattered pressure $|\boldsymbol{p}^{sc}|$ calculated under the system of cylinders (*dotted line*)

The comparison between these two arrays are reflected in Fig. 25.7, where in the right upper corner the arrangement of the shifted array is presented. As predicted by the analytical approach [7], on the low-frequency interval the behaviour of both the systems is identical. Our numerical calculations confirm the analytical prediction [7] that the closeness of the wave properties for the two discussed geometries takes place only for low frequencies.

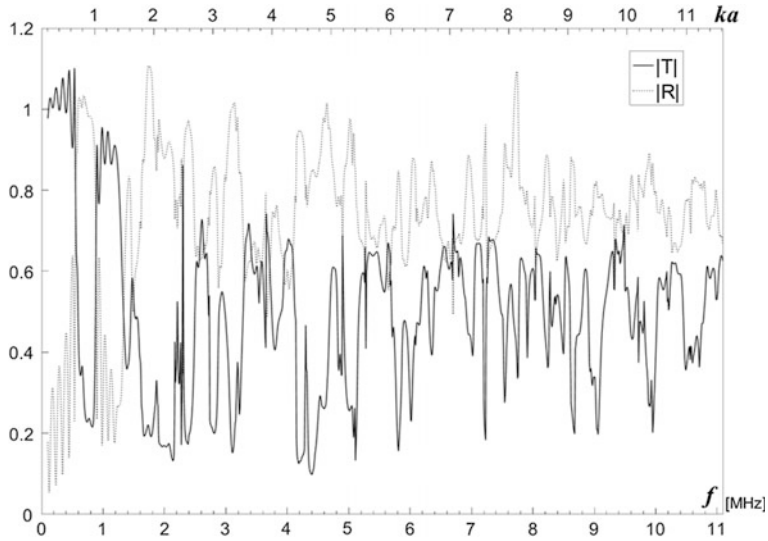

Fig. 25.6 Transmission ***T*** and reflection ***R*** coefficients versus frequency and ***ka*** (*upper bound*)

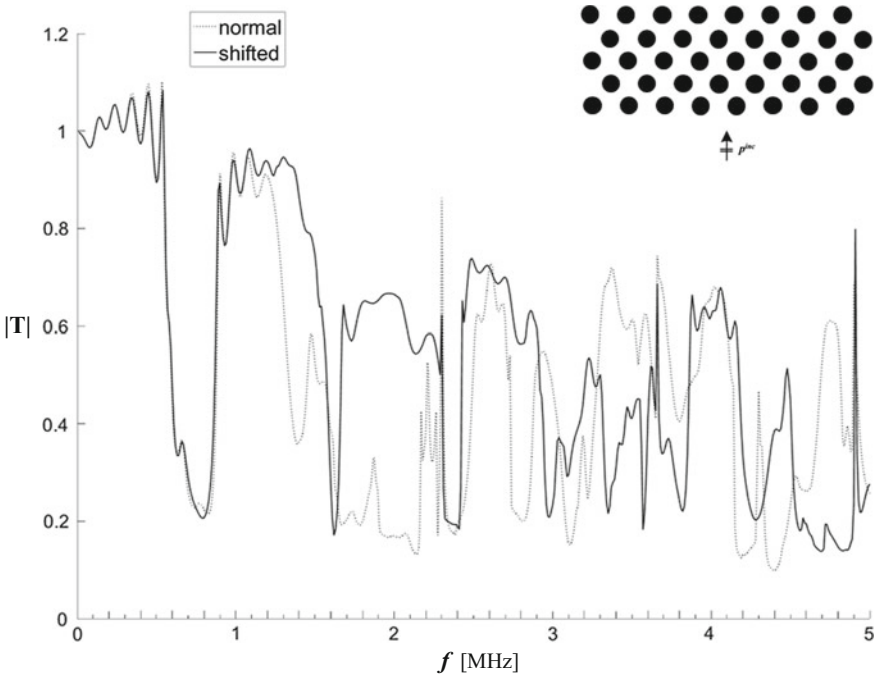

Fig. 25.7 Comparison between the transmission coefficients of two different arrangements for the periodic structure

25.5 Natural Experiment

In order to perform the experimental study, the steel sample with a periodic system of cylindrical holes has been produced as a system of drillings (Fig. 25.8a). Then, the through-transmission technique is applied in the experimental measurements: the transducer, which transmits ultrasound waves is placed on one side of the sample and the receiver on the opposite side. The schematic representation of this approach is shown in Fig. 25.8b.

In the presented experimental results the industrial low-frequency ultrasonic flaw detector UCD-60N with working frequencies 0.01–2.5 MHz has been used. The list of the ultrasonic transducers used in the measurements is presented in Table 25.1:

First four probes in this list are commercially available and the last four are specially produced in the ultrasound laboratory for the purpose of the experimental work. The PZT-19 is used as the material of piezoelectric elements. The protector is made of a polymerized epoxy and represents the thin membrane with the thickness

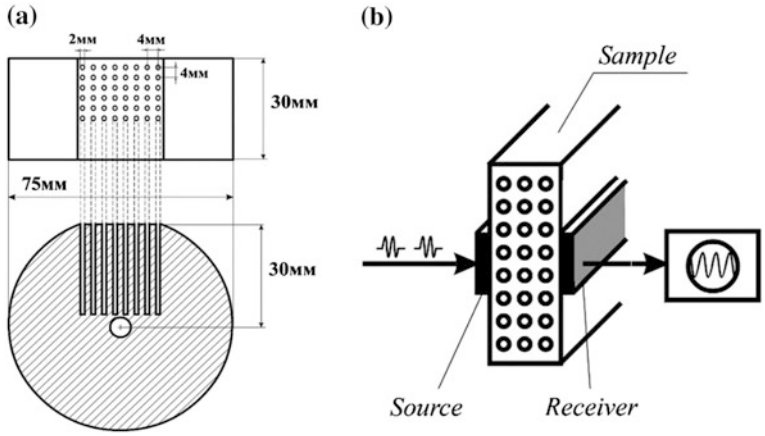

Fig. 25.8 Steel sample with cylindrical holes and the through-transmission technique for the measurements

Table 25.1 US transducers

No	Basic frequency (MHz)	Shape	Size (cm)
1.	2.5 (c)	Round	$d = 1.4$
2.	1.25 (c)	Round	$d = 2.8$
3.	0.64 (c)	Round	$d = 2.8$
4.	0.61 (c)	Round	$d = 1.4$
5.	0.33	Round	$d = 1.6$
6.	0.25 (0.73)	Round	$d = 3.0$
7.	0.16	Rectangular	2.0×0.8
8.	0.14	Rectangular	1.5×0.5

less than a half of the ping length. To neutralize inertial properties of the transducer element, the epoxy with lead oxide filling is used as a damper device. Such an installation equalizes the damper characteristic impedance with wave impedance and increases the attenuation of waves which propagate inside the transducer. The lithium grease is used as a contact medium between the US probe and the scanning sample.

An electrical square pulse with the basic frequency equal to the resonance frequency of the piezoelectric element is delivered to this element by a generator. Then, the transducer generates the elastic wave inside the solid and after that the wave passing through the material is registered by the receiving transducer at the opposite side of the sample. The obtained data at the receiving transducer is sent to the main device. After digitalization, this data is displayed as the amplitude-time response (also known as the A-scan in the ultrasonic non-destructive testing) on the display of the ultrasonic flaw detector.

Based on this results the main conclusions about wave transmission for the basic frequency can be done. For example, A-scans for three different frequencies are demonstrated in Fig. 25.9. The signal propagated through the material without the system of cylindrical holes is denoted by the white line while the signal passed through material with the array of holes is marked by the black line. As can be seen from the analysis of the amplitude in Fig. 25.9 and the transmission coefficient in Fig. 25.7, the main prediction performed by the numerical calculations is satisfactory by its precision, since we can observe significant decay of the wave energy at $f = 0.64\,\mathbf{MHz}$, almost complete transmission at $f = 0.33\,\mathbf{MHz}$ and a half of the energy passed at $f = 1.25\,\mathbf{MHz}$, which is in a good agreement between the numerical and the experimental results.

The proposed approach allows us to experimentally examine the behaviour of the acoustic metamaterials only for a certain limited set of frequencies. However, it

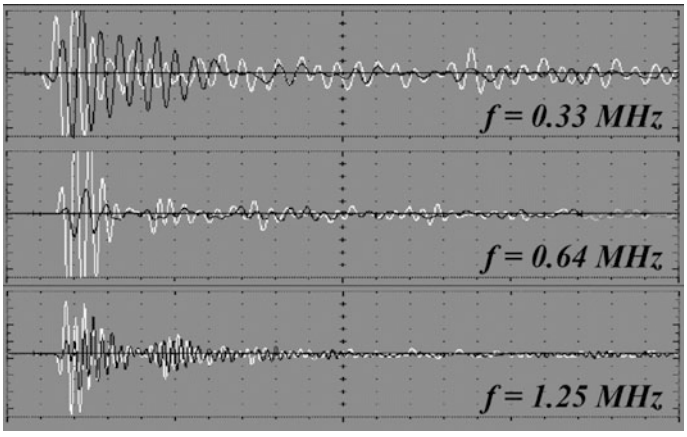

Fig. 25.9 Comparison of the signals registered by the ultrasonic flaw detector UCD-60N. *White line* shows wave transmitted through a normal material, *black line* corresponds to material with holes

should be noted that the radio pulse sequence spectrum, which induces the transmitting piezoelectric element, has not only the basic frequency component, but contains also some additional frequencies. Moreover, the transfer functions, electrical and acoustic impedances of the transducers are functions, which depend on the frequency, upon the parameters of the piezoelectric element and the parameters of the damper. As a result, the signal frequency response at the receiver contains frequency components with various amplitudes. Thus, more comprehensive analysis can be based on the spectrum estimation. In order to extract the amplitude-time characteristics, the Discrete Fourier Transform is applied to the registered signals, and the resulting data is analyzed.

Let us notice, that the natural experiment has its inaccuracy coupled with the thickness of the contact medium, the influence of the noise, the statistical errors, etc. Moreover, as shown in Figs. 25.4 and 25.5, the pressure field may be unevenly distributed on the side of the sample where the receiver collects the data, so the calculated transmission coefficient in Figs. 25.6 and 25.7 is rough. Also, the receiving transducer makes average of the captured data over the surface of the piezo-element. All this factors do not permit to measure small perturbations of the transmission coefficient. Nevertheless, the results of the performed measurements show good agreement with the numerical prediction (see Fig. 25.10).

In Fig. 25.10, the solid line denoted by "analytical 1" corresponds to the array of linear obstacles with horizontal distance between two neighbour obstacles equal to $\boldsymbol{d}_1 = 0.2\boldsymbol{a}$, where $\boldsymbol{a}$ is a half length of the segment and dashed line "analytical 2" corresponds to the array with opening equal to $\boldsymbol{d}_1 = 0.8\boldsymbol{a}$ [7].

In order to vividly demonstrate the frequency-filtering property of the new material, the special transducer with the two basic frequencies

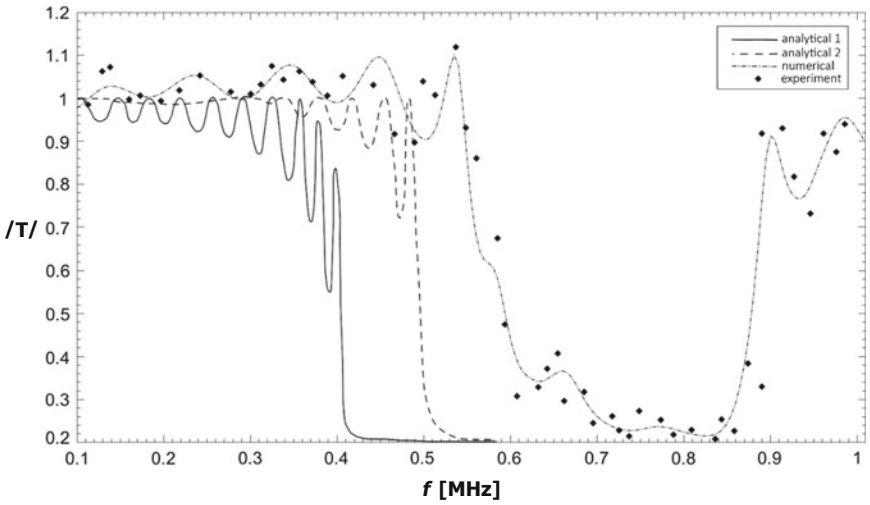

Fig. 25.10 Comparison between experimental measurements, numerical predictions and low-frequency theoretical estimates for periodic system of linear obstacles [7]

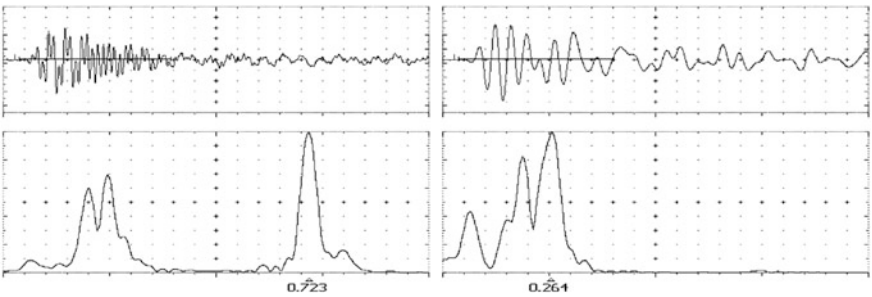

Fig. 25.11 Demonstration of the frequency filtering properties of the acoustic metamaterial. At the *left* signal transmitted through the basic material, at the *right* through the material with the array of holes

($f_1 = 0.25\,\mathbf{MHz}, f_2 = 0.72\,\mathbf{MHz}$) has been prepared in our ultrasonic laboratory. This frequencies are choosen in such a way that one of them lies in the fully transmit range and the other one—in the band gap (see Fig. 25.10). The signal passed through the basic material is demonstrated at the left part of Fig. 25.11, where the built-in device spectral representation is reflected under the radio-pulse signal. The diagram at the right-hand side of Fig. 25.11 demonstrates the wave transmitted through the material with the periodic system of holes. One can easily observe, that only low frequency passes through the acoustic metamaterial, "clearing" the radio-pulse from its high-frequency components.

25.6 Conclusions

The main conclusions which can be extracted from the present work are listed here below:

1. The BEM and the BIE simulate quite precisely the wave properties of the metamaterials; these techniques can adequately be applied to study of these materials.
2. All properties, predicted by the low-frequency analytic approach [7], are confirmed by the numerical estimation. Both analytical simulation and experimental results show that for low frequencies the structure of the wave field is quite regular, however with frequency increasing this becomes more chaotic.
3. The materials with the inner periodic array of obstacles can concentrate the energy of the wave inside the array creating a "tunnel" with an amplified pressure.
4. The geometric "shift" of each even row in the array creates a material with better acoustic permeability than the material with regular array.

5. In the high-frequency range, when a wave passes through the material, this geometry shows a ray nature and transmits the energy right to the opening between the holes.

Some different geometries with similar wave properties will be studied in the authors' further works.

Acknowledgements The authors are grateful to the Russian Science Foundation (RSCF), for its support by Project 15-19-10008.

References

1. S. Guenneau, R.V. Craster, *Acoustic Metamaterials Negative Refraction, Imaging, Lensing and Cloaking* (Springer Science+Business Media, Dordrecht, 2013). (Springer Series in Materials Science)
2. P.A. Deymier, *Acoustic Metamaterials and Phononic Crystals* (Springer, Berlin, 2013). (Springer Series in Solid-State Sciences)
3. B. Banerjee, in *An Introduction to Metamaterials and Waves in Composites* (CRC Press Taylor & Francis Group) (2011)
4. Z.Y. Liu, X.X. Zhang et al., Science **289**, 1734 (2000)
5. J.D. Achenbach, Z.L. Li, Wave Motion **8**, 225 (1986)
6. J.D. Achenbach, M. Kitahara, J. Acoust. Soc. Am. **81**, (1987)
7. E. Scarpetta, M.A. Sumbatyan, Wave Motion **25**, 61 (1997)
8. E. Scarpetta, M.A. Sumbatyan, Eur. J. Mech. A/Solids, p. 19 (2000)
9. M.A. Sumbatyan, A. Scalia, in *Equations of Mathematical Diffraction Theory* (CRC Press, Boca Raton) (2005)
10. S. Bron, in *Efficient Numerical Methods for Non-local Operators* (EMS Tracts in Mathematics), p. 14 (2010)
11. D. Brunner, M. Junge, P. Rapp, M. Bebendorf, L. Gaul, Comput. Model. Eng. Sci. **58**, 131 (2010)
12. M.H. Cho, W. Cai, Comput. Phys. Commun. **181**, 2086 (2010)
13. H. Cheng, W.Y. Crutchfield, Z. Gimbutas et al., J. Comput. Phys. **216**, 300 (2006)

Chapter 26
On the Elastic Waves Propagating Along the Edge of the Wedge with Small Opening Angle

Aleksandr O. Vatulyan and Lyubov I. Parinova

Abstract A propagation of elastic waves is studied along the ridgity rib of the wedge clamped with a finite size height. A dependence of the wave number on the non-dimensional oscillation frequency is defined by using the variational principle of Hamilton–Ostrogradskii in the case of steady-state oscillations and Ritz method. A relative phase velocity of the wave, propagating along the edge of the clamped wedge, is compared with the relative phase velocity of infinite wedge.

26.1 Introduction

Acoustics, seismology and defectoscopy investigate the problems associated with the propagation of the wedge waves along the edges of the elastic bodies. Solution of the problems, coupled with the finding of velocities of elastic waves, propagating along the edges of topographical waveguides, are used to create acoustic-electronic devices for signal processing in the radio-electronic systems. The problem of elastic wave propagation along the edge of the wedge of space isotropic material is studied in detail in the literature [1–4]. A number of papers [1, 2] is devoted to the calculation of the velocity waves, based on the method of finite elements. In the course of investigations, it was found that the wave field in the isotropic case was localized near the edge of the wedge. A waveguide is a dispersion structure. The wave velocity is dependent on oscillation frequency. The existence of the wave of mode for a wedge with a small

A.O. Vatulyan (✉)
I.I. Vorovich Institute of Mathematics,
Mechanics and Computer Science, Southern Federal University,
8a, Milchakov Street, Rostov-on-Don 344090, Russia
e-mail: vatulyan@math.rsu.ru

L.I. Parinova
Don State Technical University, 1 Gagarin Square,
Rostov-on-Don 344000, Russia
e-mail: parinovali@mail.ru

I.A. Parinov et al. (eds.), *Advanced Materials*, Springer Proceedings
in Physics 193, DOI 10.1007/978-3-319-56062-5_26

angle of the solution was proved in [5]. Waves, propagating along the edge of an infinite wedge, were studied in [6, 7], previously.

The aim of the present study is on the base of the analysis of the problem for an orthotropic elastic plate of variable stiffness to determine the value of the wave number as a function of the non-dimensional oscillation frequency.

26.2 Mathematical Formulation of the Problem

Let us consider an elastic wave, which propagates along the edge of the wedge. The wedge from the orthotropic material is clamped rigidly. The height of the wedge is equal to h. The opening angle is small and equal to 2α. The wedge section is denoted as S (Fig. 26.1).

The mass forces do not act on the wedge, and the equation of motion has the form:

$$\sigma_{mj,j} + \rho\omega^2 u_m = 0, \tag{26.1}$$

where σ_{kj} are the components of stress tensor, u_m are the components of the vector of elastic displacement, ρ is the density, m, k, $j = 1, 2, 3$, ω is the oscillation frequency.

The constitutive relations and Cauchy relations are represented in the form:

$$\sigma_{kj} = C_{kjmn}\varepsilon_{mn};\ \varepsilon_{mn} = \frac{1}{2}(u_{m,n} + u_{n,m}), \tag{26.2}$$

where C_{kjmn} are the components of the compliance tensor of material,ε_{mn} are the components of the strain tensor, m, n, k, $j = 1, 2, 3$.

Boundary conditions for the base of the wedge take the form:

$$u_m = 0,\ m = 1, 2, 3. \tag{26.3}$$

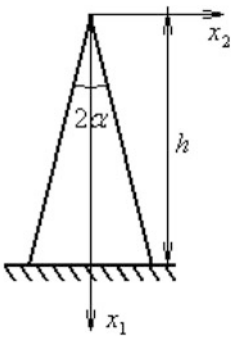

Fig. 26.1 Section of the wedge S

Boundary conditions for the wedge faces take the form:

$$\sigma_{mj} n_j\big|_S = 0,\ j = 1,2,3.\, m = 1,2,3. \tag{26.4}$$

The material is assumed isotropic and axes of an elastic symmetry coincide with coordinate axes.

The solution is searched in the form of a plane wave, propagating along the edge of the wedge:

$$u_m(x_1, x_2, x_3, t) = U_m(x_1, x_2)\mathrm{e}^{i(\gamma x_3 - \omega t)},\ j = 1,2,3, \tag{26.5}$$

where γ is a wave number, $U_m(x_1, x_2)$ are the amplitudes of the wedge waves, $m = 1,2,3$, ω is the oscillation frequency.

A boundary-value problem for the functions: $U_m = U_m(x_1, x_2)$, $m = 1,2,3$ in the case of an orthotropic material takes the form:

$$\begin{cases} C_{11}U_{1,11} + C_{12}U_{1,21} + C_{13}U_{3,1}i\gamma + C_{66}\big(U_{1,22} + U_{2,12}\big) + C_{55}\big(-\gamma^2 U_1 + U_{3,1}i\gamma\big) \\ = -\rho\omega^2 U_1 \\ C_{66}\big(U_{1,21} + U_{2,11}\big) + C_{12}U_{1,12} + C_{22}U_{2,22} + C_{23}U_{3,2}i\gamma + C_{44}\big(-\gamma^2 U_2 + U_{3,2}i\gamma\big) \\ = -\rho\omega^2 U_2 \\ C_{55}\big(U_{1,1}i + U_{3,11}\big) + C_{44}\big(U_{2,2}i + U_{3,22}\big) + \big(C_{13}U_{1,1} + C_{23}U_{2,2}\big)i - \gamma^2 C_{33}U_3 = -\rho\omega^2 U_3 \end{cases}$$

$$u_m = 0,\ m = 1,2,3,\ x_1 = h \tag{26.6}$$

$$\begin{cases} \big(C_{11}U_{1,1} + C_{12}U_{2,2} + C_{13}U_3 i\gamma\big)\sin\alpha + C_{66}\big(U_{1,2} + U_{2,1}\big)(\pm\cos\alpha) = 0 \\ C_{66}\big(U_{1,2} + U_{2,1}\big)\sin\alpha + \big(C_{12}U_{1,1} + C_{22}U_{2,2} + C_{23}U_3 i\gamma\big)(\pm\cos\alpha) = 0 \\ C_{55}\big(U_1 i\gamma + U_{3,1}\big)\sin\alpha + C_{44}\big(U_2 i\gamma + U_{3,2}\big)(\pm\cos\alpha) = 0 \end{cases}$$

where C_{ij} are elastic constants of an orthotropic material, which have known properties of symmetry and positive definiteness.

We go to the dimensionless problem, introducing the dimensionless parameters:

$$\begin{gathered} \frac{C_{11}}{C_{55}} = \gamma_1, \frac{C_{22}}{C_{55}} = \gamma_2, \frac{C_{33}}{C_{55}} = \gamma_3, \frac{C_{44}}{C_{55}} = \gamma_4, \frac{C_{12}}{C_{55}} = \gamma_5, \\ \frac{C_{66}}{C_{55}} = \gamma_6, \frac{C_{23}}{C_{55}} = \gamma_7, \frac{C_{13}}{C_{55}} = \gamma_8, \frac{\rho\omega^2 h^2}{C_{55}} = \beta, \gamma h = \mu. \end{gathered} \tag{26.7}$$

We need to find the value of the wave number μ, depending on the setting β in which the problem (26.6) has a non-trivial solution.

There is no a separation of variables in the anisotropic case. Therefore, we cannot go to the polar coordinate system in the equations of motion in the studied case. Therefore, we use the approximate method, based on the variational approach, to solve the problem and finding the value β.

The variational principle of Hamilton–Ostrogradskii [8] in the case of steady-state oscillations in the absence of mass and surface forces takes the form:

$$\delta(W-K)=0;\ W=\frac{1}{2}\int\limits_S \sigma_{ij}\,\overline{\varepsilon_{ij}}dS,\ K=\frac{1}{2}\omega^2\int\limits_S \rho U_i^2 dS,$$

where W is an analog of the specific potential energy, K is an analog of the kinetic energy, $\overline{\varepsilon_{ij}}$ are the complex-conjugate quantities to the components of the strain tensor ε_{ij}.

Passing to non-dimensional parameters, introduced above, we obtain the following variational equation, $\delta M[U_i]=0$, where

$$M[U_i]=\int\limits_S M_0 dS, \tag{26.8}$$

and the integrand has the form:

$$\begin{aligned} M_0 = {} & (\gamma_1 U_{1,1}+\gamma_5 U_{2,2}+i\gamma\gamma_8 U_3)\overline{U_{1,1}}+(\gamma_5 U_{1,1}+\gamma_2 U_{2,2}+i\gamma\,\gamma_7 U_3)\overline{U_{2,2}} \\ & +(\gamma_8 U_{1,1}+\gamma_7 U_{2,2}+i\gamma\,\gamma_3 U_3)\overline{iU_3}+\gamma_6(U_{1,2}+U_{2,1})\overline{(U_{1,2}+U_{2,1})} \\ & +(i\gamma U_1+U_{3,1})\overline{(i\gamma U_1+U_{3,1})}+(i\gamma U_2+U_{3,2})\overline{(i\gamma U_2+U_{3,2})} \\ & -\beta\,(U_1^2+U_2^2+U_3^2) \end{aligned} \tag{26.9}$$

26.3 The Model of the Plate of Variable Stiffness

The oscillations of the wedge-shaped region are divided into two tasks: symmetric and antisymmetric vibrations. There are not typically studied types of movements for the symmetric case. Therefore, let us consider an antisymmetric case.

We assume that the components satisfy the following parity relations on odd x_2-coordinate:

$$U_1(x_1,-x_2)=-U_1(x_1,x_2),U_2(x_1,-x_2)=U_2(x_1,x_2),U_3(x_1,-x_2)=-U_3(x_1,x_2) \tag{26.10}$$

We take into account the properties of the wave field of localization and consider that the opening angle α has a small value. We take the classic hypothesis theory of anisotropic plates of variable stiffness to find the stationary value of functional (26.8):

$$U_1=-x_2W'(x_1),U_2=W(x_1),U_3=-i\gamma x_2 W(x_1). \tag{26.11}$$

We integrate (26.9) on x_2 and make a change of variables: $x_1=zh$. By using (26.11), in the result we find that the problem of constructing the dispersion curves is reduced to the problem of finding the stationary value of the quadratic functional M:

$$M[W] = \int_0^1 M_0 dz \tag{26.12}$$

where

$$M_0 = \left(\gamma_1 W_{zz}^2 - 2\gamma_8 \mu W_{zz} W + \gamma_3 W^2 \mu^2 + 4\mu W_z^2\right) \frac{2}{3} z^3 \mathrm{tg}^3 \alpha$$
$$- \kappa^2 \left(\left(W_z^2 - W^2 \mu\right) \frac{2}{3} z^3 \mathrm{tg}^3 \alpha + 2W^2 z \mathrm{tg}\alpha \right)$$

the dimensionless parameters γ_1, γ_3, γ_8 are determined in accordance with (26.7).

One of the approximate methods for finding the stationary functional values, namely the Ritz method will be used to find the stationary value of the functional. Thus, the solution $W(z)$ will be searched in the class of functions restricted at $z = 0$ and satisfying the boundary conditions at $z = 1$.

We represent the solution in the form: $W = (z-1)^2 \sum_{n=1}^{N} c_n \varphi_n(z)$, where coordinate functions are chosen as system functions: $\varphi_n(z) = z^{n-1}$, $n = 1, 2, \ldots$

Then the functional (26.12) takes the form of a quadratic function of N variables:

$$M(c_1, c_2 \ldots c_n) = \int_0^1 M_1 dz, \tag{26.13}$$

where $M_1 = M_1(c_1, c_2 \ldots c_n, z)$.

For example, when $N = 2$, we have $M_1(c_1, c_2, z) = k_{11} c_1^2 + k_{12} c_1 c_2 + k_{22} c_2^2$, where $k_{ij} = k_{ij}(z)$, $i, j = 1, 2$.

By integrating (26.13) by z, and assuming $\mathrm{tg}\alpha = t$, we get that k_{ij}, i, $j = 1, 2$, take the following forms:

$$k_1 = \frac{1}{1260}\left\{t^3\left[3\gamma_3\mu^2 + (-56\gamma_8 + 224)\mu + 840\gamma_1\right] + \beta\left[t^3(3\mu - 56) - 84t\right]\right\}$$
$$k_2 = \frac{1}{3780}\left\{t^3\left[2\gamma_3\mu^2 + (12\gamma_8 + 132)\mu + 1008\gamma_1\right] + \beta\left[t^3(2\mu - 33) - 27t\right]\right\}$$
$$k_{12} = \frac{2}{945}\left\{t^3\left[\gamma_3\mu^2 + (-6\gamma_8 + 60)\mu + 252\gamma_1\right] + \beta\left[t^3(\mu - 15) - 18t\right]\right\}$$

By using a condition of stationary of the functional M, we obtain a linear homogeneous system in respect to c_k. Table 26.1 presents dimensionless parameters γ_i, obtained from ratios (26.7) for materials under consideration.

In the result, we obtain a system of linear algebraic equations. By equating the determinant of the system to zero, we get an algebraic equation connecting β and μ. We explored the convergence of the method according to the number of coordinate functions. We have showed that 3 or 4 coordinate functions allow us to reach the

Table 26.1 Elastic constants of orthotropic materials studied

Material	γ_1	γ_2	γ_3	γ_4	γ_5	γ_6	γ_7	γ_8
Barite	3.15	2.8	3.72	0.42	1.71	3.15	1.04	0.96
Austenitic steel	2.04	2.04	1.67	1.0	0.76	2.04	1.12	1.12

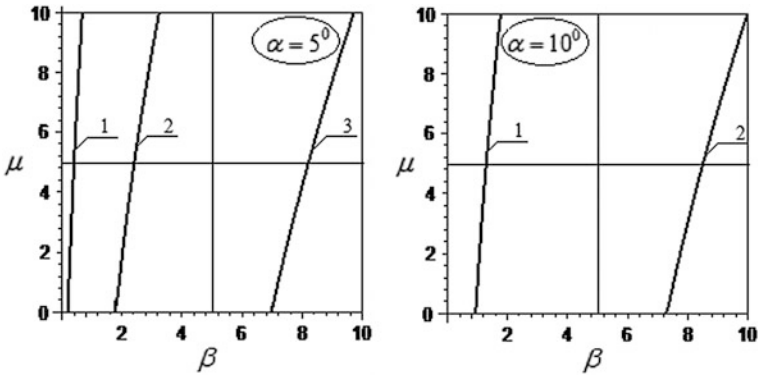

Fig. 26.2 Dependence of wave number μ on parameter β for barite

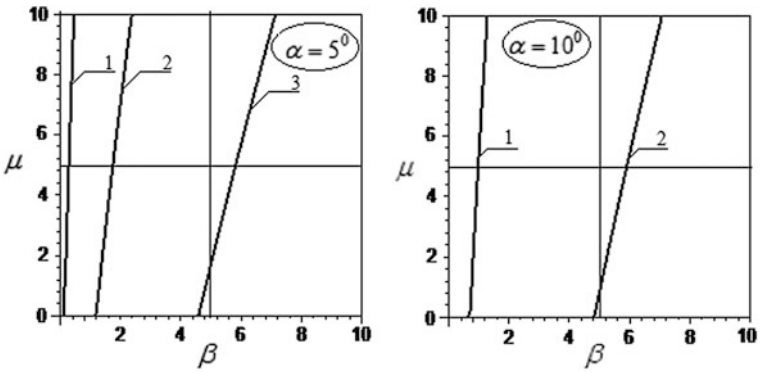

Fig. 26.3 Dependence of wave number μ on parameter β for austenitic steel

accuracy of the order of 1%. We built dispersion relations and found the numerical values, obtained for two orthotropic materials (barite and austenitic steel) at different opening angles α of wedge.

Plots of the dependence of wave number μ on parameter β for the both orthotropic materials are shown in Figs. 26.2 and 26.3. The corresponding numerical data in dependence on number of coordinate functions are present in Tables 26.2 and 26.3.

Table 26.2 Values of the wave number μ for the angle of wedge opening $\alpha = 5°$ (material is the austenitic steel)

No. of mode	β	Number of coordinate functions					
		$N = 3$	$N = 4$	$N = 5$	$N = 6$	$N = 7$	$N = 8$
1 mode	1	44.657	46.990	47.740	47.856	47.874	47.875
	2	81.161	90.245	94.791	96.255	96.621	96.688
	3	111.283	128.057	138.382	143.015	144.605	145.012
	4	137.588	161.934	178.793	187.940	191.822	193.080
	5	161.251	192.832	216.423	230.880	238.005	240.748
2 mode	2	11.699	13.857	14.177	14.211	14.213	14.213
	3	23.305	27.823	28.960	29.201	29.225	29.228
	4	32.989	39.686	41.924	42.598	42.700	42.713
	5	41.490	50.207	53.721	55.050	55.316	55.358
3 mode	5	0	0.421	3.138	3.465	3.482	3.483

Table 26.3 Values of the wave number μ for the angle of wedge opening $\alpha = 5°$ (material is the barite)

No. of mode	β	The number of coordinate functions					
		$N = 3$	$N = 4$	$N = 5$	$N = 6$	$N = 7$	$N = 8$
1 mode	1	28.432	28.946	29.010	29.015	29.015	29.015
	2	54.045	57.564	58.466	58.593	58.604	58.605
	3	75.756	83.970	87.103	87.811	87.912	87.922
	4	94.797	108.227	114.755	116.777	117.173	117.225
	5	111.887	130.559	141.196	145.311	146.342	146.515
2 mode	2	2.083	2.862	2.897	2.898	2.898	2.898
	3	14.008	16.045	16.303	16.322	16.323	16.323
	4	22.376	25.631	26.270	26.349	26.354	26.354
	5	29.210	33.672	34.850	35.050	35.067	35.068

The influence of the accuracy of the determination of dispersed branches depending on the number of coordinate functions was investigated for austenitic steel.

It was shown that 3 or 4 coordinate functions were required to define small values β for the points of the first dispersion branch with an accuracy of less than 1% for the angle $\alpha = 5°$ in the case of austenitic steel. At the same time, 4 or 5 coordinate functions were required to define small values β for the points of the second dispersion branch. This transverse-isotropic material has a third branch of the dispersion. To determine the coordinate points of the branch with an error not exceeding 1% were enough 5 or 6 coordinate functions.

26.4 Comparison with the Problem of Wave Propagation Along the Edge of Infinite Wedge

Previous works [6, 7] studied the problem of wave propagation along the edge of an infinite wedge with a triangular cross-section. Formulae have been obtained to calculate the relative phase velocities in the orthotropic case. The comparison of results using the Ritz method was obtained with known results obtained by using geometric-acoustic theory in the isotropic case [4].

Let us compare the relative phase velocity of propagation of the elastic wave along the edge of the clamped wedge having a finite height with the same parameters for the infinite wedge.

Relative phase velocity was defined by the formula:

$$\psi = \frac{c}{c_2} \tag{26.14}$$

where

$$c_2 = \sqrt{\frac{\rho}{C_{55}}} \text{ and } c_2 = \frac{\sqrt{\beta}}{\mu}, \tag{26.15}$$

β is the non-dimensional oscillation frequency. The comparative plots of relative phase velocity in dependence on non-dimensional oscillation frequency for the wave propagating along the edge of the clamped finite wedge and along the infinite wedge for barite are presented in Fig. 26.4.

Figure 26.4 shows an absence of dispersion in the case of an infinite wedge (2). A dependence of the relative velocity on the non-dimentional oscillation frequency (1) appears in the case of propagation of elastic waves along the edge of the finite rigidly clamped wedge.

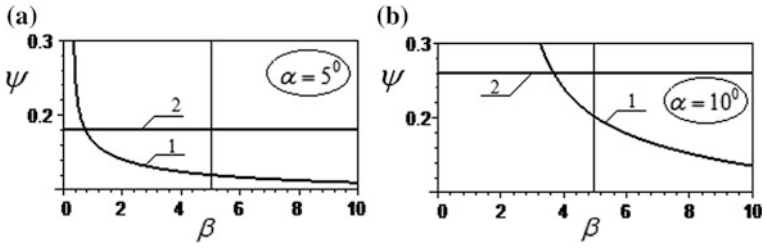

Fig. 26.4 Dependence of relative phase velocity on non-dimensional oscillation frequency for the wave, propagating along edge of clamped wedge *1* and infinite wedge *2*, for barite: **a** $\alpha = 5°$ and **b** $\alpha = 10°$

References

1. P.E. Lagasse, Electron. Lett. **8**, 372 (1972)
2. P.E. Lagasse, I.M. Mason, E.A. Ash, IEEE Trans. Son. Ultrason. **20**, 143 (1973)
3. A.A. Maradudin, R.F. Wallis, D.L. Mills, R.L. Ballard, Phys. Rev. B **6**, 1106 (1972)
4. S.V. Biryukov, Yu.V. Guljaev, V.V. Krylov, V.P. Plesskii, *Surface Acoustic Waves in Inhomogeneous Media* (Nauka, Moscow, 1991), 414 p. (in Russian)
5. I.V. Kamockii, Algebra Anal. **20**(1), 86 (2008)
6. A.O. Vatulyan, L.I. Parinova, Vestnik DSTU **5**(4), 491 (2005) (in Russian)
7. L.I. Parinova, in *Proceedings of the III School-seminar*, vol. 113, DSTU, Rostov-on-Don, 15–19 Nov 2004 (in Russian)
8. S.G. Mihlin, *Variational Methods in Mathematical Physics* (Gostehizdat, Moscow, 1957), 476 p. (in Russian)

Chapter 27
BEM Formulation for 3D Static Analysis in Magnetoelectroelastic Solids

Leonid A. Igumnov, Ivan P. Markov and Aleksandr K. Lyubimov

Abstract The three-dimensional static boundary element method formulation is presented in this chapter. Both piezoelectric and piezomagnetic phases are present in considered magnetoelectroelastic materials. These materials are able of converting energy among electric, magnetic and mechanical fields. The boundary element technique is based on the displacement boundary integral representation. Static fundamental solutions are employed in the form of the integrals along a unit circumference. The point collocation scheme with the mixed boundary elements is used for spatial discretization. The generalized displacements and tractions are interpolated by the linear and constant shape functions, respectively. Boundary geometry is approximated by eight-node quadrilateral elements with quadratic shape functions. Simple numerical example with known exact solutions is considered to validate the proposed boundary element formulation. To establish versatility of the present approach a more complex example is presented.

27.1 Introduction

Magnetoelectroelastic materials (MME) belong to the class of materials with multifield behavior. Such materials have a special feature namely an electromagnetic coupling effect due to combination of piezoelectric and piezomagnetic phases. Significant interactions between electric, magnetic and elastic fields render magnetoelectroelastic materials especially attractive in many important engineering and technological applications, such as energy harvesting systems, multifunctional devices, smart and adaptive structures like sensors, actuators, transducers and so on. Correct simulation of coupled response is very important for effective design and operation of structures made of magnetoelectroelastic materials. Consequently, it is of particular interest to develop a numerical formulation to model the coupled

L.A. Igumnov · I.P. Markov (✉) · A.K. Lyubimov
Research Institute for Mechanics, National Research Lobachevsky State University of Nizhni Novgorod, 23 Bldg. 6, Gagarin Avenue, 603950 Nizhny Novgorod, Russia
e-mail: markov@mech.unn.ru

I.A. Parinov et al. (eds.), *Advanced Materials*, Springer Proceedings in Physics 193, DOI 10.1007/978-3-319-56062-5_27

electro-magneto-mechanical response of magnetoelectroelastic three-dimensional (3D) solids with complex geometry, arbitrary boundary conditions and under various mechanical, electric or magnetic loadings.

Although certain number of works [1–10] devoted to different analytical and numerical approaches for modeling of magnetoelectroelastic solids under static loading conditions was presented over the past two decades, more often than not these works are restricted to two-dimensional case or simple problems geometries and boundary conditions. The Boundary Element Method (BEM) is well suited to solve general three-dimensional boundary value problems of linear magnetoelectroelasticity and has well-recognized advantages over universal numerical approaches like Finite Element Method and Finite Difference Method. Fundamental solution, or as often referred to as Green's function, and its derivatives are the cornerstones of the conventional boundary element formulations. Regarding full-space 3D Green's functions for magnetoelectroelastic materials, various expressions can be found in the literature [11–13].

The aim of the present chapter is to formulate and implement a conventional direct boundary element formulation for the three-dimensional static analysis of fully coupled linear magnetoelectroelastic solids. MEE material can have arbitrary degree of anisotropy. Proposed BEM technique is based on the integral representation of the fundamental solutions. Procedure of spatial discretization is relying on concept of mixed boundary elements [14]. Analytical solutions available in the literature are used to validate the presented boundary element approach. As an illustration, new numerical results are also provided.

27.2 Statement of the Problem

We consider a three-dimensional, homogenous solid occupying the region $\Omega \subset R^3$ with the boundary $\Gamma = \partial\Omega$. Under the assumption of static elastic fields, quasi-static electric and magnetic fields, in the absence of body forces, electric charge and electric current, the basic relations for linear magnetoelectroelasticity are:

$$\sigma_{ij,j} = 0 \text{ in } \Omega, \quad i,j = \overline{1,3}, \tag{27.1}$$

$$D_{i,i} = 0 \text{ in } \Omega, \tag{27.2}$$

$$B_{i,i} = 0 \text{ in } \Omega, \tag{27.3}$$

$$\sigma_{ij} = C^E_{ijlm}\varepsilon_{lm} - e_{kij}E_k - q_{kij}H_k \text{ in } \Omega,\ k,l = \overline{1,3}, \tag{27.4}$$

$$D_i = e_{ijk}\varepsilon_{jk} + \gamma_{ij}E_j + \lambda_{ij}H_j \text{ in } \Omega, \tag{27.5}$$

$$B_i = q_{ijk}\varepsilon_{jk} + \lambda_{ij}E_j + \mu_{ij}H_j \text{ in } \Omega, \tag{27.6}$$

$$\varepsilon_{ij} = \frac{1}{2}(u_{i,j} + u_{j,i}) \text{ in } \Omega, \tag{27.7}$$

$$E_i = -\phi_{,i} \text{ in } \Omega, \tag{27.8}$$

$$H_i = -\psi_{,i} \text{ in } \Omega, \tag{27.9}$$

where σ_{ij}, D_i, B_i are the stress tensor, the electric displacement vector and the magnetic induction vector, respectively; ε_{ij}, E_i, H_i are the elastic strain tensor, the electric field vector and the magnetic field vector; u_i, ϕ, ψ are the elastic displacement vector, the electric potential and the magnetic potential, respectively. C^E_{ijkl}, e_{ijk}, q_{ijk} are the elasticity tensor, the piezoelectric and the piezomagnetic coefficients; λ_{ij}, γ_{ij}, μ_{ij} are the magnetoelectric coefficients, the dielectric permittivity tensor and the magnetic permeability tensor. The following symmetry relations are satisfied for the material constants:

$$C^E_{ijkl} = C^E_{klij} = C^E_{jikl} = C^E_{ijlk}, \quad \gamma_{ij} = \gamma_{ji}, \quad \mu_{ij} = \mu_{ji}, \quad e_{ijk} = e_{ikj}, \quad q_{ijk} = q_{ikj}, \quad \lambda_{ij} = \lambda_{ji}. \tag{27.10}$$

Mechanical, electric and magnetic boundary conditions on the external boundary are stated as follows

- Dirichlet boundary conditions:

$$u_i = \tilde{u}_i \text{ on } \Gamma^u, \tag{27.11}$$

$$\phi = \tilde{\phi} \text{ on } \Gamma^\phi, \tag{27.12}$$

$$\psi = \tilde{\psi} \text{ on } \Gamma^\psi. \tag{27.13}$$

- Neumann boundary conditions:

$$t_i = \sigma_{ij}n_j = \tilde{t}_i \text{ on } \Gamma^t, \tag{27.14}$$

$$D_n = D_i n_i = \tilde{D}_n \text{ on } \Gamma^D, \tag{27.15}$$

$$B_n = B_i n_i = \tilde{B}_n \text{ on } \Gamma^B, \tag{27.16}$$

where t_i is the traction vector, n_i denotes the outward unit normal vector to the boundary and tilde symbol indicates a prescribed value.

Employing the extended variable notation introduced by Barnett and Lothe [15], linear magnetoelectroelastic problem may be formulated in compact form. To this end, the following generalized entities are defined [11]:

$$U_k = \begin{cases} u_k, & k = \overline{1,3}, \\ \phi, & k = 4, \\ \psi, & k = 5, \end{cases} \tag{27.17}$$

$$T_k = \begin{cases} t_k, & k = \overline{1,3}, \\ D_n, & k = 4, \\ B_n, & k = 5, \end{cases} \tag{27.18}$$

$$C_{ijkl} = \begin{cases} C^E_{ijkl}, & i,j,k,l = \overline{1,3}, \\ e_{lij}, & i,l,j = \overline{1,3},\ k = 4, \\ e_{ikl}, & i,l,k = \overline{1,3},\ j = 4, \\ q_{lij} & i,l,j = \overline{1,3},\ k = 5, \\ q_{ikl} & i,l,k = \overline{1,3},\ j = 5, \\ -\lambda_{il} & i,l = \overline{1,3}\, j = 4,\ k = 5 \text{ or } \mathrm{k} = 4,\ j = 5, \\ -\gamma_{il} & i,l = \overline{1,3}, j,k = 4, \\ -\mu_{il} & i,l = \overline{1,3}, j,k = 5, \end{cases} \tag{27.19}$$

This way, in terms of the generalized variables the governing equations can be expressed as

$$C_{ijkl} U_{k,li} = 0. \tag{27.20}$$

It can be noted that (27.20) are similar to corresponding equations of linear elasticity.

27.3 BEM Formulation

Analytical solutions of the magnetoelectroelastic equations stated in previous section can only be obtained for very specific cases of geometry and boundary conditions. For the static analysis of the homogenous 3D MEE structures with general configuration, we employ a boundary element approach. Using the extended form of Somigliana identity:

$$U_k(\mathbf{x}) = \int_\Omega \big(g_{jk}(\mathbf{x},\mathbf{y}) T_k(\mathbf{y}) - h_{jk}(\mathbf{x},\mathbf{y}) U_k(\mathbf{y})\big) \mathrm{d}\Gamma(\mathbf{y}), \quad \mathbf{x} \in \Omega, \tag{27.21}$$

displacement boundary integral equations can be obtained as follows

$$c_{jk}U_k(\mathbf{x}) = \int_\Gamma g_{jk}(\mathbf{x},\mathbf{y})T_k(\mathbf{y})\mathrm{d}\Gamma(\mathbf{y}) - \int_\Gamma h_{jk}(\mathbf{x},\mathbf{y})U_k(\mathbf{y})\mathrm{d}\Gamma(\mathbf{y}), \quad \mathbf{x}\in\Gamma, \quad (27.22)$$

where U_k and T_k are the generalized displacements and tractions as introduced earlier; c_{jk} are the free terms; g_{jk} and h_{jk} are the generalized displacement fundamental solution and the traction fundamental solution at a field point $\mathbf{y}$ due to an applied unit source at a source point $\mathbf{x}$.

In present formulation, the boundary Γ is discretized with eight-node quadrilateral elements with quadratic shape functions. The spatial discretization of the boundary integral equations (27.22) is performed by a collocation procedure. Following the idea of mixed boundary elements the generalized variables on the boundary are interpolated through their nodal values inside each boundary element by the linear and constant shape functions, therefore the corresponding collocation nodes are split. The static displacement fundamental solution can be expressed in an integral form as follows

$$g^S_{jk}(\mathbf{x},\mathbf{y}) = \frac{1}{8\pi^2 r}\int_{|\mathbf{d}|=1}\Gamma^{-1}_{jk}(\mathbf{d})\mathrm{d}S(\mathbf{d}), \quad j,k=\overline{1,5}, \quad (27.23)$$

where $\Gamma_{jk}(\mathbf{d}) = C_{ijkl}d_i d_l$, S is a unit circumference on a unit sphere with center at $\mathbf{x}$ intersected by the plane perpendicular to $\mathbf{r}=\mathbf{y}-\mathbf{x}$ and $r=|\mathbf{r}|$. The traction fundamental solution is obtained from the constitutive equations and definition of the traction vector as

$$h_{jk}(\mathbf{x},\mathbf{y}) = C_{ijpl}g_{pk,l}(\mathbf{x},\mathbf{y})n_i(\mathbf{y}), \quad p=\overline{1,5}, \quad (27.24)$$

where $n_i(\mathbf{y})$ is the external unit normal vector to the boundary.

27.4 Numerical Examples

In the first example a magnetoelectroelastic beam with dimensions $L=0.2\,\mathrm{m}$, $w=0.04\,\mathrm{m}$ and $h=0.02\,\mathrm{m}$ is considered [5], as depicted in Fig. 27.1. The beam is subjected to mechanical loading at its upper surface $x_3=+h/2: t_3=p(x_1)=p_0\sin(\pi x_1/L)$ with $p_0=-10\,\mathrm{Pa}$.

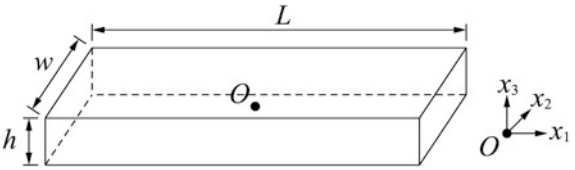

Fig. 27.1 Geometry of a magnetoelectroelastic beam

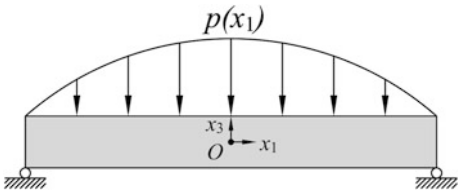

Fig. 27.2 Sketch of a simply supported magnetoelectroelastic beam

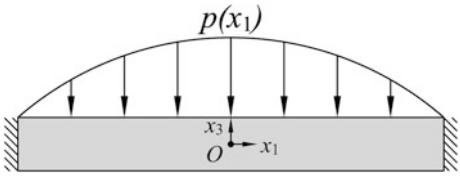

Fig. 27.3 Sketch of a clamped mangnetoelectroelastic beam

Two sets of boundary conditions along the faces $x_1 = \pm L/2$ are examined, specifically: electric and magnetic potentials are fixed at zero and beam either simply supported or clamped at both ends as illustrated in Figs. 27.2 and 27.3, respectively. The rest of surface is free of generalized tractions. The material tensors are given as follows [5]:

$$\mathbf{C}^E = \begin{bmatrix} 166 & 77 & 78 & 0 & 0 & 0 \\ 77 & 166 & 78 & 0 & 0 & 0 \\ 78 & 78 & 162 & 0 & 0 & 0 \\ 0 & 0 & 0 & 43 & 0 & 0 \\ 0 & 0 & 0 & 0 & 43 & 0 \\ 0 & 0 & 0 & 0 & 0 & 44.5 \end{bmatrix} \text{GPa},$$

$$\mathbf{e} = \begin{bmatrix} 0 & 0 & 0 & 0 & 11.6 & 0 \\ 0 & 0 & 0 & 11.6 & 0 & 0 \\ -4.4 & -4.4 & 18.6 & 0 & 0 & 0 \end{bmatrix} \text{C}/\text{m}^2,$$

$$\boldsymbol{\gamma} = \begin{bmatrix} 11.2 & 0 & 0 \\ 0 & 11.2 & 0 \\ 0 & 0 & 12.6 \end{bmatrix} \cdot 10^{-9}\text{C}/\text{Vm},$$

$$\mathbf{q} = \begin{bmatrix} 0 & 0 & 0 & 0 & 550 & 0 \\ 0 & 0 & 0 & 550 & 0 & 0 \\ 580.3 & 580.3 & 699.7 & 0 & 0 & 0 \end{bmatrix} \text{N}/\text{Am},$$

$$\boldsymbol{\lambda} = \begin{bmatrix} 5 & 0 & 0 \\ 0 & 5 & 0 \\ 0 & 0 & 3 \end{bmatrix} \cdot 10^{-12}\text{Ns}/\text{VC},$$

$$\boldsymbol{\mu} = \begin{bmatrix} 5 & 0 & 0 \\ 0 & 5 & 0 \\ 0 & 0 & 10 \end{bmatrix} \cdot 10^{-6} \mathrm{Ns}^2/\mathrm{C}^2.$$

For the simply supported case, Table 27.1 shows the comparison of the presented boundary element approach with the exact solutions and results by Ding and Jiang [5]. For the clamped beam, results, obtained with the proposed formulation, are listed in Table 27.2 alongside with those by Ding and Jiang [5]. It should be noted no exact solutions was found for the clamped beam yet.

The obtained results for the simply supported case compare favorably against two-dimensional boundary element solutions provided by Ding and Jiang [5].

For the next example, a square magnetoelectroelastic plate with a central square hole [6] is considered, as depicted in Fig. 27.4. The dimensions of the plate are

Table 27.1 Results for the simply supported beam

Point (m)		u_3 (m)	ϕ (V)	ψ (A)
(0.0, 0.02, 0.0)	Present formulation	−1.9922E-09	−2.2961E-02	−1.8018E-03
	Exact	−2.0000E-09	−2.3140E-02	−1.8080E-03
	Ding and Jiang [5]	−1.9770E-09	−2.3000E-02	−1.7940E-03
(0.025, 0.02, 0.0)		−1.8406E-09	−2.1215E-02	−1.6646E-03
		−1.8470E-09	−2.1380E-02	−1.6710E-03
		−1.7960E-09	−2.1230E-02	−1.5880E-03
(0.05, 0.02, 0.0)		−1.4089E-09	−1.6241E-02	−1.2741E-03
		−1.4140E-09	−1.6370E-02	−1.2790E-03
		−1.3780E-09	−1.6250E-02	−1.2580E-03
(0.075, 0.02, 0.0)		−7.6275E-10	−8.8003E-03	−6.8951E-04
		−7.6520E-10	−8.8570E-03	−6.9210E-04
		−7.6920E-10	−8.7980E-03	−6.8200E-04
(0.00, 0.02, 0.01)		−1.9860E-09	−8.8213E-03	−2.1707E-03
		−1.9930E-09	−8.7280E-03	−2.1650E-03
		−1.9720E-09	−8.8070E-03	−2.1650E-03
(0.025, 0.02, 0.01)		−1.8349E-09	−8.1504E-03	−2.0056E-03
		−1.8420E-09	−8.0630E-03	−2.0180E-03
		−1.8640E-09	−8.1320E-03	−2.0030E-03
(0.05, 0.02, 0.01)		−1.4045E-09	−6.2377E-03	−1.5352E-03
		−1.4090E-09	−6.1720E-03	−1.5440E-03
		−1.3740E-09	−6.0970E-03	−1.5590E-03
(0.075, 0.02, 0.01)		−7.6039E-10	−3.3557E-03	−8.3134E-04
		−7.6280E-10	−3.3400E-03	−8.3570E-04
		−7.6980E-10	−3.2810E-03	−8.3330E-04

Table 27.2 Results for the clamped beam

Point (m)		u_3 (m)	ϕ (V)	ψ (A)
(0.0, 0.02, 0.0)	Present formulation	−4.46884E-10	−2.02073E-02	−1.88074E-03
	Ding and Jiang [5]	−4.23100E-10	−2.08600E-02	−1.82700E-03
(0.025, 0.02, 0.0)		−3.90664E-10	−1.84451E-02	−1.74348E-03
		−3.71100E-10	−1.90600E-02	−1.69400E-03
(0.05, 0.02, 0.0)		−2.45280E-10	−1.34221E-02	−1.35259E-03
		−2.37200E-10	−1.39800E-02	−1.31900E-03
(0.075, 0.02, 0.0)		−7.76060E-11	−5.88912E-03	−7.67559E-04
		−8.22200E-11	−6.31720E-03	−7.54000E-04
(0.00, 0.02, 0.01)		−4.45004E-10	−1.55589E-02	−2.02107E-03
		−4.21400E-10	−1.64300E-02	−1.96300E-03
(0.025, 0.02, 0.01)		−3.89255E-10	−1.48802E-02	−1.85555E-03
		−3.69900E-10	−1.56600E-02	−1.80300E-03
(0.05, 0.02, 0.01)		−2.45211E-10	−1.29425E-02	−1.38411E-03
		−2.37100E-10	−1.34500E-02	−1.35200E-03
(0.075, 0.02, 0.01)		−7.95330E-11	−1.00107E-02	−6.78672E-04
		−8.39100E-11	−1.01700E-02	−6.71800E-04

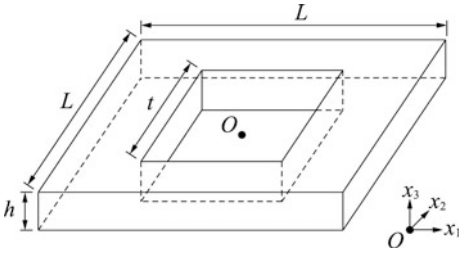

Fig. 27.4 Geometry of a magnetoelectroelastic square plate with a square hole

$L \times L \times h$ with $L = 1.0\,\text{m}$. A square hole has a side length of $t = 0.6\,\text{L}$. Outer lateral faces of the plate are simply supported and have zero electric and magnetic potentials prescribed. At the upper surface of the plate, a constant uniformly distributed traction $t_3 = 1\,\text{Pa}$ is applied as it is shown in Fig. 27.5. The rest of the plate's surface (including inner boundary) is free of generalized tractions. The material constants are the same as in the previous example. Figures 27.6, 27.7, 27.8 illustrate variations of the vertical displacements u_3, electric potential ϕ and magnetic potential ψ along the thickness direction x_3 on the edge located at the inner boundary at $x_1 = 0.3\,\text{L}$ and $x_2 = 0.3\,\text{L}$ for three h/L ratios. To simplify the comparison, the considered results are normalized by the corresponding maximum values.

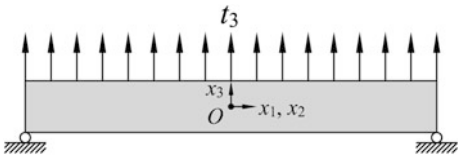

Fig. 27.5 Sketch of a magnetoelectroelastic square plate with simply supported outer boundary

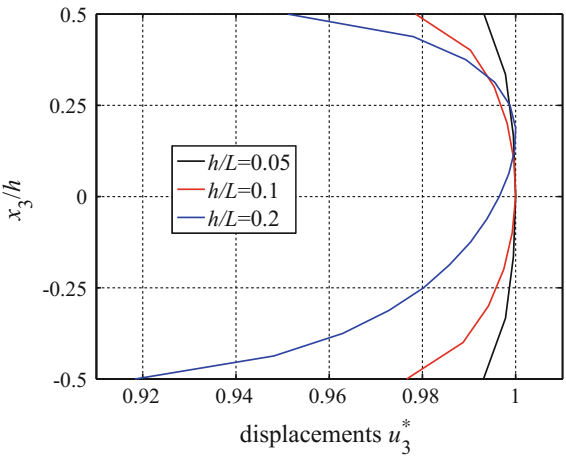

Fig. 27.6 Through-thickness dependence of dimensionless displacements u_3^* at (0.3 L, 0.3 L, x_3)

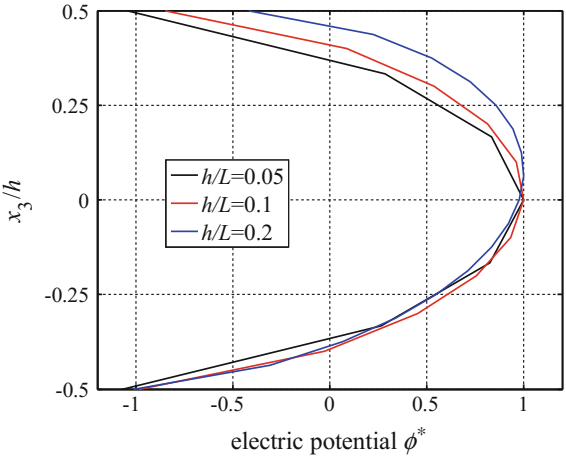

Fig. 27.7 Through-thickness dependence of dimensionless electric potential ϕ^* at (0.3 L, 0.3 L, x_3)

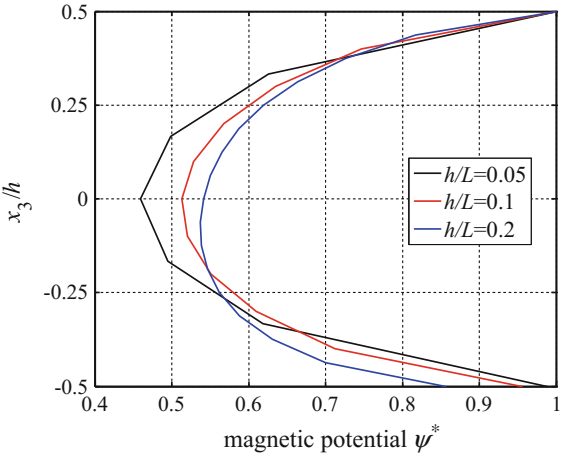

Fig. 27.8 Through-thickness dependence of dimensionless magnetic potential ψ^* at (0.3 L, 0.3 L, x_3)

27.5 Conclusions

In this chapter, we have presented a direct boundary element approach for the static analysis of the three-dimensional general anisotropic magnetoelectroelastic solids. The standard contracted notation is used to simplify the formulation. The proposed BEM technique is based on the spatial discretization with mixed boundary elements, which is a distinctive feature compared to conventional isoparametric formulations. The implemented 3D Green's functions are expressed in an integral form.

First, the proposed formulation is applied to three-dimensional problem with known analytical solution. Excellent agreement is obtained for displacements, electric and magnetic potentials at ten different field points. Maximum relative error did not exceed 0.45%.

For the second example, a static response of relatively thick magnetoelectroelastic square plate with square hole is considered. Obtained results indicate that thickness to length ratio has much greater effect on the values of the vertical displacements than on the values of the electric and magnetic potentials.

Acknowledgements The reported study was funded by Russian Foundation for Basic Research (RFBR), according to the research projects No. 16-38-60097 mol_a_dk, No. 16-38-50142, by the grant of the President of the Russian Federation for state support of young Russian scientists MK-5395.2016.1 and by the Russian Science Foundation under grant No. 16-19-10237 regarding studying the influence of the thickness to length ratio on the static response of the magnetoelectroelastic square plate with a square hole.

References

1. E. Pan, P.R. Heyliger, Int. J. Solids Struct. **40**, 6859 (2003)
2. P.R. Heyliger, E. Pan, AIAA J. **42**, 1435 (2004)
3. E. Pan, J. Appl. Mech. **68**, 608 (2001)
4. J. Wang, L. Chen, S. Fang, Int. J. Solids Struct. **40**, 1669 (2003)
5. H. Ding, A. Jiang, Comput. Struct. **82**, 1599 (2004)
6. J. Liu, P. Zhang, G. Lin, W. Wang, S. Lu, Eng. Anal. Bound. Elem. **68**, 103 (2016)
7. H.J. Ding, A.M. Jiang, P.F. Hou, W.Q. Chen, Eng. Anal. Bound. Elem. **29**, 551 (2005)
8. X.-C. Li, W.-A. Yao, Eng. Anal. Bound. Elem. **30**, 709 (2006)
9. X. Zhu, Z. Huang, A. Jiang, W.Q. Chen, N. Nishimura, Eng. Anal. Bound. Elem. **34**, 927 (2010)
10. A. Milazzo, C. Orlando, Compos. Struct. **94**, 3710 (2012)
11. E. Pan, Z. Angew. Math. Phys. **53**, 815 (2002)
12. F.C. Buroni, A. Saez, Proc. R. Soc. A **466**, 515 (2010)
13. L. Xie, C. Zhang, C. Hwu, E. Pan, Eur. J. Mech. A Solid. (2016) (in press)
14. L.A. Igumnov, I.P. Markov, Probl. Strength Plast. **76**, 191 (2014)
15. D.M. Barnett, J. Lothe, Phys. Status Solidi B **67**, 105 (1975)

Chapter 28
Boundary Element Method in Three Dimensional Transient Poroviscoelastic Problems

Aleksandr A. Ipatov, Leonid A. Igumnov and Aleksandr A. Belov

Abstract The present paper is dedicated to dynamic behavior of poroelastic and poroviscoelastic solids. Poroviscoelastic formulation is based on Biot's theory of poroelasticity in combination with elastic-viscoelastic correspondence principle. The correspondence principle is applied to describe viscoelastic properties of a skeleton of the porous material. Classical models of viscoelasticity are employed such as Kelvin-Voigt model standard linear solid model and model with weakly singular kernel. The problem is treated in Laplace domain. Direct boundary integral equation system is used to perform a solution. Mixed boundary element discretization is introduced to obtain discrete analogues. Time-step method based on Runge-Kutte nodes of numerical inversion of Laplace transform is applied to perform solution in time domain. A problem of Heaviside-type vertical load acting on a slab bonded on a poroviscoelastic halfspace and a problem of poroviscoelastic cube with cavity subjected to a normal internal pressure are considered. The comparison of dynamic responses when poroviscoelastic material is described by different viscoelactic models is presented. Viscosity parameter influence on dynamic responses of displacements and pore pressure is studied. Surface waves on poroviscoelastic halfspace are modelled with the help of boundary element method.

28.1 Introduction

Mechanics of advanced materials, such as poro-, visco- or poroviscoelastic materials, is relevant to such disciplines as geophysics, geo- and biomechanics, seismology, constricting, petroleum engineering. Wave propagation in porous/viscous media is an important issue of these disciplines. Considering wave propagation on a

A.A. Ipatov (✉) · L.A. Igumnov · A.A. Belov
Research Institute for Mechanics, National Reasearch Lobachevsky State University of Nizhni Novgorod, Nizhny Novgorod 23 Prospekt Gagarina, bld. 6, Russia
e-mail: ipatov@mech.unn.ru

L.A. Igumnov
e-mail: igumnov@mech.unn.ru

I.A. Parinov et al. (eds.), *Advanced Materials*, Springer Proceedings in Physics 193, DOI 10.1007/978-3-319-56062-5_28

half-space, one of most interesting effects are surface waves, in particular the Rayleigh wave is interest due to its miserable consequence in earthquakes. Study of wave propagation processes in saturated porous media originates from Frenkel [1] and Biot [2, 3]. The implementation of the solid viscoelastic effects in the theory of poroelasticity was first introduced by Biot [4]. Recent time have been made many significant achievements on wave propagation in porous media [5–7], but it is still very complex problems, mostly because of the inertial viscosity and mechanical coupling in porous media, and that's why large part of transient response problems can only be solved via numerical methods.

Classical formulations for boundary integral equation (BIE) method with its discretization and traditional boundary element schemes are successful approaches for solving three-dimensional isotropic problems of dynamic elasticity. Extension of BIE method and BEM to anisotropic problems, and, problems where material models are different from elastic, needs development of special new schemes. Today there are two fundamentally different approaches for constructing such numerical scheme: direct solving in time domain [8, 9], or solving in Laplace or Fourier domain [10, 11]. Unfortunately in three-dimensional case it is not always possible to construct required fundamental solutions in time, considering porous materials it is only possible in Laplace or Fourier domain. The first BEM formulations for Biot's poroelastodynamics was performed with Laplace transform usage. So the Laplace transform is the main method for three-dimensional transient problems in porous media. Shanz and Cheng [12] presented an analytical solution in the Laplace domain and analytical time-domain solution without considering viscous coupling effect, and then governing equations was extended for saturated poroviscoelastic media by using the Kelvin–Voigt model and obtained an analytical solution in the Laplace domain for the 1D problem [13].

A classical three-dimensional formulation is employed for study of viscoelastic parameters influence on dynamic responses in poroviscoelastic solids. The present work is dedicated to the development of 3d poroviscodynamic problems numerical modeling technique based on using the Boundary Element Method (BEM) in Laplace domain. The extension to poroviscoelasticity of the solution will be done in Laplace domain with the help of the elastic-viscoelastic correspondence principle.

The time domain formulations based on analytical inversion of Laplace transform applied to fundamental solutions was presented by Chen and Dargush [14]. There are fundamental solutions in time for quasi-static problems of poro- and viscoelasticity, but they are quite unmanageable, also it's impossible to account damping effects. As well, this approach is characterized by high computing costs and low stability rate. A new method, called Convolution Quadrature Method (CQM) was introduced by Lubich in 1988 [15, 16]. Nowadays CQM became a widely applied method in time-step boundary element schemes build on Laplace domain fundamental solutions [5, 17]. CQM helps to get rid of fundamental solutions in time requirement and shows better stability but is still costly. Work [18] addresses the issue of Runge-Kutta-based CQM usage. Various combinations of

this CQM modification with BEM stepping schemes were developed in [19, 20]. An overview of different boundary element approaches based on CQM is presented in [21]. Works [20, 22] estimate the accuracy and precision of Runge-Kutta-based CQM. In present paper, a similar boundary element scheme, based on the time-step method for numerical inversion of Laplace transform is considered. A modification of the scheme with variable integration step based on highly oscillatory quadrature approach is performed.

28.2 Mathematical Model

We consider a homogeneous solid Ω in three-dimensional space R^3, and $\Gamma = \partial\Omega$ is the boundary of Ω. Solid Ω is taken as isotropic poroviscoelastic. Basic poroelastic material is a two-phase material consisting of an elastic skeleton and compressible fluid or gas filler. Porous material of a volume V can be constructed as follows:

$$V = V^f + V^s$$

where V is the total volume, V^f is the summary pore volume and V^s is the volume of the skeleton. It is assumed that filler can openly seep through the pores and all closed pores are assumed as a part of the skeleton. Then a correspondence principle is applied to the skeleton, so we extend poroelastic formulation to poroviscoelasticity.

Considering a boundary-value problem for Biot's model of fully saturated poroelastic continuum in Laplace domain in terms of 4 unknowns (displacements $\bar{u}_i$ and pore pressure $\bar{p}$) the set of differential equations take the following form [5]:

$$\begin{aligned} &G\bar{u}_{i,jj} + \left(K + \frac{G}{3}\right)\bar{u}_{j,ij} - (\psi - \beta)\bar{p}_{,i} - s^2(\rho - \beta\rho_f)\bar{u}_i = -\bar{F}_i, \\ &\frac{\beta}{s\rho_f}\bar{p}_{,ii} - \frac{\phi^2 s}{R}\bar{p} - (\psi - \beta)s\bar{u}_{i,i} = -\bar{a}, \quad x \in \Omega, \end{aligned} \tag{28.1}$$

$$\begin{aligned} &\bar{u}'(x,s) = \tilde{u}', \quad x \in \Gamma^u, \quad \bar{u}' = (\bar{u}_1, \bar{u}_2, \bar{u}_3, \bar{p}), \\ &\bar{t}'_n(x,s) = \tilde{t}'_n, \quad x \in \Gamma^\sigma, \quad \bar{t}' = (\bar{t}_1, \bar{t}_2, \bar{t}_3, \bar{q}), \end{aligned}$$

where Γ^u and Γ^σ denotes boundaries for boundary conditions of 1st and 2nd kind respectively, G, K are elastic moduli, $\phi = V^f/V$ is porosity, $\bar{F}_i$, $\bar{a}$ are bulk body forces,

$$\beta = \frac{\kappa\rho_f\phi^2 s}{\phi^2 + s\kappa(\rho_a + \phi\rho_f)}, \quad \psi = 1 - \frac{K}{K_s} \quad \text{and} \quad R = \frac{\phi^2 K_f K_s^2}{K_f(K_s - K) + \phi K_s(K_s - K_f)}$$

are constants reflecting interaction between skeleton and filler, κ is permeability. Further, $\rho = \rho_s(1-\phi) + \phi\rho_f$ is a bulk density, $\rho_s,\ \rho_a,\ \rho_f$ are solid, apparent mass density and filler density respectively, K_s, K_f are elastic bulk moduli of the skeleton and filler respectively. Apparent mass density $\rho_a = C\phi\rho_f$ was introduced by Biot to describe dynamic interaction between fluid and skeleton. C is a factor depending on the pores geometry and excitation frequency.

Formulation of boundary integral equations method and its direct approach can be found in [5, 23, 24]:

$$\begin{bmatrix} \hat{u}_j \\ \hat{p} \end{bmatrix} = \int\limits_{\Gamma} \begin{bmatrix} \hat{U}_{ij}^s & -\hat{P}_j^s \\ \hat{U}_i^f & -\hat{P}^f \end{bmatrix} \begin{bmatrix} \hat{t}_i \\ \hat{q} \end{bmatrix} d\Gamma - \int\limits_{\Gamma} \begin{bmatrix} \hat{T}_{ij}^s & -\hat{Q}_j^s \\ \hat{T}_i^f & -\hat{Q}^f \end{bmatrix} \begin{bmatrix} u_i \\ \hat{p} \end{bmatrix} d\Gamma,$$

where $\begin{bmatrix} \hat{U}_{ij}^s & -\hat{P}_j^s \\ \hat{U}_i^f & -\hat{P}^f \end{bmatrix}$, $\begin{bmatrix} \hat{T}_{ij}^s & -\hat{Q}_j^s \\ \hat{T}_i^f & -\hat{Q}^f \end{bmatrix}$—matrices of fundamental and singular solutions.

Displacement vector at internal points is linked with boundary displacements and tractions as follows:

$$u_l(x,\mathrm{s}) = \int\limits_{\Gamma_k} U_{lj}^s(x,y,s)\,t_j(y,s)\,d_yS - \int\limits_{\Gamma_k} T_{lj}^s(x,y,s)\,u_j(y,s)\,d_yS,\ l = 1,2,3, \quad x \in \Omega,$$

where U_{lj} and T_{lj}—components of fundamental and singular solution tensors.

Poroviscoelastic solution is obtained from poroelastic solution by means of the elastic-viscoelastic correspondence principle, applied to skeleton's moduli K and G. Forms of $\bar{K}(s)$. $\bar{G}(s)$ for different viscoelastic models in Laplace domain are following:

Kelvin-Voigt model: $\bar{K}(s) = K\left[1 + \frac{s}{\gamma}\right]$, $\bar{G}(s) = G\left[1 + \frac{s}{\gamma}\right]$.

Standard linear solid model: $\bar{K}(s) = K \cdot \left[(\omega^2 - 1)\dfrac{is}{is+\gamma} + 1\right]$, $\bar{G}(s) = G \cdot \left[(\omega^2 - 1)\frac{is}{is+\gamma} + 1\right]$.

Model with weakly singular kernel: $\bar{K} = \frac{K}{1+hs^{\alpha-1}}$, $\bar{G} = \frac{G}{1+hs^{\alpha-1}}$

Where γ,ω, h and α are model parameters [23–25].

28.3 Boundary Element Approach

Boundary-value problem (28.1) can be reduced to the boundary integral equation (BIE) system as follows [5, 24, 26]:

$$\alpha_\Omega \bar{u}_k(x,s) + \int_\Gamma \left(\tilde{T}_{ik}(x,y,s)\bar{u}_i(y,s) - \tilde{T}^0_{ik}(x,y,s)\bar{u}_i(x,s) - \tilde{U}_{ik}(x,y,s)\bar{t}_i(y,s)\right)d\Gamma = 0,$$

$$(x \in \Gamma), \quad \bar{t} = (\bar{t}_1, \bar{t}_2, \bar{t}_3, \bar{q})^T, \quad \bar{u} = (\bar{u}_1, \bar{u}_2, \bar{u}_3, \bar{p})^T,$$

where $\tilde{U}(x,s)$, $\tilde{T}(x,s)$—fundamental and singular solutions, $\tilde{T}^0(x,s)$ contains the isolated singularities.

Boundary surface of our homogeneous solid is discretized by quadrangular and triangular elements, which are assumed as singular quadrangular elements. We use reference elements: square $\xi = (\xi_1, \xi_2) \in [-1,\ 1]^2$ and triangle $0 \le \xi_1 + \xi_2 \le 1$, $\xi_1 \ge 0$, $\xi_2 \ge 0$, and each boundary element is mapped to a reference one by the following formula:

$$y_i(\xi) = \sum_{l=1}^{8} N^l(\xi) y_i^{\beta(k,l)}, \quad i = 1,2,3,$$

where l—local node number in element k, $\beta(k,l)$—global node number, $N^l(\xi)$—shape functions. Goldshteyn's displacement-stress mixed model [27] is performed. To discretize the boundary surface eight-node biquadratic quadrilateral elements are used, generalized displacements and tractions—are approximated by linear and constant shape functions, respectively.

Subsequent applying of collocation method leads to the system of linear equations. As the collocation nodes we take the approximation nodes of boundary functions. For each homogeneous domain of the solid linear equations written in generalized displacements approximation nodes are as follows:

$$\frac{1-\alpha_\Omega}{2} u_i^m + \sum_{k=1}^{N}\sum_{l=1}^{4} A_{ij}^{m,k,l} u_j^{\chi(k,l)} = \sum_{k=1}^{N_1} B_{ij}^{m,k} t_j^k - \sum_{k=1}^{N_2}\sum_{l=1}^{4} D_{ij}^{m,k,l}\left(u_j^{\chi(k,l)} - u_j^{\overline{\chi}(\overline{k},l)}\right),$$

$$N = N_1 + N_2.$$

Linear equations written in generalized tractions approximation nodes take following form:

$$\frac{1-\alpha_\Omega}{8} u_i^m + \sum_{k=1}^{N}\sum_{l=1}^{4} A_{ij}^{m,k,l} u_j^{\chi(k,l)} = \sum_{k=1}^{N_1} B_{ij}^{m,k} t_j^k - \sum_{k=1}^{N_2}\sum_{l=1}^{4} D_{ij}^{m,k,l}\left(u_j^{\chi(k,l)} - u_j^{\overline{\chi}(\overline{k},l)}\right),$$

$$N = N_1 + N_2$$

To boundary elements with no contact corresponds the first term in both equations, to satisfy the contact conditions between elements k and $\overline{k}$—second one.

Formulae to accounted coefficients A, B and D are:

$$A_{ij}^{m,k,l} = \int_{-1}^{1}\int_{-1}^{1}\left[R^l(\xi)T_{ij}(x^m, y^k(\xi), s) - \delta_{\chi(k,l),m,}T_{ij}^0(x^m, y^k(\xi))\right]J^k(\xi)d\xi_1 d\xi_2,$$

$$B_{ij}^{m,k} = \int_{-1}^{1}\int_{-1}^{1} U_{ij}(x^m, y^k(\xi), s)J_k(\xi)d\xi_1 d\xi_2,$$

$$D_{ij}^{m,k,l} = \int_{-1}^{1}\int_{-1}^{1} R^l(\xi)U_{ij}(x^m, y^k(\xi), s)J_k(\xi)\alpha_j^{\chi\bar{\chi}}(y^k(\xi))d\xi_1 d\xi_2,$$

where s is the parameter of Laplace transform. Gaussian quadrature are used to calculate integrals on regular elements. But if an element contains a singularity, algorithm of singularity avoiding or order reducing is applied [26]. When singularity is excluded we use an adaptive integration algorithm. An appropriate order of Gaussian quadrature is chosen from primarily known necessary precision, if it is impossible, the element is subdivided to smaller elements recursively.

28.4 Laplace Transform Inversion

CQM is generally a method to calculate a convolution integral:

$$y(t) = f(t) * g(t) = \int_0^t f(t-\tau)g(\tau)d\tau$$

from one of the convoluted functions ($f(t)$) known in Laplace domain and some discrete values of another one ($g(t)$) [5, 15, 16]. The idea consists in rewriting the convolution integral in the following form with the help of the inverse Laplace transform formula:

$$\int_0^t f(t-\tau)g(\tau)d\tau = \frac{1}{2\pi i}\lim_{R\to\infty}\int_{c-iR}^{c+iR}\bar{f}(s)\underbrace{\int_0^t e^{s(t-\tau)}g(\tau)d\tau}_{x(t,s)}ds, \tag{28.2}$$

where $\bar{f}(s)$ denotes the function in Laplace domain.

Calculating $x(t,s)$ numerically is the only approximation to be used in scope of CQM. $x(t,s)$ is obviously the solution of the following Cauchy problem:

$$\frac{d}{dt}x(t,s) = sx(t,s) + g(t), x(0,s) = 0.$$

A scheme to solve this problem defines the particular case of CQM. Employing a linear multistep method to solve for $x(t,s)$, evaluating the outer integral in (28.2) with the help of residue theory and expanding $\bar{f}(\gamma(z)/\Delta t)$ in power series by z, we get the convolution integral in the following form [5]:

$$y(n\Delta t) = \sum_{k=0}^{n} \omega_{n-k}(\Delta t) g(k\Delta t), \quad n = 0, 1, \ldots N. \tag{28.3}$$

Coefficients $\omega_n(\Delta t)$ can be computed by means of integral Cauchy formula:

$$\omega_n(\Delta t) = \frac{1}{2\pi i} \int\limits_{|z|=R} \bar{f}\left(\frac{\gamma(z)}{\Delta t}\right) z^{-n-1} dz = \frac{R^{-n}}{2\pi} \int\limits_{0}^{2\pi} \bar{f}\left(\frac{\gamma(Re^{i\varphi})}{\Delta t}\right) e^{-in\varphi} d\varphi. \tag{28.4}$$

In (28.4) function $\bar{f}(\gamma(z)/\Delta t)$ is analytical in domain with radius R, and $\gamma(z)$ is characteristic function. Methods based on Backward differentiation formula (BDF) only of the order ≤ 6 are applicable in this formulae, because they are zero-stable. For BDF of 2nd order (traditional method, or 2nd order Euler) we have $\gamma(z) = 3/2 - 2z + z^2/2$ [5].

Time-step method for numerical inversion of Laplace transform is similar to CQM, but the difference is that CQM is based on the convolution theorem, but Time-step method based on the time-domain integration theorem. We apply time-domain integration theorem to derivative of $f(t)$ in order to obtain the original function from $\bar{f}(s)$, with respect to $f(0) = 0$:

$$f(t) = \int\limits_{0}^{t} f'(\tau) d\tau.$$

In this case (28.3), (28.4) will be rewritten as:

$$f(0) = 0, \quad f(n\Delta t) = \sum_{k=1}^{n} \omega_k(\Delta t), \quad n = 1, \ldots N,$$

$$\omega_n(\Delta t) = \frac{R^{-n}}{L} \sum_{l=0}^{L-1} \bar{f}(s) e^{-in\varphi}, \quad s = \frac{\gamma(z)}{\Delta t}, \quad z = \mathrm{R}e^{i\varphi}, \quad \varphi = 2\pi\frac{l}{L}.$$

Various modifications can be applied to the method in different ways of $\omega_n(\Delta t)$ calculation. For varied step by φ and linear approximation of the integrand function we obtain

$$\omega_n(\Delta t) = \frac{R^{-n}}{2\pi}\sum_{k=0}^{L-1}\left[\bar{f}(s_k)s_k e^{-in\varphi_k} + \bar{f}(s_{k+1})s_{k+1}e^{-in\varphi_{k+1}}\right]\frac{(\varphi_{k+1}-\varphi_k)}{2},$$
$$s_k = \frac{\gamma(Re^{i\varphi_k})}{\Delta t}$$

or, basing on the highly oscillatory quadrature [24]:

$$\omega_n(\Delta t) = \frac{R^{-n}}{2\pi}\sum_{k=0}^{L-1}\frac{\varphi_{k+1}-\varphi_k}{2}e^{-in\frac{\varphi_k+\varphi_{k+1}}{2}}\left[D_1(w)\bar{f}(s_k)s_k + D_2(w)\bar{f}(s_{k+1})s_{k+1}\right],$$
$$s_k = \frac{\gamma(Re^{i\varphi_k})}{\Delta t}w = -n\frac{\varphi_{k+1}-\varphi_k}{2}, \quad D_{1,2}(w) = \begin{cases} \frac{\sin w}{w} \pm \frac{w\cos w - \sin w}{w^2}i & \text{where} \quad |w| > w_*, \\ e^{\mp wi} & \text{where} \quad |w| \le w_*, \end{cases}$$

here w_* is specific key value.

Substituting basic linear multistep method for Runge-Kutta method taking into account Butcher tableau $\frac{c|A^T}{b^T}$, $A \in R^{m\times m}$, $b, c \in R^m$, we obtain the following representation [21, 22]:

$$f(0) = 0, \quad f(n\Delta t) = b^T A^{-1}\sum_{k=1}^{n}\omega_k(\Delta t), \quad n = 1, \ldots N.$$

Formulae for coefficients $\omega_n(\Delta t)$ can still be used here taking into account that now they contain matrices instead of scalars. Characteristic function $\gamma(z)$ takes the following form [21, 22]:

$$\gamma(z) = A^{-1} - zA^{-1}[1]b^T A^{-1}, [1] = (1, \ldots, 1)^T.$$

Radau (Radau IIA) scheme [21] is chosen to further represent Runge-Kutta family. Some advantages of a time-step method are shown in [28].

28.5 Numerical Results

28.5.1 Slab Bonded on a Halfspace

The numerical modelling of a problem of a Heaviside-type impact load acting on a slab situated above a fluid saturated foundation is considered. Fluid saturated slab and foundation are modeled as a poroelastic or poroviscoelastic media. Problem of a vertical Heaviside-type load $P(t) = P_0 H(t)$, $P_0 = 1000\,\mathrm{N/m^2}$ on a slab bonded on a halfspace is considered (Fig. 28.1).

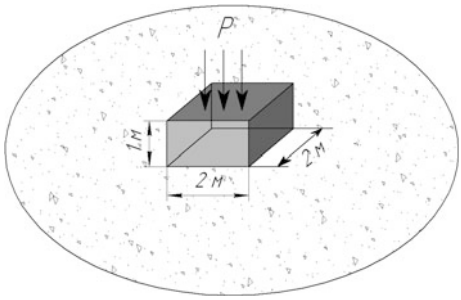

Fig. 28.1 Slab bonded on a halfspace

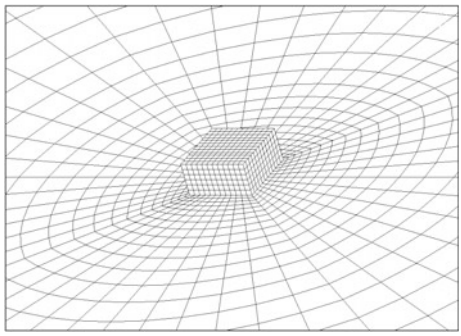

Fig. 28.2 Boundary element mesh

Poroelastic material parameters are: $K = 8 \cdot 10^9\,\mathrm{N/m^2}$, $G = 6 \cdot 10^9\,\mathrm{N/m^2}$, $\rho = 2458\,\mathrm{kg/m^3}$, $\phi = 0.66$, $K_s = 3.6 \cdot 10^{10}\,\mathrm{N/m^2}$, $\rho_f = 1000\,\mathrm{kg/m^3}$, $K_f = 3.3 \cdot 10^9\,\mathrm{N/m^2}$, $k = 1.9 \cdot 10^{-10}\,\mathrm{m^4/(N \cdot s)}$, that corresponds to Berea sandstone [5]. The reference point $P(10;0;0)$ is situated on a surface of a halfspace. To obtain numerical solution for displacements at reference point a boundary element mesh was employed (Fig. 28.2).

The convergence was studied in a case of poroelastic slab and halfspace (Figs. 28.3 and 28.4). Were considered BE meshes with different sampling degree: (a) slab—64 el., halfspace—132 el.; (b) slab—256 el., halfspace—548 el.; (c) slab—576 el., halfspace—1252 el.; (d) slab—1024 el., halfspace—2308 el.

For a further calculations BE mesh «c» (Fig. 28.2) was chosen. Vertical displacements at reference point in case of poroelastic slab on a poroviscoelastic halfspace are presented on Figs. 28.5 and 28.6. Vertical displacements at reference point in case of model with weakly singular kernel are presented on Figs. 28.7 and 28.8.

Poroelastic and poroviscoelastic solutions obtained by means of different viscoelastic models are given on Figs. 28.5, 28.6, 28.7 and 28.8. The comparison of dynamic responses with different values of viscoelastic parameter for each model is presented. An effect of inner displacements wave field restructuring is demonstrated in the case of standard linear solid model, when properties of poroviscoelastic material were changing from instantaneous to equilibrium (Fig. 28.6).

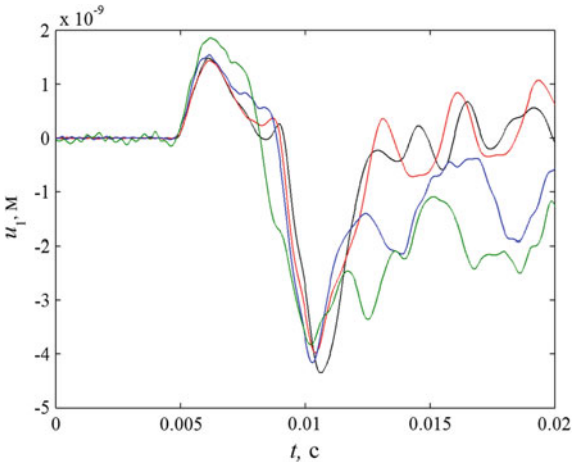

Fig. 28.3 Displacements u_1. *Green solid line* solution on mesh «**a**»; *blue solid line* solution on mesh «**b**»; *red solid line* solution on mesh «**c**»; *black solid line* solution on mesh «**d**»

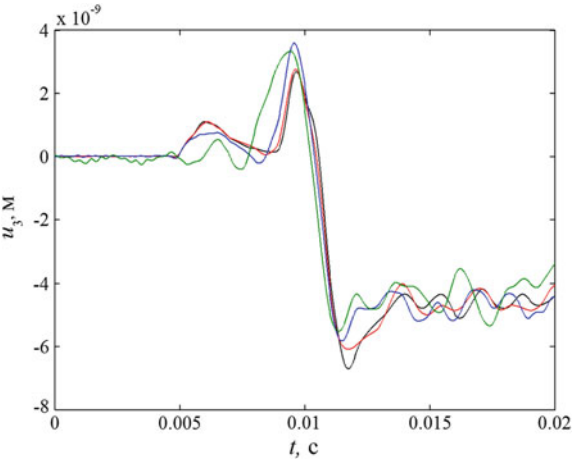

Fig. 28.4 Displacements u_3. *Green solid line* solution on mesh «**a**»; *blue solid line* solution on mesh «**b**»; *red solid line* solution on mesh «**c**»; *black solid line* solution on mesh «**d**»

28.5.2 Cube with a Spherical Cavity

A poroviscoelastic cube, with side lengths $L = 2$ m, and containing a spherical cavity of radius $R = 0.5$ m is considered (see Fig. 28.9). The cube is clamped at the face $x_3 = -1$ m and cavity is subjected to a normal internal pressure:

$$P(t) = \begin{cases} 0, & \text{for } t \le 0\,\text{s}, \\ P_0 t/0.0005, & \text{for } 0 \le t \le 0.0005\ \text{s}, \\ P_0, & \text{for } t > 0.0005\ \text{s}, \end{cases} \quad P_0 = 10^5\ \text{Pa}.$$

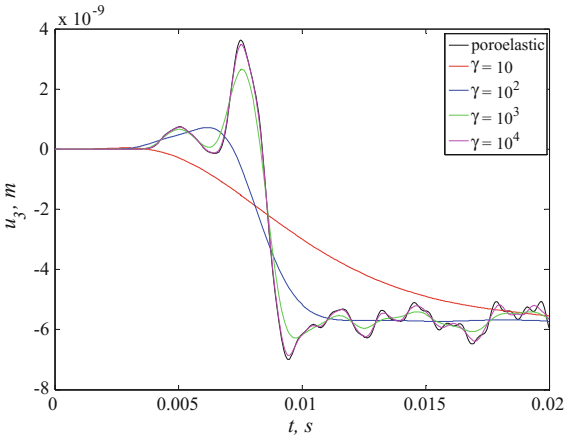

Fig. 28.5 Case of Kelvin-Voigt model

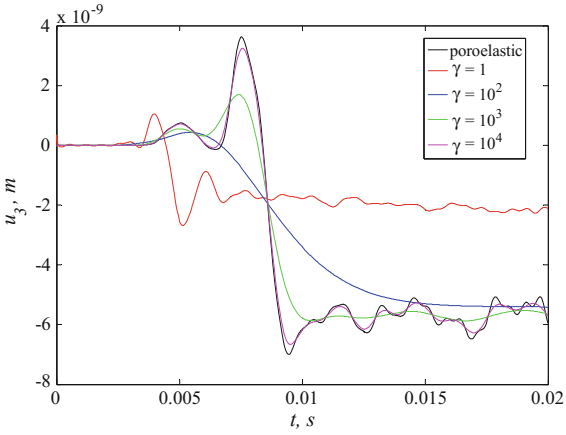

Fig. 28.6 Case of standard linear solid model

Poroelastic material parameters are: $K = 8 \cdot 10^9\,\mathrm{N/m^2}$, $G = 6 \cdot 10^9\,\mathrm{N/m^2}$, $\rho = 2458\,\mathrm{kg/m^3}$, $\phi = 0.66$, $K_s = 3.6 \cdot 10^{10}\,\mathrm{N/m^2}$, $\rho_f = 1000\,\mathrm{kg/m^3}$, $K_f = 3.3 \cdot 10^9\,\mathrm{N/m^2}$, $k = 1.9 \cdot 10^{-10}\,\mathrm{m^4/(N \cdot s)}$ (Berea sandstone).

The BEM mesh employed consists of 432 boundary elements and 436 nodes. Figures 28.10, 28.11, 28.12 and 28.13 shows the transient response of the displacements $u_3(t)$ and pore pressure p at the nodal point with the coordinates (0, 0, 1) m. For poroviscoelastic analysis, parameters of standard model: $\omega = 2$, $\gamma = 1000$, 100, 1 and 0.1; parameters of weakly singular model: $\alpha = 0.1$, 0.5 and 0.9, h = 1, 2 and 4.

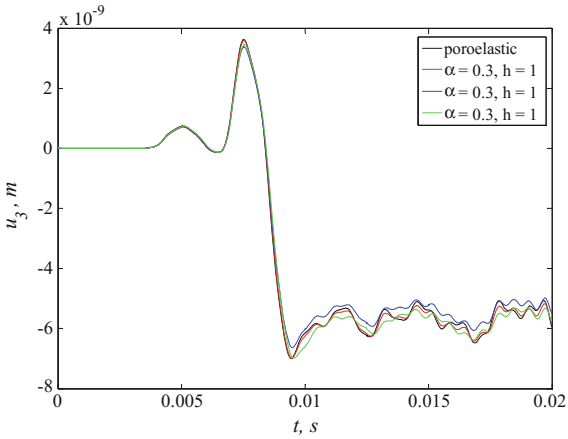

Fig. 28.7 Poroviscoelastic slab

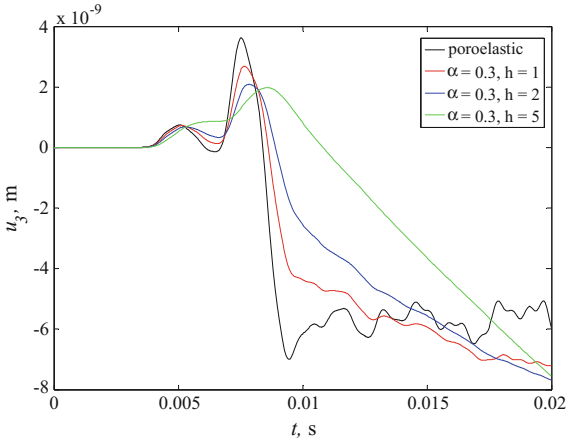

Fig. 28.8 Poroviscoelastic halfspace

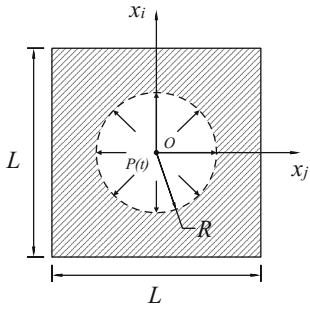

Fig. 28.9 A cube containing a spherical cavity

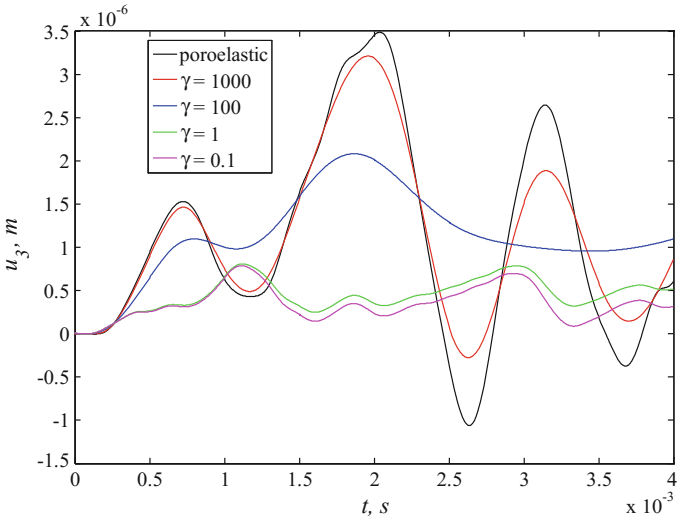

Fig. 28.10 Displacements u_3 in case of standard linear solid model

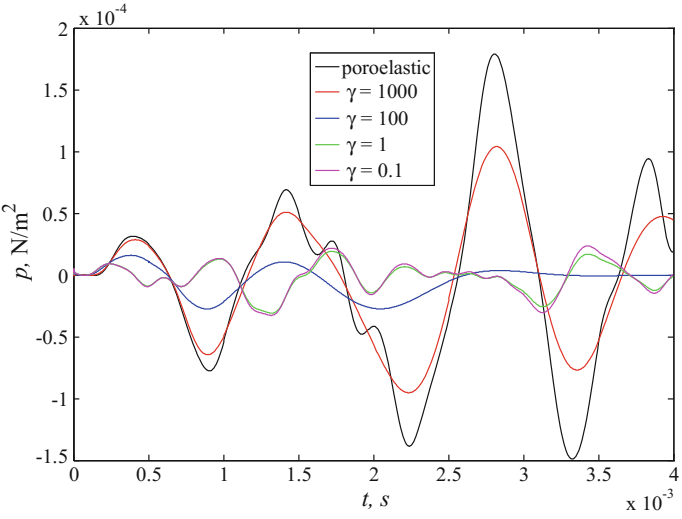

Fig. 28.11 Pore pressure p in case of standard linear solid model

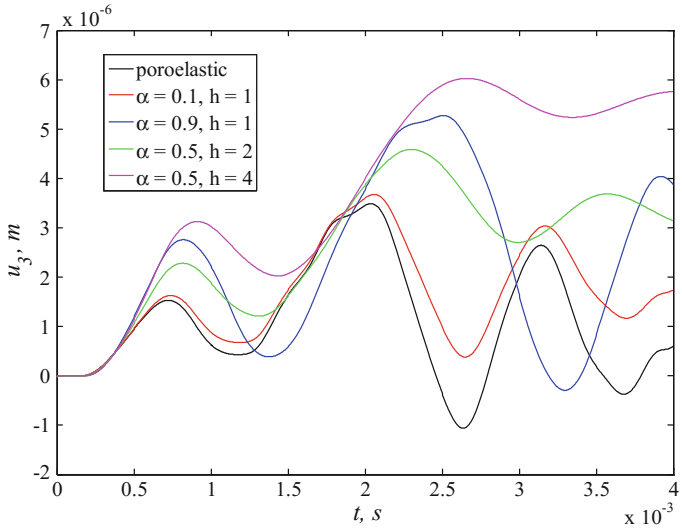

Fig. 28.12 Displacements u_3 in case of model with weakly singular kernel

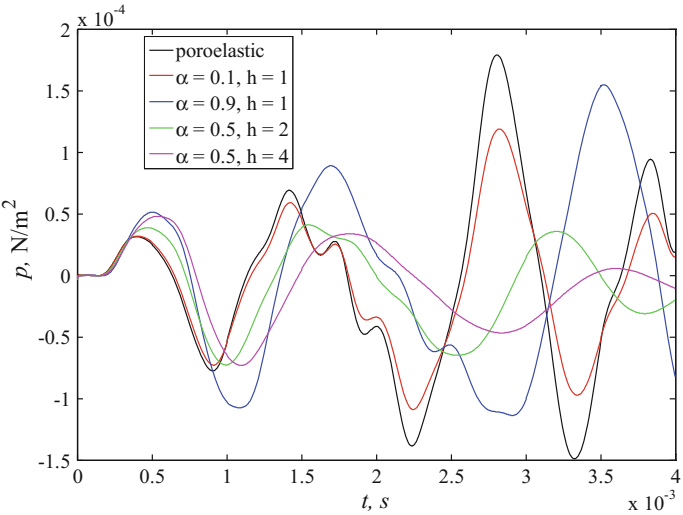

Fig. 28.13 Pore pressure p in case of model with weakly singular kernel

28.6 Conclusions

Isotropic poroviscoelastic solids and halfspace are considered. Results of numerical experiments are employed. A Laplace domain BEM approach for the transient analysis of the three-dimensional linear poroviscoelastic solids based on the correspondence principle has been presented. The poroviscoelastic media modelling is based on Biot's theory of fully saturated poroelastic material in combination with the elastic-viscoelastic corresponding principle. Kelvin-Voigt, standard linear solid and weakly singular models are considered as viscoelastic constitutive models.

Boundary integral equations method and boundary element method are applied in order to solve three dimensional boundary-value problems. Regularized BIE system is considered. We used mixed boundary elements to perform the spatial discretization. Gaussian quadrature and hierarchic integrating algorithm are used for integration over the boundary elements. Numerical inversion of Laplace transform is done by means of time-step method based on Runge-Kutte nodes.

A problem of Heaviside-type vertical load acting on a slab bonded on a poroviscoelastic halfspace and a problem of poroviscoelastic cube with cavity subjected to a normal internal pressure are solved. The comparison of dynamic responses when poroviscoelastic halfspace is described by different viscoelastic models is presented. An influence of viscoelastic parameter on Rayleigh wave response is demonstrated. Obtained results for the transient response of the displacements show the effect of the transition from instantaneous to equilibrium viscoelastic moduli within the framework of the standard linear solid model, such effect was earlier demonstrated in [24, 29]. An influence of material viscosity on transient responses of displacements and pore pressure is presented.

Acknowledgements The work was financially supported by Russian Scientific Foundation (grant 16-19-10237) at the part of obtaining numerical solutions in poroelastic formulation and con vergence study, and at the part of obtaining numerical results in poroviscoelastic formulation by RFBR (grants Nos. 16-31-00450, 15-08-02817, 15-08-02814, 16-38-50143).

References

1. J. Frenkel, J. Phys. **8**, 230 (1944)
2. M.A. Biot, J. Acoust. Soc. Am. **12**, 155 (1941)
3. M.A. Biot, J. Acoust. Soc. Am. **2**, 182 (1955)
4. M.A. Biot, J. Acoust. Soc. Am. **27**(5), 459 (1956)
5. M. Schanz, *Wave Propagation in Viscoelastic and Poroelastic Continua* (Springer, Berlin, 2001)
6. R. de Boer, Appl. Mech. Rev. **49**(4), 201 (1996)
7. V.N. Nikolaevskiy, J. Eng. Mech. **131**(9), 888 (2005)
8. D. Nardini, C.A. Brebbia, in *Boundary Element Methods in Engineering,* ed. by C.A. Brebbia (Springer, Berlin, 1982)
9. W.J. Mansur, *A Time-Stepping Technique to Solve Wave Propagation Problems Using the Boundary Element Method.* Ph.D. thesis. University of Southampton (1983)

10. T.A. Cruze, F.J. Rizzo, J. Math. Anal. Appl. **22**(1), 244 (1968)
11. V.A. Babeshko, Proc. USSR Acad. Sci. **284**, 73 (1985)
12. M. Schanz, A.H.D. Cheng, Acta Mech. **145**, 1 (2000)
13. M. Schanz, A.H.D. Cheng, J. Appl. Mech., **68**, 192 (2001)
14. J. Chen, G.F. Dargush, Int. J. Solids Struct. **32**(15), 2257 (1995)
15. C. Lubich, Numer. Math. **52**, 129 (1988)
16. C. Lubich, Numer. Math. **52**, 413 (1988)
17. M. Schanz, H. Antes, in *Porous Media: Theory, Experiments and Numerical Applications*, ed. by W. Ehlers, J. Bluhm (Springer, Berlin, 2002), p. 383
18. C. Lubich, A. Ostermann, Math. Comput. **60**, 105 (1993)
19. M.P. Calvo, E. Cuesta, C. Palencia, Numer. Math. **107**, 589 (2007)
20. L. Banjai, M. Messner, M. Schanz, Comput. Methods Appl. Mech. Eng. **245–246**, 90 (2012)
21. L. Banjai, M. Schanz, in *Fast Boundary Element Methods in Engineering and Industrial Applications*, ed. by U. Langer (Springer, Berlin, 2012), p. 145
22. L. Banjai, C. Lubich, J.M. Melenk, Numer. Math. **119**, 1 (2011)
23. A.G. Ugodchikov, N.M. Hutoryanskii, *Boundary element method in deformable solid mechanics [Metod granichnykh elementov v mekhanike deformiruemogo tverdogo tela]* (Kazan State University, Kazan, 1986)
24. V.G. Bazhenov, L.A. Igumnov, *Boundary Integral Equations & Boundary Element Methods in treating the problems of 3D elastodynamics with coupled fields* [*Metody granichnyh integralnyh uravneniy i granichnyh elementov v reshenii zadach tryohmernoy dinamicheskoy teorii uprugosti s sopryazhyonnymi polyami*] PhysMathLit, Moscow (2008)
25. R. Cristensen, in *Introduction to the theory of viscoelasticity* (Mir, Moscow, 1974)
26. A.V. Amenitsky, A.A. Belov, L.A. Igumnov, I.S. Karelin, *Problems of Strength and Plasticity*, **71**, 164 (2009) (in Russian). http://www.unn.ru/e-library/ppp.html?anum_eng=113
27. R.V. Goldshteyn, *Boundary Integral Equations Method: Numerical Aspects & Application in Mechanics* (*Mechanics: New in Foreign Science*) [*Metod granichnyh integralnyh uravneniy: Vychislitelniye aspekty i prilozheniya v mehanike (Mehanika: novoye v zarubezhnoy nauke)*]: collected works (Mir, Moscow, 1978), p. 183 (in Russian)
28. L.A. Igumnov, A.N. Petrov, A.A. Ipatov, Probl. Strength Plast. **75**(4), 273 (2013)
29. L.A. Igumnov, A.A. Ipatov, T.A. Sabaeva, Probl. Strength Plast. **76**(2), 106 (2014)

Chapter 29
Finite Element Homogenization of Periodic Block Masonry by the Effective Moduli Method

Anna A. Nasedkina and Amirtham Rajagopal

Abstract The study is devoted to the determination of the effective material properties of masonry based on its internal structure. Masonry is considered as a periodic composite consisting of bricks and mortar. According to the classical method of determining effective moduli for composites, in order to describe internal microstructure we consider a representative volume cell, which enables us to determine effective properties of an equivalent anisotropic material. The problem for the representative volume cell is simulated and analyzed using finite element method.

29.1 Introduction

Masonry structure consists of bricks and mortar arranged in a periodic manner. Due to different mechanical properties of its constituents, masonry structure can be considered as a two-phase composite, which is essentially heterogeneous. Global behaviour of such composite structure can be determined from the behaviour of its phases with the help of homogenization theory. With this approach masonry structure can be treated as an effectively elastic homogeneous medium.

A comprehensive but computationally expensive approach is to model each brick and mortar joint in the structure, taking into account their linear and nonlinear constitutive behaviours. This approach would be impractical for a large masonry structure.

A.A. Nasedkina (✉)
I.I. Vorovich Institute of Mathematics, Mechanics and Computer Science, Southern Federal University,
8a, Milchakova Street, Rostov-on-Don 344090, Russia
e-mail: nasedkina@math.sfedu.ru

A. Rajagopal
Indian Institute of Technology
Hyderabad, Kandi, Hyderabad 502285, Telangana, India
e-mail: rajagopal@iith.ac.in

I.A. Parinov et al. (eds.), *Advanced Materials*, Springer Proceedings in Physics 193, DOI 10.1007/978-3-319-56062-5_29

The simulation methodology for the composite masonry structure is considered in the following steps. At microlevel the models of representative volumes are considered that take into account exact structure of masonry and mechanical properties of its constituents. Mathematical models of representative volumes are then transformed into finite element models. The effective properties of the composite are then determined by a homogenization method. Subsequently, after finding the average macroscopic stresses and strains at macrolevel the compound structure can be considered as an elastic material with effective properties.

As masonry structure represents a periodic composite, homogenization procedures for masonry can be done not only numerically, but also analytically and semi-analytically. Analytical homogenization methods described in the literature suggest two-step and one-step homogenization scheme. In two-step homogenization methods, head joints and bed joints of the mortar are introduced step-wise. Examples of such methods are a multilayer system of Pande et al. [1] with alternating mortar joints or a two-step technique of Pietruszczak and Niu [2], where the first step consisted in consideration of homogenized matrix with head joints as elliptical inclusions and the second step considered a laminate structure with continuous bed joints. The reported drawbacks of the two-step homogenization lie in the fact that the results depend on the step order, and geometric configuration such as bond patterns is not fully taken into account, as well as the thickness of masonry is often neglected.

Later one-step approaches free from these disadvantages have been introduced. Most of these approaches are semi-analytical by nature, as they include application of the finite element method. For example, Anthoine [3] suggested a one-step homogenization technique with periodic boundary conditions and numerical solution by finite element method. Another one-step homogenization by using asymptotic method in combination with finite element method was proposed by Cecchi and Rizzi [4]. Fully analytical homogenization was done by Bati et al. [5], who used elliptical cylinders as approximations for rectangular bricks, where brick units were considered as inclusions. Wang et al. [6] used one-step periodic eigenstrain homogenization method, where the effective material properties of the masonry were determined based on a strain energy approach, the periodicity of field quantities was imposed by Fourier series, and the Eshelby tensor for the unit cell was derived to relate the disturbance field with the eigenstrain field. Klusemann and Svendsen [7] made a comparative study on the homogenization methods for multi-phase elastic composites based on Eshelby theory and Mori Tanaka theory. Sacco [8] presented a nonlinear homogenization procedure for periodic masonry with linear constitutive relationship for the bricks and nonlinear constitutive law for mortar joints. Another nonlinear homogenization technique for masonry structures was suggested by Quinteros et al. [9]. Recent nonlinear methodology for the analysis of masonry structures based on an equilibrated macro-element was proposed by Addessi et al. [10].

Numerical calculation of effective properties of masonry by finite element method using stress-prescribed or strain-prescribed analysis for a representative volume element of masonry structure was done by Kumar et al. [11] and Rivieccio [12].

In this paper, we apply the effective moduli method for composites to calculate effective properties of masonry structure. The effective moduli method has been widely used in mechanics of composites [13]. According to this method, in order to describe internal microstructure, a representative volume element is considered. Several boundary value problems with special boundary conditions for a representative volume are solved by the finite element method. The post processing of the solution gives averaged characteristics of the stress-strain state that allow computing the full set of the effective moduli of the composite.

We demonstrate the proposed method for an example of a representative unit cell of periodic masonry structure. The homogenization variants are studied for a periodicity cell and for an enlarged block consisting of several cells, which constitute periodic larger cells. For the set of boundary conditions, the boundary conditions of the first kind (for displacements) are considered. This known form of boundary conditions permits to obtain constant fields of stresses and strains for homogeneous media. The results of the finite element computation of elastic stiffness matrix for masonry structure by the effective moduli method are compared to the results obtained in [12] using strain-prescribed analysis.

29.2 Effective Moduli Method for Linear Elastic Material

Let us consider heterogeneous elastic material in a representative volume Ω of a composite body. Then in the frames of static linear theory of elasticity we have the following system of equations:

$$\nabla \cdot \boldsymbol{\sigma} = \mathbf{0}, \tag{29.1}$$

$$\boldsymbol{\sigma} = \mathbf{c} \cdot \cdot \boldsymbol{\varepsilon}, \tag{29.2}$$

$$\boldsymbol{\varepsilon} = \frac{1}{2}(\nabla \mathbf{u} + \nabla \mathbf{u}^T) \tag{29.3}$$

where $\boldsymbol{\sigma}$ is the second rank stress tensor, $\mathbf{c}$ is the fourth rank tensor of elastic stiffness, $\boldsymbol{\varepsilon}$ is the second rank strain tensor, $\mathbf{u} = \mathbf{u}(\mathbf{x})$ is the displacement vector, $\mathbf{x} = (x_1, x_2, x_3) \in \Omega$, and the symbol $\cdot\cdot$ in (29.2) stands for a tensor contraction.

In vector-matrix notation, system (29.1)–(29.3) can be presented in the form:

$$\mathbf{L}^T(\nabla) \cdot \mathbf{T} = 0, \mathbf{T} = \mathbf{C} \cdot \mathbf{S}, \mathbf{S} = \mathbf{L}(\nabla) \cdot \mathbf{u}, \tag{29.4}$$

where $\mathbf{L}^T(\nabla) = \begin{bmatrix} \partial_1 & 0 & 0 & 0 & \partial_3 & \partial_2 \\ 0 & \partial_2 & 0 & \partial_3 & 0 & \partial_1 \\ 0 & 0 & \partial_3 & \partial_2 & \partial_1 & 0 \end{bmatrix}, \nabla = \begin{bmatrix} \partial_1 \\ \partial_2 \\ \partial_3 \end{bmatrix}, \mathbf{T} = [\sigma_{11} \quad \sigma_{22} \quad \sigma_{33} \quad \sigma_{23} \quad \sigma_{13} \quad \sigma_{12}]$ is the pseudo-vector of stresses σ_{ij}, $\mathbf{C}$ is the 6×6 matrix of elastic stiffness, $\mathbf{S} = [\varepsilon_{11}, \varepsilon_{22}, \varepsilon_{33}, 2\varepsilon_{23}, 2\varepsilon_{13}, 2\varepsilon_{12}]$ is the pseudo-vector of strains ε_{ij}. Here the correspondence law $(ij) \leftrightarrow \alpha$ is used between the indices $ij, i, j = 1, 2, 3$, and one-dimensional array $\alpha = 1, 2, 3, 4, 5, 6$: $(11) \leftrightarrow (1)$; $(22) \leftrightarrow (2)$; $(33) \leftrightarrow (3)$; $(23), (32) \leftrightarrow (4)$; $(13), (31) \leftrightarrow (5)$; $(12), (21) \leftrightarrow (6)$.

We note that the elastic stiffness matrix for heterogeneous elastic medium depends on the coordinates $\mathbf{C} = \mathbf{C}(\mathbf{X})$ and its components can vary throughout the representative volume. Having set the appropriate boundary conditions at $\Gamma = \partial\Omega$, we can find the solutions of the problem (29.1)–(29.3) or (29.4) for heterogeneous medium in the representative volume Ω. Then the comparison of the solution characteristics averaged over Ω (such as stresses, etc.) with analogous values for homogeneous medium (the comparison medium) will permit to determine the effective elastic stiffnesses. It should be noted that for anisotropic media in order to determine the full set of the effective moduli it is necessary to solve several problems of the considered types for different boundary conditions, and the number of such problems depends on crystallographic system of the comparison medium.

Let us adopt that for a linear elastic homogeneous comparison medium the same (29.1)–(29.3) are satisfied with constant moduli of elastic stiffness $\mathbf{c}^{\text{eff}}$, which are to be determined.

Let us assume that on the boundary $\Gamma = \partial\Omega$ the following boundary condition takes place:

$$\mathbf{u} = \mathbf{x} \cdot \boldsymbol{\varepsilon}_0, \mathbf{x} \in \Gamma, \tag{29.5}$$

where $\boldsymbol{\varepsilon}_0$ is a value that does not depend on $\mathbf{x}$. Then $\mathbf{u} = \mathbf{x} \cdot \boldsymbol{\varepsilon}_0$, $\boldsymbol{\varepsilon} = \boldsymbol{\varepsilon}_0$, $\boldsymbol{\sigma} = \boldsymbol{\sigma}_0 = \mathbf{c}^{eff} \cdot \cdot \boldsymbol{\varepsilon}_0$ will give the solution for the problem (29.1)–(29.3), (29.5) in the representative volume Ω for the homogeneous comparison medium.

Let us now solve the same problem (29.1)–(29.3), (29.5) for heterogeneous medium and assume that for this medium and for the comparison medium the averaged stresses are equal $\langle\boldsymbol{\sigma}\rangle = \langle\boldsymbol{\sigma}_0\rangle$, where the angle brackets denote the value, which was averaged by the volume:

$$\langle \ldots \rangle = (1/\Omega) \int_{\Omega} (\ldots) d\Omega \tag{29.6}$$

Hence we obtain that for the effective elastic stiffness of the composite the equation $\langle\boldsymbol{\sigma}\rangle = \mathbf{c}^{\text{eff}} \cdot \cdot \boldsymbol{\varepsilon}_0$ is satisfied, where $\boldsymbol{\varepsilon}_0$ is the known value from the boundary condition (29.5). Consequently, even in the assumption of an anisotropy of general form for the comparison medium, we can calculate all the stiffness moduli c^{eff}_{ijlm}. Indeed, setting in (29.5) $\boldsymbol{\varepsilon}_0 = \varepsilon_0(\mathbf{e}_l\mathbf{e}_m + \mathbf{e}_m\mathbf{e}_l)/2$, $\varepsilon_0 = \text{const}$, for fixed indices l and

m ($\mathbf{e}_l$, $\mathbf{e}_m$ are the unit vectors of the Cartesian coordinate system), we get the computation formulae for the elastic moduli c_{ijlm}^{eff}: $c_{ijlm}^{\text{eff}} = \langle \sigma_{ij} \rangle / \varepsilon_0$. An important justification for the choice of the boundary condition $\mathbf{u} = \mathbf{x} \cdot \boldsymbol{\varepsilon}_0$ for $\mathbf{x} \in \Gamma$ consists in the fact that with this boundary condition the following equalities for stresses and strains of heterogeneous medium and comparison medium take place $\langle \boldsymbol{\varepsilon} \rangle = \langle \boldsymbol{\varepsilon}_0 \rangle$, $\langle \boldsymbol{\sigma} \cdot \cdot \boldsymbol{\varepsilon} \rangle = \langle \boldsymbol{\sigma}_0 \cdot \cdot \boldsymbol{\varepsilon}_0 \rangle$. Therefore such boundary condition insures that heterogeneous medium and homogeneous comparison medium have equal mechanical potential energies.

In order to solve the problem (29.1)–(29.3), (29.5) for heterogeneous composite material by the finite element method, we formulate the weak statement of this problem and use a well-known technique of finite element approximations. Let Ω_h be a region occupied by the corresponding finite element mesh $\Omega_h \subseteq \Omega$, $\Omega_h = \cup_k \Omega^{ek}$, where Ω^{ek} is a separate finite element with number k.In case of static problems, we can find an approximation to the weak solution on the $\mathbf{u}_h \approx \mathbf{u}$finite element mesh Ω_h in the following form:

$$\mathbf{u}_h = \mathbf{N}_u^T(\mathbf{x}) \cdot \mathbf{U}, \tag{29.7}$$

where $\mathbf{N}_u^T$ is the matrix of the basis functions for displacements, $\mathbf{U}$ is the vector of the nodal displacements.

According to the conventional finite element technique, we approximate the weak formulation of problem by the problem in a finite dimensional space related to the basis functions $\mathbf{N}_u^T$. Substituting (29.6) and similar representations for the projection functions into the weak problem statement for Ω_h, we obtain the system of finite element equations with respect to the nodal displacements $\mathbf{U}$:

$$\mathbf{K} \cdot \mathbf{U} = \mathbf{F}, \tag{29.8}$$

where $\mathbf{K} = \sum_k^a \mathbf{K}^{ek}$ is the global finite element matrix obtained from the corresponding element matrices as a result of the assembling process ($\sum^a$), $\mathbf{F} = \sum_k^a \mathbf{F}^{ek}$ is the global vector of external influences obtained from the element vectors $\mathbf{F}^{ek}$, which are defined by external influences and the main boundary conditions.

The element matrices $\mathbf{K}^{ek}$ are given by the formulae $\mathbf{K}^{ek} = \int_{\Omega^{ek}} (\mathbf{L}(\nabla) \cdot (\mathbf{N}^{ek})^T)^T \cdot \mathbf{c} \cdot \mathbf{L}(\nabla) \cdot (\mathbf{N}^{ek})^T d\Omega$, where $\mathbf{N}^{ek}$ is the matrix of approximate basis functions, defined for each finite element.

29.3 Numerical Model for a Representative Unit Cell of Masonry Structure

According to the technique of micromechanical homogenization, we consider the model a representative volume, which takes into account important characteristicsof the composite structure. Ideally, a representative volume should be a region large

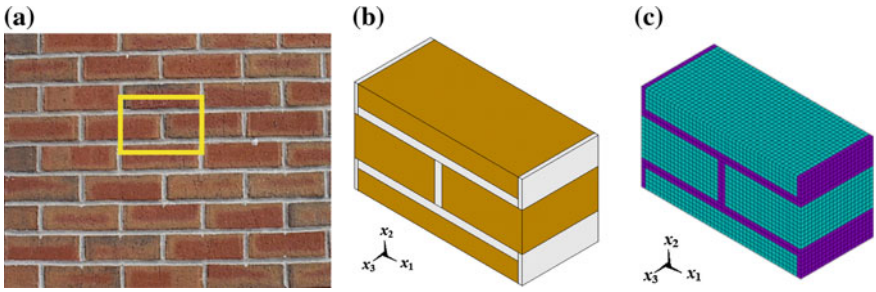

Fig. 29.1 Masonry wall (**a**), basic unit cell (**b**) and its finite element model (**c**)

enough compared to the sizes of the inhomogeneities but small enough compared to the distances where the slow variables significantly change.

For a periodic masonry structure as a representative volume we consider a classical unit cell of masonry wall one brick thick (Fig. 29.1a) that represents the unit of periodicity in horizontal and vertical directions [6, 12]. The basic unit cell illustrated in (Fig. 29.1b) contains one complete brick unit, four one-quarter-sized brick units, and mortar joints between the bricks. Such choice of a representative volume enables us to describe the microstructure of masonry in exact way. Each break has dimensions of 210 mm (length) $\times$ 50 mm (height) $\times$ 100 mm (thickness). Thickness of mortar is assumed equal to 10 mm.

Numerical analysis is carried out with the help of ANSYS finite element software [14]. We mesh the solid model of the representative unit cell with 3-D 8-node cubic elements Solid45 with the element size of 5 mm. The corresponding finite element model of the representative unit cell is shown in (Fig. 29.1c). The resulting finite element mesh consists of 21,120 elements.

The considered representative unit cell represents a composite structure consisting of two phases: brick and mortar. For calculation of effective properties of the composite, we assume that each phase is isotropic. The Young's modulus of the brick is 2×10^{11} Pa, and Young's modulus of the mortar is 2×10^{10} Pa. The Poisson's ratio for both materials is equal to 0.15.

In general, for a composite structure an anisotropic mechanical behavior is considered, hence the effective elastic stiffness matrix $\mathbf{C}^{\text{eff}}$ for a masonry structure has size of 6×6, and therefore comprises 36 components.

The components of the effective elastic stiffness matrix are obtained from the solutions of six problems with six different boundary conditions, which are derived from (29.5). Each row of the effective stiffness matrix is obtained by applying one boundary condition at a time. The components of the averaged stress pseudo-vector are defined by (29.6). Below the six boundary-value problems are given, which enable us to determine six rows of the effective elastic stiffness matrix:

Problem 29.1

$$\begin{aligned}
&\varepsilon_{011} \neq 0 \Rightarrow u_1 = x_1\varepsilon_{011}, u_2 = u_3 = 0, \mathbf{x} \in \Gamma;\\
&C_{11}^{\text{eff}} = \langle\sigma_{11}\rangle/\varepsilon_{011};\ C_{12}^{\text{eff}} = \langle\sigma_{22}\rangle/\varepsilon_{011};\ C_{13}^{\text{eff}} = \langle\sigma_{33}\rangle/\varepsilon_{011},\\
&C_{14}^{\text{eff}} = \langle\sigma_{23}\rangle/\varepsilon_{011};\ C_{15}^{\text{eff}} = \langle\sigma_{13}\rangle/\varepsilon_{011};\ C_{16}^{\text{eff}} = \langle\sigma_{12}\rangle/\varepsilon_{011}
\end{aligned} \tag{29.9}$$

Problem 29.2

$$\begin{aligned}
&\varepsilon_{022} \neq 0 \Rightarrow u_2 = x_2\varepsilon_{022}, u_1 = u_3 = 0, \mathbf{x} \in \Gamma;\\
&C_{21}^{\text{eff}} = \langle\sigma_{11}\rangle/\varepsilon_{022};\ C_{22}^{\text{eff}} = \langle\sigma_{22}\rangle/\varepsilon_{022};C_{23}^{\text{eff}} = \langle\sigma_{33}\rangle/\varepsilon_{022},\\
&C_{24}^{\text{eff}} = \langle\sigma_{23}\rangle/\varepsilon_{022}, C_{25}^{\text{eff}} = \langle\sigma_{13}\rangle/\varepsilon_{022};\ C_{26}^{\text{eff}} = \langle\sigma_{12}\rangle/\varepsilon_{022}
\end{aligned} \tag{29.10}$$

Problem 29.3

$$\begin{aligned}
&\varepsilon_{033} \neq 0 \Rightarrow u_3 = x_3\varepsilon_{033}, u_1 = u_2 = 0, \mathbf{x} \in \Gamma;\\
&C_{31}^{\text{eff}} = \langle\sigma_{11}\rangle/\varepsilon_{033};\ C_{32}^{\text{eff}} = \langle\sigma_{22}\rangle/\varepsilon_{033};\ C_{33}^{\text{eff}} = \langle\sigma_{33}\rangle/\varepsilon_{033},\\
&C_{34}^{\text{eff}} = \langle\sigma_{23}\rangle/\varepsilon_{033};\ C_{35}^{\text{eff}} = \langle\sigma_{13}\rangle/\varepsilon_{033};\ C_{36}^{\text{eff}} = \langle\sigma_{12}\rangle/\varepsilon_{033}
\end{aligned} \tag{29.11}$$

Problem 29.4

$$\begin{aligned}
&\varepsilon_{023} = \varepsilon_{032} \neq 0 \Rightarrow u_1 = 0, u_2 = \frac{1}{2}x_3\varepsilon_{023}, u_3 = \frac{1}{2}x_2\varepsilon_{023}, \mathbf{x} \in \Gamma;\\
&C_{41}^{\text{eff}} = \langle\sigma_{11}\rangle/(2\varepsilon_{023});\ C_{42}^{\text{eff}} = \langle\sigma_{22}\rangle/(2\varepsilon_{023});\ C_{43}^{\text{eff}} = \langle\sigma_{33}\rangle/(2\varepsilon_{023}),\\
&C_{44}^{\text{eff}} = \langle\sigma_{23}\rangle/(2\varepsilon_{023});\ C_{45}^{\text{eff}} = \langle\sigma_{13}\rangle/(2\varepsilon_{023});\ C_{46}^{\text{eff}} = \langle\sigma_{12}\rangle/(2\varepsilon_{023})
\end{aligned} \tag{29.12}$$

Problem 29.5

$$\begin{aligned}
&\varepsilon_{013} = \varepsilon_{031} \neq 0 \Rightarrow u_1 = \frac{1}{2}x_3\varepsilon_{013}, u_2 = 0, u_3 = \frac{1}{2}x_1\varepsilon_{013}, \mathbf{x} \in \Gamma;\\
&C_{51}^{\text{eff}} = \langle\sigma_{11}\rangle/(2\varepsilon_{013});\ C_{52}^{\text{eff}} = \langle\sigma_{22}\rangle/(2\varepsilon_{013});\ C_{53}^{\text{eff}} = \langle\sigma_{33}\rangle/(2\varepsilon_{013}),\\
&C_{54}^{\text{eff}} = \langle\sigma_{23}\rangle/(2\varepsilon_{013});\ C_{55}^{\text{eff}} = \langle\sigma_{13}\rangle/(2\varepsilon_{013});\ C_{56}^{\text{eff}} = \langle\sigma_{12}\rangle/(2\varepsilon_{013})
\end{aligned} \tag{29.13}$$

Problem 29.6

$$\begin{aligned}
&\varepsilon_{012} = \varepsilon_{021} \neq 0 \Rightarrow u_1 = \frac{1}{2}x_2\varepsilon_{012}, u_2 = \frac{1}{2}x_1\varepsilon_{012}, u_3 = 0, \mathbf{x} \in \Gamma;\\
&C_{61}^{\text{eff}} = \langle\sigma_{11}\rangle/(2\varepsilon_{012});\ C_{62}^{\text{eff}} = \langle\sigma_{22}\rangle/(2\varepsilon_{012});\ C_{63}^{\text{eff}} = \langle\sigma_{33}\rangle/(2\varepsilon_{012}),\\
&C_{64}^{\text{eff}} = \langle\sigma_{23}\rangle/(2\varepsilon_{012});\ C_{65}^{\text{eff}} = \langle\sigma_{13}\rangle/(2\varepsilon_{012});\ C_{66}^{\text{eff}} = \langle\sigma_{12}\rangle/(2\varepsilon_{012})
\end{aligned} \tag{29.14}$$

29.4 Results and Comparison with Other Homogenization Methods

The solutions of the problems (29.9)–(29.14) permit to determine the average macroscopic stresses and strains in the basic unit cell. The resulting effective stiffness matrix obtained after solving problems (29.9)–(29.14) for $\varepsilon_{0ij} = \varepsilon_0 = 1$, $i,\ j = 1, 2, 3$ is given by

$$\mathbf{C}^{\text{eff}} = 10^{12} \cdot \begin{pmatrix} 0.1499 & 0.0154 & 0.0248 & 0 & 0 & 0 \\ 0.0154 & 0.0957 & 0.0167 & 0 & 0 & 0 \\ 0.0248 & 0.0167 & 0.1694 & 0 & 0 & 0 \\ 0 & 0 & 0 & 0.0470 & 0 & 0 \\ 0 & 0 & 0 & 0 & 0.0659 & 0 \\ 0 & 0 & 0 & 0 & 0 & 0.0428 \end{pmatrix}, \tag{29.15}$$

where zero components of $\mathbf{C}^{\text{eff}}$ are negligibly small numbers. From (29.15) it can be seen that the stiffness matrix of masonry is symmetric and that masonry structure exhibits orthotropic behavior, since only nine components are independent and different from zero.

Application of the effective moduli method to a larger periodic cell of masonry wall containing four basic unit cells (Fig. 29.2) has produced similar values of the components of the effective stiffness matrix:

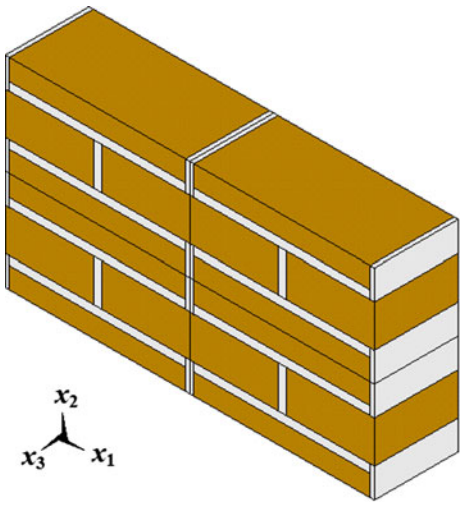

Fig. 29.2 Model of a larger periodic cell of a masonry wall

$$\mathbf{C}_l^{\text{eff}} = 10^{12} \cdot \begin{pmatrix} 0.1474 & 0.0152 & 0.0244 & 0 & 0 & 0 \\ 0.0152 & 0.0939 & 0.0164 & 0 & 0 & 0 \\ 0.0244 & 0.0164 & 0.1693 & 0 & 0 & 0 \\ 0 & 0 & 0 & 0.0461 & 0 & 0 \\ 0 & 0 & 0 & 0 & 0.0653 & 0 \\ 0 & 0 & 0 & 0 & 0 & 0.0414 \end{pmatrix} \quad (29.16)$$

Therefore, one basic unit cell can be considered as a representative volume for masonry wall.

As it can be seen from (29.15), (29.16), the effective elastic stiffnesses of the composite have significantly different values in the directions x_1, x_2 and x_3, This anisotropy of the properties is due only to a geometric structure of the composite, as both phases of masonry are taken isotropic. Figures 29.3, 29.4, 29.5, 29.6, 29.7 and 29.8 demonstrate the distribution of stresses $T_\alpha = \sigma_{ij}$ in the basic unit cell in the problems with numbers $\alpha = 1, 2, 3, 4, 5, 6$, respectively, i.e. the distribution of stresses which averaged values give diagonal components of the effective stiffness matrix.

As the Young's moduli for the brick and mortar differ by one order of magnitude, the brick material will be stiffer in the directions where there is less mortar material. Hence, the overall stiffness of the structure has the largest value in the direction of the masonry wall thickness, i.e. in the x_3-axis. In this case, under the tension along x_3 (Fig. 29.5) in the major part of the composite the directions of tension along the thickness go only along the brick material, which is stiffer. In the case of the tension along the length, i.e. in the x_1-axis (Fig. 29.3), the directions of tension cross both materials of brick and mortar. However, the zones filled by the

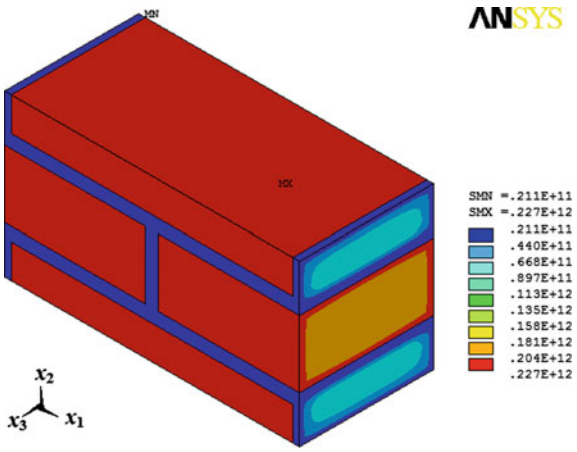

Fig. 29.3 Distribution of axial stresses σ_{11} in Problem 29.1

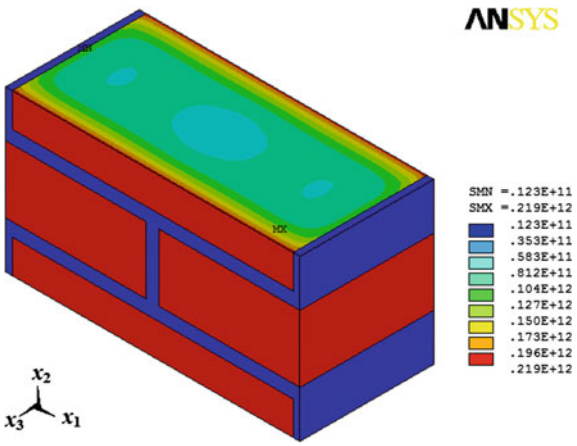

Fig. 29.4 Distribution of axial stresses σ_{22} in Problem 29.2

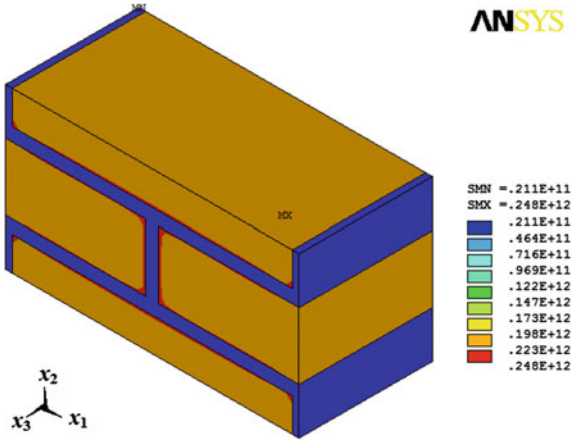

Fig. 29.5 Distribution of axial stresses σ_{33} in Problem 29.3

mortar go along a whole basic unit cell, therefore the whole structure remains almost as stiff as in the case of the tension along x_3-axis. The masonry composite is softer along the direction of the height of the masonry wall, i.e. in the x_2-axis (Fig. 29.4), because here under the tension along x_2-axis, the whole layer of soft mortar is undergoing uniform tension.

The moduli c_{ij} at $i \neq j,\ i,j = 1,2,3$ are considerably smaller than the axial tension-compression moduli, because for the considered basic unit cell both brick and mortar Poisson's ratios are small.

The shear moduli are also smaller than the axial moduli, because the shear strains in all cases entirely influence the soft layers of mortar. The average shear stresses $T_5 = \sigma_{13}$ in the Problem 29.5 (Fig. 29.7) are greater than the shear stresses $T_4 = \sigma_{23}$ from the Problem 29.4 (Fig. 29.6) and $T_6 = \sigma_{12}$ from the Problem 29.6 (Fig. 29.8), as in the Problem 29.5 they act mostly on the brick material.

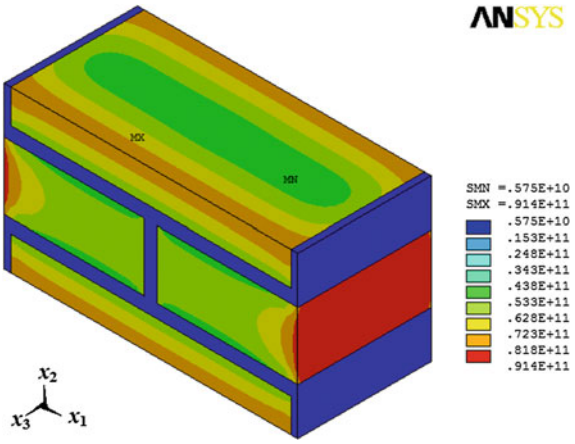

Fig. 29.6 Distribution of shear stresses σ_{23} in Problem 29.4

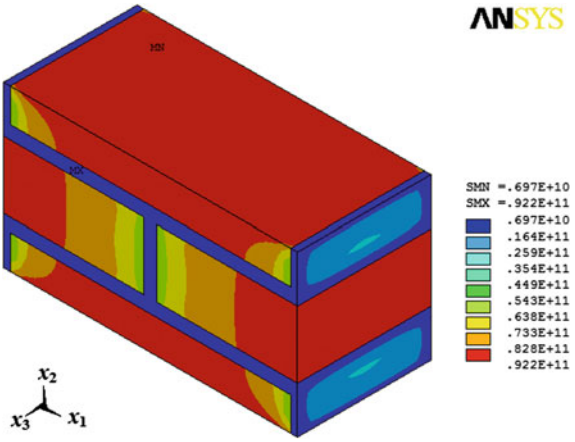

Fig. 29.7 Distribution of shear stresses σ_{13} in Problem 29.5

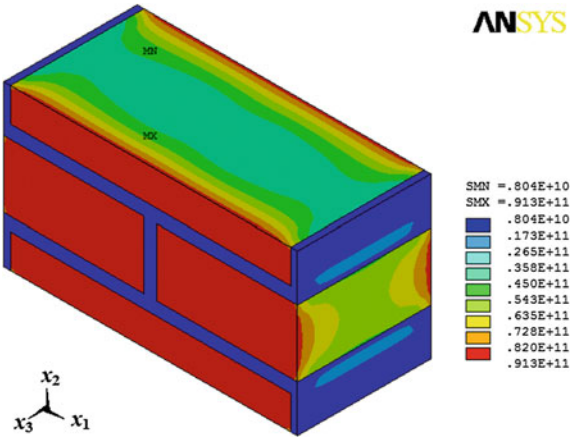

Fig. 29.8 Distribution of shear stresses σ_{12} in Problem 29.6

To verify the effective moduli method, we consider strain-prescribed analysis used in [11, 12] to obtain the effective stiffness matrix for the same input data of material properties and dimensions of the basic unit cell.

In the strain-prescribed analysis, the stiffness matrix is computed by means of the finite element method from the solutions of six problems with six different loading conditions, which are three cases of normal strains in x_1, x_2 and x_3 directions and three cases of shear strains in x_2x_3, x_1x_3 and x_1x_2, planes. In an assumption of a generally anisotropic mechanical behavior, the stress-strain relationship is written in the following form:

$$\begin{pmatrix} \langle\sigma_1\rangle \\ \langle\sigma_2\rangle \\ \langle\sigma_3\rangle \\ \langle\sigma_4\rangle \\ \langle\sigma_5\rangle \\ \langle\sigma_6\rangle \end{pmatrix} = \begin{pmatrix} \langle C_{11}\rangle & \langle C_{12}\rangle & \langle C_{13}\rangle & \langle C_{14}\rangle & \langle C_{15}\rangle & \langle C_{16}\rangle \\ \langle C_{21}\rangle & \langle C_{22}\rangle & \langle C_{23}\rangle & \langle C_{24}\rangle & \langle C_{25}\rangle & \langle C_{26}\rangle \\ \langle C_{31}\rangle & \langle C_{32}\rangle & \langle C_{33}\rangle & \langle C_{34}\rangle & \langle C_{35}\rangle & \langle C_{36}\rangle \\ \langle C_{41}\rangle & \langle C_{42}\rangle & \langle C_{43}\rangle & \langle C_{44}\rangle & \langle C_{45}\rangle & \langle C_{46}\rangle \\ \langle C_{51}\rangle & \langle C_{52}\rangle & \langle C_{53}\rangle & \langle C_{54}\rangle & \langle C_{55}\rangle & \langle C_{56}\rangle \\ \langle C_{61}\rangle & \langle C_{62}\rangle & \langle C_{63}\rangle & \langle C_{64}\rangle & \langle C_{65}\rangle & \langle C_{66}\rangle \end{pmatrix} \cdot \begin{pmatrix} \langle\varepsilon_1\rangle \\ \langle\varepsilon_2\rangle \\ \langle\varepsilon_3\rangle \\ \langle\varepsilon_4\rangle \\ \langle\varepsilon_5\rangle \\ \langle\varepsilon_6\rangle \end{pmatrix}, \tag{29.17}$$

where $\sigma_1 = \sigma_{11}$, $\sigma_2 = \sigma_{22}$, $\sigma_3 = \sigma_{33}$, $\sigma_4 = \sigma_{23}$, $\sigma_5 = \sigma_{13}$, $\sigma_6 = \sigma_{12}$; $\varepsilon_1 = \varepsilon_{11}$, $\varepsilon_2 = \varepsilon_{22}$, $\varepsilon_3 = \varepsilon_{33}$, $\varepsilon_4 = \varepsilon_{23}$, $\varepsilon_5 = \varepsilon_{13}$, $\varepsilon_6 = \varepsilon_{12}$; the angle brackets denote average values of the corresponding quantities within the considered representative unit cell by (6). Only a single column of the stiffness matrix is obtained by applying one loading condition out of the six, according to the relation:

$$\langle C_{kl}\rangle = \frac{\langle\sigma_k\rangle}{\langle\varepsilon_l\rangle}, \tag{29.18}$$

where $k, l = 1, 2, 3, 4, 5, 6$.

Application of the strain-prescribed analysis gives the following components of the homogenized stiffness matrix [12]:

$$\mathbf{C}^{\text{hom}} = 10^{12} \cdot \begin{pmatrix} 0.141 & 0.014 & 0.021 & 0 & 0 & 0 \\ 0.011 & 0.083 & 0.011 & 0 & 0 & 0 \\ 0.022 & 0.013 & 0.173 & 0 & 0 & 0 \\ 0 & 0 & 0 & 0.072 & 0 & 0 \\ 0 & 0 & 0 & 0 & 0.142 & 0 \\ 0 & 0 & 0 & 0 & 0 & 0.071 \end{pmatrix} \tag{29.19}$$

Comparison of (29.19) with (29.15), (29.16) shows that the effective moduli method and the strain-prescribed analysis give close values of the first 3×3 components of the resulting stiffness matrix for masonry structure. The difference in shear components is greater due to different boundary conditions used in these two methods.

29.5 Conclusion

The effective moduli method has been considered for a homogenization procedure of a masonry structure. Masonry was represented by a two-phase composite material consisting of brick and mortar phases. A basic unit cell of masonry wall was considered as a representative volume to describe internal microstructure of masonry composite. A boundary-value problem for a heterogeneous linear elastic material was formulated and finite element approximation was provided. According to the effective moduli method, a comparison of the solution characteristics averaged over representative volume with analogous values for homogeneous comparison medium enabled to determine the effective properties for masonry structure. Six problems with special boundary conditions of the first kind were solved to obtain six rows of the effective stiffness matrix. It was shown that such form of boundary conditions ensured constant fields of stresses and strains for homogeneous media.

In a model for a basic unit cell of masonry wall an exact geometry of masonry was taken into account. For validation, a numerical analysis was also carried out for an enlarged block consisting of several basic unit cells. The results of the finite element computation of elastic stiffness matrix for masonry structure by the effective moduli method were compared to the results obtained in [12] using strain-prescribed analysis. The comparison of the results showed good correspondence between two homogenization methods for non-shear components of the stiffness matrix.

Acknowledgements The first author would like to acknowledge the support from Southern Federal University.

References

1. G.N. Pande, J.X. Liang, J. Middleton, Comput. Geotech. **8**, 243 (1989)
2. S. Pietruszczak, X. Niu, Int. J. Solids Struct. **29**(5), 531 (1992)
3. A. Anthoine, Int. J. Solids Struct. **32**(20), 137 (1995)
4. A. Cecchi, N.L. Rizzi, Int. J. Solids Struct. **38**, 29 (2001)
5. S.B. Bati, G. Ranocchiai, L. Rovero, J. Eng. Mech. **125**(8), 922 (1999)
6. G. Wang, S. Li, H.-N. Nguyen, N. Sitar, J. Mater. Civ. Eng. **19**(3), 269 (2007)
7. B. Klusemann, B. Svendsen, Techn. Mech. **30**(4), 374 (2010)
8. E. Sacco, Eur. J. Mech. A/Solids **28**, 209 (2009)
9. R.D. Quinteros, S. Oller, L.G. Nallim, Compos. Struct. **94**, 724 (2012)
10. D. Addessi, A. Mastrandrea, E. Sacco, Eng. Struct. **70**, 82 (2014)
11. P.G. Rivieccio, *Homogenization Strategies and Computational Analyses for Masonry Structures via Micro-mechanical Approach*, Ph.D. Thesis, Ingegneria delle Costruzioni, 2006
12. N. Kumar, H. Lambadi, M. Pandey, A. Rajagopal, Int. J. Comp. Methods Eng. Sci. Mech. **17** (1), 7 (2016)
13. R.M. Christensen, *Mechanics of Composite Materials* (Krieger Publishing Company, 1991), 348 p
14. *ANSYS Mechanical APDL Theory Reference*. ANSYS Rel. 14.5 (Canonsburg: ANSYS Inc., 2012)

Chapter 30
Stress Assessment for a Pipeline Segment with Volumetric Surface Defects Repaired Using Composite Materials

M.I. Chebakov, G. Zecheru, A. Dumitrescu and R.D. Nedin

Abstract In the present study, we have considered several issues for a damaged pipeline with one or two volumetric surface defects, subjected to internal pressure loading. The problem of an optimal repair system for a pipe using a composite material wrap is considered. The analysis of the most efficient repair wrap properties was performed; some practical recommendations are provided.

30.1 Introduction

The maintenance of safety and reliability of transmission pipelines is vital in the petroleum industry. Such pipelines often suffer from various defects especially weld defects, cracks, defects due to corrosion and erosion. The common repair methods presently used are based on the employment of the techniques involving welding.

In conditions of the necessity of applying the pipe repair techniques without suspending its operation (in order to avoid significant financial losses), special measures need to be taken when welding directly on an in-service pipeline. One of the possible ways to avoid them is to develop alternative in-service repair techniques that do not require welding, like the use of composite materials repair systems. Therefore, the mechanical engineering problems of proper modeling and development of such repair systems for transmission pipelines are of great importance [1–3].

In the present research, we have considered two problems for a damaged segment of a pipeline subjected to inner pressure. The first one assumed that on the pipe surface there were two volumetric surface defects due to corrosion/erosion

M.I. Chebakov · R.D. Nedin (✉)
Vorovich Institute of Mathematics, Mechanics and Computer Science, Southern Federal University, 8a, Milchakova Street, Rostov-on-Don 344090, Russia
e-mail: rdn90@bk.ru

G. Zecheru · A. Dumitrescu (✉)
Petroleum-Gas University of Ploieşti, 39, Bulevardul Bucureşti, 100680 Ploieşti, Romania
e-mail: andrei.upg@gmail.com

I.A. Parinov et al. (eds.), *Advanced Materials*, Springer Proceedings in Physics 193, DOI 10.1007/978-3-319-56062-5_30

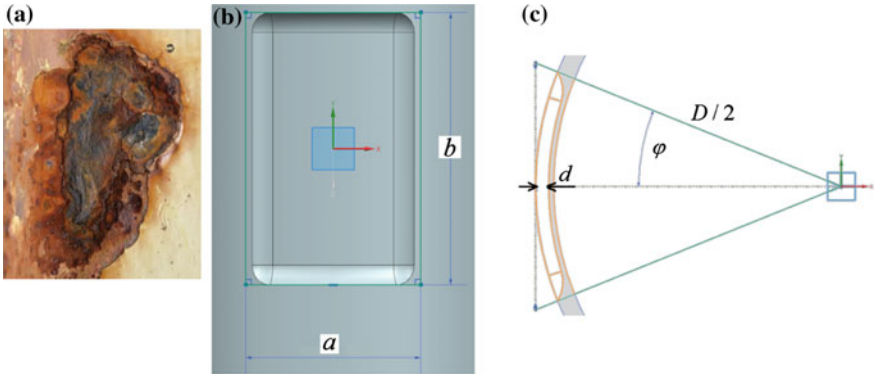

Fig. 30.1 **a** A defect on a pipe surface due to corrosion. **b** The machined pocket in the defect area. **c** Cross-sectional view of the pocket. Here a is the longitudinal size of the defect, D is the pipe outside diameter, φ is the half opening defect angle, d is the defect depth

which have been technologically processed by machining a "pocket" in order to reduce the stress concentration effects in each defect zone (see Fig. 30.1). As a result of further machining, the edges of the pocket were blended with a certain radius of curvature. The second problem considered was a static problem for the same pipe with two processed defects when the pipe was additionally strengthened by applying a layered composite material wrap (consisting of several composite layers bonded by an adhesive). The machined defects under the wrap were preliminarily filled by a special polymer (filler). In this case we have analyzed the influence of the chosen composite material and the filler on the pipe stress distribution in order to obtain the most efficient and optimal wrap properties that could provide in-service repair of the damaged pipeline. In this way, the proposed approach leads to cost reduction of repairs of damaged transmission pipelines.

To carry out the finite element (FE) analysis of the considered pipeline segments, we used the package Siemens NX. For the described pipe with defects, we built a general FE-model depending parametrically on the initial data and on all the problem parameters including geometry and materials of the pipe, wrap and fillers, operating pressure, dimensions and locations of the defects. As testing specimens, we examined pipe segments made of API X52 steel with various geometry and defects parameters. In every considered case, we assessed the inhomogeneous stress distribution in the defects area and revealed the most dangerous zones from the viewpoint of the analysis of stress concentrators. A comparative analysis of the solutions obtained in the two packages showed their good agreement. The conducted series of computational experiments also allowed us to select the most hazardous geometrical parameters and relative locations of the defects. At the same time we revealed a range of allowable defect parameters for which it is not necessary to replace the pipe segment during repairs.

30.2 Finite Element Model

Both stated problems require a series of computational experiments. One of the best ways to optimize the numerical solutions of a large number of similar problems is to use the automation of calculations. To carry out the finite element (FE) analysis of the considered pipeline segments, we used the package Siemens NX. For the described pipe with defects, we built a general FE-model with the help of which it was possible to achieve the automatic execution of the main stages of the finite element simulation like editing model geometry and materials properties, creating/refreshing a finite element mesh, and (re)calculating the solution. We have also developed the efficient algorithm of automatic generation of the optimal FE mesh based on the initial geometrical data (see Figs. 30.2 and 30.3).

To solve the problems stated, we have performed linear elastic analysis; the nonlinear analysis was not needed here because in such a pipe only stresses lower than the yield stress are allowed.

The pipe itself and the fillers were meshed by 3D 10-node FE based on the general 3D elasticity theory, while the wrap was meshed by 2D 4-node FE based on the classical laminate theory in order to obtain the most adequate solution. In

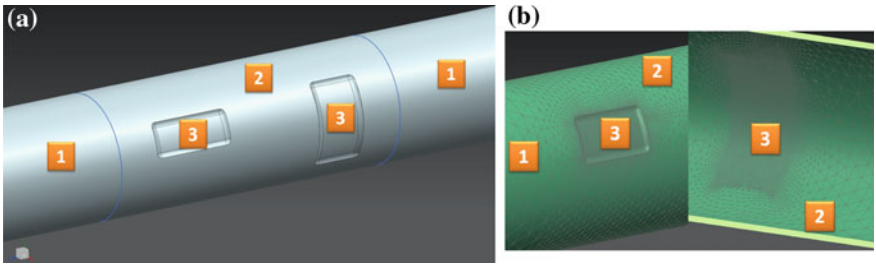

Fig. 30.2 **a** Sectioning of the pipe body for further FE meshing. **b** FE meshes refinement at the pipe exterior and inner surfaces by large (*1*), middle (*2*) and small FE (*3*) depending on the zone

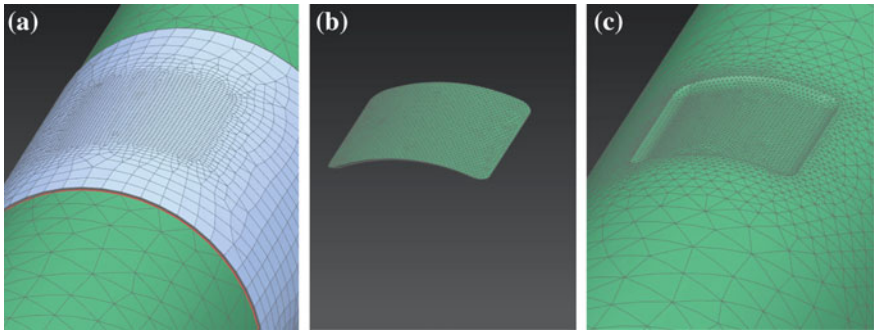

Fig. 30.3 FE meshing of the composite wrap (**a**), fillers (**b**) and the steel pipe (**c**)

Fig. 30.3 an example of FE-meshing of each part of the whole FE model is depicted. In order to get an adequate solution, we have provided proper compliance of the meshes of different parts of the model.

In the framework of the general FE model built, one may set any geometrical and physical properties of each layer of the laminate composite. In the present paper, we give the results for the layer-like laminate with identical composite layers bonded by identical adhesive layers (see Fig. 30.13).

30.3 Computational Experiments

As testing specimens, we have examined pipe segments made of API X52 steel with the following parameters: Young modulus E = 2.1 × 10^5 MPa, density $\rho = 7800$ kg/m^3, Poisson coefficient $v = 0.3$, yield stress $\sigma_y = 360$ MPa. We have tested the specimens with various geometry and defects parameters. The results are shown below for the standard pipe with exterior diameter $D = 323.9$ mm and wall thickness $t = 8$ mm. The operating inner pressure was 7 MPa. As a composite material for the wrap layers, fiberglass was chosen with the fibers in the circumferential direction (see Table 30.1).

The other constants assumed for the orthotropic composite material are $v_1 = v_2 = v_3 = 0.3$, $E_2 = E_3 = 2$ GPa, $G_{12} = G_{13} = 1$ GPa, $G_{23} = 0.5$ GPa.

For the problem considering the unwrapped pipe with one defect, a sensitivity analysis was performed in order to find a set of dimensionless parameters and to obtain some similarity criteria allowing us to estimate the maximum levels of stress distribution by extrapolating the results for other pipes without the need for additional calculations. For the problem with two defects, we have investigated the dependence of the relative position of the two defects on the non-uniform distribution of stresses, and we have proposed a set of dimensionless parameters uniquely characterizing the way the two defects influence one another. In every considered case, we have assessed the inhomogeneous stress distribution in the defects area and revealed the most dangerous zones from the viewpoint of the analysis of stress concentrators.

Table 30.1 Material properties

	Reinforcement material	Mechanical properties of composite materials (circumferential direction)		
		Elastic modulus (GPa)	Tensile strength (MPa)	Elongation (%)
Composite material (orthotropic)	Fiberglass	30	300	2
Adhesive	–	17	40	30
Filler	–	30	60	1

The conducted series of computational experiments for the unwrapped pipe allowed us to select the most hazardous geometrical parameters and relative locations of the defects and to reveal the optimal conditions of processing defect zones including cutting shape of a pocket and parameters of edge blending inside it for a number of specific cases. At the same time, we revealed a range of allowable defect parameters for which it is not necessary to replace the pipe segment during repairs.

Secondly, we considered a problem for the same damaged pipe which was then repaired by filling the cut pockets and setting the composite wrap on it. The FE model developed allows to set any dimensions and location for each defects. We have performed a computational analysis of the problem of the defects mutual influence (interaction). Three series of numerical experiments have been conducted differing from each other by the defects location and sizes.

In the first series of computational experiments, we have located the defects at the same cross-section circumference at different distances from each other. The sizes of each defect are $a = 76.2$ mm, $\varphi = 26.96$ deg, $d = 6$ mm, $r = 19$ mm (blending curvature radius). The 3 mm composite wrap consists of four 0.5 mm fiberglass layers bonded by 0.25 mm adhesive layers. In Figs. 30.4, 30.5 and 30.6 the case of the angular distance $\gamma = 5^\circ$ between the defects is depicted. In this case, there is a significant interaction between them (change in the stress distributions) only if the distance does not exceed the defect circumferential size; at the closest defects edges, stresses always reduce up to 2 times (see Fig. 30.4). In all the double figures below, the figure to the left presents the results for the unwrapped steel pipe, and the figure to the right shows the results for the repaired (wrapped) pipe. The wrap contour is outlined by the black line.

The stress graphs for two angular distances between the defects are depicted in the defect area on the trajectory in the middle of the defect area (see Figs. 30.7 and 30.8). It can be seen from these figures that, firstly, the wrap significantly reduces

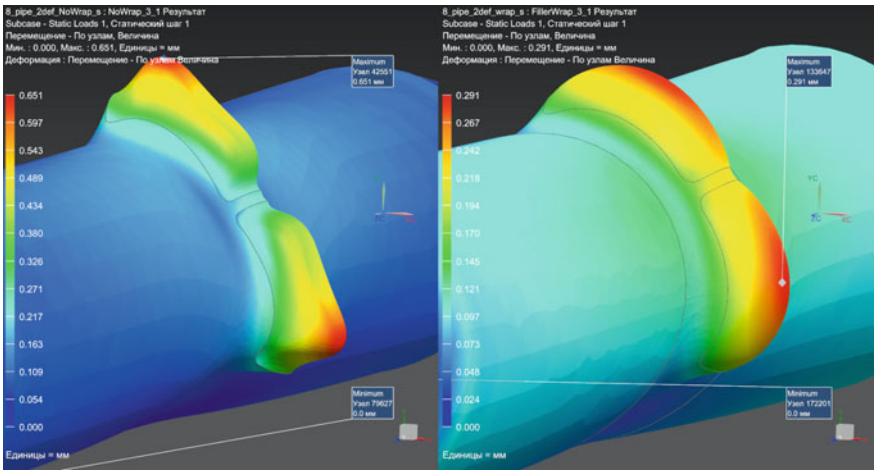

Fig. 30.4 Displacement field of the unwrapped (*left*) and wrapped (*right*) pipe

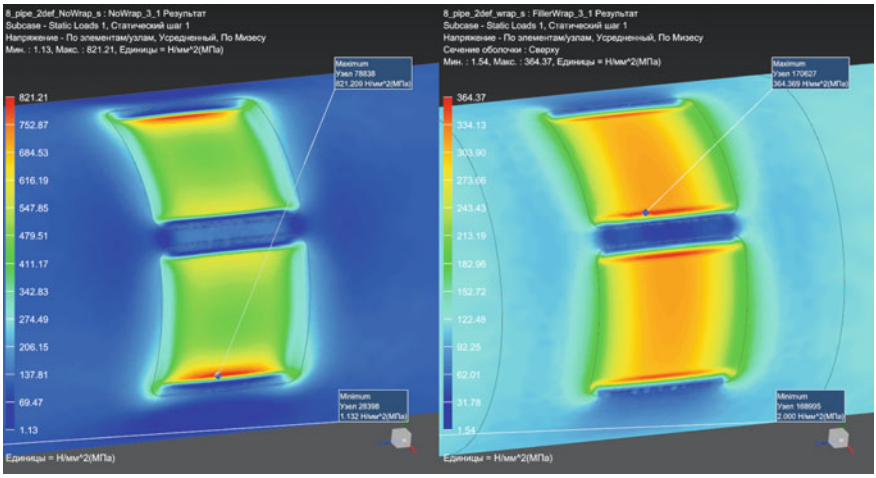

Fig. 30.5 Stress field (von Mises, averaged) of the unwrapped (*left*) and wrapped (*right*) pipe.The fillers and the wrap are not displayed

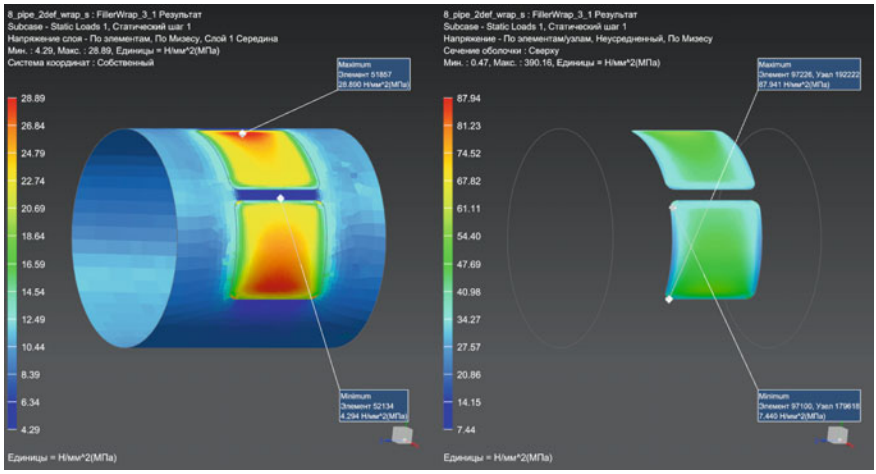

Fig. 30.6 Stress field (von Mises, averaged) of the wrap outer layer (*left*) and the fillers (*right*)

the stress level and, secondly, it makes the stress distribution even and rids of concentrators at the defects sides.

Secondly, we have conducted the experiments for the same pipe and wrap for the case in which the defects were located on one longitudinal line. In case we vary the longitudinal distance between two machined defects of the same rectangular shape (with the same fixed circumferential location), stress distribution in each of them does not change significantly for any chosen distance.

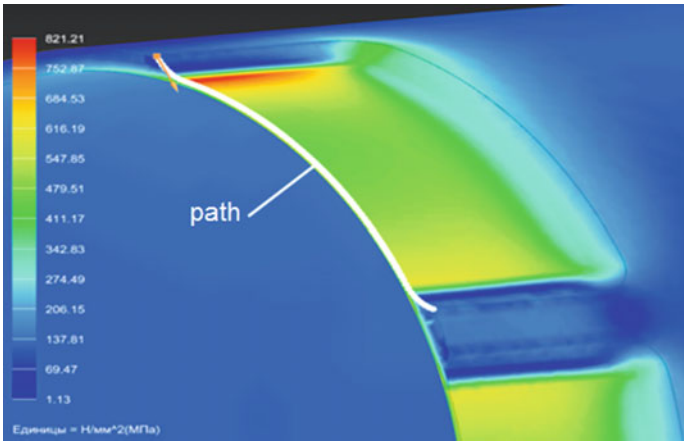

Fig. 30.7 Trajectory in the middle of the defect area

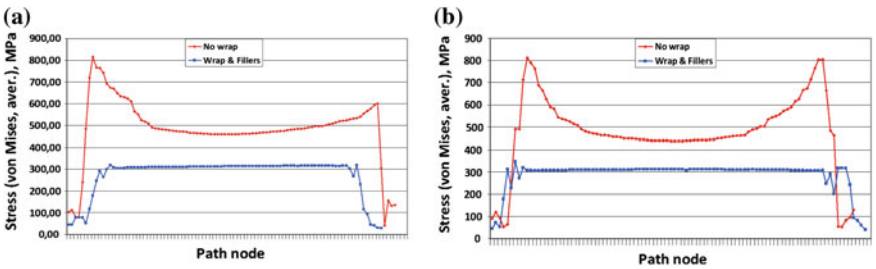

Fig. 30.8 Graphs of Von Mises stresses on the middle cross-sectioning path of the defect area in the circumferential direction: **a** case of small circumferential distance between two defects, $\gamma = 5°$; **b** case of large distance, $\gamma = 85°$

We have also investigated a number of situations with an arbitrary defects locations and shapes, for their different angular and longitudinal coordinates. As an example of FE calculations for a pipe in such case, see Figs. 30.9 and 30.10. As previously, it can be seen from the numerical results that the wrap is rather efficient from the viewpoint of stress-strain state of the steel pipe.

Furthermore, we have provided a comparison between the laminate and homogeneous wraps (see Fig. 30.11) and have estimated their influence on stress-strain state. We have analyzed the case of an arbitrary location of the defects presented in Figs. 30.9 and 30.10 for the same standard pipe (323.9 mm/8 mm) considered before. On the basis of the computational results (see Figs. 30.11, 30.12 and 30.13), it can be revealed that there is almost no difference between the laminate and homogeneous structure from the viewpoint of the stress-strain state.

Furthermore, we have analysed the effect of total wrap thickness on the stress-strain state. Considering again the case of an arbitrary location of the defects

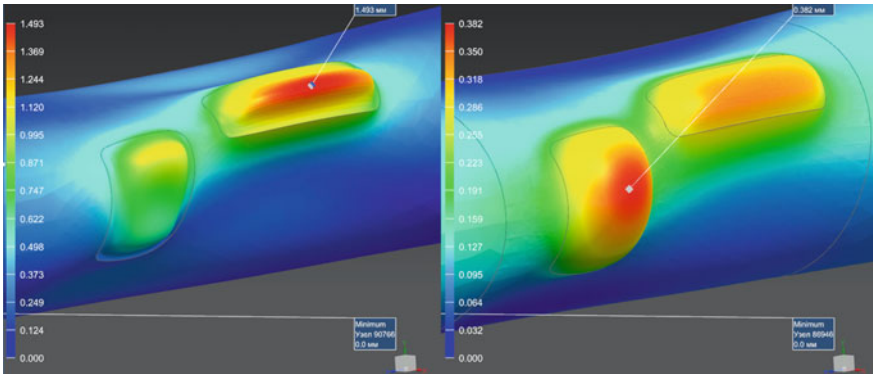

Fig. 30.9 Comparison of the displacement fields for the unwrapped (*to the left*) and wrapped (*to the right*) pipe in case of arbitrary shapes and location of the initial defects

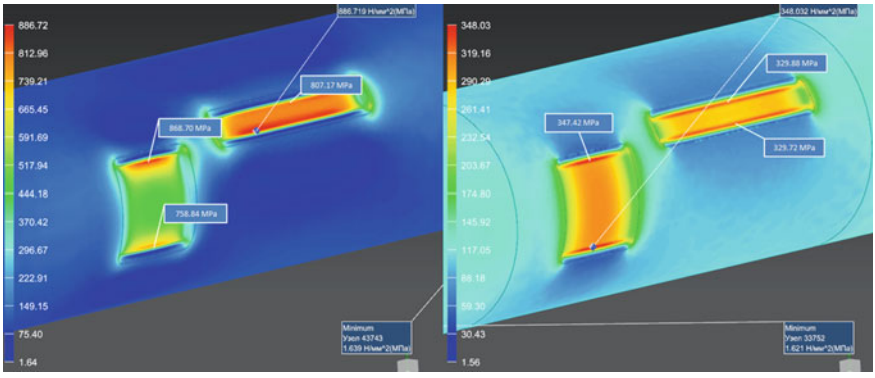

Fig. 30.10 Comparison of the Von Mises stress fields for the unwrapped (*to the left*) and wrapped (*to the right*) pipe in case of arbitrary shapes and location of the initial defects

presented in Figs. 30.9 and 30.10, we have varied the composite thickness; the adhesive (0.25 mm) is the same. Figures 30.14, 30.15 and 30.16 present the maximum displacements and stress in the steel pipe and also the maximum stress in the wrap and the fillers. The approximately selected zone in these figures corresponds to the most efficient range of the wrap thicknesses.

On the basis of the computational results obtained, it can be concluded that depending on the wrap thickness, maximum stress and strain may reduce up to 4 times. For the particular case considered for the standard pipe (323.9 mm/8 mm), the range of the efficient wrap thickness is about 6–19 mm.

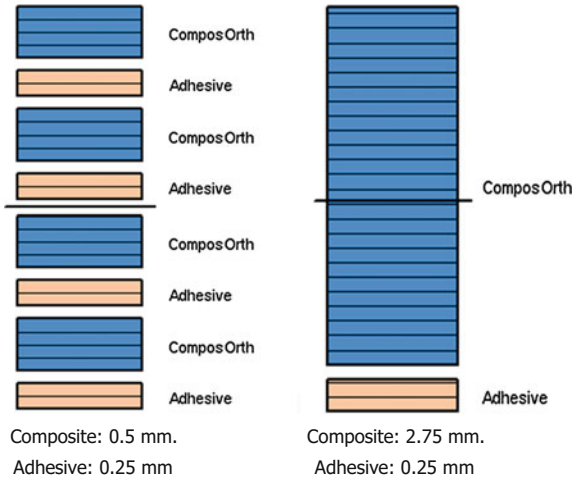

Fig. 30.11 Structure of laminate and homogeneous wraps compared. The total thickness of both wraps is 3 mm

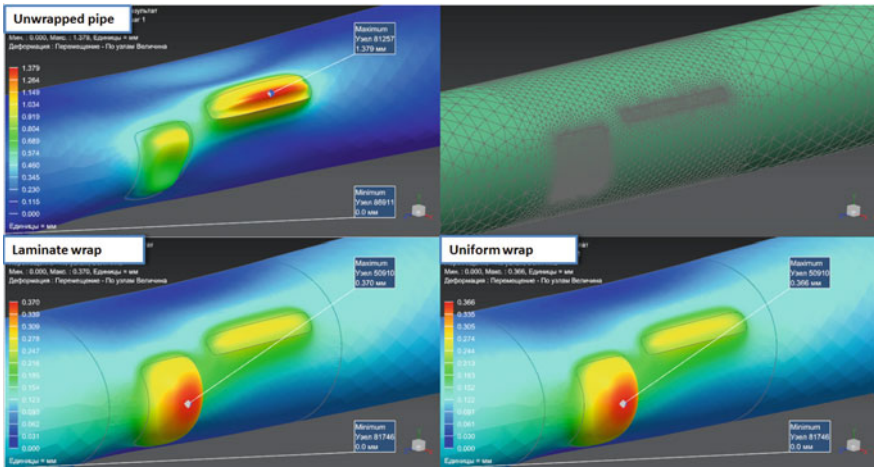

Fig. 30.12 Displacements comparison for the whole structure

30.4 Conclusion

Several problems for the damaged pipeline subjected to internal pressure loading and containing one or two volumetric surface defects have been solved. The defects were caused by surface corrosion and subsequently exposed to a mechanical treatment in order to eliminate the stress concentration effects. The problem of an optimal repair system for a pipe using a laminate composite wrap has been

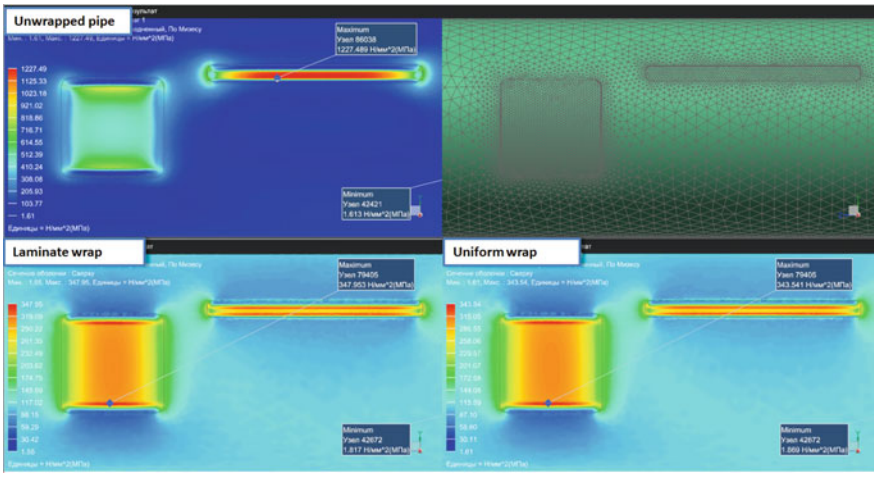

Fig. 30.13 Von Mises stress fields for the pipes with laminate and uniform wraps compared with the unwrapped pipe

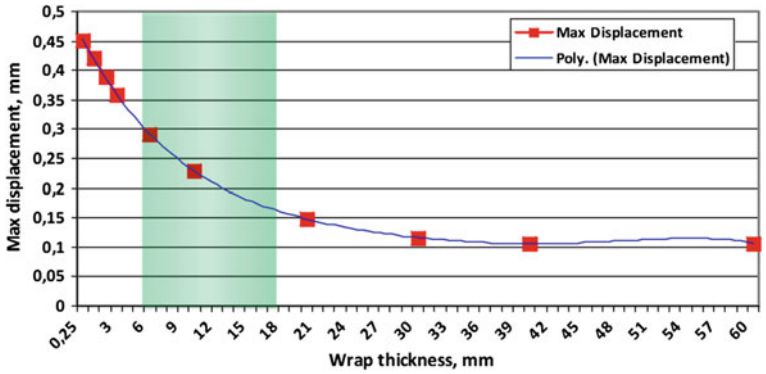

Fig. 30.14 Maximum displacement of the whole structure

considered. The proposed approach on the alternative in-service repair method leads to significant cost reduction of repairs of damaged transmission pipelines.

The generalized FE model was built allowing to calculate stresses and deformations of the wrapped pipe with two arbitrary machined defects. A series of computational experiments on defects interaction was conducted for the cases of circumferential, longitudinal and arbitrary defects locations. The comparison of laminate and homogeneous wraps was performed. The influence of the wrap thickness on the stress-strain state was also investigated. The results obtained were analyzed, and some recommendations were provided in order to obtain the most efficient wrap properties.

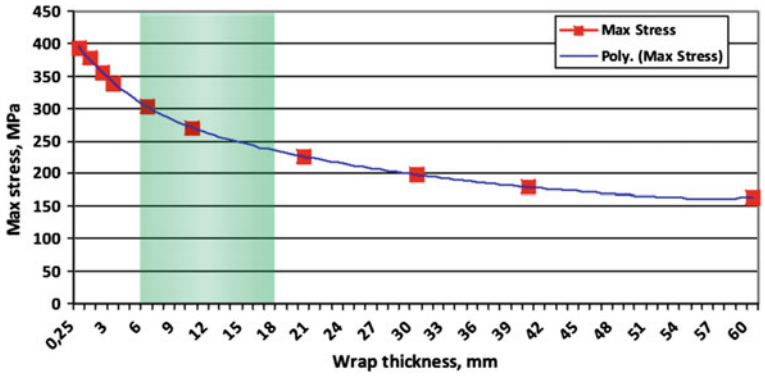

Fig. 30.15 Maximum Von Mises stress on the steel pipe

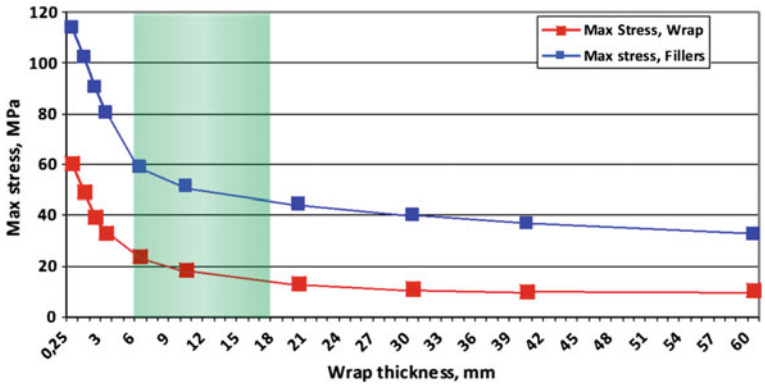

Fig. 30.16 Maximum Von Mises stresses on the outer composite layer of the wrap and the fillers

The main results of the solutions analysis consist in the following. Concerning defects location and their mutual influence, we have revealed that for the longitudinal location there is almost no interaction between defects for any distance. In case of circumferential location, there is a significant interaction when the distance does not exceed the defect angular size; at the closest defects edges, stresses always reduce, up to 2 times. For the arbitrary location, due to complex stress and strain behavior, FE calculation is required for each specific case. We have validated numerically the efficiency of the proposed laminate wraps: depending on wrap thickness, maximum stress and strain values may reduce up to 4 times, and stress distribution always become smooth and regular in the whole defect area. As for the wrap structure, we have investigated an issue of difference between laminate and homogeneous structures of the wrap; for the specific case considered in the present research, there was almost no difference between them from the viewpoint of the stress-strain state. We have also performed the analysis on a selection of the

adequate wrap thickness. By means of the developed FE model, the most efficient range of the wrap thickness can be calculated. For the particular case considered for the standard pipe (323.9 mm/8 mm), the approximate range is about 7–20 mm.

Acknowledgements The research was conducted with the support of the Project "INNOPIPES" # 318874 in the framework of the European Program FP7-PEOPLE-2012-IRSES, and the Grant of the President of the Russian Federation MK-5440.2016.1.

References

1. A.A. Lyapin, M.I. Chebakov, A. Dumitrescu, G. Zecheru, Mech. Compos. Mater. **51**(3), 333 (2015)
2. G. Zecheru, P. Yukhymets, G. Draghici, A. Dumitrescu, Rev. Chim. **66**(5), 710 (2015)
3. G. Zecheru, I.E. Lata, G. Draghici, A. Dinita, Mater. Plast. **48**(1), 88 (2011)
4. M.I. Chebakov, A. Dumitrescu, I. Lambrescu, R. Nedin, in *Innovative Solutions in Repair of Gas and Oil Pipelines* (2016), pp. 228–234

Chapter 31
Modeling of Corrosion in Filler Defect in the Repair of Pipes Overlay Composite Bandage

A.V. Cherpakov, M.I. Chebakov, G. Zecheru and A. Dumitrescu

Abstract In the current study, it is studied a problem of the simulations of stress state in the damaged section of the pipeline segment at its repair by introducing a composite band. The simulation was performed in ANSYS finite element software. Damage is modeled as single defect having a rectangular shape. The edges of the defect are rounded to the correct configuration with a specific radius *R*. Pipe model is loaded by internal pressure. It is taken into account X52 grade steel. The stress state of the pipe is studied for its two variants: (i) the model without defect and composite shell, (ii) the model of the defect with the filler and the composite shell (bandage). We studied the inhomogeneous stress field in the elastic deformation region. Stresses were calculated along two axes passing through the center of defect (the defect located on the main axis directed along the tube axis and in the radial direction). Modeling of stress state was performed for a defect imitating corrosive delamination of the layers. The delamination of corrosion in the defect area was modelled as a cavity of small volume. Corrosion is simulated as a detachment between the defect metal and composite filler.

31.1 Introduction

By exploiting oil and gas pipelines, various types of damage arise, some of which are corrosive defects and cracks as possible technological defects in the form of dents. These damages can lead to critical situations, which require additional diagnostics to identify and repair the damaged section of pipeline. Up to date, various methods are developed such as a repair of corrosion defects. One of the

A.V. Cherpakov (✉) · M.I. Chebakov
Southern Federal University, Rostov-on-Don, Russia
e-mail: alex837@yandex.ru

A.V. Cherpakov
Don State Technical University, Rostov-on-Don, Russia

G. Zecheru · A. Dumitrescu
Petroleum-Gas University of Ploiesti, Ploiesti, Romania

I.A. Parinov et al. (eds.), *Advanced Materials*, Springer Proceedings in Physics 193, DOI 10.1007/978-3-319-56062-5_31

promising methods for repair of oil and gas pipelines, have proved themselves good enough was the use of steel sleeves, welding and overlay composite shroud. Repair techniques using the composite band (winding) are described in detail by many authors, in particular in [1–5]. The study of the mechanical properties of the composite shroud and polymeric filler has been widely discussed [6–10].

In this paper, we used the finite element method to examine the stress-strain behavior of a metal pipe in the presence of the defect with volume shape. The hollow space of the defect was filled with composite polymer of specific properties and reinforcement caused by winding the multilayer composite. In this approach, for the repair of the damaged pipeline, it is necessary to take into account the stress concentration in the area of the defect caused by the large difference between the modulus of elasticity and strength properties of the pipe material and filler.

In the production of works on repairing the damaged pipeline, between the pipe and metal composite filler may be located a defect in the form or no sizing peeling layer above applied filler on corrosion or untreated surface. This type of defect can occur during operation of the pipeline.

31.2 Methods

The objective of this study is to determine the state of stress in the area of the defect with simulation of the corrosion bundle filler of pipeline based on numerical simulation of metal in the ANSYS finite element software.

We studied the pipe model with a composite shell for the repair of oil and gas pipes. Defective construction scheme is shown in Fig. 31.1. Data for the calculation

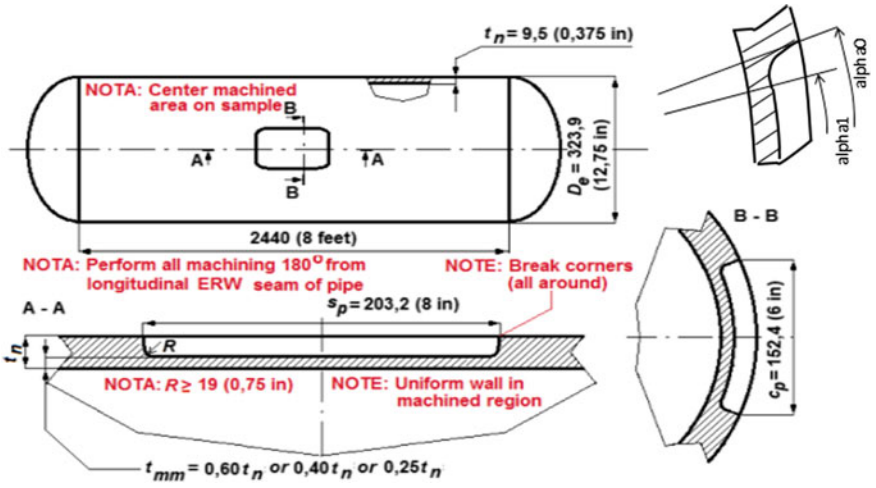

Fig. 31.1 Schematics of the structure with defect

Table 31.1 Calculation data for defective pipe

Region	Property name	Value
Steel	Material	X52
	Yield stress	σ_p = 360 MPa
	Considered critical stress	0.7 × 360 = 252 MPa
	Mechanical properties	$E_1 = 2.1 \times 10^{11}$ MPa, ρ_1 = 7700 kg/m^3
Pipe	External pipe diameter	D_e = 323.9 mm
	Pipe length	L_p = 2440 mm
	Pipe thickness	t_n = 9.5 mm
	Internal pressure	$P = 1.6 \times 10^6$ Pa (16 bar)
Defect	Length × width × depth	L_d = 203.2 mm × L_w = 152.4 mm × d = 0.6 × 9.5 = 5.7 mm
	Apparent defect depth	d/t_n = 0.6
	Angle of defect location relatively rounded edges	$\alpha_1 = 34.71°$
	Angular opening of defect	$\alpha_0 = 53.91°$
	Diameter of rounded edges	19 mm
	Radial area rounding	0–9.6°; 44.31°–53.91°
	Rounding region along the tube	0–0.0135 m; 0.176–0.2032 m

are present in Table 31.1. Table 31.2 shows the parameters of the composite material bandage.

Figure 31.2 presents full-bodied model pipe with a defect and finite element partition in the defect area in ANSYS software. The simulation used a finite element SOLID187. The number of elements in the simulation exceeded 160,000.

Figure 31.3 shows a model of the composite shell in the form of bandage on the pipe repair. In the simulation, the composite used finite element SOLID187 for the final defect. In the simulation, bandage used 3D finite element SOLID186. It has the ability to simulate different layers of different materials. The number of elements in the simulation exceeded 210,000.

In this stage, a distribution of stresses on the thickness of the pipe without defect was obtained. At this stage, the load inside the tube was taken as the equipartition and equal to $P = 1.6 \times 10^6$ Pa (16 bar). The distribution of stresses in the defect-free area of the pipe, derived from the FEM calculations, are present in Fig. 31.4.

Table 31.2 Parameters of the properties of various materials taken in the design of pipe models

Region	Property	Value
Filler	Geometry data vary depending on size of VSD	
	Mechanical properties	E_2 = 30 GPa, υ_2 = 0.3, ρ_2 = 1250 kg/m^3
Bandage	Geometry data	
	Inner radius equals pipe outer radius	R_1 = 0.16195 m
	Wall thickness	h_2 = 0.0045 m
	Length	0.3032 m
	Half of length for calculations	l_2 = 0.1516 m
	Overlapping distance of bandage	0.05 m
	Composite thickness	0.5 mm
	Mechanical properties	E_3 = 20.1 GPa, υ_3 = 0.316, ρ_3 = 1600 kg/m^3
	Adhesive thickness	0.25 mm
	Mechanical properties	E_4 = 17 GPa, υ_4 = 0.316, ρ_4 = 1600 kg/m^3

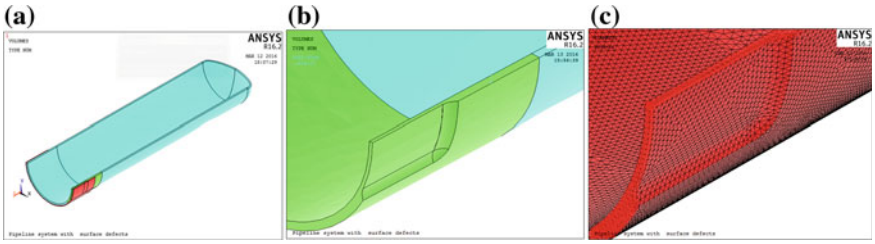

Fig. 31.2 **a** Volumetric defect model, **b** construction of finite element mesh by partitioning the defect area. **c** model with composite shell

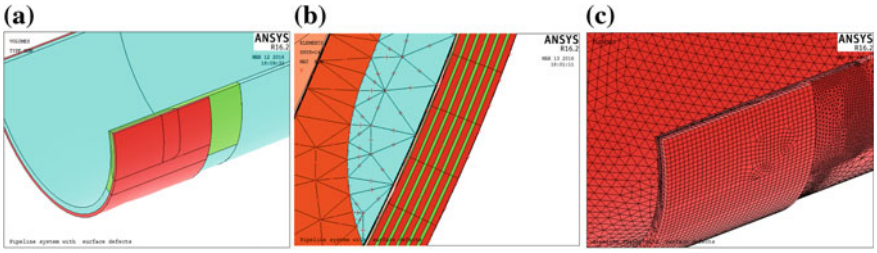

Fig. 31.3 Model shell in damaged area (**a**, **b**); finite element model mesh partition in place of the defect (**c**)

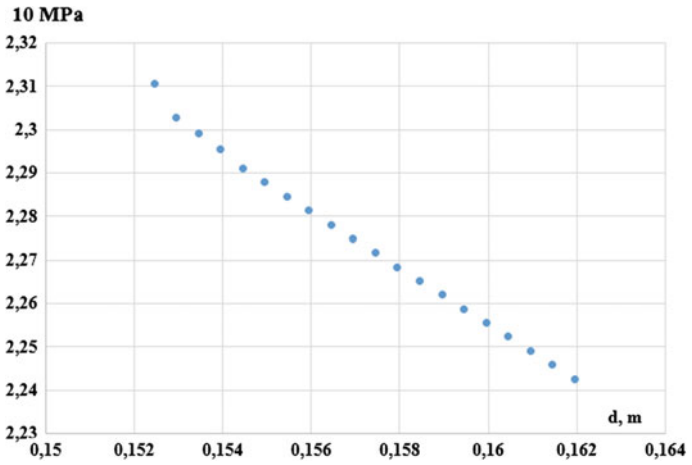

Fig. 31.4 Distribution of the stress state of the thickness of the main wall of the pipe

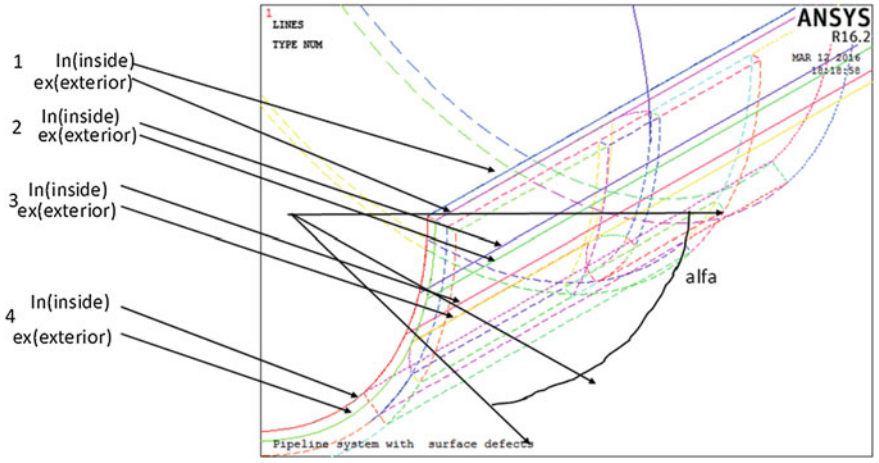

Fig. 31.5 Line information gathering inside the pipe (*inside*) and outer (*exterior*) surface of tube

31.2.1 Calculation of Stress State of Pipe with Defect Without Bandage

By studying stress state, the fields of special interest for existing defect are four zones, shown in Fig. 31.5: (1) $\alpha = 0°$ (conditional defect center); (2) its center locates in the zone, restricted by line under $\alpha = 11.075°$ and this area locates at the distance $L_d/4$ from the edge of the defect; (3) the zone, located on the front line of a stress concentrator (at the bottom of rounding the edges of the defect), $\alpha = 22.150°$; (4) the zone located in radial direction.

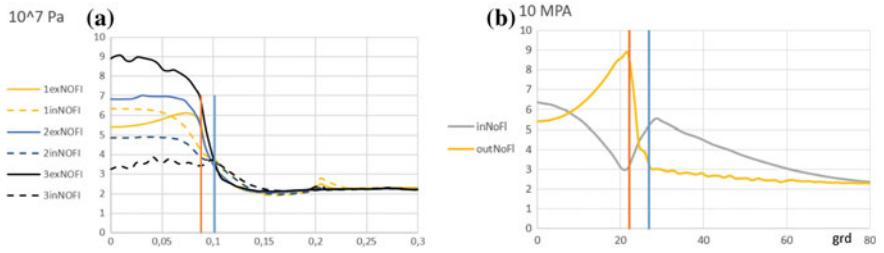

Fig. 31.6 **a** Mises stress distribution along the pipe without bandage in three zones differing by diameter; lines show location of the tape area edges: *1* $\alpha = 0$; *2* $\alpha = 11.075°$; *3* $\alpha = 22.155°$; **b** Mises stress distribution, as measured by line 4, extends in a radial direction through the center (bandage is absent and the lines show location of the tape area edges)

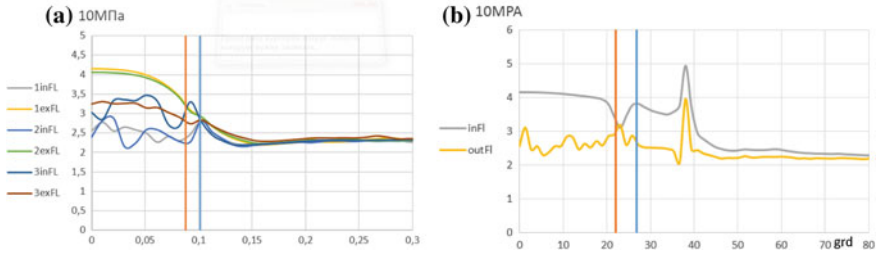

Fig. 31.7 **a** Mises stress distribution over the length of defect pipe with bandage at three different places along diameter; lines show location of the tape area edges: *1* $\alpha = 0°$, *2* $\alpha = 11.075°$, *3* $\alpha = 22.155°$; **b** Mises stress distribution, as measured by a line extending radially through the center of the defect (bandage is presence and lines show rounding the edges of area location)

In this stage, we calculated stress distribution along the length of the defect in the four zones. Stresses collected along symmetrically located lines on inner and outer surfaces of the pipe. Qualitative analysis shows that the ratio of maximum stress, measured on tube outside in presence of defect to the value of the tube inside, takes the following values (σ_{ex}/σ_{in}): 1.18 (line 1), 1.4 (line 2), 2.25 (line 3). The maximum stresses drop in the stress concentrator area, at the beginning of rounding the edges (the defect base). The curvature of the base region defines comparative growth of stresses (see Fig. 31.6b).

31.2.2 Stress State of the Pipe with a Defect in Presence of Bandage

The results are obtained by finite element modeling of stress state at a pressure 1.6 MPa inside the pipe. An analysis of the stress state of the pipe with the bandage

indicates that the stresses decreased. The level of stresses in the defect area is twice the level of the tension in the main pipe. The results are shown in Fig. 31.7.

31.2.3 Stress State of Defect with Detachment of Composite Shell

Delamination of the composite shell is modeled taking into account its small thickness and circular shape. The simulated corrosion defect has a rounded area of 10 mm in diameter and within of the shell volume is present the air cavity of 0.5 mm in depth (see Fig. 31.8). We conduct a stress state analysis.

The results of calculation of the stress state shown in Fig. 31.9, where red vertical lines indicate the place of rounding the edges of defect. Figure 31.9 shows the zones of defined voltage: M1—the stress distribution of defect at the metal surface; M2—the stress distribution on the inner side of the pipe; F1—the stress

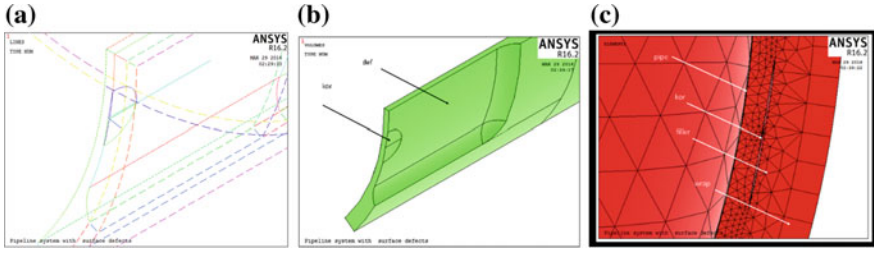

Fig. 31.8 **a** Construction lines, describing defect, **b** location of defect simulating corrosion (kor), **c** finite element mesh in place of disposition of defect presenting it as corrosive delamination of the composite

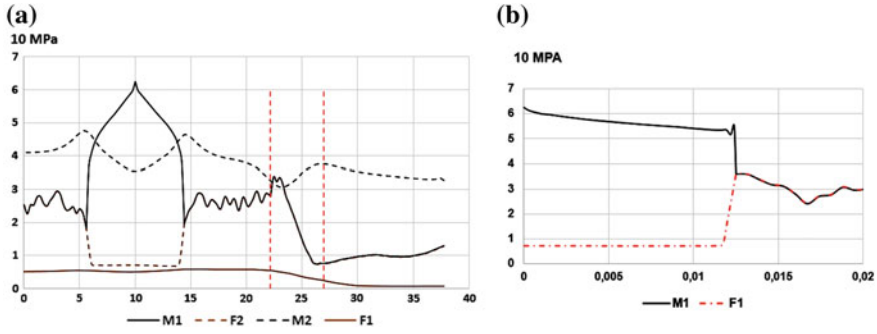

Fig. 31.9 **a** Mises stress distribution, the distribution of the stress state in the radial direction in various zones of the defect; **b** Mises stress distribution, stress distribution in the defect at the delamination of the composite in parallel to main axis of the tube

distribution on the inner side of the composite in a contact with the metal; F2—the stress distribution on the outer side of the composite in contact with the shell.

An analysis of the stress state in the area of corrosion defect indicates that the stress in the center of the corrosion spot is 2.5 times greater than the stress in an area, where there is no corrosion and thus detachment of the composite tape metal on the surface of the defect. The level of the stress state in the corrosion spot depends on the covering the concentrator surface of the metallic pipe. The value of stress state on the surface of the composite tape decreased more than two times compared to the entire surface, uncoupled with the metallic pipe. This suggests that it is necessary to take into account the strength factor of the pipe metal.

31.3 Conclusions

1. We considered stress state in the pipe with a defect of rectangular shape with rounded inner edges in the case of the overlay bandage of composite coatings for the repair of the pipeline. Analysis of stress state shows that for the selected pipe model with a defect, stress state decreases after repair more than two times. This evidences on efficiency of the repaired defective pipe.
2. An analysis of the stress state of corrosion at delamination of the composite metal tape from inside of the pipe defect shows that the stress state increases in the field of corrosion spots, and it depends on the parameters of concentrator. This case should be considered as a safety factor in the operation of the pipeline.

Acknowledgements The authors gratefully acknowledge the support of European Commission, Marie Curie Program, contract No. PIRSES-GA-2012-318874, Project "Innovative Non-Destructive Testing and Advanced Composite Repair of Pipelines with Volumetric Surface Defects (INNOPIPES)" and the Southern Federal University (Proposal No. 213.01-2014/03VG).

References

1. J.M. Duell, J.M. Wilson, M.R. Kessler, Int. J. Press. Vessels Pip. **85**, 782 (2008)
2. Kyu-Hyeon Lee, Sang-Hoon Rhee, Biomaterials **30**, 3444 (2009)
3. A. Valor, F. Caleyo, L. Alfonso, D. Rivas, J.M. Hallen, Corros. Sci. **49**(2), 559 (2007)
4. F. Caleyo, J.C. Velázquez, A. Valor, J.M. Hallen, Corros. Sci. **51**(9), 1925 (2009)
5. MKh Khalajestani, M.R. Bahaari, Int. J. Press. Vessels Pip. **123–124**, 77 (2014)
6. M.A. Abanilla, Y. Li, V.M. Karbhari, Composites **37**, 200 (2006)
7. S.B. Brahim, R.B. Cheikh, Compos. Sci. Technol. **67**, 140 (2007)
8. J.M. Duell, J.M. Wilson, M.R. Kessler, Int. J. Press. Vessels Pip. **85**, 782 (2008)
9. H. Ghiasi, D. Pasini, L. Lessard, Compos. Struct. **90**, 1 (2009)
10. P.J. Herrera-Franco, A.A. Valadez-Gonzalez, Composites **36**, 597 (2005)

Chapter 32
Ultrasonic and Magnetic Flow Inspection Methods of Identification of Cracks in the Pipe Coupled with Artificial Neural Networks

Arkadiy N. Soloviev, Boris V. Sobol and Pavel V. Vasiliev

Abstract The ultrasonic and magnetic flow inspection methods of identification of crack-like defects in coated pipes are proposed. The identification of inner defects was performed using ultrasonic methods and an artificial neural network approach. Model of a pipe cross-section with an inner coating and the propagation of an ultrasonic wave were developed. A cross-section of the pipe, reinforced by inner annular coat, and the magnetic field propagation in permanent magnets were modeled. The identification of several geometric parameters of defects was carried out. The influence of different geometric parameters of the defects on the performance of neural networks is investigated. The optimal structure of the neural networks and the form of training vectors for methods of ultrasonic testing and magnetic flow inspection are established.

32.1 Introduction

Nondestructive testing is an essential part of examination of industrial safety, technical diagnostics and used to evaluate the technical condition of industrial equipment units without the use of destructive operations and stopping production.

A.N. Soloviev (✉)
Department of Theoretical and Applied Mechanics, Don State Technical University,
1, Gagarin Square, 344010 Rostov-on-Don, Russia
e-mail: solovievarc@gmail.com

A.N. Soloviev
Institute of Mathematics, Mechanics and Computer Sciences,
Southern Federal University, 8a, Milchakov Street, 344000 Rostov-on-Don, Russia

B.V. Sobol · P.V. Vasiliev
Department of Information Technologies, Don State Technical University,
1, Gagarin Square, 344010 Rostov-on-Don, Russia
e-mail: b.sobol@mail.ru

P.V. Vasiliev
e-mail: lyftzeigen@mail.ru

I.A. Parinov et al. (eds.), *Advanced Materials*, Springer Proceedings
in Physics 193, DOI 10.1007/978-3-319-56062-5_32

The purpose of non-destructive testing is to improve the operational safety of technical devices, buildings and structures, used and exploited at hazardous production facilities, achieved by improving the reliability, reproducibility, comparability of results of non-destructive testing and decision, based on these results, timely and appropriate solutions to ensure industrial safety of dangerous production facilities.

Nondestructive testing is an integral part of technical diagnostics; it is used for the evaluation of the technical state of assemblies of industrial equipment without destructive operations. Among such methods, ultrasonic testing method is predominant; it is based on the ability of sound waves reflect from the interface between two elastic media that have different acoustic properties [1–4].

The simulation of the propagation of an ultrasonic wave in solids can be performed by the finite-element method (FEM). COMSOL software was chosen as a tool for modeling the propagation of an ultrasonic wave in a pipe with a thin ring coating.

Defect identification and the subsequent defect localization are topical problems. This problem refers to the sphere of non-destructive testing of the properties and parameters of an object in an inverse problem on the mechanics of deformable solids [5].

Among the non-destructive testing methods, one of the leading position is occupied by the magnetic flaw detection method. Magnetic inspection is a highly effective method for the detection of surface and subsurface defects. It is based on the receipt of information about the magnetic scattered field around the ferromagnetic objects. In the location of the defect areas, there is a redistribution of the magnetic flux and the formation of magnetic scattered fields. Information on the magnetic flux density may be obtained by using devices based on the Hall effect, the so-called Hall sensors.

There are some effective methods based on magnetic inspection [6–9]. It is used typically an inspection of objects made of ferromagnetic materials. With these methods, the magnetizing objects and measurement of the parameters involved in magnetic inspection are used in all cases. Depending on the magnetic properties of the material (coercive force, magnetic permeability, remanent induction), the shape and dimensions of inspection products are used two methods: the applied magnetic field and the residual magnetization.

Modern computational tools allow one to apply methods and technologies, based on the artificial neural networks for solving identification problems [10–13].

32.2 Statement of the Direct and Inverse Problems

In the direct problem, the forced oscillations of an elastic body are considered, which are described by the following boundary-value problem [14]:

$$\sigma_{ij,j} = \rho\ddot{u}_i; \quad \sigma_{ij} = c_{ijkl}u_{k,l}, \quad i = 1,2,3 \tag{32.1}$$

$$u_i|_{S_u} = u_i^{(0)}, \quad \sigma_{ij}n_j|_{S_t} = p_i, \quad \sigma_{ij}n_j|_{S_d} = q_i \tag{32.2}$$

where u_i are the unknown components of the displacement vector; $u_i^{(0)}$ and p_i, q_i are the known components of the displacement vector and surface loads; σ_{ij} and c_{ijkl} are the components of the stress tensors and elastic constants; ρ is the density; S_u, S_t are the surfaces of a body on which the displacement and stress vector, respectively, are present; and S_d are the inner surfaces of a tunnel crack in the direction of Ox_3 axis.

To identify defects (cracks, inclusions, or cavities), it is necessary to determine their configuration; thus, the surfaces S_d are unknown, which means that the considered problems are inverse geometric problems of the theory of elasticity. Hereinafter, it is assumed that the crack edges do not interact and are free from stresses, $q_i = 0$. To solve the inverse problems of the surface S_d reconstruction, additional information is needed besides that stated in the boundary value problem (32.2). Such information can be the amplitude-time characteristics (ATC) of the displacement wave field $\overline{U}$ measured on the free surface:

$$u_i = U_i(\bar{x}_k, t), \ t \in [0, T] \text{ and } k = 1,2,\ldots,n, \ \bar{x}_k \in S_t \tag{32.3}$$

where T is the typical time of signal reflection and n is the number of measurement points.

Thus, the input information set X is obtained, which can be used for the reconstruction of the geometric parameters of a crack.

The propagation of the magnetic field in a cubic region inside which there is the hollow cylinder component (pipe fragment) with two permanent magnets on its outer surface considered. The problem is solved in current-free approach when the eddy current component is missing and magnetic field vector H satisfies the equation $\nabla \times H = 0$. In this case, the Gauss law for the magnetic field gives the following system of differential equations:

$$\nabla \times B_k = 0, \quad B_k = \mu_k(H_k + M_k), \quad H_k = -\nabla V_k, \quad k = 1,2,\ldots,N \tag{32.4}$$

where B_k, M_k are the magnetic induction vector and the magnetization of the material, respectively, V_k is the scalar magnetic potential, μ_k is the permeability tensor of second rank, the subscript k is the number of subfield with no summing on it.

As boundary condition, the normal component of the magnetic induction vector is equal to zero, where S is the outer boundary of the region.

$$B_k \cdot n|_S = 0 \tag{32.5}$$

and conditions of matching at the internal interfaces (equality of the normal components of the magnetic potential of magnetic induction vectors).

32.3 Method Concept of Ultrasonic Inspection

The identification of a defect is based on the radiation into object and the subsequent reception of reflected ultrasonic waves with the analysis of the obtained data for the purpose of the identification of the defects and the determination of their size, position, and occurrence depth.

The modeling of the shadow and echo methods of ultrasonic testing was performed. According to the echo method, a transducer both generates oscillations and receives echo signals that are reflected from defects. This technique provides a rather precise determination of the defect coordinates, such as the occurrence depth and position in a studied object (with respect to the transducer). According to the shadow method, two transducers used are located at two sides of a studied object on one acoustic axis. In this case, one of the transducers (generator) generates oscillations and the other (receiver) receives them. The indicator of a defect significantly changes the amplitude of the received signal (a defect creates an acoustic shadow). Figure 32.1 (at right) presents AFC of the signals of different identification methods.

After a series of experiments for a studied object and analyses of the results, conclusions can be made about structure and characteristics of the object, including possible defects. The use of a unique artificial neural-network device can make the analysis of the results more effective [15]. Unlike [15], this study describes different ultrasonic testing techniques and their combinations, which can improve the identification of both horizontal and vertical defects.

For the modeling of the propagation of an ultrasonic wave, COMSOL software with the Solid Mechanics module was used in the Time-Dependent mode. The sources of ultrasonic disturbances were points on the outer surface of a pipe. The signal modeling was performed using the parameters that are shown in Table 32.1.

An ultrasonic signal at the frequency of 10 MHz is present in the form of a negative sine function with a Hanning window function. The input signal is created based on pre-generated data using linear interpolation. In Fig. 32.1 (at left and right), the form of the input signal and amplitude-frequency characteristic of the received signal reflected from a crack and inner surface of a pipe are shown.

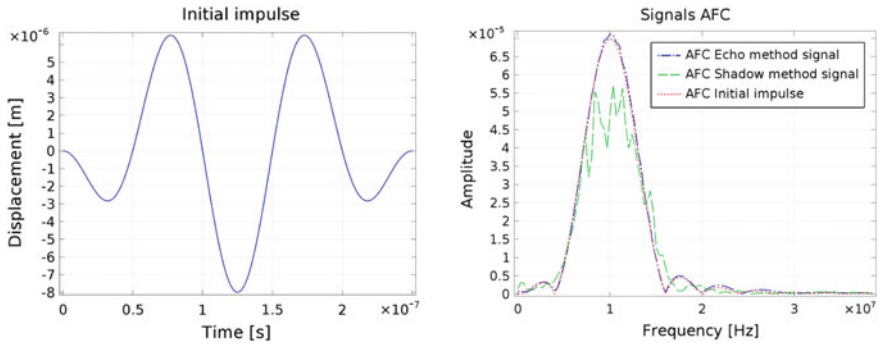

Fig. 32.1 Form of the input signal (*left*), and AFC of the received signal (*right*)

32.4 Finite Element Modeling of Pipe with Ultrasonic Wave Propagation and Its Calculation

A defect has an elliptical shape; its height significantly exceeds its width. The defect edges do not interact. Special attention is paid to the development of the finite-element mesh and subdividing it into the region of a defect and points of initial impulse of an ultrasonic wave (Fig. 32.2).

In this model, the finite element size Δx_{max} is established as $\lambda_L/8 = 7.7425 \times 10^{-5}$ m for structural steel domain and for aluminum domain, where λ_L is the length of a longitudinal ultrasonic wave that propagates in the direction of the initial impulse.

The critical step time Δt, that is used in the solution of the finite-element method with the use of the chosen solver, is equal to $\Delta x_{max}/C_{ph}$, where C_{ph} is the phase velocity of an ultrasonic wave. Thus, the critical value $\Delta t_c = \frac{\Delta x_{\max}}{C_{ph}} = 1.25 \times 10^{-8}$ s,

Table 32.1 Parameters of modeling

Outer pipe diameter	720 mm
Thickness of the pipe wall	9 mm
Thickness of the coating	0.27 mm
Material of the pipe wall	Structural steel ($E = 210$ HPa, $v = 0.28$)
Material of the stringer	Aluminum ($E = 382$ HPa, $v = 0.35$)
Steel density	7850 kg/m^3
Aluminum density	2700 kg/m^3

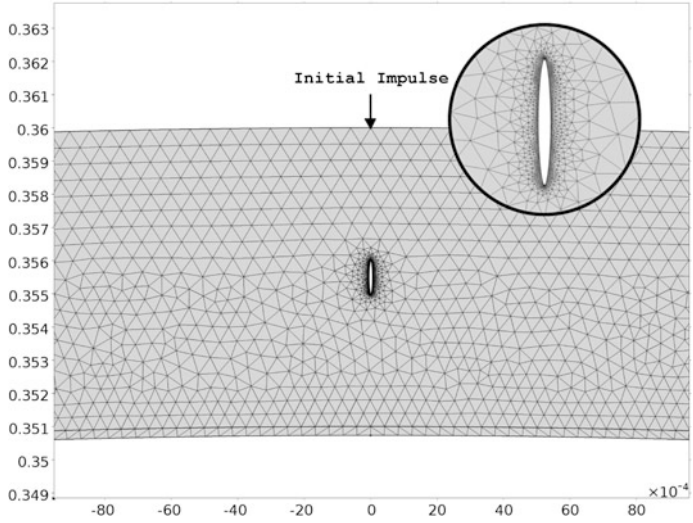

Fig. 32.2 Fragment of a pipe in the defect zone in the COMSOL software

for the values of the finite element size $\Delta x_{max} = 7.7425 \times 10^{-5}$ m and $\Delta x_{max} = 7.9 \times 10^{-5}$ m. To obtain a more accurate result, it was decided to establish the value of the step time lower than Δt_c and equal to 1×10^{-8} s.

Within the formulated problems, a series of model calculations was performed with different parameters of a crack defect.

The length l of a crack varies in the interval of 10–40% of the pipe-wall thickness. The depth of defect occurrence y_0 is determined by the condition that the distance from the inner and outer surfaces of a pipe is not less than 10% of its thickness. The angle of rotation of a crack α varies from 0° to 180°.

Figure 32.3 shows the propagation of an ultrasonic wave in a pipe at different positions of a crack ($\alpha = 0°$ at left and $\alpha = 90°$ at right).

As a result of the calculations of the simulation model that were performed using the COMSOL software, the amplitude-time characteristics of an ultrasonic wave were obtained for the combinations of the defect parameters determined earlier (Fig. 32.4 presents one of this combinations: $\alpha = 90°$, $l = 1$ mm, $y_0 = 5$ mm).

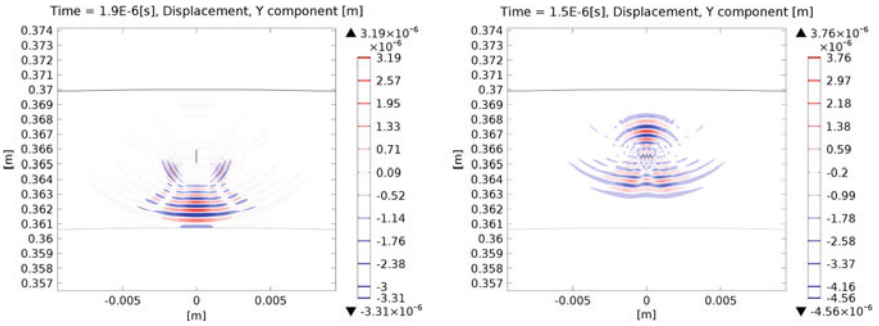

Fig. 32.3 Propagation and reflection of an ultrasonic wave in the defect zone: crack in a vertical position (*left*); crack in a horizontal position (*right*)

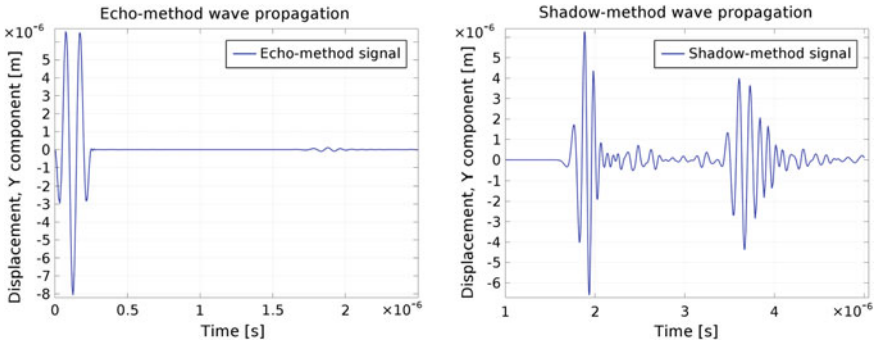

Fig. 32.4 ATC of an ultrasonic wave on the outer surface of a pipe (*left*) obtained at the analysis by the echo method; ATC of an ultrasonic wave on the inner surface of a pipe (*right*) obtained at the analysis by the shadow method

32.5 Method Concept of Magnetic Flow Inspection

Magnetic inspection is a set of non-destructive testing methods used for detection of the defects in ferromagnetic metals (iron, nickel, cobalt, and a number of alloys based on them). Such defects as cracks, hairline, non-metallic inclusions, lack of fusion, flakes can be detected by the magnetic method. Identification of defects is possible in the case they are located on the surface of the inspected object, or located at a shallow depth.

The proposed method is based on obtaining information of the magnetic scattered field around the ferromagnetic inspection objects. In the location of the defect areas, there is a redistribution of the magnetic flux and the formation of magnetic scattered fields.

After processing received information, the artificial neural networks approach (feed forward ANN) may be applied for localization and reconstruction of geometrical parameters of defects.

32.6 Finite Element Modeling of Pipe with Magnetic Flow Redistribution and Its Calculation

Parameters used in building the model correspond to the real values of pipe dimensions and permanent magnets strength (see Table 32.2).

Both internal and external defects of different configurations are modeled. Crack-like defects were modeled by using the parameters such as height, width, depth, orientation relative to the longitudinal axis of the tube. Defect representing zero adhesion between the pipe wall and the coating is realized as 5% loss of tube material. The defect that simulates the effects of corrosion corresponds to 1–3% material loss (Fig. 32.5).

The finite element three-dimensional model of a pipe with an inner coating, weakened by various defects, is developed. The inspected area contains permanent magnets, adjacent by the different poles to the pipe surface. Figure 32.6 shows the location of the magnets on the pipe and the distribution of the magnetic flux density in the inspection area.

Table 32.2 Parameters of the model

Inner diameter	100 mm
Wall thickness	2.5 mm
Internal coating thickness	1 mm
Pipe material	Structural steel ($\mu_k = 100$)
Coating material	Aluminum ($\mu_k = 1.000022$)
Environment box	Air ($\mu_k = 1.00000037$)
Magnet size	$10 \times 10 \times 10$ mm^3
Magnet field strength	750 kA/m

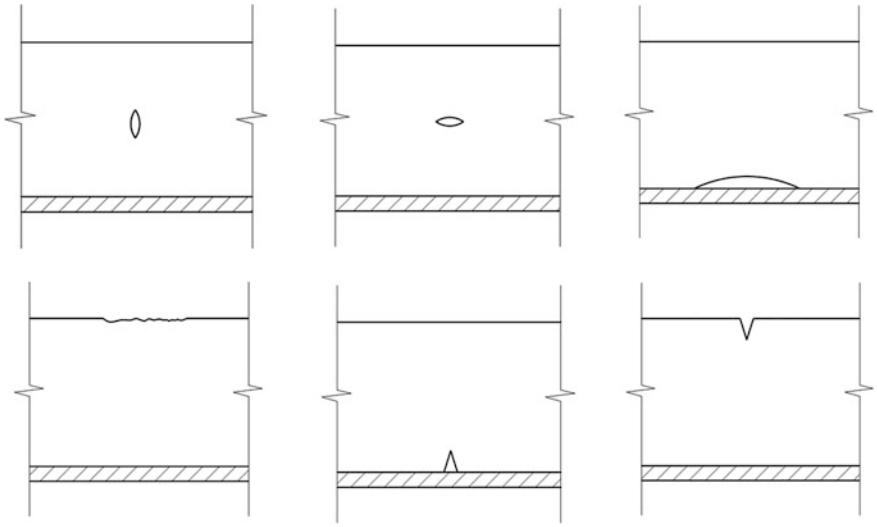

Fig. 32.5 Different types of modeled defects (*vertical inner crack*, *horizontal inner crack*, exfoliation, corrosion, defect between pipe wall and coating, surface defect)

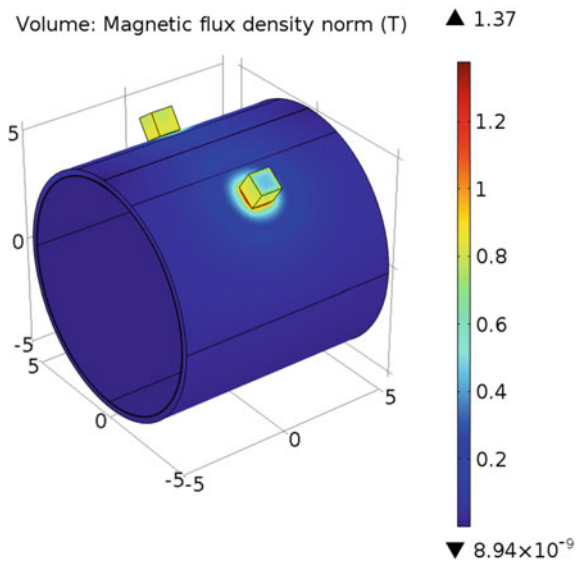

Fig. 32.6 Distribution of magnetic flux density on a piece of pipe

COMSOL Multiphysics is used as the finite element simulation tool. The Magnetic Fields and No Currents interface are used to implement the magnetic flaw detection method. They are used to calculate the magnetostatic fields of the permanent magnets and the magnetic fields of current-free sources.

The effect of environment size on the value of magnetic flux density in the area of the defect, obtained from the top surface of the pipe, is established. The relative environment size is obtained 5 times greater than the pipe. Figure 32.7 represents the defect influence on the distribution of magnetic flux density.

The influences of the height and width of a defect on the value of the magnetic flux density in the defect region are established. These parameters are varied from 1 to 90% relatively to the pipe wall thickness (Fig. 32.8).

So, it was found that the changes of the geometric parameters such as the height and width of the defect affect the values of the magnetic flux density obtained on the outer surface of the pipe. It is worth noting that the impact exerted by the value of width is much less than that of height. It is also found that variations of these parameters provide unambiguous effects at values greater than 5% relatively to the tube wall thickness.

As part of the problem, a series of numerical experiments with different parameters of crack-like defects are carried out. Defect height l ranges from 1 to

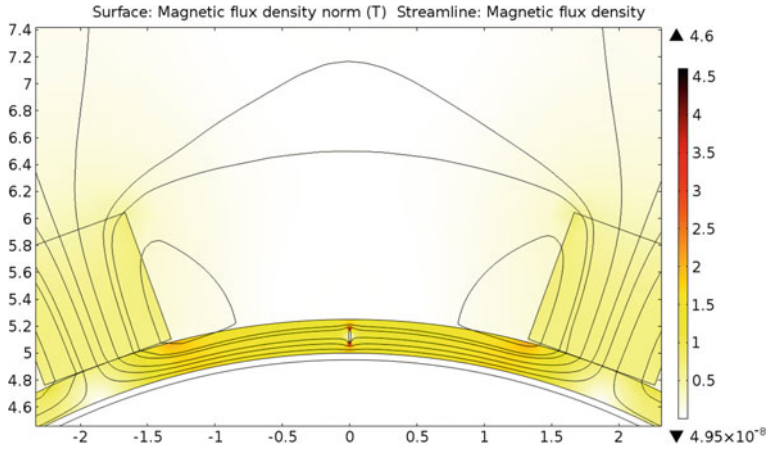

Fig. 32.7 Redistribution of the magnetic flux density in the defect region

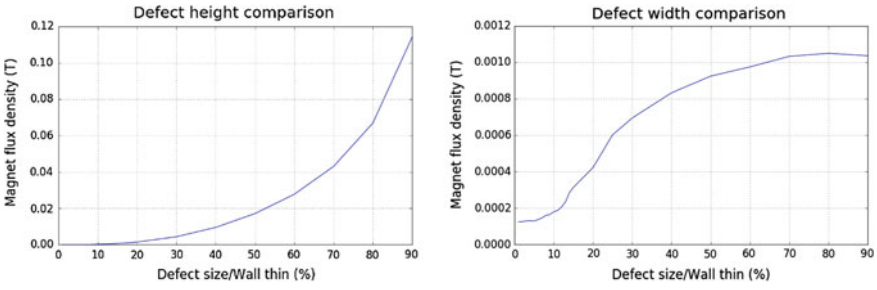

Fig. 32.8 Influence of defect geometrical parameters on the flux density in the defect area

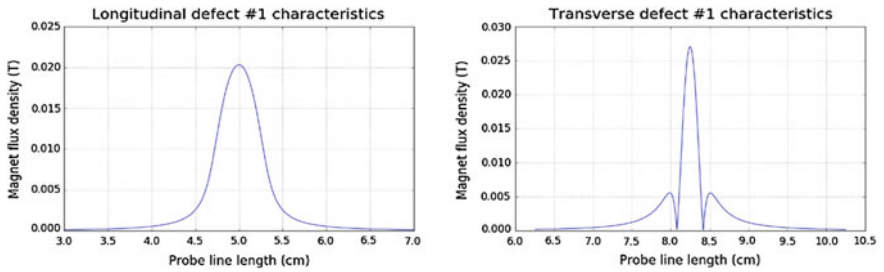

Fig. 32.9 Characteristics of longitudinally oriented defect: data from longitudinal scan-line (*left*), and from transverse scan-line (*right*)

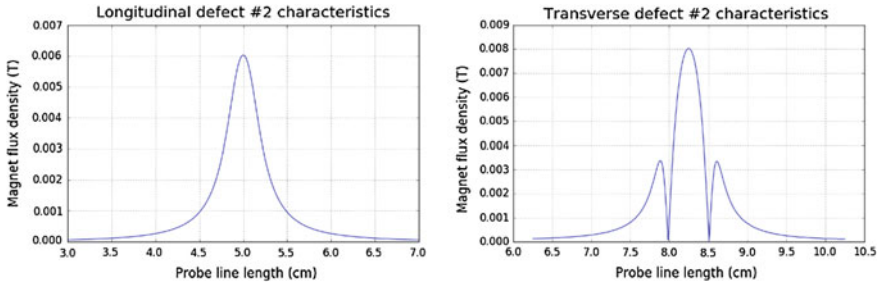

Fig. 32.10 Characteristics of transversely oriented defect; data from longitudinal scan-line (*left*), and from transverse scan-line (*right*)

50% relatively to the pipe wall thickness. Defect width h ranges from 1 to 50% relative to the pipe wall thickness. The depth of the defect y_0, determined in the range of minimum and maximum values, is defined by the limit values: 10% indentation from the inner surface on the pipe wall thickness and 10% indentation from the outer surface on the pipe wall thickness. Moreover, we considered cases longitudinally and transversely oriented defects, surface defects, defects representing zero adhesion between the pipe wall and the coating, as well as simulated the effects of corrosion.

As a result, data characterizing the defects were obtained for different configurations of geometrical parameters (Figs. 32.9 and 32.10).

32.7 Applying Artificial Neural Networks

To determine non-linear relationships between the defect parameters (height, width, depth) and the output data of the inspected object (amplitude-frequency characteristics in the first case and magnetic flux density in the second case), an approach based on artificial neural networks is applied. Neural networks are a tool of

non-linear simulations. Usually they are used to model complex relationships between inputs and outputs in order to find regularities in the data.

For the reconstruction of the geometric parameters of the defects, the multilayer feed-forward networks (Feed-forward neural networks, FFNN) are applied. The following learning algorithms were used:

(i) RProp (Resilient back propagation) used only the sign of the partial derivative, which acts independently on each synaptic weight.
(ii) BP (Back Propagation) is the most common method of teaching FFNN. For training, we used antigradient network errors.

Creation of the training set is an important step in problem solving. The set effect on further education, functioning and efficiency of artificial neural networks.

In the case of ultrasonic inspection method, to obtain the amplitude–frequency characteristics of the oscillations of the studied object, the discrete Fourier transform (DFT) is used. So we obtain pairs of frequency and amplitude values. Then, the most relevant of these pairs are selected. Each of crack parameter sets corresponds to a specific ultrasonic-wave characteristic [16–18].

As a result, the prepared training vector consists of ten amplitude-frequency pairs for each of the received signals and their time ranges. To train the ANN coding a training set into the input vectors of ANN is performed. Part of the encoding procedure is to normalize the data. The normalization means the mapping data in the interval [−1, 1]. Well-proven features of Fast Artificial Neural Network library (FANN) were used for the organization of the process of training and testing neural networks.

After the end of the learning process of the neural network, the process of testing begins. It is previously unknown data given to the input of the neural network, and the output values are obtained, that characterize parameters of the defect or its type.

In the case of ultrasonic inspection method, we established that the most optimal activation functions in the context of the formulated problem were the hidden Sigmoid Stepwise (step-by-step approximation to sigmoid function) and output Sin Symmetric (periodic sinusoidal activation function) functions. The most optimal algorithm of neural network learning for solving the formulated problem is Resilient Propagation (RProp). We used 10,000 epochs; this number is the most reasonable for correct artificial neural network learning and for providing a satisfactory level of its performance.

In the case of a magnetic flux inspection, the following data are used to construct the training set: in the case of longitudinal scan line, there are peaks of the surge, as well as the ratios of width at several levels, to its peak value. In the case of transverse scan line, there are several peaks characteristic of the surge, as well as the ratios of width at several levels, to its maximum peak value, as shown in Fig. 32.11.

As a result, the prepared learning vector consists of 9 values: $(k_1, k_2, k_3, w_1, w_2, w_3, w_4, w_5, w_6)$. Where k_1, k_2, k_3 are the peak values of the surge, getting both from longitudinal and transverse scan lines; w_1–w_6 are the ratios of width at several levels, to its peak value of k_1 (Fig. 32.11).

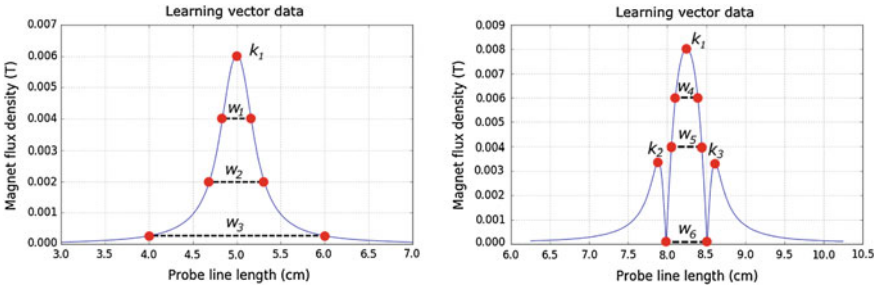

Fig. 32.11 Data for building ANN learning vectors

As a result of different variations of the geometric parameters, values of defects and their types were formed training sets which sizes make up 37,500, and 1200, respectively.

In contrast to previous work [15], it was decided to use several neural networks that solve the problem of reconstructing the defect parameters, thus improving the total efficiency of the ANN. Thus a separate neural network has been established to define each geometric defect parameter. As a result, the ANN were used with the following structures:

(i) (9-4-4-1), (9-6-6-1), (9-4-4-4-1) to determine the geometric parameters of the defect. Configuration (9-4-4-1) means that the neural network has nine input values, four neurons in the first hidden layer, four neurons in the second hidden layer and one output value.

(ii) (9-10-4-2) to determine the types of defects such as a zero adhesion, corrosion, surface defect and the defects between the pipe and coating. In this case, the structure has nine input values, ten hidden neurons in the first layer, four neurons in the second hidden layer, and two output values, which coding the defect type in binary format.

It was found that the most optimal activation function in the context of the problem, are hidden Sigmoid Stepwise (step-by-step approximation of a sigmoid function) and the output Sin Symmetric (periodic sinusoidal activation function). The optimal algorithm for training a neural network to solve the problem is the Resilient Propagation (RProp). In training process were used from 5000 to 15,000 epochs for different structures of artificial neural networks. That amount is the most acceptable for current task. In the case of using more number of training epochs, there are overfitting and paralysis occurs. Thus, such a number of periods are sufficient for correct training an artificial neural network, while achieving a satisfactory level of its operation. Earlier developed software-analytical system is used to establish the optimal structures of neural networks [19].

32.8 Results and Conclusions

The results were obtained using the trained ANN. The training sample was based on the data from the outer surface of the pipe, which modeled the echo method. The results obtained by the ANN were trained based on the data from both the outer and inner pipe surfaces. They are a result of the combination of the shadow and echo methods. It is noteworthy that a higher error of the ANN occurred at the value of the rotation angle of crack on 80°–100°.

Table 32.3 presents the results of the work of the artificial neural network at its different configurations. In the Structure column, the numbers of neurons in the input, hidden, and output layers are indicated. Tables 32.4 and 32.5 show the results of using the artificial neural network on the identification of different defect parameters.

The analysis of the obtained results showed that the average error in the defect identification in the case of the echo method was 22.74%; for the combination of the shadow and echo methods, it was 0.72%.

In the result of this study, the model implementing methods of magnetic flaw inspection coupled with approach of artificial neural networks was built. As part of the task identification and reconstruction of some defects, geometric parameters were found out.

These results indicate that the location and identification of the parameters of various defects (whose size is not less than 8.5% relatively to the pipe wall thickness) is possible with the use of neural network technology based only on the

Table 32.3 Results of the work of an artificial neural network at its different configurations with the use of the echo method and the combination of the shadow and echo methods

Structure	Error (%) (echo method)	Error (%) (combination)
21-12-3	35.9	2.4
21-15-3	29.2	3.2
21-24-3	**22.74**	1.8
21-12-6-3	33.4	**0.72**

Table 32.4 Results of the ANN performance (echo method)

Parameter	Error (%)
Depth of defect occurrence (y_0)	7.5
Size of the defect (l)	27.2
Position of the defect (angle of rotation) (α)	33.4

Table 32.5 Results of the ANN performance (combination of methods)

Parameter	Error (%)
Depth of defect occurrence (y_0)	0.1
Size of the defect (l)	0.3
Position of the defect (angle of rotation) (α)	1.78

Table 32.6 ANN error of height defect identification

ANN structure	Learning algorithm	Error (%)
(9-7-4-4-1)	RProp	22.3
(9-4-4-1)	**RProp**	**14.6**
(9-10-10-1)	RProp	17.9
(9-5-3-1)	BP	25.4

Table 32.7 ANN error of width defect identification

ANN structure	Learning algorithm	Error (%)
(9-3-5-5-3-1)	RProp	33.3
(9-6-6-1)	**RProp**	**21.5**
(9-15-5-1)	RProp	28.1

Table 32.8 ANN error of depth defect identification

ANN structure	Learning algorithm	Error (%)
(9-5-5-1)	RProp	18.2
(9-4-4-4-1)	**RProp**	**4.2**
(9-4-3-1)	BP	10.7

information about the density of the magnetic flux, obtained from the outer surface of the control object.

Tables 32.6, 32.7 and 32.8 demonstrate the results of defect identification with different neural network structures, learning algorithms and defect types.

Configured and trained neural networks to determine the defect type showed the following results:

(i) defect simulating zero adhesion between the pipe and the coating has been identified in 371 cases out of 400 (ANN operation error: 7.25%);
(ii) defect representing corrosion at the outer surface of the tube has been identified in 22 cases out of 400 (ANN operation error: 94.5%);
(iii) defect, located between the pipe and the coating, was identified in 388 cases out of 400 (ANN operation error: 3%);
(iv) surface defect was identified successfully in all cases.

In conclusion, it should be noted that the proposed methods of identification of crack-like defects solve successfully the problem. Moreover, proposed methods complement each other; it makes them suitable for the identification of various defects configurations.

Acknowledgements This work was supported by internal Grant of DSTU and RFBR No. 14-08-00142_a.

References

1. V.G. Gerasimov, A.D. Pokrovskii, V.V. Sukhorukov, *Non-Destructive Testing* (High School, Moscow, 1992) (in Russian)
2. I. Ermolov, N. Aleshin, A. Potapov, *Non-Destructive Testing* (High School, Acoustic Methods of Control, Moscow, 1991) (in Russian)
3. M.A. Willcox, *A Brief Description of NDT Techniques* (NDT Equipment Limited, Toronto, 2003)
4. I.G. Derenskii, in *Don Engineering Vestnik,* vol. 1 (2011) (in Russian). http://ivdon.ru/magazine/archive/n1y2011/370
5. A.O. Vatul'yan, *Inverse Problems in the Mechanics of Deformable Solids* (Fizmatlit, Moscow, 2007) (in Russian)
6. D. Stegemann, B. Raj in *Encyclopedia of Materials: Science and Technology*, vol. 1 (2002)
7. P. Wang, Y. Gao, G.Y. Tian, H. Wang, NDT&E Int. **64**, 7 (2014)
8. Y. Sun, Y. Kang, Chen Qiu, NDT&E Int. **44**, 1 (2011)
9. B.J. Nestleroth, R.J. Davis, NDT&E Int. **40**, 77 (2007)
10. A.N. Solov'ev, P.S. Kurbatova, N.I. Saprunov, S.N. Shevtsov, in *Proceedings of the X International Conference on Current Problems of the Continuum Mechanics*, Rostov-on-Don, (2006), p. 175 (in Russian)
11. A.S.N. Huda, S. Taib, K.H. Ghazali, M.S. Jadin, ISA Trans. **53**, 717 (2014)
12. A.N. Soloviev, C.H. Nguyen, Vestn. Don State Tech. Univ. **14**(2) (2014), p. 84 (in Russian)
13. A.N. Soloviev, N.D.T. Giang, S.H. Chang, in *Advanced Materials: Physics, Mechanics and Applications*, vol. 152. ed. by S.-H. Chang, I.A. Parinov, V.Y. Topolov (Springer Cham, Heidelberg, New York, Dordrecht, London, 2014), p. 137 (Chapter 12)
14. V. Novatskii, *Theory of Elasticity* (Mir, Moscow, 1975) (in Russian)
15. A.N. Solov'ev, B.V. Sobol', A.A. Krasnoshchekov, Russ. J. Non-destruct. Test. **8**, 23 (2014)
16. A.N. Solov'ev, Z.C. Nguen, Ecol. Vestn. Sci. Cent. ChES **1**, 76 (2014) (in Russian)
17. R. Sikora, T. Chady, Int. J. Appl. Electromagn. Mech. **9**(4), 391 (1998)
18. Z. Waszczyszyn, L. Ziemianski, Comput. Struct. **79**(22–25), 2261 (2001)
19. B.V. Sobol, P.V. Vasiliev, in *Proceedings of the Conference* "*Modern Problems of Multi-level Education*", Rostov-on-Don, 27 Sept–4 Oct 2013 (in Russian)

Chapter 33
Indentation of a Functionally Graded Coating on an Elastic Substrate by a Sphero-Conical Indenter

Leonid I. Krenev, Evgeniy V. Sadyrin, Sergey M. Aizikovich and Tatiana I. Zubar

Abstract In the present chapter, the axially symmetric static elastic contact problem about the interaction of a smooth sphero-conical punch and an inhomogeneous layer bonded to an elastic half-space is considered. Young's modulus and Poisson ratio of the layer vary by depth according to arbitrary functional laws. The mixed problem on indentation of a sphero-conical punch into a continuously inhomogeneous half-space is reduced to a system of dual integral equations. The kernel transforms are approximated with the expressions of special kind, allowing us to obtain the analytical solution. Using the asymptotic method, the numerically analytical approximate solution is constructed.

33.1 Introduction

Creation of thin films and coatings on surface of machine parts can significantly change their physical and mechanical properties, without affecting the volume. The construction of modern coatings is aimed at creating, on the one hand, thinner coatings, and on the other hand, inhomogeneous coatings of complex structure (multilayered or functionally graded coatings [1]). Complex microstuctured coatings are discussed in [2]. High performance of these coatings is achieved due to the

L.I. Krenev · E.V. Sadyrin (✉) · S.M. Aizikovich
Research and Educational Center "Materials",
Don State Technical University, 1, Gagarin Square,
Rostov-on-Don 344000, Russia
e-mail: evgeniy.sadyrin@gmail.com

L.I. Krenev · S.M. Aizikovich
I.I. Vorovich Institute of Mathematics, Mechanics
and Computer Science, Southern Federal University,
8a, Milchakov Street, Rostov-on-Don 344090, Russia

T.I. Zubar
A.V. Luikov Heat and Mass Transfer Institute, National Academy
of Sciences of Belarus, 15 P. Brovka Street, Minsk 220072, Belarus

I.A. Parinov et al. (eds.), *Advanced Materials*, Springer Proceedings
in Physics 193, DOI 10.1007/978-3-319-56062-5_33

combination of the properties of materials from which the coating consists. Such coatings can be used for wear [3], corrosion [4], erosion [5, 6] protection, in medicine [7], aerospace industry [8], nano- and microelectronics [9] etc. To study, certify and perform diagnostics of such coatings nano- and microindentation methods are becoming increasingly popular [10]. For delicate researches the spherical indenters are often used, which are typically made as sphero-cones [11]. Indentation analysis of complex structured coating requires development of appropriate mathematical models. Usually unloading part of experiment is assumed to be fully elastic [11], and such modeling can be done in the framework of the theory of elasticity. Some elastic contact problems for functionally graded coatings were considered in [12]. Indentation of a blunted conical indenter into a multi-layered coating, that can be considered as an elastically graded material with constant piecewise distributions of characteristics, was previously studied in [13], where the authors reduced the problem to a Fredholm integral equation and then solved it numerically. Another approach is to use special analytical approximation of the kernel transform of integral equation of the problem, which allows one to obtain solution in analytical form [14]. In [15], this method was used to solve the axisymmetric problem about indentation of a soft functionally graded elastic coating by a flat-based punch. In the present chapter, we used this approach to construct the numerical analytical solution of axially symmetric static problem about elastic indentation of a smooth sphero-conical indenter into an inhomogeneous layer (coating), bonded to an elastic half-space (substrate).

33.2 Problem Statement

Let us consider the half-space Ω. Its mechanical characteristics vary continuously by depth within the layer adjacent to the surface, then stabilize and remain constant further on. The layer thickness is H. The cylindrical coordinate system (r, φ, z) is associated with the half-space. We assume that $0 \le r < \infty$, and $z < 0$. Let us denote the displacements along the axes (r, φ, z) as u, v, w. We also denote radial, angular, normal and tangential stresses as $\sigma_r, \sigma_\varphi, \sigma_z, \tau_{r\varphi}, \tau_{rz}, \tau_{\varphi z}$, respectively.

The rigid blunt conical punch indents into the surface Γ of the half-space Ω. The sphere is located at the top of the punch, it is approximated by the parabolic surface. Under the load P the indenter moved over the distance δ along the z-axis. We consider that the punch surface is described by the quadratic function $z = \varphi_1(r) = -\delta + (1/2R)r^2$, $r \le r_1$ in the vicinity of the initial point of contact. Further the punch shape is described by the linear function $z = \varphi_2(r) = \alpha + \mathrm{tg}(\beta)r$, $r_1 \le r \le a$. Outside the indenter the surface of the half-space is not loaded.

In what follows we assume that the Lame coefficients $M(z)$ and $\lambda(z)$ are continuous functions of z-coordinate such that

$$\begin{aligned}
&1.\ \mathrm{M}(z) = \mathrm{M}(-H) = \mathrm{M}^S, \quad \Lambda(z) = \Lambda(-H) = \Lambda^S - \infty \le z \le -H \\
&2.\ \mathrm{M}(z) = \mathrm{M}^C(z), \quad \Lambda(z) = \Lambda^C(z), \quad -H \le z \le 0 \\
&3.\ \mathrm{M}^C(-H) = \mathrm{M}^S, \quad \Lambda^C(-H) = \Lambda^S
\end{aligned} \tag{33.1}$$

where H is the thickness of the inhomogeneous layer bonded to the underlying half-space, i.e. the depth from which we assume the thermo-mechanical characteristics of the half-space to be constant. The upper index S corresponds to the underlying homogeneous half-space, the upper index C corresponds to the inhomogeneous layer, $\Lambda_*,\ \Lambda^*,\ \mathrm{M}_*,\ \mathrm{M}^*$ are arbitrary constants.

Along with a pair of Lame coefficients for describing the elastic behavior of isotropic solid we used: shear modulus G and Poisson ratio v or Young's modulus E and Poisson ratio v, which are connected with Lame coefficients Λ and M as

$$G = \mathrm{M} = \frac{E}{2(1+v)}, \quad \Lambda = \frac{Ev}{(1+v)(1-2v)}, \quad E = \frac{\mathrm{M}(2M+3\Lambda)}{M+\Lambda}, \quad v = \frac{\Lambda}{2(\mathrm{M}+\Lambda)} \tag{33.2}$$

Under the action of the central applied force P the punch moved over the distance δ along the axis z. The boundary conditions at the assumptions made and in the condition of smooth sphere and cone connection are of the form

$$\begin{aligned}
&z = 0,\ \tau_{zr} = \tau_{z\varphi} = 0,\ \begin{cases} \sigma_z = 0, & r > a \\ w = -\delta + r^2/2R, & 0 \le r \le r_1 \\ w = -\delta_1 + \mathrm{tg}(\beta)(r - r_1), & r_1 \le r \le a \end{cases} \\
&\mathrm{tg}(\beta) = r_1/R
\end{aligned} \tag{33.3}$$

At the boundary of the bonding of the inhomogeneous layer with the homogeneous half-space, when $z = -H$ due to continuity of the bonding conditions for displacements and their derivatives must be carried out:

$$\sigma_z^C(r,-H) = \sigma_z^S(r,-H),\ \tau_{rz}^C(r,-H) = \tau_{rz}^S(r,-H), u^C(r,-H) = u^S(r,-H), \tag{33.4}$$

$$w^C(r,-H) = w^S(r,-H)$$

At infinity, when $(r,-z) \to \infty$ displacements, strains and stresses disappear:

$$\lim_{z\to-\infty}\left(u, w, \varepsilon_r, \varepsilon_\varphi, \varepsilon_z, \varepsilon_{rz}, \sigma_r, \sigma_\varphi, \sigma_z, \tau_{rz}\right) = 0, \lim_{r\to\infty}\left(u, w, \varepsilon_r, \varepsilon_\varphi, \varepsilon_z, \varepsilon_{rz}, \sigma_r, \sigma_\varphi, \sigma_z, \tau_{rz}\right) = 0. \tag{33.5}$$

It is required to determine the distribution of the contact normal stresses under the punch.

33.3 Construction of the Closed Approximate Numerical Analytical Solution

We use the results obtained in [15]. Let us make the change of variables and denote:

$$\lambda = H/a; \quad r' = r/a; \quad \rho' = \rho/a; \quad L'(\gamma) = L(\gamma, 0), \quad \beta'(\rho' a) = \beta(\rho), \quad r_1' = r_1/a, \quad R' = R/a. \tag{33.6}$$

(hereinafter we omit the primes), we find that the problem is reduced to solving the system of dual integral equations of the form:

$$\begin{cases} \begin{cases} \int\limits_0^\infty P_1(\gamma) L(\lambda\gamma) \mathrm{J}_0(r\gamma) d\gamma = \Delta(0)(-\delta + \frac{1}{2R} r^2 - \frac{1}{2R} r_1^2 + \delta_1 - \mathrm{tg}(\beta)(r - r_1)), & r \le r_1 \\ \int\limits_0^\infty P_1(\gamma) \mathrm{J}_0(r\gamma) \gamma d\gamma = 0, & r \ge r_1 \end{cases} \\ \begin{cases} \int\limits_0^\infty P_2(\gamma) L(\lambda\gamma) \mathrm{J}_0(r\gamma) d\gamma = \Delta(0)(-\delta_1 + \mathrm{tg}(\beta)(r - r_1)), & 0 \le r \le 1 \\ \int\limits_0^\infty P_2(\gamma) \mathrm{J}_0(r\gamma) \gamma d\gamma = 0, & r > 1 \end{cases} \end{cases}$$
$$\Delta(0) = 2\mathrm{M}(0)(\Lambda(0) + \mathrm{M}(0))(\Lambda(0) + 2\mathrm{M}(0))^{-1} \tag{33.7}$$

Using operators:

$$U_1^t \varphi(r) = \frac{d}{dt} \int\limits_0^t \frac{r\varphi(r) dr}{\sqrt{t^2 - r^2}}; \quad U_1^t J_0(r\gamma) = \cos t\gamma; \quad U_1^t 1 = 1; \quad U_1^t r = \frac{\pi}{2} t; \quad U_1^t r^2 = 2t^2; \tag{33.8}$$

$$U_2^t \varphi(r) = \int\limits_0^\infty \frac{r\varphi(r) dr}{\sqrt{r^2 - t^2}}; \quad U_2^t J_0(r\gamma) = \gamma^{-1} \cos t\gamma \tag{33.9}$$

we transform (33.7) to

$$\begin{cases} \begin{cases} \int\limits_0^\infty P_1(\gamma) L(\lambda\gamma) \cos t\gamma \, d\gamma = g_1(t) = \Delta(0) \left(-\delta + \frac{1}{R} t^2 - \frac{r_1^2}{2R} + \delta_1 - \frac{\pi}{2} \mathrm{tg}(\beta) t + \mathrm{tg}(\beta) r_1\right), & 0 \le t \le r_1 \\ \int\limits_0^\infty P_1(\gamma) \cos t\gamma \, d\gamma = 0, & r_1 < t < \infty \end{cases} \\ \begin{cases} \int\limits_0^\infty P_2(\gamma) L(\lambda\gamma) \cos t\gamma \, d\gamma = g_2(t) = \Delta(0) \left(-\delta_1 + \frac{\pi}{2} \mathrm{tg}(\beta) t - \mathrm{tg}(\beta) r_1\right), & \mathrm{r}_1 < t \le 1 \\ \int\limits_0^\infty P_2(\gamma) \cos t\gamma \, d\gamma = 0, & 0 \le t \le r_1, \quad 1 < t < \infty \end{cases} \end{cases} \tag{33.10}$$

We approximate the kernel transform of the dual integral equation using expression:

$$L(\lambda\alpha) = L_N(\lambda\alpha) = \frac{R_1(\lambda^2\alpha^2)}{R_2(\lambda^2\alpha^2)} = \prod_{i=1}^{N} \frac{\lambda^2\alpha^2 + A_i^2}{\lambda^2\alpha^2 + B_i^2} \tag{33.11}$$

and obtain the solution of the problem analytically.

Let us introduce the functions:

$$q(t) = \begin{cases} q_1(t) = \int\limits_0^\infty P_1(\alpha)\cos\,\alpha t d\alpha, & 0 \le t \le r_1 \\ q_2(t) = \int\limits_0^\infty P_2(\alpha)\cos\,\alpha t d\alpha, & r_1 < t \le 1 \end{cases} \tag{33.12}$$

Then (33.10) can be written as

$$\begin{aligned} R_1(-D)q_1(t) &= R_2(-D)g_1(t), \quad D = \frac{d^2}{dt^2}, \quad t \in [0; r_1] \\ R_1(-D)q_2(t) &= R_2(-D)g_2(t), \quad D = \frac{d^2}{dt^2}, \quad t \in [0; 1] \end{aligned} \tag{33.13}$$

where the polynomials R_1 and R_2 are defined as in (33.11).

The solution of differential equations (33.13) can be represented by the sum of the general solution of homogeneous equations and the specific solution of inhomogeneous equations in some parts of the domain:

$$q(t) = \begin{cases} q_1(t) = \Delta(0)\left[\sum\limits_{i=1}^{N} C_i^1\,\mathrm{ch}(A_i\lambda^{-1}t) + \sum\limits_{i=1}^{N} D_i^1\,\mathrm{sh}(A_i\lambda^{-1}t)\right. \\ \qquad \left. + L_N^{-1}(0)\left(-\delta + \frac{4S_1 - r_1^2}{2R} + \frac{1}{R}t^2 + \delta_1 - \frac{\pi t - 2r_1}{2}\mathrm{tg}(\beta)\right)\right], \quad 0 \le t \le r_1 \\ q_2(t) = \Delta(0)\left[\sum\limits_{i=1}^{N} C_i^2\,\mathrm{ch}(A_i\lambda^{-1}t) + \sum\limits_{i=1}^{N} D_i^2\,\mathrm{sh}(A_i\lambda^{-1}t)\right. \\ \qquad \left. + L_N^{-1}(0)\left(-\delta_1 + \frac{\pi t - 2r_1}{2}\mathrm{tg}(\beta)\right)\right], \quad 0 \le t \le 1 \end{cases} \tag{33.14}$$

where $S_1 = \lambda^2 \sum_{i=1}^{N} (A_i^{-2} - B_i^{-2})$, and coefficients $C_i^j, D_i^j, j = 1, 2; i = 1, 2, ..., N$ are unknown and determined further by substituting this type of solution into integral equation (33.10). Let us introduce the notation $\tilde{A}_i = A_i\lambda^{-1}, \tilde{B}_i = B_i\lambda^{-1}$.

Using the inverse Fourier transform in (33.14), we obtain the expression for $P(\alpha) = P_1(\alpha) + P_2(\alpha)$.

The expression for the distribution of contact normal stresses is obtained using the inverse Hankel transform:

$$
\begin{aligned}
p_1(r) = \frac{2}{\pi}\Delta(0)\Bigg\{ & -\frac{2}{R}L_N^{-1}(0)\sqrt{r_1^2 - r^2} \\
& + L_N^{-1}(0)\left(-\delta + \delta_1 + \frac{4S_1 + r_1^2}{2R} - \frac{(\pi - 2)\mathrm{tg}(\beta)r_1}{2}\right)\frac{1}{\sqrt{r_1^2 - r^2}} \\
& + L_N^{-1}(0)\frac{\pi}{2}\mathrm{tg}(\beta)\left(-\ln\left(\frac{1 + \sqrt{1 - r^2}}{\mathrm{r}_1 + \sqrt{r_1^2 - r^2}}\right)\right) \\
& + L_N^{-1}(0)\left(-\delta_1 + \frac{\pi - 2r_1}{2}\mathrm{tg}(\beta)\right)\frac{1}{\sqrt{1 - r^2}} \\
& + \sum_{i=1}^{N} C_i^2\left(\frac{\mathrm{ch}(\tilde{A}_i)}{\sqrt{1 - r^2}} - \tilde{A}_i\int_r^1 \frac{\mathrm{sh}(\tilde{A}_i x)dx}{\sqrt{x^2 - r^2}}\right) \\
& + \sum_{i=1}^{N} D_i^2\left(\frac{\mathrm{sh}(\tilde{A}_i)}{\sqrt{1 - r^2}} - \tilde{A}_i\int_r^1 \frac{\mathrm{ch}(\tilde{A}_i x)dx}{\sqrt{x^2 - r^2}}\right) \\
& + \sum_{i=1}^{N} C_i^1\left(\frac{\mathrm{ch}(\tilde{A}_i r_1)}{\sqrt{r_1^2 - r^2}} - \tilde{A}_i\int_r^{r_1} \frac{\mathrm{sh}(\tilde{A}_i x)dx}{\sqrt{x^2 - r^2}}\right) \\
& + \sum_{i=1}^{N} D_i^1\left(\frac{\mathrm{sh}(\tilde{A}_i r_1)}{\sqrt{r_1^2 - r^2}} - \tilde{A}_i\int_r^{r_1} \frac{\mathrm{ch}(\tilde{A}_i x)dx}{\sqrt{x^2 - r^2}}\right)\Bigg\}, \quad 0 \le r \le r_1 \\
p_2(r) = \frac{2}{\pi}\Delta(0)\Bigg\{ & -L_N^{-1}(0)\frac{\pi}{2}\mathrm{tg}(\beta)\left(-\ln\left(\frac{1 + \sqrt{1 - r^2}}{r}\right)\right) \\
& + L_N^{-1}(0)\left(-\delta_1 + \frac{\pi - 2r_1}{2}\mathrm{tg}(\beta)\right)\frac{1}{\sqrt{1 - r^2}} \\
& + \sum_{i=1}^{N} C_i^2\left(\frac{\mathrm{ch}(\tilde{A}_i)}{\sqrt{1 - r^2}} - \tilde{A}_i\int_r^1 \frac{\mathrm{sh}(\tilde{A}_i x)dx}{\sqrt{x^2 - r^2}}\right) \\
& + \sum_{i=1}^{N} D_i^2\left(\frac{\mathrm{sh}(\tilde{A}_i)}{\sqrt{1 - r^2}} - \tilde{A}_i\int_r^1 \frac{\mathrm{ch}(\tilde{A}_i x)dx}{\sqrt{x^2 - r^2}}\right)\Bigg\}, \quad r_1 < r \le 1
\end{aligned}
\tag{33.15}
$$

We assume that the transition from the sphere to the cone is smooth and the contact stresses are limited. Hence:

$$
\begin{aligned}
& L_N^{-1}(0)\left(-\delta + \delta_1 + \frac{4S_1 + r_1^2}{2R} - \frac{(\pi - 2)\mathrm{tg}(\beta)r_1}{2}\right) + \sum_{i=1}^{N} C_i^1\,\mathrm{ch}(\tilde{A}_i r_1) \\
& \quad + \sum_{i=1}^{N} D_i^1\,\mathrm{sh}(\tilde{A}_i r_1) = 0
\end{aligned}
\tag{33.16}
$$

The punch displacement δ is determined from the condition of the absence of stresses on the boundary of the contact zone: $p_2(1) = 0$

$$L_N^{-1}(0)\left(-\delta_1 + \frac{\pi - 2r_1}{2}\mathrm{tg}(\beta)\right) + \sum_{i=1}^{N} C_i^2 \,\mathrm{ch}(\tilde{A}_i) + \sum_{i=1}^{N} D_i^2 \,\mathrm{sh}(\tilde{A}_i) = 0$$

$$\delta = \left(\frac{\pi}{2}\,\mathrm{tg}(\beta)(1 - r_1) + \frac{4S_1 + r_1^2}{2R\lambda^2}\right) + L_N(0)\sum_{i=1}^{N} C_i^1 \,\mathrm{ch}(\tilde{A}_i r_1) + L_N(0)\sum_{i=1}^{N} D_i^1 \,\mathrm{sh}(\tilde{A}_i r_1)$$
$$+ L_N(0)\sum_{i=1}^{N} C_i^2 \,\mathrm{ch}(\tilde{A}_i) + L_N(0)\sum_{i=1}^{N} D_i^2 \,\mathrm{sh}(\tilde{A}_i) \tag{33.17}$$

The constants $C_i^j, D_i^j,\ i = 1\ldots N, j = 1, 2$ are determined from the system of linear algebraic equations obtained by substituting the expression for $P_1(\alpha)$, $P_2(\alpha)$ in (33.10):

$$\sum_{i=1}^{N} C_i^1 \tilde{A}_i \frac{\tilde{B}_m \,\mathrm{sh}(\tilde{A}_i r_1) + \tilde{A}_i \,\mathrm{ch}(\tilde{A}_i r_1)}{\tilde{B}_m^2 - \tilde{A}_i^2} + \sum_{i=1}^{N} D_i^2 \tilde{A}_i \frac{\tilde{B}_m \,\mathrm{ch}(\tilde{A}_i r_1) + \tilde{A}_i \,\mathrm{sh}(\tilde{A}_i r_1)}{\tilde{B}_m^2 - \tilde{A}_i^2}$$
$$= L_N^{-1}(0)\frac{2}{R}\frac{1 + \tilde{B}_m}{\tilde{B}_m^2}, \quad m = 1, 2, \ldots N,$$

$$\sum_{i=1}^{N} D_i^1 \frac{\tilde{B}_m \tilde{A}_i}{\tilde{B}_m^2 - \tilde{A}_i^2} + \sum_{i=1}^{N} D_i^2 \frac{\tilde{B}_m \tilde{A}_i}{\tilde{B}_m^2 - \tilde{A}_i^2} = 0, \quad i = 1, 2, \ldots N$$

$$\sum_{i=1}^{N} C_i^1 \frac{\tilde{A}_i \tilde{B}_m \,\mathrm{sh}(\tilde{A}_i r_1)\,\mathrm{ch}(\tilde{B}_m r_1) - \tilde{A}_i^2 \,\mathrm{ch}(\tilde{A} r_1)\,\mathrm{sh}(\tilde{B}_m r_1)}{\tilde{B}_m^2 - \tilde{A}_i^2}$$
$$+ \sum_{i=1}^{N} D_i^1 \frac{\tilde{A}_i \tilde{B}_m \,\mathrm{ch}(\tilde{A}_i r_1)\,\mathrm{ch}(\tilde{B}_m r_1) - \tilde{A}_i^2 \,\mathrm{sh}(\tilde{A}_i r_1)\,\mathrm{sh}(\tilde{B}_m r_1)}{\tilde{B}_m^2 - \tilde{A}_i^2}$$
$$= L_N^{-1}(0)\frac{\pi}{2}\,\mathrm{tg}(\beta)\frac{\mathrm{sh}(\tilde{B}_m r_1)}{\tilde{B}_m} + L_N^{-1}(0)\frac{2r_1}{R\tilde{B}_m^2}\left(\frac{\tilde{B}_m \,\mathrm{sh}(\tilde{B}_m r_1) - \mathrm{ch}(\tilde{B}_m r_1)}{\tilde{B}_m}\right), \quad m = 1, 2, \ldots N$$

$$\sum_{i=1}^{N} C_i^2 \frac{\tilde{A}_i \tilde{B}_m \,\mathrm{sh}(\tilde{A}_i) + \tilde{A}_i^2 \,\mathrm{ch}(\tilde{A}_i)}{\tilde{B}_m^2 - \tilde{A}_i^2} + \sum_{i=1}^{N} D_i^2 \frac{\tilde{A}_i \tilde{B}_m \,\mathrm{ch}(\tilde{A}_i) + \tilde{A}_i^2 \,\mathrm{sh}(\tilde{A}_i)}{\tilde{B}_m^2 - \tilde{A}_i^2}$$
$$= L_N^{-1}(0)\frac{\pi}{2}\,\mathrm{tg}(\beta)\frac{1}{\tilde{B}_m}, \quad m = 1, 2, \ldots N$$

Taking into account (33.16), (33.17), we write the expression for $p_1(r)$, $p_2(r)$:

$$p_1(r) = \frac{2}{\pi}\Delta(0)\left\{-\frac{2}{R}L_N^{-1}(0)\sqrt{r_1^2 - r^2} + L_N^{-1}(0)\frac{\pi}{2}\mathrm{tg}(\beta)\left(-\ln\left(\frac{1+\sqrt{1-r^2}}{\mathrm{r}_1+\sqrt{r_1^2-r^2}}\right)\right)\right.$$
$$- \sum_{i=1}^{N} C_i^2\left(\tilde{A}_i\int_r^1 \frac{\mathrm{sh}(\tilde{A}_i x)dx}{\sqrt{x^2-r^2}}\right) - \sum_{i=1}^{N} D_i^2\left(\tilde{A}_i\int_r^1 \frac{\mathrm{ch}(\tilde{A}_i x)dx}{\sqrt{x^2-r^2}}\right)$$
$$\left. - \sum_{i=1}^{N} C_i^1\left(\tilde{A}_i\int_r^{r_1} \frac{\mathrm{sh}(\tilde{A}_i x)dx}{\sqrt{x^2-r^2}}\right) - \sum_{i=1}^{N} D_i^1\left(\tilde{A}_i\int_r^{r_1} \frac{\mathrm{ch}(\tilde{A}_i x)dx}{\sqrt{x^2-r^2}}\right)\right\}, \quad 0 \le r \le r_1 \tag{33.18}$$

$$p_2(r) = \frac{2}{\pi}\Delta(0)\left\{-L_N^{-1}(0)\frac{\pi}{2}\mathrm{tg}(\beta)\left(-\ln\left(\frac{1+\sqrt{1-r^2}}{r}\right)\right)\right.$$
$$\left. - \sum_{i=1}^{N} C_i^2\left(\tilde{A}_i\int_r^1 \frac{\mathrm{sh}(\tilde{A}_i x)dx}{\sqrt{x^2-r^2}}\right) - \sum_{i=1}^{N} D_i^2\left(\tilde{A}_i\int_r^1 \frac{\mathrm{ch}(\tilde{A}_i x)dx}{\sqrt{x^2-r^2}}\right)\right\}, \quad r_1 < r \le 1 \tag{33.19}$$

The value of load P is determined from the equilibrium conditions for the indenter as

$$P = \frac{2\pi}{\lambda^2}\int_0^1 p(r)rdr = \frac{4}{\lambda^2}\int_0^1 q(t)dt.$$

Consequently,

$$P = \frac{4\Delta(0)}{\lambda^2}\left\{\left(-\frac{2r_1^3}{3R} - \frac{\pi}{4}\mathrm{tg}(\beta)(1-r_1^2) + \frac{2S_1 r_1}{R}\right)L_N^{-1}(0)\right.$$
$$+ \sum_{i=1}^{N} C_i^1\tilde{A}_i^{-1}\left(\mathrm{sh}(\tilde{A}_i r_1) - \tilde{A}_i r_1\,\mathrm{ch}(\tilde{A}_i r_1)\right) + \sum_{i=1}^{N} D_i^1\tilde{A}_i^{-1}\left(\mathrm{ch}(\tilde{A}_i r_1) - \tilde{A}_i r_1\mathrm{sh}(\tilde{A}_i r_1)\right)$$
$$\left. + \sum_{i=1}^{N} C_i^2\tilde{A}_i^{-1}\left(\mathrm{sh}(\tilde{A}_i) - \tilde{A}_i\mathrm{ch}(\tilde{A}_i)\right) + \sum_{i=1}^{N} D_i^2\tilde{A}_i^{-1}\left(\mathrm{ch}(\tilde{A}_i) - \tilde{A}_i\,\mathrm{sh}(\tilde{A}_i)\right)\right\} \tag{33.20}$$

33.4 Conclusion

In the present chapter, the numerical analytical solution of axially symmetric static problem about indentation of a smooth sphero-conical punch into an inhomogeneous layer, bonded to an elastic half-space is constructed. The kernel transforms of the systems of pair integral equations of the problem are approximated by the

expressions of a special kind, allowing us to obtain an approximate analytical solution. Expressions for displacements and load are derived. These expressions can be used for nanoindentation analysis of homogeneous and inhomogeneous coatings on elastic substrates.

Acknowledgements This work was supported by RFBR grant Nos. 15-07-05208-a, 15-57-04084-Bel_mol_a and BRFBR grant No. F15RM-069.

References

1. S.M. Aizikovich, V.M. Aleksandrov, A.S. Vasiliev, L.I. Krenev, I.S. Trubchik, in *Analytical Solutions of Mixed Axisymmetric Problems for Functional-Graded Media* (Moscow, Fizmatlit, 2011) p. 192 (in Russian)
2. V.A. Eremeyev, Acta Mech. **227**(1) (2016)
3. E. Sigolo, J. Soyama, G. Zepon, C. Shyinti Kiminami, W. Jose Botta , C. Bolfarini, Surf. Coat. Technol. **302** (2016)
4. H. Duan, K. Du, C. Yan, F. Wang, Electrochim. Acta **51** (2006)
5. O.V. Kudryakov, V.N. Varavka, I.Y. Zabiyaka, I.S. Morozkin, in *Proceedings of the XI International Conference* "*Fundamental and Applied Science*", vol. 19 (2015)
6. V.N. Varavka, O.V. Kudryakov, A.V. Ryzhenkov, in *Piezoelectrics and Nanomaterials: Fundamentals, Developments and Applications*, chap. 5 (Nova Science Publishers, NY, USA, 2015), p. 105
7. A. Simchi, E. Tamjid, F. Pishbin, A.R. Boccaccini, Nanomed. Nanotechnol. Biol. Med. **7** (2011)
8. G. Troncin, M.B. Marshall, Tribol. Int. **100** (2016)
9. A. Inberg, P. Livshits, Z. Zalevsky, Y. Shacham-Diamand, Microelectron. Eng. **98** (2012)
10. O.V. Kudryakov, V.N. Varavka, I.Y. Zabiyaka, I.S. Morozkin, Int. Res. J. **46**(4), part 2 (2016)
11. A.C. Fischer-Cripps, in *Nanoindentation* (Springer Science & Business Media, 2013), p. 198
12. M.A. Guler, F. Erdogan, Mech. Mater. **38**(7) (2006)
13. A. Constantinescu, A.M. Korsunsky, O. Pison, A. Oueslati, Int. J. Solids Struct. **50**(18) (2013)
14. S.M. Aizikovich, A.S. Vasiliev, J. Appl. Math. Mech. **77**(1) (2013)
15. S.S. Volkov, S.M. Aizikovich, Y. Wang, I. Fedotov, Acta Mech. Sin. **29**(2) (2013)

Chapter 34
Researching the Properties of Nanocomposite Coatings by the Methods of Indent-Diagnostics

V.N. Varavka, O.V. Kudryakov, I. Yu. Zabiyaka and I.S. Morozkin

Abstract In this paper, the thin coatings, consisting of various metal and ceramic alternating layers, have been chosen as object of researches. The coatings were deposited using an ion plasma spraying setup equipped with a magnetron evaporation system. The thickness of each of the layers has composed 8–30 nm, while the general thickness of the coating does not exceed 10 μm. Their strength and erosive properties have been investigated. The strength of coatings was characterized as a complex of the physical-mechanical properties, which are measured with use of various schemes of a discrete and continuous indentation and are defined by the term "indent-diagnostics". By results of researches a good correlation between data of indent-diagnostics of coatings and data of erosive tests is obtained. It has allowed us to recommend a methods of laboratory indent-diagnostics for an evaluation of the erosion resistance of nanocomposite coatings instead of conducting a complex bench or full-scale tests.

34.1 Introduction

One of the most common applied problems of diagnostics of materials is the reliable prediction of hardly identifiable performance properties of a material according to other characteristics of this material that can be measured using simple and standardized techniques and tests. This problem becomes even more complicated if the object of examination, measurement, and operation is a coating with micron thickness. This is true, for example, for the study of materials and coatings that are resistant to droplet impingement erosion. This kind of erosion is undergone

V.N. Varavka (✉) · O.V. Kudryakov · I.Yu. Zabiyaka
Don State Technical University, Rostov-on-Don, Russia
e-mail: varavkavn@gmail.com

I.S. Morozkin
Rostov State Transport University, Rostov-on-Don, Russia

I.A. Parinov et al. (eds.), *Advanced Materials*, Springer Proceedings in Physics 193, DOI 10.1007/978-3-319-56062-5_34

by the blade system of powerful steam turbines: the cooling steam becomes wet and the resulting drip condensate becomes a source of erosion of the turbine blades rotating at high speed. The resistance of the material of the blades to droplet impingement erosion can be measured only in cost-intensive long-term bench or full-scale tests. The theoretical works, which were devoted to studying of properties of nonhomogeneous coatings [1–3], deal with the general tendencies only, but do not consider peculiarities of a coating's structure and the complicated nature of external affects. These circumstances significantly limits possibilities of research and applied development of the whole group of functional materials to which also nanocomposite coatings belong.

34.2 Methods

34.2.1 Objective

The aim of this study was to examine the strength and erosion resistance of nanocomposite coatings, determine the correlation between these properties, and, as a consequence, explore the possibility of predicting the erosion resistance of coatings according to the strength properties of the coatings.

34.2.2 Object of Study

The following 2D metal-ceramic nanocomposite coatings were selected for the study: Ti/C, Ti/Mo, TiN/MoN, Ti/AlSi, TiN/AlSiN, Ti/Zr(Nb), and TiN/Zr(Nb)N. The coatings were deposited using an ion plasma spraying setup equipped with a magnetron evaporation system. The coating deposition modes were selected so as to provide the formation of dense (defect-free, nonporous) nanolayers with a nanocrystalline structure and compressive stresses in the coating. Samples of steel AISI 420 with a sorbitol structure (quenching + high-temperature tempering) with a surface roughness of R_z = 0.08 μm were used as a substrate. The chemical composition of the coating was determined by the composition of the magnetron target (electrode) and the composition of the gas in the vacuum chamber of the setup. The coating composition was additionally controlled using an X-Max EDAX energy-dispersive electron probe microanalyzer (Oxford Instruments); the amorphous components of the coatings were identified by X-ray diffraction analysis on a DRON-7 diffractometer using Fe$K\alpha$ radiation.

The structure of the nanocomposite coatings was studied using a Mira Tescan 3 LMU scanning electron microscope (SEM) operating in a wide range of magnifications including the nanolevel of the structure. The microstructures of some types of the studied coatings are shown in Fig. 34.1. The typical structure of a 2D-nanocomposite coating is shown in Fig. 34.1a. This structure was found in the

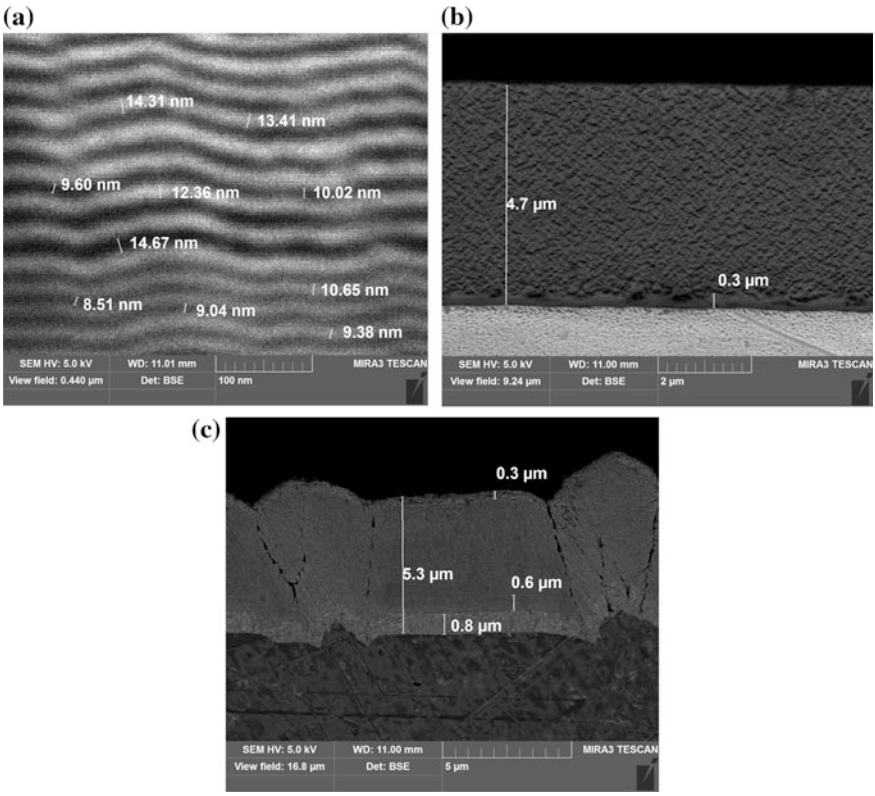

Fig. 34.1 Cross-sectional microstructure of the nanocomposite coatings (SEM images): **a** the nanolayers of the TiN/MoN coating, **b** the amorphized Ti/AlSi coating, and **c** the TiN/Zr(Nb)N coating

Ti/C, Ti/Zr(Nb), Ti/Mo, and TiN/MoN coatings. A characteristic feature of these coatings is the presence of dense defect-free nanolayers exhibiting no signs of a grain structure. Figure 34.1b shows an example of an amorphized structure of the coating. The formation of this structure is attributed to the presence of silicon in the system. Figure 34.1c shows the effect of the substrate topography on the coating quality: the initial surface roughness of the base metal (steel AISI 420) is responsible for the occurrence of growth defects, discontinuities, and stresses in the coating, which adversely affect both the strength and erosion resistance of the coating despite the presence of nanolayers in it.[1]

[1]A growth defect of a coating is understood as the violation of the homogeneity of a coating during the layer-by-layer deposition (growth) of the coating. For example, at a high roughness of the substrate, the layer-by-layer growth is violated, because the number of layers on the protrusions and depressions of the relief is not the same. This feature leads to the formation of internal interfaces (boundaries) and fragmentation of the coating structure.

34.2.3 Results

In this study, the physical-mechanical properties of coatings were examined by indentation and scratching at different scale levels under the action of varying indentation load. Vickers microhardness (*HV*) was determined using a DuraScan 20 hardness tester with the automatic (electro-optical) measurement of the indent. The nanohardness was determined using a NanoScan-3D scanning nanohardness tester (Technological Institute for Superhard and Novel Carbon Materials, Troitsk, Russia) under continuous instrumental indentation. The summarized results of measurements of the geometrical parameters of the coatings, obtained by SEM metallography, and the tensile properties, determined by the indentation method, are shown in Table 34.1. Despite the use of a load of 10 g, which is the minimum possible load for the DuraScan 20 instrument, the determined microhardness of the coatings of some systems was lower than the expected value. This fact is indicative of the effect of a "soft" substrate (steel AISI 420) and characterizes microhardness as a less reliable method for the diagnostics of these coatings than nanohardness.

The adhesion and scratch resistance of the coatings, the coefficient of friction between the different regions of the material, and other physical-mechanical properties were determined in sclerometric tests conducted using a multimodule scratch tester (CSM Instruments, Switzerland). Using the CSM scratch tester, the most informative data set with a wide range of strength parameters was derived. The nanocomposite coatings of all the studied systems were tested in the loading mode with a variable normal load linearly increasing from 0.03 to 30 N. The mode provided the indenter penetration through the entire thickness of the coating into the base metal at a scratching rate of 5 mm/min and a rate of rise of load to 30 N/min. The test time was 1 min; the scratch length was 5 mm. The scratch-test conditions are shown in Fig. 34.2a; one of the test results (for the TiN/AlSiN coating) is represented in Figures 34.2b–d.

The technique for determining the strength characteristics of the coating in the scratch tests was as follows. During loading, the instrument recorded plots of variation in the normal force, the coefficient and force of friction (Fig. 34.2b), the penetration depth of the indenter during the application of load, and the residual depth after the removal of load (Fig. 34.2c), as well as the signal of the acoustic emission sensor (Fig. 34.2d), whose reflections characterize the occurrence of cracks. The two axes of abscissas in Figures 34.2b–d are the scales of variation in load (in newtons) and crack length (in millimeters). The micrographs of the scratch (Figures 34.2b–d show the optical image of the scratch above the plots) are used to determine the time of crack nucleation in the coating (Lc1, not shown in Fig. 34.2) and the incipient (Lc2) and complete delamination of the coating (Lc3). In Figures 34.2b–d, the left-hand side of the scratch and the plots (to the left of Lc2) corresponds to the coating, while the right-hand side (to the right of Lc3) characterizes the base metal.

CSM scratch testers have a high-precision optical positioning system with a CCD camera that provides the examination of scratches at high magnifications. However, in some cases, the identification of the morphological features of the

Table 34.1 Results on the indentation of samples with nanocomposite coatings

Type of coating	Microhardness (at load of 10 g)	Indentation depth $h_{0.01}$ (μm)	Coating thickness h (μm)	Layer thickness (nm)	Continuous indentation	
					Nanohardness (GPa) (at load of 1 mN)	Elastic modulus E (GPa)
Ti/AlSi	499–655 $HV_{0.01}$	0.76-0.87	4.7–9.3	Amorph	7.2 (3.44*)–9.2**	148(76*)–232
Ti/Mo	776 $HV_{0.01}$	0.70	4.32	–	–	–
TiN/MoN	1974 $HV_{0.01}$	0.44	5.32	8.5-14.6	–	–
Ti/C	482 $HV_{0.01}$	0.89	2.2-2.9	10.1-12.5	7.1	179
Ti/Zr(Nb)	480 $HV_{0.01}$	0.89	5.4	10-12	7.36	141
TiN/Zr (Nb)N	270 $HV_{0.01}$	1.18	1.9-5.3	10.2-15.0	7.48	133
	–	–	7.1	25-30	3.95	180
TiN/AlSiN	948 $HV_{0.01}$	0.64	5.1	Amorph	8.01	166

*At a load of 10 mN

**In the cross-microsection

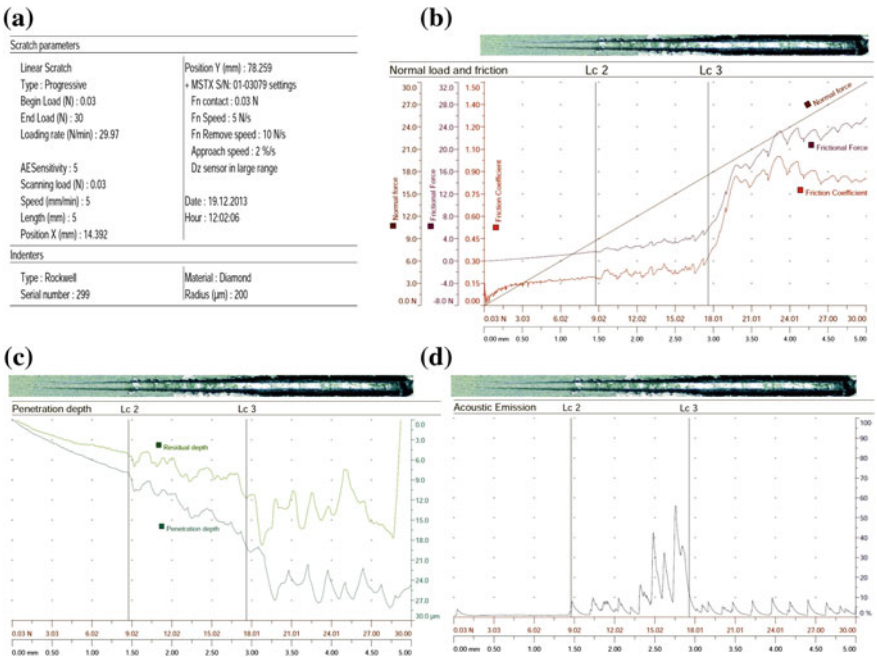

Fig. 34.2 Conditions (**a**) and results (**b–d**) of the scratch test of the nanocomposite coating of the TiN/AlSiN system: sclerometric force diagrams (**b**), the penetration depth of the indenter (**c**), and acoustic emission (**d**)

sclerometric surface required a higher resolution. To this end, SEM images of the scratch were used; the images were studied after a similar superposition on the sclerometric diagrams. In particular, Fig. 34.3 shows the SEM image of the same scratch as in the upper portion of Figures 34.2b–d, to be more precise, a fragment of the scratch in the region of incipient delamination of the coating (Lc2). In the phase contrast mode (see the right-hand side of Fig. 34.3), it is clearly evident that, for the TiN/AlSiN coating, the instants of crack nucleation (Lc1) and incipient delamination (Lc2) coincide. This feature is characteristic of thin hard coatings with a relatively low adhesion to the base metal. The capillary nature of the cracks before the cleavage regions in Fig. 34.3 suggests that the coating has an amorphous structure.

The results of determination of the physical-mechanical properties of the studied coatings using a multimodule CSM scratch tester are shown in Table 34.2. Here, the incipient delamination of the coating Lc2 is characterized by critical values of load P_1 and depth p_1, while the complete delamination Lc3 is described by critical values of P_2 and p_2, respectively.

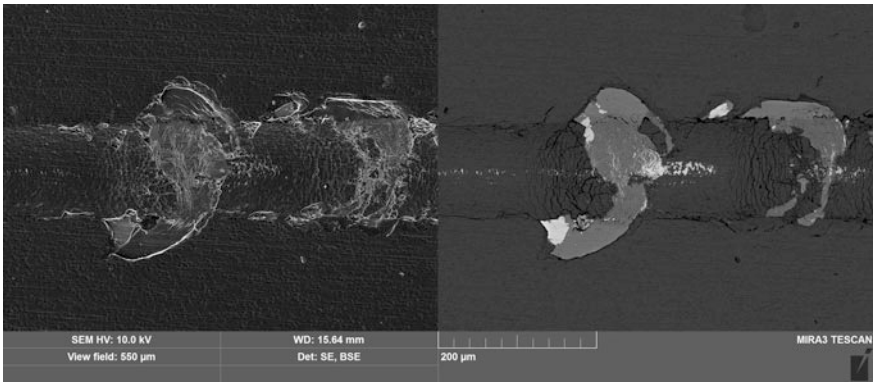

Fig. 34.3 Secondary electron (*left*) and backscattered electron (*right*) SEM images of the scratch of the TiN/AlSiN coating in the region of incipient delamination Lc2; the direction of travel of the indenter during scratching is from left to right

Table 34.2 Results on the indentation of samples with nanocomposite coatings

Type of coating	Critical applied load P_1 (N)	Critical depth* p_1 (μm)	Average friction coefficient in coating f_1	Average friction coefficient in substrate f_2	Critical tangential force N_1 (N)	Complete coating cleavage force P_2 (N)	Critical depth* p_2 (μm)
Ti/AlSi	3.54–6.39	1.65–3.1	0.165–0.226	0.9	0.54–0.7	12.7–17.0	2.30–8.75
Ti/Mo	–	–	0.3–0.477	0.85	3.37	6.89	2.30
TiN/MoN	8.3	3.13	0.05–0.27	0.35–0.6	2.55	14.3	3.41
Ti/C	6.89	5.15	0.3–0.9	1.0	5.86	–	–
Ti/Zr(Nb)	6.23	–	0.246	0.9	1.51	13.09	–
TiN/Zr(Nb)N	1.36–6.31	1.64–6.53	0.149–0.38	0.8–1.1	0.23–2.39	4.58–9.07	4.44–6.48
TiN/AlSiN	8.83	5.48	0.183	0.9	1.62	17.54	11.71

*Determined from the plot of residual depth (see the "Residual depth" curve in Fig. 34.2c)

34.2.4 Analysis

Analysis of the data on the physical-mechanical properties of the coatings derived by the different indentation methods (see Tables 34.1 and 34.2) shows that none of the properties taken separately can unambiguously and reliably characterize the erosion resistance of the coatings. Therefore, a multiparametric optimization [4] of the strength properties of the coatings was conducted via integrating the ray diagrams. An example of this diagram for nanocomposite coatings of three systems is shown in Fig. 34.4. The relative values of nine physical-mechanical properties listed in Tables 34.1 and 34.2 are plotted along the axes of the ray diagram: $HV_{0.01}$, nanohardness, E, P_1, p_1, f_1, N_1, P_2, and p_2. Since the number of parameters is quite

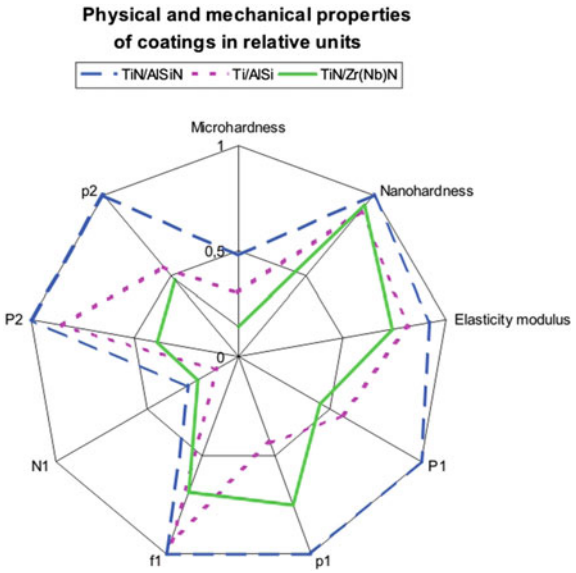

Fig. 34.4 Ray diagram of the physical-mechanical properties of nanocomposite coatings of the TiN/AlSiN, Ti/AlSi, and TiN/Zr(Nb)N systems according to the data of Tables 34.1 and 34.2

large (nine) and no correlations of each of the parameters taken separately with erosion-resisting properties have been revealed, upon switching to the relative values of the parameters, their coefficients of significance (specific weights) were assumed to be equally probable. The maximum value of the property obtained during the tests (concerning the coatings of all the seven studied systems) was taken as a unit of each of the parameters except for the friction coefficient, for which the minimum value was taken as a relative unit. The area of the polygon in the diagram corresponding to each of the coatings was used as an integrated statistical relative estimation of the strength of the coatings; it was an optimization variable: the larger the area of the polygon, the greater the total strength of the coating. Area S of the polygon was calculated as the sum of the areas of its constituent n triangles:

$$S = \frac{1}{2}\left[a_1 a_n + \sum_{i=1}^{n-1}(a_i a_{i+1})\right]\sin\frac{2\pi}{n}$$

where n is the number of rays (properties) of the diagram and a_i is the relative value of the property of the coating in the diagram.

According to the multiparametric optimization results, the ion plasma nanocomposite coatings of the studied systems can be arranged in the following descending order with respect to strength (i.e., the set of nine physic-mechanical properties): TiN/AlSiN, TiN/MoN, Ti/AlSi, Ti/C, Ti/Mo, Ti/Zr(Nb), TiN/Zr(Nb)N (Fig. 34.5). The fact that the TiN/Zr(Nb)N nitride system is the last in this series is attributed to the technological defects arising during formation—substrate topography, discontinuities, growth effects, and stresses—rather than to the nature and properties of the coating (see Fig. 34.1c).

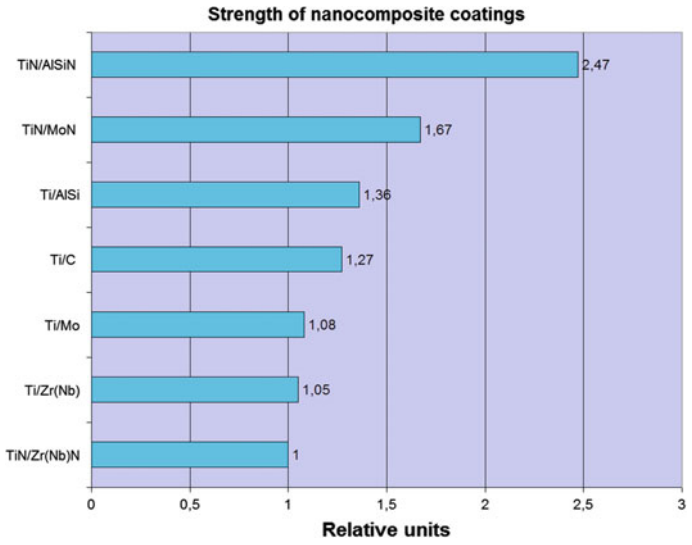

Fig. 34.5 Integrated strength of nanocomposite coatings of the different systems

Erosion tests were conducted, using a unique special-purpose Eroziya-M test bench of the Moscow Power Engineering Institute (National Research University), which is employed for studying the resistance of materials and coatings to the effects of a high-velocity stream of liquid droplets [5–7]. The bench provides the simulation of different conditions of interaction of the liquid particles with the surface of materials, in particular, real conditions of the droplet impingement erosion of the blades of steam turbines. In this case, the variational parameters are the droplet diameter d_{dr} = 20–1200 μm and the collision velocity of liquid droplets with samples C_{coll} = 200–600 m/s. The test results are used to plot curves of the erosive wear of materials or coatings at fixed values of C_{coll} and d_{dr} in coordinates of test time t (min) or erodent (liquid) flow rate m (kg/m^2) *versus* wear, i.e., the loss of sample weight M (kg). In the general case, the droplet-impingement erosion wear occurs in three successive stages: (i) incubation, during which $M = 0$; (ii) transition, which begins at time m_0 and where the development of wear occurs at a maximum average rate $\partial M/\partial m \rightarrow \max$; (iii) an asymptotic stage of steady wear, during which $\partial M/\partial m \rightarrow \min$ [8, 9].

In [10–12], it is shown that thin coatings perform a protective function only in the case of preservation of continuity. Therefore, comparison of the erosion resistance of the studied small-thickness nanocomposite coatings against each other and with other materials can be correctly conducted only according to the duration of incubation period m_0, during which the coating maintains its continuity. In addition, at the transition stage ($m > m_0$), there arises the problem of separating the contributions to the wear of the coating and the substrate. Therefore, the m_0 values of the materials and coatings obtained under identical conditions of bench tests were used as an antierosion index.

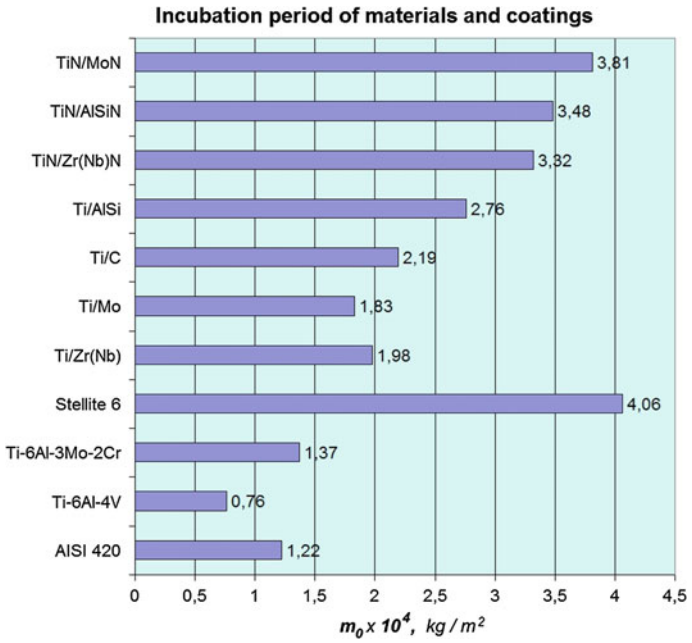

Fig. 34.6 Erosion resistance of typical blade materials and nanocomposite coatings of the different systems in the bench tests with the parameters of collision C_{coll} = 250 m/s and d_{dr} = 800 μm

To compare the erosion resistance indices, steel AISI 420 (a sorbitol structure after quenching and high-temperature tempering) is commonly taken as a base blade material (reference). The low m_0 value of the Ti-6Al-4V titanium alloy (see Fig. 34.6) is attributed to the fact that the samples were tested in an annealed state. The Ti-6Al-3Mo-2Cr alloy, in common with Ti-6Al-4V, is a two-phase titanium alloy ($\alpha + \beta$) of the martensite type. However, unlike Ti-6Al-4V, the Ti-6Al-3Mo-2Cr samples were tested in a precipitation-hardened state after quenching and aging.

The best results on erosion resistance are provided by the use of Stellite 6, which shows a multiple decrease in the rate of droplet-impingement erosion wear compared to other materials [7]. The m_0 value of this alloy is the highest (see Fig. 34.6). However, in terms of technology, ion plasma coatings are more promising than stellite, which is used to protect the blades in the form of cast plates welded or soldered to the leading edges of a blade. This feature significantly complicates the manufacturing technology of blades and causes the occurrence of stress concentrators in the blades.

Among the studied nanocomposite coatings, the amorphized coatings of the Ti/AlSi and TiN/AlSiN systems are more resistant to the effects of droplet impingement than pure metal composites. Under these conditions, the nanocomposites of nitride systems exhibit the highest erosion resistance. The m_0 value of

these composites is on the level of that of stellite. However, the most important result follows from comparison of the test data on the strength and erosion resistance of the ion plasma nanocomposite coatings: the sequence of arrangement of coatings in Figs. 34.5 and 34.6 is almost the same. An exception is provided by the coating of the TiN/Zr(Nb)N system, which had the lowest physical-mechanical properties (see Fig. 34.5) and exhibited one of the highest erosion resistances (see Fig. 34.6). This feature is attributed to the fact that the samples with this coating selected for strength tests had the above technological defects (see Fig. 34.1c) in order to show the effect of the quality of the coating on the properties thereof. In the preparation of the samples for erosion tests, these technological defects were eliminated.

It can be concluded that there is a satisfactory correlation between the set of physical-mechanical properties of the ion plasma nanocomposite coatings (nine characteristics obtained by the different indentation methods) and the erosion resistance of these coatings. This feature provides the possibility of a qualitative comparative prediction of the resistance of various coatings to droplet impingement erosion, which can be measured only in bench or full-scale tests, from the set of their physical-mechanical properties measured in the laboratory.

34.3 Conclusions

Thus, the used set of nine physical-mechanical properties that determine the strength of the coatings provides high coincidence with the results of erosion tests and can be recommended for the comparative characterization of the resistance of different coatings to droplet impingement erosion. In general, scratch tests provide more complete and accurate information on the erosion resistance of coatings than other types of indentation do. None of the nine measured properties of the coatings taken separately gave satisfactory agreement with the results of the erosion tests.

The nitride systems of nanocomposites exhibit the highest integrated strength (the set of nine studied physical-mechanical characteristics) and antierosion properties of all the examined coatings. A positive effect on these properties is also exerted by the amorphization of the coatings.

The quality of ion plasma coatings, which is determined by the preparation of the substrate surface and the technological mode of coating deposition, has a significant impact on the properties of the coatings. The presence of growth defects, porosity, and stresses in the coating and irregularities and discontinuities on the substrate surface dramatically reduces both the integral estimate of strength and the erosion resistance of the coating regardless of the coating composition. Using the example of the TiN/Zr(Nb)N coating, it has been shown that all the used indentation techniques are sensitive to these effects and nanoindentation exhibits the lowest sensitivity.

Acknowledgements The work was carried out with partial financial support from Russian Foundation for Basic Research (Project No. 15-08-06181).

References

1. S. Aizikovich, L. Krenev, I. Sevostianov, I. Trubchik, L. Evich, ZAMM – J. Appl. Math. Mech. **91**(6), 493 (2011)
2. S.S. Volkov, A.S. Vasiliev, A.A. Belov, SYu. Litvinchuk, S.M. Aizikovich, Int. J. Eng. Sci. **112**, 63 (2017)
3. L.I. Krenev, S.M. Aizikovich, Y.V. Tokovyy, Y.-C. Wang, Int. J. Solids Struct. **59**, 18 (2015)
4. I.G. Zedgenidze, *Planning of Experiment for Studying Multicomponent Systems* (Nauka, Moscow, 1976), p. 390 (in Russian)
5. L.I. Seleznev, V.A. Ryzhenkov, Technol. Metal. **3**, 19 (2007) (in Russian)
6. V.A. Ryzhenkov, A.I. Lebedeva, A.F. Mednikov, Therm. Eng. **58**(9), 713 (2011)
7. A.F. Mednikov, V.A. Ryzhenkov, L.I. Seleznev, A.I. Lebedeva, Therm. Eng. **59**(5), 414 (2012)
8. V.N. Varavka, O.V. Kudryakov, J. Friction Wear **36**(1), 71 (2015)
9. V.N. Varavka, O.V. Kudryakov, J. Friction Wear **36**(2), 153 (2015)
10. O.V. Kudryakov, V.N. Varavka, J. Strength. Technol. Coat. **10**, 40 (2012) (in Russian)
11. O.V. Kudryakov, V.N. Varavka, I.Y. Zabiyaka, I.S. Morozkin, in *Proceedings of the XI International Conference* "*Fundamental and Applied Science*". Technical Sciences, vol. 19 (Science and Education Ltd, Sheffield, GB, 2015), p. 6
12. O.V. Kudryakov, V.N. Varavka, I.Y. Zabiyaka, I.S. Morozkin, Int. Res. J. **46**(4), part 2, 117 (2016)

Chapter 35
The Influence of the Elemental Composition of Friction Materials on the Composition, Microrelief and the Mechanical Characteristics of Metal Counterbody's Surface Layers

Andrey V. Sidashov, Alexey T. Kozakov, Vladimir I. Kolesnikov and Vladimir P. Sergienko

Abstract Experimental study of microscopic mechanisms of interaction of polymer composite materials and counterbody metal in a friction unit are carried out. Polymer composites were modified by introduction of various additives containing boron, alkali metals, tungsten and others. The analysis of the surface topography of the counterbody material was conducted by using atomic force microscopy. Electron microscopy and X-ray photoelectron spectroscopy were applied for the interpretation of the obtained results. It is shown that by changing the modifying additives in the material matrix and varying friction modes it is possible both to control the composition of the frictional transfer film on the metal counterbody and to change the microrelief of metal.

35.1 Introduction

The problem of increasing the wear resistance of materials in tribological conjunction railway wheel—polymer composite brake shoe is an important scientific and technical task for railway transport [1]. One of the promising ways to solve this

A.V. Sidashov (✉) · V.I. Kolesnikov
Rostov State Transport University, 2 Narodnogo Opolcheniya,
Rostov-on-Don 344038, Russia
e-mail: sav_teor_meh@rgups.ru

A.T. Kozakov
Scientific Research Institute of Physics, Southern Federal University,
194, Stachki Avenue, Rostov-on-Don 344090, Russia
e-mail: kozakov_a@mail.ru

V.P. Sergienko
V.A. Biely Metal-Polymer Research Institute, National Academy of Sciences
of Belarus, 32 a, Kirova Street, Gomel 246050, Belarus

I.A. Parinov et al. (eds.), *Advanced Materials*, Springer Proceedings
in Physics 193, DOI 10.1007/978-3-319-56062-5_35

problem is to study the microscopic mechanisms of interaction of polymer composite materials with metal.

The composition of surface layers at undamaged parts of the working surface of the railway wheel, at the surface of various defects and in depth of wheel tread was experimentally and theoretically studied in a range of scientific works [2–6]. It was found that there are certain exchange diffusion processes between metal of the wheel surface and material of composite brake shoe. These processes lead to transferring of atoms of chemical elements, entering into the composition of contacting materials, from one surface to another [3, 4].

Further, under the influence of temperature and power factors in a friction unit, the transferred atoms of elements entering into the friction materials diffuse from the wheel surface into depth of metal, and then they are found in large quantities at grain boundaries. In [4], it was shown that, after segregating at grain boundaries of the wheel surface layer, atoms of elements both of impurity composition of the metal wheel and transferred from the brake shoe material can embrittle grain boundaries and reduce the strength and wear resistance of the wheel surface layer.

According to some segregation theories, atoms on grain boundaries of a polycrystalline metal can not only reduce its strength properties, but also improve them [7]. In metallurgical engineering, it is known that mechanical properties of bulk, grain boundaries and binding forces between grains can be controlled by adding a small amount of alloying elements into the bulk of metal at the production stage and purifying steel from harmful impurity such as sulfur, phosphorus, bismuth, etc. [8]. In this regard, in [2] it was proposed to use segregation mechanisms for hardening the surface layers of the wheel by introduction of small amounts of modifying additives into the structure of a composite brake shoe. In this case, at the process of unsteady friction, atoms of the additives could be transferred onto the working surface of the wheel and facilitate hardening of metal structure. According to [7], atoms of boron, molybdenum, and tungsten proved to be at grain boundaries in the binary and ternary metal systems strengthen bonding forces between the grains, while atoms of alkaline metals such as sodium, potassium or barium occurred at grain boundaries cause their embrittlement. It is typical for industrial steels and alloys as well. Authors of [9, 10] proved theoretically and experimentally that the modification of compositions of indenters' materials and surface layers of metal counterbodies with boron, molybdenum and tungsten compounds leads to hardening of their friction surface.

In this regard, one of the objectives of the present work is the development of the ideas represented in [9, 10] to study the composition of frictional transfer films and its influence on the morphology and wear properties of the metal counterbody, since the atoms of elements entering into the brake shoe material can penetrate onto grain boundaries only from the transfer films located on the wheel surface.

The aim of this work is the experimental confirmation of the presence of hardening modifying additives in transfer films caused by frictional interaction of metal-polymer pairs and studying their impact on the micro-relief of the metal counterbody surface.

35.2 Materials and Methods of Research

The commercial friction material containing synthetic rubber, phenol resins, various disperse fillers (metal barytes and oxides) and reinforcing mineral fibers were used as a basic composition of friction material. The compounds containing boron, alkali metals, tungsten: borax + WO_3, technical borax ($Na_2B_4O_710H_2O$; Russian National Standard 8429-77), KBF_4 were used as target modifying additives for commercial friction materials. Table 35.1 presents the compositions of the materials.

The chemical composition and chemical bonding in transfer films were studied by X-ray photoelectron spectroscopy using a system of surface analysis SPECS. The topography analysis of the friction surface of the metal counterbody was carried out with atomic force microscopy (AFM) using a scanning probe microscope Solver-47 M (NT-MDT). To scan it, a probe NSG11 in a static contact mode was used. Clamping force of the probe to surface was 1 μN. The scanning was carried out on areas of 50 × 50 μm^2, 10 × 10 μm^2, 3 × 3 μm^2. Before scanning, the samples were sustained in acetone and ethanol for 24 h, and then washed with distilled water. Programs Callisto, N_Surf and Nova were used for signal processing and analysis of the surface roughness.

Tribological tests were carried out on a laboratory tribometer according to the scheme "rotating disk—fixed indenter". The scheme of the test is shown in Fig. 35.1. The pressure in the friction unit was 1.0 and 3.0 MPa, linear sliding velocity is 1.0 and 5.0 m/s, and friction time is 10 h. For friction wear tests metal samples of counterbodies were made of high carbon steel 65G (Russian National Standard 14959-79), which is similar in chemical composition to the metal of the wheel steel [2, 11].

35.3 Research of Friction Surface Microrelief

AFM methods were used to carry out the analysis of 12 samples of metal counterbodies after the friction tests, and a steel sample before the test. 12 samples were grouped into 6 groups. In each group, a friction pair consists of materials of the same composition but of different friction modes. Data about the composition of the samples and test modes are shown in Table 35.1.

The analysis of the surface geometry at a level below 1 μm was conducted by Fourier transform of topography image and by filtered images. In Fourier transform there were found the wavelengths corresponding to the maximum spectral power of the image. On the prepared initial and filtered images subjectively there were chosen three largest, three average and three smallest structural elements (grains). Then there were determined diameter of the round grains and the width and length of the elongated ones. A statistical analysis of the results was carried out for each of the three selections.

Table 1 Composition of friction materials and friction modes of the samples

Properties		Number of metal counterbody's sample											
		1	2	3	4	5	6	7	8	9	10	11	12
		Group of materials											
		I		II		III		IV		V		VI	
Friction modes	Velocity (m/s)	1	5	1	5	1	5	1	5	1	5	1	5
	Pressure (MPa)	1	1	1	3	1	3	1	3	1	3	1	3
Research method		XPS AFM		AFM		XPS AFM		XPS AFM		AFM		XPS AFM	
The composition of the friction pair (mass.% additive)		Basic composi-tion (BC)		BC + borax + WO_3 (2.5%)		BC + borax + WO_3 (5%)		BC + borax (5%)		BC + $K[BF_4]$ (2.5%)		BC + K $[BF_4]$ (5%)	

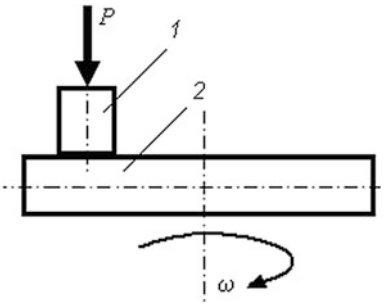

Fig. 35.1 Scheme of tribological tests: *1* fixed indenter, *2* rotating disk [9, 10]

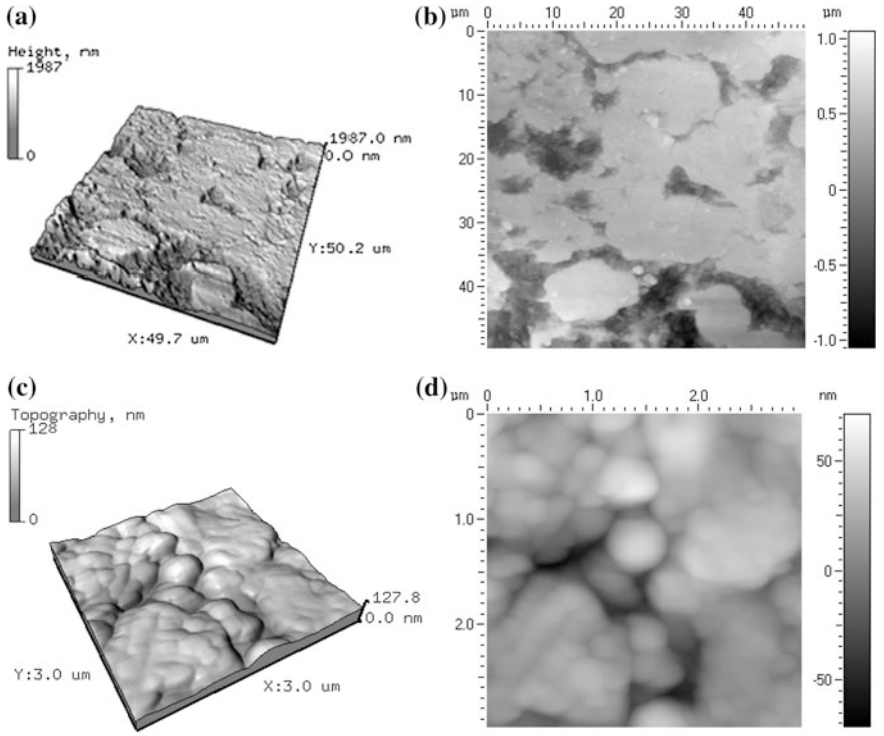

Fig. 35.2 The topography of steel counterbody surface before friction loading (scanning area **a**, **b** —50 × 50 µm^2, **c**, *d*—3 × 3 µm^2)

Figures 35.2, 35.3, 35.4, 35.5 and 35.6 present the results of the friction surface topography studies: (i) the initial metal counterbody not subjected to friction loading; (ii) unmodified basic composition of friction material and metal pair after friction (samples 1 and 2 in Table 35.1); (iii) after friction in pair with a friction material,

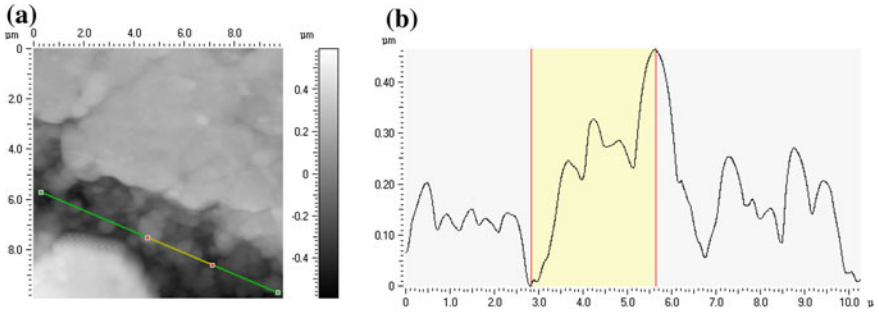

Fig. 35.3 Topography (**a**) and the profile along the chosen direction of the sample surface (**b**), not subjected to friction tests (10 × 10 μm^2)

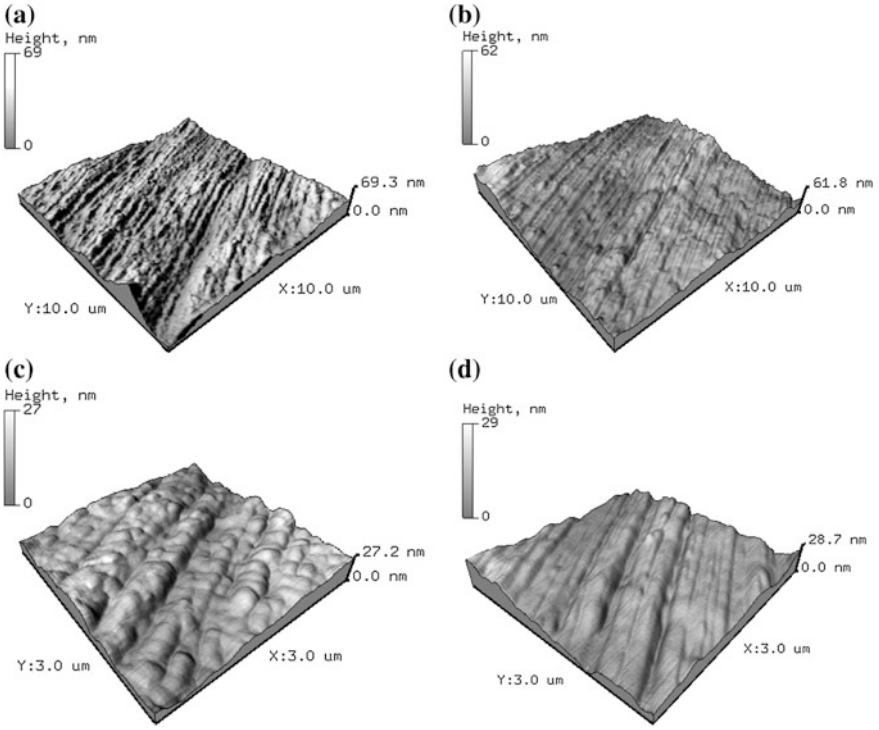

Fig. 35.4 Topography of the friction surface of samples No. 1 from Table 35.1 (**a**, **c**) and No. 2 (**b**, **d**) (the scanning area **a**, **b** 10 × 10 μm^2, **c**, **d** 3 × 3 μm^2)

modified with a mixture of borax and tungsten trioxide (samples 5 and 6); (iv) after friction in pair with a friction material modified with K[BF_4] (samples 11 and 12).

Measurements under scanning probe microscope on the scanning field of 50 × 50 μm^2 (Fig. 35.3) showed that the surface of the steel before the friction test

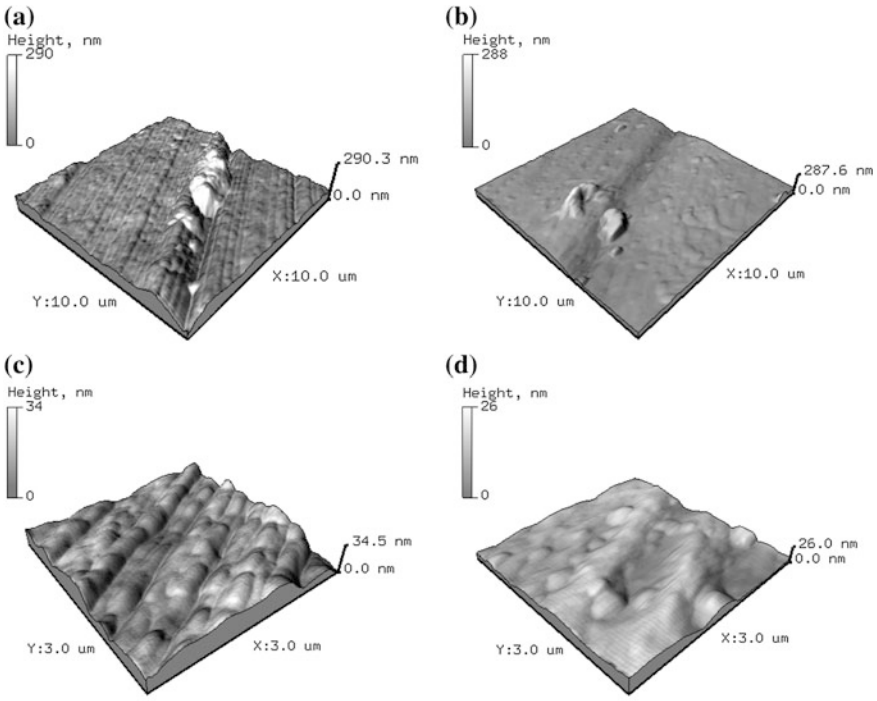

Fig. 35.5 The topography of the friction surface of samples No. 5 from Table 35.1 (**a**, **c**) and No. 6 (**b**, **d**) (the scanning area is **a**, **b** 10 × 10 μm^2, **c**, **d** 3 × 3 μm^2)

is a developed topography conditioned with relatively smooth surface regions (plateau) and pits with a depth until to 1–2 μm and more.

The arithmetic mean deviation of the surface profile (standard length is 10 μm) on the flat parts of the surface was about 16 nm, while the deviation for the pits was equal to 80 nm. The granular structure of the material (without a specific orientation) is clearly visible in the pits (scanning field of 10 × 10 μm^2) (Fig. 35.3).

Large grains of spherical shape at the pits have a diameter of 500–600 nm, average diameter 200–300 nm. The maximum deviation of the surface profile on a base length of 10 μm for a particular sample was 458 nm. Grain size estimated while scanning the area of 3 × 3 μm^2 was about 0.2–0.5 μm.

The study of twelve steel samples of the same chemical composition in a pair of the friction material with six different compositions by using a scanning probe microscope after the friction test at different sliding velocity and specific load in the friction unit allows us to discover: (a) the regularity of reducing the surface roughness in each of six groups at the transition from the sliding velocity of 1–5 m/s; and (b) the regularity of changing the friction surface morphology for each of six groups (2 samples per group), consisting in that after the test at sliding

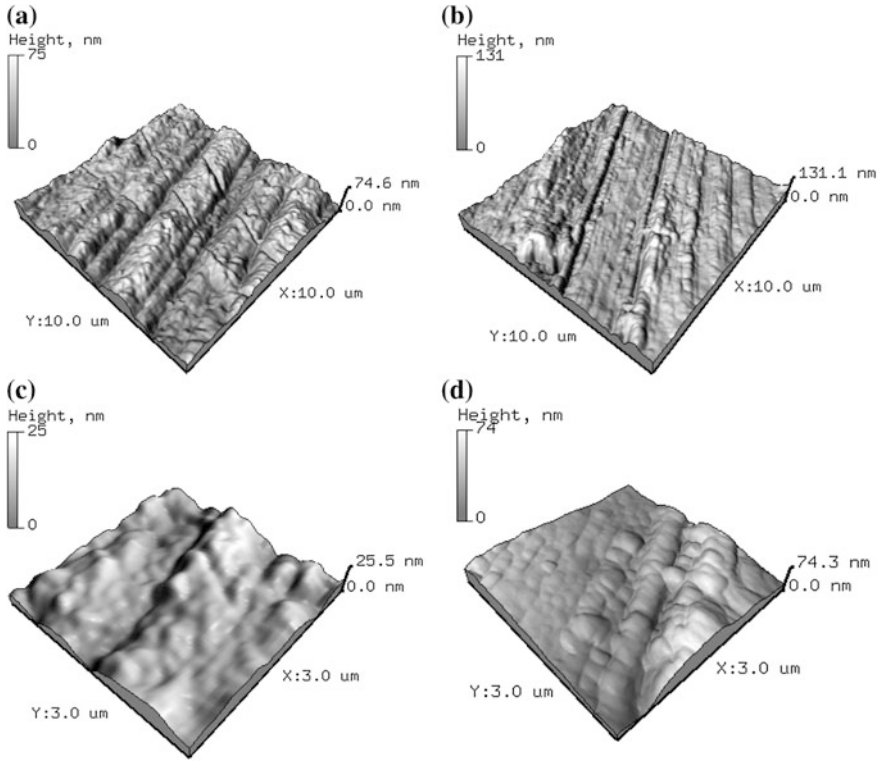

Fig. 35.6 Topography of the friction surface of samples No. 9 (**a**, **c**) and No. 10 (**b**, **d**) of Table 35.1 (the scanning area **a**, **b** 10 × 10 μm^2, **c**, **d** 3 × 3 μm^2)

velocity of 1 m/s on samples there is observed an orientation of grains of structural elements of the material surface layer on the friction track towards the sliding direction, and at a speed of 5 m/s separate grains can be only guessed, combining in lines towards the sliding direction (Figs. 35.4, 35.5 and 35.6, the images of scanning area of 3 × 3 μm^2).

In spite of the general regularities in the changes of metal samples morphology after the friction test, in each group grain size and shape differed depending on the composition of the friction material. Samples Nos. 4–6, obtained by adding tungsten modifier, include surface area, that morphologically differ from the typical ones for this sample. These areas can be described as the friction grooves, locally filled with wear particles, formed during friction. It is likely that they may be wear particles of the friction material of the brake shoe formed at the friction process and transferred to steel. The latter may mean that the relief formed on the friction surfaces of the discussed samples has a high impact on the wear of the shoe material.

Sample No. 9 does not contain strongly marked orientation of the granules on the surface towards the sliding of the counterbody that is typical for samples of the other groups obtained at the same conditions. At the same time, during increasing sliding velocity (sample No. 10) such orientation of the granules begins to emerge. It can be assumed that the material of the brake shoe with modifying additive K [BF_4] significantly reduced the impact of the friction process on the modification of the surface layers of steel. The comparison of the results, obtained from the AFM-images (Figs. 35.2, 35.3, 35.4, 35.5, 35.6 and 35.7) and graphs (Figs. 35.8 and 35.9), confirm the hypothesis about the influence of the composition of modifying additives on the relief of the metal counterbody's surface. As it can be seen from Figs. 35.8 and 35.9, the largest roughness of the friction surface is observed after the addition of WO_3, while the smallest is in the case of using modifying additive K [BF_4].

Comparison of the results received from ASM-images (Figs. 35.2, 35.3, 35.4, 35.5, 35.6 and 35.7) and charts (Figs. 35.8 and 35.9) confirms the assumption of

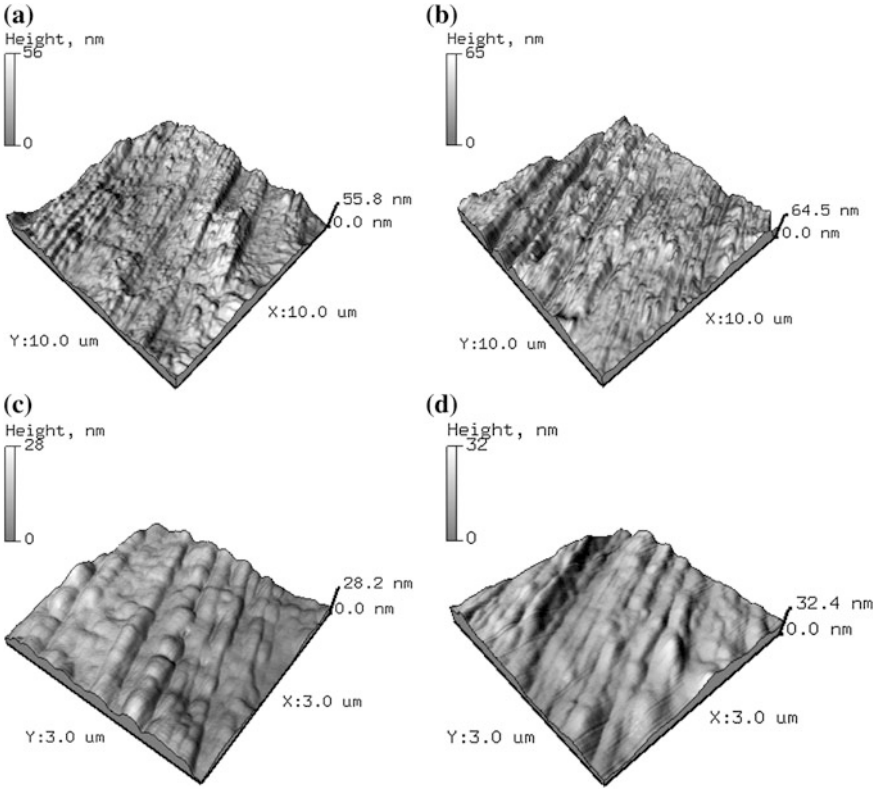

Fig. 35.7 The topography of the friction surface of samples No. 11 (**a**, **c**) and No. 12 (**b**, **d**) of Table 35.1 (the scanning area **a**, **b** 10 × 10 μm^2, **c**, **d** 3 × 3 μm^2)

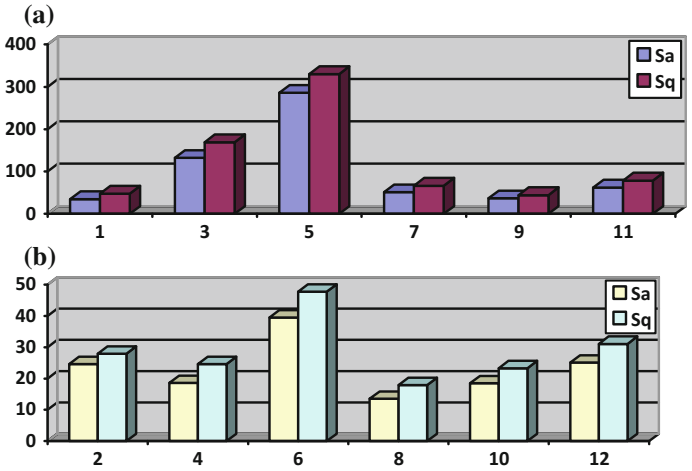

Fig. 35.8 Values of the arithmetic mean (*Sa*) and mean square (*Sq*) deviations of asperity height on the scanning area of 50 × 50 μm^2 for sliding velocity of 1 m/s (**a**) and 5 m/s (**b**)

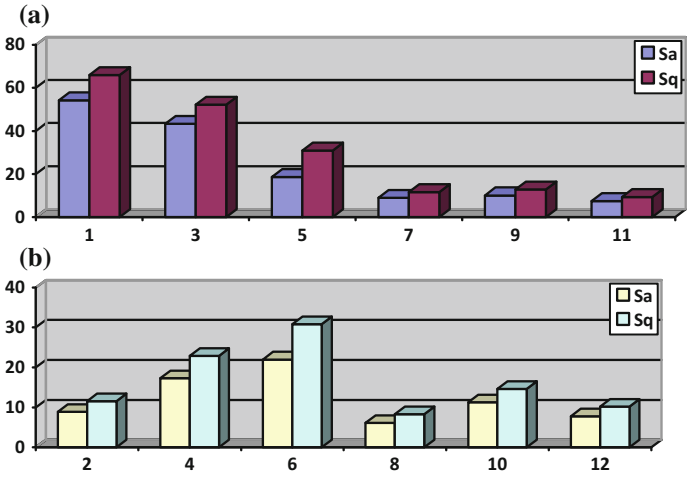

Fig. 35.9 The values of the arithmetic mean (*Sa*) and mean square (*Sq*) deviations of asperity height on the scanning an area of 10 × 10 μm^2 for sliding velocity of 1 m/s (**a**) and 5 m/s (**b**)

influence of structure of the modifying additives on a relief of a surface of a metal counterbody. It should be noted that the roughness for the relatively weak friction mode (v = 1 m/c, P = 1 MPa), defined on different areas (50 × 50 μm^2 and 10 × 10 μm^2) in the case of samples 1 and 5, 6 changes radically. In the case of interaction with the shoe of the basic composition, the roughness on the counterbody's surface on the area of 50 × 50 μm^2 is less than the roughness on the same

area after the interaction with the shoe containing WO_3. When measuring the roughness on the scanning area of $10 \times 10\ \mu m^2$, the situation is reversed (Figs. 35.8 and 35.9). In case of heavier friction mode, when the relative sliding velocity and the pressure in the friction unit increase, the results are more univalent: the roughness measured on both areas is more in the case of interaction with the shoe containing WO_3. At the same time, regardless of the scanning area, the roughness of the metal counterbody is less while using friction material containing $K[BF_4]$ in the friction pair.

35.4 Composition of Friction Surfaces. Discussion of Results

To understand the mechanisms of this impact, there were obtained X-ray spectra of steel 65G surfaces before friction and spectra of the friction surfaces of the same steel after its interaction with the shoe composite material of the initial basic composition and modified with various purposeful additives (Table 35.1). Results of the qualitative and quantitative analysis of the transfer film composition are presented in Table 35.2.

Figures 35.10 and 35.11 show the survey spectra from the studied surfaces. These spectra give information on the composition of 65G steel surface before the friction and on a transfer film on the surface after friction in pair with the composite modified by an additive containing tungsten. From Figs. 35.10 and 35.11 and

Table 35.2 Elemental composition of the steel counterbody's surface of the friction pair

Element	Properties					
	Steel 65 G (after 10 min. of profiling by Ar^+ ions)	Number of counterbody's sample				
		1	2	5	6	12
Sodium	–	1.9	2.2	–	5.8	–
Barium	–	13.6	24.0	17.6	29.4	11.7
Iron	45.3	11.4	15.4	19.3	9.8	12.5
Fluorine	–	0.3	1.1	–	–	1.6
Oxygen	45.4	43.5	37.0	42.2	33.4	45.4
Calcium	–	0.7	0.8	2.2	2.7	0.361
Carbon	9.3	24.5	14.9	13.8	12.8	23.0
Molybdenum	–	1.0	0.2	–	–	0.5
Boron	–	–	0.6	–	–	
Sulfur	–	1.9	1.6	1.9	1.7	1.7
Phosphorus	–	–	–	–	–	–
Silicon	–	0.5	1.4	0.8	0.7	1.2
Aluminum	–	0.7	0.8	1.6	2.0	1.15
Tungsten	–	–	–	0.6	1.7	–
Potassium	–	–	–	–	–	0.9

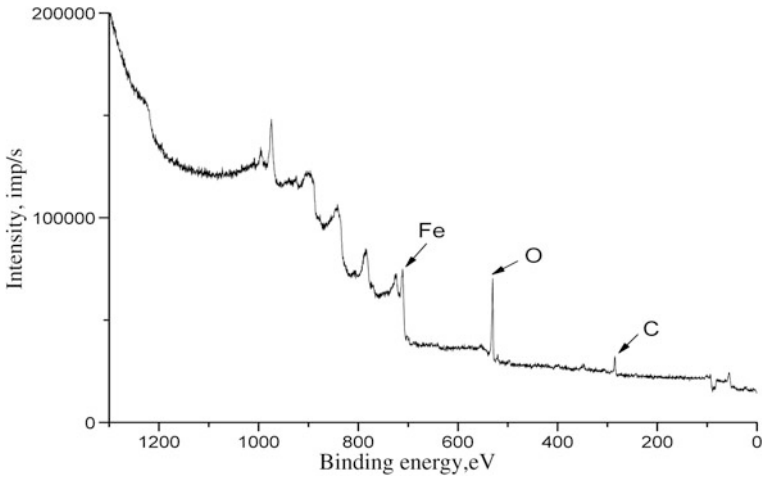

Fig. 35.10 XPS spectrum of 65G steel (after 10 min of profiling with argon ions Ar^+) obtained by X-Ray photoelectron spectrometer with scanning pitch 0.45 eV

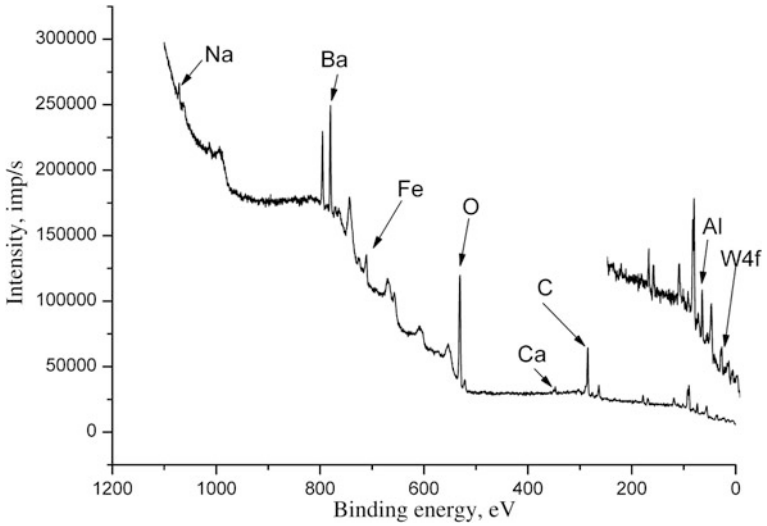

Fig. 35.11 XPS spectrum of transfer film after friction of brake shoe of commercial composition with tungsten modifier III in a heavy mode. The spectrum is obtained by electronic spectrometer with scanning pitch 0.45 eV

Table 35.2, it follows that in the composition of surface of 65G steel there are iron, hydrocarbon contaminants and oxygen which atoms belong to the oxide film on the surface, and a part of them is adsorbed. The most notable result of the friction is the emergence of intense 3D X-ray photoelectron lines of barium in the survey

spectrum in Fig. 35.11. Its emergence testifies about the transfer film formation, the main component of which is barium (this line dominates also in case of compositions with modifying additives). In Fig. 35.11, electron lines of sodium and tungsten additives, and various fillers of brake shoe material are nearly invisible.

On the right side of Fig. 35.11, there is an insert, which in enlarged scale shows a section of the spectrum from 0 to binding energy of carbon (E_b = 284.6 eV). In this section one can reliably distinguish a number of electronic lines relating both to modifiers (Na, W), and to the composition of composite brake shoe (C, Ba Al, Ca). Analysis of Table 35.2 gives information on the elemental transfer processes from brake shoe's material onto the surface of the metal counterbody. It is seen that barium, iron, oxygen and carbon are the main components of the transfer film.

In case of heavier friction modes, the quantity of barium and iron on the friction surface increase and oxygen and carbon reduce (let us compare samples 1 and 2, and also 5 and 6). Similarly, the content of modifying additives increases with an increase of friction intensity in the friction film. However, the content of modifying additives is always less than its content in the friction material.

Thus, XPS data testify about the presence of all elements belonging to purposeful additives in the transfer film. It allows associating remarked in Fig. 35.2 and in the diagrams in Figs. 35.8 and 35.9 regularities of relief changes while adding various additives to the composition of brake shoe's material with chemical composition of the transfer films and chemical compounds in them formed by atoms of purposeful modifying additives.

The analysis of Tables 35.1 and 35.2, and Figs. 35.8 and 35.9 shows that the composition of the transfer film is to a large extent determined by the bulk composition of the polymer composite brake shoe. In particular, barium is one of the major components of commercial friction materials. Therefore, the barium content in the transfer film reaches 30%. Table 35.2 and Fig. 35.11 also show that the elements of additives including strengthening the structure of metal sufficiently well transit into transfer film. Although their content in transfer film increases as pressure and sliding velocity increase, however, their content in the film is negligible.

Combined analysis of diagrams in Figs. 35.8 and 35.9 and Tables 35.1 and 35.2 shows that purposeful additives influence the roughness of a contact surface. Depending on the scanning area (50 × 50 μm^2 or 10 × 10 μm^2), this influence is manifested in different ways. For example, adding WO_3 significantly increases the roughness, measured in the area of 50 × 50 μm^2 in both friction modes, and in the area 10 × 10 μm^2 in a heavier friction mode (v = 5 m/s). At the same time the introduction of additives containing potassium and sodium ($Na_2B_4O_710H_2O$ and $K[BF_4]$) into the frictional material reduces the roughness of the friction surface measured over both scanning areas. The increase of roughness in the presence of WO_3 can be justified by the high value of the melting temperature of the given oxide, reaching 2130 °C.

Apparently, oxide particles are not completely destroyed with friction that leads to abrasive wear type and increasing of surface roughness. As shown in Table 35.2, sodium and potassium go from shoe within transfer film formed in the contact area. The analysis of the binding energies of the internal levels of sodium and potassium in the X-ray photoelectron spectrum of the transfer film shows that they are either

transferred in the form of compounds or form new connections during already the formation of the transfer film. In particular, rather low melting temperature of the modifier $K[BF_4]$, which according to [12] is 570 ºC, indicates that the given modifier can be destroyed at friction temperatures.

We can assume that $K[BF_4]$ is destroyed at friction partially or completely forming new compounds. Barium is a part of the friction material in the form of the compounds BaO, BaS, $BaSO_4$. The analysis of binding energies of Ba3d, S2p, O1s levels in the transfer film allows suggesting that barium gets over to the transfer film mainly in the form of these compounds. This conclusion corresponds to the high melting temperature of BaO, BaS, $BaSO_4$, respectively equal to 1923, 2205 and 1350 °C [12].

Thus, the transfer film consists of a number of oxides and compounds of potassium, sodium, barium, aluminum, silicon, possibly, iron, etc., among which the barium compounds are the most part in accordance with Table 35.2 and Figs. 35.10 and 35.11. It is known that metal oxides and salts, which are located on the surface of iron and its oxides are surface active substances [13]. The same should be noted in this particular case.

It is necessary to consider the reference data [12] about the surface tension of liquid metals entering into the metal-polymer system studied. The surface tension of W, Fe, Ba, Na, K is respectively, 2316, 1850, 267, 117 and 53.8 mN/m. For comparison, we convey the surface tension of some salts of barium, potassium and sodium at the same temperatures [13]. The surface tension of $BaSO_4$, Na_2SO_4, K_2SO_4, $NaBO_2$, KBO_2 is respectively, equal to 1250, 183.7, 144.3, 201.7, 142.4 mN/m. These data show that the formation on the surface of films both pure barium, sodium and potassium and their oxides and salts should lead to lowering of surface energy of the metal counterbody [13].

In this regard, the greatest effect can be expected for potassium and its salts. Acting at friction as surface active substances, in accordance with Rehbinder effect they can facilitate the deformation of a solid body. This effect makes possible to understand the reduction of the surface roughness after the friction of the friction material with additives containing potassium and sodium.

By considering that the sodium-containing modifying additive (borax) in samples 5 and 6 is used simultaneously with a modifier WO_3 (and these two additives may act on the surface microrelief in opposite directions), it cannot be excluded that such a complex additive may differently affect the microrelief of the friction surface in different modes, which is confirmed by the data in Figs. 35.8 and 35.9.

35.5 Conclusion

1. The composition of transfer films can be controlled by introducing a variety of purposeful additives into the brake shoe material.
2. Modifying additives, despite their small amount in the composition of the brake shoe material and transfer films, have a significant impact on the microrelief of the metal counterbody.

Acknowledgements The first and third authors are grateful to the Russian Scientific Foundation (RSCF) for its support by Project 16-19-10467.

References

1. V.I. Kolesnikov, in *Thermophysical Processes in Metal Polymeric Tribosystems* (Science, Moscow, 2003), p. 279
2. V.I. Kolesnikov, A.T. Kozakov, A.V. Sidashov, V.N. Kravtchenko, A.P. Sytchev, in *Friction and Lubrication in Machinery and Mechanism*, vol. 8, (2006), p. 22
3. V.I. Kolesnikov, A.T. Kozakov, A.V. Sidashov, V.N. Kravtchenko, A.P. Sytchev, Friction Wear **27**(4), 361 (2006)
4. V.I. Kolesnikov, A.T. Kozakov, A.V. Sidashov, in *Deformation and Fracture of Materials*, vol 12 (2007), p. 38
5. V.I. Kolesnikov, S.B. Bulgarevich, A.T. Kozakov, A.V. Sidashov, M.V. Boyko, Bull South Sci Cent Russ Acad Sci **3**(A3), 9 (2007)
6. V.I. Kolesnikov, A.T. Kozakov, N.A. Myasnikova, A.V. Sidashov, in *Bulletin of Southern Scientific Center of The Russian Academy of Sciences. Vol. II. Physics, Chemistry, Mechanics*, vol. 20 (Publishing House of Russian Scientific Centre of Russian Academy of Sciences, Rostov-on-Don, 2007)
7. D. Briggs, M.P. Seach (eds.), *Practical Surface Analysis by Auger and X-ray Photoelectron Spectroscopy* (John Wiley & Sons, Chichester, New York, Brisbane, Toronto, Singapore, 1984), p. 533
8. G. Fhilippov, V. Sinelnikov, in *Proceedings of International Heavy Haul Association STS—Conference* "*Wheel/Rail Interface*", vol. 1 (Moscow, 1999), p. 255
9. A.T. Kozakov, S.I. Yaresko, A.V. Sidashov, in *Modification and Analysis of Steels and Alloys Surface* (Rostov State Transport University, Rostov-on-Don, 2015), p. 378
10. V.I. Kolesnikov, A.T. Kozakov, A.P. Sergienko, A.P. Sytchev, A.V. Sidashov, A.V. Kupreev, in *Friction and Lubrication in Machinery and Mechanism*, vol. 8 (2009) p. 23
11. O.A. Bannykh, N.N. Alexandrov (eds.), *Mechanical Engineering. Encyclopedia. Vol. II-2. Steels. Cast Irons* (Mechanical Engineering, Moscow, 2000), p. 784
12. A.P. Babitchev, N.A. Babushkina, A.M. Bratkovskiy, et al., in *Physical Quantities: Reference Book*, ed. by I.S. Grigoriev, E.Z. Meilikhova (Energoatomisdat, Moscow, 1991), p. 1232
13. L.L. Kunin, in *Surface Phenomena in Metals*, ed. by Y.A. Klyachko (State Scientific and Technical Publishing House of Literature about Ferrous and Nonferrous Metallurgy, Moscow, 1955), p. 304

Chapter 36
Definition of Stress-Strain State in Layered Cylindrical Constructions at Pulse Loading

I.P. Miroshnichenko

Abstract This article analyzes the characteristics of the stress-strain state of layred cylindrical constructions made of transversely isotropic materials under pulse influences arising due to the curvature of the surface of the examined structures and the physical and mechanical properties of materials of layers.

36.1 Introduction

In the study of elastic displacements, stresses and strains in layered constructions of anisotropic materials, it is successfully used generalized method of scalarization for dynamic elastic fields in transversely isotropic media [1]. In this method, these fields can be expressed in terms of scalar potentials corresponding to quasi-longitudinal, quasi-transverse and purely transverse waves. In this case, such a scalarization is possible if the objects under consideration are tensors with respect to the subgroup of general coordinate transformations when a local affine basis has one invariant vector, which coincides with the axis of material symmetry of the material.

The results of using this method for solving a variety of applications have been published in [2–6]. Based on the tensor relations of the pointed method, it was developed the scientific and methodological approaches [2, 7–9] for the determination of stress-strain state in layered cylindrical constructions made of isotropic and transversely isotropic materials. These approaches take into account the characteristics of all types of waves propagating in these materials, wave processes in layered constructions and the influence of the curvature of the surface of the constructions under consideration at a given spatial and temporal distribution of sources of pulsing impact on the outer and inner surfaces of the constructions under consideration.

I.P. Miroshnichenko (✉)
Don State Technical University, Rostov-on-Don, Russia
e-mail: ipmir@rambler.ru

I.A. Parinov et al. (eds.), *Advanced Materials*, Springer Proceedings in Physics 193, DOI 10.1007/978-3-319-56062-5_36

The proposed scientific and methodical approaches allow us analyze of arisen in the construction of complex stress-strain state formed not only the primary disturbance, but also disturbances caused by multiple reflections of waves from the boundaries of layers, interference phenomena and diffraction in randomly selected areas of the construction at any time as the during loading, and upon its completion.

To analyze the features of the effect of the surface curvature of the cylindrical construction and physico-mechanical properties of transversely isotropic layered materials, we performed computational and theoretical study using the proposed scientific-methodological approaches and corresponding original software.

36.2 Calculation Scheme, Initial Propositions

Let us consider a layered cylindrical construction (Fig. 36.1), referred to a cylindrical coordinate system $\{z, \Theta, Z\}$, the axis of which coincides with the axis of symmetry of the material layers made of transversely isotropic materials. The layers are numbered 1, 2, …, N, starting with the internal boundary layers with specified radii r_0, r_1,….,r_N. The layers may be of any thickness and made of different isotropic and transversely isotropic construction materials with their individual physical and mechanical characteristics. Some areas (V_1, V_2, V_3, …) of the structure are subject to external influence, independent of time and coordinates.

Impact has a pulse character (a single pulse or several pressure pulses). Restrictions on the pulse shape and the areas of their application are not definite.

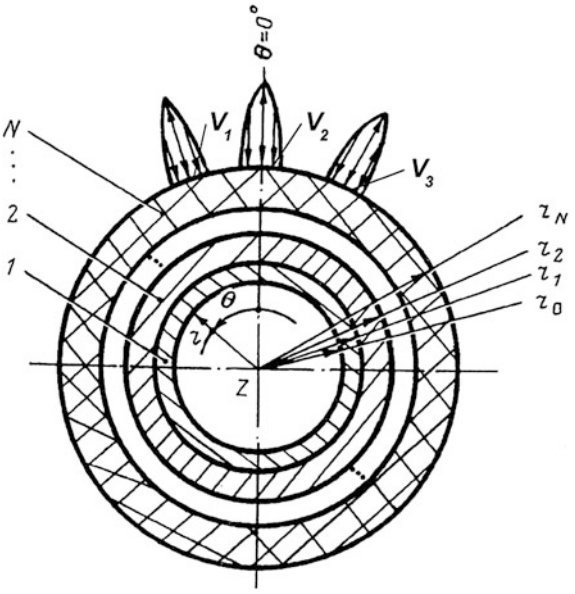

Fig. 36.1 Layered cylindrical construction

Under this impact, it is arisen complex stress-strain state in the construction, formed not only the primary disturbance, but also disturbances caused by multiple reflections of waves from the boundaries of layers, interference and diffraction phenomena.

36.3 Features of Influence of Surface Curvature on the Stress-Strain State

It is known that in the cylindrical constructions by the focusing effect of the curved surface, the concentration of wave energy arises, which leads to the increase of the amplitude values of stresses. A numerical study of the effect of the curvature on the value of the amplitude values of the radial stresses σ_{rr} in the cylindrical construction, on the base of method [2]. The calculation scheme is present in Fig. 36.2.

The geometrical characteristics of the construction, referred to a cylindrical coordinate system $\{r, \theta, z\}$ were given by radiuses of outer $(r_1 = 1\,m)$ and inner $(r_0 = 0.1\,\mathrm{m})$ surfaces. The relative thickness of the construction defined as $\alpha = (r_1 - r_n)/r_1$ was 0.9 at $r = r_0$, which corresponds to the construction in which there is the influence of surface curvature.

The construction material had the following physical and mechanical characteristics: density ρ = 2700 kg/m^3, elastic moduli C_{11} = 107 GPa, $C_{12} = C_{13}$ = 55.3 GPa, C_{44} = 25.9 GPa; absorption coefficients of longitudinal g'' = 2 m^{-1} and transverse χ = 1 m^{-1} waves.

Impact was a pressure pulse $P(\theta, t)$, with amplitude P_0, applied to the external surface $(r = r_1)$, the pressure does not depend on the coordinate. The pressure

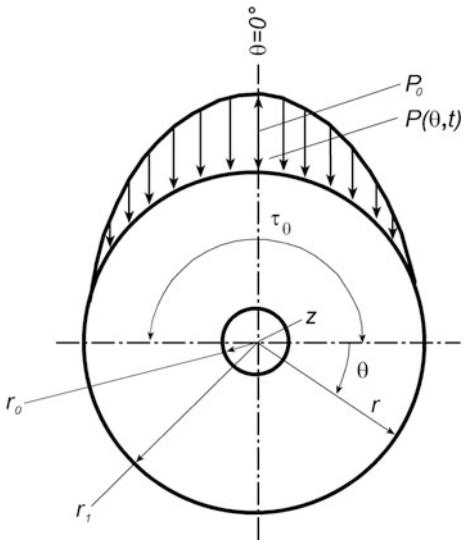

Fig. 36.2 The calculation scheme

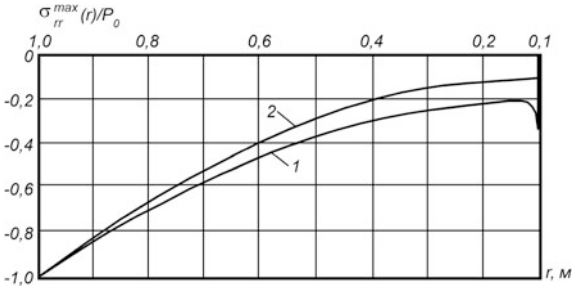

Fig. 36.3 The relationship $\sigma_{rr}^{\max}$ (1), calculated in accordance with the specified initial data. At the same time, there is shown a similar relationship (2) obtained for the equivalent plate thickness

distribution on the coordinate θ was given in the form of half-sine pulse at the $\theta = 0$ with a duration $\tau_\theta = \pi$, and its change in time t is stated as a Gaussian function with a duration $\tau = 1$ μs.

First, the calculated dependence of the stress σ_{rr} for a fixed value of r in time t from $t = 0$ to $t = 150$ μs with step $h_t = 0.1$ μs. Then from this dependence, we selected the maximum value of $\sigma_{rr}^{\max}$ with simultaneous recording the values of r and the time t. The similar sequence of operations is repeated for all r from r_1 to r_0 with the steps $h_r = 10^3$ m.

Figure 36.3 shows the relationship $\sigma_{rr}^{\max}(r)$ (1), calculated in accordance with the specified initial data. At the same time, there is shown a similar relationship (2) obtained for the equivalent plate thickness. Analysis of the given dependencies shows that the section from $r = 1$ m to $r = 0.9$ m, they are the same, and then, the nature of their change is different. It should be noted that in the section adjacent to $r = 0.1$ m, extremum of dependence (1) takes place.

The dependence (2) presents exponential decreasing amplitude of stress $\sigma_{rr}^{\max}$ from r_1 to r_0. It is caused by the absorption of wave energy in the construction material, determined by the given coefficients g'' and x'', which correspond to losses of longitudinal and transverse waves and are the imaginary parts of the wave numbers of the pointed types of waves.

Dependence 1 is more complex and depends not only on the pointed absorption in the material, but also on the increment of the amplitude of stress, induced by wave energy concentration or, in other words, is a consequence of the curvature of the construction surface under consideration.

On the section from $r = 1$ m to $r = 0.9$ m ($\alpha = 0.1$ at $r = 0.9$ m), the pointed increment is small, so dependencies (1) and (2) coincide. Further, the parameter α increases, and the increment increases, due to the dependence (1) compared to the dependence (2) has higher amplitude values of $\sigma_{rr}^{\max}$. For large values α (from $\alpha = 0.8$ at $r = 0.2$ to $\alpha = 0.9$ to at $r = 0.1$ m), the growth rate of $\sigma_{rr}^{\max}$ increases. Subsequent reduction of amplitude of $\sigma_{rr}^{\max}$ occurs since the time t of reaching by the front of the inner surface pulse $(r = r_0)$ of construction and the beginning of the reflection process.

Figure 36.4 shows dependencies $\sigma_{rr}^{\max}(r, g'')$ calculated for different values of g'' at the section from $r = 0.3$ m to $r = 0.1$ m at times t prior to achieving pulse front

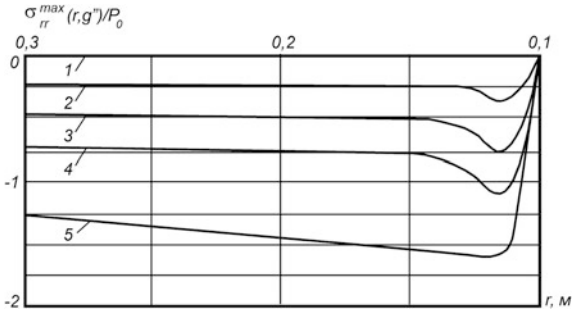

Fig. 36.4 dependencies $\sigma_{rr}^{\max}$ (r, g'') calculated for different values of g''

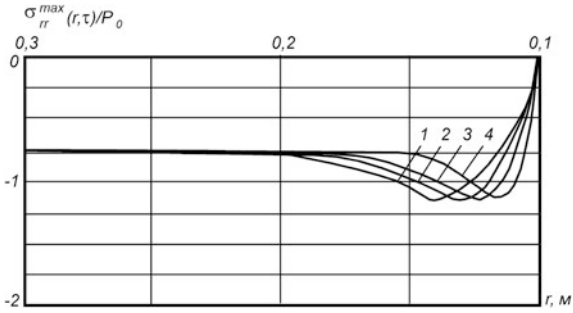

Fig. 36.5 Analysis of the dependencies shows that the position of the extremum is determined by the duration of the load action τ

inner surface of the structure, by this: $g'' = 5\ \mathrm{m}^{-1}$ (1); $2\ \mathrm{m}^{-1}$ (2); $1\ \mathrm{m}^{-1}$ (3); $0.5\ \mathrm{m}^{-1}$ (4); $0.25\ \mathrm{m}^{-1}$ (5).

Analysis of dependencies (2)–(5) shows that the change in the values of amplitudes $\sigma_{rr}^{\max}$ is proportion to the coefficients g'', and the nature of these relationships is similar to (the position of extremum corresponds to the same value of r and occurs in the same time t). Note that when a large absorption in the material, an extremum is absent, due to the liquidation of increment owing to the effect of the surface curvature of the construction expressed by wave energy absorption in the material.

Figure 36.5 shows the dependencies $\sigma_{rr}^{\max}(r, \tau)$ for various values of load action duration τ; the dependencies correspond to $\tau = 5$ μs (1), 4 μs (2), 3 μs (3), 2 μs (4). Analysis of the dependencies shows that the position of the extremum is determined by the duration of the load action τ.

Figure 36.6 shows the dependencies $\sigma_{rr}^{\max}(r, \rho)$ obtained by changing the density ρ and the fixed values of the elastic moduli C_{ij} and a fixed density ρ and different values of the elastic moduli C_{ij}, so that the speed of propagation of longitudinal waves v_l in the material of construction is equal to the values shown in Table 36.1. This table gives the number of dependencies, corresponding to these combinations of density ρ and moduli C_{ij}.

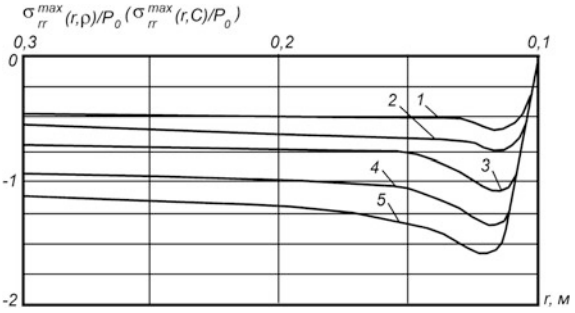

Fig. 36.6 The number of dependencies, corresponding to these combinations of density and moduli C_{ij}

Table 36.1 The position of the extremum is determined only by the duration τ

	Number of dependence (speed v_l, m/s)				
	1	2	3	4	5
	v_l = 8445	v_l = 7138	v_l = 6295	v_l = 5694	v_l = 5238
Density ρ = 2700 kg/m^3					
C_{11} (GPa)	192.5	137.9	107	88.3	74.1
$C_{12} = C_{13}$ (GPa)	103.7	74.3	55.3	47.5	39.9
C_{44} (GPa)	44.4	31.8	25.9	20.4	17.1
Elastic Moduli C_{11} = 107 GPa; $C_{12} = C_{13}$ = 55.3 GPa; C_{44} = 25.9 GPa					
Density ρ (kg/m^3)	1500	2100	2700	3300	3900

Analysis of the dependencies shows that they are identical in pairs, and their nature depends on the speed v_l, independently on that through which physical-mechanical characteristic, it has been defined. The position of the extremum is determined only by the duration τ.

Figure 36.7 shows dependencies $\sigma_{rr}^{\max}(r, r_1, g'')$ for the constructions with different thicknesses; their values were given by changing the radius of the outer surface r_1 with a constant radius of the inner surface r_0 = 0.1 m, by this coefficient g'' = 0.5 m^{-1} in Fig. 7a; g'' = 1 m^{-1} in Fig. 36.7b and g'' = 2 m^{-1} in Fig. 36.7c. For clarity, these figures show combined surface $r = r_1$ for all constructions.

Figure 36.7 shows that there is a dependence (10), which characterizes the level of amplitude values of $\sigma_{rr}^{\max}$ in these structures in dependence on r_1 and g''. The practical significance of the dependence is the ability to select the most optimal geometry of designed construction and material for its production.

The presented results of the study reveal the features of the surface curvature influence on the levels of amplitude values and the distribution of radial stresses in cylindrical constructions. They show patterns of change for different combinations of influencing factors and allow one to propose one of the possible approaches to the evaluation of designed constructions.

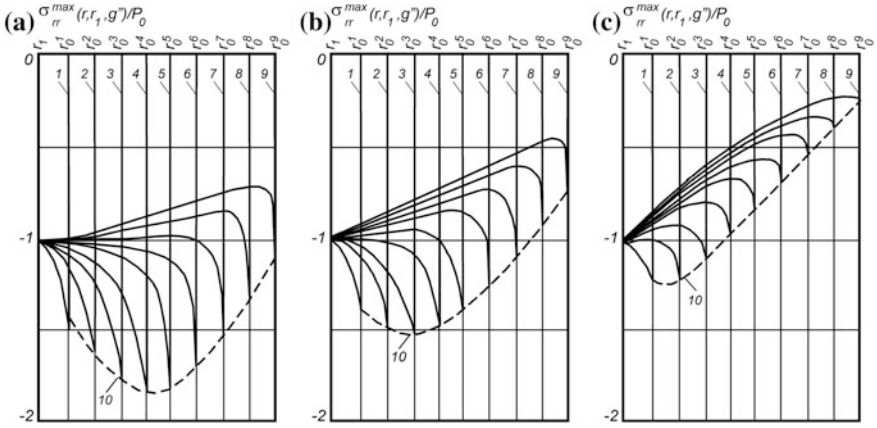

Fig. 36.7 characterizes the level of amplitude values of $\sigma_{rr}^{\max}$ in these structures in dependence on r_1 and g''

36.4 Features of Influence of Anisotropy of Constructional Materials on the Stress-Strain State

The study of the effect of material anisotropy of the stress-strain state in monolayered cylindrical construction ($r_0 = 3 \cdot 10^{-3}$ m and $r_1 = 0.5$ m), made of transversely isotropic materials with different degrees of anisotropy. The calculations were made under the influence of the pressure pulse n the form of a Gaussian function at $z = 0$ ($\tau_z = 0.1$ m, where τ_z is the pulse length along coordinate z). The dependence of pressure on time t is also established as a Gaussian function with a duration of $\tau = 1$ μs.

Material 1 had the following physical and mechanical characteristics: $\rho = 1650$ kg/m^3; $C_{11} = 6.43$ GPa; $C_{12} = 1.95$ GPa; $C_{13} = 0.569$ GPa; $C_{33} = 1.48$ GPa; $\overset{(L)}{g''} = 3$ m^{-1}; $\overset{(L)}{g''} = 2$ m^{-1}. For material 2, listed physical and mechanical properties differed only value $C_{11} = 3$ GPa.

Comparative analysis of the characteristics of the materials 1 and 2 shows that material 1 has a more pronounced anisotropy because $\overset{(l)}{V}(90^o)/\overset{(l)}{V}(0^o) = 2.07$, and for the material 2, this ratio is 1.42 (where $\overset{(l)}{V}$ is the velocity of propagation of quasi-longitudinal waves along the pointed directions). Figure 36.8 shows the distribution of radial stresses $\sigma_{rr}^{\max}(r,z)$ at time $t = 1.1$ μs and $t = 1.2$ μs, while in Fig. 36.8a for the material 1, and in Fig. 36.8b for the material 2.

Analysis of the results shows that a pulse extending in the material from a point influence on the outer surface $(r = r_0)$, the pulse extends and its amplitude decreases. In this case, its extension in the material 2 along z-axis is greater than in the material 1. This is because of anisotropy properties of these materials. Reducing

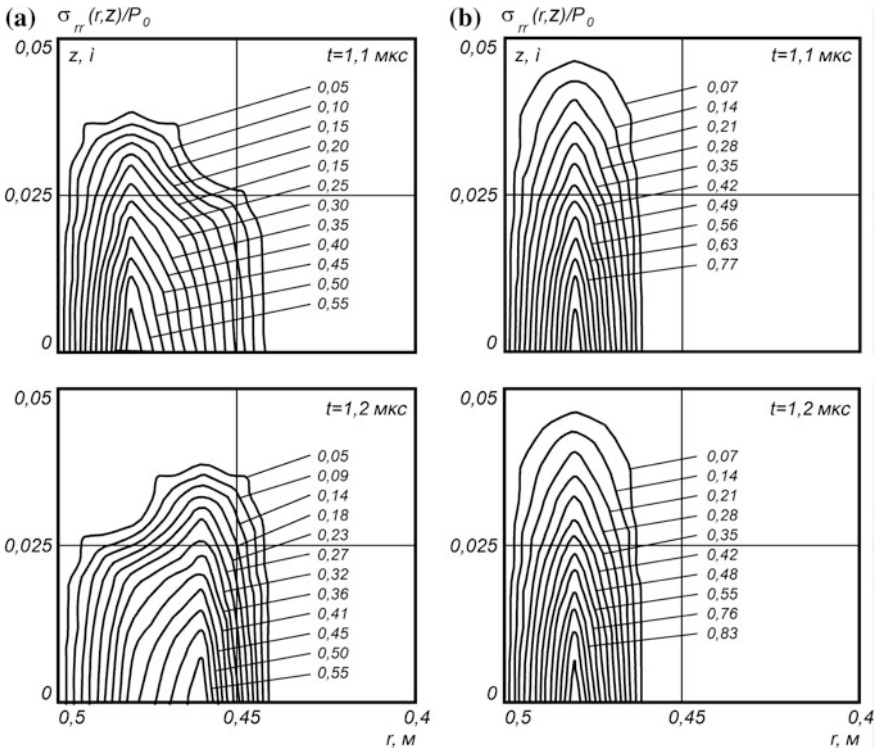

Fig. 36.8 The distribution of radial stresses $\sigma_{rr}^{\max}(r, z)$ at time $t = 1.1$ μs and $t = 1.2$ μs

the amplitude consists in absorption of wave energy by these materials and is no feature only of anisotropic composite materials. This result shows the particular manifestations of anisotropy of construction materials of the layers and should be taken into account by processing calculation estimates of promising constructions.

36.5 Conclusion

The presented theoretical and numerical results clearly demonstrate the capabilities of the proposed scientific and methodological approach. It allows the analysis of stress-strain state in layered cylindrical structures made of transversely isotropic materials, under repeated impacts of local dynamic loads, taking into account features of wave processes occurring in these structures. The results are the most appropriate to use for the solution of applied problems to create advanced constructions of the new anisotropic composite materials, quality control of their manufacturing and the diagnosis of the state during the operation in mechanical engineering, shipbuilding, aircraft, etc.

Acknowledgements This work was partially supported by the Russian Foundation for Basic Research (grant No. 16-08-00740).

References

1. V.P. Sizov, *Izvestiya of Russian Academy of Science. Mechanics of Solids* **5**, 55 (1988)
2. V.P. Sizov, I.P. Miroshnichenko, in *Elastic Waves in Layered Anisotropic Structures* (LAP LAMBERT Academic Publishing, Saarbrucken, Germany, 2012), p. 270.
3. V.P. Sizov, I.P. Miroshnichenko, in *Physics and Mechanics of New Materials and their Applications*, eds. by I.A. Parinov, S.H. Chang (Nova Science Publishers, New York, 2013), p. 203
4. I.P. Miroshnichenko, in *Advanced Materials. Physics, Mechanics and Applications*, eds. by S.-H. Chang, I.A. Parinov, V.Y. Topolov. Springer Proceedings in Physics, vol 152 (Springer, Heidelberg, New York, Dordrecht, London, 2014), p. 163.
5. I.P. Miroshnichenko, V.P. Sizov, in *Advanced Materials—Studies and Applications*, eds. by I.A. Parinov, S.H. Chang, S. Theerakulpisut. (Nova Science Publishers, New York, 2015), p. 353
6. I.P. Miroshnichenko, in *Proceedings of the 2015 International Conference on "Physics, Mechanics of New Materials and Their Applications", devoted to the 100th Anniversary of the Southern Federal University*, eds. by I.A. Parinov, S.-H. Chang, V.Y. Topolov (Nova Science Publishers, New York, 2016), p. 509.
7. I.P. Miroshnichenko, V.P. Sizov, Izvestia of higher school. North-Caucases region. Nat. Sci. **2**, 19 (1999) (in Russian).
8. I.P. Miroshnichenko, V.P. Sizov, Izvestia of higher school. North-Caucases region. Nat. Sci. **3**, 40 (1999) (in Russian).
9. I.P. Miroshnichenko, V.P. Sizov, Izvestiya of Russian academy of science. Mech. Solids. **1**, 97 (2000) (in Russian).

Chapter 37
Compressive Strength and Shrinkage Test of Flowing Concrete Using Fly Ash and Naphtalene-Based Superplasticizer

Retno Trimurtiningrum and Aman Subakti

Abstract Flowing concrete is a high workability concrete with a slump greater than 7.5 in. (190 mm) without any bleeding and segregation. The workability is achieved due to the use of plasticizing admixture, since the addition of water will result lower compressive strength. Flowing concrete usually used in area that highly congested, used for concrete repair and often desirable for use in mass placements because the cement content can be kept low, which minimizes heat development. Fly ash is a by-product from the coal combustion and widely used as a cementitious and pozzolanic ingredient in concrete. Fly ash has glassy, solid or hollow spherical shape. The spherical shape of fly ash influences the workability of concrete. The aimed of this research is to investigate the influence of fly ash on the compressive strength and the shrinkage test of flowing concrete. The content of fly ash varied as 0, 15, 25, 35 and 50% of cementitious material. Naphtalene was used as superplasticizer. The test results showed that the highest compressive strength was 46.26 MPa in 28 days and the smallest shrinkage was 0.0352% in 144 h from the mixtures with 50% of fly ash.

37.1 Introduction

Concrete is a composite material consisting of fine and course aggregates, bonded together with cement paste, and hardens over time. For many years, concrete becomes one of popular material used for buildings, especially high-rise buildings.

R. Trimurtiningrum (✉)
Department of Civil Engineering, Universitas 17 Agustus 1945, Surabaya, Indonesia
e-mail: neno_s47@yahoo.com

A. Subakti
Department of Civil Engineering, Institut Teknologi Sepuluh Nopember, Surabaya, Indonesia
e-mail: subaktiaman@yahoo.com

I.A. Parinov et al. (eds.), *Advanced Materials*, Springer Proceedings in Physics 193, DOI 10.1007/978-3-319-56062-5_37

Workability and flow-ability concrete in reinforcement area play an important role in achievement of homogeneity and quality of concrete as it is required.

Flowing concrete is a high workability concrete with a slump greater than 7.5 in. (190 mm) without any bleeding and segregation. Flowing concrete is commonly used in congested locations such as slabs, mats, columns and also useful for pumping because it reduces pumping pressure and increases both the rate and distance that the concrete can be pumped [1]. In conventional concrete mixtures, workability relates to the amount of water in the mixtures, but the addition of water will result lower compressive strength.

Fly ash is a by-product from the combustion of pulverized coal, is widely used as a cementitious and pozzolanic ingredient in hydraulic cement concrete. Fly ash particles have glassy, solid or hollow spherical shape. Nowadays, fly ash has been concerned to replace partial of cement in order to improve the properties of concrete. Previous research [3], showed influence of fly ash particles (see Fig. 37.1) on the properties of freshly mixed, unhardened concrete, the strength development and other properties of hardened concrete. Using fly ash as partial replacement of concrete decreases the demand of cement so that reduces the CO_2 emission from the cement industry [4].

Superplaticizers are chemical admixtures used where well-dispersed particle suspension is required [5]. The action of the superplasticizer is to prevent or delay the flocculation and to disperse the cement particles within the paste [6]. Therefore, the use of superplasticizer in the concrete improve workability of fresh-concrete. In this research, *naphtelene sulphonate* is used as the superplasticizer because the cost is low.

The aimed of this research is to investigate the influence of fly ash on the workability of concrete and hardened-state of concrete such as compressive strength and the shrinkage test of flowing concrete.

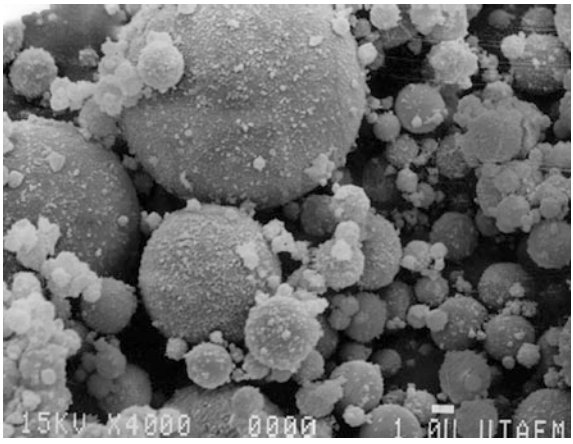

Fig. 37.1 Fly ash in 4000× magnificence [3]

37.2 Methods

37.2.1 Materials

Cement. The cement used in this research was Portland cement of type I from PT. Semen Gresik, Indonesia, corresponding to SNI 15-2049-94 with the chemical composition shown in Table 37.1.

Fly ash. This research used fly ash obtained from Jawa Power Paiton, Indonesia. The chemical composition of fly ash is shown in Table 37.2.

Based on ASTM C618-03, chemical composition of fly ash is classified fly ash into two classes. The sum of the first three constituents (SiO_2, Al_2O_3, and Fe_2O_3) must exceed 70% to be classified as ASTM C 618 Class F fly ash, whereas their sum must only exceed 50% to be classified as an ASTM C 618 Class C fly ash [3]. Therefore, in this research we used class F fly ash.

Aggregates. Crushed gravel was used as coarse aggregate with 20 mm maximum diameter and fine aggregates were from natural river sand from East Jawa, Indonesia. Physical properties of fine and coarse aggregates are present in Table 37.3.

Superplasticizer. This research used naphtelene sulphonated-based superplasticizer ***CONPLAST SP442*** from Fosroc.

37.2.2 Experimental Procedure

Mixture proportions. There were 5 mixtures prepared for this research. The mixture was divided based on the percentage of fly ash. The content of fly ash varied as 0% (controlled specimen), 15, 25, 35 and 50% weight of cementitious material. Mixture

Table 37.1 Chemical composition of Portland cement of type I

Compound			SNI 15-2049-94	% by weight
Silicon dioxide (silica)	SiO_2	%	–	20.75
Aluminum oxide (alumina)	Al_2O_3	%	–	6.2
Iron oxide	Fe_2O_3	%	–	3.24
Calcium oxide (lime)	CaO	%	–	64.16
Magnesium oxide	MgO	%	Max 6.0	1.30
Sulphur trioxide	SO_3	%	Max 3.5	1.98
Loss of ignition	LOI	%	Max 5.0	1.13
Alkali (Na_2O + 0.658 K_2O)	–	%	Max 0.6	0.17
Tricalcium silicate	C_3S	%	–	57.70
Dicalcium silicate	C_2S	%	–	11.15
Tricalcium aluminate	C_3A	%	–	10.95
Tetracalcium aluminate ferrite	C_4AF	%	–	10.89

Table 37.2 Chemical composition of fly ash

Compound	% by weight
SiO_2	53.20
Fe_2O_3	12.59
Al_2O_3	10.38
CaO	11.20
MgO	4.86
Na_2O	2.12
K_2O	1.31
SO_3	1.3
LOI	0.38

Table 37.3 Physical properties of fine and coarse aggregates

Physical properties	Sand	Crushed gravel
Moisture content (%)	0.6	3.225
Specific gravity	2.71	2.79
Water absorption (%)	1.937	1.17
Bulk density (kg/m^3)	1525	1467

Table 37.4 Concrete mixtures for f'c = 40 MPa/m^3

Mixtures	Cement (kg)	Fly ash (kg)	Water (kg)	Fine aggregate (kg)	Coarse aggregate 5-10 mm (kg)	Coarse aggregate 10–20 mm (kg)	Super plasticizer (L)
FA-0	403.13	0	193.5	1011.11	488.09	339.18	3.225
FA-15	360.60	63.63	182.25	1021.63	493.17	342.71	4.242
FA-25	336.65	112.22	177.75	1014.96	489.95	340.47	4.489
FA-35	310.74	167.32	173.25	1005.23	485.25	337.21	4.781
FA-50	237.18	237.18	148	1040.95	502.50	349.19	4.744

Designations for FA-X: *FA*—fly ash; *X*—percentage of fly ash in cementitious material

proportions of concrete are shown in Table 37.4. Concrete mixtures were mixed with naphtelene sulphonated-based superplasticizer with maximum 1% of cementitious material.

The cylindrical specimens of concrete for compressive strength test were prepared with the size of 150 mm in diameter and 300 mm in height and were cured by submerged into the water at room temperature in laboratory. The specimens of concrete for shrinkage test were prepared with the size of 25 × 25 × 285 mm^3 and were covered with plastic and left in ambient condition at room temperature in laboratory (Figs. 37.2 and 37.3).

Some methods that use for testing the concrete mixtures are slump test according to ASTM C143 [7], setting time of concrete by penetration resistance according to ASTM C403 [8], compressive concrete strength according to ASTM C39 [9] and shrinkage test method at ambient temperature according to ASTM 157 [10].

Fig. 37.2 Specimens for compressive strength tests

Fig. 37.3 Specimens for shrinkage test

37.3 Results and Discussion

37.3.1 Slump Test Result

This test result determined the workability of the concrete mixtures. Figure 37.4 shows the influence of fly ash replacement percentage on slump test result.

Result shown in Fig. 37.4 concluded that fly ash influence the workability of the concrete mixtures. The higher of fly ash percentage in the mixture caused the greater workability of concrete. The spherical shape of fly ash particles and the increasing of paste volume due to the replacement of cement ratio greater than 1 influence the concrete workability. Moreover, the naphtelene sulphonated-based superplasticizer also influences the workability of concrete. Slump measurements of

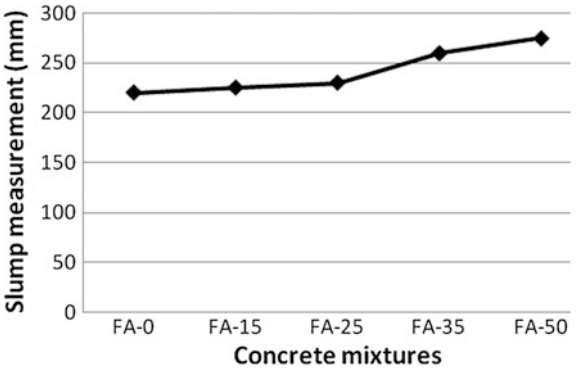

Fig. 37.4 The influence of fly ash on the workability of concrete mixtures

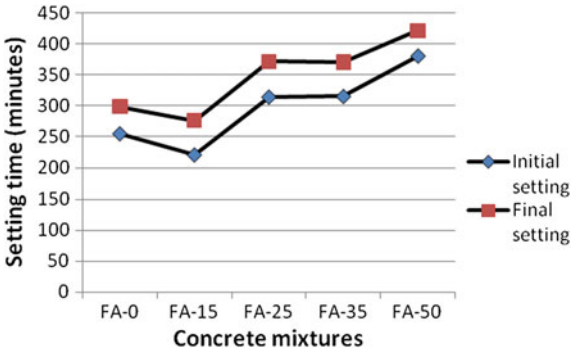

Fig. 37.5 Influence of fly ash on the setting time of concrete mixtures

all the mixtures were about 220–275 mm and provided the required slump of flowing concrete.

37.3.2 Setting Time of Concrete Result

Setting time is time required for stiffening the cement paste. The purpose of this test is to record the initial setting time (when cement paste starts losing its plasticity) and the final setting time (when cement paste completely loses its plasticity). Figure 37.5 shows a relation of fly ash percentage and setting time for concrete.

It is generally shown that higher percentage of fly ash leads to longer both initial and final setting time of concrete. Higher percentage of fly ash content in concrete mixture means more amount of fly ash replacing cement. Because of lesser cement content, both initial and final setting time increased. Superplasticizer also contributes in increasing the setting time. Mixture that has higher fly ash percentage content corresponds to greater amount of superplasticizer, because the percentage of superplasticizer is about 1% of cementitious material in each mixture.

Figure 37.5 also shows that setting time of FA-15 mixture is faster than other mixtures because the ambient temperature when mixing also influences the setting time. Higher temperature decreases the setting time, because of rapid chemical reaction in cement paste.

37.3.3 Compressive Strength Test Result

Figures 37.6 and 37.7 show dependencies for compressive strength of flowing concrete on fly ash content in the mixture.

It is shown that at the early age of concrete, mixture with higher percentage of fly ash develops lower compressive strength, otherwise when concrete reach 28 days, mixture with higher percentage of fly ash results higher compressive strength than concrete without fly ash. It is because higher percentage of fly ash mixture contains less of cement, which plays an important role in hydration process. Moreover, the pozzolanic reaction is also a slow reaction, it requires more time to react completely [11], therefore in early age, higher percentage of fly ash decreases the compressive strength.

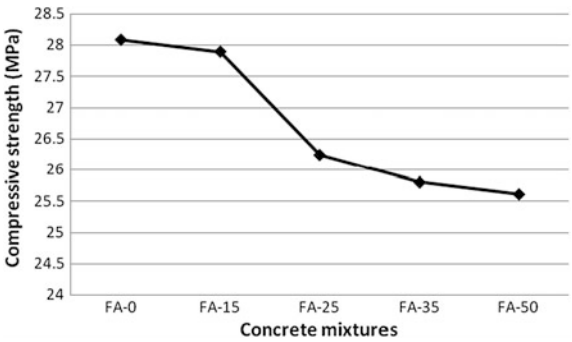

Fig. 37.6 Influence of fly ash on the 7-days compressive strength of concrete

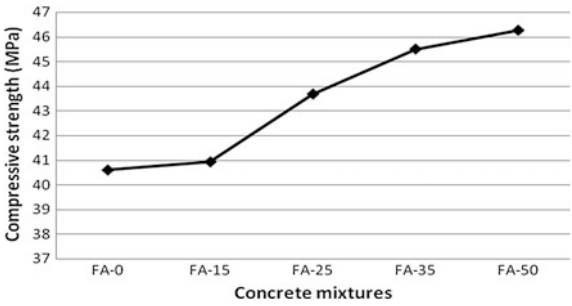

Fig. 37.7 Influence of fly ash on the 28-days compressive strength of concrete

In later age, fly ash increases the compressive strength. It is because the pozzolanic reaction with calcium hydroxide is derived from the hydration of Portland cement to form calcium silicate hydrate (CSH) [2] and the small size of fly ash particles causes denser concrete [12]. Moreover, the spherical shape of fly ash increases the workability of fresh concrete, so that a water can be reduced. Therefore, mixture with higher percentage of fly ash has lower water-cementitious ratio that influences the concrete strength. The highest compressive strength is 46.26 MPa at 28 days obtained by the FA-50 mixture.

The trends of the strength development of the fly ash concretes show the same result with previous research conducted by P. Nath that fly ash in concrete decreased strength at the earlier age as compared to the control concrete, however they gather more strength or very close to control concrete strength on later age [13].

37.3.4 Shrinkage Test Result

This test method determines the change in length of drying mortar. Figure 37.8 illustrates dependencies of the mortar shrinkage on fly ash percentage in the concrete mixture.

The result shows that higher percentage of fly ash in the mortar mixture results in smaller change in length. It is because the mixture has lesser water content, so that the change in length of mortar due to the temperature and the evaporation of water will have the smaller shrinkage percentage. The smallest change in length is 0.0352%, obtained by the FA-50 mixtures. This result is appropriate with previous research, conducted by Chindaprasirt that drying shrinkage of ordinary Portland cement mortar bars is higher than the fly ash mix mortar bars, because fine fly ash reduces the drying shrinkage, which was mainly related to the reduced water content and hence the lower water and binder ratio of the mixes [14].

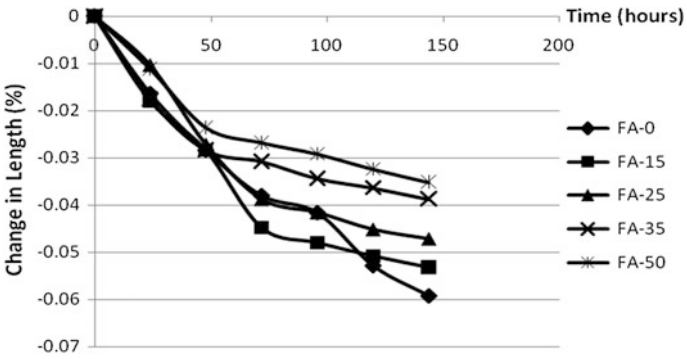

Fig. 37.8 Effect of fly ash on the change in length of concrete mortar

37.4 Conclusion

(i) The increase of fly ash percentage influences the slump test result. Concrete with fly ash is more workable than the ordinary Portland cement concrete. It is because fly ash has spherical shapes particles that influence the concrete workability. Besides, the superplasticizer also influences the workability of concrete.

(ii) Higher percentage of fly ash leads to longer both initial and final setting time of concrete. It is because the mixture has less cement content, which plays an important role in hydration process to form the calcium-silicate gel.

(iii) Concrete with fly ash as partial replacement of cement tends to have lower strength in the earlier age than the ordinary Portland cement concrete. Otherwise, in later age concrete with fly ash has higher strength compared to controlled specimen. The maximum compressive strength is 46.26 MPa at 28 days obtained by the FA-50 mixture. It is because the lower water and cementitious ratio due to water reduction and the pozzolanic reaction between fly ash and calcium hydroxide.

(iv) Higher percentage of fly ash results in smaller change in length. It is because the mixtures have lesser water content, so that the change in length of mortar specimen due to the temperature and the evaporation of water will have the smaller shrinkage percentage. The smallest change in length is 0.0352%, obtained by the FA-50 mixtures.

References

1. *ACI 212.3R-10*, in *Report on Chemical Admixtures for Concrete*. American Concrete Institute (2010)
2. *ACI 232.1R-12*, *Report on the Use of Raw or Processed Natural Pozzolans in Concrete* (American Concrete Institute, 2012)
3. ACI 232.2R-03, in *Use of Fly Ash in Concrete* (American Concrete Institute, 2003)
4. K. Klara, R. Hela. in *Use of Green Cement in Concrete for Friendly Building Construction. Latest Trends in Sustainable and Green Development*. ISBN: 978-1-61804-132-6
5. https://en.wikipedia.org/wiki/Superplasticizer
6. Chakkamalayath Jayasree, *Ravindra Gettu* (Manu Santhanam, The Indian Concrete Journal, 2011)
7. *ASTM C143*, in *Standard Test Method for Slump of Hydraulic-Cement Concrete* (ASTM International, PA, USA, 2005)
8. *ASTM C403*, in *Standard Test Method for Time of Setting of Concrete Mixtures by Penetration Resistance* (ASTM International, PA, USA, 2008)
9. *ASTM C39*, in *Standard Test Method for Compressive Strength of Cylindrical Concrete Specimens* (ASTM International, PA, USA, 2001)
10. *ASTM C157*, in *Standard Test Method for Length Change of Hardened Hydraulic-Cement Mortar and Concrete* (ASTM International, PA, USA, 2014)

11. B. Kondraivendhan, B. Bhattacharjee, International Journal of Sustainable Built Environment **4**, 270 (2015)
12. Chindaprasirt Prinya, Chai Jaturapitakkul, Theerawat Sinsiri, Cement Concr. Compos **27**, 425 (2005)
13. P. Nath, P. Sarker, Procedia Eng **14**, 1149 (2011)
14. C. Prinya, S. Homwuttiwongb, V. Sirivivatnanonc. Cement Concr. Res. **34**, 1087 (2004)

Part IV
Applications of Advanced Materials

Chapter 38
Optical Nanowaveguides Based on Zinc Oxide Plasmonic Materials

A.M. Lerer, P.E. Timoshenko, T. Yu. Chernikova, E.M. Kaidashev and A.J. Emaimo

Abstract The numerical study of nanowaveguides containing ZO, AZO, GZO and other materials are studied in infrared range. The dispersion equation for the waveguides, containing an arbitrary number of layers, is solved numerically by the separation of method variables in cylindrical coordinates. The integral-differential equations in vector form of the electromagnetic waves propagation in nanowaveguides, containing a finite width plasmon films, are obtained and calculated by the Galerkin' method. The opportunity of surface plasmon-polariton propagation with a large deceleration ratio is shown.

38.1 Introduction

The surface TM-wave (surface plasmon-polariton, SPP) with a large deceleration ratio can propagate at the interface of plasma-insulator or metal-dielectric in optical range. The phenomenon [1, 2] allows one to create plasmonic waveguides conducting the light signals in the volumes smaller than the diffraction limit. It can significantly reduce the size and increase the efficiency of optical integrated circuits. The main shortcoming of plasmon waveguides are strong losses due to the large absorption in metals. The metal waveguides provide a large deceleration at wavelengths less than micrometer. The main aims of the nanophotonic circuits developers [2] are to extend the operating band of plasmon waveguides and to achieve an optimal balance of SPP localization and waveguide losses.

A.M. Lerer · P.E. Timoshenko (✉) · T.Yu. Chernikova · A.J. Emaimo
Department of Physics, Southern Federal University, Rostov-on-Don, Russia
e-mail: P.E.Timoshenko@GMail.com

P.E. Timoshenko · E.M. Kaidashev
Laboratory of Nanomaterials, Southern Federal University, Rostov-on-Don, Russia

I.A. Parinov et al. (eds.), *Advanced Materials*, Springer Proceedings in Physics 193, DOI 10.1007/978-3-319-56062-5_38

Recently, the new materials based on ZO, AZO, GZO, ITO and other were created [3, 4]. So the goal of this paper is a numerical study of the dispersion characteristics of nanowaveguides, containing such materials in the infrared range. Subject matter of the study is the following nanowaveguides: (i) semi-infinite dielectric structures, the new material, dielectric, (ii) planar nanowaveguides, formed by plane-parallel dielectric layers, the new material, and (iii) planar nanowaveguides, formed by the finite thickness films of the new material lying on the multilayered dielectric substrate.

The well-known analytical expressions [2] calculating the wavelength and the decay constant of SPP are used to study the first type waveguides. The optimal wavelength ranges for spread of SSP are found. The ranges are used to investigate the second type nanowaveguides.

The dispersion equation for the second type waveguide, containing an arbitrary number of layers, is obtained and solved numerically. The waveguide is a prototype of the third type nanowaveguide that can be practically implemented.

The way to find the complex propagation constant in waveguide structures with small losses is proposed. The properties of SPP propagating in offered structures are investigated and applied to study the third type nanowaveguides. The solution of the integral-differential equations in vector form of the electromagnetic waves propagation in nanowaveguides containing a finite width plasmon films is given by the Galerkin' method. The possibility of SPP propagation with a large deceleration ratio is shown.

38.2 Statement of the Problem

The development of computer chips with the replacement of electrical connections with optical ones is up-to-date. Planar dielectric waveguide [2] (PDW) is the basis of integral optics. Silicon PDWs were used in the last case. In most cases a PDW is a dielectric strip on a dielectric substrate with a lesser refractive index. The size of a PDW can be approximately calculated as

$$L \approx \frac{\lambda}{2n},$$

where λ is the wavelength in vacuum, n is the wave deceleration coefficient in the waveguide. To reduce the sizes of PDWs, n needs to be reduced. One of the possible ways of use is plasmonic materials, which have $\mathrm{Re}\varepsilon(\lambda) < 0$ in their optical ranges. Recently, we used Au, Ag and Cu. There is a possibility of SPP wave propagation on the dielectric-plasmonic material boundary. In which two problems arises.

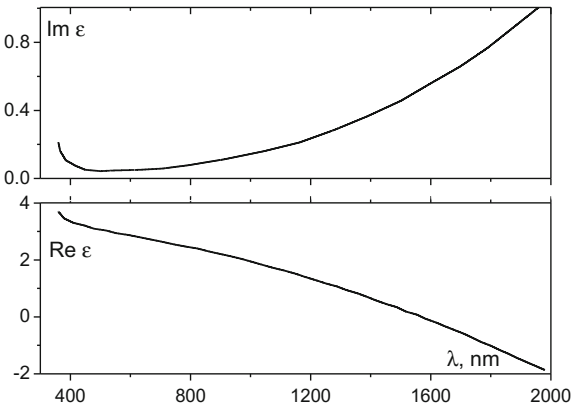

Fig. 38.1 Dielectric constant of AZO [3]

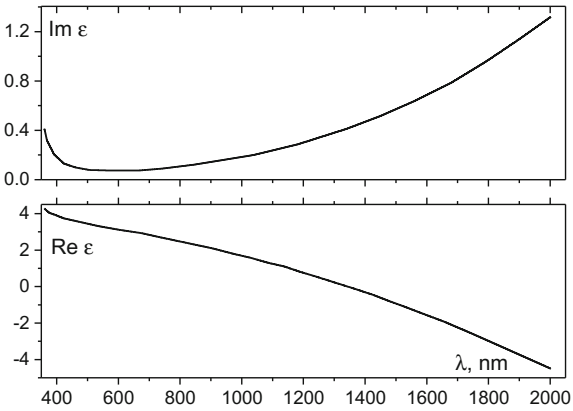

Fig. 38.2 Dielectric constant of GZO [3]

The first and basic problem is high losses. The propagation length of SPP is less then few wavelengths. The surface waves are used in the development of non-reflective optical coatings [5]. Although they limit the waveguide usage of SPP. Trials to find an optimum construction has not been successful. The second problem is SPP in metals have a huge deceleration only in the visible spectrum.

Lately, there has been a rise of new materials, which have $\mathrm{Re}\varepsilon_{metal}(\lambda) < 0$ in their optical range [3, 4]. It is important to firstly take note of ZnO, doped Al and Ga (Figs. 38.1 and 38.2). These materials were even given specific names—AZO and GZO, respectively. In Figs. 38.3 and 38.4 are the refractive indexes of two other materials—HfN, ZrN.

We are theoretically studying the possibility of using new plasmonic materials in waveguides, photonic crystals, and different types of diffraction gratings. Part of these researches is present in this work.

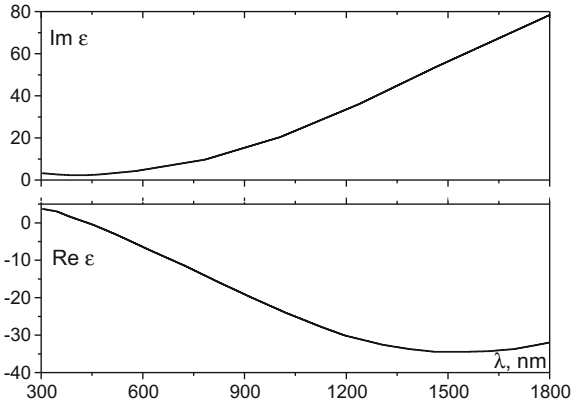

Fig. 38.3 Dielectric constant of HfN [4]

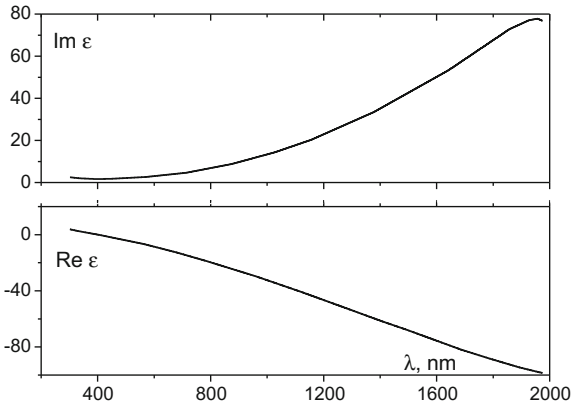

Fig. 38.4 Dielectric constant of ZrN [4]

38.3 Waves on the Dielectric—Plasmonic Material Boundary

An accurate formula was used for the calculation of the SPP [2]:

$$n = n' - in'' = \frac{\beta}{k} = \sqrt{\frac{\varepsilon\,\varepsilon_{pl}}{\varepsilon + \varepsilon_{pl}}}$$

where β is the complex propagation constant, k is wave constant in free space; ε, ε_{pl} are refractive indices of the dielectric and plasmonic materials, the dependence on time is $\exp(i\omega t)$.

Figure 38.5 shows the results of the calculations of the dispersion characteristics of SPP, that disseminate at the dielectric—plasmonic material boundary. Continuous curves represent the dielectric with $n = 1.77$, while the ones with dashes, ZnO. Curve 1 corresponds to HfN, 2—TiN, 3—ZrN. The propagation length of a wave L is understood as the distance at which it fades e times.

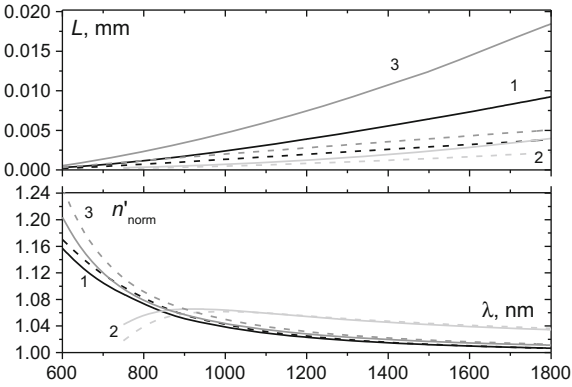

Fig. 38.5 Dispersion characteristics of SPP, $n'_{norm} = n'/\sqrt{\mathrm{Re}\varepsilon}$, ε is the permittivity of a dielectric in a specific wavelength

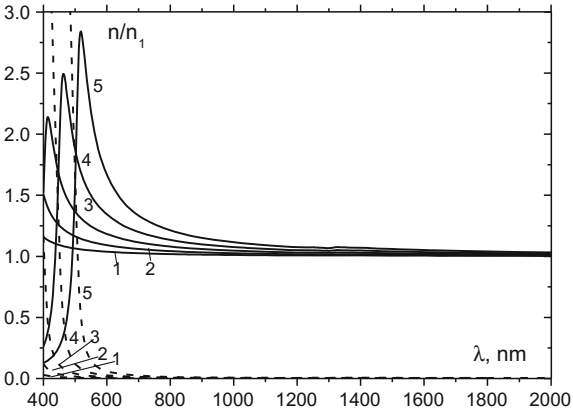

Fig. 38.6 Real and imaginary part of the normalized deceleration coefficient of SPP in the structure of silver-dielectric (n_1 is the refractive index)

SPP can also be seen on the metal-dielectric boundary (Fig. 38.6) with high losses, propagation length comparable with wavelength. The greater n' (that is, the shorter the wavelength), the greater the loss and the shorter the propagation length. In comparison with metallic layers, a big deceleration coefficient can be derived when $\lambda \geq$ 800 nm.

38.4 Planar Waveguides

The dispersion relation was derived for the calculations of random numbers of dielectric layers with complex dielectric constants. The equation is written in the form of recurrent formulae. An approximate method of finding the complex roots of complex functions is described in [6].

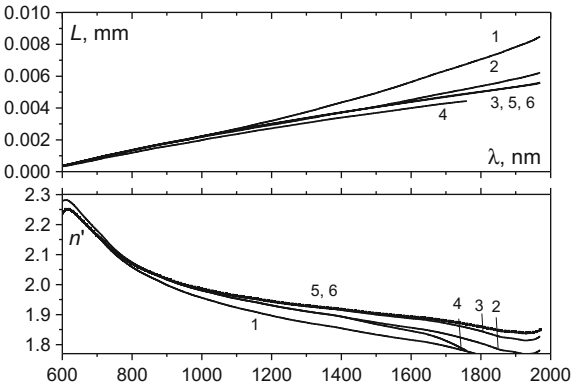

Fig. 38.7 Dispersion characteristics of planar waveguides: *1* h_1 = 100 nm, h_2 = 200 nm; *2* h_1 = 100 nm, h_2 = 400 nm; *3* h_1 = 100 nm, h_2 = 1000 nm; *4* h_1 = 50 nm, h_2 = 1000 nm; *5* h_1 = 200 nm, h_2 = 1000 nm; *6* h_1 = 400 nm, h_2 = 1000 nm

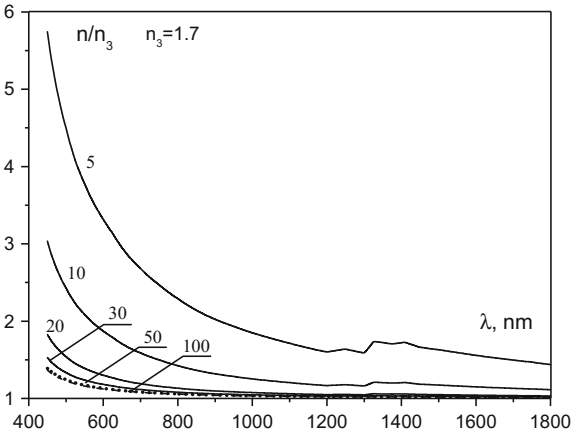

Fig. 38.8 Real part of the normalized deceleration ratio of SPP in a silver film layered structure in between two dielectrics

The investigated structure consists of the substrate with n = 1.77, a h_2-thick layer of ZnO, a h_1-thick layer of ZrN. As it can be seen in Fig. 38.7, the deceleration coefficient n' in the range of wavelengths far from the critical wavelengths weakly depends on the thickness of both ZnO layer and ZrN layer wavelengths range. This affirms the existence of SPP at the phase boundary of these dielectrics. The more the critical wavelength n' is approached losses reduce with reduction in the thickness of ZnO layer.

The deceleration is greater in thin (with thickness less than 30–50 nm) layers made of plasmonic materials in between two dielectrics (Figs. 38.8 and 38.9).

As it is shown in Figs. 38.8 and 38.9, a deceleration ratio greater than the refractive index of the substrate can be obtained. This property of SPPs seems promising for the development of real planar nanowaveguides. In paper [6], it is shown that the best properties are owned by waveguides-dielectric substrate, thin metallic slate, dielectric substrate.

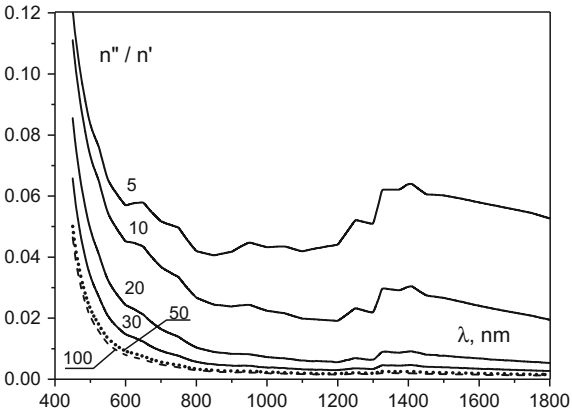

Fig. 38.9 The imaginary part of the normalized deceleration ratio of SPP in a silver film layered structure in between two dielectrics

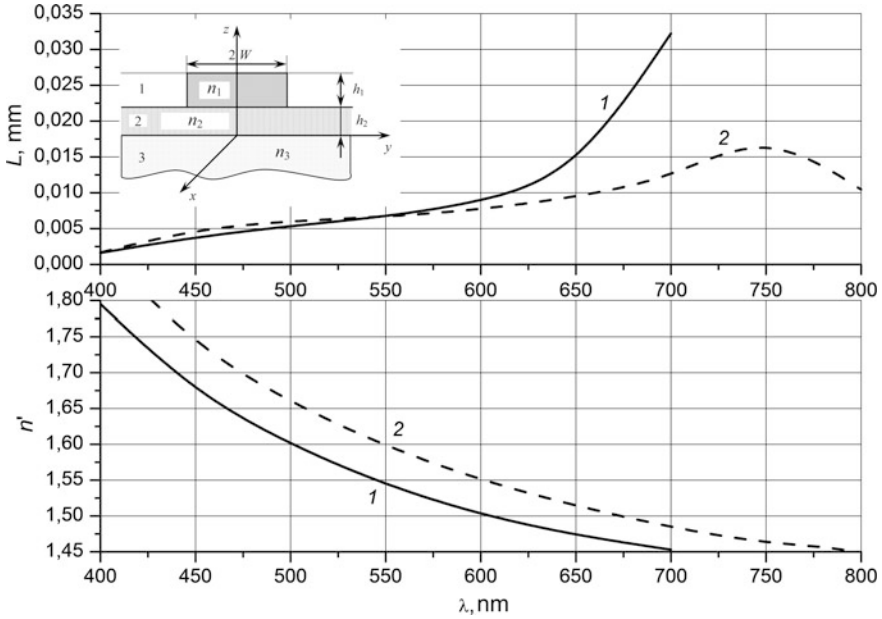

Fig. 38.10 Dispersion characteristics of waveguide with GZO material: n_1—ZnO, n_3 = 1.45, W = 100 nm, h_1 = 100 nm, h_2 = 100 nm: *1* rectangular waveguide, *2* waveguide-prototype

38.5 Rectangular Waveguides

The structure of the rectangular waveguide is presented in Fig. 38.10. There are two methods used in calculation. The first method is the strict volume integral method, which is described in [6]. The second method is the method of effective dielectric

constants (EDCs). The EDCs method is easy and suitable for realization. It consists of two stages.

Let us consider the first stage. The waveguide is divided into N_x multilayered wave guiding structures by vertical lines. In general, each structure has various amounts of horizontal layers. Each of these waveguides is taken as infinite (planar) in a horizontal direction. If a structure is continuous in a vertical direction, then the deceleration coefficient of the waveguide is equal to the refractive index of the dielectric. If the selected structure cannot permit the dissemination of its own waves (for example, in a structure made up of two partially infinite dielectrics in the vertical direction with dielectric constants of the same sign), the deceleration coefficient of the waveguide is equals to the refractive index of the waveguide in study. If in the chosen structure, dissemination of personal waves are allowed, the deceleration coefficient of these waveguides can be found.

In the second stage, a planar waveguide (vertically semi-infinite layers), made up of N_x layers is studied. The refractive index of the n-th layer is the deceleration coefficient found in the first stage. The deceleration coefficient of waves, disseminating in the waveguide is found. They are taken as the deceleration coefficient of the initial waveguide with a complex form of a c-section.

The strict volume integral method is used to verify the EDC method. In the wavelength range, in which surface wave propagation is allowed, the EDC method ensures the precision of the calculation of the parameters of the nanoplasmonic waveguides for practical purposes.

The dispersion characteristics of waveguides, containing layers of ZnO (layer number 1) and GZO (layer 2) are shown in Fig. 38.10. The waveguide-prototype is a waveguide with $W \to \infty$.

Figures 38.11 and 38.12 show the characteristics of waveguides, consisting of substrates with $n = 1.77$, a layer of 400 nm thick, the film made from a plasmonic material 100 nm thick, with width w. The results for the wave guide with ZrN are in Fig. 38.11, but Fig. 38.12 shows the comparison between waveguides made from

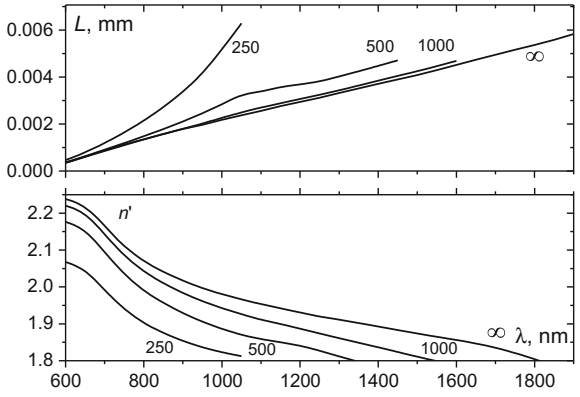

Fig. 38.11 Dispersion characteristics of rectangular waveguides of ZrN. The numbers of the *curve w* are in nanometers

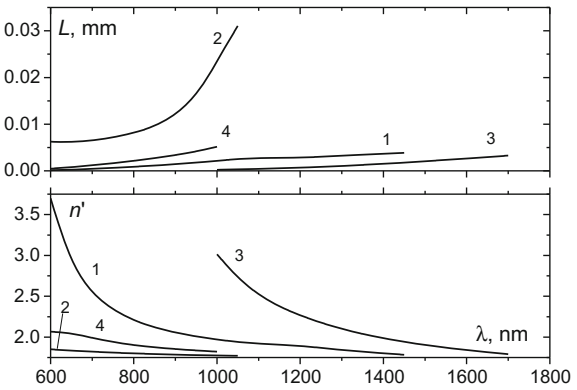

Fig. 38.12 Dispersion characteristics of rectangular waveguides with w = 250 nm: *1* HfN film, *2* ITO, *3* TiN, *4* ZrN

different plasmonic materials. Reduction in the width of the waveguide reduces the working range of wave lengths, deceleration coefficient, but significantly reduces losses. From these pictures—diagrams, a conclusion can be made that optical waveguides with metallic slates likewise have great losses, the propagation length is comparable with the wavelength.

The rectangular waveguide made from new plasmonic materials can work in the infrared spectrum; the loss is great, the propagation length of some wavelengths. It is possible that this is enough for chips with thick packages.

38.6 Conclusions

The Galerkin method is used to find the exact solution of a vector integral-differential equation to describe electromagnetic wave diffraction on three-dimensional bodies with complex dielectric permeability. Three types of nanowaveguide were simulated: (i) semi-infinite dielectric structures, the new material, dielectric, (ii) planar nanowaveguides, formed by plane-parallel dielectric layers, the new material, and (iii) planar nanowaveguides, formed by the finite thickness films of the new material lying on the multilayered dielectric substrate.

Acknowledgements The authors acknowledge the support of the Russian Ministry of Education and Science, provided by grant 16.219.2014/K "The synthesis methods development, the theoretical and experimental investigation of the nanostructures based on ZnO performs to create photodetectors, optical nanoantennas, piezo- and chemosensors", and the Internal Grant project of Southern Federal University in 2014–2016, provided by grant 213.01.-07.2014/08PCHVG, for carrying out this research study.

References

1. E.M. Kaidashev, N.V. Lyanguzov, A.M. Lerer, E.A. Raspopova, Tech. Phys. Lett. **40**(7), 79 (2014)
2. A.D. Rakic, A.B. Djurisic, J.M. Elazar, M.L. Majewski, Appl. Opt. **37**(22), 5271 (1998)
3. G.V. Naik, J. Kim, A. Boltasseva, Opt. Mater. Express **1**(6), 1090 (2011)
4. G.V. Naik, V.M. Shalaev, A. Boltasseva, *Proc. SPIE 7754, Metamaterials: Fundamentals and Applications III*, 77540M (2010)
5. A.M. Lerer, E.A. Tsvetyanskii, Tech. Phys. Lett. **38**(11), 995 (2012)
6. A.M. Lerer, I.V. Donets, G.A. Kalinchenko, P.V. Makhno, Photon. Res. **2**(1), 31 (2014)

Chapter 39
Superconducting Film Concentrator of the Magnetic Field

Levan P. Ichkitidze, Sergei V. Selishchev, Nikolai Yu Shichkin and Dmitri V. Telyshev

Abstract The superconducting film magnetic field concentrator is investigated. It is established that nanostructuring of an active strip of the concentrator on superconducting branches and cuts (width of cuts is 20 nm) allows one to increase several times concentration coefficient of a magnetic field and, therefore, to lower threshold sensitivity of magnetic field sensor. Thus higher values of concentration coefficient are reached in magnetic field concentrator based on films from a low-temperature superconductor compared to concentrator based on films from a high-temperature superconductor.

In most of the magnetic field sensors (MFSs), high resolution, i.e. low threshold magnetic sensitivity $\delta B_0 \leq 1$ nT, is achieved through the use of magnetic field concentrator (MFC) based on superconducting films. They lower δB_0 in MFS, in which different structures can serve as magneto sensitive elements (MSEs): the Josephson transitions, Hall sensors, sensors on spintronic effects, etc. [1].

Nanostructuring of the active strip of MFC, i.e. its partition into alternating superconducting branch and cuts, having nanosized width and thickness, leads to an additional increase of its concentration coefficient [2]. This further reduces δB_0, and thereby improves the resolution (efficiency) of MFS. In [3] for planar MFS with a superconducting film magnetic flux transformer (MFT), we calculated values of concentration coefficient, however, not taken into account the possibility of varying the size of MSE and inductance of MFT receiving rings.

The purpose of this work is the calculation of the concentration coefficient of the magnetic field in the planar sensor, when active strip of the concentrator is located in nanostructured state and without nanostructuring. Here we take into account the inductance of the MFC receiving rings.

L.P. Ichkitidze (✉) · S.V. Selishchev · N.Y. Shichkin · D.V. Telyshev
National Research University "MIET", 124498 Zelenograd, Moscow, Russia
e-mail: leo852@inbox.ru

I.A. Parinov et al. (eds.), *Advanced Materials*, Springer Proceedings in Physics 193, DOI 10.1007/978-3-319-56062-5_39

Figure 39.1 shows a schematically image of the MFC. Here are shown Fig. 39.1a MFC in the form of superconducting rings, between which MSE is enclosed; Fig. 39.1b active strip of superconducting rings and MRE on an enlarged scale; Fig. 39.1c cuts are located at the same distance width of the active strip; Fig. 39.1d cuts are located at the same distance on half the width of the active stripe, located far from MSE; Fig. 39.1e cuts are located at the same distance on half the width of the active stripe, located near to MSE.

The width of the active MFC-strip w_s is less than the width of the remaining sections of the MFC on an order of magnitude or more. This leads to an increase in the density of the shielding current in the active strip, consequently, to an increased concentration of an external magnetic field near active MFC-strip and MSE [3].

The concentration coefficients were calculated for cases, when the active strip has no cuts F_0 (see Fig. 39.1b), and F, when there are cuts on the active strip (see Fig. 39.1c–e). Location of the slots on the active strip, size width of MSE and values of London depth of penetration λ were varied, taking into account only the projection of the magnetic field perpendicular to the substrate surface.

In an external magnetic field B_0 a magnetic flux which shield the ring 1 (Fig. 39.1), is defined as: $\phi = AB_{ext}$, where $A = \pi D^2/4$ is the size of the ring, D is the diameter of the ring. The shielding current I_S has a magnitude $I_S = \phi/(L+M)$, where L is the inductance of the ring, M is the sum of mutual inductances between the parts of the MFC and MSE. It is known that the value of L on an order of magnitude or more higher than the total induction M. In this case for I_S, we write:

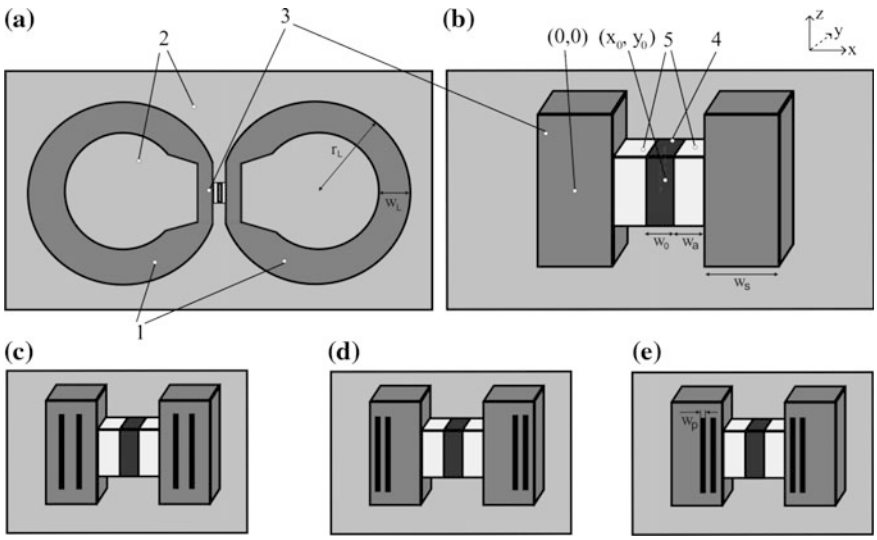

Fig. 39.1 Schematically image of the MFC with different locations of the cuts across the width of the active stripes: **a** MFC, *1* superconducting ring of the MFC, *2* dielectric substrate; **b** active stripes and MSE on a larger scale (*drawing without scale*), *3* active strip, *4* MSE, *5* insulating film; **c**, **d**, **e** cuts are located at various locations of active strip

$$I_s = \frac{\pi D^2 B_0}{4L}, \tag{39.1}$$

$$L = \left(\frac{\mu_0 D}{2}\right)\left(\ln\frac{4D}{w_L} - 2 + \frac{7w_L}{2D}\right), \tag{39.2}$$

where w_L is the width of the ring, $\mu_0 = 4\pi \cdot 10^{-7}$ H/m is a magnetic field constant.

The inductance L of ring of the MFC is much more than inductance L_S of the active strip. Formula (2) is given for the "thin ring" ($D, w_L \gg d, d$ is the thickness of the ring), but it is in the order of logarithmic accuracy is almost identical with L for the "thick ring" ($D, w_L \geq d$) [4]. In the case when the active strip consists of several branches, each with inductance L_i, the total inductance increases slightly concerning L_S.

The calculations use the formula to calculate the magnetic field created by a rectangular strip with uniform distribution of current I_S [5]:

$$B = \frac{\mu_0 I_S}{8\pi l h}\left[\int_{-2h}^{0}\int_{-l}^{0}\frac{(x_0 - x)}{(y_0 - y)^2 + (x_0 - x)^2}dxdy + \int_{-2h}^{0}\int_{0}^{+l}\frac{(x_0 - x)}{(y_0 - y)^2 + (x_0 - x)^2}dxdy\right]. \tag{39.3}$$

However, in a superconducting strip, the current flows non-uniformly: on the edges the current density is higher than in the middle. Considered the case of heterogeneous distribution of current on the active band width is described by the expressions:

$$J_x = J_e^{-\frac{x+l}{\lambda}}, \tag{39.4}$$

$$\frac{I_s}{2} = 2hJ_e\int_{-l}^{0} e^{-\frac{x+l}{\lambda}}dx, \tag{39.5}$$

where J_x, J_e are the current density at the point x and at the edges of the active strip during the exponential distribution of current, respectively. Values J_e are determined using (39.4) and (39.5) that half of the total I_S current flows in the half of the active strip. For the other half of the active strip, formulas (39.3)–(39.5) have similar forms. For the exponential current distribution, the magnetic field analogous to (39.3) are calculated by formula:

$$B_i = \frac{\mu_0 I_i}{8\pi\lambda h}\left[\int_{-2h}^{0}\int_{-l}^{0}\frac{e^{-\frac{x+l}{\lambda}}(x_0 - x)}{(y_0 - y)^2 + (x_0 - x)^2}dxdy + \int_{-2h}^{0}\int_{0}^{+l}\frac{e^{-\frac{l-x}{\lambda}}(x_0 - x)}{(y_0 - y)^2 + (x_0 - x)^2}dxdy\right], \tag{39.6}$$

According to (39.3)–(39.6), it is determined the magnetic field created by *i*-superconducting branch on MSE. These data allow us to calculate the following parameters:

$$F_0 = \frac{<B_0>}{B_0}, \tag{39.7}$$

$$F = \frac{<B>}{B_{ext}} \cdot \frac{1}{K_L}, \tag{39.8}$$

$$K_L = \frac{(\sum_{i=1}^{n} L_i^{-1})^{-1}}{L} \sim \frac{w_S}{\sum_{i=1}^{n} w_i}, \tag{39.9}$$

where w_S is the width of an active stripe; w_i is the width of *i*-th branch; n is the number of superconducting branches, $n = 1$ for a continuous (without nanostructuring) active strip; $n \geq 2$ for nanostructured active strip; $l\,and\,h$ are the half-width and half-thickness of *i*-th branch, respectively; $I_i/4\lambda h \leq J_c, J_c$ is the critical current density of the superconducting film of MFC; λ is the London depth of penetration of the magnetic field in the superconductor; K_L is the growth factor of the total inductance of the active strip; B_0 is the external magnetic field; $<B>$, $<B_0>$ are the averaged across the width of the MSE magnetic fields, generated by the current in the active strip with cuts and without them, respectively. Values of B_i, B and B_0, determined according to (39.1)–(39.3), were averaged across the width of the active strip; the average values $<B>$ and $<B_0>$ were used in (39.7) and (39.8).

Due to the fact that the length of the active strips and the slits are many times greater than MSE, (39.3)–(39.9) reflects only the projections of x and y, and the projection of z is not taken into account. Note that the case $i = 1$ corresponds to a solid (without nanostructuring) active strip. In all calculations, it was assumed that the width of the slot w_p coincides with the width of the gap w_a between the nearest edges of the MFC and MSE, and the width of the active stripe and its branches multiply of w_a.

Research of dependence F_0 and F from the width w_0 was conducted. Table 39.1 shows the results of calculations. We considered three values w_0: 0.2, 1 and 5 μm. For calculations, we took the following numerical values: $\lambda = 50\,\text{nm}, 250\,\text{nm}$; $J_c = 10^{10}\,\text{A/m}^2$, $h = 10\,\text{nm}$, $w_s = 30\,\mu\text{m}$, $w_a = w_p = 20\,\text{nm}$. When $r_L = D/2 = 1\,\text{mm}$

Table 39.1 Dependence of concentration coefficient on the width of MSE

w_0 (μm)	F_0		F	
	$\lambda = 50\,\text{nm}$	$\lambda = 250\,\text{nm}$	$\lambda = 50\,\text{nm}$	$\lambda = 250\,\text{nm}$
5.0	211	157	267	212
1.0	677	438	742	502
0.2	1766	954	1828	1021

(radius of the ring) and $w_L = 0.8$ mm (thickness of the ring), it was approximately achieved the minimum value of L, that was used in (39.2). For calculations on the active strip, slots were applied uniformly (see Fig. 39.1) in the amount of two pieces.

Table 39.1 shows that the reduction of the width of MSE increases as F_0, as F, reflecting the positive effect of the nanostructuring of the active strip. Threshold sensitivity depends on the concentration factor as $\delta B_0 \sim 1/F$, [3], therefore use as the MFC films from low-temperature superconducting (LTSC) materials (e.g., epitaxial layers of niobium, $\lambda = 50$ nm) is most effective compared to the use of films of high temperature superconducting (HTSC) materials (for example, Y-123 and Bi-2223, $\lambda \geq 250$ nm). Particularly low value δB_0, i.e. high efficiency MFC, is realized when MSE has a narrow width (0.2 μm) and $F \sim 1828$.

When the current is uniformly distributed over the cross section of the active strip, the concentration factor F_0^h as determined according to (39.3), is low. Indeed, with $w_0 = 5.0$ μm and $\lambda = 50$ nm, the value $F_0^h = 42$ is much smaller than in the case of $F_0 = 211$ (inhomogeneous current distribution in a continuous active strip).

Also the study of dependence of F from the method of application of cuts on the active strip with $\lambda = 50$ nm was conducted. The calculations showed that the optimum can be case, when the cuts are closer to MSE (see Fig. 39.1e). In this case, $F \sim 1899$, which is approximately in 1.05 times larger compared with the case, where the slits are distant from MSE $F \sim 1801$ (see Fig. 39.1d), and almost in 1.04 times higher compared with the case where the slits evenly over the strip $F \sim 1828$.

Note that the MFC or MFT from superconducting film can significantly lower the threshold sensitivity of the MFS. In particular, the combined MFS type "sandwich" consisting of a superconducting film concentrator of the structure of spintronics as MSE, managed to obtain a resolution $\delta B_0 \leq 5$ fT on the level of resolution of the SQUID [1]. Thus estimated F_0 agrees well with the measured values [6]. It should be noted that according to (39.1), (39.2), (39.3) and (39.7) in the order of magnitude $F_0 \sim D/(w_0 + w_p)$, i.e. for improvement of F_0, it is required to increase the diameter D of the receiving ring, that leads to an increase of the geometric dimensions of a continuous (without nanostructuring) MFS. However, the nanostructuring of the MFS allows one to further increase the concentration coefficient and the need to increase D is disappears. For example, for a solid (without nanostructuring) MFS obtained, we calculated value of $F_0 = 1766$, when the diameter $D = 2$mm and the parameters shown in Table 39.1. However, after the nanostructuring of the active strip, while maintaining the same parameters value F_0 can be reduced and, accordingly, reduce the previous value D in F/F_0 time. Obviously, such a situation can be realized, when also large value of F does not allow to reduce δB_0, as it is limited by the noise of MSE or structural noise of the MFS. It is seen that nanostructuring of the active strips can reduce either the resolution or the geometric dimensions of the MFC, which is a significant factor for improving its effectiveness. Obviously, in the latter case, geometrical dimensions of the MFS are sharply reduced, as they are practically determined by the size of the MFC (see Fig. 39.1).

We fix that the important fact that the natural non-uniform current distribution in the superconductor in the design allows one to achieve high values of the concentration coefficient, which is further enhanced by the nanostructuring of the active stripes of the MFC. However, with homogeneous current distribution in the active strip, in particular, for example, when it represents a normal metal, the concentration coefficient according to (39.3) can has a small value ≤ 100, for the input parameters of the MFC reviewed by us.

Thus, from the analysis of the results, it follows: the nanostructuring of the active strip of superconducting film magnetic field concentrator for parallel branch and cuts, changing the width of the magnetically sensitive element, and the use of low-temperature superconducting materials, allows one to achieve a significant increase in the coefficient of concentration of the magnetic field and, thereby, lowering the threshold of sensitivity of magnetic field sensor.

In modern medicine, new biocompatible materials (nanomaterials with ferromagnetic or superparamagnetic particles, carbon nanotubes, etc.), non-invasive diagnosis and monitoring of active implanted devices (artificial heart, various stimulants, measurement of blood flow velocity, etc.) are actual. Required tasks will probably be solved with the use of magnetic field sensors with superconducting film magnetic field concentrator with nanostructured active stripes.

Acknowledgements This work was supported by the Ministry of Education and Science of the Russian Federation, agreement No. 14.581.21.0014 (Project ID RFMEFI58115X0014).

References

1. D. Robbes, Sens. Actuators A **129**(1), 86 (2006)
2. L.P. Ichkitidze, A.N. Myronyuk, Nano Microsyst. Tech. **1**, 47 (2012) (In Russian)
3. L.P. Ichkitidze, Nano Microsys. Tech. **9**, 38 (2013) (In Russian)
4. A.V. Saveliev, N.P. Chubinskiy, Radio Electron. Mag. E-zine. **2**, 1 (2015). http://jre.cplire.ru/mac/feb15/3/text.html
5. D.V. Vagin, S.I. Kasatkin, P.A. Polyakov, in *Proceedings Hardware and Software Control Systems, Control and Measurement*, 18–20 October 2010, Moscow, 000240 (2010)
6. M. Pannetier-Lecoeur, Q. Herreros, H. Dyvorne et al., Rev. Sci. Instrum. **84**, 095116 (2013). doi:10.1063/1.4821657

Chapter 40
Comparison Between Applied Theory and Final Element Method for Energy Harvesting Non-homogeneous Piezoelements Modeling

Arkadiy N. Soloviev, Pavel A. Oganesyan, A.S. Skaliukh, Le V. Duong, Vijay Kumar Gupta and Ivan A. Panfilov

Abstract The chapter is devoted to modeling of non-uniformly polarized piezoelectric devices. We suggest that applying specific types of preliminary polarization can lead to significant growth of the electroelastic parameters of the device. Such parameters are electro-mechanical coupling coefficient, bandwidth of the transducer, maximum output voltage in circuit with resistor, eigen frequencies. Different approaches to modeling were tested and compared during study, including finite-element method in different packages and applied theory based on known plate models.

40.1 Introduction

The goal of present study is to develop a mathematical model, program tools and design workflow for efficient non-homogeneously polarized piezo-transducers. Such devices can be used as sensor, actuators, parts of energy harvesting systems, etc. Described materials and devices have very wide range of usage, different models were presented in papers like to [1, 2]. Common approach is to use

A.N. Soloviev (✉) · I.A. Panfilov
Don State Technicla University, 1, Gagarin Street, Rostov-on-Don 344000, Russia
e-mail: soloviev.arc@gmail.com

A.N. Soloviev · P.A. Oganesyan · A.S. Skaliukh
Vorovich Institute of Mathematics, Mechanics and Computer Science, Southern Federal University, 8a Milchakov Street, Rostov-on-Don 344090, Russia

L.V. Duong
Department of Mechanical Engineering, Le Quy Don Technical University, 100000 Hanoi, Vietnam

V.K. Gupta
Design and Manufacturing, PDPM Indian Institute of Information Technology, Jabalpur, India

I.A. Parinov et al. (eds.), *Advanced Materials*, Springer Proceedings in Physics 193, DOI 10.1007/978-3-319-56062-5_40

multipart design to create complicated structure of piezoelectric device. However, in this study we present preliminary polarization technique that leads to less number of parts in the design. Finite element analysis was performed in ACELAN and ANSYS software. ACELAN software provides additional capabilities for measuring preliminary polarization field and transferring it to the direct problem model. ANSYS software was used for simplified polarization modeling, but it provided specific elements for electric circuits. Calculation results were compared for verification where it was possible. Applied theory was tested against FEM numerical examples and it acceptable accuracy for presented models was proven.

40.2 Mathematical Formulation of the Problem

The mathematical model of each separate elastic or electro-elastic body is the same as in [3, 4]: piezoelectric transducer Ω is presented by a set of areas $\Omega_j = \Omega_{pk}$; $k = 1, 2,..., Np$; $j = k$ with the properties of piezoelectric materials, and a set of areas $\Omega_j = \Omega_{em}$; $m = 1,2,...,Ne$; $j = Np + m$ with the properties of elastic materials. It is appropriate to describe the physical-mechanical processes taking place in the media Ω_{pk} and Ω_{em} within the framework of piezoelectricity (electric-elasticity) and elasticity theory.

We assume that the following constitutive equations are satisfied (piezoelectric medium is $\Omega_j = \Omega_{pk}$):

$$\rho_{pk}\ddot{\mathbf{u}} + \alpha_{dj}\rho_j\dot{\mathbf{u}} - \nabla\cdot\boldsymbol{\sigma} = \mathbf{f}_j; \quad \nabla\cdot\mathbf{D} = 0 \tag{40.1}$$

$$\boldsymbol{\sigma} = \mathbf{c}_j^E\cdots(\boldsymbol{\varepsilon} + \beta_{dj}\underline{\boldsymbol{\varepsilon}}) - \mathbf{e}_j^T\cdot\mathbf{E};\ \mathbf{D} + \varsigma_d\dot{\mathbf{D}} = \mathbf{e}_j\cdots(\boldsymbol{\varepsilon} + \varsigma_d\underline{\boldsymbol{\varepsilon}}) + \ni_j^S\cdot\mathbf{E}, \tag{40.2}$$

$$\boldsymbol{\varepsilon} = (\nabla\mathbf{u} + \nabla\mathbf{u}^T)/2; \quad \mathbf{E} = -\nabla\varphi \tag{40.3}$$

where $\rho(x, t)$ is the continuous function of coordinates (density); $u(x)$ is the displacement vector-function; σ is the stress tensor, $\mathbf{f}$ are the mass forces; f are the mass forces; D is the electric induction vector; c_j^E are the components of the elastic constant tensor; e_j is piezoelectric stress coefficients; ε is the strain tensor; E is the electric field vector; $\varphi(x)$ is the electric potential function; $\ni_j^S$ are the components of the dielectric permittivity tensor; α_{dj}, β_{dj}, ζ_d are non-negative damping coefficients, and the other symbols are the standard designations for theory of electric-elasticity with the exception of index "j", corresponding for area Ω_j. (For elastic media $\Omega_j = \Omega_{ek}$ the piezomodules e_j are equal to zero).

For the media $\Omega_j = \Omega_{em}$ with pure elastic properties, only stress fields would be considered. Similar (40.1)–(40.3) and constitutive relationships are used with neglect electric fields and piezoelectric connectivity effects. Equations (40.1)–(40.3) are added to the mechanical and electrical boundary conditions, as well as the initial conditions in the case of non-stationary problem. Numerical modeling of devices that can be described with (40.1)–(40.3) are performed using finite element method.

In addition to previous equations, all material properties are handled as functions of coordinates:

$$\rho_k = \rho_{pk}(x)\ \mathbf{c}_j^E = \mathbf{c}_j^E(x)\ \boldsymbol{\varepsilon}_{aj}^S = \boldsymbol{\varepsilon}_{aj}^S(x)\ \mathbf{e}_j^T = \mathbf{e}_j^T(x) \tag{40.4}$$

$$\text{for tensors } \mathbf{c}_j^E \text{ and } \ni_j^S - g = g^i + |P|(g^a - g^i), \quad \text{for tensor } \mathbf{e}_j^T - g = |P|g^a \tag{40.5}$$

there g is corresponding tensor components, i marks isotropic state, a marks anisotropic state. Tensor of piezoelectric constants $\mathbf{e}_j^T$ will be zero for isotropic bodies. In previous papers [4], we presented specific moduli of ACELAN software for non-homogeneous polarization describing, presenting and modeling. Spline theory [5] was used for mesh-to-mesh transition of inhomogeneous polarization fields in vector form. In some cases, with simple polarization field we were able to describe it using one of predefined function available in ACELAN:

1. Exponential function $F(x, y) = c_1 e^{c_2 x + c_3 y}$
2. Polynomial function $F(x, y) = c_1 x^2 + c_2 y^2 + c_3 xy + c_4 x + c_5 y + c_6$
3. Heaviside step function $F(x) = \begin{cases} a, x \le t, \\ b, x > t; \end{cases}$
4. Double Heaviside step function $F(x) = \begin{cases} a, x \le t_1, \\ b, t_1 < x \le t_2, \\ c, t_2 < x; \end{cases}$
5. Sin $F(x) = a\ \sin(bx + s) + c$.

Numerical example of device with advanced properties was also presented in study [4]. It is a model of plain piezoelectric transducer (see Fig. 40.1) with free boundaries and electrodes on upper and lower plains. Material was PZT-4, the model included a study of damping with coefficients $\alpha = 2.7 \cdot 10^2, \beta = \zeta = 3.84 \cdot 10^{-8}$. Length of the rod was 1 cm, its thickness changed in numerical experiments from 0.025 to 0.200 cm. Oscillations were excited by the voltage of 200 V. Modes are present in Fig. 40.2. Three types of applied polarization are present in Fig. 40.3. Numerical results for polarization Type 2 are present in Table 40.1.

Let us call homogeneous polarization field Type 0 to describe results. As we can see, for the second eigen-mode huge, growth of bandwidth was discovered with specific type of polarization (Type 2). Similar results we obtained for combination of the third eigen-mode and polarization of Type 3.

Electromechanical coupling coefficient was enlarged up to 3.5 times for the second mode and up to 1.5 times for the third mode.

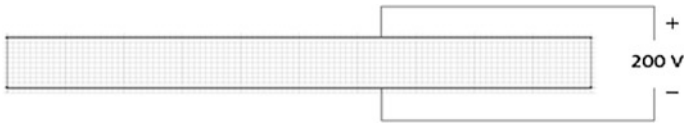

Fig. 40.1 Scheme of the transducer

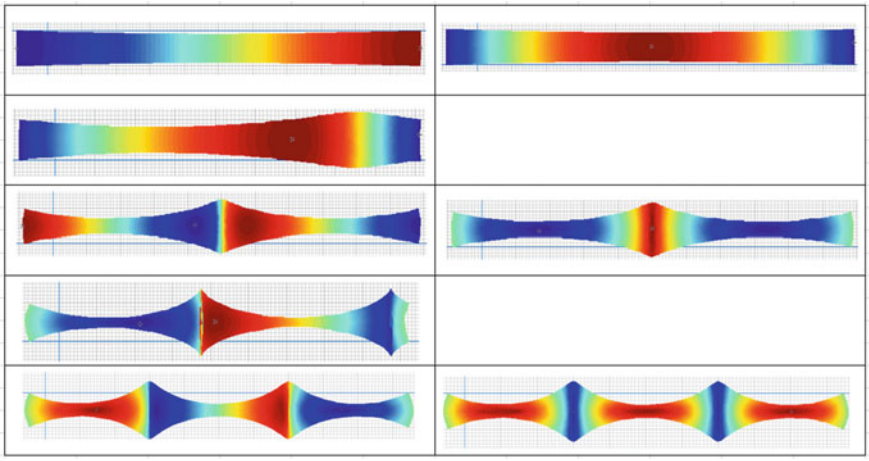

Fig. 40.2 Eigen-modes with displacement distribution (*left column*) and distribution of *x*-component of stress (*right column*). Modes without electromechanical coupling omitted

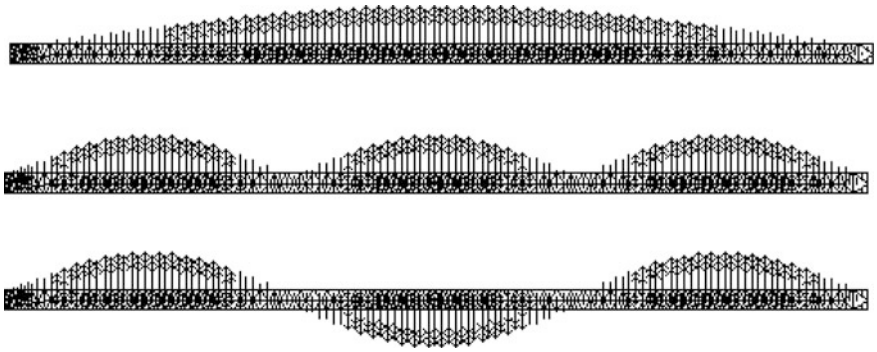

Fig. 40.3 Three types on inhomogeneous polarization, named type 1 (*top*), type 2 (*middle*), type 3 (*bottom*)

40.3 Simplified Polarization Modeling

The important question in this study can be formulated as follows: do we need to perform full polarization modeling in all types of numerical examples? Is it possible to avoid full computation and to use simplified model of polarization? We suggest to use model with blocks of uniformly polarized material combined into single body to mimicrate exact fields (Fig. 40.4). We modeled two layered transducer with top active layer and passive metallic bottom layer of similar sizes and proportions that was used in study [6].

Table 40.1 Numerical results for the second eigen mode

Width (cm)	0.2			0.1		
Polarization type	Type 0	Type 2	Type 3	Type 0	Type 2	Type 3
Displacement, U, m	$4.5 \cdot 10^{-7}$	$9.5 \cdot 10^{-7}$	$4.5 \cdot 10^{-7}$	$1.05 \cdot 10^{-6}$	$2.3 \cdot 10^{-6}$	$1.05 \cdot 10^{-6}$
Threshold, U, m	$2.25 \cdot 10^{-7}$			$5.25 \cdot 10^{-7}$		
Start of band, Hz	$4.78 \cdot 10^{4}$	$4.743 \cdot 10^{4}$	$4.822 \cdot 10^{4}$	$5.076 \cdot 10^{4}$	$4.95 \cdot 10^{4}$	$5.042 \cdot 10^{4}$
End of band, Hz	$4.895 \cdot 10^{4}$	$5.008 \cdot 10^{4}$	$4.934 \cdot 10^{4}$	$5.202 \cdot 10^{4}$	$5.248 \cdot 10^{4}$	$5.164 \cdot 10^{4}$
Bandwidth, Hz	1150	2650	1120	1260	2980	1220
Bandwidth growth (%)	0.00	130.43	−2.61	0.00	136.51	−3.17
Width (cm)	0.05			0.025		
Polarization type	Type 0	Type 2	Type 3	Type 0	Type 2	Type 3
Displacement, U, m	$2.2 \cdot 10^{-6}$	$4.6 \cdot 10^{-6}$	$2.1 \cdot 10^{-6}$	$4.4 \cdot 10^{-6}$	$9.5 \cdot 10^{-6}$	$4.2 \cdot 10^{-6}$
Threshold, U, m	$1.1 \cdot 10^{-6}$			$2.2 \cdot 10^{-6}$		
Start of band, Hz	$5.135 \cdot 10^{4}$	$5.002 \cdot 10^{4}$	$5.09 \cdot 10^{4}$	$5.15 \cdot 10^{4}$	$5.014 \cdot 10^{4}$	$5.102 \cdot 10^{4}$
End of band, Hz	$5.272 \cdot 10^{4}$	$5.288 \cdot 10^{4}$	$5.205 \cdot 10^{4}$	$5.287 \cdot 10^{4}$	$5.3 \cdot 10^{4}$	$5.215 \cdot 10^{4}$
Bandwidth, Hz	1370	2860	1150	1370	2860	1130
Bandwidth growth (%)	0.00	108.76	−16.06	0.00	108.76	−17.52

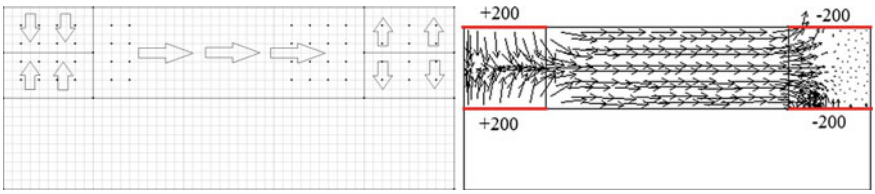

Fig. 40.4 Simplified blocks of polarization (*left*) compared to full vector field (*right*)

Varying size of electrodes from 5 to 20% of top surface of the device, we measured frequencies and electro-mechanical coupling coefficients (EMCC) for both full and simplified models. Results are present in Table 40.2. For some models (5, 20% electrodes) results are significantly different. Full polarization shows less EMCC because of unpolarized areas near borders. But in some cases (15%) results are relatively close.

Depending on geometry, electrodes and preliminary polarization, some models can be reduced to avoid extra computational time without significant accuracy loss.

Table 40.2 Modeling techniques comparison

Electrode size (%)	Homogenous	5		10	
Model	S	S	F	S	F
Resonance frequency, Hz	$3.54 \cdot 10^4$	$3.53 \cdot 10^4$	$3.13 \cdot 10^4$	$3.56 \cdot 10^4$	$3.14 \cdot 10^4$
Antiresonance frequency, Hz	$3.69 \cdot 10^4$	$3.74 \cdot 10^4$	$3.22 \cdot 10^4$	$3.74 \cdot 10^4$	$3.27 \cdot 10^4$
EMCC (%)	28.72	32.89	23.43	30.97	28.06
EMCC Growth (%)	0.00	14.52	−18.41	7.81	−2.31
Electrode size (%)		15		20	
Model		S	F	S	F
Resonance frequency, Hz		$3.60 \cdot 10^4$	$3.19 \cdot 10^4$	$3.62 \cdot 10^4$	$3.18 \cdot 10^4$
Antiresonance frequency, Hz		$3.76 \cdot 10^4$	$3.33 \cdot 10^4$	$3.74 \cdot 10^4$	$3.31 \cdot 10^4$
EMCC (%)		28.42	28.89	25.41	27.68
EMCC growth (%)		−1.05	0.58	−11.52	−3.64
Electrode size (%)		5	10	15	20
Max vertical displacement, simplified model, m		$1.08 \cdot 10^5$	$1.08 \cdot 10^5$	$1.09 \cdot 10^5$	$1 \cdot 10^5$
Integrated vertical displacement, simplified model, m^2		$3.48 \cdot 10^8$	$3.49 \cdot 10^8$	$3.52 \cdot 10^8$	$3.25 \cdot 10^8$
Max vertical displacement, full model, m		$8.94 \cdot 10^6$	$1.19 \cdot 10^5$	$1.29 \cdot 10^5$	$1.34 \cdot 10^5$
Integrated vertical displacement, full model, m^2		$2.87 \cdot 10^8$	$3.80 \cdot 10^8$	$4.11 \cdot 10^8$	$4.28 \cdot 10^8$

Fig. 40.5 Transducer scheme

40.4 Applied Theory

Part of transducer described in Sect. 40.3 can be modeled using applied theory. Let us reduce our model further into shape shown in Fig. 40.5.

Let's analyze one layered piezo-transducer with length L and thickness h; x-axes are placed on the middle line of the transducer. Presented theory is based on ideas described in [6, 7]. Equations to describe part with transverse polarization can written as follows:

$$\begin{aligned}
\sigma_{11} &= c_{11}\varepsilon_{11} + c_{12}\varepsilon_{22} + c_{13}\varepsilon_{33} + e_{31}\frac{\partial\phi}{\partial z} & \sigma_{23} &= c_{44}\left(\frac{\partial u_y}{\partial z} + \frac{\partial u_z}{\partial y}\right) + e_{15}\frac{\partial\phi}{\partial y} \\
\sigma_{22} &= c_{12}\varepsilon_{11} + c_{11}\varepsilon_{22} + c_{13}\varepsilon_{33} + e_{31}\frac{\partial\phi}{\partial z} & \sigma_{13} &= c_{44}\left(\frac{\partial u_x}{\partial z} + \frac{\partial u_z}{\partial x}\right) + e_{15}\frac{\partial\phi}{\partial x} \\
\sigma_{33} &= c_{13}\varepsilon_{11} + c_{13}\varepsilon_{22} + c_{33}\varepsilon_{33} + e_{33}\frac{\partial\phi}{\partial z} & \sigma_{12} &= \left(\tfrac{c_{11}}{2} - \tfrac{c_{12}}{2}\right)\left(\frac{\partial u_x}{\partial y} + \frac{\partial uy}{\partial z}\right) \\
D_1 &= e_{15}\left(\frac{\partial u_x}{\partial z} + \frac{\partial u_z}{\partial x}\right) - g_{11}\frac{\partial\phi}{\partial x} \\
D_2 &= e_{15}\left(\frac{\partial u_y}{\partial z} + \frac{\partial u_z}{\partial y}\right) - g_{11}\frac{\partial\phi}{\partial y} \\
D_3 &= e_{31}\varepsilon_{11} + e_{31}\varepsilon_{22} + e_{33}\varepsilon_{33} - g_{33}\frac{\partial\phi}{\partial z}
\end{aligned} \tag{40.6}$$

Extracting ε_{33} from equation for σ_{33} gives us

$$\varepsilon_{33} = -\frac{c_{13}e_{11} + c_{13}\varepsilon_{22} + e_{33}\frac{\partial\phi}{\partial z}}{c_{33}}$$

Let us substitute above equation into (40.6) and assume ε_{22} = 0:

$$\begin{aligned}
\sigma_{11} &= c_{11}\varepsilon_{11} - c_{13}\frac{c_{13}e_{11} + e_{33}\frac{\partial\phi}{\partial z}}{c_{33}} + e_{31}\frac{\partial\phi}{\partial z} \\
\sigma_{22} &= c_{12}\varepsilon_{11} - c_{13}\frac{c_{13}e_{11} + e_{33}\frac{\partial\phi}{\partial z}}{c_{33}} + e_{31}\frac{\partial\phi}{\partial z}
\end{aligned} \tag{40.7}$$

Potential distribution will be found as:

$$\phi(x,y,z) = \frac{V_0 z\left(\frac{2z}{h} - 1\right)}{h} + \frac{V_0 z\left(\frac{2z}{h} + 1\right)}{h} + \Phi(x)\left(1 - \frac{4z^2}{h^2}\right), \tag{40.8}$$

where V_0 is the function that describes potential distribution on the surface of the plate.

Displacement distribution can be found as

$$\mathbf{u}(x,y,z) = -\frac{\partial U_z(x)}{\partial x} * z. \tag{40.9}$$

Using (40.7), (40.8) in (40.6) allows one to extract V_0:

$$V_0 = \frac{1}{8}\frac{\left[-e_{31}\frac{\partial^2 U_z(x)}{\partial x^2}h^2 c_{33} + e_{33}c_{13}\frac{\partial^2 U_z(x)}{\partial x^2}h^2 + 8e_{33}^2\Phi(x) + 8g_{33}c_{33}\Phi(x)\right]}{e_{33}^2 + g_{33}c_{33}}$$

Evaluating linear bending moment M_{11} and linear transverse force Q_1 as

$$M_{11} = \int\limits_{-h/2}^{h/2} \sigma_{11} z dz$$
$$= \frac{1}{12}\left\{ -c_{11}\frac{\partial^2 U_z(x)}{\partial x^2} - \frac{c_{13}\left[c_{13}\frac{\partial^2 U_z(x)}{\partial x^2} + \frac{8e_{33}}{h^2}(V_0 - \Phi(x)\right]}{c_{33}} + \frac{8e_{31}}{h^2}[V_0 - \Phi(x)] \right\} h^3 \tag{40.10}$$

$$Q_1 = -\frac{\partial M_{11}}{\partial x}$$
$$= \frac{1}{12}\left\{ -c_{11}\frac{\partial^3 U_z(x)}{\partial x^3} - \frac{c_{13}\left[c_{13}\frac{\partial^3 U_z(x)}{\partial x^3} - \frac{8e_{33}}{h^2}\frac{\partial \Phi(x)}{\partial x}\right]}{c_{33}} - \frac{8e_{31}}{h^2}\frac{\partial \Phi(x)}{\partial x} \right\} h^3$$

Equations for displacements and potential have the forms:

$$\begin{gathered} \frac{\partial Q_1}{\partial x} - p(x) - W^2 \rho h U_z(x) = 0 \\ \int\limits_{-h/2}^{h/2} \left(\frac{\partial D_3}{\partial x} + \frac{\partial D_1}{\partial x} \right) dz = 0 \end{gathered} \tag{40.11}$$

where ρ is the density, $p(x)$ is the external load, $W = 2\pi\omega$, ω is the frequency. After all substitutions, we have the equation set:

$$\begin{cases} -\frac{1}{12}\left(-c_{11} + \frac{c_{13}^2}{c_{33}}\right) h^3 \frac{\partial^4 U_z(x)}{\partial x^4} - \frac{1}{12}\left(\frac{8c_{13}e_{33}}{h^2 c_{33}} - \frac{8e_{31}}{h^2}\right) h^3 \frac{\partial^2 \Phi(x)}{\partial x^2} \\ \qquad\qquad -p(x) - W^2 \rho h \frac{\partial U_z(x)}{\partial x} = 0 \\ \left(-e_{31} + \frac{e_{33}c_{13}}{c_{33}}\right)\frac{\partial^2 U_z(x)}{\partial x^2} + K\Phi(x) - KV_0 - \frac{2}{3}g_{11}\frac{\partial^2 \Phi(x)}{\partial x^2} = 0 \end{cases} \tag{40.12}$$

where $K = \frac{8e_{33}^2}{h^2 c_{33}} + \frac{8g_{33}}{h^2}$.

The second part with longitudinal polarization can be described in similar way. For the ease of material constants numeration, local coordinate system with starting position at $(L, 0)$ must be added.

Switching z- and x-axes will lead us to needed simplification, letting us to use initial equations. Potential distribution can be described with following function:

$$\phi(x, y, z) = \Phi(z)$$

Extract D_3, M_3 and Q_3, using similar approach as before:

$$D_3 = \left(-\frac{e_{31}^2}{c_{11}} - g_{33}\right)h\frac{\partial \Phi(z)}{\partial z} - \frac{1}{8}\left(2e_{33} - \frac{2c_{13}e_{31}}{c_{11}}\right)h^2\frac{\partial^2 U_x(z)}{\partial z^2}$$

$$M_3 = \frac{1}{24}\left(\frac{2c_{13}}{c_{11}} - 2c_{33}\right)h^3\frac{\partial^2 U_x(z)}{\partial z^2} + \frac{1}{8}\left(2e_{33} - \frac{2c_{13}e_{31}}{c_{11}}\right)h^2\frac{\partial \Phi(z)}{\partial z}$$

$$Q_3 = -\frac{1}{24}\left(\frac{2c_{13}}{c_{11}} - 2c_{33}\right)h^3\frac{\partial^3 U_x(z)}{\partial z^3} - \frac{1}{8}\left(2e_{33} - \frac{2c_{13}e_{31}}{c_{11}}\right)h^2\frac{\partial^2 \Phi(z)}{\partial z^2}$$

After substitution of D_3, M_3 and Q_3 into system (40.11), we have all needed equations for the second part of the transducer:

$$\begin{cases} -\frac{1}{8}\left(-\frac{2e_{31}c_{13}}{c_{11}} + 2e_{33}\right)h^2\frac{\partial^3 \Phi(z)}{\partial z^3} - \frac{1}{24}\left(\frac{2c_{13}^2}{c_{11}} - 2c_{33}\right)h^3\frac{\partial^4 U_x(z)}{\partial z^4} \\ \qquad\qquad -p(z) - W^2\rho h U_x(z) = 0 \\ \left(-\frac{e_{31}}{c_{11}} - g_{33}\right)\frac{\partial^2 \Phi(z)}{\partial z^2} + \frac{1}{4}\left(\frac{e_{31}c_{13}}{c_{11}} - e_{33}\right)h\frac{\partial^3 U_x(z)}{\partial z^3} = 0 \end{cases} \tag{40.13}$$

Second equation in (40.11) can be integrated twice to achieve next form:

$$\left(-\frac{e_{31}}{c_{11}} - g_{33}\right)\Phi(z) + \frac{1}{4}\left(\frac{e_{31}c_{13}}{c_{11}} - e_{33}\right)h\frac{\partial U_x(z)}{\partial z} + C_1 z + C_2 = 0$$

It allows to extract $\Phi(z)$ and use it in the first equation of (40.13).

$$\Phi(z) = \frac{1}{4(e_{31}^2 + g_{33}c_{11})}\left[(e_{31}c_{13} - e_{33}c_{11})h\frac{\partial U_x(z)}{\partial z} + 4c_{11}(C_1 z + C_2)\right] \tag{40.14}$$

$$\left[-\frac{1}{12}\left(\frac{c_{13}^2}{c_{11}} - c_{33}\right) - \frac{1}{16}\frac{\left(-\frac{e_{31}c_{13}}{c_{11}} + e_{33}\right)(e_{31}c_{13} - e_{33}c_{11})}{e_{31}^2 + g_{33}c_{11}}\right]h^3\frac{\partial^4 U_x(z)}{\partial z^4}\,p(z) - W^2\rho h U_x(z) = 0 \tag{40.15}$$

First of all, we need to solve together (40.12) and (40.15). First step is to find common solutions for homogeneous differential equations. Upper index will show if function belongs to the first or to the second model. So, $U^1(x)$ and $\Phi^1(x)$ will be solutions for (40.12), $U^2(x)$ and $\Phi_2(x)$ are the solutions for (40.13), obtained from (40.14). Common solutions are:

$$
\begin{aligned}
U^1(x) &= C_1 e^{\lambda_1 x} + C_2 e^{\lambda_2 x} + C_3 e^{\lambda_3 x} + C_4 e^{\lambda_4 x} + C_5 \cos(\lambda_5 x) + C_6 \sin(\lambda_6 x) \\
\Phi^1(x) &= T_1 C_1 e^{\lambda_1 x} + T_2 C_2 e^{\lambda_2 x} + T_3 C_3 e^{\lambda_3 x} + T_4 C_4 e^{\lambda_4 x} + T_5 C_5 \cos(\lambda_5 x) + T_6 C_6 \cos(\lambda_6 x) \\
U^2(z) &= C_7 e^{\alpha_1 z} + C_8 e^{\alpha_2 z} + C_9 \cos(\alpha_5 z) + C_{10} \sin(\alpha_6 z) \\
\Phi^2(z) &= T_7 C_7 e^{\alpha_1 z} + T_8 C_8 e^{\alpha_2 z} + T_9 C_9 \cos(\alpha_5 z) + T_{10} C_{10} \sin(\alpha_6 z) + C_{11} z + C_{12}
\end{aligned}
\tag{40.16}
$$

In this system, values of λ, α, T can be found after substitution of material constants and geometrical sizes into (40.12) and (40.14) by using the characteristic polynomials. Constants C_1 and C_2 from (40.14) are labeled in (40.16) as C_{11} and C_{12} for numeration purposes. Input of inhomogeneous part that represents external load, can be described as $\left[-\frac{p(x)}{W^2 \rho h}\right]$.

Let us analyze boundary conditions with fixed edged of the transducer. Both ends have zero potential, contact zone has condition for fields equality, in local coordinates we have twelve conditions as follows:

$$
\begin{array}{ll}
U^1(0) = 0 & U^1(L) = U^2(0) \\
\Theta^1(0) = 0 & M^1(L) = M^2(0) \\
\Phi^1(0) = 0 & \Theta^1(L) = \Theta^2(0) \\
U^2(L) = 0 & Q^1(L) = Q^2(0) \\
\Theta^2(L) = 0 & \Phi^1(L) \int_{-h/2}^{h/2} (1-(\frac{2x}{h})^2) dx \\
\Phi^2(L) = 0 & \frac{h}{D^1(L) = D^2(0)} = \Phi^2(0)
\end{array}
\tag{40.17}
$$

Boundary conditions (40.17) allow us to obtain a system of linear equations from (40.16), and evaluate coefficients $C_1 - C_{12}$, which lead us to the solution of the initial problem. In numerical experiment, we used values $V_0 = 100$ V, $p(x) = 1000$ N/m^2, $\omega = 1000$ Hz in both FEM (ACELAN software) and applied theory to compare results. In series of experiments, difference between maximum displacements was about 3–4%. The same accuracy was achieved in measurements of potential. Figures 40.6 and 40.7 show results from numerical experiments obtained by ACELAN software and MAPLE software based on applied theory.

For further analysis, we varied thickness of the transducer. Numerical results can be seen in Table 40.3.

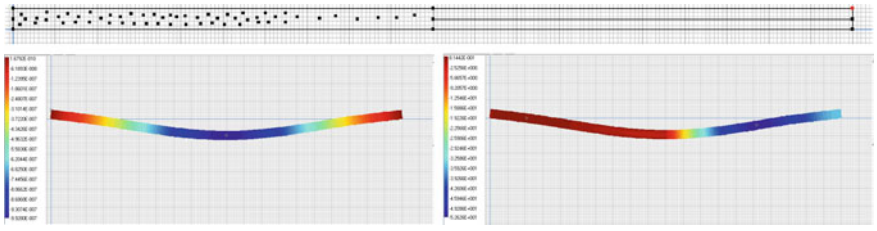

Fig. 40.6 Geometry of FEM model (*top*); U (*left*) and Φ (*right*) distributions (*bottom*)

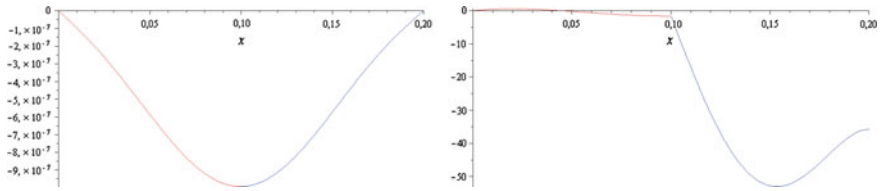

Fig. 40.7 *U* (*left*) and Φ (*right*) distributions obtained from applied theory

Table 40.3 Theory and FEM comparison

Method	Applied theory	FEM
Maximum of displacement *U*, m	$9.928 \cdot 10^{-7}$	$9.935 \cdot 10^{-7}$
Maximum of potential Φ, V	−52.26	−53.016

40.5 Conclusion

In previous work [4], we presented the results of studies of cylindrical and planar transducers for EMCC growth with some types of polarization. In view of the results presented in this paper, it is possible to construct the optimal process development and modeling effective piezoelectric devices, combining applied theory calculations with the block polarization and clarifying the calculation for a given configuration of electrodes, taking into account the inhomogeneous polarization. Software necessary for this approach, is developed in form of MAPLE and ANSYS programs, as well as executable files for ACELAN software. The collection of data allows the software to meet certain challenges, namely static problem to determine the frequency response, the circuit analysis is connected to the resistance of the converter. It allowed the sharing of certain parts of the developed software modules with the optimization tools in ACELAN package to determine the optimal polarization field in semi-automated mode.

Acknowledgements This work was partially supported by RFBR grant Nos. 16-01-00354-a and 16-58-52013 MNT_a.

References

1. D. Ballhause, M. D'Ottavio, B. Kröplin, E. Carrera, Comput. Struct. **83**, 1217 (2005)
2. S.V. Gopinathan, V.V. Varadan, V.K. Varadan, Smart Mater. Struct. **9**, 24 (2000)
3. P.A. Soloviev, P.A. Oganesyan, A.S. Skaliukh, in *Advanced Materials—Studies and Applications*, Chapter 12, vol. 169, eds. by I.A. Parinov, S.-H. Chang, S. Theerakulpisut (Nova Publishers, 2015).
4. A.V. Belokon, A.S. Skaliukh, in *Mathematical Modeling of Irreversible Processes of Polarization* (Fizmatlit, Moscow, 2010), p. 328 (In Russian).

5. J. Meinguet, in *Proceedings of the NATO Advance Study Institute Calgary*, 1978, vol. 163 (Kluwer Academic Publishers, Dordrecht, Boston, London, 1979)
6. A.O. Vatulian, I.P. Getman, N.B. Lapnitskaya, Appl. Mech. **27**(10), 101 (1991)
7. A.O. Vatul'yan, A.A. Rynkova, *J. Appl. Mech. Tech. Phys.* **42**(1), 164 (2001)

Chapter 41
Study of the Output Characteristics of Ferroelectric Ceramic Beam Made from Non-polarized Ceramics PZT-19: Experiment and Modeling

Arkadiy N. Soloviev, V.A. Chebanenko, Yu N. Zakharov, E.V. Rozhkov, I.A. Parinov and Vijay Kumar Gupta

Abstract In this chapter, non-polarized ferroelectric ceramic beams with varying degrees of the roughness of opposite surfaces were investigated. It was found that under the influence of harmonic three-point mechanical loading at the resonance frequency, created by proof mass of 3.1 g in the middle of the beam, all samples without exception generated a voltage between 0.2 and 0.55 V at the electric load resistance of 360 kΩ. The maximum voltage was achieved in the samples when the rougher side (proof mass located at "upper surface" and rough side—at "lower surface") was subjected to tensile stress. In addition, mathematical modeling was conducted for similar problem within the theory of flexoelectricity for beams.

A.N. Soloviev (✉)
Don State Technical University, 1, Gagarin Square,
Rostov-on-Don 344000, Russia
e-mail: solovievarc@gmail.com

V.A. Chebanenko
South Scientific Center of RAS, 41, Chekhov Street,
Rostov-on-Don 344022, Russia
e-mail: valera.chebanenko@yandex.ru

A.N. Soloviev · V.A. Chebanenko · E.V. Rozhkov · I.A. Parinov
Vorovich Mathematics, Mechanics and Computer Science Institute,
Southern Federal University, 8a, Milchakov Street
Rostov-on-Don, Rostov-on-Don 344090, Russia

Y.N. Zakharov
Physics Research Institute, Southern Federal University,
194, Stachki Avenue, Rostov-on-Don 344090, Russia
e-mail: delta-46@mail.ru

V.K. Gupta
PDPM Indian Institute of Information Technology,
Design and Manufacturing Jabalpur, Jabalpur, India

I.A. Parinov et al. (eds.), *Advanced Materials*, Springer Proceedings
in Physics 193, DOI 10.1007/978-3-319-56062-5_41

The possibility of occurrence of electric potential in the non-polarized piezoceramic samples was shown. Nevertheless, the values of electric potential were much lower than the experimental.

41.1 Introduction

In recent years, a lot of studies on estimation of the effect of various electrophysical and geometrical parameters on the performance and energy efficiency of the piezoelectric generators (PEGs) were conducted. Most of these works dealt with cantilever type PEGs. A review of these works was made in a number of monographs and articles [1–5]. Problems connected with axial type PEG have not received so much interest, though this type of design has some advantages. These advantages are caused by that such a PEG can operate at substantially higher mechanical stresses than cantilever type generators. We have selected for this study three-point type of excitation of the PEG's active element with the proof mass at its center. This type of excitation occupies an intermediate position between the axial and cantilever type PEGs. This design allowed us to explore the output parameters of PEG in resonance harmonic loading mode of an active element with proof mass, and also gave us opportunity to study influence of loading application on both sides of the piezoelectric beam. Lateral impact of proof mass at the center of the beam leads to its elastic deflection, which leads to the compression of upper and stretching the lower electrode layers, and creates (or change existing stationary ones) the counter-directed strain gradients in this layers. The possibility of a polarization under the influence of the strain gradient was firstly pointed out by Mashkevich and Tolpygo [6, 7]. They have also obtained expression for the relationship between the amplitudes of the polarization and the strain gradient for the acoustic wave in the diamond-type structures. The first step in building a phenomenological description of the phenomenon was made by [8]. Some aspects of the description of the symmetry under the scheme proposed in [8] discussed by [9]. In the same paper was an attempt to describe the microscopic flexoelectrical effect for the case of static strain gradient. Experimentally effect was investigated by [10]. The value of proportionality coefficient between the polarization and the strain gradient obtained from experiment was four orders of magnitude greater than rough theoretical estimate.

The aim of this work is to study the effect of the lateral impact under the three-point scheme of mechanical loading on the possibility of obtaining an electrical response from non-polarized ferroelectric ceramic beams. Moreover, we also perform theoretical study of the possibility of creating an electric potential in the non-polarized ferroelectric ceramic beams under the influence of the dynamic inertial load.

41.2 Experiment

Four batches of ceramic beams were made from PZT-19 (Russian analog of PZT-5) with sizes 50 × 4 × 0.7 mm^3. Electrodes made from silver were applied on larger surfaces. Before application of the electrodes, the samples were given identical thickness sizes with the help of machining process on both opposite surfaces. Then in batches Nos. 2–4 consisting of 10 pieces, one of the surfaces of each specimen was processed with grinding powders which had different grain sizes of 5, 10 and 20 μm, respectively. With the help of this technique, different depth of diffusion of Ag was achieved during sintering process on the ceramic surface, thus creating at opposite sides of specimen the cermet layers of different thickness. At the boundaries of these layers with bulk of ceramic beams in batches Nos. 2–4, non-equivalent gradients of mechanical strain and tangential compressive stresses were formed. The compressive stress was caused by the difference of coefficients of thermal expansion for Ag and ferroelectric material when cooled from 730 °C down to room temperature after sintering. Figure 41.1 shows a hypothetical scheme of the distribution strain gradient and stress in the surface layers and the bulk of sample (Fig. 41.1a), as well as scheme of the device for three-point mechanical loading (Fig. 41.1b). Figure 41.2 shows a photograph of a test set-up and its block diagram.

The test set-up consists of the exciter of mechanical vibrations—electromagnetic shaker VEB Robotron 11077 (6), on desktop (5) of which three-point mechanical loading device with piezoceramic beam and proof mass M_n is set; optical sensor of mechanical displacement (7); optical sensor controller (8); acceleration sensor (9),

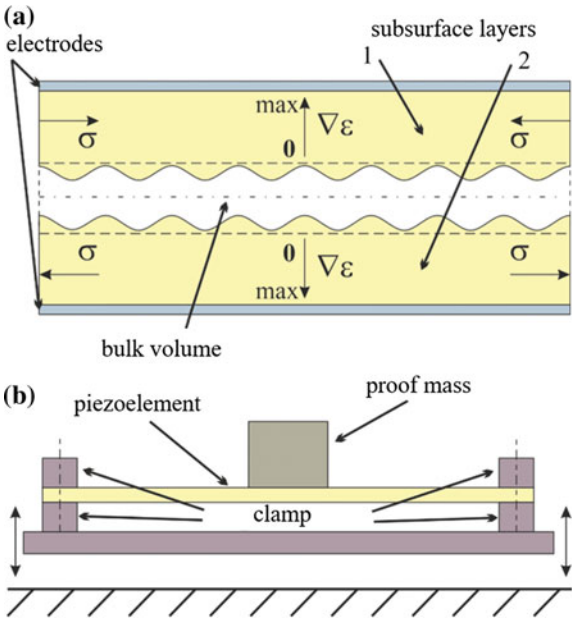

Fig. 41.1 Hypothetical scheme of distribution of static strain gradient $\nabla\varepsilon$ at the boundaries of sintered ceramic layers with bulk (*1 upper layer*, *2 lower layer*) and tangential compressive stress σ in the electrode layers (**a**); scheme of the device for three-point mechanical loading (**b**)

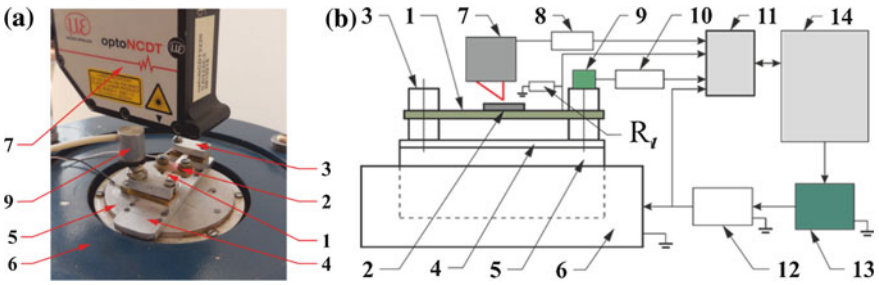

Fig. 41.2 General view of the test set-up (**a**) and its block diagram (**b**): *1* piezoceramic beam, *2* proof mass, *3* 1st fixing point, *4* base, *5* worktable of the electromagnetic shaker, *6* shaker, *7* optical linear displacement sensor, *8* optical sensor's controller, *9* ADXL-103 acceleration sensor (located at 2nd fixing point), *10* acceleration sensor's controller, *11* ADC/DAC E14–440D external unit, *12* power amplifier, *13* signal generator, *14* computer, R_l is the electric load resistance

located at fixing point of specimen; acceleration sensor controller (10); external ADC/DAC module E14-440D developed by L-Card (11); power amplifier LV-102 50 W (12); signal generator AFG 3022B Tektronix (13); computer (14) and electric load resistance R_l. Electric response from mechanical loading of specimen is measured across the resistor R_l by ADC unit. Optical sensor (7) measures the mechanical displacement of the surface of M_s. The acceleration sensor ADXL-103 measures the acceleration of worktable.

41.3 Results of Experiment

Figure 41.3 shows the relationships between the electrical response of specimen and acceleration of worktable, typical for beams from batches No. 1 (Fig. 41.3a) and No. 3 (Fig. 41.3b), selected on the basis of recurrence of the effect in the batch. Analysis of Fig. 41.3a (for beam No. 3 from batch No. 1—3B1) shows that in the batch No. 1 after sintering of Ag, electrical polarization P_{res} stable to cyclic mechanical load is created by static strain gradients at the boundaries of sintered layers with the bulk of ceramics and by tangential compressive stresses in the near-electrode layers. This conclusion is illustrated by curves 1 and 2, the first of which was obtained before the turn of the beam on 180°, second curve—after the turn. The output electrical signal from 0.1 to 0.4 V from the impact of proof mass for various values of acceleration is due to the compression of the surface layer 1 and stretching of layer 2 (Fig. 41.1b). In this batch for each position of the surfaces of the beam relative to proof mass, the output voltages of the greater number of samples coincided, indicating the identity of the polarization P_{res} created at the opposite sides.

Figure 41.3b shows a 25% increase in the electrical response (from 0.26 to 0.5 V, depending on the acceleration) of the sample 6B3 when rougher face is located on the opposite side of the M_n. In this case, like in batch No. 1, deflection beam under M_n is created by mechanical tensile stress with an opposite direction to

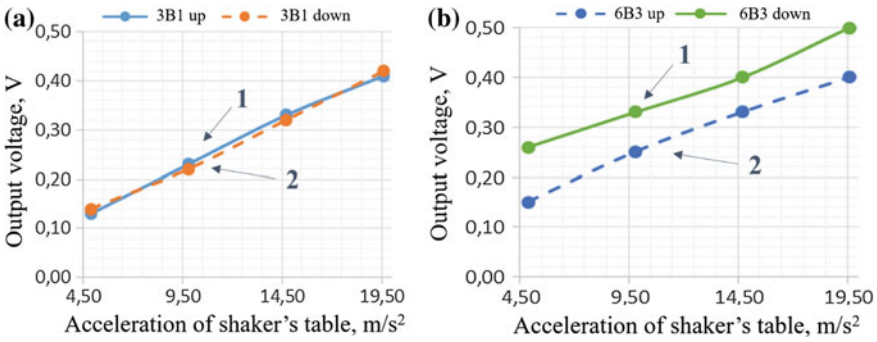

Fig. 41.3 Relationship between electrical response to mechanical impact of $M_n = 3.1$ g and acceleration of the worktable: before (*curve 1*) and after (*curve 2*) rotation of the specimens on 180°. Beams from batches No. 1 (**a**) and No. 3 (**b**)

the current ones, created during the formation of the cermet layer at the surface. The difference in the magnitude of the output voltage can account for higher values of P_{res} of the surface.

The main result of this study is the fact of occurrence of P_{res} at the opposite surfaces of the beams from PZT-19 ceramics after sintering of Ag. The magnitude of P_{res} depends on the degree of roughness of the surface before the application of the electrodes, and the electrical response is the arithmetic sum of the signals arising from the compression of one and tension of opposite beam surfaces. Due to the fact that the effect was investigated at room temperature in the ferroelectric phase of PZT-19, it is impossible to treat it uniquely as flexoelectrical and "giant." At the same time, most likely, it can occur in a very thin transition layer: border of cermet layer—volumetric, homogeneous bulk of ceramic. Assuming that the thickness of this layer is about 1 μm, it generates on resitive load of 360 kΩ electric potential with the electric field strength up to 50 kV/cm.

41.4 Mathematical Modeling

Most of the works devoted to the modeling of flexoeffect in solids [11–14, 17] used a variational approach proposed by [15]. We will follow the same path. We write the variational principle for electroelastic body:

$$\delta \int_{t_1}^{t_2} dt \iiint_V \left[\frac{1}{2}\rho|\ddot{\mathbf{u}}|^2 - \left(W^L - \frac{1}{2}\varepsilon_0|\nabla\phi|^2 + \mathbf{P}\cdot\nabla\phi\right)\right] dV + \int_{t_1}^{t_2} dt \iiint_V (\mathbf{q}\cdot\delta\mathbf{u} + \mathbf{E^0}\cdot\delta\mathbf{P}) dV + \int_{t_1}^{t_2} dt \iint_S (\mathbf{t}\delta\mathbf{u}) = 0 \tag{41.1}$$

where V is the volume of the body, ρ is the density, $\mathbf{u}$ is the displacement vector, W^L is the density of internal energy, ε_0 is an electric constant, $\mathbf{P}$ is the polarization vector, φ is the electric potential, $\mathbf{q}$ is the internal force, $\mathbf{E^0}$ is the internal electric field, S is the surface bounding volume V, $\mathbf{t}$ is the surface force.

To account for the effect of the strain gradient, we will use the density of the potential energy in the form [16]:

$$W^L(\mathbf{P},\mathbf{S},\nabla\nabla\mathbf{u}) = \frac{1}{2}\mathbf{P}\cdot\mathbf{a}\cdot\mathbf{P} + \frac{1}{2}\mathbf{S}:\mathbf{c}:\mathbf{S} + \mathbf{P}\cdot\mathbf{d}:\mathbf{S} + \mathbf{P}\cdot\mathbf{f}:\nabla\nabla\mathbf{u} + \frac{1}{2}\nabla\nabla\mathbf{u}:\mathbf{g}:\nabla\nabla\mathbf{u}, \tag{41.2}$$

where, $\mathbf{a}$ is the inverse dielectric susceptibility, $\mathbf{S}$ is the tensor of small deformations, $\mathbf{c}$ is the tensor of elastic moduli, $\mathbf{d}$ is the piezomoduli tensor, $\mathbf{f}$ is the tensor of flexoelectric moduli, $\mathbf{g}$ is the tensor describing pure nonlocal elastic effects, $\nabla\nabla\mathbf{u}$ is the strain gradient.

Substituting the expression for the potential energy (41.2) in the first term of the variational principle (41.1) we obtain:

$$\delta\int_{t_1}^{t_2} dt \iiint_V \left[W^L - \frac{1}{2}\varepsilon_0|\nabla\varphi|^2 + \mathbf{P}\cdot\nabla\varphi\right]dV = \int_{t_1}^{t_2} dt \iiint_V \left(\frac{\partial W^L}{\partial\mathbf{P}}\delta\mathbf{P} + \frac{\partial W^L}{\partial\mathbf{S}}\delta\mathbf{S} + \frac{\partial W^L}{\partial(\nabla\nabla\mathbf{u})}\delta(\nabla\nabla\mathbf{u}) - \varepsilon_0\nabla\varphi\delta(\nabla\varphi) + \mathbf{P}\delta(\nabla\varphi) + \nabla\varphi\delta\mathbf{P}\right)dV \tag{41.3}$$

Due to the fact that the deformation in the considered problem is small, we can move from a general statement to the two-dimensional case to simplify the problem. We introduce the Euler-Bernoulli hypothesis for beams:

$$\mathbf{u} = \left\{-x_3\frac{\partial w_a(x_1,t)}{\partial x_1}, 0, w_a(x_1,t)\right\}^T. \tag{41.4}$$

The expressions for the components of the strain tensor and strain gradient that take into account hypotheses (41.4) take the following form:

$$S_{11} = -x_3\frac{\partial^2 w_a}{\partial x_1^2}, \quad S_{11,3} = -\frac{\partial^2 w_a}{\partial x_1^2}. \tag{41.5}$$

Also we introduce the following simplifications for the polarization vector:

$$\mathbf{P}(x_1,x_3,t) = \{0,0,P(x_1,x_3,t)\}. \tag{41.6}$$

To simplify further calculations we assume the following notation:

$$a = a_{33}, \quad c = c_{1111}, \quad d = d_{311}, \quad f = f_{3113}, \quad g = g_{113113}. \tag{41.7}$$

With given hypotheses and notation entered, the density of the potential energy takes the form:

$$W^L = \frac{1}{2}aP^2 + \frac{1}{2}cx_3^2\left(\frac{\partial^2 w_a}{\partial x_1^2}\right)^2 - dx_3 P\frac{\partial^2 w_a}{\partial x_1^2} - fP\frac{\partial^2 w_a}{\partial x_1^2} + \frac{1}{2}g\left(\frac{\partial^2 w_a}{\partial x_1^2}\right)^2. \tag{41.8}$$

Substituting the expression for the potential energy density (41.8) into (41.3), we obtain:

$$\begin{aligned}&\int_{t_1}^{t_2} dt \iiint_V \rho\ddot{w}_a \delta w_a dV + \int_{t_1}^{t_2} dt \iiint_V \left[\left(aP - dx_3\frac{\partial^2 w_a}{\partial x_1^2} - f\frac{\partial^2 w_a}{\partial x_1^2} + \frac{\partial\varphi}{\partial x_3}\right)\delta P\right.\\ &+ \left(cx_3^2\frac{\partial^2 w_a}{\partial x_1^2} - dx_3 P - fP + g\frac{\partial^2 w_a}{\partial x_1^2}\right)\delta\left(\frac{\partial^2 w_a}{\partial x_1^2}\right) + \left(P - \varepsilon_0\frac{\partial\varphi}{\partial x_3}\right)\delta\left(\frac{\partial\varphi}{\partial x_3}\right)\\ &\left.+ \left(-\varepsilon_0\frac{\partial\varphi}{\partial x_1}\right)\delta\left(\frac{\partial\varphi}{\partial x_1}\right)\right] dV = 0\end{aligned} \tag{41.9}$$

Since the polarization variation δP is arbitrary, then

$$P = \frac{1}{a}\left(-dx_3\frac{\partial^2 w_a}{\partial x_1^2} - f\frac{\partial^2 w_a}{\partial x_1^2} + \frac{\partial\varphi}{\partial x_3}\right). \tag{41.10}$$

Substituting (41.10) into (41.9) we obtain:

$$\begin{aligned}&\int_{t_1}^{t_2} dt \int_0^L \rho A_p \ddot{w}_a \delta w_a dx_1 + \int_{t_1}^{t_2} dt \int_0^L \left\{\left[\left(c - \frac{d^2}{a}\right)I_p - \frac{2df}{a}H_p - \left(\frac{f^2}{a} - g\right)A_p\right]\frac{\partial^2 w_a}{\partial x_1^2}\right.\\ &\left.+ \iint_S \left(\frac{d}{a}x_3 + \frac{f}{a}\right)\frac{\partial\varphi}{\partial x_3} ds\right\}\delta\left(\frac{\partial^2 w_a}{\partial x_1^2}\right) dx_1 = 0\end{aligned} \tag{41.11}$$

where

$$A_p = \iint_S dS, \quad H_p = \iint_S x_3 dS, \quad I_p = \iint_S x_3^2 dS.$$

We introduce the notation for the right factor in the first term of the integrand of the second integral in (41.11):

$$EI^* = \left(c - \frac{d^2}{a}\right) I_p - \frac{2df}{a} H_p - \left(\frac{f^2}{a} - g\right) A_p, \tag{41.12}$$

where EI^* is the effective bending stiffness of the flexoelectrical beam.

We assume that the electric field is linear in the thickness of the beam, then

$$E_3 = -\frac{\partial \varphi}{\partial x_3} = const = -\frac{v(t)}{h}, \tag{41.13}$$

where $v(t)$ is the electric potential between two electrodes on the large surfaces of the beam.

Since voltage is measured across the load resistance R_l (see Fig. 41.2b), the current flowing through the resistor is equal to the time derivative of the averaged electric displacement D_3

$$i(t) = \frac{v(t)}{R_l} = \frac{d}{dt}\left(\frac{1}{h} \iiint_V D_3 dV\right), \tag{41.14}$$

where $D_3 = -\varepsilon_0 \nabla \varphi + P$. In view of (41.10) we obtain the equation of electric circuit with flexoelectrical coupling:

$$\frac{v(t)}{R_l} = -\frac{BL}{h}\left(\varepsilon_0 + \frac{1}{a}\right)\dot{v}(t) + \frac{1}{h}\int_0^L \left(\frac{d}{a} H_p + \frac{f}{a} A_p\right) \frac{\partial^2 \dot{w}_a}{\partial x_1^2} dx_1 \tag{41.15}$$

Since the oscillations in the beam are excited by the moving clamp (see Fig. 41.1b), the absolute displacement $w_a(x_1, t)$ should be expanded to movement of clamp $w_b(t)$ and the relative movement of the beam $w(x_1, t)$:

$$w_a(x_1, t) = w(x_1, t) + w_b(t). \tag{41.16}$$

To solve the problem of forced oscillations of flexoelectrical beam, we will use the modified Rayleigh-Ritz method, by analogy with [17]. Relative movements of the beam can be expressed as series expansion:

$$w(x_1, t) = \sum_{k=1}^{N} \eta_k(t) \xi_k(x_1) \tag{41.17}$$

where N is the number of modes of oscillations taken into account, $\eta_k(t)$ are the unknown generalized coordinates, $\xi_k(x_1)$ are the known cinematically admissible trial functions that satisfy the boundary conditions.

To find $\xi_k(x_1)$ we need to solve the problem of free oscillations for the beam clamped at both ends with a concentrated mass in the middle (see Fig. 41.4).

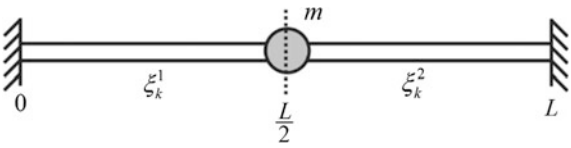

Fig. 41.4 Kinematic scheme of the problem

To account for the effect of the concentrated mass, we need to express the function $\xi_k(x_1)$ as follows:

$$\xi_k(x_1) = \begin{cases} \xi_k^1(x_1), & x_1 \le \frac{L}{2} \\ \xi_k^2(x_1), & x_1 > \frac{L}{2} \end{cases} \tag{41.18}$$

where $\xi_k^1(x_1)$ corresponds to shape of oscillations of the beam's left side, $\xi_k^2(x_1)$ corresponds to shape of oscillations of the beam's right side, L is the length of the beam, m is the value of the proof mass (see Fig. 4).

Solution in general form for each side of the beam can be expressed as

$$\begin{aligned} \xi_k^1(x_1) &= a_1 \sin(\beta x_1) + a_2 \cos(\beta x_1) + a_3 \sinh(\beta x_1) + a_4 \cosh(\beta x_1) \\ \xi_k^2(x_1) &= a_5 \sin(\beta x_1) + a_6 \cos(\beta x_1) + a_7 \sinh(\beta x_1) + a_8 \cosh(\beta x_1) \end{aligned} \tag{41.19}$$

We write the boundary conditions for the edges of beam and coupling conditions in the center of the beam:

$$\begin{array}{ccc} & \xi_k^1\left(\frac{L}{2}\right) = \xi_k^2\left(\frac{L}{2}\right) & \\ \xi_k^1(0) = 0 & \xi_k^{1\prime}\left(\frac{L}{2}\right) = \xi_k^{2\prime}\left(\frac{L}{2}\right) & \xi_k^1(L) = 0 \\ \xi_k^{2\prime}(0) = 0 & \xi_k^{1\prime\prime}\left(\frac{L}{2}\right) = \xi_k^{2\prime\prime}\left(\frac{L}{2}\right) & \xi_k^{2\prime}(L) = 0 \\ & \xi_k^{1\prime\prime\prime}\left(\frac{L}{2}\right) = \xi_k^{2\prime\prime\prime}\left(\frac{L}{2}\right) - \alpha\beta^4 \xi_k^1\left(\frac{L}{2}\right) & \end{array} \tag{41.20}$$

where $\alpha = \frac{m}{\rho A L}$, ρ is the density of the beam, A is the cross-section area of the beam.

Satisfying the boundary conditions, we obtain a homogeneous system of 8 equations with 8 unknowns:

$$\Lambda = \begin{pmatrix} a_{11} & \dots & a_{18} \\ \vdots & \ddots & \vdots \\ a_{81} & \cdots & a_{88} \end{pmatrix}. \tag{41.21}$$

In order to find the eigenvalues β_i, we need to find the determinant of this system. Since $\det(\Lambda) = 0$ is the transcendental equation, it will be solved with the help of Newton's method. After obtaining set of β_i, we calculate the coefficients a_i for the required number of oscillation modes N.

Substituting the representations (41.16) and (41.17) into (41.11) and (41.15), we obtain a set of differential equations describing forced oscillations of flexoelectric beam connected to the load resistance

$$\begin{aligned} &\mathbf{M}\ddot{\boldsymbol{\eta}}(t)+\mathbf{D}\dot{\boldsymbol{\eta}}(t)+\mathbf{K}\boldsymbol{\eta}(t)-\boldsymbol{\Theta}v(t)=\mathbf{p} \\ &C_f\dot{v}(t)+\frac{v(t)}{R}+\boldsymbol{\Theta}^T\dot{\boldsymbol{\eta}}(t)=0 \end{aligned} \tag{41.22}$$

where $\mathbf{D}=\mu\mathbf{M}+\gamma\mathbf{K}$ is the matrix of Rayleigh type damping. The remaining coefficients are

$$\begin{aligned} C_f &= \frac{BL}{h}\left(\varepsilon_0+\frac{1}{a}\right) \\ M_{kl} &= \rho A_p\int_0^L \xi_k(x_1)\xi_l(x_1)dx_1+m\xi_k\left(\frac{L}{2}\right)\xi_l\left(\frac{L}{2}\right) \\ K_{kl} &= EI^*\int_0^L \xi_k''(x_1)\xi_l''(x_1)dx_1 \\ \theta_l &= \frac{1}{h}\left(\frac{d}{a}H_p+\frac{f}{a}A_p\right)\int_0^L \xi_l''(x_1)dx_1 \\ p_l &= -\ddot{w}_b(t)\left[\int_0^L \rho A_p\xi_l(x_1)dx_1+m\xi_l\left(\frac{L}{2}\right)\right] \end{aligned} \tag{41.23}$$

where C_f is the effective capacitance, M_{kl} are the elements of the mass matrix, K_{kl} are the elements of stiffness matrix, θ_l are the elements of electromechanical coupling vector, p_l is the effective mechanical load vector. Also, it should be noted that the second terms in the expressions for M_{kl} and p_l are responsible for the effect of concentrated mass.

We assume that the excitation is harmonic:

$$\begin{aligned} w_b(t) &= W_0\mathrm{e}^{i\omega t} \\ \mathbf{p} &= \mathbf{p_0}\mathrm{e}^{i\omega t} \end{aligned} \tag{41.24}$$

Then the solution will be obtained in the form:

$$\begin{aligned} \boldsymbol{\eta}(t) &= \mathbf{H}e^{i\omega t} \\ v(t) &= Ve^{i\omega t} \end{aligned} \tag{41.25}$$

After substituting (41.24) and (41.25), equation set (41.22) takes the form:

$$\begin{aligned}&\left[-\omega^2\mathbf{M}+i\omega(\mu\mathbf{M}+\gamma\mathbf{K})+\mathbf{K}\right]\mathbf{H}-\mathbf{\Theta}V=\mathbf{p}_0\\&\left(i\omega C_f+\frac{1}{R}\right)V+i\omega\mathbf{\Theta}^T\mathbf{H}=0\end{aligned}\tag{41.26}$$

From the second equation of the set (41.26), we express V as

$$V=-\frac{i\omega\mathbf{\Theta}^T\mathbf{H}}{i\omega C_f+\frac{1}{R}}\tag{41.27}$$

Then we substitute (41.27) into the first equation of the set (41.26) and express $\mathbf{H}$ as

$$\mathbf{H}=\left[-\omega^2\mathbf{M}+i\omega(\mu\mathbf{M}+\gamma\mathbf{K})+\mathbf{K}+\frac{i\omega\mathbf{\Theta}\mathbf{\Theta}^T}{i\omega C_f+\frac{1}{R}}\right]^{-1}\mathbf{p}_0\tag{41.28}$$

Substituting this expression for $\mathbf{H}$ back to (41.27), we obtain an expression for V:

$$V=-\frac{i\omega\mathbf{\Theta}^T}{i\omega C_f+\frac{1}{R}}\left[-\omega^2\mathbf{M}+i\omega(\mu\mathbf{M}+\gamma\mathbf{K})+\mathbf{K}+\frac{i\omega\mathbf{\Theta}\mathbf{\Theta}^T}{i\omega C_f+\frac{1}{R}}\right]^{-1}\mathbf{p}_0\tag{41.29}$$

These expressions (41.28) and (41.29) are the solution of the system (41.26). Now we carry out some numerical experiments to test the model.

41.5 Numerical Experiment

As input parameters of the model, we will use the initial data from the experiment. We consider a piezoceramic beam made of non-polarized ceramics PZT-19, which has the geometrical and physical properties shown in Table 41.1, obtained from [17–20].

Table 41.1 The geometrical and physical properties

Geometrical dimensions ($L_0 \times b \times h$)	$50 \times 4 \times 0.7$ mm^3
Working length (L)	35 mm
Density (ρ)	7280 kg/m^3
Elastic moduli (c)	114.8×10^9 Pa
Relative permittivity (ε)	682.6
Inverse dielectric susceptibility (a)	1.657×10^8 Nm^2/C^2
Flexoelectrical factor (μ_{12})	2×10^{-6} C/m
Flexoelectrical modulus (f)	−331 Nm/C
Higher order elastic modulus (g)	1.75×10^{-6} N

Since non-polarized ceramic is a center-symmetrical material, the piezoelectric modulus d in such material will be equal to zero. An inverse dielectric susceptibility was calculated using the formula $a = (\varepsilon\varepsilon_0 - \varepsilon_0)^{-1}$, and flexoelectrical modulus $f = -a\mu_{12}$. Magnitude of the movement of shaker's working table (Fig. 41.2, item 5) is equal to 0.1 mm.

It should be noted that due to design features of the experimental setup, the proof mass size is about 20% of the working surface of the beam (see Fig. 41.2a), and its width is greater than the width of the beam by 4 times. The approach we use, where the proof mass is considered as a point, cannot provide matching of calculated amplitude-frequency characteristics with the experimental ones.

For the qualitative comparison with experiment, we are interested in the first oscillation mode. That is why we suppose $N = 3$. We have obtained amplitude-frequency characteristics for the displacement of the middle point of the beam (Fig. 41.5) and for voltage from different load resistances (Fig. 41.6). In addition, we have calculated similar to experiment (Fig. 41.3) relationship between acceleration of working table and output voltage, when resistive load was 360 kΩ. Estimated resonant frequency was 504 Hz and experimental one was 346 Hz.

Figure 41.5 shows that the maximum displacement at the resonance is about 1 mm, which is consistent with the data from the optical displacement sensor (Fig. 41.2b, item 7).

The values of voltage, shown in Figs. 41.6 and 41.7, differ from those obtained in the experiment. Nevertheless, they reflect the qualitative characteristic of the voltage dependence of the magnitude from frequency and load resistance. This difference may indicate inaccurate input data, as well as the non-linearity of the phenomenon under investigation.

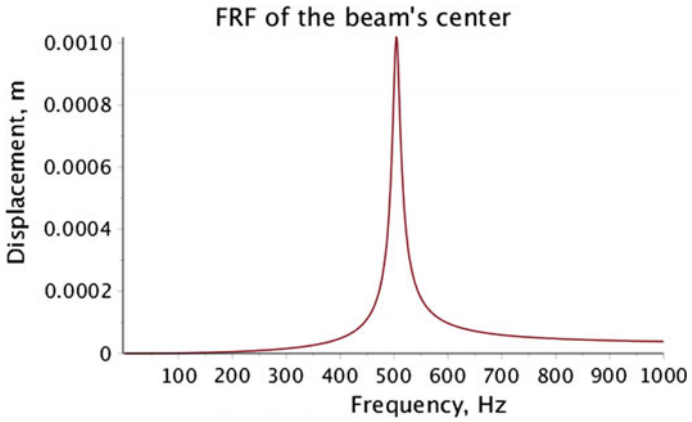

Fig. 41.5 Frequency response of the beam's center displacement obtained from the numerical experiment

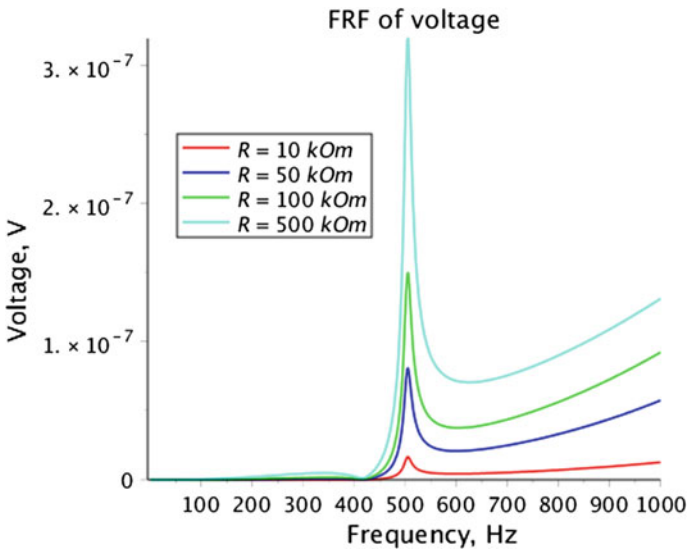

Fig. 41.6 Frequency response of the voltage across the resistor with different values of the load resistance obtained from the numerical experiment

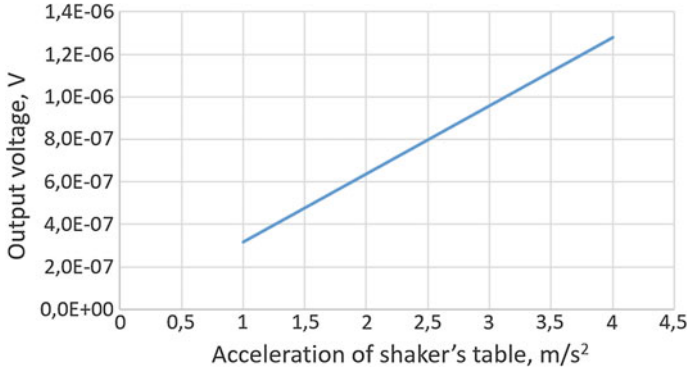

Fig. 41.7 Relationship between electrical response to mechanical impact of $M_n = 3.1$ g and acceleration of the worktable on resonsnce frequence when $R_l = 360$ kΩ, obtained from numerical experiment

Because the definition of material constants that affect the higher order effects (such as flexoelectrical effect), is a complex and unsolved research problem, in our case, we can try to vary the factor μ_{12}.

It was found that during variation when a certain value of the coefficient is achieved, effective bending stiffness (41.12) becomes negative. Therefore, we chosed the closest value in the vicinity of the transition point equal to 10^{-3} and obtained frequency response of voltage.

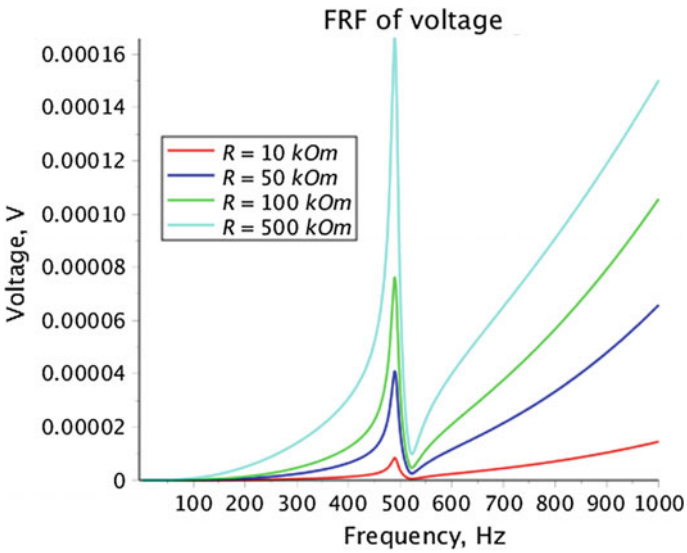

Fig. 41.8 Frequency response of the voltage across the resistor with different values of the load resistance derived from the numerical experiment, when $\mu_{12} = 10^{-3}$

It can be seen from Fig. 41.8 that the voltage value is increased by three orders of magnitude. However, these values are sufficiently small in comparison with the experimental ones. Furthermore, the resonance frequency slightly decreased to 491 Hz. The amount of movement of the beam mid-amplitude remained unchanged.

The results obtained in the numerical experiment showed the possibility of occurrence of an electric potential in the non-polarized piezoceramic beam and its qualitative characteristics. Nevertheless, the problem is not fully solved and requires further investigation.

41.6 Conclusion

The main result of the experimental part of the study is the fact of occurrence of P_{res} at the opposite surfaces of the beams made from PZT-19 ceramics after application of Ag electrodes. The values obtained of the output voltage 0.5 V for non-polarization of beam with thickness 0.7 mm are already of practical interest for multi-layered active elements of the PEG. Further studies of this effect in materials with Curie temperatures below room temperature and relaxor ferroelectrics are required.

The main result of the theoretical part of the work is the formulation and solution of a similar to the experiment the problem of forced oscillations of flexoelectrical

beam with inertial loading. It is shown that the electric potential may arise in non-polarized specimens, but its value is small compared with the experimental results. Variation of constant μ_{12} responsible for the magnitude of the arising potential, is possible only to a certain point, when the effective stiffness EI^* becomes negative, and the results lose their physical meaning. It is possible that the introduction of non-linear formulation of the problem, including the effect of pre-stress in the surface layer will give a similar result to the experimental data. The applicability of this approach will be discussed in the further works.

Acknowledgements The work was supported by the Ministry of Education of the Russian Federation (as part of the base part of the state task Project 1880) and the Russian Foundation for Basic Research (grants Nos. 16-08-00740_a, 15-08-00849_a). I.A. Parinov acknowledges financial support from Ministry of Education and Sciences of Russia in the framework of "Organization of Scientific Research" Government Assignment (grant No. 654).

References

1. A. Erturk, D.J. Inman, *Piezoelectric Energy Harvesting* (John Wiley & Sons, New York, 2011)
2. Y.C. Shu, I.C. Lien, J. Micromech. Microeng. **16**(11), 2429 (2006)
3. S. Priya,·D.J. Inman, in *Energy Harvesting Technologies* (Springer, New York, 2009)
4. V.A. Chebanenko, V.A. Akopyan, I.A. Parinov, in *Piezoelectrics and Nanomaterials: Fundamentals, Developments and Applications.* ed. by I.A. Parinov (Nova Science Publishers, New York, 2015), p. 243
5. V.A. Akopyan, I.A. Parinov, Y.N. Zakharov, V.A. Chebanenko, E.V. Rozhkov, in *Advanced Materials—Studies and Applications.* eds. I.A. Parinov, S.-H. Chang, S. Theerakulpisut (Nova Science Publishers, New York 2015), p. 417
6. V.S. Mashkevich, K.B. Tolpygo, Sov. Phys. JETP **4**, 455 (1957)
7. K.B. Tolpygo, Solid State Phys. **4**, 1765 (1962)
8. S.M. Kogan, Solid State Phys. **5**(10), 2829 (1963)
9. V.L. Indenbom, E.B. Loginov, M.A. Osipov, Kristallografiya. **26**(6), 1157 (1981)
10. I.S. Zeludev, Czech J. Phys. **16**(5), 368 (1966)
11. A. Abdollahi, C. Peco, D. Millán, M. Arroyo, I. Arias, J. Appl. Phys. **116**(9), 093502 (2014)
12. S. Hu, S. Shen, Sci. China Phys. Mech. Astron. **53**(8), 1497 (2010)
13. M.S. Majdoub, P. Sharma, T. Cagin, Phys. Rev. B. **77**, 125424 (2008)
14. R. Maranganti, N.D. Sharma, P. Sharma, Physical Review B **74**(1), 014110 (2006)
15. R.D. Mindlin, in *Problems of Continuum Mechanics* (1961), p. 282
16. E. Sahin, S. Dost, Int. J. Eng. Sci. **26**(12), 1231 (1988)
17. Q. Deng, M. Kammoun, A. Erturk, P. Sharma, Int. J. Solids Struct. **51**(18), 3218 (2014)
18. W. Ma, L.E. Cross, Appl. Phys. Lett. **82**(19), 3293 (2003)
19. A.V. Belokon, A.S. Skaliuh, in *Mathematical Modeling of Irreversible Processes of Polarization* (2010) (in Russian)
20. X. Liang, S. Hu, S. Shen, J. Appl. Mech. **80**(4), 044502 (2013)

Chapter 42
Modeling the Interaction of Piezoelectric Actuators with Elastic Structures

Evgenia V. Kirillova, Wolfgang Seemann and Maria S. Shevtsova

Abstract In this paper, we formulate the contact problem of an actuator on an isotropic layer. The appropriate integro-differential system of equations is solved for a 2D model. We start with calculating the unknown stresses in the contact area using the Petrov-Galerkin method and proceed with obtaining the wave fields using the integral equation. Finally, we analyse the obtained wave fields in the considered isotropic structure and compare them with the results obtained by means of an engineering approach.

42.1 Introduction

Monitoring the condition of components relevant in terms of safety and functionality is absolutely essential in many different industrial sectors. The use of Condition Monitoring (CM) allows observing dynamically loaded components and structures. The structural integrity of large-scale constructions and highly loaded critical components can be monitored by means of precise recording and describing their natural oscillation conditions or analysing wave propagation. Condition monitoring has been practised for many years. In contrast to the conventional nondestructive controlling, which supposes more or less regular but time limited inspection of constructions, the sensors during CM remain on or in the observed structure for an extended period of time and are permanently or periodically checked. Thus, the damage can be detected almost immediately through the

E.V. Kirillova (✉) · M.S. Shevtsova
RheinMain University of Applied Sciences, 18 Kurt-Schumacher-Ring,
Wiesbaden 65197, Germany
e-mail: Evgenia.Kirillova@hs-rm.de

M.S. Shevtsova
e-mail: Maria.Shevtsov@hs-rm.de

W. Seemann
Karlsruhe Institute of Technology, 10 Kaiserstrasse,
76131 Karlsruhe, Germany

I.A. Parinov et al. (eds.), *Advanced Materials*, Springer Proceedings
in Physics 193, DOI 10.1007/978-3-319-56062-5_42

changes of sensor signals and appropriate measures can be taken. Lamb waves [1] have considerable potential for the identification of defects in elastic structures since they can propagate at long distances, can be generated without great effort and their wave characteristics can be easily measured [2, 3]. New CM systems use elastic waves to monitor the condition of structures and components. To do this, the test object is deliberately excited. While passing through the object, the waves (depending on their type and quality) interact with the defects in the object. The comparison of the measured signals in undamaged and damaged states makes it possible to identify the type and scope of damage [4]. In all control and observation tasks based on the use of elastic waves, the exact knowledge of wave propagation in the construction as well as the interaction of waves with the construction components and defects is essential in order to develop appropriate evaluation strategies.

Numerous methods exist today to excite and measure elastic waves, however, the piezo element method is the most frequently used one. Piezo elements can be both applied to the structure or embedded into the structure [5]. They are of extremely low weight and small size, do not require high production costs and can be simultaneously used as actuators and sensors. These facts explain the wide range of applications of piezo elements in condition monitoring with the aid of excitation of elastic waves [3, 4, 6]. When elastic waves are generated by piezo elements, the longitudinal deformations appear in the piezo element and lead to the vibrations of the elastic continuum surface. The first investigations of the interaction between a piezo element and an elastic structure that were performed by means of simplified models (beams, shells, plates) showed that the occurring contact stresses are shear stresses which concentrate on the edge of the contact area [7, 8]. That is why the interaction was described with the help of concentrated forces (pin-force models) on the boundaries of the piezo element in opposite directions [9]. This simplified model of producing Lamb waves by means of piezo actuators has been widely applied [7]. It is also used to describe high frequency oscillations in elastic structures. Specifically, this model is used in the structures with isotropic [6, 10] as well as anisotropic characteristics [2, 11].

To analyse the mechanical behaviour of the systems consisting of an electromechanical part (a piezoceramic actuator or a sensor) and a purely mechanical part, it is necessary to study the dynamic interactions between the piezo electric system parts and the mechanical structures. These interactions can be described with the help of integro-differential equations for unknown contact stresses and for the displacements in the contact area in the case of the corresponding modeling with mechanical stresses between the system parts.

42.2 Problem Statement

Let us consider vibrations of a medium that occupies the volume $D = \{(x, y, z) | -\infty < x, y < \infty; -h \le z \le 0\}$ (see Fig. 42.1). The lower boundary is free, whereas a thin piezoelectric plate with the thickness of h_0 is glued in the domain Ω

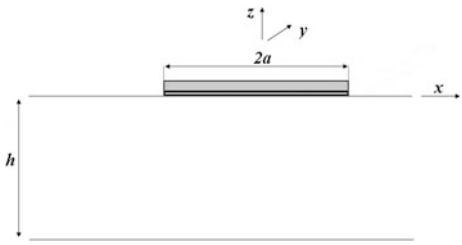

Fig. 42.1 The scheme of the loaded structure

on the upper boundary. The displacements during harmonic vibrations of the piezoelectric plate are $\mathbf{u} = \{\ u_x \quad u_y \quad u_z\ \}^T \cdot e^{-i\omega t}$. The displacements of the actuator are assumed to be known and determined by the function $\mathbf{u}|_{z=0} = \{\ v_x \quad v_y \quad 0\ \}^T|_{z=0} = \mathbf{f}(x, y)$ in the contact area. The aim of this study is to determine the wave field in the considered layer.

Lame's equations for the steady-state harmonic vibration have the form:

$$L\mathbf{u} + \rho\omega^2\mathbf{u} = 0. \tag{42.1}$$

The bottom surface of the structure is free of stress:

$$\boldsymbol{\tau}|_{z=-h} = 0. \tag{42.2}$$

The surface displacements cause unknown contact shear stresses in the domain Ω

$$\boldsymbol{\tau}|_{z=0} = \begin{cases} \mathbf{q}, & (x, y) \in \Omega \\ 0, & (x, y) \notin \Omega \end{cases}, \tag{42.3}$$

where $\mathbf{q}$ is unknown.

42.3 An Integral Representation of the Wave Field

In order to solve the formulated problem, we apply an approach based on the use of integral representations of the wave fields excited in the elastic medium by surface loads. When we use these representations jointly with the contact conditions of the structure and the actuator and take into account the small thickness of the actuator in comparison with the wavelengths propagating in the system, we can reduce it to the boundary value problem for a system of integro-differential equations with respect to the unknown contact stresses under the actuator. After calculating the unknown contact stresses, the wave fields excited in the system can be calculated using integral representations. The solution of the initial problem can be written as follows [12]:

$$\mathbf{u}(x,y,z) = \iint\limits_{\Omega} \mathbf{k}(x-\xi, y-\zeta, z)\mathbf{q}(\xi,\zeta)d\xi d\zeta, \tag{42.4}$$

where $\mathbf{k}$ is the Green's matrix of the considered elastic medium. Let us apply the Fourier transform by x, y to (3.1) with the parameters α_1, α_2 [11]:

$$\mathbf{U}(\alpha_1, \alpha_2, z) = \mathbf{K}(\alpha_1, \alpha_2, z)\mathbf{Q}(\alpha_1, \alpha_2), \tag{42.5}$$

where $\mathbf{U}$, $\mathbf{K}$, $\mathbf{Q}$ are the Fourier transforms from $\mathbf{u}$, $\mathbf{k}$, $\mathbf{q}$.

The solution of the problem can be thus rewritten as follows:

$$\mathbf{u}(x,y,z) = \frac{1}{4\pi^2}\int\limits_{\Gamma_1}\int\limits_{\Gamma_2} \mathbf{K}(\alpha_1, \alpha_2, z)\mathbf{Q}(\alpha_1, \alpha_2)e^{-i(\alpha_1 x + \alpha_2 y)}d\alpha_1 d\alpha_2, \tag{42.6}$$

The integration contours Γ_1 and Γ_2, in accordance with the limiting absorption principle [13], go along the real axis, deviating when traversing the poles of Fourier transform $\mathbf{K}$ of the Green's matrix $\mathbf{k}$.

For the given type of displacements, only shear contact stresses appear under the actuator, thereby, $\mathbf{q} = \{\, q_x \quad q_y \quad 0 \,\}$, and taking into account only the first two columns of the Green's matrix $\mathbf{k}_1 = \{\, k_{11} \quad k_{21} \quad k_{31} \,\}^T$ and $\mathbf{k}_2 = \{\, k_{12} \quad k_{22} \quad k_{32} \,\}^T$, respectively, the solution (4) can be rewritten as follows:

$$\begin{aligned}\mathbf{u}(x,y,z) = &\iint\limits_{\Omega} \mathbf{k}_1(x-\xi, y-\zeta, z)q_x(\xi,\zeta)d\xi d\zeta \\ &+ \iint\limits_{\Omega} \mathbf{k}_2(x-\xi, y-\zeta, z)q_y(\xi,\zeta)d\xi d\zeta.\end{aligned} \tag{42.7}$$

When $\mathbf{q} = \{\, q_x \quad q_y \quad 0 \,\}$, the Fourier symbol of the contact stresses under an actuator has the form

$$\mathbf{Q} = \int\limits_{-\infty}^{\infty}\int\limits_{-\infty}^{\infty} \mathbf{q}(x,y)e^{i(\alpha_1 x + \alpha_2 y)}dxdy = \{\, Q_x \quad Q_y \quad 0 \,\}^T, \tag{42.8}$$

and taking into account the continuity requirement of a displacement field in the contact area:

$$u_x\big|_{z=0} = v_x, \quad u_y\big|_{z=0} = v_y, \quad (x,y) \in \Omega, \tag{42.9}$$

we obtain following integral equations from (8), (9):

$$\begin{aligned}\frac{1}{4\pi^2}\int_{\Gamma_1}\int_{\Gamma_2}\left(\mathrm{K}_{11}(\alpha_1,\alpha_2,0)Q_x+\mathrm{K}_{12}(\alpha_1,\alpha_2,0)Q_y\right)e^{-i(\alpha_1 x+\alpha_2 y)}d\alpha_1 d\alpha_2 = v_x\\ \frac{1}{4\pi^2}\int_{\Gamma_1}\int_{\Gamma_2}\left(\mathrm{K}_{21}(\alpha_1,\alpha_2,0)Q_x+\mathrm{K}_{22}(\alpha_1,\alpha_2,0)Q_y\right)e^{-i(\alpha_1 x+\alpha_2 y)}d\alpha_1 d\alpha_2 = v_y\end{aligned}. \quad (42.10)$$

The wave field **u**, excited by the actuator, is thus defined by the representation (6) after the contact stresses **q** have been calculated.

The numerical calculations will be performed for the 2D case in domain $D=\{(x,z)|-\infty<x<\infty;-h\le z\le 0\}$, when the contact area is described as follows $\Omega=\{(x,z)|\quad |x|<a;z=0\}$. In this case the solution (6) takes the form:

$$\mathbf{u}(x)=\left\{\frac{1}{2\pi}\int_{\Gamma}K(\alpha,z)Q_x(\alpha)e^{-i\alpha x}d\alpha\quad 0\right\}^T, \quad (42.11)$$

where $K(\alpha,z)=K_{11}$ is the first element of the Fourier-symbol of the Green's matrix for the elastic structure in case of plane strain [12]. The integration contour, shown in Fig. 42.2, coincides almost everywhere with the real axis. The real poles of $K(\alpha,z)$ will be bypassed at the bottom in case of the positive poles, when the negative poles will be bypassed at the top (in case of the absence of backward waves). According to the boundary conditions, the integral (42.10) is transformed into the form:

$$\frac{1}{2\pi}\int_{\Gamma}K(\alpha,0)Q_x(\alpha)e^{-i\alpha x}d\alpha=v_x, \quad (42.12)$$

where $Q_x(\alpha)=\int_{-\infty}^{\infty}q_x(x)e^{i\alpha x}dx$, thus

$$\frac{1}{2\pi}\int_{\Gamma}K(\alpha,0)\int_{-\infty}^{\infty}q_x(\xi)e^{i\alpha\xi}d\xi e^{-i\alpha x}d\alpha=v_x. \quad (42.13)$$

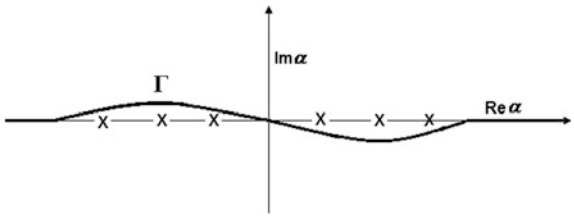

Fig. 42.2 Integration contour

42.4 Petrov-Galerkin Method for the Integral Equation Solution

In order to solve the integral (42.13) with respect to the unknown function $q_x(x)$, we apply the Petrov-Galerkin method. This method is a type of the projection methods, which is based on the idea of representation of the correct solution $\tilde{q}(x)$ by an approximate solution $q_N(x)$, which is composed of functions $\varphi_i(x)$ according to

$$\tilde{q}(x) \approx q_N(x) = \sum_{i=1}^{N} C_i \varphi_i(x), \tag{42.14}$$

which depends on the unknown parameters $C_i, \quad i = 1, \ldots, N$, while $\varphi_i(x)$ is a system of linearly independent basis functions in L_2 and $\varphi_i(x) = \varphi\left(\frac{x - x_i}{\Delta x}\right)$, $\Delta x = \frac{2a}{N}$, $x_i = -a + \left(i - \frac{1}{2}\right)\Delta x$, when

$$\varphi(\xi) = \begin{cases} 1 - |\xi|, & |\xi| < 1 \\ 0, & |\xi| > 1 \end{cases}. \tag{42.15}$$

The unknown coefficients C_i are determined by solving the linear algebraic system:

$$\begin{cases} a_{11}C_1 + a_{12}C_2 + \ldots + a_{1n}C_n = f_1 \\ a_{21}C_1 + a_{22}C_2 + \ldots + a_{2n}C_n = f_2 \\ \ldots\ldots\ldots\ldots\ldots\ldots\ldots\ldots \\ a_{n1}C_1 + a_{n2}C_2 + \ldots + a_{nn}C_n = f_n \end{cases}, \tag{42.16}$$

obtained by projection of the unknown function q in L_2 on the system of the basis functions φ_i

$$(\mathrm{K}q_N - f, \varphi_i)_{\mathbf{L}_2} = 0, i = 1, \ldots, N. \tag{42.17}$$

The elements a_{ij} are calculated as follows

$$a_{ij} = \frac{(\Delta x)^2}{2\pi} \int_{\Gamma} K(\alpha, 0)\Phi^2(\alpha\Delta x) e^{-i\alpha\left(x_i - x_j\right)} d\alpha, \tag{42.18}$$

where $\Phi(\alpha) = \int_{-1}^{1} \varphi(x) \cdot e^{i\alpha x} dx = \frac{\sin^2(\alpha/2)}{(\alpha/2)^2}$, $f_i = \int_{-\infty}^{\infty} f(x)\varphi_i(x)dx$.

The function $K(\alpha, 0)$ is an even function (see Fig. 42.3), therefore, let us perform the transition to the contour Γ^+ in the integral (42.18). This contour coincides almost everywhere with the positive real semi-axis, and bypasses the positive real poles (in case of the absence of backward waves) at the bottom.

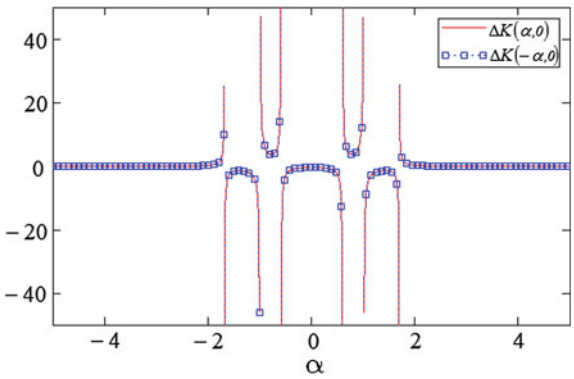

Fig. 42.3 Function of the green's matrix determinant $\Delta K(\alpha, 0)$ (*red line*) and $\Delta K(-\alpha, 0)$ (*blue points*) at $\omega = 1$, steel layer

During the transition to the contour Γ^+, the dependence of the integrand on $|x_i - x_j| = \left|-a + \left(i - \frac{1}{2}\right)\Delta x - \left(-a + \left(j - \frac{1}{2}\right)\Delta x\right)\right| = |i - j|\Delta x$ appears. Thus, the a_{ij} components are expressed in terms of N integrals as follows

$$a_{ij} = \frac{(\Delta x)^2}{\pi} \int\limits_{\Gamma^+} K(\alpha, 0)\Phi^2(\alpha\Delta x)\cos(\alpha\Delta x|i - j|)d\alpha. \tag{42.19}$$

After the C_j coefficients have been calculated from the system (42.16), the wave field $\mathbf{u}(x, z)$ can be obtained in each point (x, z) using the relation

$$\mathbf{u}(x, z) \approx \mathbf{u}_N(x, z) = \frac{\Delta x}{2\pi} \int\limits_{\Gamma} K(\alpha, z)\Phi(\alpha\Delta x)\mathbf{Q}e^{-i\alpha x}d\alpha, \tag{42.20}$$

where $\mathbf{Q} = \left\{ Q_N = \sum_{j=1}^{N} C_J e^{i\alpha x_j} \quad 0 \right\}^T$.

42.5 Results and Analysis

In order to operate with the dimensionless parameters, we have divided them by the following values: $h_0 = h$ is the thickness of the layer, $\rho_0 = \rho$ is the layer's material density, $\mu_0 = \mu$ is the shear modulus. The dimensionless vibration frequency has been calculated using the formula

$$\omega = \frac{f \cdot h \cdot 2\pi}{c_s}. \tag{42.21}$$

where $c_s = \sqrt{\mu/\rho}$ is the S-wave velocity. The calculations have been performed for steel and duraluminum layers. In both cases, the thickness of the layers was taken equal to $h = 10\,\text{mm}$, thus $h_0 = 10^{-2}\,\text{m}$. The following mechanical parameters were accepted for the steel and duraluminium layers, respectively: $\rho_{st} = 7480\,\text{kg/m}^3$ and $\rho_d = 2700\,\text{kg/m}^3$ are the densities; $\mu_{st} = 78\,\text{GPa}$ and $\mu_d = 26.5\,\text{GPa}$ are the shear moduli; $\nu_{st} = 0.28$ and $\nu_d = 0.34$ are Poisson's ratios. The dimensionless speeds and frequencies have been obtained using the formulas $c_0 = \sqrt{\mu_0/\rho_0}$ and $f_0 = c_0/h_0$, respectively.

Figure 42.4 shows the functions of the contact stresses $q_N(x)$ calculated for the steel (Fig. 42.4a), and duraluminium (Fig. 42.4b) layers at different frequency values $\omega = 1.1,\ 1.5,\ 4$ and for $N = 20$. Further increase of N does not cause a significant change of the numerical solution.

The amplitudes of the displacement field on the top of the steel (Fig. 42.5a) and duraluninium (Fig. 42.5b) layers are presented below.

Figure 42.6 shows the distribution of the displacement field on the outer surface of a steel layer at low frequencies $\omega = 1.1$ (Fig. 42.6a) and at higher frequencies $\omega = 4$ (Fig. 42.6b), when the radius of the contact area $a = 1$. The displacements were calculated by means of two methods: by solving the contact problem as well as using the engineering approach. According to the second method, the action of the actuator has been approximated by the concentrated forces, applied to the boundary points $x = \pm a$ of the actuator:

$$\tau_{xz}|_{z=0} = C(\delta(x-a) + \delta(x+a)), \tag{42.22}$$

where $C = \int_0^a q(x)dx$ is a coefficient which represents the amplitude of an applied load. In this case, the displacement field was calculated by means of contour integration [14].

It can be concluded that the distributions of the displacement fields obtained by two different methods at high frequencies differ significantly near the vibration source (see Fig. 42.6b), but with an increase of x-coordinate both methods give similar results. However, the two methods give calculation results, which are in a good agreement both near the vibration source and at an essential distance from it (see Fig. 42.6a) at low frequencies.

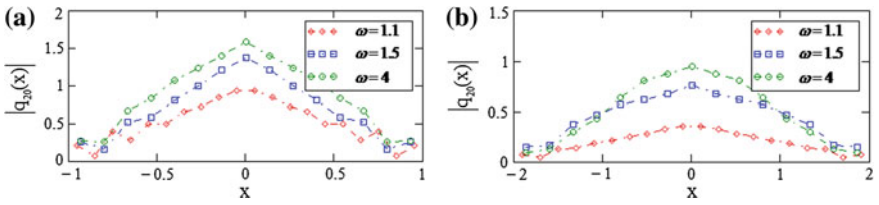

Fig. 42.4 Functions of contact stresses $q(x)$ for steel (**a**) and duraluminium (**b**) layers; $a = 1$ and $a = 2$, respectively

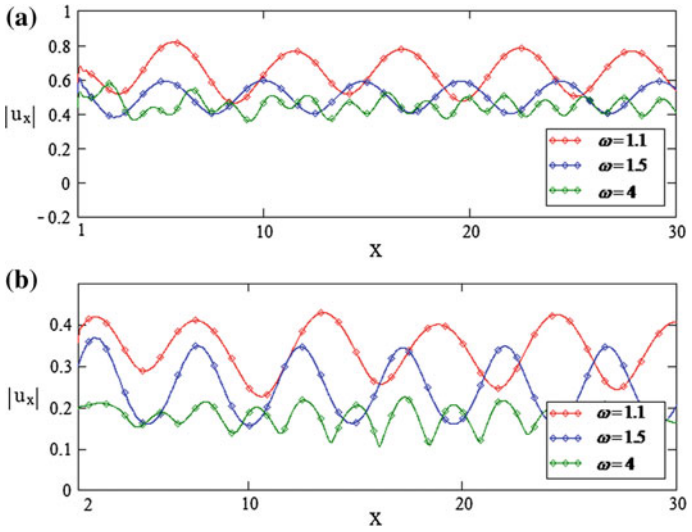

Fig. 42.5 Displacement field for steel (**a**) and duraluminium (**b**) structures at $z = 0$: $a = 1$ and $a = 2$, respectively

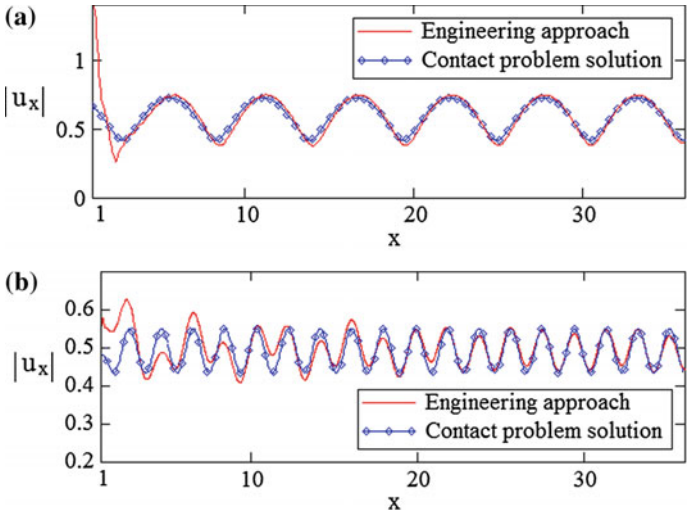

Fig. 42.6 Comparison of the displacement fields obtained by means of the engineering approach and the contact problem solution at $z = 0$ and $\omega = 1.1$ (**a**) and $\omega = 4$ (**b**)

42.6 Conclusions

The contact problem for an actuator glued on an isotropic structure was formulated and solved. The displacement fields were calculated by the solution of an appropriate integro-differential system by means of the Petrov-Galerkin method and using the engineering approach, when the action of the actuator has been approximated by the concentrated forces applied to the boundary points of the actuator. The solutions of the considered problem were obtained for the steel and duraluminium structures with different width of a contact area. The wave fields in the considered isotropic structures obtained by solving the contact problem were analyzed and compared with the results calculated using the engineering approach. It was shown that both methods give coincident results far from the vibration source at both low and high frequencies. In the vicinity of the actuator, the results are in a good agreement at low frequencies, whereas they are considerably different at high frequencies.

Acknowledgements The work is supported by the Federal Ministry of Education and Research, Germany and the Russian Foundation for Basic Research (grant No. 16-58-52013 MNT_a).

References

1. H. Lamb, Proc. Roy. Soc. Lond. Ser. A. **93**(651), 293 (1917)
2. A. Raghavan, C.E.S. Cesnik, in *48th AIA/ASME/ASCE/ASH/ASC Structures, Structural Dynamics, and Materials Conference* (2007)
3. K. Diamanti, C. Soutis, Structural health monitoring for aircraft composite structures. Prog. Aerosp. Sci **46**, 342 (2010)
4. W. Ostachowicz, P. Kudela, P. Malinowski, T. Wandowski, Mech. Syst. Signal Process **23**, 1805 (2009)
5. Z. Su, L. Ye, in *Identification of Damage Using Lamb Waves* (Springer, 2009)
6. V. Giurgiutiu, in *Elsevier Academic Press* (2008)
7. E.F. Crawley, J. Luis, AIAA J **25**, 1373 (1987)
8. V. Giurgiutiu, A.N. Zagrai, J. Intell. Mater. Syst. Struct **11**, 959 (2000)
9. Z. Chaundhry, C.A. Rogers, J. Intell. Mater. Syst. Struct **5**, 347 (1994)
10. A. Raghavan, C.E.S. Cesnik, Smart Mater. Struct **14**, 1448 (2005)
11. A. Karmazin, E. Kirillova, W. Seemann, P. Syromyatnikov, in *Proceedings IMECE* (2010)
12. E. Glushkov, N. Glushkova, O. Kvasha, W. Seemann, Smart Mat. Struct **16**(3), 650 (2007)
13. V. Babeshko, E. Glushkov, Z. Zinchenko, *Dynamics of Inhomogeneous Linearly Elastic Media* (Nauka, Moscow, 1989). (In Russian)
14. A. Karmazin, *Time-efficient Simulation of Surface-excited Guided Lamb Wave Propagation in Composites*, PhD thesis (2012)

Chapter 43
Finite Element Simulation of Dissipative Heating of Piezoelectric Vibratory Gyroscopes

Andrey V. Nasedkin and Evgenia I. Shprayzer

Abstract The chapter describes the methodology of finite element solutions of linear and nonlinear problems of dissipative heating of piezoelectric vibratory gyroscopes, working in the mode of steady-state oscillations. The continual formulations of these problems and their finite element approximations are presented. The chapter also presents the numerical algorithms for solving the problems of dissipative heating of vibratory gyroscopes using non-standard features of finite-element software ANSYS and its command language APDL.

43.1 Introduction

Solid piezoelectric vibratory gyroscopes are among the most common types of gyroscopic devices, widely used in systems of navigation and control [1]. These gyroscopes operate on the resonance frequencies and register the frequency of rotation due to the Coriolis forces. These resonators can have various geometric structures depending upon the designs [2]. The use of piezoelectric materials for vibratory gyroscopes became popular because piezoelectric devices can have small sizes and low price, and they are robust and reliable. Now the finite element method was widely used for numerical design of different piezoelectric devices and piezoelectric vibratory gyroscopes [3–5].

The present investigation focuses on the effect of dissipative heating, since the angular velocity sensors are sensitive to changes of temperature, which cause a

A.V. Nasedkin (✉)
I. I. Vorovich Institute of Mathematics, Mechanics and Computer Science,
Southern Federal University, 8a, Milchakova Street,
Rostov-on-Don 344090, Russia
e-mail: nasedkin@math.sfedu.ru

E.I. Shprayzer
Department of Theoretical and Applied Mechanics,
Don State Technical University, Gagarin Sq, Rostov-on-Don 344000, Russia
e-mail: shprayzer@gmail.com

I.A. Parinov et al. (eds.), *Advanced Materials*, Springer Proceedings
in Physics 193, DOI 10.1007/978-3-319-56062-5_43

reduction of the frequency of vibration occurring due to a change of piezomoduli. The chapter is organized as follows. Section 43.2 presents the mathematical statement of the harmonic problem for piezoelectric vibratory gyroscopes. The finite element approximations of the considered harmonic problems for piezoelectric devices with rotation effects are given in Sect. 43.3. Section 43.4 describes the thermal problems for determination of temperature fields due to energy dissipation from harmonic oscillations. For these problems we formulate the linear and non-linear problems of dissipative heating for constant material moduli of piezoelectric bodies and for material moduli depending on temperature fields, respectively. In Sect. 43.5 we describes the finite element equations for considered problems of dissipative heating, we discuss the implementation of the proposed approaches in the finite element software ANSYS, and we suggest an iterative algorithm for solving non-liner problems of dissipative heating.

43.2 Mathematical Formulation of the Problem for Piezoelectric Vibratory Gyroscope

The piezoelectric vibratory gyroscopes like ordinary gyroscopic sensors are designed to record the rotation concerning the inertial reference frame (absolute coordinate system). Their operating principle is usually as follows. The voltage $\Delta\varphi$ is applied at one of the pairs of electrodes and varied periodically with frequency $f = \omega/(2\pi)$: $\Delta\varphi = \tilde{V}_{inp}\exp(j\omega t)$. In the result of these periodic external influences the gyroscope will oscillate with the same frequency ω, and in the coordinate system related to its non-deformed state (in the relative coordinate system) the displacements $\mathbf{u}(\mathbf{x},t)$ and the electrical potential $\varphi(\mathbf{x},t)$ can be written as: $\mathbf{u} = \tilde{\mathbf{u}}(\mathbf{x})\exp(j\omega t)$, $\varphi = \tilde{\varphi}(\mathbf{x})\exp(j\omega t)$, where the symbol "tilde" (it is not shown below) means the amplitude values of the corresponding quantities. Let us assume that there is an additional (secondary) motion of the total structure in the form of the rotation with an angular velocity vector $\mathbf{\Omega} = \{\Omega_x, \Omega_y, \Omega_z\} = \{\Omega_1, \Omega_2, \Omega_3\}$.

Then the equation of the linear theory of piezoelectricity in a non-inertial (relative) reference system associated with the rotating body V in the steady-state oscillation mode for the amplitude values has the following form [5]:

$$\mathbf{L}^*(\nabla)\cdot\mathbf{T} = \rho\left(-\omega^2\mathbf{u} + j\omega\,\alpha_d\,\mathbf{u} + 2j\omega\,\mathbf{\Omega}\times\mathbf{u} + \mathbf{\Omega}\times(\mathbf{\Omega}\times\mathbf{u})\right), \tag{43.1}$$

$$\nabla^*\cdot\mathbf{D} = 0, \tag{43.2}$$

$$\mathbf{T} = (1 + j\omega\,\beta_d)\,\mathbf{c}^E\cdot\mathbf{S} - \mathbf{e}^*\cdot\mathbf{E}, \tag{43.3}$$

$$\mathbf{D} = \mathbf{e}\cdot\mathbf{S} + \boldsymbol{\varepsilon}^S\cdot\mathbf{E}, \tag{43.4}$$

$$\mathbf{S} = \mathbf{L}(\nabla) \cdot \mathbf{u},\ \mathbf{E} = -\nabla\phi, \tag{43.5}$$

$$\mathbf{L}^*(\nabla) = \begin{bmatrix} \partial_1 & 0 & 0 & 0 & \partial_3 & \partial_2 \\ 0 & \partial_2 & 0 & \partial_3 & 0 & \partial_1 \\ 0 & 0 & \partial_3 & \partial_2 & \partial_1 & 0 \end{bmatrix}, \nabla = \begin{Bmatrix} \partial_1 \\ \partial_2 \\ \partial_3 \end{Bmatrix}, \tag{43.6}$$

where ρ is the density; $\mathbf{T} = \{\sigma_{11}, \sigma_{22}, \sigma_{33}, \sigma_{23}, \sigma_{13}, \sigma_{12}\}$ is the array of the components of the stress tensor σ_{ij}; $\mathbf{D}$ is the electric flux density vector or the electric displacement vector; $\mathbf{S} = \{\varepsilon_{11}, \varepsilon_{22}, \varepsilon_{33}, 2\varepsilon_{23}, 2\varepsilon_{13}, 2\varepsilon_{12}\}$ is the array of the components of the strain tensor ε_{ij}; $\mathbf{E}$ is the electric field vector; $\mathbf{c}^E$ is the 6×6 matrix of elastic stiffness, measured at constant electric field; $\mathbf{e}$ is the 3×6 matrix of piezomoduli; $\boldsymbol{\varepsilon}^S$ is the 3×3 matrix of dielectric permittivities, measured at constant strains; α_d, β_d are the damping coefficients; $(\ldots)^*$ is the operation of transposition for matrices and vectors.

For completeness, the boundary conditions should be added to the system of differential (43.1)–(43.6). There are two types of boundary conditions: mechanical and electric.

To formulate the mechanical boundary conditions, we assume that the boundary $S = \partial V$ is divided into two subsets S_σ and S_u $(S = S_\sigma \cup S_u)$ for dynamic and kinematic boundary conditions, respectively. The dynamic boundary conditions given at S_σ take the form:

$$\mathbf{L}^*(\mathbf{n}) \cdot \mathbf{T} = \mathbf{p}_S, \quad \mathbf{x} \in S_\sigma, \tag{43.7}$$

where $\mathbf{n}$ is the external unit normal to S, and $\mathbf{p}_S$ is the amplitude of external surface loads.

On the remaining part S_u of boundary S, we pose known the amplitude of mechanical displacements vector $\mathbf{u}_S$

$$\mathbf{u} = \mathbf{u}_S, \quad \mathbf{x} \in S_u. \tag{43.8}$$

Note that for piezoelectric gyroscope, usually, $\mathbf{p}_S = 0$, i.e. the part S_u is free from stresses, and $\mathbf{u}_S = 0$, i.e. the part S_u is rigidly fixed.

To set the electric boundary conditions, we assume that the surface S is also subdivided into two subsets: S_D and S_φ $(S = S_D \cup S_\varphi)$.

The region S_D does not contain electrodes, so the following conditions hold

$$\mathbf{n}^* \cdot \mathbf{D} = -\sigma_S, \quad \mathbf{x} \in S_D, \tag{43.9}$$

where σ_S is the given surface density of electric charge, and usually, $\sigma_S = 0$.

The subset S_φ is the union of $M+1$ regions $S_{\varphi k}$ $(k \in J_Q \cup J_V$, $J_Q = \{1, 2, \ldots, m\}$, $J_V = \{0, m, m+1, \ldots, M\})$, that does not border on each other and are covered with infinitely thin electrodes. At these regions, we set the following boundary conditions:

$$\varphi = \Phi_k, \quad \mathbf{x} \in S_{\varphi k}, \quad k \in J_Q, \tag{43.10}$$

$$\int\limits_{S_{\varphi k}} \mathbf{n}^* \cdot \mathbf{D}\, dS = -Q_k, \quad I_k = \pm \dot{Q}_k, \, \mathbf{x} \in S_{\varphi k}, \quad k \in J_Q, \tag{43.11}$$

$$\varphi = V_k, \quad \mathbf{x} \in S_{\varphi k}, \quad S_{\varphi 0} \neq \wedge, \quad k \in J_V, \tag{43.12}$$

where the variables Φ_k, V_k do not depend on $\mathbf{x}$; Q_k is the overall electric charge on $S_{\varphi k}$, and the sign "$\pm$" in (43.11) is chosen in accordance with the accepted direction of the current I_k in the electric circuit.

Features of equations for piezoelectric vibratory gyroscopes are associated with (43.1). The term $2j\rho\omega\, \boldsymbol{\Omega} \times \mathbf{u}$ represents the Coriolis forces, caused by the Coriolis acceleration (turning acceleration), and the term $\rho\, \boldsymbol{\Omega} \times (\boldsymbol{\Omega} \times \mathbf{u})$ represents the centripetal forces. If we compare the solutions of problems (43.1)–(43.12) in the absence of rotation ($\boldsymbol{\Omega} = 0$) and with rotation ($\boldsymbol{\Omega} \neq 0$), then we can conclude about the appearance of rotation and about the magnitude of its angular velocity. We would like to note that the piezoelectric vibratory gyroscopes are often made with multielectrode covering for convenience of registration of rotation.

43.3 Finite Element Modelling of Harmonic Vibration for Piezoelectric Gyroscope

For numerical solution of the piezoelectric problems for piezoelectric vibratory gyroscopes, we can use the finite element method (FEM). Let V_h is a region of the corresponding finite element mesh, $V_h \subseteq V$. For harmonic problem, we can find the approximate solution $\{\mathbf{u}_h \approx \mathbf{u}, \, \varphi_h \approx \varphi\}$ in the next form:

$$\mathbf{u}_h(\mathbf{x}) = \mathbf{N}_u^*(\mathbf{x}) \cdot \mathbf{U}, \quad \varphi_h(\mathbf{x}) = \mathbf{N}_\varphi^*(\mathbf{x}) \cdot \boldsymbol{\Phi}, \tag{43.13}$$

where $\mathbf{N}_u^*$ is the matrix of the shape functions (basis functions) for the displacements; $\mathbf{N}_\varphi^*$ is the row vector of the shape functions for electric potential; $\mathbf{U}$, $\boldsymbol{\Phi}$ are the vectors of nodal amplitudes of displacements and electric potential, respectively.

In accordance with standard finite element technique, we approximate the continual weak formulation of the piezoelectric problem in finite-dimensional spaces connected with the shape functions $\mathbf{N}_u^*$ and $\mathbf{N}_\varphi^*$. Substituting (43.13) and similar expressions for projects functions into the weak formulation of the piezoelectric problem in V_h, we obtain the following finite element system [5]:

$$-\omega^2 \mathbf{M}_{uu} \cdot \mathbf{U} + i\omega \left(\mathbf{C}_{uu} + \mathbf{G}_{uu}\right) \cdot \mathbf{U} + \left(\mathbf{K}_{uu} - \mathbf{K}^c_{uu}\right) \cdot \mathbf{U} + \mathbf{K}_{u\varphi} \cdot \mathbf{\Phi} = \mathbf{F}_u, \quad (43.14)$$

$$-\mathbf{K}^*_{u\varphi} \cdot \mathbf{U} + \mathbf{K}_{\varphi\varphi} \cdot \mathbf{\Phi} = \mathbf{F}_\varphi, \quad (43.15)$$

where

$$\begin{aligned} \mathbf{M}_{uu} &= \int\limits_{V_h} \rho \mathbf{N}_u \cdot \mathbf{N}^*_u \, dV, \quad \mathbf{C}_{uu} = \alpha_d \mathbf{M}_{uu} + \beta_d \mathbf{K}_{uu}, \\ \mathbf{G}_{uu} &= 2 \int\limits_{V_h} \rho \, \mathbf{N}_u \cdot \mathbf{\Theta} \cdot \mathbf{N}^*_u \, dV, \end{aligned} \quad (43.16)$$

$$\mathbf{K}_{uu} = \int\limits_{V_h} \mathbf{B}^*_u \cdot \mathbf{c}^E \cdot \mathbf{B}_u dV, \quad \mathbf{B}_u = \mathbf{L}(\nabla) \cdot \mathbf{N}^*_u, \quad (43.17)$$

$$\mathbf{K}_{u\varphi} = \int\limits_{V_h} \mathbf{B}^*_u \cdot \mathbf{e}^* \cdot \mathbf{B}_\varphi \, dV, \quad \mathbf{K}_{\varphi\varphi} = \int\limits_{V_h} \mathbf{B}^*_\varphi \cdot \boldsymbol{\varepsilon}^S \cdot \mathbf{B}_\varphi \, dV, \quad \mathbf{B}_\varphi = \nabla \mathbf{N}^*_\varphi, \quad (43.18)$$

$$\mathbf{\Theta} = \begin{bmatrix} 0 & -\Omega_3 & \Omega_2 \\ \Omega_3 & 0 & -\Omega_1 \\ -\Omega_2 & \Omega_1 & 0 \end{bmatrix}, \quad \mathbf{K}^c_{uu} = \int\limits_{V_h} \rho \, \mathbf{N}_u \cdot \mathbf{\Theta}^* \cdot \mathbf{\Theta} \cdot \mathbf{N}^*_u \, dV, \quad (43.19)$$

and for generation of the matrices, concerned with rotation, the following formulae were used:

$$\mathbf{\Omega} \times \mathbf{u} = \mathbf{\Theta} \cdot \mathbf{u}, \quad \mathbf{\Omega} \times (\mathbf{\Omega} \times \mathbf{u}) = \mathbf{\Theta} \cdot \mathbf{\Theta} \cdot \mathbf{u} = -\mathbf{\Theta}^* \cdot \mathbf{\Theta} \cdot \mathbf{u}, \quad (43.20)$$

Here $\mathbf{M}_{uu}$ is the mass matrix, $\mathbf{C}_{uu}$ is the damping matrix, $\mathbf{K}_{uu}$ is the stiffness matrix, $\mathbf{K}_{u\varphi}$ is the matrix of piezoelectric coupling, $\mathbf{K}_{\varphi\varphi}$ is the matrix of dielectric permittivities, $\mathbf{G}_{uu}$ is the Coriolis damping matrix, $\mathbf{K}^c_{uu}$ is the stiffness matrix due to centrifugal force; $\mathbf{F}_u$, $\mathbf{F}_\varphi$ are the vector of generalized nodal forces and the vector of generalized charges, resulting from the accounting inhomogeneous main boundary conditions.

Finite element analysis of piezoelectric vibration gyroscopes based on the solution of (43.14)–(43.19) is implemented in the computer software ANSYS, and some examples of the analysis of the vibratory gyroscope with using ANSYS can be found, for example, in [6–9].

43.4 Modelling of Dissipative Heating

As it is well known [10–13], piezoelectric vibratory gyroscopes like others piezoelectric devices, in case of harmonic oscillations become warm. In this situation, the solution of the problem about determination of temperature fields for steady oscillations of piezoelectric vibratory gyroscopes due to energy dissipation is an important issue. The general theory of dissipative heating was developed in [14] and later used for many problems, including the problems for the piezoelectric bodies ([15, 16], and others).

For modeling of dissipative heating, we introduce the non-stationary heat conduction problem for the same body V. This problem is described in the linear formulation with the heat equation:

$$\rho\, c_\varepsilon\, \dot{\theta} + \nabla^* \cdot \mathbf{q} = W, \quad \mathbf{q} = -\,\mathrm{k} \cdot \nabla\theta, \tag{43.21}$$

where θ is the temperature increase under natural state, c_ε is the specific heat, $\mathbf{q}$ is the heat flux vector, $\mathbf{k}$ is the 3×3 matrix of coefficients of thermal conductivity, W is the density of power of volumetric heat sources.

In addition, in the formulation of the problem we must include the boundary and initial conditions. Among the boundary conditions, in the problems for overwhelming majority of gyroscopes, we can consider only the condition of convective heat transfer:

$$\mathbf{n}^* \cdot \mathbf{q} = -h_f(\theta_f - \theta), \quad \mathbf{x} \in S, \tag{43.22}$$

where h_f is the heat transfer coefficient, θ_f is the ambient temperature.

The initial condition for the time t_{in} can be written as

$$\theta = \theta_{in}(\mathbf{x}), \quad t = t_{in}, \tag{43.23}$$

i.e. for the initial moment t_{in} the temperature is assumed known $\theta_{in}(\mathbf{x})$ for all points $\mathbf{x}$ of V.

The problem (43.21)–(43.23) describes the change of the body temperature field over the time interval $t \in [t_{in}, t_{end}]$ with some end time t_{end} under the influence of power density of heat sources. $W = W(\mathbf{x}, t)$ This problem is the classic problem of heat conduction for convective heat transfer and can be successfully solved numerically by the finite element method, for example, with ANSYS software.

In the case of harmonic oscillations of the gyroscope, its heating occurs due to the dissipation of energy. This irreversible part of the energy is determined by the model of Rayleigh damping adopted in (43.1) and (43.3). It can be expressed by the function of density of elastic energy dissipation D during oscillation period by the formula:

$$D = D_K + D_\Pi + D_\Omega, \tag{43.24}$$

where

$$D_K = \frac{1}{2}\omega^2 \alpha_d \rho(\mathbf{u}'^* \cdot \mathbf{u}' + \mathbf{u}''^* \cdot \mathbf{u}''), \quad D_\Omega = \omega^2 \rho(\mathbf{u}'^* \cdot \Theta \cdot \mathbf{u}' + \mathbf{u}''^* \cdot \Theta \cdot \mathbf{u}''), \tag{43.25}$$

$$D_\Pi = \frac{1}{2}\omega^2(\mathbf{S}^*(\mathbf{u}') \cdot \mathbf{c}^E \cdot \mathbf{S}(\mathbf{u}') + \mathbf{S}^*(\mathbf{u}'') \cdot \mathbf{c}^E \cdot \mathbf{S}(\mathbf{u}'')), \quad \mathbf{u}' = \operatorname{Re}\mathbf{u}, \quad \mathbf{u}'' = \operatorname{Im}\mathbf{u} \tag{43.26}$$

Here, D_K is the function of dissipation density of the kinetic energy, D_Ω is the function of dissipation density of energy of oscillations associated with rotary motion, D_Π is the function of dissipation density of the elastic potential energy.

Assuming that all irreversible energy during oscillation is converted into heat, we suppose that $D = W$.

If we assume that the material moduli of the piezoelectric gyroscope are not depend on the temperature, the problem of heating temperature is linear. This problem includes solution of the problem of electroelasticity (43.1)–(43.12), determination of the dissipation function D from the electroelastic problem and solution of the heat conduction problem (43.21)–(43.23) with heat sources $D = W$.

The problem becomes non-linear in case with accounting dependencies of the temperature for the moduli $\mathbf{c}^E = \mathbf{c}^E(\mathbf{x}, \theta)$, $\mathbf{e} = \mathbf{e}(\mathbf{x}, \theta)$, $\boldsymbol{\varepsilon}^S = \boldsymbol{\varepsilon}^S(\mathbf{x}, \theta)$ in (43.3) and (43.4). Such dependences of piezoceramic moduli are known from the literature ([17–20], and others), and the investigation of the temperature instability of the piezoelectric vibratory gyroscopes with changing moduli of piezoceramic materials for different temperatures was carried out in [21], but without solving the problem of temperature heating.

One algorithm for solution of this problem by the finite element method with software ANSYS is described in the next section. It is an iterative and requires a non-standard use of ANSYS features and its command language APDL.

43.5 Finite Element Modelling of Dissipative Heating

For the calculation of the temperature field, we approximate the unsteady heat conduction problem (43.21)–(43.23) using the finite element method.

The field of the temperature $\theta_h \approx \theta$ is calculated for finite element mesh in the region V_h, but with the temperature finite elements, in the form:

$$\theta_h(\mathbf{x}) = \mathbf{N}_\theta^*(\mathbf{x}) \cdot \mathbf{T}(t), \tag{43.27}$$

where $\mathbf{N}_\theta^*$ is the row vector of the shape functions for temperature; $\mathbf{T}$ is the vector of nodal temperature.

Finite element equation for thermal problem with convection surfaces is well-known and can be written in the form:

$$\mathbf{C}_{\theta\theta} \cdot \dot{\mathbf{T}} + \mathbf{K}_{\theta\theta} \cdot \mathbf{T} = \mathbf{F}_{\theta} + \mathbf{F}_{\theta D}, \tag{43.28}$$

where

$$\begin{gathered} \mathbf{C}_{\theta\theta} = \int\limits_{V_h} \rho c_{\varepsilon} \mathbf{N}_{\theta} \mathbf{N}_{\theta}^{*} dV, \quad \mathbf{K}_{\theta\theta} = \int\limits_{V_h} \mathbf{B}_{\theta}^{*} \cdot \mathbf{k} \cdot \mathbf{B}_{\theta} dV \\ + \int\limits_{S_h} h_f \mathbf{N}_{\theta} \mathbf{N}_{\theta}^{*} dS, \quad \mathbf{B}_{\theta} = \nabla \mathbf{N}_{\theta}^{*}. \end{gathered} \tag{43.29}$$

Here $\mathbf{C}_{\theta\theta}$ is the matrix of the heat capacity, $\mathbf{K}_{\theta\theta}$ is the matrix of heat conductivity, $\mathbf{F}_{\theta}$ is the vector of external thermal influences. These values are standard for finite element analysis of heat conduction problems, but $\mathbf{F}_{\theta D} = \int_{V_h} \boldsymbol{N}_{\theta} D dV$ in (43.28) is additional vector, determined by the intensity of the heat sources caused by energy dissipation D.

In accordance with the damping model, (43.24)–(43.26) and (43.13), the function of the dissipation density $D_h \approx D$ is given by the formula:

$$D_h = \omega^2 [\alpha_d (K_u(\mathbf{U}') + K_u(\mathbf{U}'')) + K_{\Omega}(\mathbf{U}') + K_{\Omega}(\mathbf{U}'') + \beta_d (\Pi_u(\mathbf{U}') + (\Pi_u(\mathbf{U}''))], \tag{43.30}$$

where

$$K_u(\mathbf{U}) = \frac{1}{2} \rho \mathbf{U}^{*} \cdot \mathbf{N}_u \cdot \mathbf{N}_u^{*} \cdot \mathbf{U}, \quad K_{\Omega}(\mathbf{U}) = \rho \mathbf{U}^{*} \cdot \mathbf{N}_u \cdot \boldsymbol{\Theta} \cdot \mathbf{N}_u^{*} \cdot \mathbf{U}, \tag{43.31}$$

$$\Pi_u(\mathbf{U}) = \frac{1}{2} \mathbf{U}^{*} \cdot \mathbf{B}_u \cdot \mathbf{c}^{E} \cdot \mathbf{B}_u^{*} \cdot \mathbf{U}, \quad \mathbf{U}' = \operatorname{Re} \mathbf{U}, \quad \mathbf{U}'' = \operatorname{Im} \mathbf{U}. \tag{43.32}$$

We note that we cannot take into account the terms with $K_{\Omega}(\mathbf{U}')$ and $K_{\Omega}(\mathbf{U}'')$ in (43.30), because under the conditions of our problem the gyroscope rotation occurs in considerably shorter time than its major oscillations occur. In addition, (43.30) depends on adopted model of damping. Moreover, the previously used model of Rayleigh damping is often used model of frequency-independent damping, when the first coefficient is equal to zero, and the second coefficient is inversely proportional to the frequency and expressed through the Q-factor Q_d

$$\alpha_d = 0, \quad \beta_d = \frac{1}{\omega Q_d} \tag{43.33}$$

Thus, partial formula for the function of dissipation density can be adopted instead of (43.30) with a frequency-independent damping coefficient (43.33):

$$D_h = \omega^2 \beta_d (\Pi_u(\mathbf{U}') + (\Pi_u(\mathbf{U}'')). \tag{43.34}$$

In finite element solution of linear problems of dissipative heating, the most difficult step is the determination of the function of dissipation and transfer the obtained values to the temperature problem. However, the use of frequency-independent damping model makes it very easy to implement the solution of such problems in the finite element software ANSYS. In fact, since the procedure for calculating the elastic potential energy $\Pi_u^{em}(\mathbf{U})$ for a single piezoelectric finite element V^{em} is programmed in ANSYS, we have access to $\Pi_u^{em}(\mathbf{U})$ by the command ETABLE and we can use the quite developed tools of programming language APDL ANSYS. After harmonic analysis in ANSYS according (43.14)–(43.19), we can calculate the element elastic potential energies $\Pi_u^{em}(\mathbf{U}')$ and $\Pi_u^{em}(\mathbf{U}'')$, also we can code the calculation of element function of dissipation density D_h^{em} according (43.34) with $\Pi_u^{em}(\mathbf{U}')$, $\Pi_u^{em}(\mathbf{U}'')$ and we can memorize the calculated values of D_h^{em} in the suitable arrays. Next we can proceed to the problem of the temperature on the same geometric finite element mesh (43.28) and transfer the saved values D_h^{em} in this problem for the element vectors $\mathbf{F}_{\theta D}^{em}$. Then, the solution of the problem of thermal conductivity (43.28) with the corresponding initial conditions allows us to find in ANSYS the temperature field of dissipative heating in the selected time interval.

By using ANSYS software, we can also implement the solution of nonlinear problems of dissipative heating in which the piezoelectric body is considered to be dependent on the temperature by some given laws:$\mathbf{c}^E = \mathbf{c}^E(\mathbf{x}, \theta)$, $\mathbf{e} = \mathbf{e}(\mathbf{x}, \theta)$, $\boldsymbol{\varepsilon}^S = \boldsymbol{\varepsilon}^S(\mathbf{x}, \theta)$.

Then, as in [6, 7], we propose the following iterative algorithm for the simulation of the temperature heating of the piezoelectric vibration gyroscopes in ANSYS.

1. Assume the counter of iterations i is equal to 1 and the medium moduli are equal to their initial table values: $\mathbf{c}^{E(i)} = \mathbf{c}^E$, $\mathbf{e}^{(k)} = \mathbf{e}$, $\boldsymbol{\varepsilon}^{S(i)} = \boldsymbol{\varepsilon}^S$. We define a sequence of time intervals $t \in \left[t_{in}^{(i)}, t_{end}^{(i)}\right]$ $\left(t_{end}^{(i)} = t_{in}^{(i+1)}\right)$ and according to (43.23), we also define the initial temperature field $\mathbf{T}_{in}^{(i)}$.
2. In step i, first, we solve the problem of piezoelectricity (43.14)–(43.19) on the harmonic oscillations. After solving this problem, we find and memorize the field of amplitudes of displacements $\mathbf{U}^{(i)}$.
3. We compute the averaged of dissipation function $D_h^{(i)}$ by the field $\mathbf{U}^{(i)}$ from (43.34) (more precisely, we compute the array of element values $D_h^{(i)em}$).
4. Values of dissipation function are used in the heat conduction problem as heat sources $\mathbf{F}_{\theta D}^{(i)}$. Solving the problem of heat conduction (43.28) with the initial conditions $\mathbf{T}_{in}^{(i)}$ on the time interval $\left[t_{in}^{(i)}, t_{end}^{(i)}\right]$, we find the temperature field $\mathbf{T}_{end}^{(i)}$ at the end time.

5. By the given dependencies of temperature moduli, we define new moduli $\mathbf{c}^{E(i+1)} = \mathbf{c}^{E}(\theta^{(i)})$, $\mathbf{e}^{(i+1)} = \mathbf{e}(\theta^{(i)})$, $\boldsymbol{\varepsilon}^{S(i+1)} = \boldsymbol{\varepsilon}^{S}(\theta^{(i)})$.
6. If in the selected norm $\left\|\mathbf{c}^{E(i)} - \mathbf{c}^{E(i+1)}\right\| / \left\|\mathbf{c}^{E(i)}\right\| \le \varepsilon$, $\left\|\mathbf{e}^{(i)} - \mathbf{e}^{(i+1)}\right\| / \left\|\mathbf{e}^{(i)}\right\| \le \varepsilon$, $\left\|\boldsymbol{\varepsilon}^{S(i)} - \varepsilon^{S(i+1)}\right\| / \left\|\boldsymbol{\varepsilon}^{S(i)}\right\| \le \varepsilon$, where ε is given as the relative error, we are completing the iteration process. Otherwise, we assume $i := i+1$, replace $\mathbf{T}_{in}^{(i)}$ by previously found values $\mathbf{T}_{end}^{(i)}$, and proceed to step 2.

Note that in the step 5, the material moduli depend on the space variables $\mathbf{x}$, since according $\theta^{(i)} = \theta^{(i)}(\mathbf{x})$ the interpolation formulae are defined by calculated values of the temperature field $\mathbf{T}_{in}^{(i)}$ at the nodes of the finite element mesh. So we have a set of these moduli separately for each finite element V^{em}.

As we can see, the solution of nonlinear problems of dissipative heating in ANSYS is much more difficult than linear, but nevertheless, advanced command language APDL ANSYS allows us to implement this algorithm.

43.6 Concluding Remark

In present chapter, we have been proposed some models and numerical methods for dynamic behaviors of piezoelectric devices with rotation effect and dissipative heating. The numerical examples, given in [6, 7, 22], show the efficiency of the described technique in addition to standard finite element techniques for the investigations of various vibratory gyroscopes, piezoelectric transformers and devices for which the Coriolis' forces or the temperature effects under dissipative heating are important.

Acknowledgements The first author is grateful to the Russian Scientific Foundation (RSCF), for its support by Project 15-19-10008. The second author is grateful to the Don State Technical University for its support.

References

1. V. Apostolyuk, *Coriolis Vibratory Gyroscopes: Theory and Design, Cham* (Springer International Publ, Switzerland, 2016)
2. A.K. Singh, Defence Sci. J **57**, 95 (2007)
3. Y. Kagawa, T. Tsuchiya, T. Kawashima, IEEE Trans. Ultrason. Ferroelect. Freq. Control **43**, 509 (1996)
4. Y. Kagawa, T. Tsuchiya, T. Sakai, IEEE Trans. Ultrason. Ferroelect. Freq. Control **48**, 180 (2001)
5. A.V. Nasedkin, *Modeling of Piezoelectric Transducers in ANSYS* (SFedU Press, Rostov-on-Don, 2015). (In Russian)
6. A.V. Nasedkin, in *Piezoceramic Materials and Devices*. ed. I.A. Parinov (Nova Science Publ., NY, 2010), p. 177

7. A.V. Nasedkin, E.I. Shprayzer, in *10th HSTAM International Congress on Mechanics. 25–27 May 2013, Chania, Crete, Greece. Congress Proceedings*, Chania, Hellenic Society for Theoretical and Applied Mechanics, Technical University of Crete, paper 192 (2013)
8. Y. Tao, X. Wu, D. Xiao, Y. Wu, H. Cui, X. Xi, B. Zhu, Sensors and Actuators A **168**, 286 (2011)
9. X.S. Wu, W.Y. Chen, Y.P. Lu, Q.J. Xiao, G.Y. Ma, W.P. Zhang, F. Cui, J. Micromech. Microeng **19**, 125008 (2009)
10. E. Ando, Y. Kagawa, IEEE Trans. Ultrason. Ferroelect. Freq. Control **39**, 432 (1992)
11. K. Kanayama. IEEE Ultrason. Symp. 901 (1998)
12. S.S. Rao, M. Sunar, AIAA J **31**, 1280 (1993)
13. Z. Zhang, L. Feng, Y. Sun, Proc. Eng **15**, 752 (2011)
14. V.G. Karnaukhov, *Coupled Thermoviscoelastic Problems* (Naukova Dumka, Kiev, 1982). (In Russian)
15. V.G. Karnaukhov, J. Therm. Stress **28**, 783 (2005)
16. I.F. Kirichok, Int. Appl. Mech **45**, 215 (2009)
17. Z. Gubinyi, C. Batur, A. Sayir, F. Dynys, J. Electroceram **20**, 95 (2008)
18. F. Li, Z. Xu, X. Wei, X. Yao, J. Phys. D Appl. Phys **42**, 095417 (2009)
19. R.G. Sabat, W. Ren, G. Yang, B.K. Mukherjee, in *Proceedings of the SPIE 6170, Smart Structures and Materials 2006: Active Materials: Behavior and Mechanics*, 61700A (2006)
20. S. Sherrit, G. Yang, H.D. Wiederick, B.K. Mukherjee, Proc. SPIE. 121 (1999)
21. P.S. Marinushkin, in *Proceedings of the 2011 IEEE Third School and Seminar on Fundamental Problems of Micro/Nanosystem Technologies* (NSTU, Novosibirsk, 2011), pp. 19–21 (In Russian)
22. A.V. Nasedkin, E.I. Shprayzer. Basic Probl. Radio Electron. Instrum. **15**(4), 57 (2015) (In Russian)

Chapter 44
Hyperspectral Sensor on the Structure "Semiconductors—Thin Films of PLZT"

Leonid V. Grigoryev, Mark A. Mazurov, Oleg V. Shakin and Vechaslav G. Nefedov

Abstract The chapter is devoted to the results of the study structural and photovoltaic properties of the photo resistor that is based on the structure of ferroelectric–semiconductor (dielectric–semiconductor) DP-photo resistor with field effect. Main advantage of photo resistors on the field effect before the bulky photoconductivity photo resistors is the ability to improve the shape of the spectral sensitivity, such as the rise of short-wave part of the spectrum (UV-region) and the extension in the infrared region (IR-region) of the spectral sensitivity. The use of thin-film ferroelectric allows one to dramatically expand the spectral range in the IR region and create a photodetector for hyperspectral range, which work without external cooling.

44.1 Introduction

Radiation receivers (photoelectrical sensor) capable of operating in ultra-high spectral range (hyper-spectral range) are highly required, at the present time, in correspondence with the development, as the Fourier spectroscopy as registration far infrared radiation (FIR) from of terahertz radiation. A possible solution is to create a hyperspectral receiver based on structure of dielectric–semiconductor, such as ferroelectric–semiconductor structure. In turn, the photo resistor detectors on ferroelectric–semiconductor structure favorably with those of other types of radiation detectors by their basic properties: wideband, the value of detectability, low inertia and response work without cooling. Detectability coefficient (D^*) of photo resistor detector at medium radiation modulation frequencies is higher than that of

L.V. Grigoryev (✉) · M.A. Mazurov
ITMO University, 49, Kronversky Pr., Sant-Petersburg
197101, Russia
e-mail: grigoryev@oi.ifmo.ru

O.V. Shakin · V.G. Nefedov
Sant-Petersburg State University of Aerospase Instrumentation,
67, Bolshaya Morskaya Str., Sant-Peterburg 190000, Russia

I.A. Parinov et al. (eds.), *Advanced Materials*, Springer Proceedings
in Physics 193, DOI 10.1007/978-3-319-56062-5_44

the bolometer or thermocouple transmitter and practically equal detectability of photoacoustic receiver. At low and high modulation frequencies, D^* of this detector is far above the detectability of other types of thermal radiation detectors, approaching the terahertz region for the detectability of photon detectors. Radiation receivers, whose area for receiving incident light is made of a ferroelectric, can operate in the range from UV radiation to radiation with a wavelength of 200 μm [1, 2]. In this case, the speed sensor in the registration of a single pulse is limited to the value of units and shares ns [3], which is close to the theoretical limit for this constructive scheme. To increase speed and enhance detectability, hyperspectral receiver must pass from the capacitor circuit to the construction of the sensor according to the scheme of the photoelectric device on structure of dielectric–semiconductors with field-effect detector (FED) [3]. Articles [4, 5] show the possibility of constructing photo detectors from FED scheme.

In the present chapter, we presents the results of a study of the optical and photoelectrical characteristics of a high-sensitive receiver in hyperspectral region, created by the scheme field-effect photo resistor, based on the structure of ferroelectric–semiconductor (ZnO–PLZT).

44.2 Mathematical Formulation of the Problem

Let us consider the thin-film structure of the semiconductor–dielectric (SD), which uses dielectric layer as a thin-layer ferroelectric. We confine ourselves to homogeneous in volume and on surface the semiconductor layer and ferroelectric layer. Let χ is the affinity energy: the amount of energy that must be imparted to an electron to transfer it to the state corresponds to the conduction band of ferroelectric. Energy affinity in the semiconductor and ferroelectric is different. The condition of thermodynamic balance of the electrons in the SD system consists in equality of chemical potentials in all parts of the system, i.e. the existence of a common Fermi level. To find the distributions of electric field $E(x)$, and electron density $n(x)$, we solve the equations set of the electrical conductivity, diffusion and Poisson's equation:

$$\begin{aligned} j &= e\mu n(x)E(x) - eD_0\frac{dn(x)}{dx}; \\ D_0 &= kT\mu; \\ \frac{dD(x)}{dx} &= -4\pi e n(x). \end{aligned} \tag{44.1}$$

For ferroelectrics, the relationship between electric field E and induction D is not linear and can be described for the case of a ferroelectric, which has phase transition of the second kind by the relation:

$$\begin{aligned} D &= E + 4\pi P_{sp} + 4\pi P_{ind} = \varepsilon_{eff} E + 4\pi P_{sp}; \\ \varepsilon_{eff} &= 1 + 4\pi\chi_{eff}; \quad \chi_{eff} = \frac{1}{\left(\beta + 3\zeta P_{sp}^2 + 4\zeta P_{sp}^4\right)}. \end{aligned} \tag{44.2}$$

Since the spontaneous polarization P_{sp} does not depend on the coordinates, then the Poisson equation can be written as

$$\frac{dE(x)}{dx} = -\frac{4\pi e n(x)}{\varepsilon_0 \varepsilon_{eff}}. \tag{44.3}$$

Near surface to a ferroelectric layer, a semiconductor forms the space charge region (SCR) in which increase of conductivity is observed. The concentration of charge carriers in the SCR can be expressed as follows:

$$\rho_s = -\frac{\varepsilon_0 \varepsilon_{semi} E^2(x)}{2kT} \frac{1}{\left[\frac{eE(x)x}{2kT} + 1\right]^2}; \tag{44.4}$$

In the case of low-intensity radiation incident on the semiconductor layer, which is usually observed in the opto-electronic device spectroscopy, the total photoconductivity σ_{sum} of semiconductor layer can be represented as the sum of the photoconductivity in the surface region σ_{surf} (surface photoconductivity) and photoconductivity in the volume of semiconductor σ_{bulk}:

$$\sigma_{sum} = \sigma_{surf} + \sigma_{bulk}; \tag{44.5}$$

By decreasing the depth of the absorption of light and decreasing the length of incident light, the value of volume photoconductivity can only decreases. Photoconductivity in near-surface region increases with increasing light absorption coefficient α, which can be explained by the growth of the quantity of non-equilibrium charge carrier, breeding them apart and weakening gradient of their concentration in the SCR. Growth of photoconductivity in SCR allows one to create a mode of photovoltaic device, in which the contribution of surface photoconductivity σ_{surf} is dominant. This fact allows us to achieve a significant increase in photosensitivity in the ultraviolet region of the spectrum (UV) for ZnO and to control the spectral characteristics of photoconductivity by varying the value of potential in the SCR in the visible and infrared regions of spectrum.

44.3 Experimental Results and Discussion

ZnO thin films were prepared by reactive ion-plasma sputtering of a metal target. The process of ion-plasma sputtering target was carried out by a magnetron sputtering, operating in constant current mode. Synthesis of ZnO thin film was performed in a gas atmosphere, consisting of 20% O_2 and 80% Ar_2. The pressure of the gas mixture in the reactor did not exceed 3.10 mm Hg Art., the substrate temperature does not exceed 453 °C. The magnetron metal target was made of Zn grade high purity. The thickness of the zinc oxide film according to the microscopic studies was 1.0 μm.

Thin layers of ferroelectric PLZT were obtained by the method of electron-beam evaporation of target from ceramic ferroelectric. The evaporation of ferroelectric ceramic target was carried out in a pulse mode electron beam gun at frequency of 100 Hz. As a substrate for the deposition of the ferroelectric layer, we used polished discs of quartz brand KU of 3 mm thick. The thickness of the ferroelectric layer according to optical microscopy was 7 microns.

Formation of aluminum electrodes for the photo resistor structure was carried out by a magnetron sputtering.

Sample ZnO–PLZT structures (Fig. 44.1), in which a layer ZnO, was synthesized on a pre-heated to temperature 420 K substrate in further will be referred as "Sample 1", and the sample ZnO–PLZT structures, in which a layer ZnO, was synthesized on a substrate without heating hereinafter will be referred as "Sample 2".

The study of the structural properties of ZnO films was carried out by X-ray diffraction using an automated X-ray diffractometer DRON-3M. X-Ray diffractometer uses radiation Fe–Ka. To obtain stable characteristics of X-ray radiation, influence value anode voltage on anode tube was chosen equal 25 kV. In order to discharge from the output X-ray spectrum of the line Fe–Kα, preliminary the

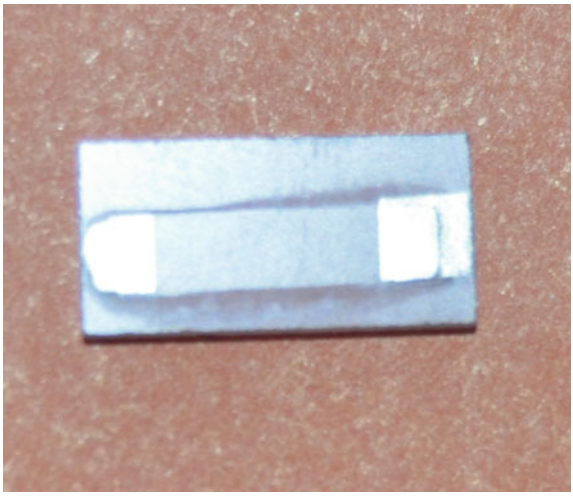

Fig. 44.1 Field-effect photoresistor from ZnO–PLZT structure

sample was placed selectively in β-absorbing filter. The measurement was conducted in the range of Bragg angle 2θ from 20º to 80º with increments $\Delta 2\theta = 0.05º$. Time pulses accumulation at the measurement point was 10 s. X-ray plots of zinc oxide films, synthesized by the method of ion plasma sputtering, are shown in Figs. 44.2 and 44.3. Figure 44.2 shows the diffraction pattern of the film, synthesized on the substrate, preheated to 420 K.

Figure 44.3 shows a X-ray plot of ZnO film, synthesized without preheating substrate.

According to X-ray analysis, both types of film have synthesized polycrystalline structure. The diffraction patterns present diffraction peak of great intensity, characteristic of hexagonal ZnO (002). It can be stated presence of the synthesized film with high structural quality and availability of dedicated texture axis in the direction of *c*-axis perpendicular to the substrate surface. Due to, increasing the temperature of the substrate in the synthesis of ZnO films led to a shift of the diffraction peaks at the same value towards lower angles (Figs. 44.2 and 44.3) and changed the intensity of the diffraction peaks responsible for the direction (100) and (002). This can be explained from the standpoint of increasing the interplanar spacing due to elastic tensile stresses in ZnO layer. In the synthesis of ZnO films on a preheated substrate, we observed a decreasing in the crystallite sizes from 20 to 11 nm. Dimensions polycrystalline grains of ZnO in the film, synthesized on the substrate, preheated to 453 K, were calculated by the formula Scherrer-Selyakova and did not exceed 11 nm. By comparing the positions of diffraction peaks in X-ray patterns for films, synthesized at the hot and cold substrates, diffraction patterns showed a shift

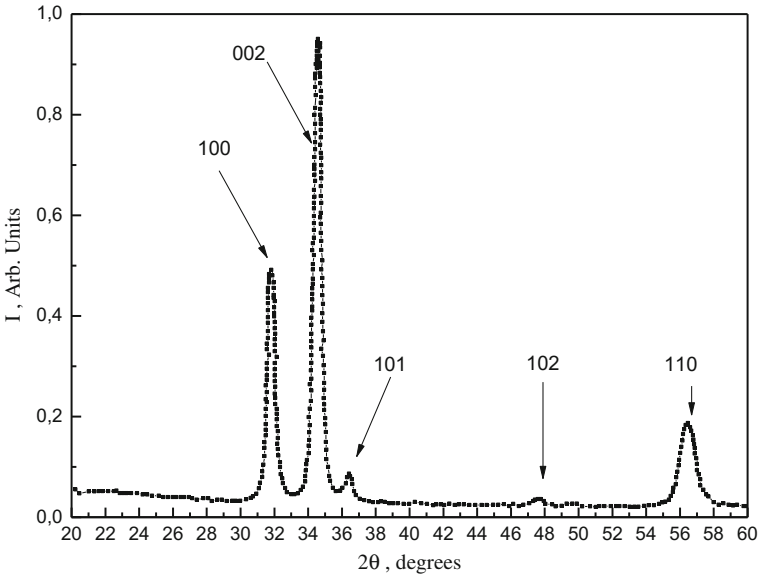

Fig. 44.2 X-ray plot of ZnO film, synthesized on the substrate, preheated to 420 K

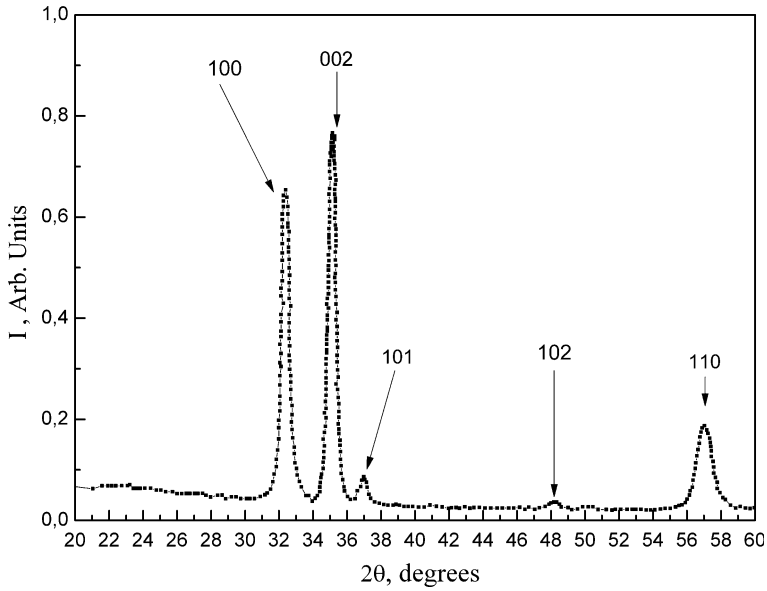

Fig. 44.3 X-ray plot of ZnO film, synthesized without preheating substrate

towards lower angles in the X-ray pattern for the film on a preheated substrate. Furthermore, it is seen that the intensity peak responsible for diffraction in the direction (002) decreased with respect to the same intensity of the peak corresponding to the diffraction pattern of the film synthesized on the preheated substrate. The intensity of the peaks (101) on the X-ray diffraction pattern, corresponding to the synthesized film on a cold substrate, on the other hand was greater compared with an intensity similar to the case of lines for film, synthesized on a hot substrate. We compared the published data on the behavior of X-ray diffraction patterns for ZnO films, synthesized by high frequency (RF) magnetron sputtering with target of ZnO [8], with the results of X-ray analysis. The corresponding films of zinc oxide, synthesized by the ion-plasma method on the hot and cold substrates showed correlated behavior of diffractograms in both cases. Moreover, we conducted the joint analysis of the X-ray diffraction pattern of the synthesized film of zinc oxide by the ion-plasma technology in an environment of a strong oxidant (plasma O_2 + Ar_2) and the X-ray diffraction pattern in the case of RF magnetron sputtering of ZnO. It shows no diffraction maxima (100) (101) (102) (110) on the X-Ray diffraction patterns of samples, prepared by RF magnetron sputtering from a zinc oxide. Minimum sizes of the polycrystalline zinc oxide films synthesized by both technologies, practically the same.

To determine the width of the forbidden zone of ZnO, transmission spectra and reflection spectra were studied in the wavelength range from 300 to 1000 nm. The spectra were obtained on a spectrophotometer Perken Elmer Lambda 25. The transmission spectra of ZnO films are shown in Fig. 44.4.

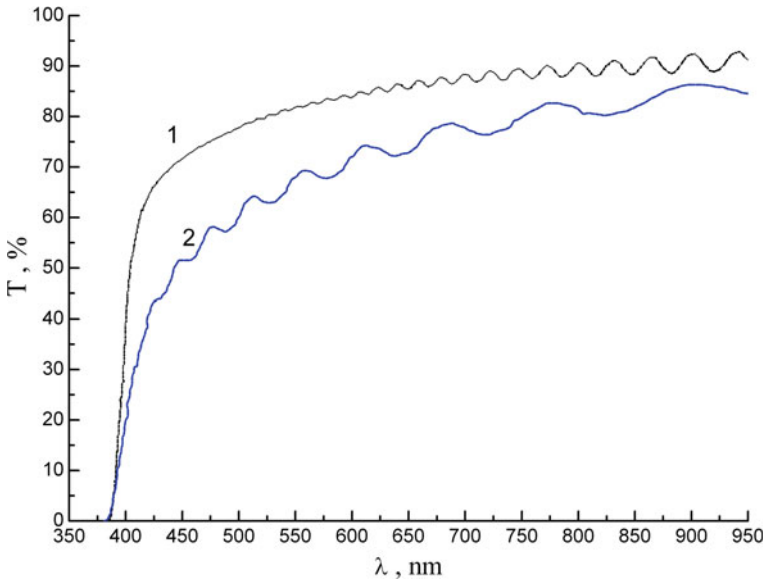

Fig. 44.4 Transmission spectra of ZnO films: *1* transmission spectra for sample 1; *2* transmission spectra for sample 2

The figure shows that in the wavelength range of 400–800 nm, transmission coefficient (T) changes in the range from 50 to 94%. In Fig. 44.4, there are oscillations of the transmission coefficient due to availability of interference effects in thin-film semiconductor. In the spectral region, where the effect of interference of light in thin films can be ignored, values of the transmission coefficient, absorption coefficient and refractive index may be calculated by the following formula:

$$T_0 = (1-R)^2\left[1+(\lambda\alpha/4\pi n)^2\right]/\left(\exp(\alpha d)-R^2\exp(-\alpha d)\right) \tag{44.6}$$

In the spectrum region, where there is clearly expressed the effect of interference of light in thin films, the transmission coefficient may be determined as

$$T = \left(1-R^2\right)/\left(1+R_{12}^2-2R_{12}\cos(4\pi nd/\lambda)\right), \tag{44.7}$$

where $R_{12} = [(n-1)/(n+1)]^2$.

The transmission spectrum has maxima at the following wavelengths:

$$\lambda_{\max} = 4nd/m,\ m = 2,4,6,\ldots. \tag{44.8}$$

The transmission spectrum has minima at the following wavelengths:

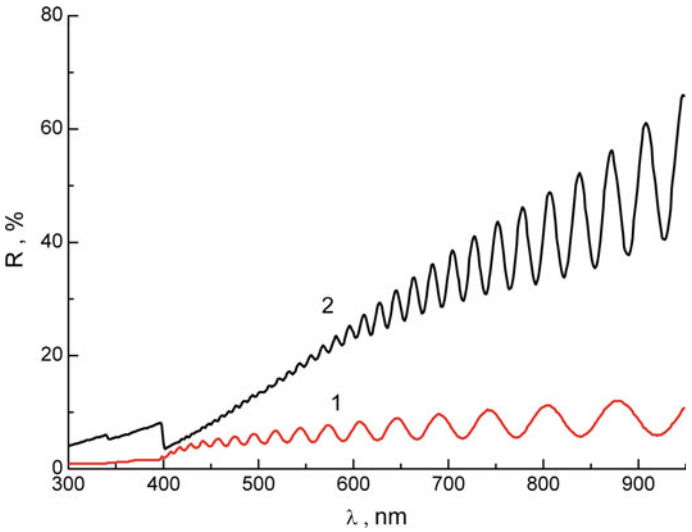

Fig. 44.5 Reflection spectra of ZnO films: *1* reflection spectrum for sample 1; *2* reflection spectrum for sample 2

$$\lambda_{\min} = 4nd/k,\ k = 1, 3, 5, \ldots. \tag{44.9}$$

From formulae (44.8) and (44.9), it is possible to derive the following expression for determining the refractive index of thin film:

$$n = (\lambda_m \lambda_{m-1}/(2d(\lambda_{m-1} - \lambda_m)). \tag{44.10}$$

From formula (44.6) and ratio $R = (1 - T)$, and taking into account formulae (44.7) and (44.8), the transmission coefficient can be expressed by the ratio of minimum to maximum value:

$$T_0^2 = T_{\min}/T_{\max} = 2n/(n^2 + 1). \tag{44.11}$$

Thus, by analyzing the transmission and reflection spectra of ZnO films, the refractive indexes of the experimental samples were determined for sample 1 (n = 2.38) and sample 2 (n = 2.33). The refractive index of sample 1 has close value of refractive index for ZnO films, synthesized by the method of reactive magnetron sputtering [8].

The reflection spectra of two samples of ZnO thin films, prepared by ion-plasma sputtering of a metal target in a gas oxidant environment, are shown in Fig. 44.5.

In reflection spectra of ZnO thin films, we also observed oscillations due to the effect of interference of light in thin films.

The reflection spectra have the maximum condition, defined as

$$\lambda_{\max} = 4nd/m, m = 1, 3, 5, \ldots, .$$

The reflection spectra have the minimum condition, defined as

$$\lambda_{\min} = 4nd/k, k = 2, 4, 6, \ldots.$$

Based on the numerical solution of (44.6) and (44.7), it was obtained the spectral characteristic of the absorption coefficient of thin films of ZnO. It then translated to the dependence of the absorption coefficient on the energy of the incident light. The value of optical band gap E_g for samples 1 and samples 2 were obtained by linear interpolation on the numerical axis and were equal to 3.28 and 3.25 eV for samples 1 and 2, respectively. The optical band gap of the sample 1 of the ZnO thin-film nanostructures most closely matches band gap in single crystal of ZnO and is equal to 3.3 eV.

In subsequent investigations of the photoelectric properties of ZnO–PLZT structure, we used the Sample 1, in which the ZnO-layer was deposited on the preheated substrate. The selection of this type of sample is due to the optical properties of the ZnO-film are similar to the properties of ZnO single crystal.

Investigation of the spectral dependence of the photoelectric current, flowing through the semiconductor layer in the photo resistor structure, carried out in the experimental facility, presented in [6, 7]. Figure 44.6 shows the spectral dependence of the photoelectric current, flowing through the photo resistor structure in the UV-range.

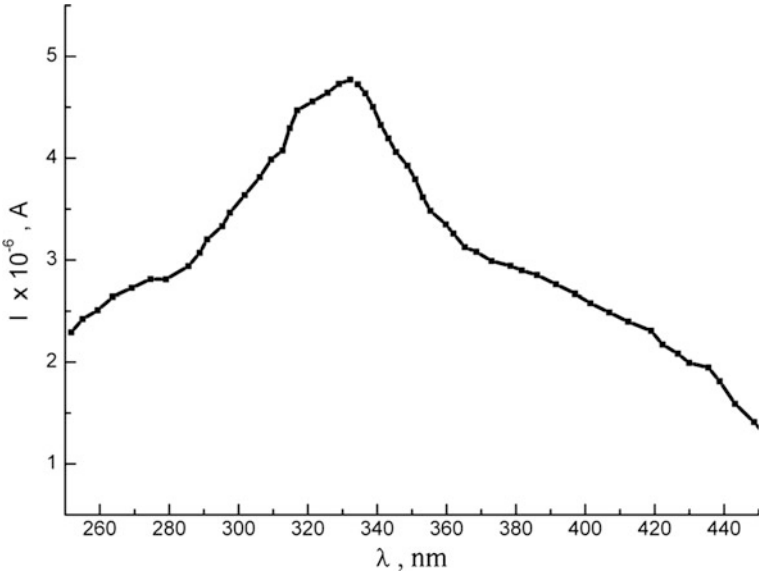

Fig. 44.6 Photoelectric current in photo resistor structure in the UV-range

Figure 44.6 indicates the spectral band of the highest spectral sensitivity in the range from 290 to 350 nm with a maximum (peak) located at 330 nm. According to above research of the ZnO thin film with optical band gap equal to 3.28 eV, the maximum spectral sensitivity should be at 370 nm. Shift of the spectral sensitivity maximum in the area of short-wave radiation can be explained by the combined effect of resonance absorption of UV radiation in the volume of the thin film of semiconductor and on the surface of ferroelectric. Moreover, it is caused by increasing contribution of the surface photoconductivity of ZnO at the interface region "semiconductor–ferroelectric". Falling UV radiation on the interface ferroelectric-semiconductors changes the electrical field in the space charge region, which leads to increased sensitivity of the photo resistor in the UV range and shift of spectral sensitivity to shorter wavelengths of the UV spectrum.

Figure 44.7 shows the spectral dependence of the photoelectric current in the visible and infrared range. In this range of lengths of waves, the ZnO thin film has a practically flat transmittance characteristic and all the falling radiation is absorbed in the surface region of the semiconductor near interface "semiconductor–ferroelectric".

Figure 44.8 shows the spectral dependence of the detectability coefficient of the photodetector in the range from 260 nm to 24 μm.

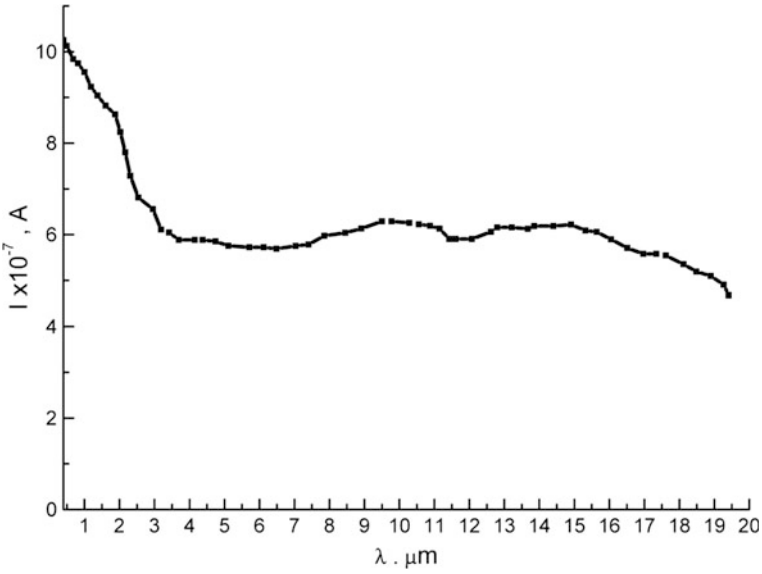

Fig. 44.7 Photoelectric current in photo resistor structure in the visible and IR range

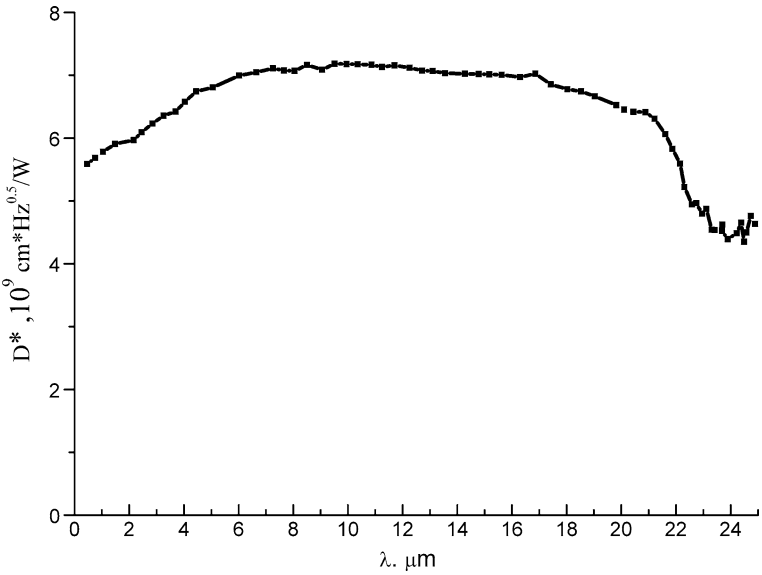

Fig. 44.8 Spectral dependence of detectability coefficient D^* for ZnO–PLZT photodetector structure

44.4 Conclusion

It is shown the possibility of creating hyperspectral photodetector on the structure of ZnO–PLZT capable to operate from solar-blind UV spectral range to the far infrared range. The shift of the spectral sensitivity of the photodetector structure in the solar-blind range is due to the contribution of photoconductivity space region charges, located in the surface region of the ZnO semiconductor near the interface of the semiconductor–ferroelectric. The value of detectability coefficient D^* of the photodetector on the ZnO–PLZT structure in hyperspectral range is comparable with the detectability coefficient D^* of a silicon photodiode at visible range. The photodetector structure of ZnO–PLZT can be integrated photodetector in a "system on a chip", created on a planar silicon technology.

Acknowledgements This work has been supported by the Ministry of Education and Science of Russian Federation (Project No. RFMEFI58114X0006).

References

1. M. Okyama, Ferroelectrics **33**(1–4), 235 (1981)
2. R.A. Valitov et al., *Technique of Submillimeter Waves* (Moscow, Soviet Radio, 1969). (In Russian)
3. V.A. Zuev, V.G. Popov, *Photoelectrical MIS-devices* (Radio and Communications, Moscow, 1983). (In Russian)
4. R.L. Abrams, O.R. Woods, Appl. Phys. Lett **19**(12), 518 (1971)
5. N.R. Agamalyan, T.A. Aslanyan, E.S. Vardyanyan, et al. Proc. NAS of Armenia Phys. **48**(2), 136 (2013)
6. L.V. Grigor'ev, V.G. Nefedov, O.V. Shakin, A.V. Mikhailov, E.N. Eliseev, J. Opt. Technol **82** (5), 315 (2015)
7. L.V. Grigor'ev, S.S. Rybin, V.G. Nefedov, O.V. Shakin, A.V. Mikhailov, E.N. Eliseev, J. Opt. Technol **82**(9), 634 (2015)
8. V.A. Krivchenko, D.V. Lopaev, V.G. Pashenko, J. Tech. Phys **28**(78), 107 (2008)

Chapter 45
Ultrasound Image Formation from Doppler Transducer

Fajar Astuti Hermawati, Sugiono and Evonda

Abstract This research aims to determine image formation of the radio frequency (RF) signal obtained from a Doppler transducer. Radio Frequency (RF) signal is the result of reflection (echo) of the ultrasonic waves when transmitted on a particular tissue or organ. Echo of the wave is then detected by the transducer, which converts the waves into electronic acoustic signals to be processed and reconstructed into an image. A shift in frequency when the affected surface ultrasound beam moves is the base of the Doppler ultrasonography. Doppler is an ultrasound probe that price is quite affordable. RFsignal from the Doppler transducer is processed in several stages. These stages are bandpass filtering, envelope detection and logarithmic compression. From the experiments, this system can form a B-mode image and the image harmonic of the RFsignal obtained from the Doppler transducer. The bandwidth value, used in the Gaussian filtering process, has an influence on the intensity value of the ultrasound image is produced. The smaller the value of the bandwidth, the better the resulting ultrasound image. The best bandwidth value that used in this study is 5. The total time required to form an ultrasound image in the seven times scanning is 87.16 s. The average time in one scanning is about 11.94 s.

45.1 Introduction

Ultrasonography (USG) is a diagnostic tool that provides images of organs and structures, noninvasively, which has advantages with much cheaper price, easy to move (portable), small and easily manipulated, and non-ionizing, as compared with other modalities such as CT scans and MRI [1–3]. Ultrasound procedures are part of routine prenatal care and provide an essential information required a physician or the midwife to offer optimal care. The ultrasound allows the physician or midwife to ensure normal development and also provides a diagnosis of possible problems

F.A. Hermawati (✉) · Sugiono · Evonda
Department of Informatics Engineering,
University 17 Agustus 1945 Surabaya, Surabaya, Indonesia
e-mail: fajarastuti@untag-sby.ac.id

I.A. Parinov et al. (eds.), *Advanced Materials*, Springer Proceedings
in Physics 193, DOI 10.1007/978-3-319-56062-5_45

to be faced. Because there are no risks to pregnant women and fetal development, there is no reason not to use ultrasound test. Ultrasound has been developed to form three-dimensional and even four-dimensional image. Because of the high mobility requirements, according to Baran and Webster [4], further research developed a portable ultrasound, including Oralkan et al. [5] offered a phased array pulse-echo image of the sector B-scan using the 128 CMUT element in 1D array transducer. Yet, the price is still relatively affordable in developing countries such as Indonesia.

Acoustic waves with a frequency from about 20 kHz to several hundred MHz that cannot be detected by the human ear is defined as ultrasound. Ultrasound for medical imaging applications typically only uses part of the spectrum of ultrasound from 1 to 15 MHz due to the combined requirements of a good resolution (small wavelength) and the penetration ability was good (not too high frequencies). It is produced by changing radio frequency (RF) electrical signals into mechanical vibrations through the transducer [6]. Radio frequency signal is the result of reflection (echo) of the ultrasonic waves when transmitted to a particular tissue or organ. Echo of the wave is then detected by the transducer, which converts the waves into electronic acoustic signals to be processed and reconstructed into an image. The reflection echo originating from these tissues hit the transducer, and then converted into electric pulses and then amplified and further shown in the form of light on the oscilloscope screen. Thus when the transducer is moved as if doing slices on a desired part of the body, and the description of these sections is illustrated on the monitor screen. The resulting image of the ultrasound is utilizing the reflected (echo) of the ultrasonic waves when transmitted to a particular tissue or organ. Echo of the wave is then detected by the transducer, which converts acoustic waves into electronic signals to be processed and reconstructed into an image [6].

To increase the resolution of the image significantly, there are two imaging techniques, that are tissue harmonic imaging and spatial compound imaging [7]. The harmonic imaging technique used to treat imaging the body wall is thick and complex, where this technique has the advantage capable of reducing artifacts and noise that occurs near the surface of the tissue. The spatial compound imaging technique uses multiple beams on the same tissue that causes it needs more time for data acquisition and reduce the frame rate imaging compound. Compound imaging techniques can also reduce the level of noise along with increased contrast and margin definition.

The base of the Doppler ultrasonography is a shift frequency when there is the movement of a surface ultrasound beam. The occurrence of surface movement information is given by the magnitude and direction of the shift [8]. In Doppler ultrasonography, ultrasound waves are transmitted with a certain frequency that is called with the source frequency form at a certain angle to the blood vessels. Because of the movement of the blood vessels, then the frequency of the transmitted back that is termed the reflector frequency has different values. This frequency difference is named the Doppler shift, which was first studied by Christian A. Doppler, an Austrian physicist, in 1800 [8].

This research aims to determine the ultrasound image formation of the RF signal obtained from a Doppler ultrasound. As known, Doppler is an ultrasound probe that has a quite affordable price. Thus, a medical ultrasound system is produced at low cost.

45.2 Method

45.2.1 Data Acquisition

In this study, the RF signal was obtained in real time from a Doppler ultrasound with the characteristics as presented in Table 45.1.

To acquire the RF signal from the Doppler probe, the probe is connected to a computer with an audio cable, as seen in Fig. 45.1. For our evaluation, we used hardware and software such as 3 MHz Doppler, an audio cable, a computer with the Windows XP operating system, the Conexant HD audio sound card, and the Windows Sound Recorder.

45.2.2 Ultrasound Image Formation

The 2D ultrasound image is formed by a large number sequence of the pulse echo that is generated by ultrasound. The echo pulses are produced by the Doppler ultrasonography which is expressed as the Radio Frequency signal. One pulse-echo resulted in one line of gray scale in the ultrasound image. An ultrasound image is arranged in 100 or more gray scale lines

Echoes are captured by the transducer elements forming an echo signal. The function of the echo signal is processed per element by applying apodosis function, focusing dynamically, and mix-down processing to reduce the time of image formation. Knowledge of the speed of sound alleviates for estimating the speed of sound in a medium that affects the sharpness of the image produced. The steps in the ultrasound image forming are described in Fig. 45.2, as follows [9]:

1. Each RF signal is processed and cut by only taking part of signal has a high magnitude that visually provides a sharper gray scale value. The purpose of these cuts is to reduce the computation time.
2. In the bandpass filtering, RF input signal is filtered using a Gaussian filter in the frequency domain to reduce noise. According to He [10], the Gaussian filter is

Table 45.1 Doppler ultrasound characteristics

Variable	Value
Nominal frequency	2.0 MHz
Working frequency	2.0 MHz ± 10%
Peak-negative acoustic pressure (P^{-})	<0.5 MPa
Output beam intensity (Iob)	<10 mW/cm^2
Spatial peak temporal average intensity (Ispta)	<50 mW/cm^2
Ultrasonic output intensity	Ispta < 5 mW/cm^2
Working mode	Continuous wave Doppler
Effective radiating area of transducer	208 mm^2 ± 15%

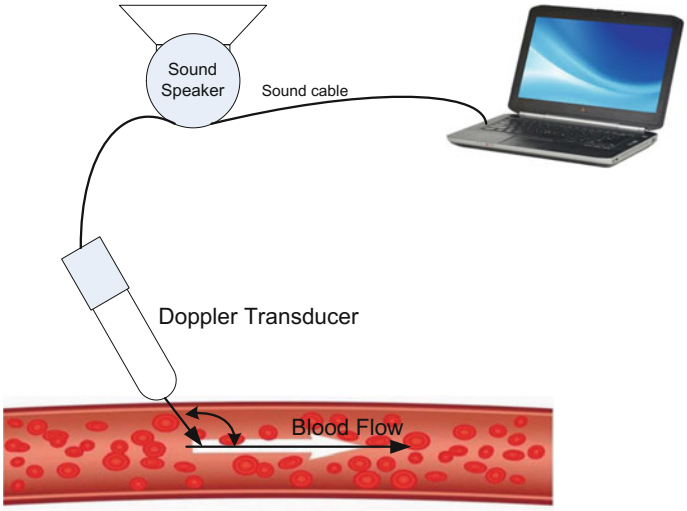

Fig. 45.1 Diagram of data acquisition

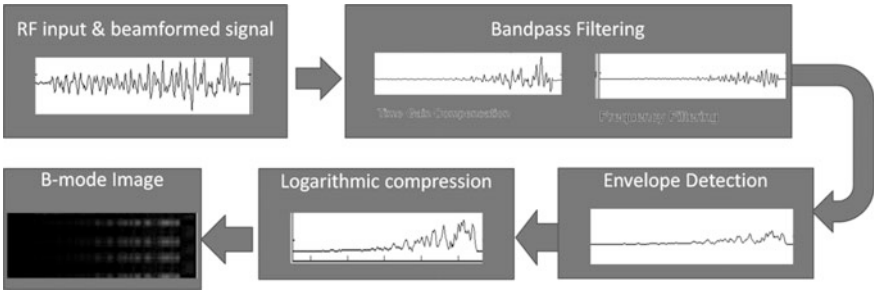

Fig. 45.2 Steps of the ultrasound image formation

best used to minimize the reconstruction error. Time gain compensation is applied before the filtering to amplify the signal. The signal amplitude is attenuated when travels through the tissue. The signal is amplified, based on the depth and the time; it takes the signal to return. Gaussian filter function, $G(x)$, used in the bandpass filter, is described as

$$G(x) = Me^{-\left(\frac{(x-f_c)^2}{2*\sigma}\right)}, \quad x = 1, 2, \ldots, n \tag{45.1}$$

where M is a magnitude and in this experiment, M = 1; n is the length of the signal x; f_c is filter center frequency that set by 1.5×10^6; σ is variance that is defined as

$$\sigma = \left(\frac{\frac{W_f}{100} f_c}{2\sqrt{2log2}} \right)^2 \tag{45.2}$$

where W_f is a bandwidth.

3. Rf signal from bandpass filtering is processed with envelope detection to get the weak positive (negative discarded) peak signals. The imaging process on this condition results a black and white image, which the image of the object being imaged become more visible, but not so obvious. The envelope signal is obtained by Hilbert transform.
4. The peak signals as the result of the envelope detection is boosted by using logarithmic compression. The imaging process on this step performs more real and vivid a visual on ultrasound.

45.3 Results and Discussion

To implement our approach, we used Matlab R2013 software. The experimental ultrasound image formation of the RF signal, obtained from Doppler transducer, is done by shifting as much as seven times, then for each time the movement is performed by recording RF signals. An example of RF signals for one recording can be seen in Fig. 45.3. For some parameters in our experiment, it can be seen in Table 45.2. Step-time, *dt*, is selected based on reference sound speed, and the number of time-step that is selected based on the time, where it takes several travels from determined one corner of the grid to the geometric opposite corner.

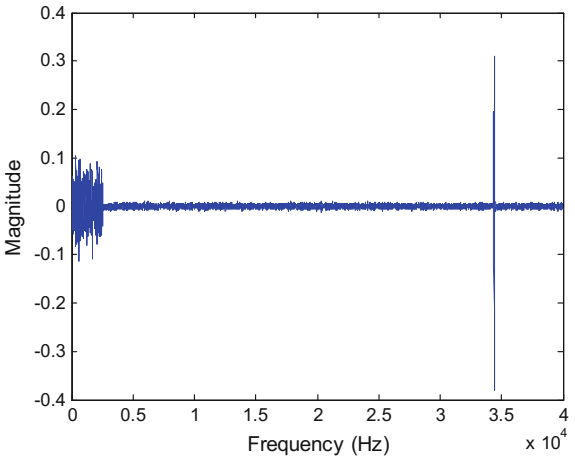

Fig. 45.3 Sample of RF signal from Doppler transducer

Table 45.2 Simulation parameters

Variable	Value
Reference sound speed	1540 m/s
dt	36.075 ns
t_{end}	57.1429 μs
Time steps	1585
Input grid size	216 × 108 grid points (40 × 20 mm)
Maximum supported frequency	4.158 MHz

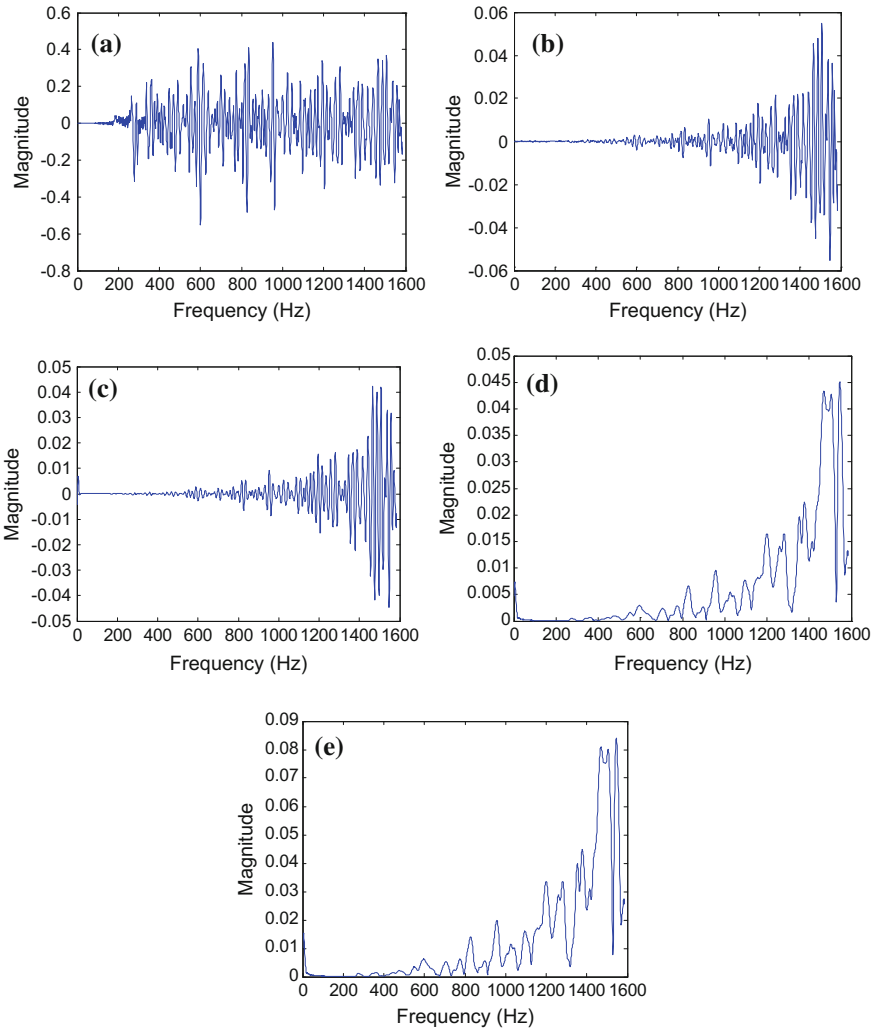

Fig. 45.4 Ultrasound image formation at a line scanning: **a** beam formed signal, **b** time gain compensation, **c** bandpass filtering, **d** envelope detection, **e** logaritmic compression

Beam formed signal is an RF signal received and reduced to 1280, as seen in Fig. 45.4a. Images, obtained from the RF signal, are subsequently filtered. In the first time, the RF signal is processed by time gain compensation. To remove the noise, it is applied a frequency filtering using transmit frequency and the second harmonic of the Gaussian filter. Figure 45.4b, c show the result of the time gain compensation process and bandpass filtering process. After the filtering process, it is continued with the frequency envelope detection process, to flatten the frequency signal generated, as seen in Fig. 45.4d. Furthermore, the logarithmic compression process, shown in Fig. 45.4e, is applied to normalize the signals generated by the compression ratio equal to 3.

The next process is to perform a linear interpolation process to enlarge the size of the sampling so that the image can be seen. The b-mode image produced can be seen in Fig. 45.5a, and the harmonic image can be seen in Fig. 45.5b. The harmonic image obtained from the same RF signal with the filter center frequency value on the Gaussian filtering process is two times of the value used in the B-mode image.

The first experiment determines the effect of changes in bandwidth of the Gaussian filter in the ultrasound image formation and get the best bandwidth value for RF signal obtained from the Doppler transducer. The values of the bandwidth W_f, used in these experiments were 30, 10 and 5. In Fig. 45.6, we can conclude that the smaller the value of the bandwidth, the more smooth signals generated. As well as the impact of the value of bandwidth used in Gaussian filtering in ultrasound

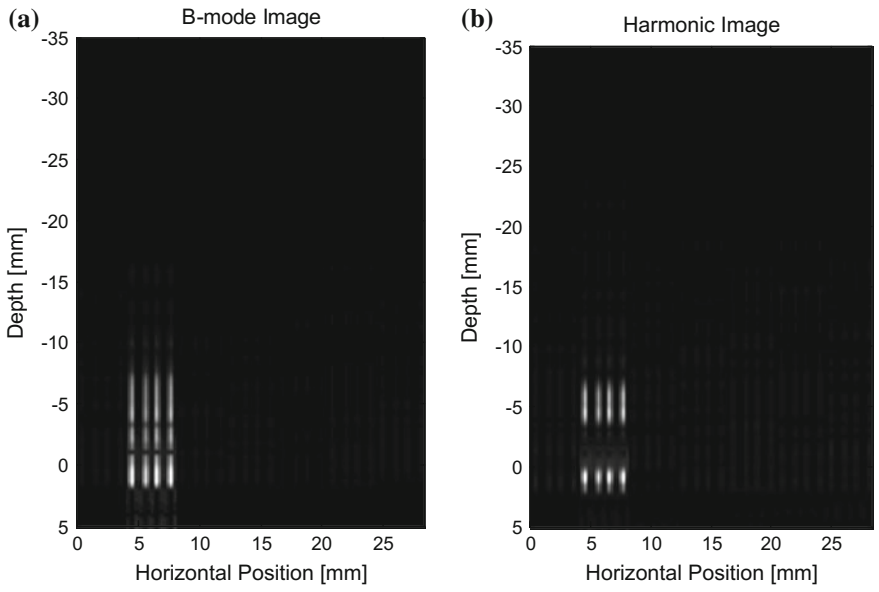

Fig. 45.5 Ultrasound image in b-mode and harmonic

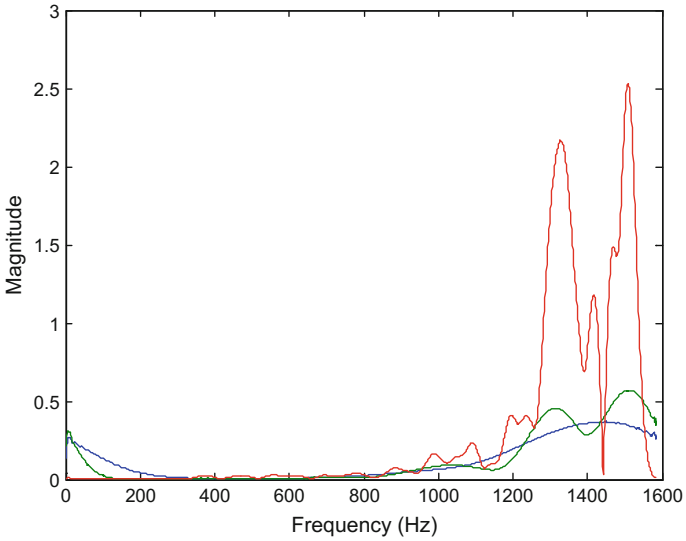

Fig. 45.6 Envelope detection signal with the different bandwidth value of Gaussian filter, $W_f = 30$ (*red line*), $W_f = 10$ (*green line*), $W_f = 5$ (*blue line*)

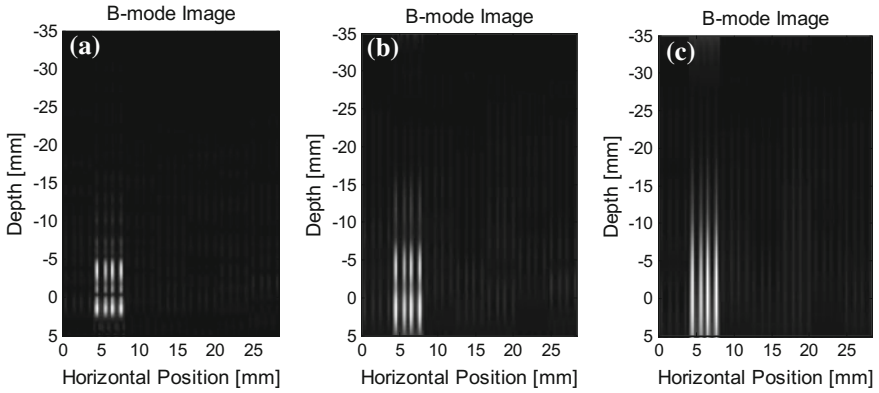

Fig. 45.7 Ultrasound image with the different bandwidth value of Gaussian filter, **a** $W_f = 30$, **b** $W_f = 10$, **c** $W_f = 5$

images produced can be seen in Fig. 45.7, in which the ultrasound image with bandwidth, $W_f = 5$, looks better visually.

The next experiment aims to determine the computational time required to generate ultrasound images in real time. The time required for the formation of an ultrasound image with the seven-time real time scanning can be seen in Table 45.3. The total time was 87.16 s. The time is long enough for seven scanning.

Table 45.3 Computing time in the ultrasound image formation

Scanning	Computation time (s)
Scan 1	15.64
Scan 2	11.031
Scan 3	11.016
Scan 4	11.18
Scan 5	11.641
Scan 6	11.152
Scan 7	11.11

45.4 Conclusion

From the experiments, it is known that B-mode ultrasound image can be formed from the RF signal obtained from the Doppler transducer device. The bandwidth value, used in the Gaussian filter process, has an influence on the intensity value of the ultrasound image produced. The smaller the value of the bandwidth, the better the resulting ultrasound image. The total time required to form an ultrasound image in the seven times scanning is 87.16 s. The average at one time scanning is about 11.94 s. For the next research, it needs to be tested by using the RF signal obtained from the convex transducer probe.

Acknowledgements Authors thank profusely The Directorate General of The Higher Education Department of Education, which has financed the program through the Letter of Agreement Implementation Research: 429.10/ST/003/LPPM/Lit/IV/2016, Date: 29 April 2016.

References

1. H.K. Gondo, T.G.A. Suwardewa, *The Publisher of Medical Books*, EGC (2012)
2. S.H.C. Ortiz, T. Chiu, M.D. Fox, Biomed. Signal Process. Control **7**, 419 (2012)
3. Y. Chen, X.M. Zhou, D.C. Liu, TELKOMNIKA **11**(4), 791 (2013)
4. J. Baran, J.G. dan Webste, in *31st Annual IEEE EMBC Conference* (2009)
5. O. Oralkan, et al. lEEE Trans Ultrason. Ferroelectr. Freq. Control. **50**(11) (2003)
6. M.S. Chaitra, et al. Int. J. Pharmacol. Pharm. Technol. (IJPPT) **1**(2) (2012)
7. V. Chan, A. Perlas, in *Atlas of Ultrasound-Guided Procedures in Interventional Pain Management* (2012)
8. D.H. Evans, Wiley, Chichester (1989)
9. S. Imardi, in *Development and Software InteRFace Function Enrichment for Ultrasound Image Visualization and Analysis*, Thesis in Jurusan Teknik Elektro Universitas Indonesia (2010) (in Indonesian)
10. P. He, *IEEE Trans. Ultra. Ferro. Freq. Contr.* **45**(1) (1998)

Chapter 46
New Methods of Complex Therapeutic Treatment and Accelerated Regeneration of Superficial Tissues of a Patient

I.A. Shvetsov, N.A. Shvetsova, A.N. Reznitchenko and A.N. Rybyanets

Abstract Development of the new therapeutic technologies and drags, accelerating natural regenerative processes in an organism, is one of the priority directions of development of modern recovery, regenerative and adaptation medicine in the developed countries. New methods and apparatus for ultrasonic therapeutic treatment, diagnostics and body aesthetics as well as a new application fields based on the advances in piezoelectric materials and ultrasonic transducer designing, visualization technologies and physical acoustics have appeared during a past decades. The Chapter reviews novel methods of ultrasonic diagnostics, complex therapeutic treatment and accelerated regeneration of superficial tissues of a patient. The methods are based on synergetic combination of different factors such as ultrasonic shear and standing waves impact, radio-frequency heating (RF), vacuum massage, as well as ultrasonically assisted drags delivery. Technological peculiarities of the ultrasonic transducer design as well as theoretical and numerical models of such transducers and corresponding HIFU fields are discussed. The results of ex vivo experiments with different tissues that prove the efficacy, safety and selectivity of new methods are presented and analyzed.

46.1 Introduction

For the last 100 years average life expectancy of the person significantly increased —modern people live much longer, than is taken away by evolution. As a result, practically each person who reached at least middle age uses the medical subjects and adaptations directed on compensation of the lost functions and/or body parts. Need for the medical actions directed on restoration and replacement of the withering bodies and tissues constantly increases—to it promotes not only noticeable aging of the population, but also high level of traumatism, significant increase the

I.A. Shvetsov · N.A. Shvetsova · A.N. Reznitchenko · A.N. Rybyanets (✉)
Institute of Physics, Southern Federal University, 194 Stachky Ave.,
Rostov-on-Don 344090, Russia
e-mail: arybyanets@gmail.com

I.A. Parinov et al. (eds.), *Advanced Materials*, Springer Proceedings
in Physics 193, DOI 10.1007/978-3-319-56062-5_46

iatrogenic adverse effects (side effects from aggressive ways of medical treatments), etc.

Recently multidimensional scientific researches on development of new medical and recovery technologies with application of methods of physiotherapy as well as to identification of opportunity and expediency of a combination of various physical and medicaments factors were conducted [1]. However obvious is that fact that application of separate narrowly targeted therapeutic methods is ineffective and does not solve all range of the problems facing recovery and regenerative medicine.

The problem of creation of the new therapeutic technologies and medicines accelerating natural regenerative processes in an organism is one of the priority directions of development of modern recovery, regenerative and adaptation medicine.

Undoubted social value and practical interest represent the scientific researches directed on identification of possibility of complex application of medicament means and hardware physical therapy for treatment, regeneration and restoration of the lost functions of an integument and superficial tissues of the person.

Ultrasonic methods are widely used for therapeutic treatment of bone and soft tissue injuries, cancer and Parkinson deceases surgery, wound and burnshealing, liver and prostate tumours treatment, tools surgery and vascular occlusion [1, 2]. New methods and apparatus for ultrasonic therapeutic treatment, diagnostics and body aesthetics as well as new features and clinical applications based on the advances in piezoelectric materials and ultrasonic transducer designing, visualization technologies and physical acoustics have appeared during a past decades [1, 3, 4].

High-intensity focused ultrasound (HIFU) are widely used for performing therapeutic, surgical or aesthetic medical procedures in target tissues of patient's body [1, 3]. Adipose tissue lysis are one of the reputed application of the HIFU systems and methods in body aesthetic therapy [3, 5, 6]. The main drawback of HIFU treatment of large volumes of tissue is small lysis volume related to small focal zone of HIFU field in lateral direction. Other disadvantage of usual HIFU therapy connected with the complex body shapes, low fat thickness, and close proximity of bones or vital organs elsewhere in the body, is a restricted number of body areas accessed for ultrasonic treatment.

Superficial tissues are one of the vital and most vulnerable parties of a human body. The social and esthetic importance and the huge market of cosmetic services define relevance and practical importance of therapy, aesthetic and regenerative medicine of superficial tissues of the person. So, we can state that the development of new effective and safe devices and ultrasonic methods for therapeutic treatment of large volume of superficial tissues (subcutaneous adipose tissue and skin) is one of the priority directions of modern aesthetic and regenerative medicine [3].

The Chapter reviews novel methods of ultrasonic diagnostics, complex therapeutic treatment and accelerated regeneration of superficial tissues of a patient. The methods are based on synergetic combination of different factors such as ultrasonic shear and standing waves impact, radio-frequency heating (RF), vacuum massage, as well as ultrasonically assisted drags delivery. Theoretical and numerical models

of ultrasonic transducers along with the results of HIFU fields modeling and technological aspects of the ultrasonic transducer designing are discussed. The efficacy, safety and selectivity of developed methods are proved by the results of ex vivo experiments with different biological tissues.

New ultrasonic methods can be used in the field of regenerative and aesthetic medicine for the accelerated healing of wounds and burns, scars removal, rejuvenation and tightening of skin, treatment of cellulitis, elimination of consequences of the disfiguring cosmetic procedures, as well as for surgical treatments of oncological diseases of a skin.

46.2 Soft Tissues Diagnostics and Therapy Using Shear Waves Generated by HIFU

46.2.1 The Acoustic Radiation Force in Biological Tissues

A volume radiation force can be generated by focusing an ultrasonic beam at a given location inside of dissipative medium. This radiation force is caused by the dissipation of the acoustic wave leading to the transfer of momentum from the acoustic wave to the medium [7].

For a dissipative medium the radiation force can be written as $F = 2\alpha I/v$, where α is the ultrasound attenuation, v is the sound speed in the medium, and I is the ultrasonic beam intensity.

This radiation force will generate shear and bulk waves propagating in the medium with respective speeds that depend on the elastic moduli λ and μ of the propagation medium.

Focused ultrasonic beam generates shear waves that propagates in the transverse direction and have axial directivity pattern. The shear wave velocity in purely elasticor viscoelastic media with negligible dispersion is directly linked to shear elastic modulus $\mu = \rho c2$, where c is the speed of the shear wave and ρ is the density of the medium, and makes typically a few meters per second in soft tissues. The Young's modulus E of the soft tissues ($\lambda \gg \mu$) can be quantitatively estimated everywhere besides the acoustic beam axis by measuring the speed of shear waves as $E \approx 3\mu = 3\rho c2$. At the focal point, the local shear modulus is linked to the rise time of the longitudinal displacements as $E = \mu(\alpha D/t_{max})2$, where t_{max} is the rising time, a is the Gaussian profile parameter of the beam ($\varphi = \exp(-r_2/a_2)$, μ is the shear modulus, and D is a dimensionless diffraction parameter [8].

The first experimental observation of shear waves generated by focused ultrasound beam in a rubber-like medium was presented in [9]. In that work it was shown that shear displacements up to 40 μm can be achieved at focal point in phantom media using HIFU with 100 μs bursts of 1.8 MHz at acoustic power 45 W. Shear waves observed in these experiments were strongly attenuative and can be used for diagnostic purposes only.

A line of diagnostic and imaging methods and devices for tissues elasticity estimation and visualization, relying on the basic concept of shear wave generation by pulsed radiation force, have been developed [10–14].

46.2.2 Shear Wave Elasticity Imaging

The method of low frequency shear wave generation using two beams with slightly different resonant frequencies was proposed and experimentally proved in [10].

Another approaches ("shear wave elasticity imaging" (SWEI) and "acoustic radiation force impulse imaging" (ARFI)), consist in focusing of long ultrasonic bursts (typically 100 μs) in tissue and measuring the resulting shear displacements at focal point using ultrasonic correlation techniques were proposed [9, 11]. The local viscoelastic properties of the tissue can be linked to the displacement induced at the focal point as a function of time. However, these techniques unable to estimate viscoelastic parameters of tissues quantitatively because the shear displacements depend on such parameters as ultrasonic ab-sorption coefficient, acoustic beam geometry, and shear wave heterogeneities in the focal point.

A new method, called "super-sonic shear imaging" (SSI), providing quantitative estimation and mapping of shear modulus of soft tissues in less than 30 ms was developed in [14]. The SSI concept is commercialized now by the company "Supersonic Imagine" (France) and the innovative MultiWave™ ultrasound system Aixplorer® for imaging of breast lesion are on the market now.

The SSI method remotely generates low-frequency shear wave in soft tissues using the acoustic radiation force emitted by the ultrasonic diagnostic array. This acoustic radiation force acts in the focal point as the dipolar source of shear waves that mainly propagates in transverse directions. It was proposed to create the high intensity shear waves by moving virtual shear source (focal point) at a supersonic speed [14]. Successive focusing the "pumping" ultrasonic beam at different depths using SSL approach can generate such supersonic shear source (source that moves faster than the shear waves in the medium). The resulting shear waves constructively interfere along a Mach cone, generating two shear waves with quasi plane fronts that propagate in opposite directions. The ratio between the speed of moving source and the speed of shear waves (the Mach number) is proportional to the angle between two plane shear waves.

46.2.3 Resonant Amplifications of Shear Waves in Soft Tissues

The shear waves with low intensity and low frequency generated remotely by HIFU in soft tissues can be used for tissue assessments and visualization [11–14]. The "pumping" HIFU with high intensity can't be used for visualization purposes according FDA requirements.

Three acoustic parameters of the ultrasound system: "the spatial peak pulse average intensity" (ISPPA < 190 W/cm^2), "the spatial peak temporal average intensity" (ISPTA < 720 mW/cm^2) and "the mechanical index" (MI < 1.9) should be met [13]. Because of strong attenuation, maximal increase in the amplitude of shear waves generated by HIFU in supersonic regime on Mach cone boundary is 1.5–2 times only [13]. Therefore, the intensity of shear waves outside a focus is very week. The generation of more intensive shear waves by therapeutic level of HIFU is also impossible because of possible thermal modification of the tissue near the focus. Thus, other designs of ultrasonic transducers and improved methods of remote generation of high intensity shear waves in soft tissues for diagnostic and therapy applications [15] meeting these contradictory demands are required.

A new concept for supersonic generation and resonant amplifications of shear waves remotely induced in soft tissues for diagnostics and therapy purposes were proposed recently [16, 17]. The concept consist in the formation inside a tissue of the "virtual resonators" of shear waves by remote excitation of a cyclically "morphing pattern" of HIFU focal points. Focal regions in this morphing pattern cyclically appear and disappear at different space locations. Radiation force excited by the HIFU in each of focal regions contributes to shear wave generation. To provide resonant amplification and constructive interference of shear wave at each focal region the following parameters must be defined and fixed: the frequency of shear waves in a tissue, distances between space locations of HIFU focal points in the "morphing pattern", as well as the repetition rates and frequencies of exciting HIFU bursts.

Two possible methods can be used for resonant amplification of shear wave:

- the radiation force applies repeatedly to a region of tissue in phase with the shear wave to amplify its amplitude;
- the focal point in the HIFU "morphing pattern" rotates in a focal plane around an axis or moves laterally between the focal points locations, to generate an amplified the shear wave.

In the last case, the linear velocity of focal zone rotation or movement must be equal or higher than the propagation velocity of shear wave in a tissue (wave resonance or supersonic regimes). At the generation of shear wave in supersonic regime all partial shear waves will constructively interfere with each other creating intense "Mach spiral" or "Mach cone" structures. The main advantages of new concept are use of dynamical focusing method for remote formation of "morphing pattern" of HIFU focal points acting inside a tissue as "virtual resonators" of shear waves, and employment of supersonic generation or wave resonance regimes for resonant amplification of shear waves in wide region of a tissue.

Different types of ultrasonic transducers (annular or sectored HIFU transducers, linear, two- or three-dimensional phased arrays etc.) can be used for practical realization of the proposed concept [16, 17].

46.2.4 Calculation and Simulation of Acoustic Fields

As a model system, multielement ultrasonic transducer, which is a piezoceramic spherical segment divided by "N" (N > 1) regular sectors of equal area has been selected. Sectors were excited simultaneously by "M" ($1 < M \leq N$) signals with different frequencies chosen from 6 dB acoustic pass-band of the ultrasonic transducer. Calculations and simulation of the HIFU field patterns for different frequency sets and configurations of sectors were performed by standard solutions of wave equations for the acoustic field by Debye method. For calculations and modeling of dynamical HIFU fields, Matlab and Ansys software packages were employed.

The result of overlapping of acoustic beams with different frequencies (frequency beats) in the focal plane is an equivalent of continuous change of the phase shift of the exciting signal supplied to the sectors. This overlapping is described by the following formula: $\varphi_i = F(f_n)$, where φ_i is the phase shift of sector i, f_n—frequency of the signal supplied to the sector n. For simulation, following parameters of the ultrasonic transducer were accepted: aperture of 85 mm, the radius of curvature of 54 mm, the thickness of the piezoelectric element of 2 mm, diameter of the hole in the segment center of 10 mm. Back electrodes of piezoceramic spherical segment were circumferentially divided into 4 regularly shaped sectors. The resonant frequency of the transducer measured using impedance analyzer was 1000 kHz. Repetition rate—the lowest common denominator for the selected set of frequencies was equal to 10 kHz. Sampling time was 0.1 s/10 = 0.01 s. Acoustic fields were calculated in water, the acoustic pressure on the surface of piezoelectric element is set to 1.5 = MPa. Table 46.1 shows the values of the phase shift in degrees at four sectors for 10 discrete focal structures at frequency set $f_1 = 980$, $f_2 = 990$, $f_3 = 1000$, $f_4 = 1010$ kHz.

Examples of acoustic pressure distribution in the focal plane for selected samples of focal structures are shown in Fig. 46.1.

Table 46.2 shows the values of the phase shift in degrees at four sectors for 10 discrete focal structure sat frequency set $f_1 = 980$, $f_2 = 990$, $f_3 = 1010$, $f_4 = 1000$ kHz. Examples of acoustic pressure distribution in the focal plane for selected samples of focal structures are shown in Fig. 46.2.

Table 46.3 shows the values of the phase shift in degrees at four sectors for 10 discrete focal structures at frequency set $f_1 = 990$, $f_2 = 980$, $f_3 = 1000$, $f_4 = 1010$ kHz. Examples of acoustic pressure distribution in the focal plane for selected samples of focal structures are shown in Fig. 46.3.

Table 46.1 Phase shifts at four sectors for 10 discrete focal structures

i/z	1	2	3	4	5	6	7	8	9	10
0	0	0	0	0	91.2	211.2	331.2	91.2	211.2	331.2
1	129.6	89.6	49.6	9.6	60.8	140.8	220.8	300.8	20.8	100.8
2	259.2	179.2	99.2	19.2	30.4	70.4	110.4	150.4	190.4	230.4
3	28.8	268.8	148.8	28.8	0	0	0	0	0	0

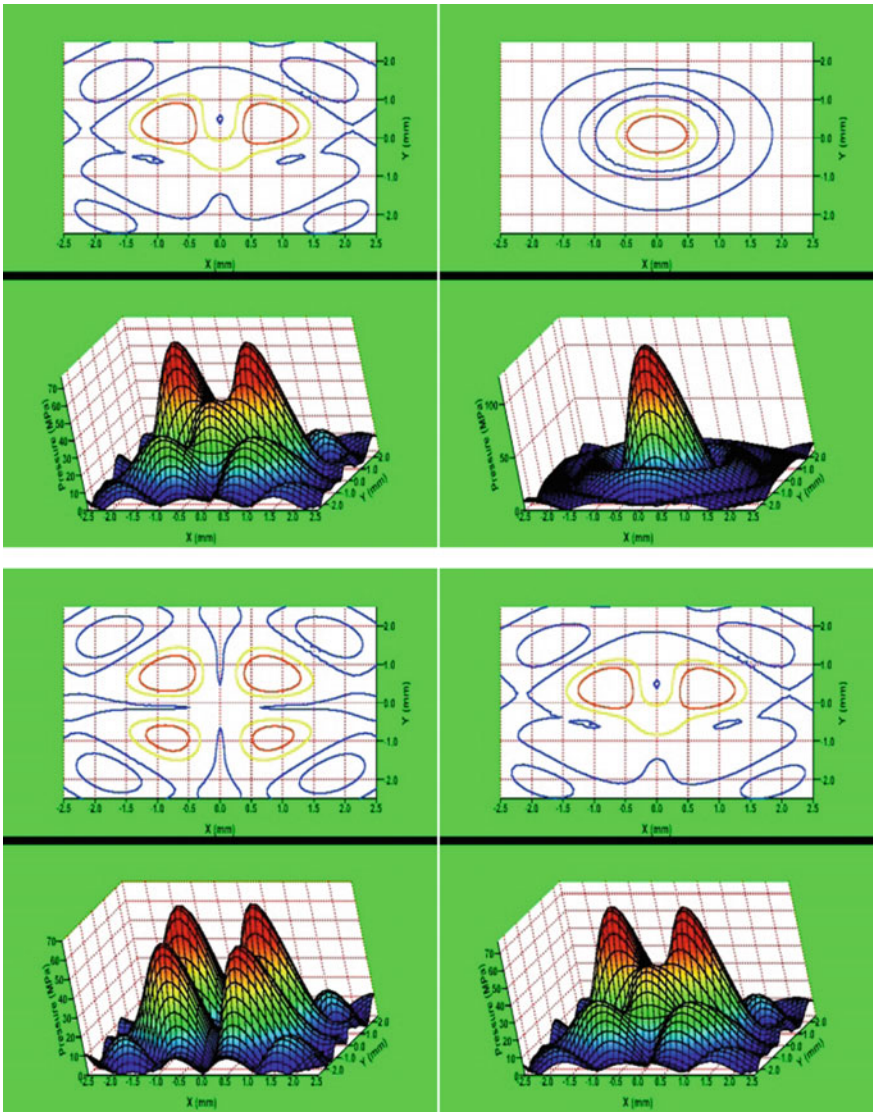

Fig. 46.1 Acoustic pressure distribution in the focal plane for selected samples of focal structures according data from Table 46.1

Table 46.2 Phase shifts at four sectors for 10 discrete focal structures

i/z	1	2	3	4	5	6	7	8	9	10
0	0	0	0	0	124.2	286.2	349.2	178.2	259.2	331.2
1	129.6	57.6	49.6	9.6	82.8	190.8	352.8	118.8	172.8	100.8
2	28.8	172.8	99.2	19.2	0	0	0	0	0	230.4
3	259.2	115.2	148.8	28.8	41.4	95.4	356.4	59.4	86.4	0

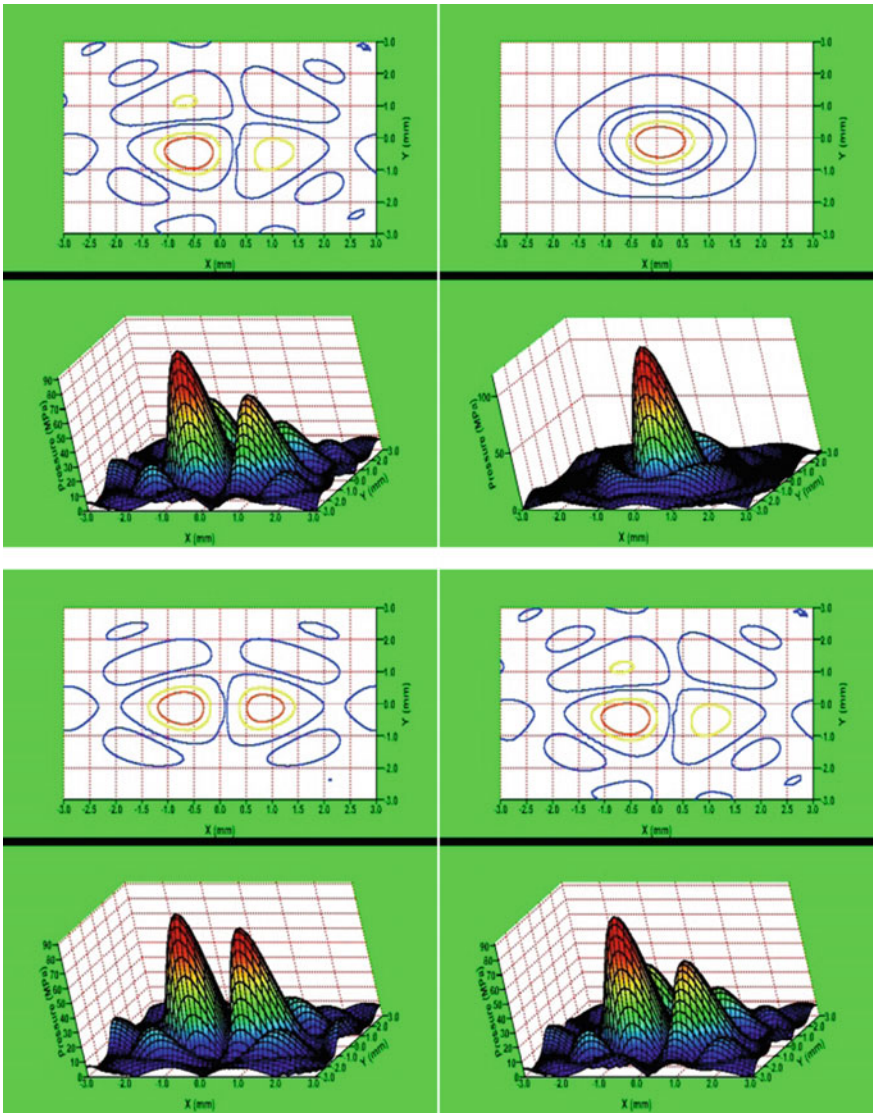

Fig. 46.2 Acoustic pressure distribution in the focal plane for selected samples of focal structures according data from Table 46.2

Table 46.4 shows the values of the phase shift in degrees at four sectors for 10 discrete focal structures at frequency set $f_1 = 1010$, $f_2 = 990$, $f_3 = 980$, $f_4 = 1000$ kHz. Examples of acoustic pressure distribution in the focal plane for selected samples of focal structures are shown in Fig. 46.4.

Table 3 Phase shifts at four sectors for 10 discrete focal structures

i/z	1	2	3	4	5	6	7	8	9	10
0	129.6	0	0	0	124.2	286.2	349.2	178.2	259.2	331.2
1	0	57.6	49.6	9.6	82.8	190.8	352.8	118.8	172.8	100.8
2	259.2	172.8	99.2	19.2	0	0	0	0	0	230.4
3	28.8	115.2	148.8	28.8	41.4	95.4	356.4	59.4	86.4	0

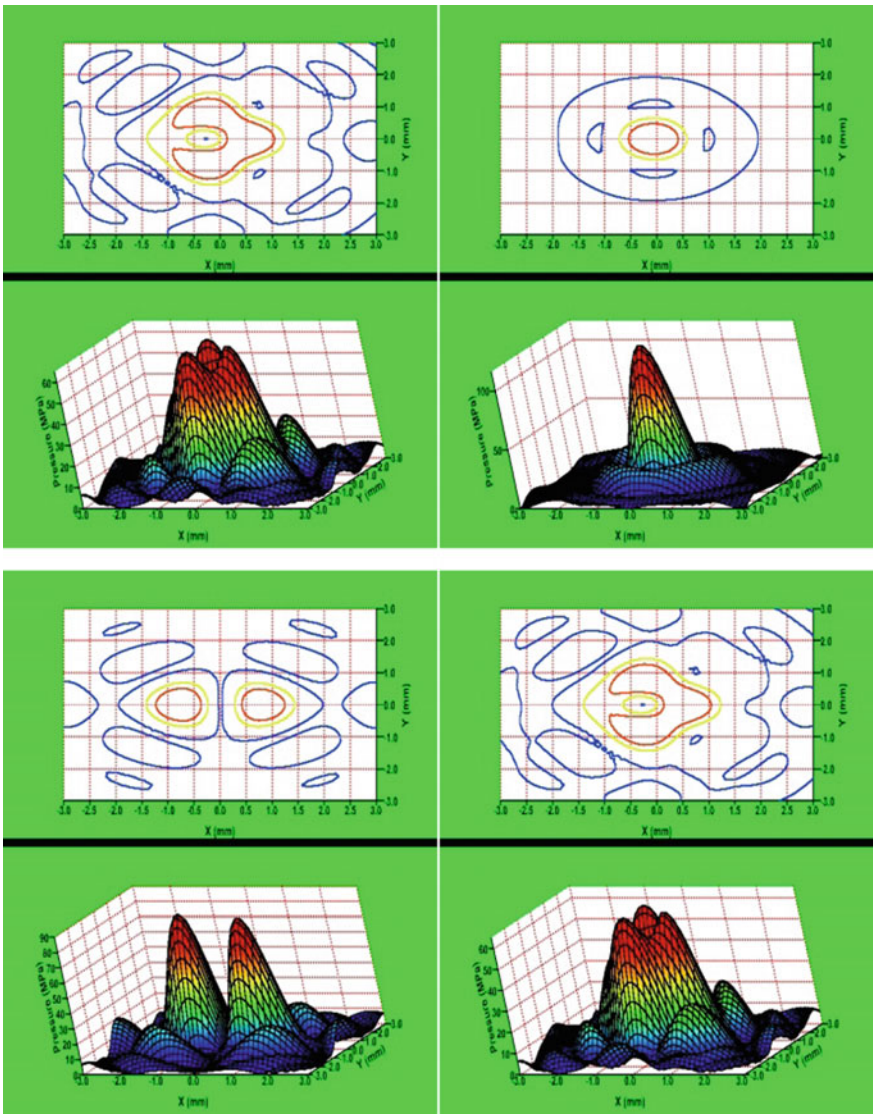

Fig. 46.3 Acoustic pressure distribution in the focal plane for selected samples of focal structures according data from Table 46.3

Table 46.4 Phase shifts at four sectors for 10 discrete focal structures

i/z	1	2	3	4	5	6	7	8	9	10
0	28.8	0	0	0	0	0	0	0	0	0
1	129.6	64.8	46.8	46.8	262.8	118.8	280.8	208.8	46.8	100.8
2	0	97.2	250.2	70.2	214.2	178.2	61.2	133.2	70.2	331.2
3	259.2	32.4	203.4	23.4	311	59.4	140.4	284.4	23.4	230.4

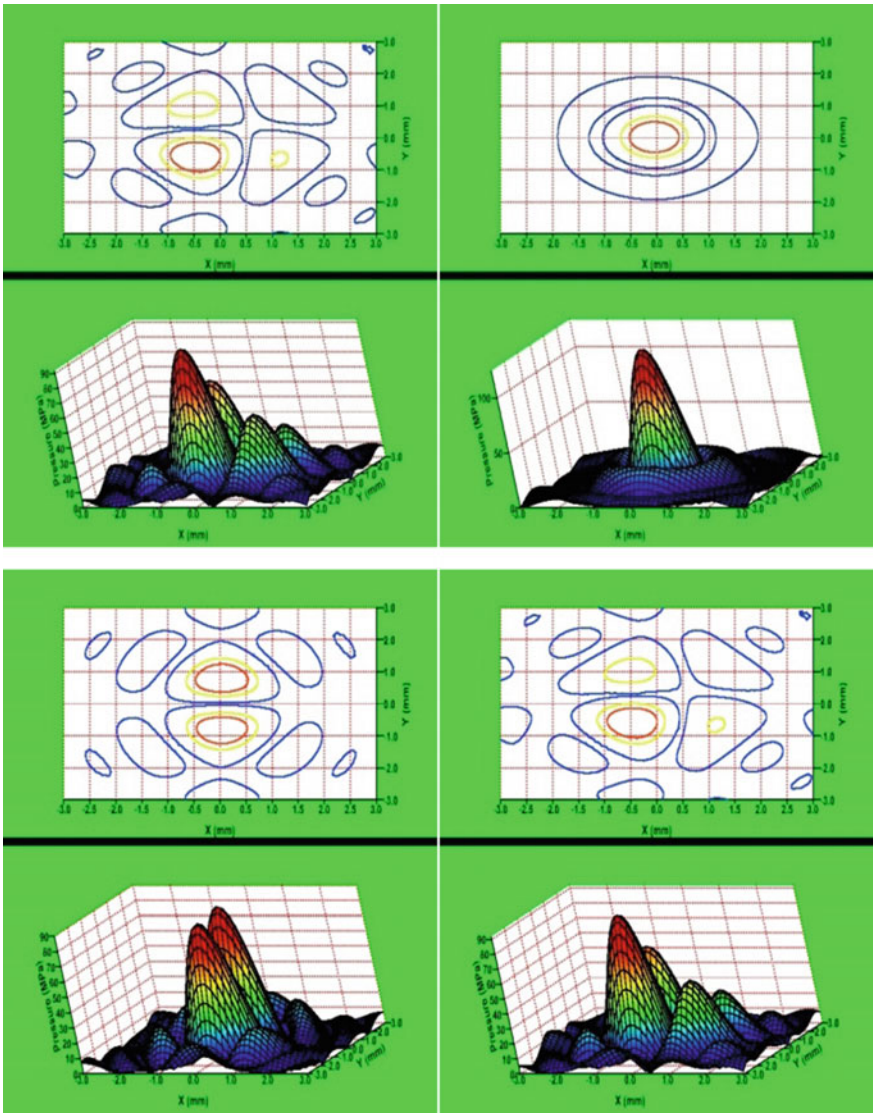

Fig. 46.4 Acoustic pressure distribution in the focal plane for selected samples of focal structures according data from Table 46.4

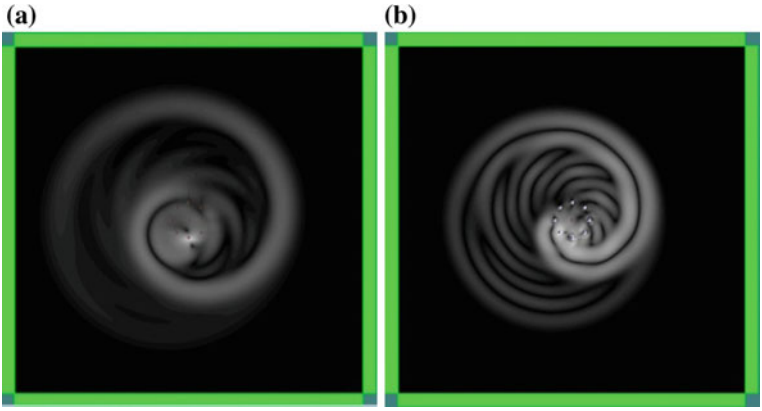

Fig. 46.5 "Mach spirals", formed by constructively interfered shear waves, generated by the rotating pattern of 1 of-axis (**a**) and 2 symmetrical HIFU focal points (**b**)

Simulation of shear wave generation in tissue by rotating pattern of HIFU focal points around a center axis in a focal plane, was performed using 3D simulation package Wave 3000™ (CyberLogic, Inc.).

"Virtual resonators" of shear waves were disposed symmetrically and switched on at appropriate delay times sequentially, simulating rotation of 1 of-axis or 2 symmetrical focal points around central axis of HIFU transducer. The resulting shear wave wave front generated by the rotation of focal points pattern at "supersonic regime" has a spiral shape and propagates in a focal plane away from the axis forming single or double "Mach spiral" structures (Fig. 46.5).

46.2.5 Experimental Validation of the Resonant Amplification Method

The experimental stand comprise a multi-channel driving circuitry, HIIFU sectored transducer and controller. The experiments were conducted on biological tissues in vitro and in oil bath. Figure 46.6 shows the photos of acoustic pressure distribution in the focal plane on the surface of a mineral oil corresponding to focal structures modeled in previous section. Using the measurement cell, equipped by piezoelectric sensors and specially designed for shear wave registration, 10 kHz shear waves of 120–140 μm amplitudes were detected in porcine samples in vitro at "pumping"HIFU acoustic power 50 W and frequencies 1 and 1.01 MHz.

For demonstration of shear wave generation by rotating HIFU pattern sectored transducer with 8 sectors combined in 2 symmetrical groups with frequency of 1 MHz was fabricated. Each group of sectors was powered simultaneously by 2 burst or sinus drive signals at 180° phase shift.

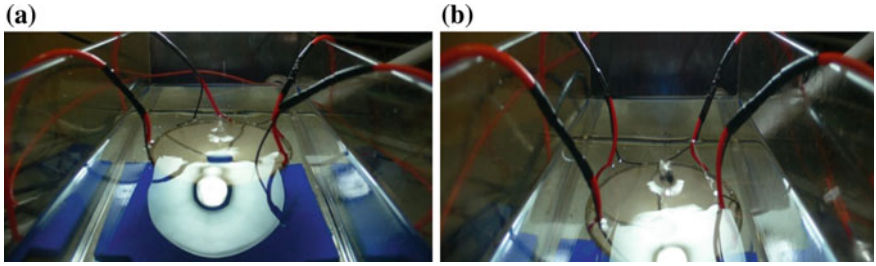

Fig. 46.6 Visualization of acoustic pressure distribution in the focal plane for selected samples of focal structures generated by sectored HIFU transducer in a mineral oil bath: **a** single focus—φ_1, φ_2, φ_3, $\varphi_4 = 0°$ and **b** four focus pattern—φ_1, $\varphi_3 = 0°$, φ_2, $\varphi_4 = 180°$

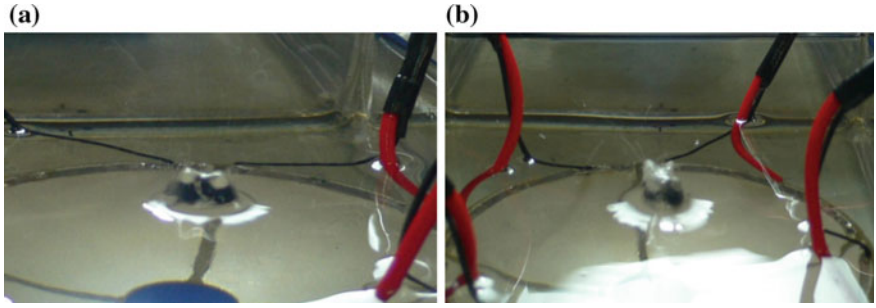

Fig. 46.7 Visualization of rotating pattern of focal points generated by dynamical HIFU transducer in a mineral oil: **a** static bi-focal off-axis focal pattern and **b** rotation of bi-focal pattern at angular velocity ω

Figure 46.7a shows resulting focal pattern of the sectored HIFU transducer appeared in oil bath comprising two symmetrical off-axis focal zones. The phase shifts of the drive signals powered to the next sector of each group are switched sequentially providing rotation of the bi-focal zones pattern visualized on Fig. 46.7b. For resonant amplification of shear waves the angular frequency of HIFU pattern rotation must be of $\omega/2\pi$ and switching frequency for the 8-sectored transducer of $8\omega/2\pi$. In present case that corresponds to angular velocity $\omega = 2186$ rad/s or about 348 rotations of focal pattern per second. At higher rotational speed, "supersonic regime" of shear wave generation with formation of appropriate "Mach spiral" was realized.

Using the measurement cell, equipped by piezoelectric sensors and specially designed for shear wave registration, shear wave of 100 μm amplitude at 10 kHz frequency generated in supersonic regime was detected in porcine samples in vitro at "pumping" HIFU acoustic power 50 W and frequency 1 MHz.

As a result of preliminary feasibility test, it was shown that shear waves with high intensity can be generated in big volume of tissue using a new method of

supersonic generation and resonant amplification of shear waves remotely induced by low intensity "pumping" HIFU.

Undesirable tissue modification by HIFU itself in this case are prevented by spatial changes in focal zones positions. Combinational effect of HIFU and intensive shear waves impact provides new therapy modality.

46.3 Application of UlSW for Body Aestetics Applications

Various methods are known for delivering acoustic energy to a target tissue region to perform a therapeutic, diagnostic and/or cosmetic procedure on a patient's body [1, 2]. Among such procedures are for example, lithotripsy, drug delivery by phonophoresis, non-invasive assaying of blood analyses, tissue ablation and lysis of fat cells for cosmetic removal of adipose tissue.

For many types of therapeutic and/or cosmetic ultrasonic applications, such as noted above lithotripsy, tissue ablation and lysis [18–21], sufficient ultrasonic energy must be delivered to destroy and remove tissue in the region. In general, the acoustic energy is delivered by focusing at least one beam of relatively intense ultrasound on the region. The high intensity focused ultrasound (HIFU) may be used to generate various mechanical and thermal effects on tissue that include local heating and/or cavitation that disrupts and destroys the tissue.

The main disadvantage of HIFU treatment of large volumes of tissue is small lysis volume related to small focal zone of HIFU field. Other disadvantage of usual HIFU therapy connected with the complex body shapes, low fat thickness, and close proximity of bones or vital organs elsewhere in the body, is a restricted number of body areas suitable for ultrasonic treatment. Some examples of enlargement of treated tissue volume using HIFU are described in [22, 23]. Non-focused ultrasound methods that frequently used for therapeutic treatment of tissue are unsuitable, in general, for lysis of adipose tissue because of strong influence or damage of intermediate tissues.

First example of using non-focused standing waves for tissue treatment is disclosed in [24]. The main drawback of this method is still a small treated volume of the treated tissue and limited body parts accessed for the treatment. It was proposed also to use ultrasonic standing waves (USW) for wound healing [25]. The use of ultrasound in body aesthetic therapy includes cellulite treatment, wrinkle reduction, skin rejuvenation, and subcutaneous adipose tissue lysis, however existing methods usually are time-consuming and not efficient. Therefore, the need exists for more efficient, safe and effective ultrasonic methods for treatment of large volumes of tissues on arbitrary body parts of a patient.

Recently, new USW methods and devices were proposed [26, 27], as an alternative to HIFU, for noninvasive therapeutic, lypolitic, or cosmetic treatment of large volumes of cellulite, subcutaneous adipose or skin tissues on arbitrary body part of a patient.

46.3.1 Tissue Treatment by USW: Modeling and Feasibility Test

Modeling of ultrasonic standing wave formation in tissue was performed using 3D finite-difference simulation package (Wave 3000™, CyberLogic, Inc.). Figure 46.8 shows the model of ultrasonic transducer and resulting USW field in porcine fat [27].

USW experimental setup consists of two facing each other PZT piezoceramic plates and a control unit with a power generator. For preventing heating and short-circuiting of the piezoceramic element electrodes, ultrasonic transducers were dipped into an oil bath. Experimental samples of target tissues (fresh porcine fat and bovine liver) were clamped between the piezoceramic plates. Figure 46.9 shows the resulting thermal lesions formed in the experimental samples by USW field. USW technology provides controllable temporal and spatial concentration of ultrasonic energy and can be used for tissue treatment and other biomedical applications.

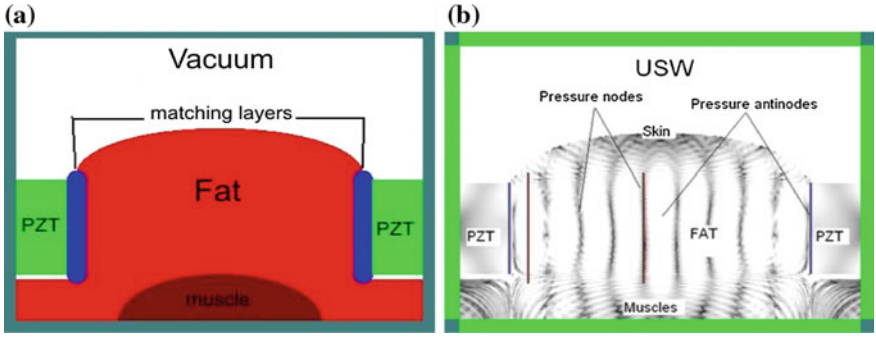

Fig. 46.8 Finite-difference model of ultrasonic transducer (**a**) and resulting USW field (**b**) in porcine fat at 30 mm distance between PZT plates 200 kHz ultrasound frequency and

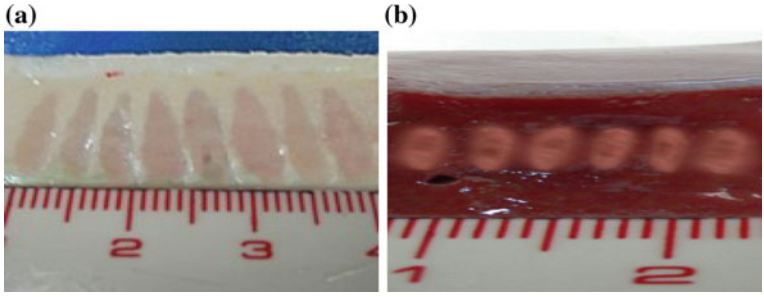

Fig. 46.9 Thermal lesions formed in porcine fat (**a**) and bovine liver (**b**) as the result of USW treatment at the following excitation protocol: driving voltage = 150–250 V, treatment time = 6 s, duty cycle = 5–10, frequency = 350 kHz; burst length = 100–200 periods

Recently, new combinational method and apparatus were proposed [28–30], as an alternative to HIFU, for noninvasive or minimally invasive lypolitic, therapeutic or cosmetic treatment of large volumes of tissues including cellulite, subcutaneous adipose or skin tissues on any desired body part of a patient. The combinational treatment method uses line of constructively interfering biologically and physically sensed factors ("moving" USW, shear waves, RF heating, vacuum massage, and phonophoresis) that can be applied to a tissue simultaneously or successively.

Unlike all existing non-focused and HIFU systems, ultrasound energy flow in "moving" USW is directed parallel to the surface of the body and fully localized in target tissue region. Resulting efficiency of "moving" USW is comparable with the intensity of HIFU at huge increase in the volume of treated tissue. Effective dynamical influence of "moving" USW on treated tissues is provided by cyclic changes of the nodal pattern of "moving" USW at specific repetition rates that correspond to the relaxation or resonant times of tissue components or living cells [31, 32]. Synergetic combination of vacuum massage with "moving" USW and RF therapeutic heating providing lower cavitation threshold and effective clearance of disrupted cell debris by blood flow along with the diagnostic possibilities and inherent treatment process control offers a great future for the combinational treatment technology.

For experimental validation of the method, the therapeutic head comprising vacuum suction cup, cylindrical piezoelement, plunger, and metal RF electrodes disposed on the plunger and outer edge of the cup was designed (Fig. 46.10).

The RF electrodes and cylindrical piezoelement was powered by the power generator on the same resonant frequencies providing formation of RF field and cylindrical USW in the target tissue. The cylindrical standing wave with the specific nodal pattern consisting of a plurality of pressure antinodes and nodes separated by an acoustic half-wavelength distance can be formed in the tissue at each particular resonance frequency.

The USW field affects target tissue by the thermal and/or non-thermal mechanisms (cavitation, micro flows, and mechanical effects). Both treatment mechanisms are most effective in the regions of the pressure amplitude maxima, which is the region of ultrasound pressure antinodes distributed throughout the tissue according to the specific nodal pattern. Synchronous excitation of RF and USW fields at the

Fig. 46.10 Therapeutic head for combinational treatment of superficial tissues comprising vacuum cup (**a**) cylindrical piezoelement (**b**) and RF electrodes (**c**)

same frequency will lead to additional RF heating. The physical reasons of the tissue heating by RF are rotations of polar molecules (dipoles) like in electrolytes and dielectrics, as well as ion movements and vibrations [29, 30].

The combinational USW and RF treatment is non-trivial, because only in the developed therapeutic head configuration USW and RF fields superimpose synchronously and coincide spatially to provide new physical and biological effects. The combination of the USW and RF impacts are further intensified by the vacuum massage providing real synergetic combinational treatment of the tissue. Figure 46.11 shows prototypes of the apparatus for combinational treatment of superficial tissues including cellulite, subcutaneous adipose or skin.

Feasibility tests of new combinational method (safety and efficiency demonstration) were made ex vivo on bovine liver samples at a standard protocol:

- 2 channel generator with additional cooling of power boards;
- RF channel—frequency 900 kHz, electric power up to 30 W max;
- Ultrasonic channel—frequency 900 kHz, electric power up to 30 W max;
- Regime of excitation—bursts 1/2,1/5, CW;
- Vacuum system—730 mmHg, pulsed or constant;
- Treatment protocol—USW alone, RF alone, RF + USW;
- Time of treatment—60 s;
- Tissue type—fresh bovine liver.

Figure 46.12 shows the results of combinational treatments of bovine liver samples. It is easy to see from Fig. 46.12, that at used powers and treatment times USW alone produce minimal (fractional) thermal modifications of the tissue. Ultrasound power increase generates noticeable heating of the piezoelement and therapeutic head and at longer exposition times can leads to burning of the skin.

In contrast, at long exposition times RF alone produce thermal tissue modifications with a strong “skin” burning under central plunger RF electrode only. Combinational treatment of target tissue by RF and USW leads to the strong thermal modifications even at minimal exposition times. However, increase in

Fig. 46.11 Prototypes of the apparatus for combinational treatment of superficial tissues comprising therapeutic head and electronic block

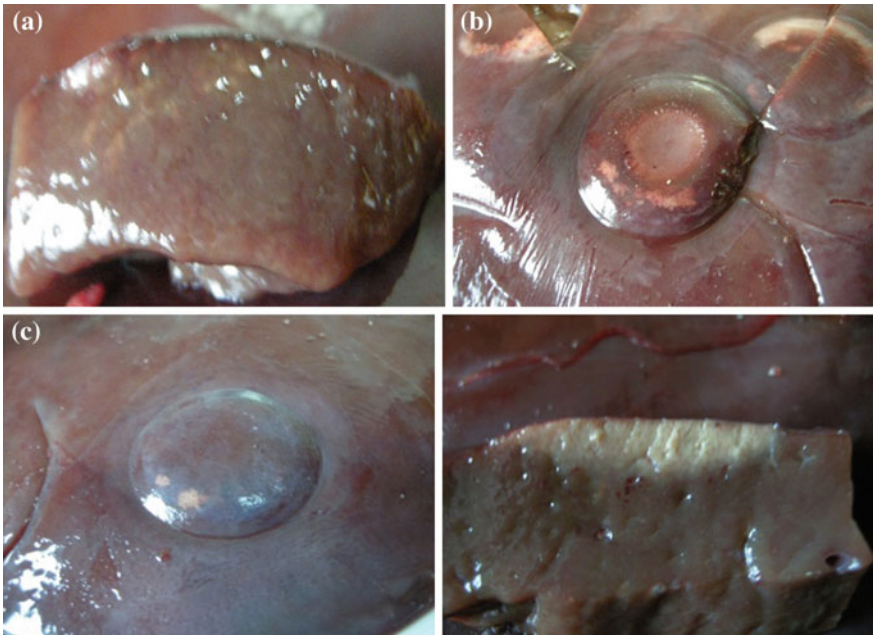

Fig. 46.12 Thermal lesions in bovine liver produced by combinational treatment using USW alone (**a**), RF alone (**b**) and USW + RF (**c**)

exposition times at fixed powers also leads to a skin burning because of RF and piezoelement heating.

It was shown in preliminary experiments on volunteers that used powers of RF and USW and expositions times are not acceptable for in vivo treatments of a patients (at used protocol, expositions of RF, USW and RF + USW lead to the skin burnings and strong pain during first 5–10 s of the treatment).

It is obvious, that for personal or home-used cosmetic devices the treatment protocols (vacuum, RF and USW levels) leading to visible skin and tissue damages or pain are unacceptable. The cosmetic device can't do harm to a patient (safety is superior to efficacy) at any regime and kind of use. So, the following treatment protocol was recommended for in vivo experiments [29, 30]:

- Vacuum—730–750 mmHg, pulsating;
- RF channel—power 15–30 W in burst mode 1/10;
- USW channel—15–30 W in burst mode 1/10;
- Treatment mode—continuous movement of therapeutic head along the body;
- Therapeutic head—internal cooling is needed for pain and burning prevention.

The combinational treatment technology can be used in the field of regenerative and aesthetic medicine for the accelerated healing of wounds and burns, removal of

scars, tightening and rejuvenation of skin, treatment of cellulitis, elimination of consequences of the disfiguring cosmetic procedures, as well as for treatments of oncological diseases of a skin.

46.4 Conclusions

The Chapter reviews novel methods of ultrasonic diagnostics, complex therapeutic treatment and accelerated regeneration of superficial tissues of a patient. The methods are based on synergetic combination of different factors such as vacuum massage, radio-frequency heating (RF), ultrasonic shear and standing waves (USW) impact, as well as ultrasonically assisted drags delivery.

Theoretical and numerical models of ultrasonic transducers along with the results of HIFU fields modeling and technological aspects of the ultrasonic transducer designing were discussed. The efficacy, safety and selectivity of developed methods and ultrasonic transducers for various therapeutic, surgical and cosmetic applications were proved by the results of ex vivo experiments with different biological tissues.

The main advantages of new methods are: reduced treatment time, bigger treated tissue volume treatment of arbitrary body part, high selectivity and safety, continuous control of the treatment process and tissue condition, and wide range of applications.

Preliminary experiments have shown that new methods of resonant amplifications and supersonic generation of remotely induced shear waves enable generation of intensive shear waves in wide tissue regions using a at low intensity of pumping HIFU. Combination of HIFU and resonantly amplified shear waves provides new therapeutic modality—Shear Waves Therapy.

Synergetic combination of vacuum massage, with “moving” USW impact and RF therapeutic heating providing lower cavitation threshold and effective clearance of disrupted cell debris by blood flow along with the diagnostic possibilities and inherent control of the treatment process offers a great future for the combinational treatment technology.

New ultrasonic methods can be used in the field of regenerative and aesthetic medicine for the accelerated healing of wounds and burns, scars removal, rejuvenation and tightening of skin, treatment of cellulitis, elimination of consequences of the disfiguring cosmetic procedures, as well as for surgical treatments of oncological diseases of a skin.

Acknowledgements This work was supported by the Ministry of Education and Science of the Russian Federation (Contract No 02.G25.31.0184 and Theme No BP0110-11/2017-44).

References

1. C.R. Hill, J.C. Bamber, G.R. ter Haar (ed.), *Physical Principles of Medical Ultrasonics*, 2nd edn. (John Wiley & Sons Ltd., 2004)
2. G.R. ter Haar, Prog. Biophys. Mol. Biol. **93**, 111 (2007)
3. A.N. Rybyanets, in *Piezoelectrics and Related Materials: Investigations and Applications* (Nova Science Publishers Inc., Chapter 5, 143, 2012)
4. W. Summer, M.K. Patrick, *Ultrasonic Therapy—A Textbook for Physiotherapists* (Elsevier, London, 1964)
5. A.N. Rybyanets, AIP Conf. Proc. **1215**, 287 (2010)
6. A.N. Rybyanets, M.A. Lugovaya, A.A. Rybyanets, AIP Conf. Proc. **1215**, 291 (2010)
7. G.R. Torr, Am. J. Phys. **52**, 402 (1984)
8. A.P. Sarvazyan et al., Ultrasound Med. Biol. **20**, 1419 (1998)
9. V.G. Andreev, V.N. Dmitriev, Y.A. Pishchal'nikov, O.V. Rudenko, O.A. Sapozhnikov, A. P. Sarvazyan, Acoust. Phys. **43**, 123 (1997)
10. M. Fatemi, J.F. Greenleaf, Science **280**, 82 (1998)
11. K. Nightingale et al., Ultrasound Med. Biol. **28**, 227 (2002)
12. J. Bercoff et al., Ultrasound Med. Biol. **13**, 143 (2003)
13. L. Lorenzen, R. Sinkus, G. Adam, *Rofo Fortschr. Geb. Rontgenstr* (Thieme Verlag Stuttgart-New York, 2003), p. 623
14. Bercoff Jeremy, Tanter Mickael, Fink Mathias, IEEE Trans. Ultrasonics, Ferroelectr., Freq. Control **51**, 396 (2004)
15. V.A. Burov, N.P. Dmitrieva, O.V. Rudenko, Doklady Biochem. Biophys. **383**, 1 (2002)
16. A.N. Rybyanets, V.A. Khokhlova, A.A. Sapozhnikov, A.A. Naumenko, M.A. Lugovaya, S. A. Shcherbinin, in *Advanced Materials—Studies and Applications* (Nova Science Publishers Inc., Chapter 23, 393, 2015)
17. A.N. Rybyanets, A.A. Naumenko, O.A. Sapozhnikov, V.A. Khokhlova, Phys. Proc. **70**, 1152 (2015)
18. Nudelman Igor, Rybyanets Andrey. US Patent No 7,709,997, 2010
19. Rybyanets Andrey. US Patent No 8,568,339, 2013
20. A.N. Rybyanets, in *Advanced Materials: Manufacturing, Physics, Mechanics and Applications*, Springer Proceedings in Physics, **175**, Chapter 43, 603 (2016)
21. A.N. Rybyanets, A.A. Naumenko, N.A. Shvetsova, V.A. Khokhlova, O.A. Sapozhnikov, A. E. Berkovich, in *Advanced Materials: Manufacturing, Physics, Mechanics and Applications*, Springer Proceedings in Physics, **175**, Chapter 44, 621 (2016)
22. W. Cribbs Robert, Hennige Carl W. US Patent 6,071,239, 2000
23. Vitek Shuki, Brenner Naama. US Patent 6,419,648, 2002
24. Bishop Richard P. US Patent 5,664,570 (1997)
25. Babaev Eilaz. US Patent 6,960,173, 2005
26. Rybyanets Andrey. US Patents Applications No 20120123304, 2012
27. A.N. Rybyanets, in *Piezoelectrics and Related Materials: Investigations and Applications* (Nova Science Publishers Inc., Chapter 5, 143, 2012)
28. A.N. Rybyanets, A.A. Naumenko, O.A. Sapozhnikov, V.A. Khokhlova, *Phys. Proc.* **70**, 1152 (2015)
29. A.N. Rybyanets, A.A. Naumenko, Phys. Proc. **70**, 1148 (2015)
30. A.N. Rybyanets, A.A. Naumenko, N.A. Shvetsova, in *Nano- and Piezoelectric Technologies, Materials and Devices* (Nova Science Publishers Inc., Chapter 1, 1, 2013)
31. K. Naugolnykh, L. Ostrovsky, *Nonlinear Wave Processes in Acoustics* (Cambridge University Press, 1998)
32. A. Sarvazyan, LA Ostrovsky, A. Rybyanets, *AIP Conf. Proc.* **6**, 020002 (2009)

Chapter 47
IMF Features of BCI FP1 EEG Signal Using EMD Methods for Cerebral Palsy

Chin-Feng Lin, Shi-Chun Lee, Shun-Hsyung Chang, Chung-Chen Chang, Ivan A. Parinov and Sergey N. Shevtsov

Abstract In the paper, the intrinsic mode function (IMF) features of Brain-computer interfaces (BCI) FP1 electroencephalogram (EEG) signals for cerebral palsy (CP) using empirical mode decomposition (EMD) methods were analyzed. The BCI FP1 EEG signals for CP and health, were decomposed into nine IMFs and one residual function (RF), respectively. $IMFERTE_6$, $IMFERTE_7$, and $IMFERTE_{RF}$ of the FP1 signals of CP were 34.36, 32.29, and 18.04%, respectively. $IMFERTE_4$, $IMFERTE_5$, $IMFERTE_9$, and $IMFERTE_{RF}$ of the BCI FP1 signals of health were 17.93, 16.53, 12.45, and 41.20%, respectively. From the analysis of results, we find that IMF6, IMF7, and RF were the important IMFs of the BCI FP1 EEG signal of CP and IMF4, IMF5, IMF9, and RF were the important IMFs of BCI FP1 EEG signal of health.

47.1 Introduction

Cerebral palsy (CP) leads to muscle and bodily disorders, associated with symptoms of cerebral damage [1]. These disorders include movement, learning, visual, and auditory perception, and cognitive processing [2]. Advanced information and communication technologies play an important role in minimizing physical dis-

C.-F. Lin (✉) · S.-C. Lee · C.-C. Chang
Department of Electrical Engineering, National Taiwan Ocean University, Keelung, Taiwan
e-mail: lcf1024@mail.ntou.edu.tw

S.-H. Chang
Department of Microeletronic Engineering, National Kaohsiung Marine University, Kaohsiung, Taiwan

I.A. Parinov
I.I. Vorovich Mathematics, Mechanics and Computer Sciences Institute, Southern Federal University, Rostov-on-Don, Russia

S.N. Shevtsov
South Scientific Center of Russian Academy of Sciences, Rostov-on-Don, Russia

I.A. Parinov et al. (eds.), *Advanced Materials*, Springer Proceedings in Physics 193, DOI 10.1007/978-3-319-56062-5_47

abilities. Brain-computer interfaces (BCIs) can assist patients with CP to solve a range of challenges in functional disorders of movement and posture [3, 4]. The characteristics of the CP electroencephalogram (EEG) that were extracted relate significantly to BCI performance accuracy. An approach involving Hjorth parameters, and data-mining classification algorithms related to CP EEG signals was used to design the BCI for patients with CP to drive an intelligent wheelchair [5]. Gait robot-aided therapy in CP was introduced, and a design concept of the user's locomotion and manipulation was demonstrated [6]. Further, an ambulatory robot for gait rehabilitation was proposed, and the aspects of human-machine interaction were demonstrated.

The Hilbert-Huang transform (HHT) time-frequency analysis method was proposed by Huang et al. [7, 8]. It is suitable for the analysis of signals with nonlinear, nonstationary, and short time durations. The HHT time-frequency analysis method includes empirical mode decomposition (EMD) and the Hilbert transform (HT). The signal was decomposed into several intrinsic mode functions (IMFs) and one residual function (RF) using the EMD method, and several IMFs and one RF were analyzed to obtain instantaneous frequencies (IFs) using HT methods. Several IMFs, IFs, and one RF were analyzed in parallel to observe the high-resolution time frequency characteristics of the signals.

In a previous study, the HHT time-frequency analysis methods for biomedical signals were reviewed [9]. EEG Signals of Clinical Alcoholics, and the sharp and spike EEG Waves of epileptics were treated using HHT methods [10–14]. In the paper, the IMFs and marginal frequencies (MFs) of BCI FP1 EEG signals of CP are discussed.

47.2 BCI FP1 EEG signal of Cerebral Palsy

Figure 47.1 shows a BCI FP1 EEG signal of CP. The sample was downloaded from subject1/session1/eeg_200605191428_epochs [15, 16]. The time duration of the sample was in the interval from 4.8052 to 7.2070 s. The P300 evoked potential was employed in the BCI system, and the sampling rates was 2048 Hz. The images of the television (TL), telephone (TP), lamp (L), door (D), window (W), and radio (R) were fashed in random sequences, and the interstimulus interval was set as 400 ms for one image. Each image was fashed for 100 ms and none of the images was fashed for the remaining 300 ms.

The images that appeared at 4.8052–5.2051, 5.2056–5.6055, 5.6060–6.0059, 6.0063–6.4063, 6.4067–6.8066, and 6.8071–7.2070 ms were marked as 'W', 'TP', 'R', 'L', 'D', and 'TL', respectively. The amplitudes of the samples from the BCI FP1 electrode were scaled to the interval [0, 1]. Figure 47.2 shows a BCI FP1 EEG signal of health. The sample was downloaded from subject6/session1/eeg_200605121427_epochs [15, 16]. The images that appeared at 4.8052–5.2051, 5.2056–5.6055, 5.6060–6.0059, 6.0063–6.4063, 6.4067–6.8066, and 6.8071–7.2070 ms were marked as 'L', 'R', 'D', 'W', 'TP', and 'TL', respectively.

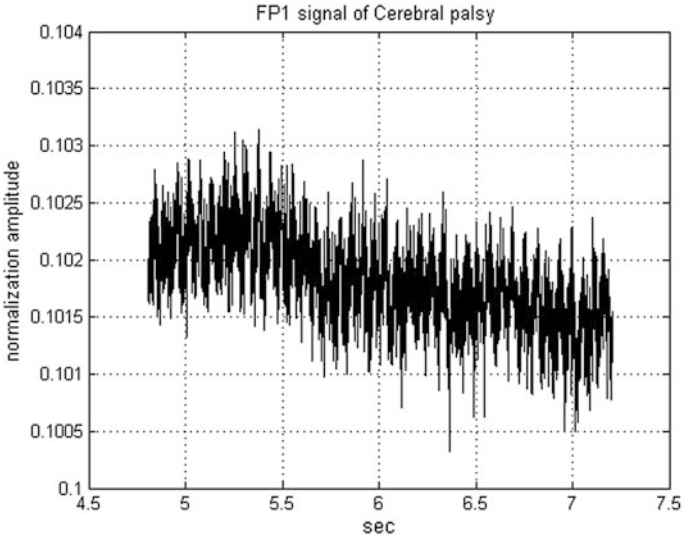

Fig. 47.1 BCI FP1 EEG signal of CP

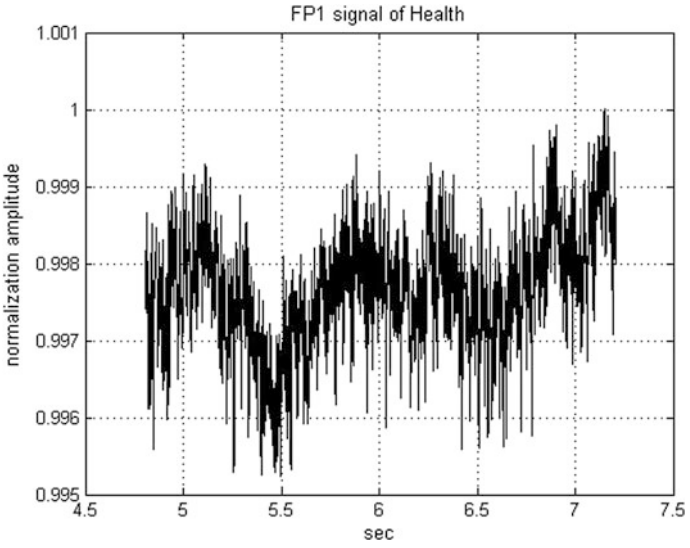

Fig. 47.2 BCI FP1 EEG signal of health

The mean, maximum, minimum, and standard deviation of the BCI FP1 EEG normalization amplitudes of the CP subject were 0.1018, 0.1031, 0.1003, and 4.0168×10^{-4} *uv*, respectively. The mean, maximum, minimum, and standard deviation of the BCI FP1 EEG normalization amplitudes of the health subject were

0.9976, 1.0000, 0.9952, and 7.033×10^{-4} *uv*, respectively. The normalization amplitudes of the BCI FP1 EEG signal of CP subject was samller than that of the BCI FP1 EEG signal for health subject.

47.3 IMF Features of FP1 EEG Signal of Cerebral Palsy

The BCI FP1 EEG signal of CP was decomposed into nine IMFs and one RF. Figure 47.3 shows the IMF1, IMF2, IMF3, and IMF4 of the BCI FP1 signal of CP. Figure 47.4 shows the IMF5, IMF6, IMF7, and IMF8 of the BCI FP1 signal of CP. Figure 47.5 shows the IMF9, and RF of the BCI FP1 signal of CP. The maximum and minimum normalization amplitudes of IMF6 of the BCI FP1 signal of CP were 0.33, and −0.23, respectively. The maximum and minimum normalization amplitudes of IMF7 of the BCI FP1 signal of CP were 0.14, and −0.33, respectively.

The BCI FP1 1 EEG signal of health was also decomposed into nine IMFs and one RF. Figure 47.6 shows IMF1, IMF2, IMF3, and IMF4 of the BCI FP1 signal of health. Figure 47.7 shows IMF5, IMF6, IMF7, and IMF8 of the BCI FP1 signal of health. Figure 47.8 shows IMF9, and RF of the BCI FP1 signal of health.

The maximum and minimum normalization amplitudes of IMF5 of the BCI FP1 signal of health were 3.29, and −3.38, respectively. The maximum and minimum

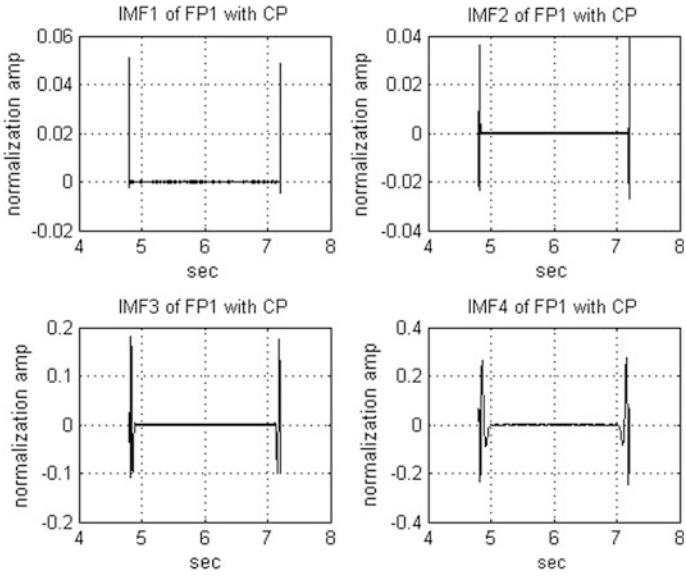

Fig. 47.3 IMF1, IMF2, IMF3, and IMF4 of the BCI FP1 signal of CP

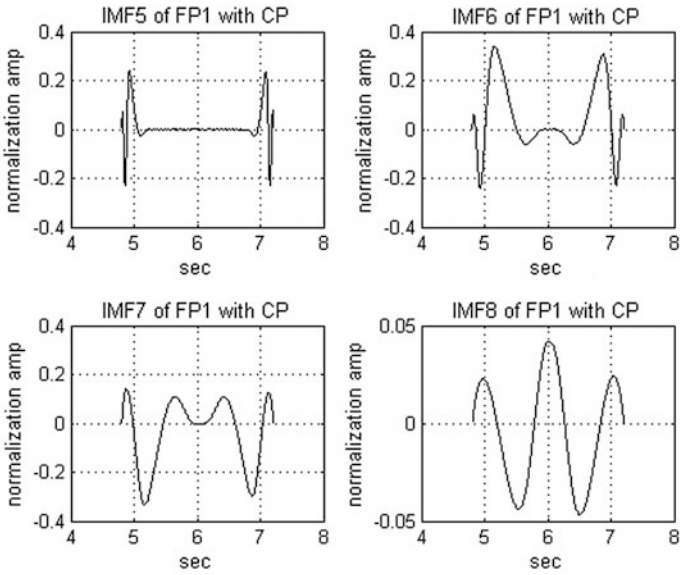

Fig. 47.4 IMF5, IMF6, IMF7, and IMF8 of the BCI FP1 signal of CP

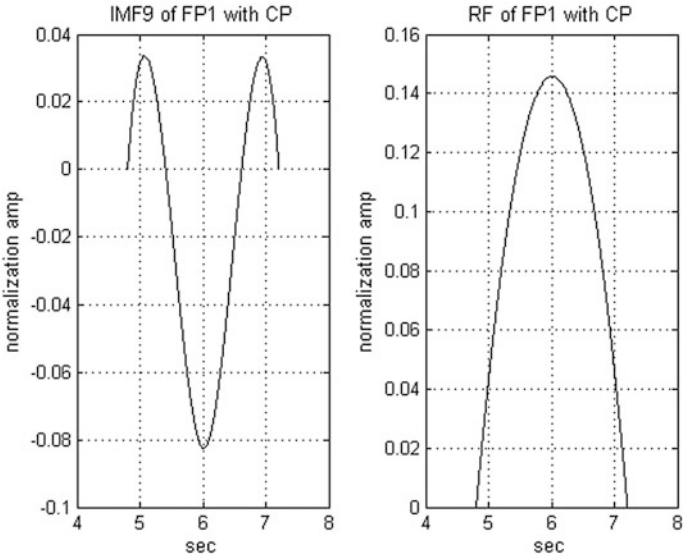

Fig. 47.5 IMF9 and RF of the BCI FP1 signal of CP

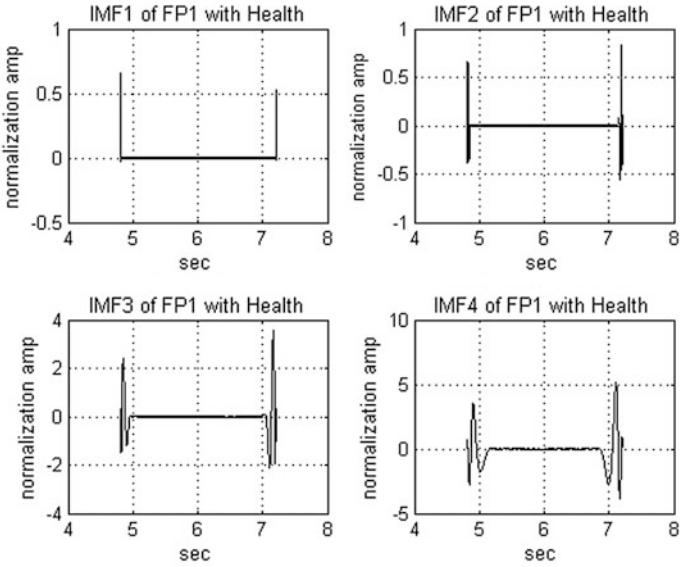

Fig. 47.6 IMF1, IMF2, IMF3, and IMF4 of the BCI FP1 signal of health

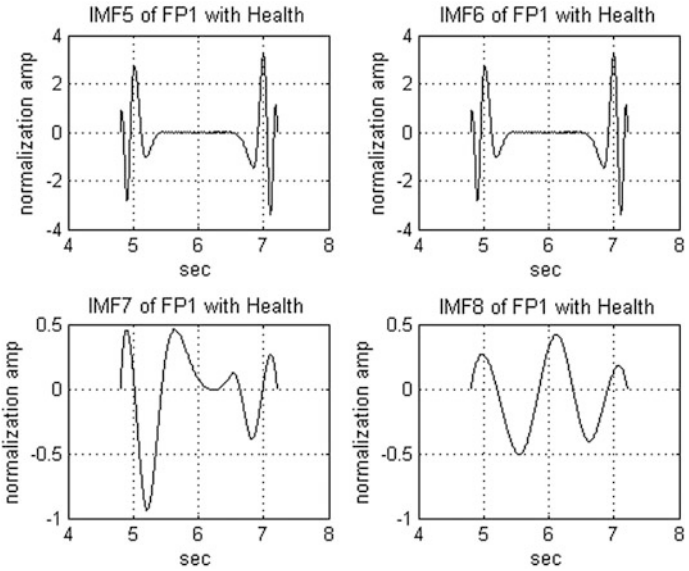

Fig. 47.7 IMF5, IMF6, IMF7, and IMF8 of the BCI FP1 signal of health

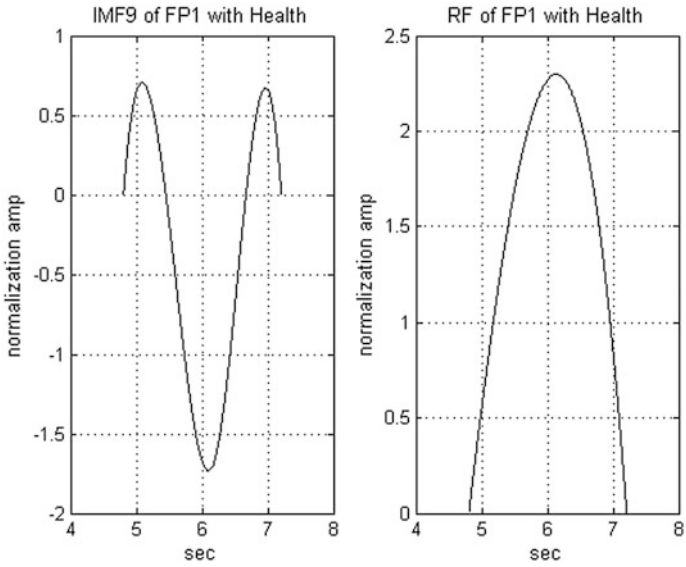

Fig. 47.8 IMF9, and RF of the BCI FP1 signal of health

normalization amplitudes of IMF5, IMF6, IMF7, and IMF8 of the BCI FP1 signal of CP were smaller than that of IMF5, IMF6, IMF7, and IMF8 of the BCI FP1 signal of health, respectively. The energy ratios of the *i*-th IMF to its referred total energy for the CP signal, $IMFERTE_i$ is given by

$$IMFERTEi = \frac{IMF_i^2(t)}{E_{ref}} \times 100\% \tag{47.1}$$

$$E_{ref} = \sum_{i=1}^{N} IMF_i^2(t) + rf^2(t)$$

The $IMFERTE_4$, $IMFERTE_5$, $IMFERTE_6$, $IMFERTE_7$, $IMFERTE_9$, and $IMFERTE_{RF}$ of the BCI FP1 signals of CP and health, respectively, were shown in Fig. 47.9. The blue and brown were shown the CP and health, respectively.

The $IMFERTE_6$, $IMFERTE_7$, and $IMFERTE_{RF}$ of the FP1 signals of CP were 34.36, 32.29, and 18.04%, respectively. The $IMFERTE_4$, $IMFERTE_5$, $IMFERTE_9$, and $IMFERTE_{RF}$ of the BCI FP1 signals of health were 17.93, 16.53, 12.45, and 41.20%, respectively.

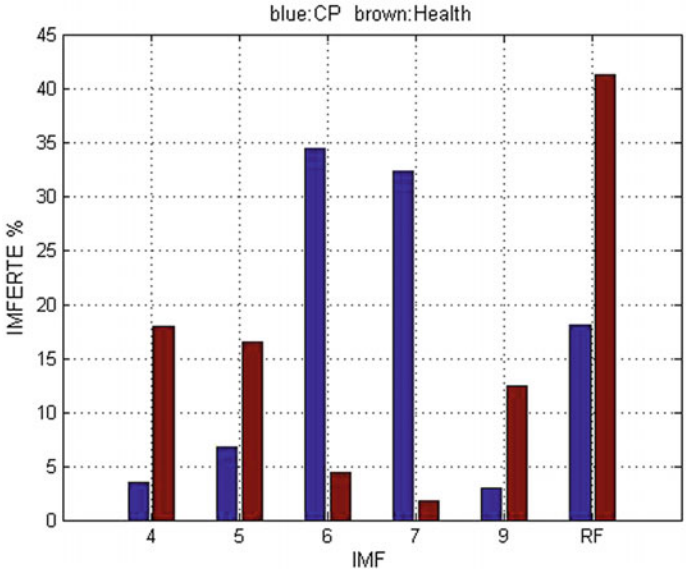

Fig. 47.9 $IMFERTE_4$, $IMFERTE_5$, $IMFERTE_6$, $IMFERTE_7$, $IMFERTE_9$, and $IMFERTE_{RF}$ of the BCI FP1 signal of CP and health, respectively

47.4 MF Features of FP1 EEG Signal of Cerebral Palsy

Figure 47.10 shows the energy ratios of the IMF6 of the wave recorded from the CP and health subjects, after obtaining the 'TL', 'TP', 'L', 'D', 'W', and 'R' images, in the δ band to its referred total energy in the BCI FP1 EEG signals. The energy ratios of the IMF6 of the wave recorded from the CP subject, after obtaining 'W', 'TP', 'R', 'L', 'D', and 'TL' images, in the δ band to its referred total energy in the BCI FP1 EEG signal were 10.42, 7.02, 0.20, 3.65, 12.02, and 7.02%, respectively. The energy ratios of the IMF6 of the wave recorded from the health subject, after obtaining 'L', 'R', 'D', 'W', 'TP', and 'TL' images, in the δ band to its referred total energy in the BCI FP1 EEG signal were 1.32, 0.31, 1.92, 0.04, 0.04, and 0.76%, respectively.

Figure 47.11 shows the energy ratios of the IMF7 of the wave recorded from the CP and health subjects, after obtaining 'TL', 'TP', 'L', 'D', 'W', and 'R' images, in the δ band to its referred total energy in the BCI FP1 EEG signal. The energy ratios of the IMF7 of the wave recorded from the CP subject, after obtaining 'W', 'TP', 'R', 'L', 'D', and 'TL' images, in the δ band to its referred total energy in the BCI FP1 EEG signal were 9.05, 6.84, 0.68, 3.91, 10.45, and 1.20%, respectively. The energy ratios of the IMF7 of the wave recorded from the health subject, after obtaining 'L', 'R', 'D', 'W', 'TP', and 'TL' images, in the δ band to its referred total energy in the BCI FP1 EEG signal were 0.13, 0.06, 0.59, 0.25, 0.01, and 0.70%, respectively. Analysis results show that the energy ratios of the IMF6 and IMF7 of

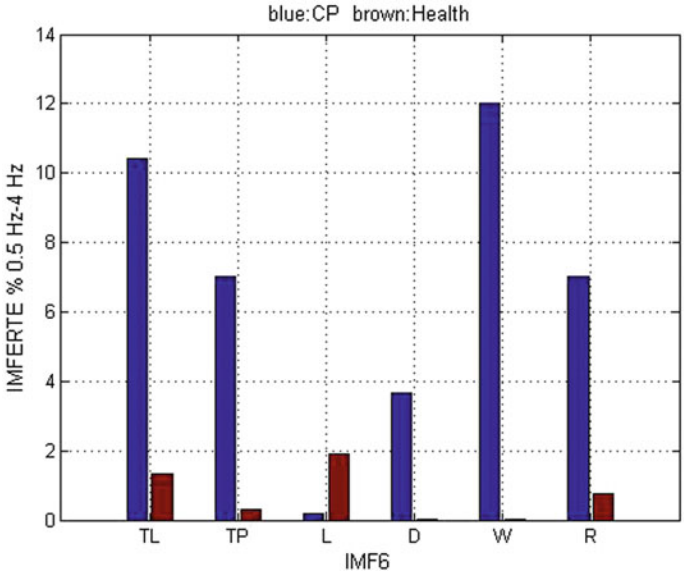

Fig. 47.10 Energy ratios of IMF6 of the wave recorded from the CP and health subjects, after obtaining 'TL', 'TP', 'L', 'D', 'W', and 'R', in the δ band to its referred total energy in the BCI FP1 EEG signal

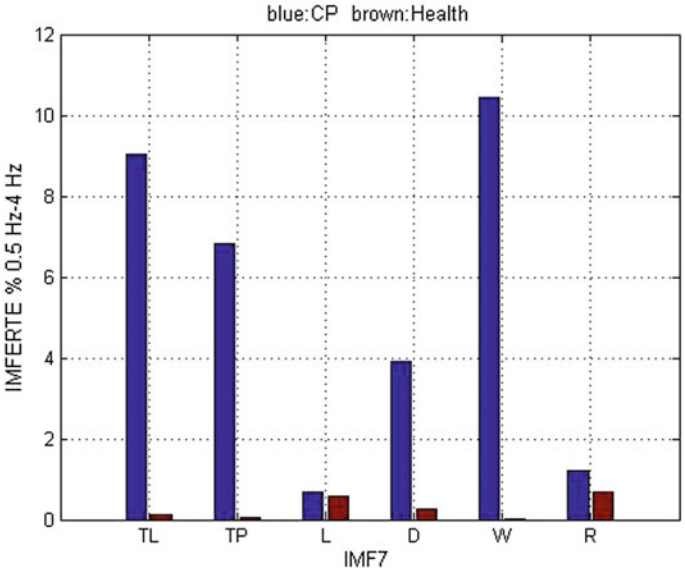

Fig. 47.11 Energy ratios of IMF7 of the wave recorded from the CP and health subjects, after obtaining 'TL', 'TP', 'L', 'D', 'W', and 'R', in the δ band to its referred total energy in the BCI FP1 EEG signal

the wave recorded from the CP subjects, after obtaining the 'TL', 'TP', 'D', and 'W' images, in the δ band to its referred total energy in the BCI FP1 EEG signals were larger than those of the IMF6 and IMF7 of the wave recorded from the health subjects. The energy ratios of the IMF6 and IMF7 of the wave recorded from the CP subjects, after obtaining the 'L', and 'R' images, in the δ band to its referred total energy in the BCI FP1 EEG signals were smaller than those of the IMF6 and IMF7 of the wave recorded from the health subjects.

Figure 47.12 shows the energy ratios of the RF of the wave recorded from the CP and health subjects, after obtaining the 'TL', 'TP', 'L', 'D', 'W', and 'R' images, in the δ band to its referred total energy in the BCI FP1 EEG signals. The energy ratios of the RF of the wave recorded from the CP subject, after obtaining 'W', 'TP', 'R', 'L', 'D', and 'TL' images, in the 0.1–0.2 Hz band to its referred total energy in the BCI FP1 EEG signal were 0.54, 3.11, 5.24, 3.17, 0.54, and 5.20%, respectively. The energy ratios of the RF of the wave recorded from the health subject, after obtaining 'L', 'R', 'D', 'W', 'TP', and 'TL' images, in the 0.1–0.2 Hz band to its referred total energy in the BCI FP1 EEG signal were 1.00, 8.76, 0.91, 11.00, 12.74, and 5.66%, respectively. Analysis results show that the energy ratios of the RF of the wave recorded from the CP subjects, after obtaining 'TL', 'TP', 'D', 'W', and 'R' images, in the δ band to its referred total energy in the BCI FP1 EEG signals were smaller than those of the RF of the wave recorded from the health subjects.

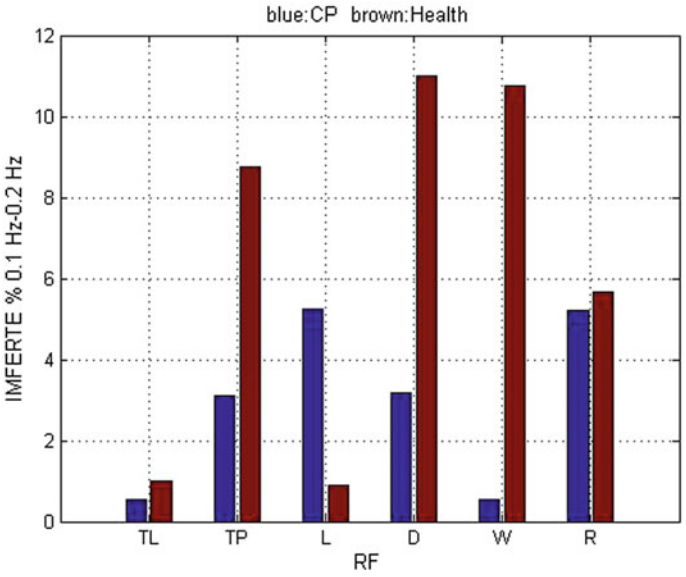

Fig. 47.12 Energy ratios of RF of the wave recorded from the CP and health subjects, after obtaining 'TL', 'TP', 'L', 'D', 'W', and 'R', in the δ band to its referred total energy in the BCI FP1 EEG signal

47.5 Conclusions

In the chapter, the BCI FP1 EEG signals of CP and health were observed, and the energy distributions of IMFs of BCI FP1 EEG signals of CP and health were demonstrated using EMD methods. IMF6, IMF7, and RF were the important IMFs of BCI FP1 EEG signal of CP. IMF4, IMF5, IMF9, and RF were the important IMFs of BCI FP1 EEG signal of health. The energy ratios of IMF6, IMF7, and RF of the wave recorded from the CP and health subjects, after obtaining 'TL', 'TP', 'L', 'D', 'W', and 'R' images, in the δ band to its referred total energy in the BCI FP1 EEG signal were investigated. A new method for energy distributions of IMFs of BCI FP1 EEG signal feature extraction of CP was presented.

Acknowledgements The authors acknowledge the support of the Union Teaching of the Ministry of Education for Medical Electronics in Taiwan, and the valuable comments of the reviewers. The research in partially supported by joint grant of the Russian Foundation for Basic Research and the Ministry of Science and Technology of Taiwan No. 16-58-52013 MNT_a. I.A. Parinov acknowledges financial support from Ministry of Education and Sciences of Russia in the framework of "Organization of Scientific Research" Government Assignment (grant No. 654).

References

1. D.W. McCandles, *Contemporary Clinical, Neuroscience*, vol. 209 (2011)
2. D. Ian, J. Faller, R. Scherer, et al., *Frontiers in Neuroengineering*, vol. 1 (2014)
3. D. Ian, M. Billinger, R. Scherer, et al., *Universal access in human-computer interaction. Design Methods, Tools, and Interaction Techniques for Inclusion*, vol. 623 (2013)
4. K.W. Krigger, Am. Fam. Physician **73**, 91 (2006)
5. M.F. Brigida, P.R. Luis, N. Lau, in *IEEE 12th International Conference on Data Mining Workshops,* vol. 33 (2012)
6. R. Raya, E. Rocon, E. Urendes, et al., Intell. Assistive Robots (2015)
7. N.E. Huang, Z. Shen, S.R. Long et al., Proc. R. Soc. Lond. A **454**, 903 (1998)
8. N.E. Huang, S.S.P. Hen, *Hilbert-Huang Transform and its Applications* (World Scientific Publishing Co., Singapore, 2005), 307 p
9. C.F. Lin, J.D. Zhu, Proc. Inst. Mech. Eng.. Part H. J. Eng. Med. **226**, 208 (2012)
10. C.F. Lin, S.W. Yeh, Y.Y. Chien et al., WSEAS Trans. Biol. Biomed. **5**(10), 249 (2008)
11. C.F. Lin, S.W. Yeh, S.H. Chang, et al., *An HHT-based Time-frequency Scheme for Analyzing the EEG Signals of Clinical Alcoholics* (Nova Science Publishers, USA, 2010), 26 p
12. C.F. Lin, B.H. Yang, T.I Peng, et al., in *Advance in Telemedicine: Technologies, Enabling Factors and Scenarios,* vol. 149 (Intech Science Publishers, Austria, 2011)
13. C.F. Lin, J.Y. Su, H.M. Wang, J. Med. Syst. **39**, 83 (2015)
14. J.D. Zhu, C.F. Lin, S.H. Chang et al., J. Med. Syst. **39**, 170 (2015)
15. http://bci.epfl.ch/p300
16. U. Hoffmann, J. Vesin, T. Ebrahimi et al., J. Neurosci. Methods **167**(1), 115 (2008)

Chapter 48
The Application of Artificial Intelligence for Cleaning Surfaces of the Solar Cells to Improve the Voltage Output

Ahmad Ridho'i

Abstract By increasing number of population, the needs of electrical energy are also increasing. The electrical energy used today still apply fossil materials to generate energy, and therefore the use of renewable energy is required to reduce the energy crisis. Renewable energy is abundant on earth of which sunlight can be used as a source of energy or alternative energy. In order the process of conversion from solar energy into electrical energy is running well, it requires care and monitoring to obtain maximum energy sources. One of the causes that lead to no optimal energy conversion process is a dirty surface of the solar cell. The dirty surface of the solar cell can be due to dust, dirty water and leaves. The dirty surface of the solar cell also disrupts the energy produced by solar conversion. This problem can be overcome by using a programmable device AVR that functions as a processor to produce a system that can monitor the voltage of the conversions generated by the solar cells. By studying the results of the solar cells voltage monitor, the device can determine whether the surface of the solar cell needs in cleaning or not. In addition to monitoring, the voltage is produced by solar cells to ensure the cleanliness of the surface of the solar cell. This device can be used to compare the light sensor generated by the LDR. By comparing LDR and the effective time of the sun, that can be converted, it is produces a voltage that can be used for charging a battery.

48.1 Introduction

Renewable energy concept was introduced in 1970. The most common definition of renewable energy (renewable) is an energy that comes from the energy that can be quickly replenished by nature, with a continuous process. Renewable energy or renewable (renewable energy) is the energy generated by natural resources such as

A. Ridho'i (✉)
Department of Electrical Engineering, Universitas 17 Agustus 1945 of Surabaya, Surabaya, Indonesia
e-mail: ridhoi@untag-sby.ac.id

I.A. Parinov et al. (eds.), *Advanced Materials*, Springer Proceedings in Physics 193, DOI 10.1007/978-3-319-56062-5_48

energy derived from natural processes that are sustainable, such as radiation (rays) of the sun, wind, biological processes, biomass and geothermal. All renewable energy is abundant, especially in the tropics where there is sunlight. Solar energy can be retrieved used as electrical energy through solar cell as energy conversion. There are two types of solar cell: monocrystalline and polycrystalline, demonstrating different characteristics such as:

(i) *Physical differences.* Difference of monocrystalline and polycrystalline solar cells can be seen in Fig. 48.1.
(ii) *Tolerance to temperature.* Monocrystalline and polycrystalline solar cells have tolerance to high and temperatures, respectively.
(iii) *Energy conversion efficiency*. Solar cell efficiency is the ratio of electrical output energy generated by solar cell to the amount of sunlight energy, received by solar cell surface.

Solar cell is a device that will work optimally in the case when sun-exposed surface is no dirty. In the use of solar cell, it is sometimes placed in remote areas or areas of high pollution on the highway and usually used as a source of energy for PJU.PJU, located on the highway. However, the dust, produced by vehicles every day, results in the buildup of dust on the surface of the solar cell. For dirty surface of the solar cell, conversion of solar energy into DC voltage that is then stored in the battery becomes maximum energy stored in the battery. For solar cell, installed in remote locations (with aim to detect energy resources of floods and landslides, as we had performed in the framework of the grant program I_bM), there is generally minimal understanding on energy sources of solar cell. So remote areas that may be

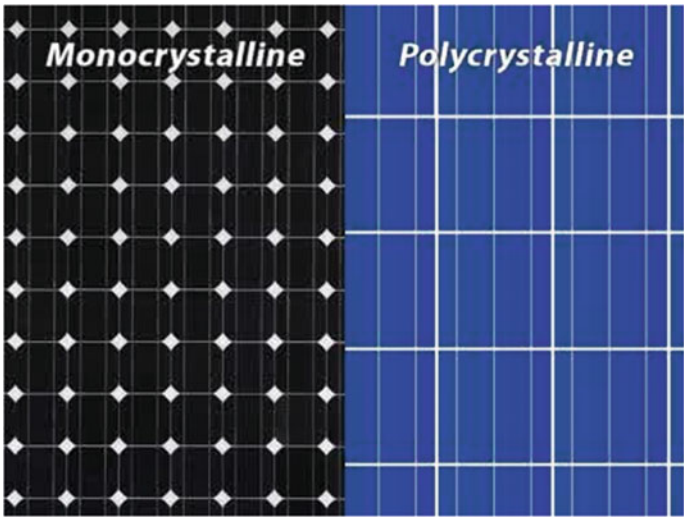

Fig. 48.1 Display of monocrystalline and polycrystalline solar cells

many trees lead to the desecration cell solar surface with the leaves of the tree landed on the surface of the solar cell.

Solar cell is composed of smaller elements called solar cells. The structure of the solar cell is shown in Fig. 48.2 in simple form.

Metal grids form one of the electrical terminals of semiconductor. The sunlight will enter through a metal grid and cause contact with semiconductor components and then electrical energy will be formed. Artireflective layer serves to increase the amount of light entering into the semiconductor. Electric energy is formed, when the hole (h^+) and electrons (e^-) arise from incoming solar light energy to the solar cell. The amount of the energy formed can be given by the following equation:

$$E_\lambda = \frac{h_c}{\lambda},$$

where E_λ is the energy of photon, h is a Planck's constant 6.6261×10^{-34} J s, c is a speed of light 3×10^8 m/s, and λ is the wavelength. All the electromagnet radiation, including sunlight can be considered as a photon particles that carry energy. The amount of energy carried is defined from the above equation. Only the photons have enough energy to form electron-hole pairs. This energy must be greater than the bandgap (threshold) of the semiconductor. Schematic and flow of electrons from the solar cell are present in Fig. 48.3.

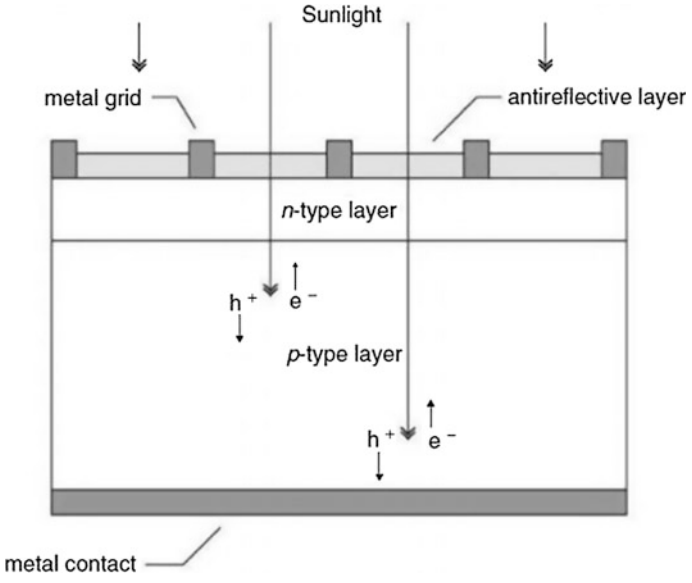

Fig. 48.2 Scheme of solar cell

Photon will go through the valence band. Photons with energy greater than the bandgap will form a hole-electron pairs in the conduction band. Valence band is part of the *p*-type layer, while the conduction band is part of *n*-type layer (see Fig. 48.2).

48.2 Method

For this study there is a block diagram in Fig. 48.4, which is the system performing voltage measurements of the solar cell and the battery voltage in real time, which uses programmable devices (microcontroller).

Voltage sensor and current sensor are used in sensor battery during charging and during use of the battery (in absence of electric load). Longevity of the battery is determined by the battery capacity and power of the electric load. Battery charging

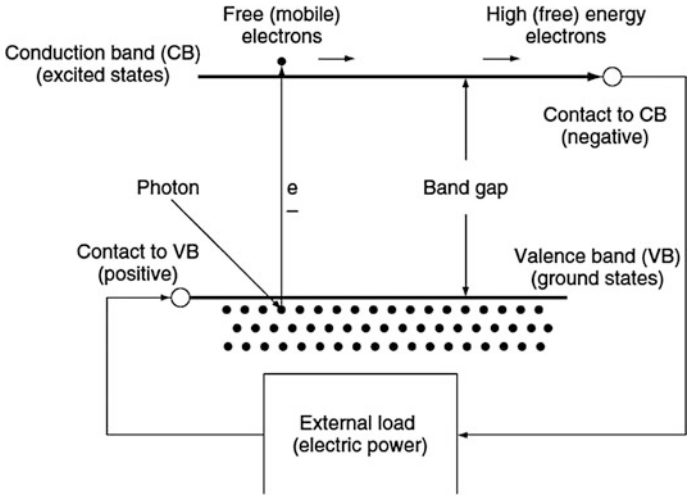

Fig. 48.3 Solar cell

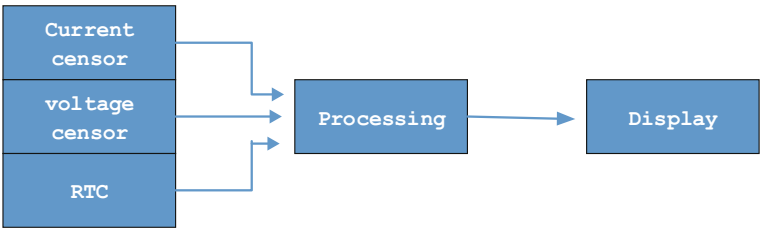

Fig. 48.4 Diagram of voltage and current monitoring

time depends on battery capacity (ampere—hour) and how many amperes of charging device. By using auto charger off (will stop charging if the battery is full), the voltage sensor and current sensor scan and detect the battery condition.

Input system is part of the system that serves to generate data from the detected voltage during battery charging and loading sensors in the system including the voltage sensor, current sensor and RTC serves as a timing reference.

Voltage sensor. Battery is a device that stores electrical energy of dc functioning; normal conditions the battery voltage ranges from 12 to 13 V (without any load). Having regard to the normal battery, the voltage range can be as a reference to the system processor (microcontroller). By using the charger circuit auto off, we can stop charging if the battery voltage is equal to the voltage charger. Measurement of the battery voltage is possible using a voltmeter (see Fig. 48.5).

Measurement Results of battery condition are present in Table 48.1.

Utilizing a voltage sensor circuit voltage divider is shown between the two resistors in Fig. 48.6.

Let us use a voltage divider obtained in accordance with the voltage change in the battery. If the maximum voltage of the battery is 12 V DC, it is necessary to divide the voltage between 0 and 5 V in order to be read by the microcontroller. To get the voltage at the voltage divider circuit, R_1 and R_2 values can be obtained as

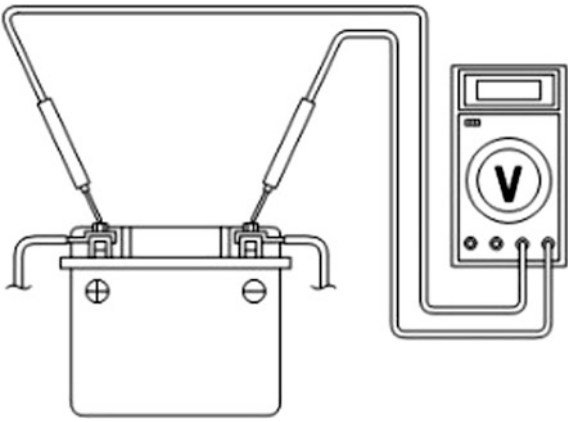

Fig. 48.5 Measurement of the battery with a voltmeter

Table 48.1 Battery condition

Condition (%)	Sealed lead acid (MF) battery/normal			Lithium battery		
	No load	On contact	With load	No load	On contact	With load
100	>12.70	>12.4	>11.4	>12.85	>12.65	>12.3
75	12.4–12.7	12.2–12.4	11–11.4	12.6–12.8	12.3–12.6	12–12.3
50	12.2–12.4	12–12.2	10.6–11	12.3–12.6	12–12.3	11.8–12
25	12–12.2	11.8–12	10.2–10.4	12–12.3	11.8–12	10.6–12
0	<11.8	<11	<10	<11.8	<11	<10.4

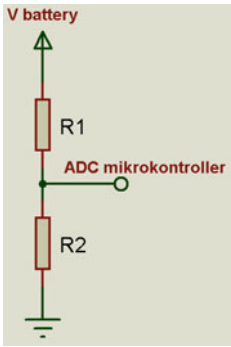

Fig. 48.6 Voltage sensor circuit; $V_{R_2} = \frac{R_2}{R_1 + R_2} . V_{battery}$

$$V_{out} = V_{in} \cdot \frac{R_2}{R_2 + R_1};\ 2V_{DC} = 12V_{DC} \cdot \frac{R_2}{R_2 + R_1}.$$

Then for R_2 = 2 kΩ, we have R_1 = 10 kΩ
At any drop 1 V, we obtain:

$$V_{out} = V_{in} \cdot \frac{R_2}{R_2 + R_1} \text{ or } V_{out} = 1.83\,V.$$

So for every decrease of 1 V on the battery, the output voltage sensor has a sensitivity equal to: V_{delta} = V_{out} (at 12 V) − V_{out} (at 11 V) = 0.17 V DC.

Current sensor uses Ohm concept. The Ohm's law states that a large electric current flowing through a conductor is always proportional to the potential difference applied to it. By using the circuit as shown in Fig. 48.7 and load resistor in series, a series circuit has large values of current, which are the same at each point, but the magnitudes of voltage across the resistors/barriers are not the same.

Let us determine the total current in the above circuit by using formula: V_{out} = $I_{total}R_p$

Then for V_{out} = 1 V DC, we obtain I_{total} = 4 A and for V_{out} = 0.75 V DC, we have I_{total} = 3 A. So the output current sensor has a sensitivity defined as a load current difference in 1 A at the output corresponds to a voltage difference of 0.25 V.

Timer (RTC). It is necessary to ensure that the sun until sunset can be detected on time. Time itself is generated by the RTC (real time clock), the output of the RTC are dates (date) and the clock (time). From plants generated by the RTC DS1307 component such as date and time, the microcontroller can read the date and time shown in the DS1307. So it can be effective to detect the time of the sun, that can be used to generate electrical energy, due to corresponding disposition of the solar cell.

Processing is part of a system, which functions to process the input parameters (voltage, current) using AVR microcontroller. The AVR microcontroller has an internal ADC—a current sensor is indispensable for conversion of value, generated

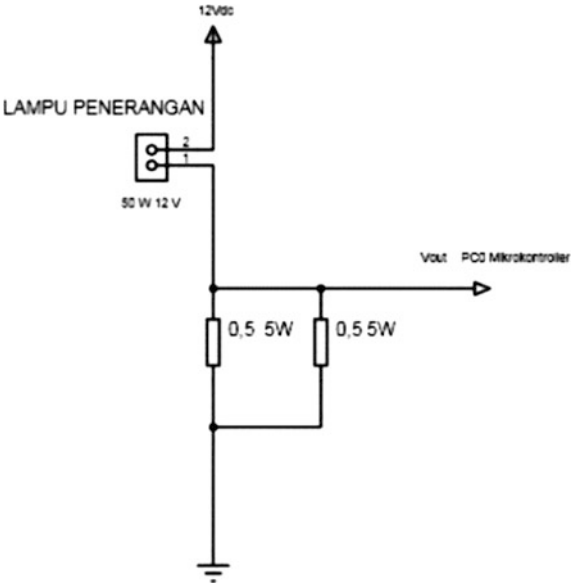

Fig. 48.7 DC current sensor circuit

by a voltage sensor. By getting the value from the conversion performed by an internal ADC-processor, it can be generates voltage value defined as

$$Volt_{acceptable} = \frac{binary_{acceptable}}{binary_{reference}} Volt_{\max\_input}$$

By using this way, the voltage and current values can be read and their values can be processed by a microcontroller, which can then be used to determine the effectiveness of the electrical energy storage in batteries.

The output (display) is section of information carried by a microcontroller that is an indicator of LCD (liquid crystal display) to provide information on voltage, current, and time. The processed values of voltage and current are displayed on the LCD, allowing us to obtain information on the battery voltage and current, which can be monitored at any time.

Planning in the planning system of voltage and current readers can determine the condition of the battery as electrical energy storage media. There are two types of planning, namely planning hardware and planning software.

Planning hardware is required to establish the system microcontroller using ATMEGA family as the processor, the processed value of the output of the voltage sensor and solar cell battery, the charging current sensor. By using the measurement of the solar cell, connected to a 16 V charger to create a system able to respond well, the voltage across the resistor can be calculated by the next way (see Fig. 48.8).

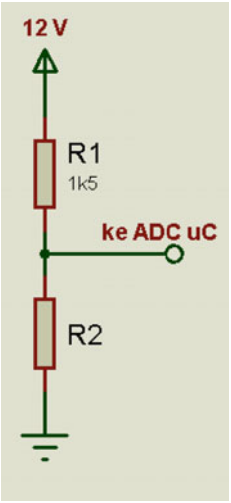

Fig. 48.8 Voltage sensor

If $R_1 = 1.5\ \text{k}\Omega$, $V_{battery} = 13.8\ \text{V}$, $V_{max\_ADCuC} = 5\ \text{V}$. Then by using the formula:

$$\frac{R_2}{R_1 + R_2} V_{battery} = V_{max\,ADCuC}$$

we obtain $R_2 = 852.273\ \Omega$.

The resistor value approaching 852.273 Ω is 820 Ω, so for the highest voltage of the battery of charging current is equal to 13.8 V, we read on the microcontroller 's internal ADC:

$$V_{inADC} = \frac{820}{820 + 1500} \times 13.8 = 4.878\,\text{V}$$

By regarding V_{inADC} voltage that is still in the allowable voltage interval, the ratio of resistors R_1 and R_2 can be used in the system as a voltage sensor. Planning processor uses AVR microcontroller (see Fig. 48.9) with planning PORTB such as LCD displays, while PORTA0 … PORTA3 are used as input voltage sensor and current sensor, which detect the voltage in the battery and the voltage in the solar cell. There are two sensors, processing circuit voltage, and two current sensors, which enable us to define the voltage before the charger circuit, used to determine the voltage of a solar cell, and estimate the voltage after the same charger to the battery voltage.

Planning software is intended in order to the system microcontroller can function according to the purpose of this study. The embedded microcontroller device is used in the form of a command programming language. Here we use the programming language C, for logic programs in the form of lowchart (see Fig. 48.10), which describes a command cycle, embedded in the microcontroller.

First microcontroller of initializing contains determination of the constants, related to the processing, performed by the microcontroller; sensor readings are

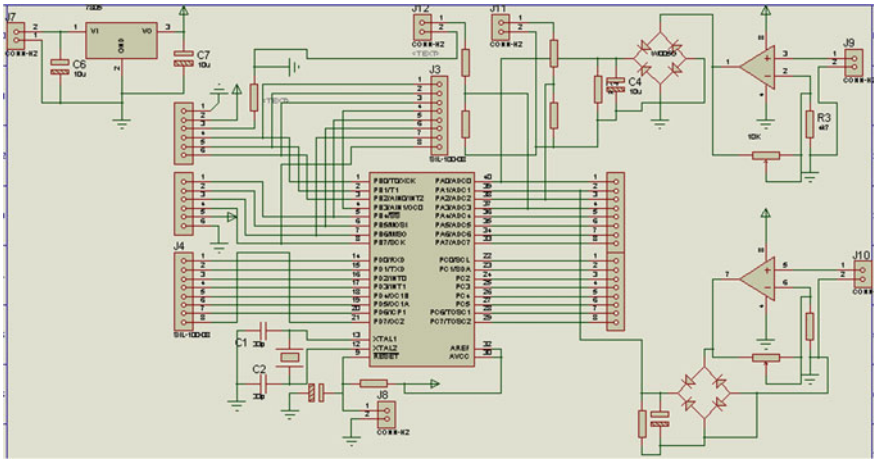

Fig. 48.9 AVR microcontroller circuit

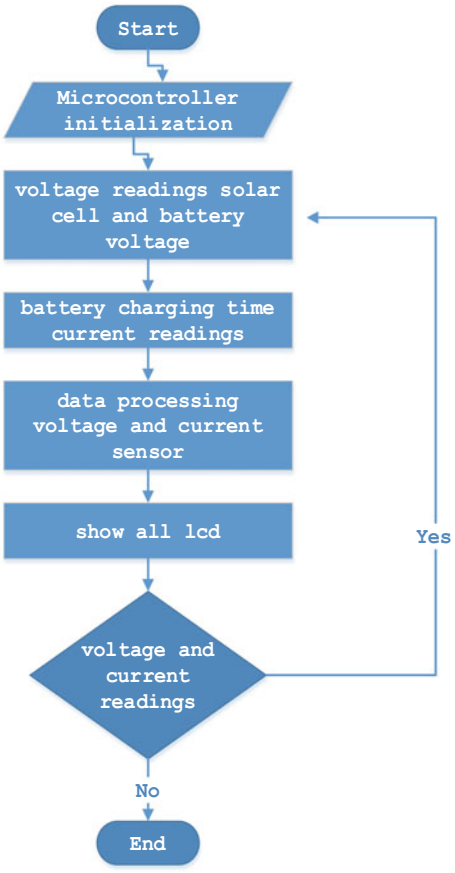

Fig. 48.10 Flowchart of logic program

conducted at intervals from sunrise to sunset. The voltage and current sensor readings are then processed and displayed on the LCD that can be observed and compared with existing measurement tools. Thus, it can be determined whether the detected voltage and current can perform battery charging. Charging stops if the read current is close to zero, as a harbinger of avoiding any conversion of sunlight energy into electrical energy.

48.3 Results and Discussion

In testing, the system carried out two major parts of testing program logic by using application software (simulator). It is performed to ensure that the program logic has been designed in accordance with the purpose of research. In addition to proving the truth, the logic level simulator program saves time and costs (Fig. 48.11).

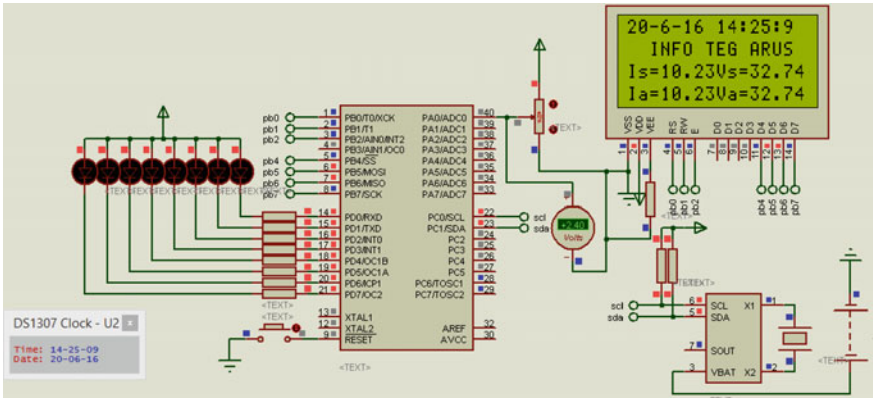

Fig. 48.11 Hardware testing with simulator

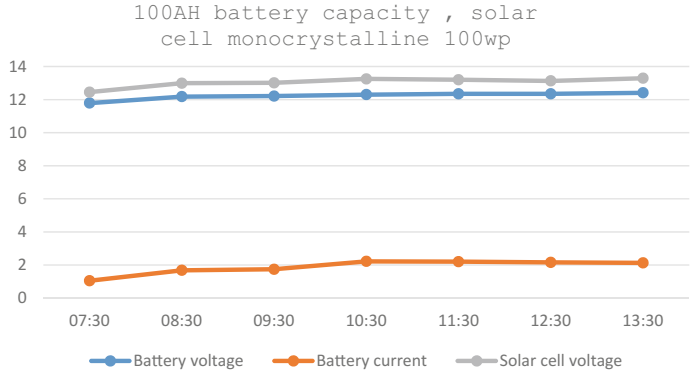

Fig. 48.12 Measurement results of voltage and current

By testing the logic test ADC0, to leave a port with a voltage range from 0 to 5 V, it can be read like the 4 × 16 LCD. Similarly, to use the time generated by the RTC, it is read the date and time, when take voltage and current on the solar cell and battery.

The results of the measurements of voltage and current on the solar cell and battery are present in Figs. 48.12 and 48.13.

The system and measuring equipments for solar cell voltage measurement are presented in Figs. 48.14 and 48.15.

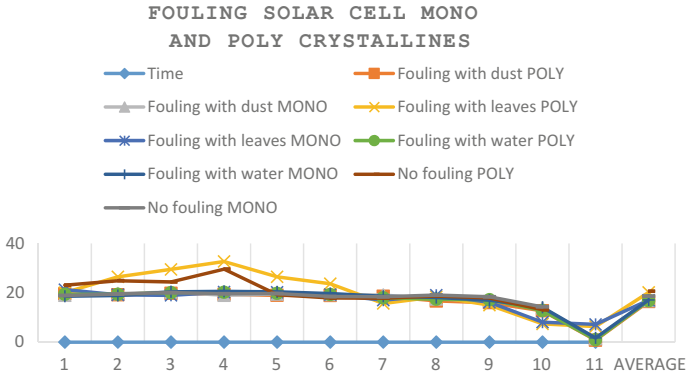

Fig. 48.13 Measurement of voltage at fouling on the solar cell poly and mono crystallines

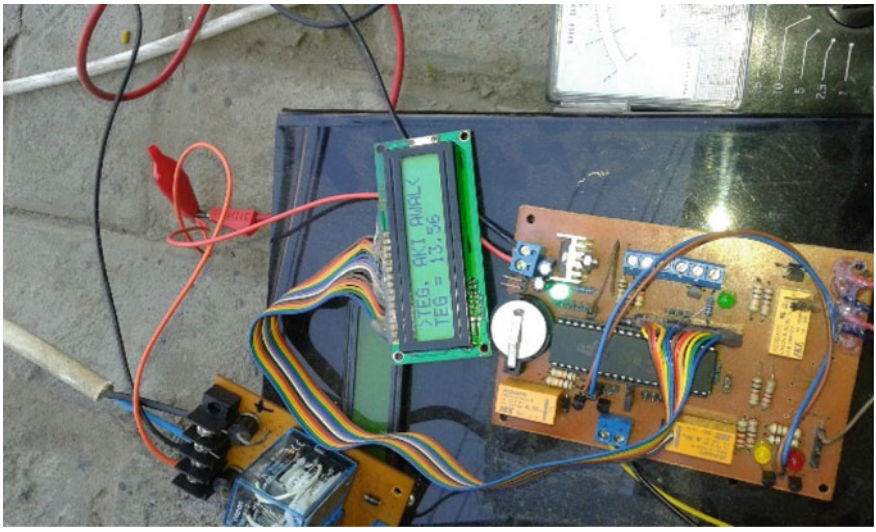

Fig. 48.14 Solar cell voltage measurement with the system and measuring tools

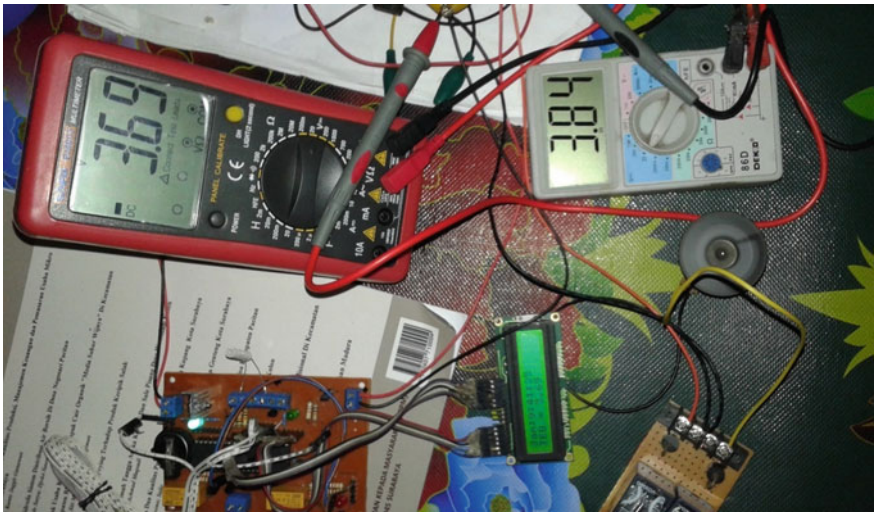

Fig. 48.15 Solar cell voltage measurement with the system and measuring equipment with drive of the dc-motor

48.4 Conclusion

1. Resistor voltage divider can be used to detect the DC voltage on the solar cell and battery, and detection is linear.
2. The closure affects the output voltage of the solar cell surface and the current generated by the solar cell; it is evident a cloudy weather affects the voltage and current produced by solar cell, battery charging is reduced further.
3. The output voltage is performed by solar cell and can be influenced by the presence of impurities that exist on the surface of solar cell, in average, a voltage drop due to fouling the polycrystalline solar cell greater compared to the solar cell of monocrystalline type.
4. Solar cell works well for alternative energy source when the sun rays directly fall on the surface of the solar cell.
5. No perpendicular placement of solar cell leads to the 80% current only and therefore the sun's surface will determine the current generated by the solar cell.
6. Overcast conditions lead to 75% decreasing for monocrystalline solar cell, reducing charging the battery.

Acknowledgements The author thanks Higher Education that has funded this research during 2015/2016.

References

1. K.J. Ayala, *The 8051 Microcontroller Architecture, Programming, and Application* (Wesh Publishing Company, 1991)
2. A.S. Sedra, *Microelectronic Circuit* (Oxford University Publishing Press Inc, 2004)
3. J. Stephen, *Fonash* (Elsevier Inc, Solar Cell Device Physics, 2010)
4. A.R. Jha, *Solar Cell Technology and Applications*, Ph.D. Thesis, Auerbach Publications, 2010
5. H. Nasution, H. Jamaluddin, J.M. Syeriff, *TELKOMNIKA*, **9**(1) (2011)
6. M. Mardiyono, R. Suryanita, A. Adnan, *TELKOMNIKA*, **10**(1) (2012)
7. U. Hasan, H. Dedid Cahya, *Sistem Charging Baterai Pada Perancangan Mobilhybrid*, Institut Teknologi Sepuluh Nopember, Surabaya, Indonesia
8. D.Y. Wafi, S. Anam, H. Suryoatmojo, *Optimasi dan Manajemen Energi Kelistrikan Di Gedung City of Tomorrow*, Jurusan Teknik Elektro, Fakultas Teknologi Industri, Institut Teknologi Sepuluh Nopember, Surabaya, Indonesia

Chapter 49
Novel Optical Interference Means to Measure Small Linear and Angular Displacements of Control Object Surfaces

I.P. Miroshnichenko, I.A. Parinov, J.-K. Wu, W.-L. Hong and M.-Y. Yeh

Abstract The results of the development and experimental study of the optical interferometric means are present for contactless measurement of small linear and angular displacement of control object surfaces in the diagnostics of the state of materials and goods by using acoustic methods of nondestructive testing.

49.1 Introduction

The development and use of high-precision contactless measuring means of small displacements of control object surfaces, based on modern laser technology and optical interferometry methods for recording information at quality control and diagnostics of materials and power components of goods by acoustic non-destructive testing (NDT) methods significantly improve the accuracy, quality and informativeness of measurements [1–7].

Currently, one of the most promising solutions for scientific and industrial problems of diagnosing the state of construction materials and goods at different stages of their life cycle and experimental research of damage processes in new

I.P. Miroshnichenko (✉)
Don State Technical University, Rostov-on-Don, Russia
e-mail: ipmir@rambler.ru

I.A. Parinov
I.I. Vorovich Mathematics, Mechanics and Computer Science Institute, Southern Federal University, Rostov-on-Don, Russia

J.-K. Wu
Department of Marine Engineering, National Kaohsiung Marine University, Kaohsiung, Taiwan

W.-L. Hong
National Kaohsiung Marine University, Kaohsiung, Taiwan

M.-Y. Yeh
Department of Microelectronics Engineering, National Kaohsiung Marine University, Kaohsiung, Taiwan

I.A. Parinov et al. (eds.), *Advanced Materials*, Springer Proceedings in Physics 193, DOI 10.1007/978-3-319-56062-5_49

constructional materials is a two-way laser interferometer with combined branches, adapted to solve measurement tasks [8–11], the type scheme of which is shown in Fig. 49.1.

This interferometer comprises optically connected in series and placed source 1 of coherent optical radiation, an optical system 2, a beam splitter 3, a reflector 4 mounted on a surface 5 of a control object 6 and a screen 7 with photodetector devices 10, mounted on its. In this case, the beam splitter 3 and the reflector 4 are arranged relative to each other under an angle α. The obtained by combining reference beam 11 and object beam 12 an interference pattern 8 presents itself a set of rings 9 with different intensities. This picture is projected onto the screen 7 and the photodetector devices 10 are mounted in the rings 9 of the interference pattern 8.

One of the main and actual directions of modification of the interferometer with respect to solving measurement tasks includes the expansion of its functionality by allowing simultaneous measurement of linear and angular components of small displacements of control object surfaces.

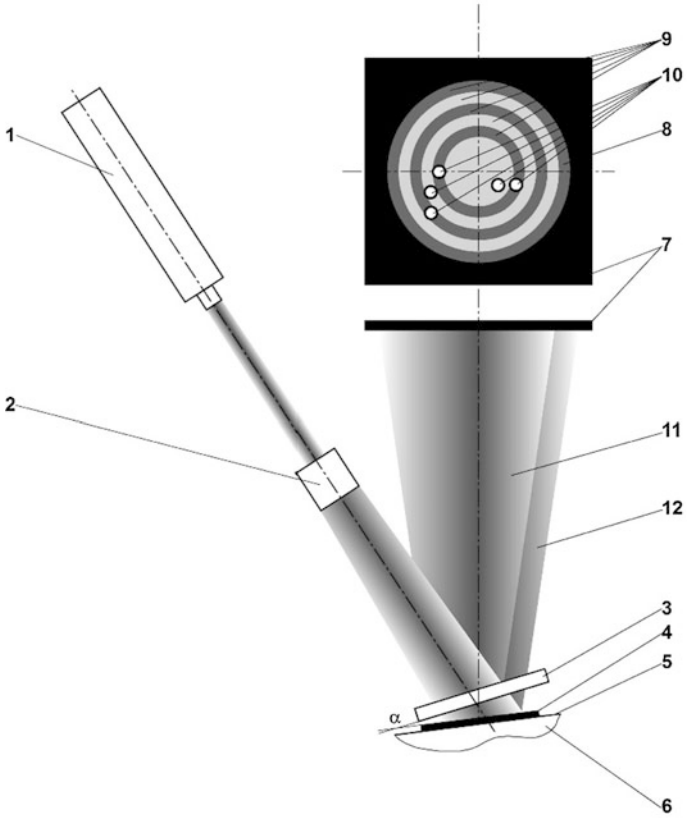

Fig. 49.1 Typical scheme of two-way laser interferometer with combined branches

The aim of the study was to develop computational and experimental grounds of the optical interferometric means for contactless measurement of linear and angular components of small displacements of control object surfaces at the diagnostics of the state of materials and goods by using acoustic NDT methods, based on the two-way laser interferometer with combined branches.

49.2 Numerical Modeling and Analysis of Results

New mathematical models have been developed which described the fields of optical interference patterns created by the interferometer under consideration. It has been proposed a new original software that implemented above mathematical models. They were secured by certificates of the Russian state registration of the computer programs. The selected results were described in detail in [12–14].

A numerical simulation of the intensity distribution in the interference patterns produced by a laser interferometer under consideration by using these mathematical models and software; we used various types of beam splitters and different cases of polarization.

Some of the results are shown in Figs. 49.2, 49.3, 49.4, and 49.5. Figure 49.2 shows the distribution of the intensity I (Θ) in the horizontal cross-section of the interference pattern along the Θ-coordinate in the field of observation of the interference pattern in the case of parallel polarization, when it is used amplitude sinusoidal grating as a beam splitter in the considered interferometer. Figure 49.3 presents the results for the case, when an amplitude sinusoidal grating with the perpendicular polarization is used as a beam splitter. Figure 49.4 shows the results for the case, when a phase sinusoidal grating with perpendicular polarization is used

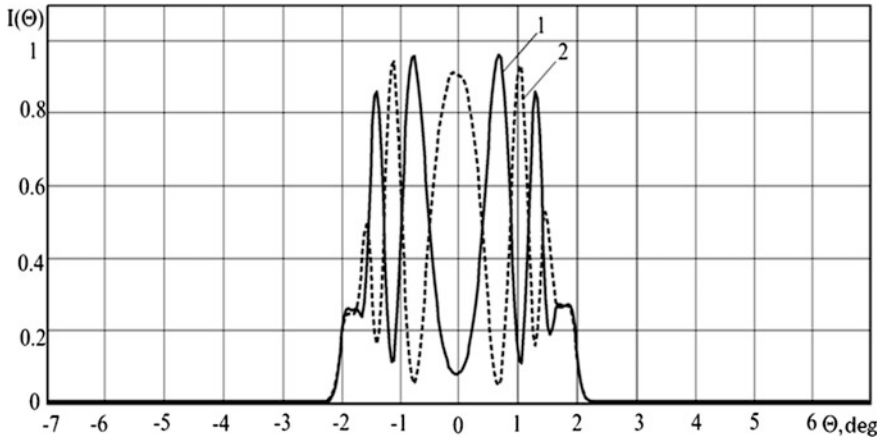

Fig. 49.2 Intensity distribution in the horizontal cross-section of the interference pattern (beam splitter is the amplitude sinusoidal grating with parallel polarization)

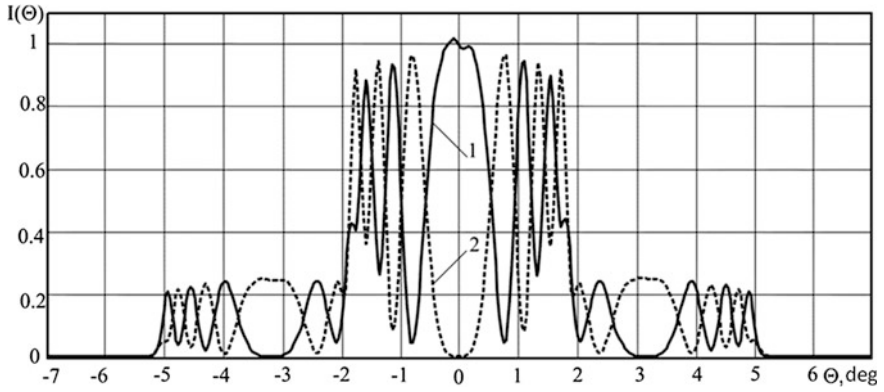

Fig. 49.3 Intensity distribution in the horizontal cross-section of the interference pattern (beam splitter is the amplitude sinusoidal grating with perpendicular polarization)

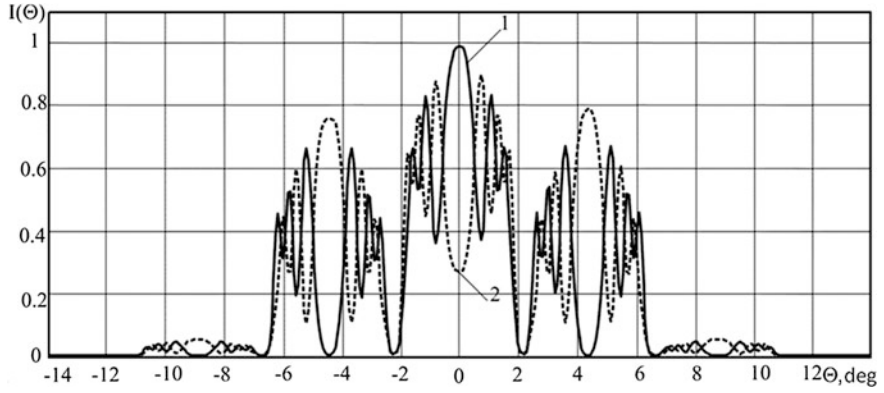

Fig. 49.4 Intensity distribution in the horizontal cross-section of the interference pattern (beam splitter is the phase sinusoidal grating with perpendicular polarization)

as a beam splitter. Figure 49.5 demonstrates the results for the case, when a phase zone plate with perpendicular polarization is used as a beam splitter. We used the following designations in Figs. 49.2–49.5: 1—dependence obtained at linear displacement $\Delta h = 0$ and angular displacement $\Delta\alpha = 0°$; 2—dependence defined at $\Delta h = \lambda/4$ and $\Delta\alpha = 0°$, where λ is the wave length of the optical radiation of source.

Analysis of the results of numerical modeling for various types of beam splitters showed that in the case of perpendicular polarization, when the electric field vector lies in a plane perpendicular to the plane of incidence, it is possible to more fully investigate the effects of diffraction properties of beam splitters on the parameters of the formed interference pattern, than in the case of parallel polarization.

The analysis results also showed that when we used as beam splitters the amplitude gratings, diffraction maxima of −1 and +1 orders are formed (see, Fig. 49.3), When we used phase gratings, besides these maxima, there are additional maxima of higher orders (see, Figs. 49.4 and 49.5).

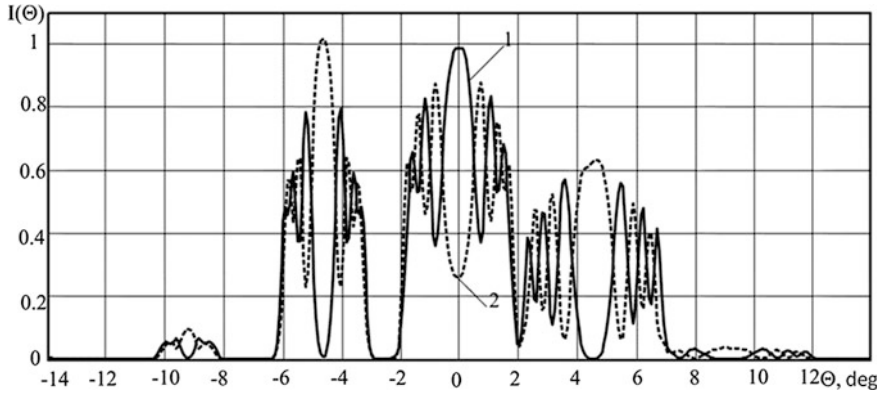

Fig. 49.5 Intensity distribution in the horizontal cross-section of the interference pattern (beam splitter is the phase zone plate with perpendicular polarization)

The application of phase gratings in solving measurement problems is rather promising, because it allows one to get at the maxima of −1, 0 and +1 orders approximately the same amplitudes of intensity variation. In this case, the amplitudes of the intensity at the maxima of −1 and +1 orders of magnitude are higher than in the corresponding maxima, formed by using an amplitude grating.

The simulation results showed that the developed mathematical models and software make it possible to investigate the influence of the beam splitter type and other parameters of the considered interferometer on the formed interference patterns. It provides the numerical determination of optimal parameters of the measurement means for given measuring system and specific measurement problem.

49.3 Method for Measuring Linear and Angular Components of Small Displacements and Its Calculation-Theoretical Grounds

The results of numerical simulation described above allowed us to develop a new method for the measurement of linear and angular components of small displacements of control object surfaces. It analyzes the intensity distributions at the maxima of −1 and +1 orders of the interference pattern. From simulation results, it follows that under comparison condition, the intensities I^{-1} and I^{+1}, respectively at the maxima of −1 and +1 orders of the interference pattern change equally, otherwise the nature of changes in intensity at the maxima of the pointed orders is different.

Measuring the intensity of I^{-1} and I^{+1} at the maxima of −1 and +1 orders of the interference pattern allows us instead of the equation with two unknowns to obtain a set of equations respectively of Δh and $\Delta\alpha$ (linear and angular components of small displacement of the control object surface) in the form:

$$\begin{cases} I^{-1} = f_1(\Delta h, \Delta\alpha); \\ I^{+1} = f_2(\Delta h, \Delta\alpha); \end{cases} \tag{49.1}$$

where $f_1(\Delta h, \Delta\alpha), f_2(\Delta h, \Delta\alpha)$ are the known dependencies, respectively, for the maxima of the −1 and +1 orders, coupling, respectively, the intensities with linear Δh and angular $\Delta\alpha$ components of small displacement of the control object surface. The values of Δh and $\Delta\alpha$ satisfying Equation set (49.1) will be correspond to actual displacement of the object.

Let us show this on specific example.

During numerical modeling, we obtained the dependencies of the intensity on h in the range from $h = 0.0052$ m to $h + 0.5\lambda$ m for the values of $\alpha = 0.07° + \Delta\alpha$ at the maxima of −1 and +1 orders. The pointed dependencies for the values of $\Delta\alpha = 0°$, $\Delta\alpha = 0.003°$, $\Delta\alpha = 0.006°$ are shown in Fig. 49.6a (at the maximum of −1 order), and 6b (at the maximum of +1 order).

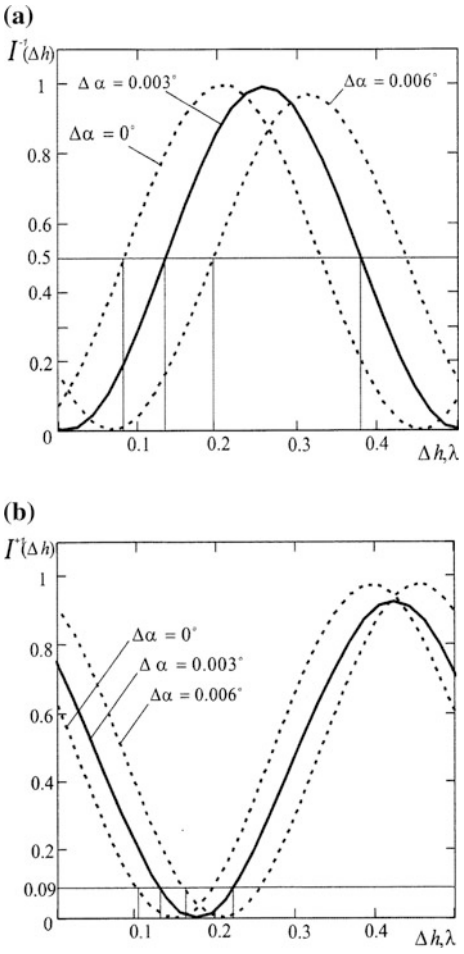

Fig. 49.6 Results of numerical modeling

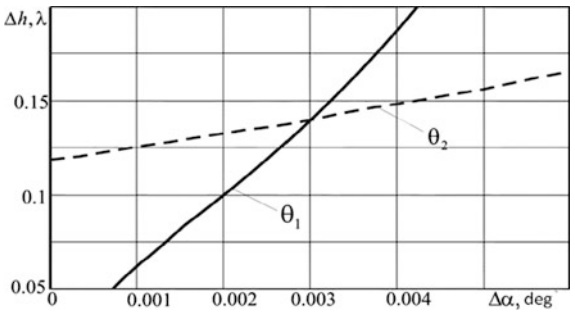

Fig. 49.7 Example of task solution

To explain the essence of this method, let in the result of measuring we obtained the values of intensity $I^{-1} = 0.5$ and $I^{+1} = 0.09$. From Fig. 49.6a, it follows that numerous pairs $\Delta\alpha$ and Δh correspond to $I^{-1} = 0.5$, for example: $\Delta\alpha = 0°$, $\Delta h = 0.08\lambda$; $\Delta\alpha = 0.003°$, $\Delta h = 0.14\lambda$; $\Delta\alpha = 0.006°, \Delta h = 0.2\lambda$; and so on; it is similar for $I^{+1} = 0.09$.

However, these sets have only one common point, which is the solution of the system of (49.1), namely point: $h = h + 0.14\lambda$, $\Delta\alpha = 0.073°$ (see Fig. 49.7). To construct the dependencies in this figure intensity, we recorded the values of intensities $I^{-1} = 0.5$ and $I^{+1} = 0.09$ in the directions Θ_1 and Θ_2, respectively, for maxima of −1 and +1 orders, at which have been measured intensities I^{-1} and I^{+1}.

These dependencies can be obtained by graphical method from the results part of which is present in Fig. 49.7. According to the results of numerical study of the developed method of measurements, it has been developed a method, realizing the proposed method of measurements by solving practical measurement problems.

49.4 Experimental Research and Analysis of Its Results

In the experimental study, we used an experimental setup that allowed us to provide a separate and simultaneous playback of the given linear and angular components of small displacements. The experimental setup is shown in Fig. 49.8.

The setup contains optically coupled and sequentially arranged source of coherent optical radiation 1 (He–Ne laser, wavelength $\lambda \approx 0.63$ μm), a focusing lens 2, an aperture of the spatial filter 3, a beam splitter 4, rigidly mounted at the device 13, a reflector 5, a screen 6, a digital photodetector 7, registration and processing device 11 (PC).

To create the simulated linear and angular components of small displacements, the reflector 5 is mounted on a piezoelectric element 8 by means of two plates 16 and 17, which are at one edge connected by a hinge 15, and on the other edge are rigidly connected to a piezoelectric element 18. The controls of a retention mechanism 12, of the piezoelectric element 8 are used for alignment of the setup

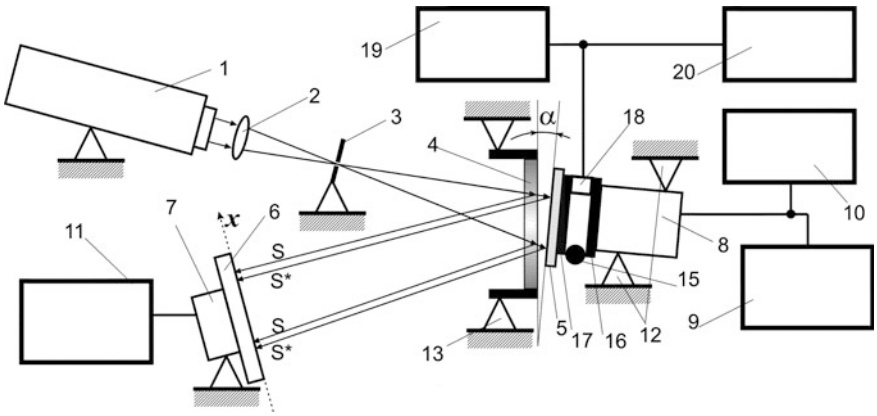

Fig. 49.8 Scheme of setup

elements. The piezoelectric elements 8 and 18 are electrically connected with the voltage sources 9 and 19 and the digital voltmeters 10 and 20, respectively.

The operation principle of the setup was the following.

The laser beam 1 after passage of the focusing lens 2 and the aperture of the spatial filter 3 was converted into a divergent beam. The beam splitter 4 divided the divergent beam into amplitude, one part is reflected from the beam splitter surface (the direction *S*–*S*), and the other is reflected from the surface of the reflector 5 (direction *S**–*S**). In the result of diffraction, maxima of −1 and +1 orders formed on the sinusoidal grating (splitter) in addition to the maximum of 0 order.

Regulators of the fastening device 12, we achieved a spatial alignment of the object beam (direction *S**–*S**) with a reference one (direction *S*–*S*) in the plane of the screen 6, in which the interference pattern is formed in the form of maxima of −1, 0, and +1 orders. The intensity was recorded photo-detector device 7, and the measurement results transmitted for processing in the PC 11.

Figure 49.9 shows a typical image of an typical interference pattern, wherein the designations −1, 0, 1 correspond to the maxima of the interference pattern of −1, 0 and +1 orders, relative position of which depends on the grating period and the distance between beam splitter 4 and screen 6.

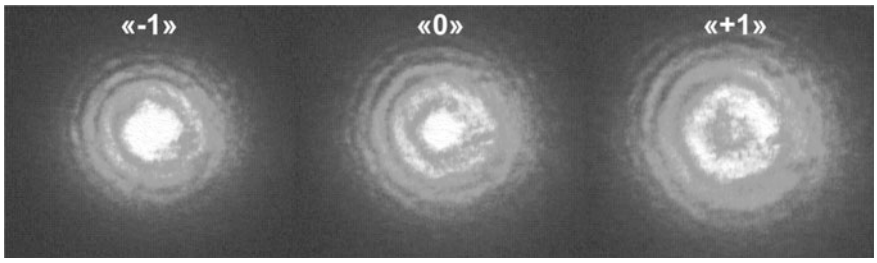

Fig. 49.9 Imagine of typical interference picture

To simulate linear components of small displacements we changed a voltage of the stabilized source 9 on the piezoelectric element 8, which shifted the reflector 5. To simulate the angular component of small displacement, we changed a voltage of the stabilized source 19 on the piezoelectric element 18; in the result, the reflector 5 rotated relatively to the hinge 15. For simultaneous simulation of linear and angular components of small displacements, we changed simultaneously the voltage on the piezoelectric elements 8 and 18. Control of the voltage on piezoelectric elements 8 and 18 was carried out by universal digital voltmeters 10 and 20, respectively.

The methodology of the experiment consisted in step-by-step setting a linear component Δh of the small displacement of the reflector 5 at a fixed angular component $\Delta\alpha$. Registration of the photodetector 7 signal was carried out at each step, and the digital images of the interference pattern at the maxima of −1, 0 and +1 orders transmitted to the device 11 as separate files of standard graphics formats for processing. The developed method of the experiment also provided the experimental simulation of the above example of the numerical solution of (49.1).

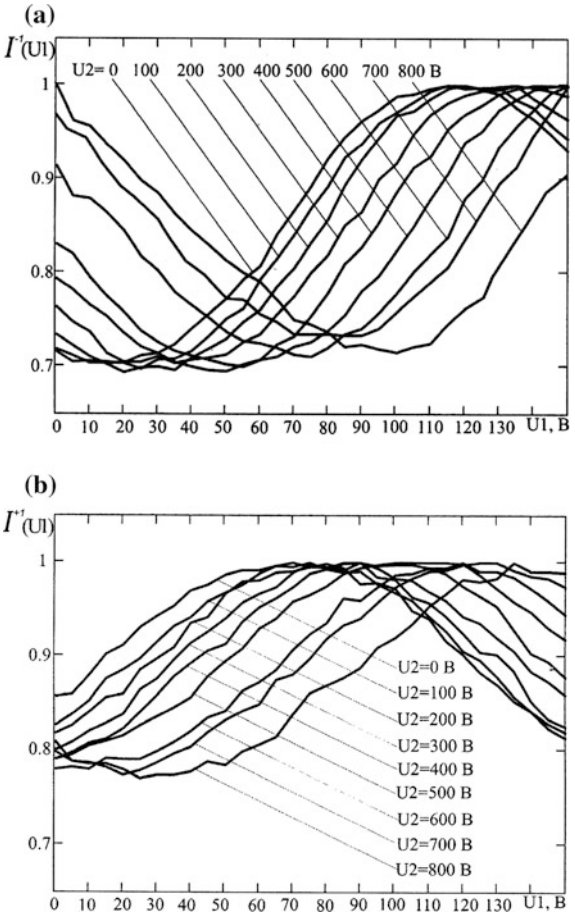

Fig. 49.10 Results of experimental modeling

During the numerical simulation, the main parameters of a mathematical model of the meter were brought into line with the parameters of the experimental setup, which allowed one to compare the results of numerical simulation and experimental study and to confirm the technical feasibility of this measurement method of small displacements.

The results of the measurements (shown in Fig. 49.10) were the dependencies of the intensity I^{-1} and I^{+1} on the linear component Δh of the small displacement of the reflector (presented by the voltage U1 at the piezoelectric transducer 8) for different values of its angular component $\Delta\alpha$ of the small displacement of reflector (presented by the voltage U2 on the piezoelectric transducer 18). These dependencies were registered in the directions Θ_1 and Θ_2, respectively at the maxima of -1 and $+1$ orders of magnitude (Fig. 49.10a, b, respectively).

Figure 49.11 presents dependencies of intensities I^{-1} and I^{+1}, obtained by comparing the results of numerical simulation and experimental study, respectively, at the maxima of -1 (Fig. 49.11a) and $+1$ (Fig. 49.11b) orders (the solid lines show the results of numerical simulation, and the dotted lines present the results of an experimental study). Analysis of these dependencies presented in Fig. 49.11 clearly confirms a technical feasibility of the developed method of the measurement of small displacements.

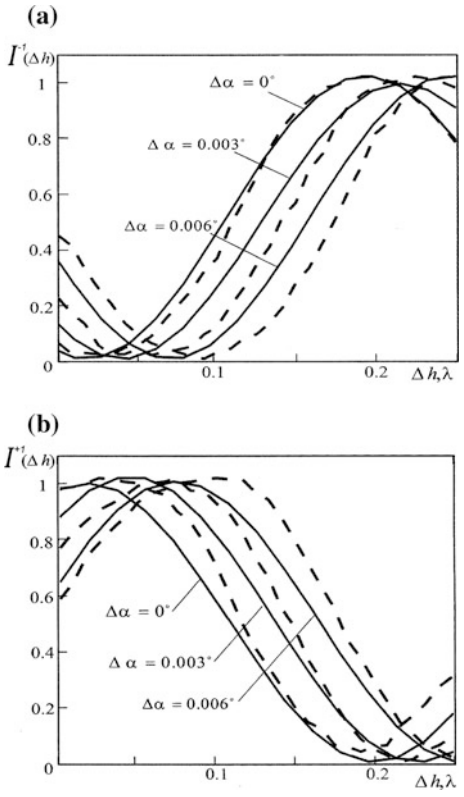

Fig. 49.11 Comparison of numerical and experimental results

49.5 Method for Measuring Linear and Angular Components of Small Displacements of Control Object Surfaces

The results of numerical simulation and experimental study allowed us to develop a new method for contactless measurement of linear and angular components of the small displacements of control object surfaces.

The method consists in that as a beam splitter, a sinusoidal grating is used. Maxima of −1 and +1 orders of the interference pattern are projected on the screen. The photodetectors are divided into two groups and placed in the areas of the maxima of −1 and +1 orders of the interference pattern. The values of the components of small displacements are determined based on the two values of the intensity, measured by using the groups of photodetectors on known dependencies for each of the maxima. The dependencies connect the intensity with the linear and angular displacements. As a result, we obtain the values of the linear and angular components of displacement simultaneously satisfying the values of the measured intensity at the maxima −1 and +1 orders.

The significant difference of the developed method compared to the conventional counterpart is to permit simultaneous contactless registration of the linear and angular components of small displacements of the control object surface by using a single optical meter of displacements. It can significantly extend its functional possibilities and the quality of the measurement results. This technical solution has been protected by Russian patent for invention [15].

49.6 Method for Measuring Linear and Angular Components of Small Displacements of Control Object Surfaces and Device for Its Realization

The above method has the shortcoming, consisting in the impossibility of the simultaneous measurement of linear and angular components of the small displacements of control object surface. In practice, by testing the real objects of control, arising displacements of their surfaces as rule have linear and angular components. So the impossibility of simultaneous recording both linear and angular components significantly reduces the information content of measurement results, requires installation of additional devices for recording the angular component of the arising displacements, complicating construction of the measuring device, etc. For this reason, the above-described method can be applied to the measurement of linear and only one angular component of small displacements provided, that the effect of the other angular component can be neglected. Thus, this fact greatly limits the functionality of the method and area of its application.

The linear and all angular components of the small displacement of control object surface can be determined based on the intensity values, measured by groups of photodetectors at maxima of −1, 0 and +1 orders. These parameters are defined by using the known for each of the maxima intensity dependencies on the linear and angular components of the small displacements of the control object surface. In this case, the measurement result is the value of the linear and angular components of the displacement, which simultaneously satisfies the measured intensity values at the maxima of −1, 0 and +1 orders of the interference pattern.

The scheme of one of the possible variants of the device that implements the proposed method is shown in Fig. 49.12, but Fig. 49.13 shows the appearance of the interference pattern in the screen area.

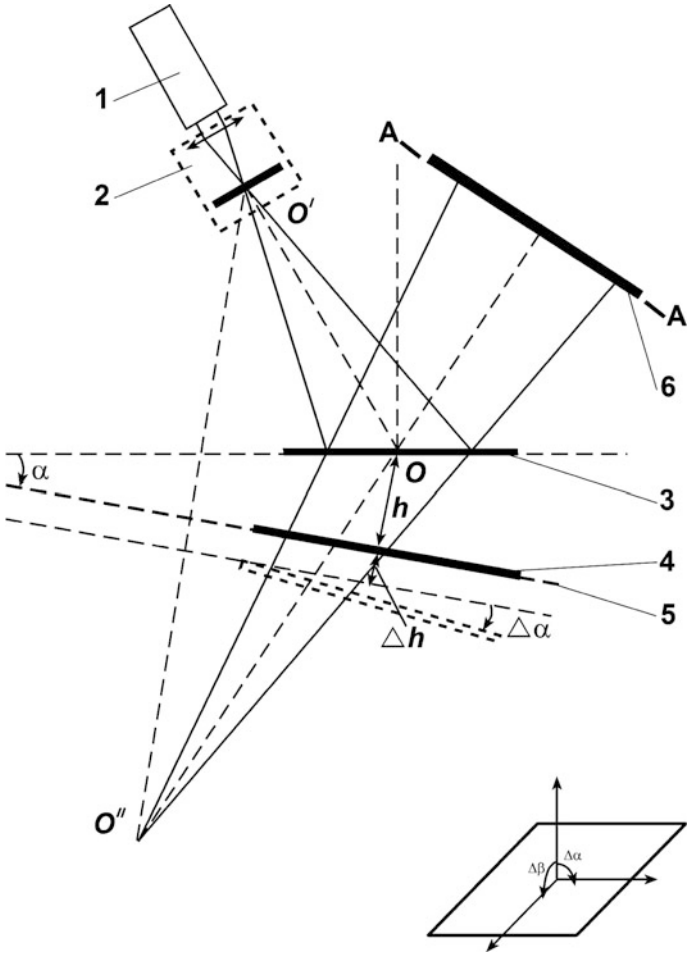

Fig. 49.12 Scheme of one of the possible variants of the device, implementing the proposed method

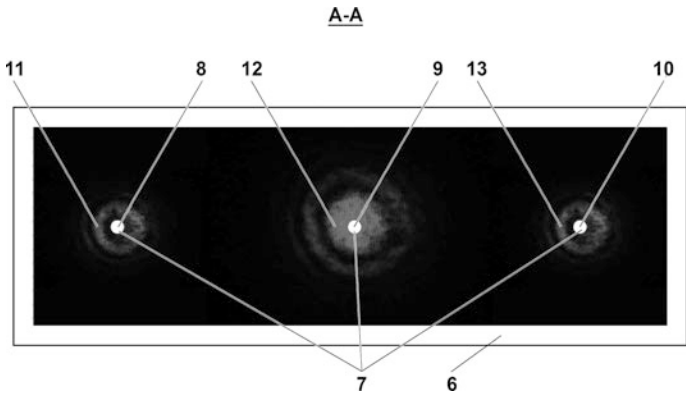

Fig. 49.13 Appearance of the interference pattern in the screen area

This device includes a source 1 of coherent optical radiation (laser); an optical system 2, which converts the radiation of the source 1 in the divergent beam; a beam splitter 3, performed in the form of a phase grating; a reflector 4 rigidly mounted on the surface 5 of the object of control; a screen 6, in which the plane, photodetectors 7 (e.g., photodiodes, etc.) are arranged with a possibility to adjust their positions. They are divided into three groups 8, 9 and 10, each of which is located in the respective areas of the maxima of −1 order 11, 0 order 12 and +1 order 13 of interference picture 14. The photodetector devices 7 are electrically connected to the system of registration, processing and displaying measurement results.

The reflector 4 is located on a distance h from the inner surface of the beam splitter 3. Reflector beam splitters 3 and 4 are arranged to each other under an angle α. It can be also a possibility, in which the reflector 4 is absent, but its function in this case is directly performed by itself reflecting surface 5 of the control object. Maxima of −1 order 11, 0 order 12 and +1 order 13 of interference picture 14 are projected onto the screen 6.

This device operates as follows. During testing, by arising the linear Δh and (or) angular $\Delta\alpha$ and $\Delta\beta$ components of the displacement of the control object surface 5, a change of the optical field intensity occurs at the maxima of −1 order 11, 0 order 12 and +1 order 13 of the interference picture 14, including corresponding areas of the location of the pointed groups 8, 9 and 10 of the photodetectors 7.

The photodetectors 7 record the intensity of optical field, and the measurement results are the intensities, obtained from each of the groups 8, 9 and 10 of the photodetectors 7. The system of registration, processing and displaying measurement results ensures registration values of intensity from each of the groups 8, 9 and 10 of the photodetectors 7 and performs their processing.

Possible option for processing is, for example, the solution of the set of equations:

$$\begin{cases} I^{-1} = f_1(\Delta h, \Delta\alpha, \Delta\beta); \\ I^{0} = f_2(\Delta h, \Delta\alpha, \Delta\beta); \\ I^{+1} = f_3(\Delta h, \Delta\alpha, \Delta\beta); \end{cases} \tag{49.2}$$

where $f_1(\Delta h, \Delta\alpha, \Delta\beta), f_2(\Delta h, \Delta\alpha, \Delta\beta), f_3(\Delta h, \Delta\alpha, \Delta\beta)$, are the known dependencies, respectively, for the maxima of −1 order 11, 0 order 12 and +1 order 13, linking intensities, respectively, with the linear Δh and angular $\Delta\alpha$ and $\Delta\beta$ components of the displacement of the control object surface 5; I^{-1}, I^{0} and I^{+1} are the values of intensity measured by each of the groups 8, 9 and 10 of the photodetectors 7, located in the relevant areas of the maxima of −1 order 11, 0 order 12 and +1 order 13 of the interference picture 14.

The result of processing are the values of linear Δh and angular $\Delta\alpha$ and $\Delta\beta$ components of the displacements of the control object surface 5, simultaneously satisfying the values of intensity I^{-1}, I^{0} and I^{+1}. The described technical solution has been also protected by Russian patent for invention.

49.7 Conclusions

1. We developed new mathematical models and software for numerical modeling of the fields of optical radiation intensity in the interference patterns generated by an optical meter of small displacements, based on the two-way laser interferometer with combined branches, taking into account both linear and angular components of a small displacement of control object surface.
2. We developed and scientifically grounded new interference method for measuring small linear and angular displacements, which allows one to combine in a single measuring device possibility of measuring both small as linear, as angular displacements of control object surfaces.
3. Application of the developed method of measuring small linear and angular displacements allows us to expand the scope of the laser interferometers to create on their basis of promising diagnostic means of technical condition of materials and goods.
4. We proposed new optical interference methods and means for contactless measurement of small linear and angular displacements of control object surfaces that implement the capabilities of the method, presented above in point 2 and extend the functionality of the known meters of small displacements.
5. Use of these results is the most useful at high-precision contactless measurements of small linear and angular displacements, in experimental studies of advanced materials and constructions, evaluation of their technical conditions

and diagnostics, the study of wave processes in layered structures and structures performed from anisotropic construction materials, the study of damage formation in high-temperature superconductive tapes in mechanical engineering, shipbuilding, aviation, energetic, etc.

Acknowledgements This work was partially supported by a grant of the Russian Foundation for Basic Research No. 16-08-00740.

References

1. I.P. Miroshnichenko, A.G. Serkin, Meas. Tech. **49**(5), 22 (2006)
2. I.P. Miroshnichenko, I.A. Parinov, E.V. Rozhkov, A.G. Serkin, Metallurgist **50**(7–8), 408 (2006)
3. V.E. Alekhin, I.P. Miroshnichenko, V.P. Sizov, Russ. J. Nondestr. Test. **43**(2), 113 (2007)
4. I.P. Miroshnichenko, A.G. Serkin, Russ. J. Nondestr. Test. **43**(4), 234 (2007)
5. V.E. Alekhin, I.P. Miroshnichenko, V.A. Nesterov, V.P. Sizov, Russ. J. Nondestr. Test. **43** (9), 592 (2007)
6. V.E. Alekhin, I.P. Miroshnichenko, A.G. Serkin, Meas. Tech. **51**(10), 26 (2008)
7. I.P. Miroshnichenko, A.G. Serkin, Metallurgist **54**(3–4), 189 (2010)
8. I.P. Miroshnichenko, I.A. Parinov, E.V. Rozhkov, A.G. Serkin, V.P. Sizov, in *Piezoelectrics and Related Materials: Investigations and Applications*, ed. by I.A. Parinov (Nova Science Publishers, New York, 2012), p. 238
9. I.P. Miroshnichenko, I.A. Parinov, E.V. Rozhkov, V.P. Sizov, V.A. Shevtsov, in *Physics and Mechanics of New Materials and their Applications*, ed. by I.A. Parinov, S.-H. Chang (Nova Science Publishers, New York, 2013), p. 145
10. I.P. Miroshnichenko, I.A. Parinov, S.-H. Chang, in *Advanced Materials—Studies and Applications*, ed. by I.A. Parinov, S.-H. Chang, S. Theerakulpisut (Nova Science Publisher, New York, 2015), p. 437
11. I.P. Miroshnichenko, I.A. Parinov, E.V. Rozhkov, S.-H. Chang, in *Advanced Materials Manufacturing, Physics, Mechanics and Applications*, vol. 175 (Springer Proceedings in Physics, Springer Cham, Heidelberg New York Dordrecht London, 2016), p. 341
12. I.P. Miroshnichenko, A.G. Serkin, V.P. Sizov, Meas. Tech. **50**(1), 9 (2007)
13. I.P. Miroshnichenko, A.G. Serkin, Russ. J. Nondestr. Test. **44**(5), 318 (2008)
14. I.P. Miroshnichenko, A.G. Serkin, V.P. Sizov, J. Opt. Technol. **75**(7), 437 (2008)
15. I.P. Miroshnichenko, A.G. Serkin, V.P. Sizov, *Method of Measurement of the Linear and Angle Displacements*. Russian Patent No. 2388994, 5 Oct 2010 (In Russian)

Chapter 50
Pump Control System Using Microcontroller and Short Message Service (SMS) Gateway for Flood Prevention

Ahmad Habib, Agus Darwanto, Elsen Ronando and Slamet

Abstract It is important to detect a water level of a river in order to control a safe level or circumstances that could cause a danger of flooding. In our experiment, we use four-level detection and send a sign to the operator to envy the message of the conditions that occur in real time. The method used utilizes the voltage of 5 V to trigger microcontroller and send a message to the server for each operator. Microcontroller will manage and process the input of the water level detection sensor, in addition to the process data sent to the server computer, other data used trigger ignition process pumps. Computer server processes the input data, obtained from the microcontroller in the form that is more flexible for graphics and allows monitoring and controlling the level of water in a river.

50.1 Introduction

Nowadays, the rapid development of information technology should lead to benefit for human life, such as to enable people to work more quickly and efficiently. Computers do not only use to run software or perform routine homework as old days. The new developments and innovations in terms of functionality have been widely elaborated by computers, either software or hardware. Thus, computers have largely recovered human role in daily activities.

In the development of electronic technologies also are emerging new advanced tools that were created by various beings in the world from trivial to useful tools. In fact, robots will replace human roles for helping life activities. It was the impact of new electronic technology or industrial automation, which a requirement in accordance with reliability, security, and efficiency of production process. Participation in industrial automation technology is not only human tools for production, it can

A. Habib (✉) · A. Darwanto · E. Ronando · Slamet
Department of Informatics Engineering, Faculty of Engineering,
University of 17 Agustus 1945 Semolowaru, Surabaya 60119, Indonesia
e-mail: habib@untag-sby.ac.id

I.A. Parinov et al. (eds.), *Advanced Materials*, Springer Proceedings
in Physics 193, DOI 10.1007/978-3-319-56062-5_50

yet alleviate human at a good quality and precision of production. For example, water removal process (water distribution) using a microcontroller controls, which extenuate human performance for controlling water pump. In this case, water pump will transfer or suck water from a river into a large river by using sensors mounted on the river.

In the large scale, the water removal process may not be done manually by humans. Therefore, it needs an automatic system for the controlling. This process is performed to prevent low-lying areas and flood prone not suffered a flood disaster. In other words, pump will automatically turn on and transfer or suck water into a large river that can accommodate water from flood prone areas. During above process, it is still done manually, which still involves a prediction. In addition, pump generator also still works manually as indicated by manual switch in high limit water. The new era now is not capable with manual controls as mentioned before, thus a new systems based on automation must be developed.

Based on the problem, we propose a pump control system using microcontroller and short message service (SMS) gateway for flood prevention. Our approach builds a pump control system based on AT89S52 microcontroller as control system and short message service (SMS) gateway as reporting system for flood prevention.

The literature review is present in the Sect. 50.2. For more details about design and instrument tools, it is explained in the Sect. 50.3. Section 50.4 describes the results and discussion of our approach. The rest of our paper in the Sect. 50.5 represents conclusions of our approach and future directions.

50.2 Literature Review

Microcontroller is a chip that can be used to control a system either in simple or complex way. Microcontroller has an input or output directly, processing bits, and a relatively simple computer software that relates directly to the input or output. In its application, the system has its own characteristics, such as a special computer software that is stored in memory for specific applications, consumes less power and cost, a circuit with simple and compact of its input or output unit. The chip in here also is simple and good for beginners or professionals in the field of electronics, thus facilitating an easy programming.

AT89S52 was the development of a microcontroller from previous versions of 8051 type, which had standard pin and assembler instructions by Atmek Corporation. The microcontroller was built by CMOS technology and volatile memory of Atmek with 8 KB internal memory program based on In-system programmable (ISP) flash memory. Figure 50.1 illustrates the architecture and PIN configuration of AT89S52 [1].

Wavecom modem is a French manufacturer or commonly called as Wavecom SA that was head quartered since 1993 in the city of Issy Les Mouline, France. The company was initially established as a technologic consulting firm and the network system of GSM. In 1996, Wavecom first started to create a design of

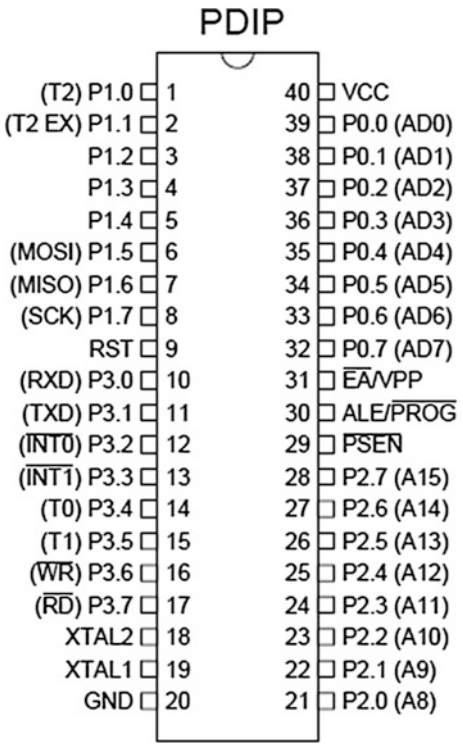

Fig. 50.1 Architecture and PIN configuration of AT89S52

module wireless GSM and special coding that was termed as AT-Command in 1997. Meanwhile, Wavecom fast rack modem was well-known in Indonesia on a cottage and large scale industry. From the benefit of short message services (SMS) and device driver of electronics, modem Wavecom was ran well in quick SMS by using quick gateway with 2–4 s for each SMS.

The advantages of using wavecom fast rack modem instead of GSM modem or hand-phone are the following:

(i) Wavecom is more stable than GSM modem or hand-phone;
(ii) Wavecom is easier to heat than GSM modem or hand-phone;
(iii) Sending short message services is faster;
(iv) AT-Command supported, it is easy to check the remaining balance, point check, and last user checks;
(v) It is more practical without batteries.

The benefits of USB types:

(i) More useful and easy to use with driver installation;
(ii) Wavecom USB modem can be installed with USB ports available in computers;
(iii) USB types in modem are faster than serial types.

The main shortcoming of the USB types consists in that the USB Wavecom modem is not stable because this type uses and receipts power from computers, so that it needs a more workable performance.

LCD was a device that can show the results (output) of microcontroller. LCD was also understood as an interaction tool between humans and microcontroller with low power. There were many types of LCD, namely M1632 type, which had two rows with 16 characters for each row. S6A0069 chip as LCD controller has CGPROM (Character Generator Read Only Memory), CGRAM (Character Generator Random Access Memory), and DDRAM (Display Data Random Access Memory). Here CGRAM is a memory to define the pattern of characters, which the characters can be modified. However, it has a drawback, such as memory access was not connected, when supply power is inactive, which it causes losing the patterns. LCD driver on S6A0069 has two registration scheme with access rules based on RS pin. Register called a command with O (low) logic in RS and registered data with 1 (high) logic in RS, respectively.

Relay is a switch operated electrically with electromechanical components as follows by electromagnetically (coil) and mechanically (switch tool). Generally electromagnetic relay is used to change switch thus the electric current is small (low power) that can conduct electricity with a higher voltage. For example, relay with 5 V electromagnetic and 50 mA can be adapted to mobilize Armature Relay as switch for transmitting electricity with 220 V—2 A parameters.

The general functions of relay, widely used in electronic equipment:

(i) To run logic functions;
(ii) To provide time delay functions;
(iii) To control high voltage circuit with support of low voltage signals;
(iv) To protect motor or other components from excess voltage or short circuit.

Transformer in the electronics plays an important role. Overall, the function of transformer is accustomed to distribute electrical energy from low to high voltage. This step take places with the same frequency. The function globally is known as step-up and step-down. Furthermore, the most important function of transformer is as communication systems.

Firstly, the function of transformer raises the electrical voltage. Step-up transformer has more secondary winding than primary winding so that transformer has more clear function as voltage booster. For example, the effect of black out in the television or computer electronics is as transformer runs.

To connect the serial type of Wavecom modem with microcontroller can use RS232 standard serial communication. To associate RS232 standard serial communication, it is required IC Max 232 as driver, which converts the voltage or TTL logic from hardware based on voltage on the computer or microcontroller or vice versa [2].

Serial communication between Wavecom modem and IC Max232 uses DB15 and DB9 connector, which modem, related with DB15 and IC Max232, is

Table 50.1 The connections between DB9 and IC Max232

Connections		Descriptions
DB9 Male	IC Max232	
Leg 3 (TD)	Pin 13 (R1 IN)	Output data from the microcontroller via IC Max232 being input for DB9
Leg 2 (RD)	Pin 14 (T1 Out)	Output data from modem via DB9 being input for IC Max232

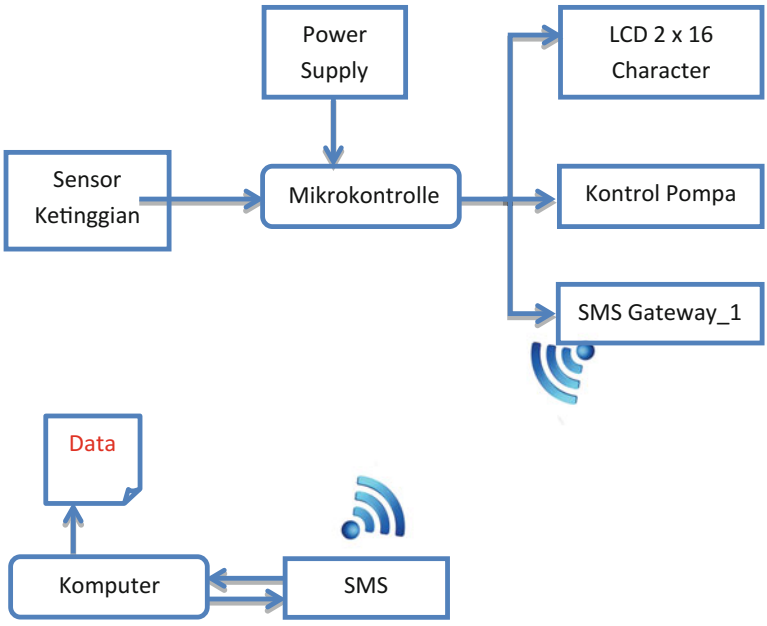

Fig. 50.2 Diagram of pump control system

associated with DB9. For more details, Table 50.1 illustrates the connection of DB9 and IC Max232.

50.3 Design and Instrument Tools

Diagram of the pump control system can be realized in Fig. 50.2. Based on the figure, the diagram defines the scheme of hardware and information systems with data flow. Thus, data can be processed and presented in graphical form. The design of hardware is aimed to scheme and builds the systems, thus the design aids to implement the real application.

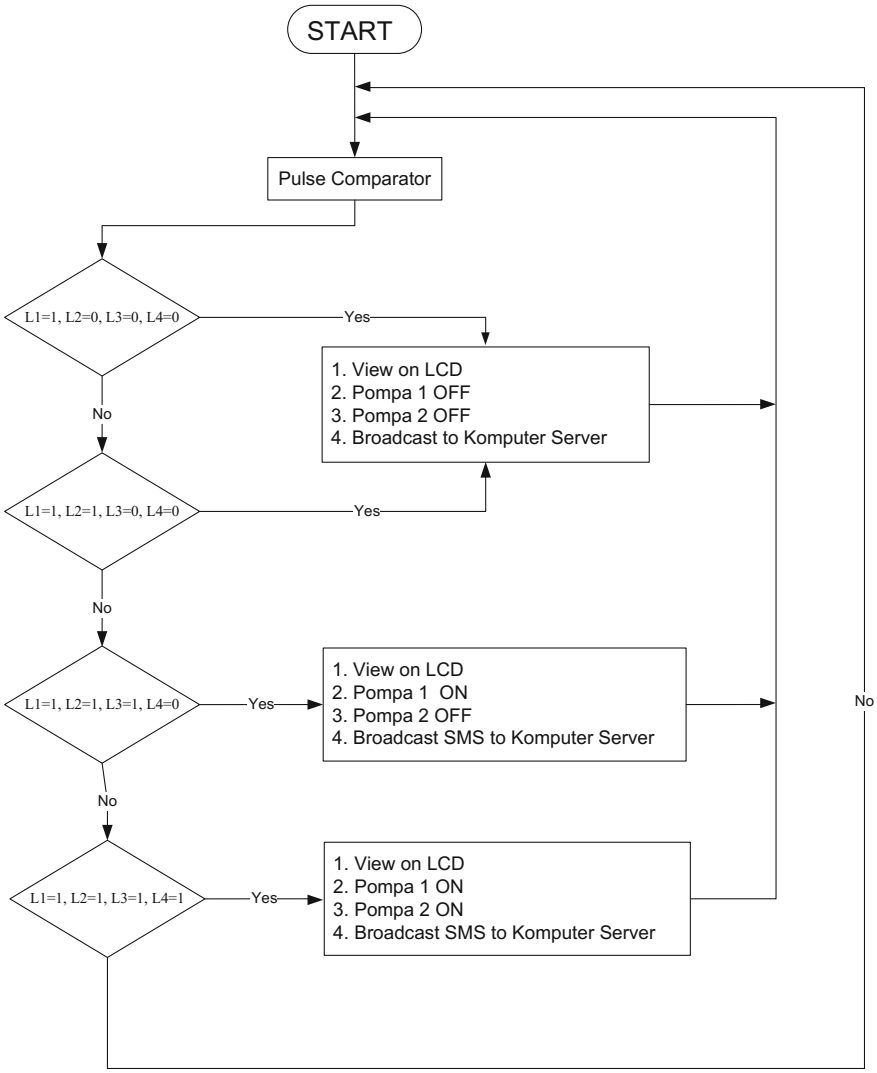

Fig. 50.3 Flowcharts of pump control system

For more details the flowchart of pump control system can be shown in Fig. 50.3, either in hardware or microcontroller sides. In this figure, all inputs exist only from the water level sensor without other input. Then the water level sensor is displayed into LCD, meanwhile a short message service is executed when the water levels are above 0 or 1 level and the execution did not deliver directly to operators but it was sent to the server computer. Further the pump turned on, when the water levels were about 3 level.

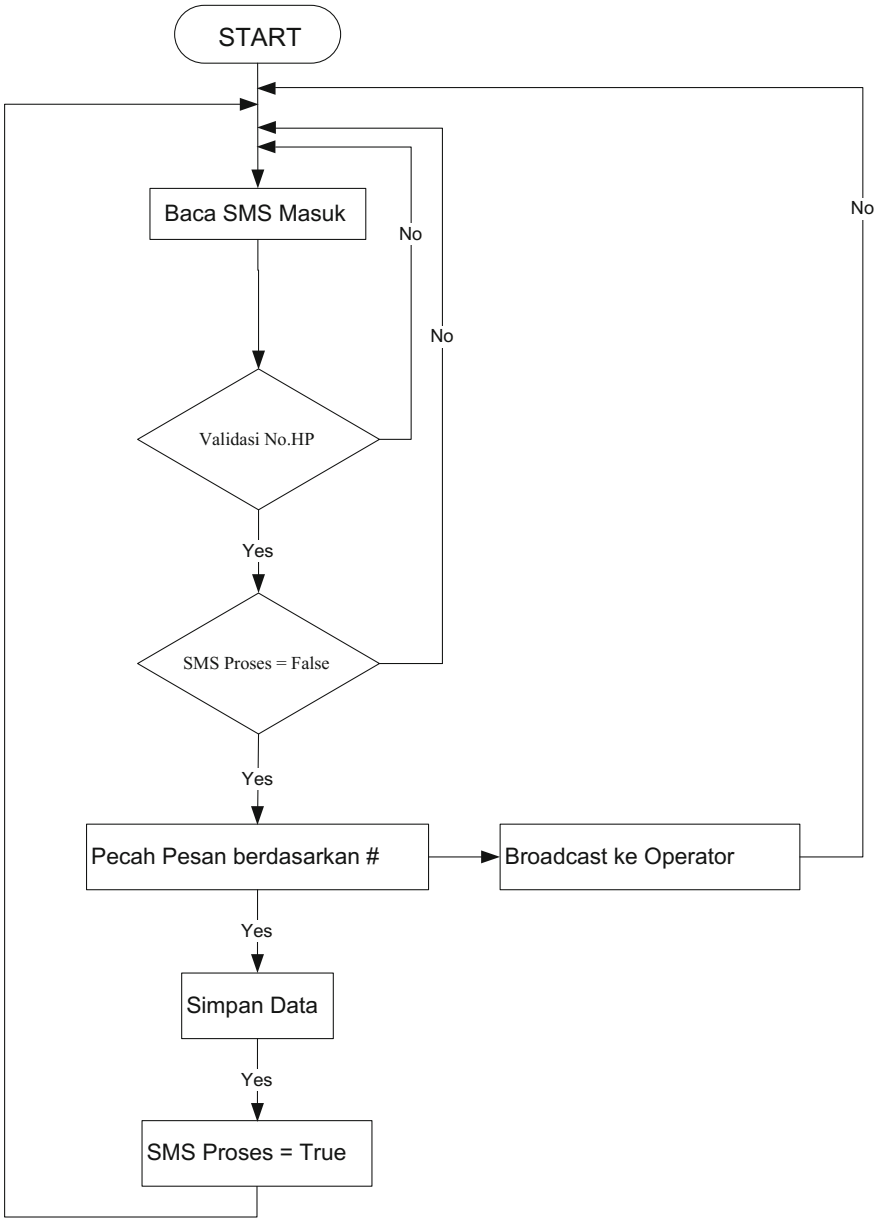

Fig. 50.4 Flowchart of sending SMS broadcast

The flowchart of sending SMS broadcast to operators is shown in Fig. 50.4. The auto-refresh information system was also constructed in Fig. 50.4.

The water sensor circuit mainly is aimed to trigger the circuits. These circuit is also a input of microcontroller as it illustrates in Fig. 50.5.

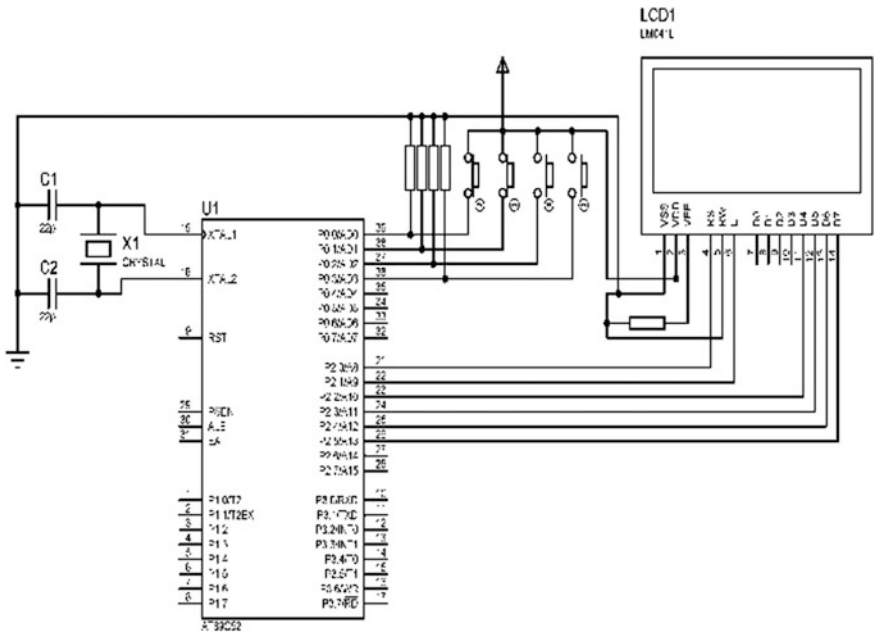

Fig. 50.5 Water sensor circuit

(i) 1 Level

The first scenario organizes a water level monitoring from first sensor for the water level at low level (the water level of 1 m from the riverbed).

(ii) 2 Level

The second level in here manages a water level monitoring from second sensor for the water sensor at middle level (the water level of 2 m from the riverbed or 1 m is higher than 1 Level).

(iii) 3 Level

The third level describes a water level monitoring from third sensor in danger level (the water level of 3 m from the riverbed or 1 m is higher than 2 Level).

(iv) 4 Level

The fourth level defines a water level monitoring from fourth sensor in critical level of floods (the water level of 4 m from the riverbed or 1 m is higher than 3 Level).

For actual sensor to detect altering water level, it is shown in Fig. 50.6.

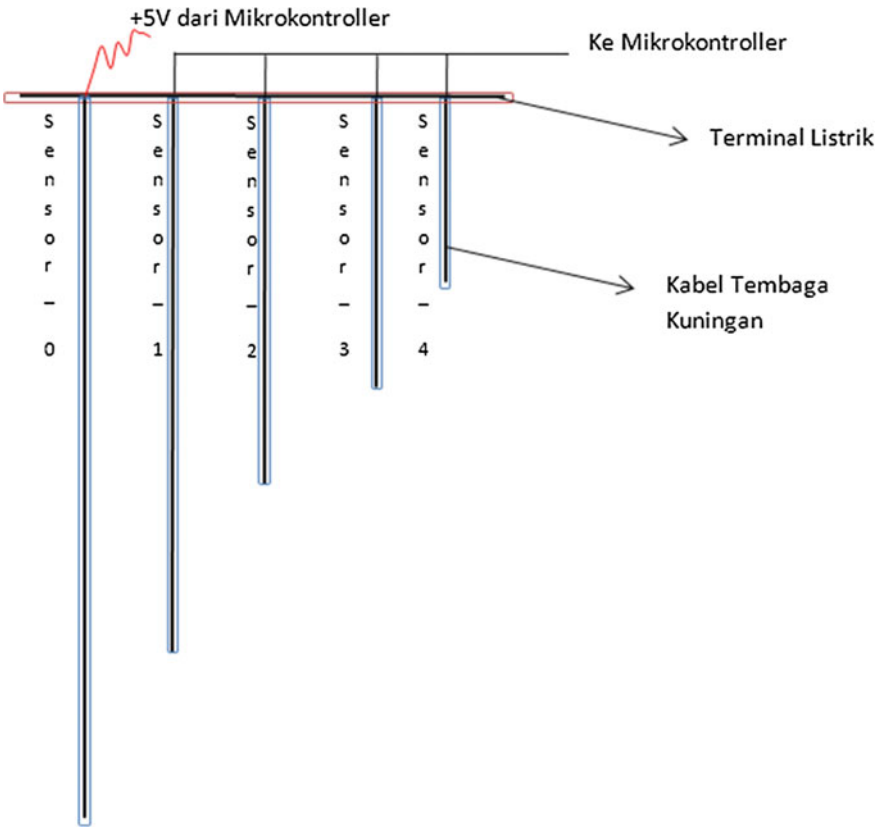

Fig. 50.6 Actual sensor of altering water level

Here water pump was controlled automatically by reviewing of triger water sensor above. The schedulling of water pump was not managed manually but automatically with the circuit of water pump as shown in Fig. 50.7, where the circuit is connected in such a way with a microcontroller.

For sending messages from modem in existing microcontroller side to modem in computer server and broadcast to all operators, it used own format. All messages were protected into databases and can be called based on requirements. The format of message is as describes in Fig. 50.8, for example: **#RP1#1#OFF#OFF** [3].

Here, computer server is a computer connected to SMS gateway modem (Wavecom serial). Computer stored data from input by obtaining from SMS gateway modem, which this modem recited data that was sent by SMS gateway modem connected with microcontroller. The main message of sending data was about fluctuating water level occurring with time. Then Input data from computer server was entered into MySQL databases and treated a report level in management system [4]. Figure 50.9 shows the input format of computer server.

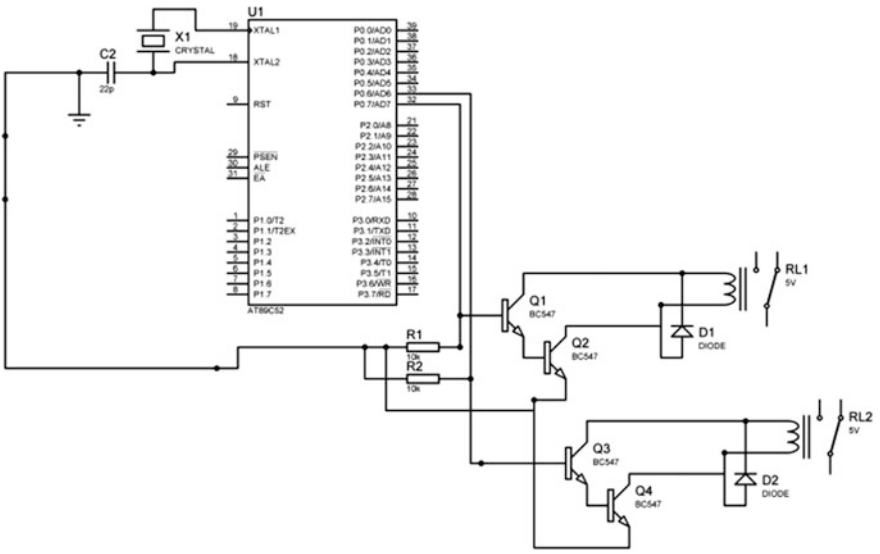

Fig. 50.7 Automated water pump circuit

Fig. 50.8 Format of messages. **Descriptions:** RPn —Pump's name [n: jagir, prapen, etc.]. X—water levels [1, 2, 3, 4]. Y—pump 1 [ON or OFF]. Z—pump 2 [ON or OFF]

#RPn#X#Y#Z

Fig. 50.9 Input format of computer server

Pump's name: [RP1]
Levels: [1, 2, 3, 4]
Pump 1: [ON or OFF]
Pump 2: [ON or OFF]
Time: [DateTime]

Information system is designed to facilitate the operator in general and particular. Information system also generated data with dynamic properties and text form; then graphical form was illustrated in this system, which aimed to transfer people of water pump data effectively and easily.

Several menu and sub-menu in this information system are as follows: in main menu, at the upper side of header, a logo about pump control was placed. In menu and sub-menu, it was located on the bottom of header. Another menu generally was positioned at the left side of website page. Meanwhile the main content was dynamically situated in the middle of display, where data is improved based on the

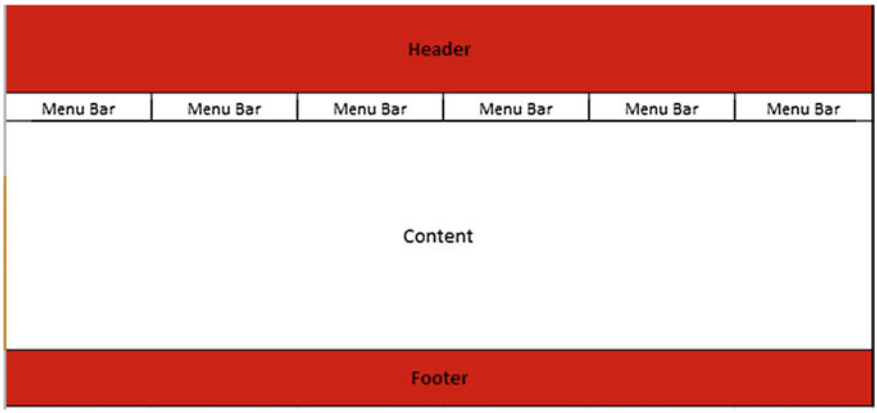

Fig. 50.10 Design of main menu

Fig. 50.11 Design of selecting time

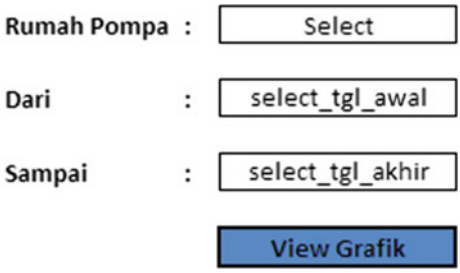

Fig. 50.12 Design of graphical results based on pump's name

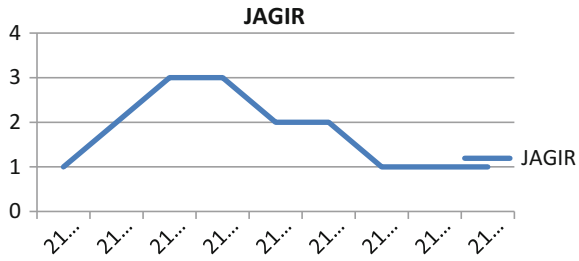

content. Footer also illustrated on the bottom of content. The design of main menu was presented in Figs. 50.10 and 50.11.

This page of the data changes of water level was based on graphical form; thus, user can simply see data required. In addition, user also can select date range of data requisite. For relating data of graphical transformation, it should be determined date range required and pump's name is required as represented in Figs. 50.10, 50.11 and 50.12.

Table entities from a database on the system are composed by *tb_rumah_pompa*, *tb_master_pompa*, *tb_level*, and *tb_pbk*. Table entities are related to one another as figured in Fig. 50.13.

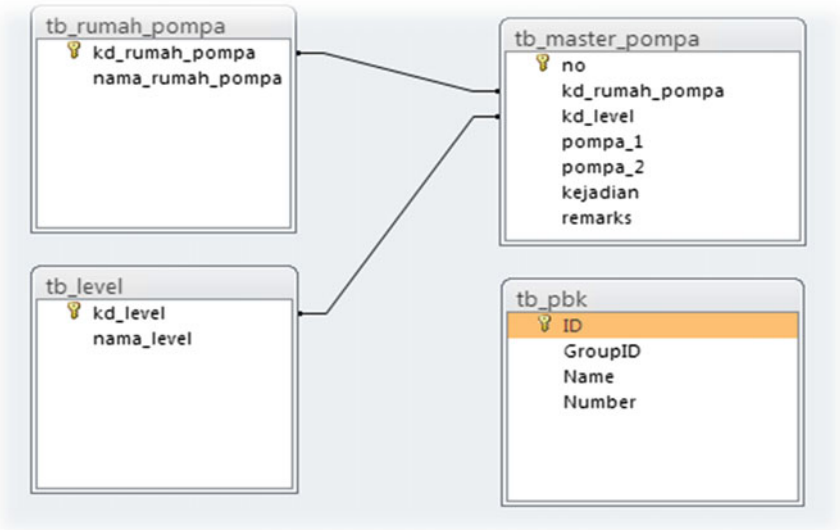

Fig. 50.13 Diagram of entity relation table

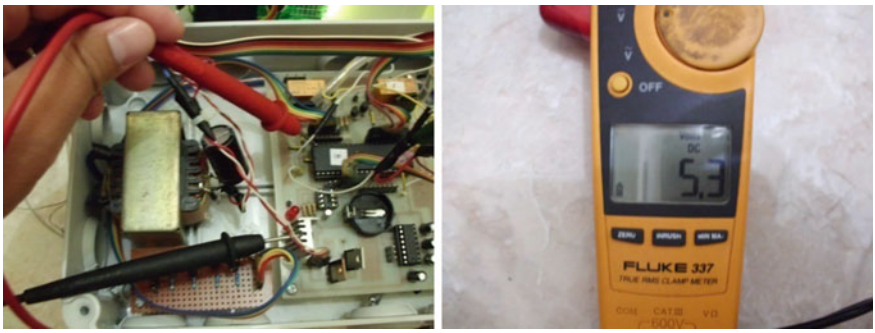

Fig. 50.14 Process of measurement of voltage circuit

50.4 Results and Discussions

Testing power supply is very important role because it is the source voltage that is supplied into electronics circuit. Results of power supply circuit obtained 16 VDC output power from 220 VAC input, from 16 VDC output was lowered again with LM7805 IC regulator until +/− 5 VDC and was delivered into electricity tools with +/− 5 VDC power. Measurement process of this scenario is present in Fig. 50.14.

If input power into microcontroller circuit exceeds a limit specified or power is greater than IC, microcontroller will be damaged. Therefore, the initial testing of

Table 50.2 Results of testing water sensor

No.	Water level	LCD display	Relay 1	Relay 2
1	0	Level 0	OFF	OFF
2	1	Level 1	OFF	OFF
3	2	Level 2	OFF	OFF
4	3	Level 3	ON	OFF
5	4	Level 4	ON	ON

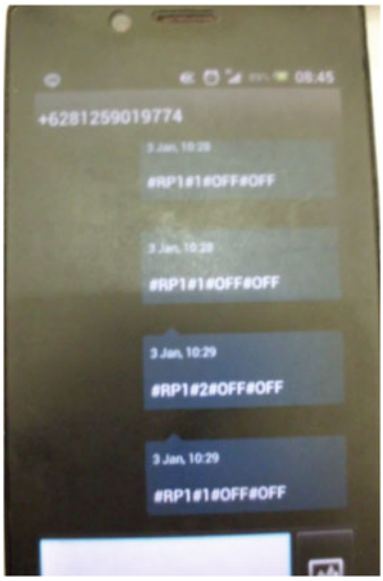

Fig. 50.15 Result of SMS gateway

power supply is an important. In addition to input power into circuit, based on limit range, power stability should be considered because it affects the results of circuit.

In testing phase of water level performance, a simple medium was tested by using small medium container with a capacity of about 10-l water and a sensor was inserted into the container. For pump, we propose a pump simulation with small suction power, namely aquarium pump (120-liter per hour). The simulation integrated two pumps: first pump was used to water level of 3 Level and second pump was used to water level of 4 Level. The results of our observations are shown in Table 50.2.

Testing the performance of SMS gateway is illustrated in Fig. 50.15. Based on this figure, it can be shown that results of data processing and data broadcasting correspond to our approach. This message in here was very important and useful to support information transfer for operators in pump's house.

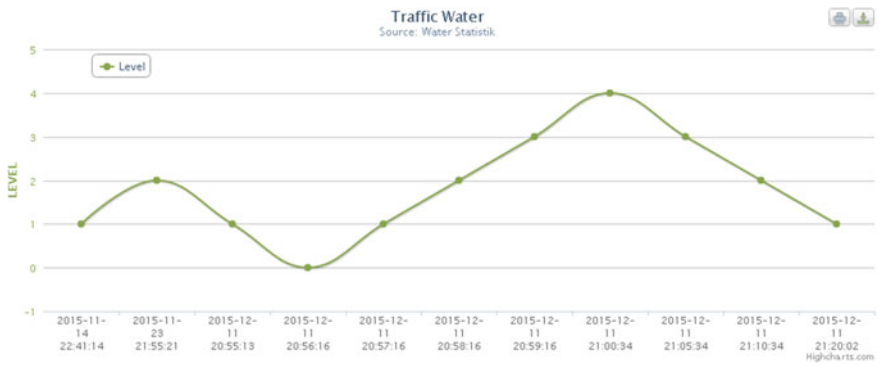

Fig. 50.16 Result plot

Based on the results, the main focus of our results was directed to obtaining data in the graphical form described in Fig. 50.16. Details of results can be seen easily and interactively thus accelerating time in making decision.

50.5 Conclusion and Future Directions

50.5.1 Conclusion

Based on our evaluation and analyses in the system, we conclude our results as follows:

1. Our approach can design flood control by using homemade sensor with copper brass, AT89S52 microcontroller, and M130B fast tract Wavecom modem (USB and serial).
2. In serial communication, baud rate modem initially is performed on AT89S52 microcontroller (depends on microcontroller) and RS232 serial. Both of these must be the same initialization, if it is not relating then the performance is not achieved. Here baud rate system used 9600 bps.
3. For the circuit that is connected to modem must have cross connection (TX modem is integrated with RX IC Max 232 and *vice versa*).
4. For water level sensor, it must be developed with converter power circuit, thus +/− 5 V indirect met—negative micro and is not directly connected on leg micro. If it was occurred, then it was happened water oxidation. Thus, it needs a voltage converter circuit using 547 and 10 K resistors.
5. For the performance of SMS transmission between modems, it depends on the provider because speed processing of provider in SMS-services also provides a major influence.

50.5.2 Future Directions

In the pump control system, we have many shortcomings. Therefore, future directions for developing our approach are required. Because it is nowadays no extended GSM signal, we will improve our approach using 3G or 4G signals. In addition, we will also apply our approach in remote areas by using Internet facilities. Renewable electrical energy to integrate and support with our approach will be established in the future.

References

1. B. Viranha, *Interfacing Komunikasi Serial PC dengan AT89S52* (2008). http://vinsenbrilyan.blogspot.co.id/2012/06/komunikasi-serial-usb-rs232-db9-pada.html/
2. P. Liga, *Pilih Mana Wavecom Serial Atau Usb* (2012). https://ligapribadi.wordpress.com/2012/10/30/pilih-mana-modem-wavecom-usb-atau-modem-wavecom-serial/
3. Beckoy, *Pemograman LCD Karakter (2 × 16) Menggunakan CV AVR* (2012). https://bekoy.wordpress.com/2012/02/15/pemrograman-lcd-karakter-2x16-menggunakan-cv-avr/
4. S. Agung, *Membangun Aplikasi SMS dengan PHP dan MYSQL* (Elex Media Komputindo, Jakarta, 2013)
5. R. Jimmy, *IC Max 232* (2010). https://jimmyrahdiansyah.wordpress.com/2010/10/05/ic-max232/
6. K. Abdul, *Buku Pertama Belajar Pemograman Java Untuk Pemula* (Mediakom, Surabaya, 2014)
7. N. Sidik, *Aplikasi dan Teknik Pemograman Mikrokontroller AVR Atmel* (Andi Publisher, Surabaya, 2012)
8. Onelka. *Mikrokontrollet AT89S52* (2010). https://onelka.wordpress.com/mikrokontroler-at89s52/
9. R. Syahban, *Mikrokontroller ATMEL AVR* (Informatika, Surabaya, 2011)

Index

I.A. Parinov et al. (eds.), *Advanced Materials*, Springer Proceedings in Physics 193, DOI 10.1007/978-3-319-56062-5